UNIVERSITY OF MALTA

DOCTOR OF PHILOSOPHY IN ENGINEERING DISSERTATION

_____

INCYLINDER HEAT TRANSFER AND FRICTION ANALYSIS IN PRESSURISED MOTORED COMPRESSION IGNITION ENGINE

_____

CARL CARUANA

Supervised by:

PROF. MARIO FARRUGIA

A dissertation submitted in fulfilment of the requirements for the award of Doctor of Philosophy in Engineering

by the

Faculty of Engineering

November 2020

Copyright Notice

Lill-għeżież tiegħi

ABSTRACT

An experimental study was performed to investigate the total mechanical friction and in-cylinder heat transfer from a pressurised motored engine. The mechanical friction study was done on a four cylinder engine, whereas heat transfer experiments were conducted on a single cylinder version of the same engine model as the four cylinder, converted in the same project.

The pressurised motored setup was modified from its conventional configuration to allow the engine to be run on gases other than air. Argon and its mixtures with air were used as the working gas. This method made it possible to test the motored engine at peak bulk gas temperatures up to 1200℃, around 600℃ higher than what is expected from conventional motoring using air. An investigation of several engine metrics in relation to the working gas was carried out. It was found that the location of peak in-cylinder pressure and location of peak bulk gas temperature are advanced from TDC by a magnitude that is directly proportional to the peak bulk gas temperature. The summation of the losses of heat and blow-by were found to show a linear increase with an increase in the peak bulk gas temperature, whereas the losses associated with the pumping of the gas showed a decrease with using gases of higher ratios of specific heats. The mechanical friction of the pressurised motored engine was found to be insensitive to the bulk gas temperature, and its effect on the combustion chamber surface temperature. It was hypothesised that this result is probably due to the gas pressure phasing with crank angle of the pressurised motored engine, which exhibits the peak gas pressure load very close to TDC where the piston lateral thrust is small. With the devised setup, the thermal load on the motored engine could be studied independently from the gas pressure load, however phasing of gas pressure with crank angle could not be changed.

For the study of the transient component of heat flux from the combustion chamber, two fast response thermocouples of the eroding type were installed; one at the valve-bridge, and another at the cylinder periphery in the squish region. The methods used for converting the temporal surface temperature measurements to heat flux were the traditional Fourier method and the Impulse Response method. The Impulse Response method was applied using basis functions obtained from a two-dimensional finite

element study of the eroding thermocouple. This analysis allowed an evaluation of the heat flow that occurs in three different types of eroding thermocouples based on Zirconia, Stainless Steel and Aluminium. It was found that significant two-dimensional effects occur at the surface of the Aluminium and Zirconia based thermocouples, whereas only minute two-dimensional heat transfer was noted for the Stainless Steel based thermocouple.

A parametric in-cylinder heat flux study was conducted, where it was found that the transient component of heat flux increases with an increase in engine speed and peak in-cylinder pressure. An increase in the transient component of heat flux was also noted with using gases of higher ratios of specific heats; however it was found that the increase in heat flux experienced with the range of gases tested was not as large as initially expected. Results from this experimental session were compared to existing zero-dimensional and one-dimensional heat flux models. It was found that zero-dimensional, one-zone models of the Annand and Woschni type are able to determine the cycle-averaged total heat flux, but unable to predict the temporal heat flux curve. On the other hand, one-dimensional heat flux models derived from the one-dimensional unsteady energy equation in the boundary layer showed very good correlation with the experimental heat flux in terms of the temporal variation, but underpredicted the magnitude.

ACKNOWLEDGEMENTS

This project would not have been possible without the help and support of several individuals. First I would like to express sincere gratitude to my advisor, Prof. Mario Farrugia, who always provided technical advice and support. His enthusiasm and dedication were fundamental. I would also like to thank him for my upbringing in the research field and academic life, together with his efforts in giving me the opportunity to meet and discuss topics of interest to this research with individuals in the automotive industry. I surely could not have asked for a better advisor!

I would like to thank Gilbert Sammut for his continuous contribution towards this project. He is also credited with the idea of shunting the exhaust gas to the intake. His advice from an industry perspective was invaluable.

Emiliano Pipitone from University of Palermo was instrumental in conveying theoretical knowledge, especially in the area of TDC determination and zero-dimensional modelling. His collaboration in setting the dynamic TDC location of our engine very early in this project was fundamental.

Prof. Martin Oldfield from University of Oxford is thanked for sharing his knowledge on the Impulse Response method, as well as his Matlab scripts.

Laboratory officer Andrew Briffa is thanked for his practical guidance. His remarkable ability to simplify problems will surely be remembered! Ing. Jean Paul Azzopardi, Joseph Curmi, Michael Curmi, Jesmond Pace, James Saliba, Kevin Farrugia and Josef Attard are thanked for their practical assistance.

My true gratitude also goes to the team at the International School for Foundation Studies, who I am honored to have been a part of during the past three years. Their support was fundamental.

Last but not least I would like to thank my parents, siblings, and fiancée Marina who have provided unconditional support and patience.

TABLE OF CONTENTS

LIST OF FIGURES

xi

xiv

LIST OF TABLES

NOMENCLATURE

AC	Alternating Current
AFR	Air-to-Fuel Ratio
AL	Aluminium
AMEP	Accessories Mean Effective Pressure
ATDC	After Top Dead Centre
BBDC	Before Bottom Dead Centre
BDC	Bottom Dead Centre
BMEP	Brake Mean Effective Pressure
BTDC	Before Top Dead Centre
CARS	Coherent Anti-Stokes Raman Scattering
CFD	Computational Fluid Dynamics
CFR	Cooperative Fuels Research
CI	Compression Ignition
CJC	Cold Junction Compensation
CR	Compression Ratio
DAQ	Data Acquisition
DC	Direct Current
DegCA	Degrees of Crank Angle
DI	Direct Injection
DOE	Design of Experiment
ECU	Electronic Control Unit
EGR	Exhaust Gas Recirculation
EVO	Exhaust Valve Open
FEA	Finite Element Analysis
FFT	Fast Fourier Transform
FMEP	Friction Mean Effective Pressure
HCCI	Homogeneous Charge Compression Ignition
HDi	High Pressure Direct Injection
IC	Internal Combustion
$IMEP_{720}$	Indicated Mean Effective Pressure over whole cycle
$IMEP_{360}$	Indicated Mean Effective Pressure over closed part of the cycle
IVC	Intake Valve Closure
LPP	Location of Peak In-Cylinder Pressure
MAP	Manifold Absolute Pressure
MEP	Mean Effective Pressure
NBS	National Bureau of Standards
NIST	National Institute of Standards and Technology
OEM	Original Equipment Manufacturer

OHC	Overhead Camshaft
PCP	Peak In-Cylinder Pressure
PID	Proportional-Integral-Derivative
PMEP	Pumping Mean Effective Pressure
ppr	Pulse Per Revolution
RCM	Rapid Compression Machine
rpm	Revolutions per Minute
RR	Reciprocating Ratio
RTD	Resistance Temperature Detector
SAE	Society of Automotive Engineers
SI	Spark Ignition
SS	Stainless Steel
TDC	Top Dead Centre
TFG	Thin Film Gauge
VFD	Variable Frequency Drive
WOT	Wide Open Throttle

LIST OF SYMBOLS

A_p	Piston Area [m^2]
$\emptyset$	Angle (or Diameter)
θ	Crank Angle [DegCA]
q'' or Q''	Heat Flux [MW/m^2]
h	Heat transfer coefficient [MW/m^{2}K] (or Enthalpy of Gas [J])
T	Temperature [K]
α	Thermal Diffusivity [m^2/s]
F_N	Piston Lateral Force [N]
f	Frequency [Hz]
x	Axial Length [m]
p	Pressure [Pa or bar]
p_{cc}	Crankcase Pressure
V	In-Cylinder Volume [m^3]
V_D	Displaced Volume [m^3]
c, c_p, c_v	Specific Heat Capacity [J/kgK]
c_i, c_e	Fluid velocity [m/s]
R	Specific Gas Constant [J/kgK]
n	Lamina Number, or Polytropic Index
γ (or $'Gamma'$)	Ratio of Specific Heats
u_x	Velocity [m/s]
Nu	Nusselt Number
Re	Reynolds Number
Pr	Prandtl Number
ρ	Density [kg/m^3]
k	Thermal Conductivity [W/mK] (or Valve Spring Stiffness [kN/m]
β	Constant, or Connecting Rod Angle [rad]
μ	Coefficient of Friction (or lubricant viscosity [Pa.s])
v_p	Piston Velocity [m/s]
v_c	Characteristic Velocity [m/s]
v_m	Mean Piston Speed [m/s]
m	Mass [kg]
s	Entropy [J/K] (or Laplace Domain)
ΔT_{G-W}	Temperature difference between bulk gas and wall [K]
j	Timestep
i	Spatial Ordinate (or complex number)
τ	Dummy Variable
t	Time [s]
D_b	Bearing Diameter [mm]
B	Bore [mm]

S	Stroke [mm]
L_B	Length of Bearing [mm]
n_c	Number of Cylinders
n_b	Number of Bearings
L_v	Valve Lift [mm]
n_v	Number of Valves
S_p	Mean Piston Speed [m/s]
P_i	Intake Pressure [kPa]
P_a	Atmospheric Pressure [kPa]
N	Engine Speed [rpm]
r_c	Compression Ratio
ω	Angular Frequency [rad/s]
Z_i, Z_e	Elevation [m]
W	Work Done [J]

Note: Variables which are not defined in this table are defined in their relevant sections in text or in figures.

1 INTRODUCTION

The topics of mechanical friction and in-cylinder heat transfer are two research subjects that have been studied for decades. Their importance in internal combustion engine research is mainly due to their direct effect on efficiency and longevity of the engine, as well as their impact on exhaust emissions which has nowadays become the most worrying factor in regards to internal combustion engine use.

It is known that the mechanical efficiency of an engine can vary from 0% at idle to 90% at full load conditions [1]. This means that at idle, all the energy output from combustion goes to sustain the mechanical friction (and pumping losses) of the engine. The impact that this has on fuel efficiency and emissions can be significant, especially when considering an urban driving cycle, in which the engine spends considerable duration at idle. At higher engine speeds and pressure loads, the mechanical efficiency of the engine improves, however the absolute magnitude of the mechanical friction losses gets larger. Other important factors such as cold start conditions, cylinder deactivation and choice of lubricant accentuate the importance of mechanical friction studies.

The total mechanical friction of an engine can be split into groups which are defined by piston-liner friction, cranktrain friction, valvetrain friction and accessory friction. It is stated that piston-liner friction is the most significant contributor, adding up to around 42% of the total mechanical friction [2]. Higher percentages up to 55% have been reported in [3] [4]. The cranktrain friction, originating mainly from the journal bearings, is also an important contributor with around 20% share of the total mechanical friction [4].

Experimental investigation of mechanical friction has proved to be challenging. This problem is especially accentuated at higher engine loads when the percentage of mechanical friction becomes small compared to the power output from combustion. This results in a typical mechanical friction measurement uncertainty of about 30% [4]. Proposed methods of mechanical friction measurement can be split into two; those performed on a fired engine, and those on a motored engine. The former provides the full representation of mechanical friction, but lacks repeatability and

measurement accuracy. On the other hand, motored friction tests offer good repeatability and measurement accuracy, but lack in the representation of all the phenomena that contribute to the mechanical friction, and their complex interactions. This limitation of obtaining reliable mechanical friction data has a repercussion on mechanical friction model development, which is a fundamental tool required at early stages of engine design.

In-cylinder heat transfer is also an important subject which has instigated many research studies from a very early age of the existence of internal combustion engines. In-cylinder heat transfer finds its prominence due to its effect on: combustion chamber surface temperature, its fluctuation, and consequent material choice, its relation to exhaust heat transfer and exhaust after-treatment, direct influence on gas emissions, lubrication film degradation, development of hot spots and consequent engine knock, design of cooling passages and cooling system, including coolant pump operation and radiator size, and several other factors.

The subject of in-cylinder heat transfer experimental measurement is a complex one. It is also further complicated by its interaction with limitations inherent in the discipline of thermometry. Furthermore, it was shown [5] [6] [7] that one location on the surface of the cylinder is not representative of the whole combustion chamber surface, but heat transfer is spatially sensitive and dependent on local gas flow characteristics and other parameters. The fitment of several thermometers to create a heat transfer map covering the combustion chamber surface is heavily limited by the accessibility through the coolant jackets. Due to the above limitations and others, several reported phenomena apparent in the magnitude and phasing of instantaneous heat transfer in relation to the bulk gas temperatures are still not completely resolved, despite the fact that different theories have emerged throughout the years. Significant discrepancies in phasing and magnitudes of instantaneous heat transfer also exist in literature. This makes the understanding of in-cylinder heat transfer particularly difficult and also poses a limitation on heat transfer model development. Despite the known limitations of some of the heat transfer models, their use is still widespread in industry for heat transfer predictions in the early design stage.

1.1 Research Problem

In the foregoing introduction it was identified that both the topics of mechanical friction and in-cylinder heat transfer are limited by the supply, or the inability to obtain reliable experimental data. This limitation results in a consequent delay in the development of solutions to improve current engine designs as well as compromises reliable predictions from engine models, particularly those used at the preliminary design stage. This research sought to improve the already existing 'pressurised motored method' to be able to provide faithful experimental data which supports model development in both areas of mechanical friction and in-cylinder heat transfer.

The next section highlights the research questions formulated during this Doctoral research, based on the experience acquired during the Masters dissertation, through the review of literature, and through discussions with individuals working in the automotive sector.

1.2 Research Questions

1. How can the conventional pressurised motored method be improved to address the current limitation of low in-cylinder bulk gas temperatures, while retaining its most significant quality of low uncertainty propagation on the FMEP?
2. To what extent are the FMEP and in-cylinder heat flux of the pressurised motored engine affected by increasing the in-cylinder bulk gas temperatures?
3. In what ways does the existing surface thermometry technology limit the in-cylinder heat flux experimental research, and how can this be improved?
4. How well do existing zero-dimensional and one-dimensional models represent the temporal variation of in-cylinder heat flux of a pressurised motored engine?

1.3 Research Methodology

This section gives a brief outline of the forthcoming chapters which details the bulk of the work conducted.

The first part of the project focused on characterising the mechanical friction of the pressurised motored engine. During this period, modifications to the setup were

investigated with the aim of improving the quality of the experimental data that can be obtained from the pressurised motored setup, mostly for mechanical friction determination. The pressurised motored engine was made to operate on a mixture of Argon with air, which allowed testing the engine at high compression temperatures. The experimental campaigns carried out are presented in Chapter 4.

In parallel, a one-dimensional simulation study was conducted to understand the limitations that predictive models present. This simulation work together with other other research involving in-cylinder heat transfer modelling is presented in Chapter 6. Furthermore, an engine was converted from four cylinder to single cylinder operation for use in the second phase of the project.

The second phase of the project regarded the experimental research on transient in-cylinder heat flux measurements. For this purpose, the modified single cylinder engine was placed on the pressurised motored setup, and the first few months were dedicated at characterising and ensuring sound operation of the engine. Two testing campaigns were planned on this setup, one targeted at mechanical friction determination, and the other related to heat transfer measurements. The mechanical friction testing campaign is detailed in the last section of Chapter 4, whereas the experimental research on in-cylinder heat transfer is detailed in Chapter 5. Chapter 5 also details a rigorous analysis that was done on the present technology of surface thermometry using eroding surface thermocouples, and its effect on the surface temperature and heat flux measurements.

2 LITERATURE REVIEW

This chapter presents a review of the most prominent literature read and consulted throughout this work. The chapter is split into three main sections. The first section highlights the research conducted on in-cylinder heat transfer modelling and experimental measurements. The review is given in a chronological timeline to reflect the progress made in this area since its very early stages of investigation. The second section contains a review on the use of surface thermocouples used for transient heat flux determination in internal combustion engine research. These two sections contain the review of the bulk of the literature search conducted in this work. The third section details the additional literature search carried out on the use of the pressurised motored method for mechanical friction determination, its advantages and limitations, and how results differ from those of the fired engine.

2.1 In-Cylinder Heat Transfer Modelling

Since the very beginning of the twentieth century, researchers sought to develop heat flux models for the in-cylinder processes of the internal combustion engine. Throughout the years, at least five different methods have been used in the prediction of heat transfer in engines. The earliest of these was the development of one-zone thermodynamic models, which later evolved into zonal models with the aim of predicting different heat flux behaviours at different parts in the combustion chamber. Later, one-dimensional models started being developed which proved able to shed new light on the boundary layer phenomena existing between the adiabatic gas core and the wall. This was followed with multi-dimensional models. In parallel to the mentioned four methods, several authors also studied the effect of radiant heat transfer, which is considered of a lesser importance than convective heat transfer, especially in motored engine operation.

2.1.1 One-Zone Models

The first consideration and discussion is on the early, global, one-zone models. One-zone models are based on the quasi-steady assumption that is represented by the use of Newton's Law of Cooling, as given in equation (2.1), where h is the heat transfer coefficient, $T_{bulkgas}$ is the bulk gas temperature, and T_{wall} is the wall temperature. The development of one-zone models was initially targeted to predict the global heat rejection and was not intended to predict the instantaneous heat transfer. However, several researchers used this form of equation to predict instantaneous heat transfer, which as a general consensus transpired to be unable to predict faithfully the instantaneous (or temporal) heat transfer shape due to an evident angular phase shift between the bulk gas temperature and heat flux which nullifies the initial assumption of a quasi-steady state. This observation will be discussed in greater detail later. When equation (2.1) is used to predict the heat flux, if the bulk gas temperature in this equation is unknown at the time of the computation, it can be replaced with the adiabatic core temperature.

$$q" = h\left(T_{\substack{bulk \\ gas}} - T_{wall}\right) \qquad \ldots (2.1)$$

As evident from equation (2.1), one-zone models assume similar conditions of heat transfer throughout the surface of the internal combustion engine. This assumption was later shown to be largely untrue as the piston usually runs hotter than the cylinder head and the liner, apart from the fact that on the surface of each of these components, heat flux is characterised by the local flow conditions, and hence varies significantly across the surface of each component. Having said this, back when one-zone models were being developed, surface thermometry was inexistent, and hence the effect of localised conditions was not yet well known. Even though this concept is well diffused nowadays, in experimental studies, obtaining surface temperature histories at different locations of the combustion chamber surface is still a real struggle and often limited by the engine geometry, valves, coolant jackets and oil galleries.

Early works on one-zone modelling were those carried out by Nusselt and Briling. These are of considerable importance as they had set the pace for more sophisticated models. It must be stated that several of the early works, such as those of Nusselt,

6

Eichelberg and Briling were written in their native language, hence could not be analysed from their original documentation. Obtaining these papers is also not an easy task. Annand [8], LeFeuvre et al. [9], Borman et al. [10] and Woschni [11] however give a very good summary of these early works and this is what will be presented here.

According to Annand [8], Woschni [11] and Borman et al. [10] the first one-zone model developed was that by Nusselt, whereby experiments done in a combustion bomb of an undisturbed mixture of air and fuel was ignited. The convective effect of combustion was separated from the radiant effect by conducting experiments on both blackened and gold-plated internal bomb surfaces. It is reported that the model developed by Nusselt made use of Newton's law of cooling to represent the convective heat flux, and Stefan's law to represent the radiation heat flux. The convective heat transfer coefficient in Nusselt's model consisted in principle of two components; one representing the turbulence effect as a function of piston speed, whereas the other was a function of pressure and bulk gas temperature aimed to represent the combustion effect on the convective heat transfer coefficient. It is noted by Annand [8] and Borman et al. [10] that in a later publication by Briling, the author presents a slightly modified version of Nusselt's correlation, altering the term representing the piston velocity effect on the heat transfer convection component. According to Annand [8] several other authors such as Eichelberg and Pflaum used the model proposed by Nusselt as the foundation for their models.

Around six decades later, Woschni [11] criticised heavily the models proposed by these authors as it was stated, based on reconstruction of experiments similar to the ones done by Nusselt, that such models will always fail to represent the forced convection effects in a reciprocating piston-cylinder arrangement because they are based on natural convection bomb experiments. Annand [8] also criticised primitive heat transfer correlations as given by Briling and Eichelberg as they lack in their dimensional consistency due to the fact that they are based on empirical correlations and not founded on theory. This raises concerns on whether such models are in fact reliable if used at conditions far from which they were derived; say higher engine speeds, or modern engine structures.

More recent one-zone models are of a semi-empirical nature, in which a dimensional analysis was favoured. In these models, a simplification of the one-dimensional energy equation was considered in a dimensionless form, usually treating the gas properties as constant and the in-cylinder pressure as being spatially uniform. Through a dimensionless analysis, several authors attempted to correlate the Nusselt number in terms of the Reynolds and Prandtl numbers, however as dictated by the energy equation, other terms such as the pressure work are of significant importance, which however were neglected in the majority of these models. These semi-empirical one-zone models, in their majority ended up in the form of equation (2.2), which is a simplification of the energy equation. Annand [8], Woschni [11] and LeFeuvre et al. [9] are amongst many of the authors who adopted this method and based their models on steady turbulent convective heat transfer. The heat transfer coefficients as suggested by Annand [8] and Woschni [11] are given by equation (2.3) and equation (2.4) respectively, where a, C, c_1 and c_2 are constants. The values of c_1 and c_2 in Woschni's model vary at different parts of the cycle.

$$Nu = C.Re^a Pr^b \qquad \ldots (2.2)$$

$$h = \left[a \left(\frac{\rho v_m B}{\mu} \right)^{0.7} \right] \frac{k}{D} \qquad \ldots (2.3)$$

$$h = 0.0128\, C\, B^{-0.2} p^{0.8} T^{-0.53} \left[c_1 v_m + c_2 \frac{V_D T_{ref}}{p_{ref} V_{ref}} (p - p_{motor}) \right]^{0.8} \ldots (2.4)$$

Annand [8] and Borman et al. [10] documented that Eichelberg was the pioneer in attempting to determine instantaneous heat flux by experiments. This was in 1923 and since thermometry technology was very limited at the time, surface temperatures had to be derived from measured sub-surface temperatures. An even earlier document by Cocker and Scoble [12] in 1913 was found to have reported transient surface temperatures with the use of thermocouples mounted at the surface of a hollow inlet valve. Later in 1961, a popular research by Overbye et al. [13] regarded an experimental investigation in which true surface temperature measurements were made, using a then-novel surface thermocouple of a co-axial construction, developed by Bendersky [14]. In the work done by Overbye et al. [13], an added advantage was that they could use an electronic computer for the harmonic analysis of the surface

thermocouple measurements. The authors performed experimental tests on a fired engine as well as a pressurised motored one; however they found difficulty to use their findings to develop a one-zone model due to a discovered angular phase shift between the measured surface temperature profile and the calculated heat flux profile. As a consequence, the model presented by Overbye et al. [13] gave the heat flux directly. This was applicable only for the pressurised motored engine. Annand [8] later criticised the model given by Overbye et al. [13] over the fact that it does not include a term having the instantaneous wall temperature. In Annand's work [8] a correlation was developed consisting of two terms, describing the convective and radiation heat transfer contribution. The model was dimensionally homogeneous, however it was stated by the same author that the term representing the radiation heat transfer was not one of great reliability because of the limited radiation experimental results published at the time. In the validation of his model, the author used data obtained only few years earlier by Overbye et al. [13].

Having given a summary of the early one-zone modelling one can reflect on similar shortcomings that were evident in the methods presented thus far. As a general consensus, these one-zone models are easy to implement and computationally efficient. This makes their use in engine modelling appealing. It was however found that these models are incapable of predicting the shape of the instantaneous heat transfer curve due to an apparent angular phase shift between the bulk gas temperature and the heat flux. Despite this, the models seemed to be sensibly adequate to provide a prediction of the cycle averaged heat flux.

It should be also noted that the models presented are not all in agreement of what the model should constitute, whether simply a convection term, or a combination of convection and radiation terms. Woschni [11] explains that Nusselt was on the forefront to consider radiation effects from combustion, representing it using Stefan's law. Annand [8] explains that Eichelberg seems to have dropped the Stefan's law term, but instead adjusted the relative powers for the two constituents in the pT group representing the convective heat transfer to shift the importance slightly onto radiation heat flux.

This disagreement on whether to include a radiation heat transfer component seemed to be an ambiguous matter at the time. The general consensus was that radiation heat

transfer contribution is negligible in spark ignition (SI) engines, but significant in compression ignition (CI) engines. Woschni [11] suggested that radiation may be better modelled if split over flame radiation and gas radiation.

2.1.2 Zonal Modelling

In a step forward towards modelling the spatial differences of heat flux in an internal combustion engine, zonal models were introduced. A zonal model divides the combustion chamber gas volume into several control volumes, each of which having its own temperature history and heat transfer coefficient. The portion of the area being affected by the gas zone needs to be also estimated. The local heat transfer coefficients can be calculated using the earlier mentioned empirical correlations, such as that by Eichelberg and Woschni [11]. Of the small number of zonal models which were encountered during the literature survey [15] [16], fired engine operations were considered.

2.1.3 One-Dimensional Models

The phenomenon reported by Overbye et al. [13] that the surface heat flux appeared angularly shifted relative to the measured surface temperature and bulk gas temperature was relatively new at the time, however it was predicted much earlier by Pfriem [17] through a theoretical analysis in 1940. After the experimental work carried out by Overbye et al. [13], the same shift between gas temperature and heat flux was also reported experimentally by Wendland [18], Annand and Ma [19], Woschni and Sihling [20] and several other researchers. With the advent of reliable surface thermometry, the computation of the heat transfer coefficient in equation (2.1) could be done from the experimentally obtained surface temperature, gas temperature and heat flux, something which up till that point was not possible. It was noted however that the heat transfer coefficient showed physically unexplainable values of zero, negative and $\pm\infty$. It was shown and explained by Wendland [18] that these peculiar observations were a result of the angular phase shift between the bulk gas temperature and heat flux. Due to this, several authors started tending towards modelling strategies involving numerical solutions of the unsteady energy equation, instead of making use of quasi-steady one-zone modelling.

Solving the energy equation usually meant that a one-dimensional assumption had to be made in the consideration of the gas adjacent to the wall. The majority of the works made use of a numerical finite difference approach [18] [21] [22]. The validation of the one-dimensional assumption is on the basis that temperature gradients in the gas normal to the wall are steeper than parallel thermal gradients during motoring, especially in flat open-chamber engines. This kind of modelling shed new light on the heat transfer problem as it allowed the evaluation of the temperature gradient set up in the boundary layer. This method also revealed the importance of the thermal energy capacitance of the gas in the boundary layer and the importance of the work done on the gas by the time-varying pressure. A significant research which promoted the use of the unsteady energy equation was that by Wendland [18] which will be discussed in greater detail in a forthcoming section. A year after Wendland [18], Goluba and Borman [21] published results from a numerical model, also utilising the unsteady energy equation, in which the boundary layer was assumed to be thin with moderate temperature variations. Turbulence was neglected and the thermal properties of the gas were assumed to be constant with temperature. The results published by Goluba and Borman [21] agree relatively well with the experimental data of the same authors. Around two decades later than the work published by Wendland [18], Lawton [22] and Nijeweme et al. [23] also considered a one-dimensional numerical solution of the unsteady energy equation. Lawton [22] used it for a motored CI engine, whereas Nijeweme et al. [23] used it for a SI engine. Other works involving the use of the energy equation are those put forward by Greif et al. [24], Dao et al. [25], Diana et al. [26], Han et al. [27] and Angelberger et al. [28].

2.1.4 Multi-Dimensional Models

Models extended in multi-dimensions started getting popular in the late 1900s and early 2000s [10] [23]. These models are theoretically capable of predicting flow fields, turbulence, gas composition and heat transfer. The model is usually involved in solving a three dimensional matrix based on the conservation equations of mass, momentum and thermal energy. For fired engine operation, the models get increasingly complex by the modelling of the combustion reaction and gas composition. In the majority of the cases, axisymmetric modelling was employed.

Although the implementation of multi-dimensional model seems appealing, authors who made use of this approach reported several uncertainties in the underlying sub-models which led to serious questions being raised about the validity of these models. According to Han et al. [27] and Nijeweme et al. [23], the main limitations surrounding multi-dimensional models regard the oversimplification inherent in modelling of the velocity and temperature fields in the boundary layer, as represented by several commercial computational fluid dynamics (CFD) codes.

The most popular approach for near-wall modelling seems to be the use of the 'law-of-the-wall'. This assumes that the hydrodynamic boundary layer is split over a viscous sub-layer in which laminar conditions prevail, connected to the turbulent core through a 'buffer layer'. This approach strictly holds true for steady and incompressible flows in pipes at moderate Reynolds numbers, however it was also used in internal combustion engine multi-dimensional modelling, at conditions far from which it was intended for [29]. Even though this approach is not one which is favoured for rigorous analysis, the use of the law-of-the-wall eliminates the need for the fine meshing required to solve explicitly the energy equation in the boundary layer, hence renders itself computationally efficient. Apart from the steady and incompressible flow assumptions inherent in the law-of-the-wall approach, other assumptions underlie its use, namely; one-dimensional flow, negligible pressure gradients and turbulence scale varies linearly with distance from the wall.

The above mentioned limitations regard the modelling of the hydrodynamic boundary layer. Other limitations also revolve around the determination of the heat flux. Nijeweme et al. [23], Han et al. [27] and Yang et al. [30] warn about the use of the Reynolds analogy in the coupling of heat transfer to momentum transfer to obtain the temperature distribution in the boundary layer. The Reynolds analogy has certain assumptions underlying its use, some of which are not really desirable in internal combustion engine studies. The Reynolds analogy assumes an isothermal boundary layer flow, no temperature gradients parallel to the wall, the turbulent Prandtl number is constant, no chemical energy release in the boundary layer and of the most inaccurate is that no pressure work is assumed present in the boundary layer. The pressure work in the boundary layer was proved by earlier one-dimensional modelling [18] to be responsible for the angular phasing of the heat flux with respect

to the bulk gas temperature, and is also responsible for the negative portion of the heat flux (*i.e.* heat flux out of the wall to gas).

The above mentioned limitations associated with the law-of-the-wall and the Reynolds analogy renders the basic form of multi-dimensional modelling less attractive than initially apparent. In fact, Nijeweme et al. [23] used the above assumptions in a CFD analysis, modelling a single cylinder version of a SI engine and results showed that the CFD underestimated the experimental heat flux by around ten times, and was also unable to predict the negative portion of the heat flux. As a result, Nijeweme et al. [23] favoured an approach of utilising a one-dimensional treatment of the boundary layer using the unsteady thermal energy equation, which similarly to Wendland [18] showed that the pressure work term is of fundamental importance to the angular phasing of the heat flux. It was additionally shown that the convective heat transfer term in the energy equation is also of fundamental importance for the magnitude of the heat flux. Other works involving multi-dimensional modelling includes that of Diana et al. [26] and Gilaber and Pinchon [29] who made use of a wall approximation function and a k-ε turbulence model. Results correlated relatively well with the experimental data, however it should be mentioned that experimental data reported by Gilaber and Pinchon [29] seemed to show no negative heat flux during the expansion process.

2.1.5 Conclusion to Heat Transfer Modelling

Having presented the main theories of heat flux modelling adopted throughout the years, some shortcomings present themselves in each of the methods considered. While multi-dimensional models are still being developed, it can be safely said that the computational effort required by these models somewhat limits their use in the present short design cycle of a new engine. Engine simulation software such as Ricardo WAVE® and GT Power®, which are largely used both for research purposes but also for commercial use by OEMs, make use of one-zone heat transfer models presented by Woschni [11] and Annand [8]. While the limitations of these one-zone models are wide-spread in inter-cycle calculations, for the purpose of estimating the global parameters of engine performance they might suffice and produce acceptable estimations. For a more rigorous analysis required by the heat

13

transfer specialist, an approach founded on theory in the one-dimension or multi-dimensions seems to be the way forward.

2.1.6 Anomalies Surrounding Heat Flux Measurements

In the preceding section, it was highlighted that early experimental heat flux measurements showed an angular phase shift with respect to the in-cylinder bulk gas temperature, where the surface heat flux anticipates the bulk gas temperature. This observation resulted in some unrest in the research community. Furthermore, due to this unsteady nature of the heat transfer, if Newton's law of cooling is employed on the experimental data of heat flux and bulk gas temperature, the ensuing heat transfer coefficient assumes values of zero, negative and $\pm\infty$. These peculiar values result from the following observations:

1. At two instances during the cycle, the heat flux was noted to change sign from positive (gas to wall) to negative (wall to gas). At the crossing points, the heat flux is logically equal to zero. At these conditions the bulk gas and wall temperatures were observed to be different. Through the use of the 'traditional' Newton's law of cooling, this results in a zero heat transfer coefficient.

2. At a certain point early in the compression stroke, and at another slightly after top dead centre (TDC) compression, the experimental heat flux was found to appear in the direction from the wall to the gas. At the same instant, however, it was found that the bulk gas temperature is higher than that of the wall. This results in a negative heat transfer coefficient.

3. When the bulk gas temperature equals the wall temperature, the observed heat flux had a magnitude other than zero. By a consideration using Newton's law of cooling, this results in positive or negative infinite heat transfer coefficients.

Even though it had been reported that the coefficient of heat transfer does not have a physical significance, authors such as Whitehouse [31] and Woschni and Sihling [20] proposed a magnitude shift for the heat transfer history such that the heat transfer coefficient could have a good physical meaning. The correction presented by Whitehouse [31] suggests that the instantaneous heat flux time history should be

shifted to zero at the inlet valve opening. On the other hand, that presented by Woschni and Sihling [20] involved shifting the instantaneous heat flux time history to zero at the point where the difference in temperature between the bulk gas temperature and wall temperature is zero. It is reported by Woschni and Sihling [20] that the magnitude shift in the instantaneous heat flux required with this proposed theory is around 1.5% of the maximum value of the local instantaneous heat flux and smaller than 15% of the time-mean local heat flux. The mentioned peculiarities were reported for motored engine operation [18] and also in fired operation [23].

2.1.7 Experimental Research on In-Cylinder Surface Temperature and Gas-Side Heat Flux

The understanding of heat transfer is vital to the design of a reliable engine. Heat transfer dictates the portion of the heat release that is rejected. It determines the products of the gaseous emissions as these are dependent on the in-cylinder temperature reached. Heat transfer also dictates the portion of the energy which is released to the exhaust, hence vital for after treatment systems and turbocharging. Materials in the engine structure, and especially the combustion chamber, sleeves and piston are heavily dependent on the wall temperature and its fluctuation. Engine knock, especially in highly boosted engines is also related to the efficient local cooling of the combustion chamber. Wall lubrication and oil film degradation are dependent on the wall temperatures [32]. This list is by no means exhaustive; however it does give an outline of the importance of surface temperature measurements and in-cylinder heat transfer understanding. For this reason, several researchers endeavoured to obtain reliable experimental data for a better understanding of the thermal field in the combustion chamber.

From a survey of literature, it was found that a wealth of research utilising surface temperature measurements occurred in the period between 1970 and 1990. Chronologically these include Whitehouse [31], Dao et al. [25], Dent and Sulaiman [33], Greif et al. [24], Alkidas [6] [34] [35], Hohenberg [5], Hoag [36], Huang and Borman [37], Mure and Rhee [38], and several others. Of the latest studies which still used the traditional method of surface thermocouples are Hendricks [39], Torregrosa et al. [7], Hennes et al. [40], Wang et al. [41] and Demuynck et al. [42].

Literature review showed that some of the classical experimental research on surface temperatures and heat flux reported spatially varying surface temperatures and heat fluxes. Spatial variations were shown in both fired and also in motored engines. At an engine speed of 1100 rpm and 1.36 bar MAP, Mure and Rhee [38] reported a spatial variation between 0.80 MW/m^2 and 2.07 MW/m^2 for a pressurised motored engine. For a fired engine, Jackson [43] reported a spatial variation of 350% on the mean heat flow.

Parametric studies of heat transfer were researched due to their importance for development of predictive heat flux models. For motored engine operation, the parameters that have a direct effect on the surface temperature and heat flux can be reduced to engine operating parameters (engine speed, PCP, coolant temperature, gas composition, etc), motion of the gas (swirl, squish and tumble), design of cooling jackets, wall material and combustion chamber surface shape.

Haog [36] showed that the use of glycol as the coolant fluid results in a decrease in the overall heat transfer to the wall when compared to the use of water as the coolant. This was attributed to a smaller convective heat transfer coefficient at the coolant jacket side for glycol, compared to water. Alkidas [34] investigated the effect of coolant temperature on heat transfer from the cylinder wall and concluded that this had no effect for the tested fired engine. His result agreed with those of French and Atkins [44], but contrasts with those of Hoag [36]. In these studies, the coolant temperature was varied as method of varying the wall temperature; however the wall temperature variation with this method was not large.

Jackson [43] studied the effect on in-cylinder heat transfer when thermally insulating the combustion chamber, such that the wall surface temperature was increased by 400°C over the non-insulated engine. In the majority of the cases, the heat flux was found to decrease for the insulated engine, with reductions of between 46% to 52%. In some cases, however, conflicting results were obtained, where the heat flux showed an increase for the insulated engine. It was hypothesised that this could be due to an increase in the convective heat transfer coefficient originating from the very high wall temperature.

From a summary of the results observed from literature, the steady-state component of heat flux seems to be much smaller than the peak of the heat flux [13] [38]. For a

pressurised motored engine, Mure and Rhee [38] reported steady-state components of heat flux between 0.027 MW/m^2 and 0.123 MW/m^2. Alkidas [34] found that when obtaining the steady-state component of heat flux, errors in the results obtained can be as high as 20%. This was determined by using thermocouples in the cylinder head recessed to different amounts from the surface, at the instrumented location.

Another subject which seems controversial is the angular location at which the instantaneous heat flux changes direction. Wendland [18] reports a change in direction of the heat flux as early as 30 DegCA ATDC for a pressurised motored engine. On the other hand, Torregrosa [7] reported a change in heat flux which is very small and occurs later than 90 DegCA ATDC, for a more modern pressurised motored engine.

In-cylinder heat transfer research is still an active topic and although the mechanisms of heat transfer in the cylinder of an internal combustion (IC) engine remain nearly unchanged from those tackled in the classical research, however engine structures now utilise new materials. The most fair comparison being the use of aluminium cylinder heads (and in some cases cylinder blocks) over the more traditional use of cast iron. Combustion chamber and piston insulating materials, such as Zirconia, have also been reported in recent studies [45], even though they started being investigated few decades ago. Higher compression ratios and optimisation of valve areas are also evident, together with optimised combustion chamber shapes. In present times, engines run much faster with higher power output densities than the engines that the classical authors studied on. These differences in IC engine design are expected to somehow be reflected in the gas-wall heat transfer.

From the reviewed recent literature, it was noted that researchers seemed to have taken a step back from the traditional parametric studies presented in classical literature, and instead seemed to have revised the heat transfer problem by looking at it from a different perspective. One particular example is the research by Demuynck et al. [42] who sought to investigate the relationship between the working gas and in-cylinder heat flux with the aim of obtaining a fuel-independent heat transfer model. Other researchers attempted the use of different types of surface thermometers, with some being custom-made with the aim of investigating the error incurred in the heat flux which originates from the surface thermometer design [40] [46] [47]. In other

works, different methods for the evaluation of heat flux from the surface temperature measurement were proposed, mainly in search to include multi-dimensional heat transfer phenomena that occur in surface thermometers [41] [48] [49].

In the next sub-section, a short literature review is presented on a few studies which investigated experimentally the boundary layer developed at the combustion chamber surface.

2.1.8 Measurement of Thermal Boundary Layer Thickness

To supplement the understanding of the unsteady nature of heat flux in IC engines which leads to the anomalies presented earlier, several researchers attempted to understand the thermal boundary layer growth and decay. This is possible by using one-dimensional models mentioned in an earlier section, and presented by authors such as Lawton [22], Greif et al. [24] and Wendland [18]. Experimental measurements of the thermal boundary layer thickness were also carried out. In the early work by Lyford-Pike and Heywood [50], a fired engine permitting visualisation through quartz glass walls was used, combined with schelieren photographs. Later, Lucht et al. [51] used Coherent Anti-Stokes Raman Scattering apparatus in a fired and motored engine. The present discussion will be limited to the experimental measurements of the thermal boundary layer thickness, however boundary layer thicknesses obtained from one-dimensional models will be discussed in Chapter 6.

From the study by Lyford-Pike and Heywood [50], it was determined that on the intake stroke, the thermal boundary layer is thin and starts increasing gradually on the compression and expansion strokes to around 2 mm. This observation is in agreement with the thermal boundary layer thickness as obtained from the one-dimensional method put forward by Lawton [22]. Lyford-Pike and Heywood [50] observed that the boundary layer stops growing when the exhaust valve opens, and at this point it separates from the cylinder wall and interacts with the bulk gas leaving the cylinder. The boundary layer thickness was only measured in the part of the cycle where the gas temperature is higher than the wall temperature.

It was also observed that the boundary layers at the cylinder head surface and piston crown are around twice to three times greater than that on the cylinder wall. The

authors [50] speculate that this is because of the different velocity flow fields at these different regions, where the piston-induced gas motion is along the cylinder wall, and perpendicular to the cylinder head surface and piston crown.

According to a parametric study done by the same authors, engine speed was found to have a significant effect on boundary layer thickness. Decreasing the engine speed led to a thicker boundary layer. Engine load did not seem to have any significant effect on the boundary layer thickness.

A striking observation made by the authors reveal that for an average boundary layer thickness of 3 mm at 90 Deg after TDC compression, the volume of the boundary layer is around 20% of the total cylinder volume at that condition. Since the average density of the gas in this boundary layer is much denser than that of the bulk gas, some 30% to 40% of the cylinder mass resides in fact in the boundary layer.

In a separate study by Lucht et al. [51], 'Coherent Anti-Stokes Raman Scattering' (CARS) was used to measure gas temperatures near the cylinder head surface of a single cylinder research engine. The authors also used an erodible K-type heat flux gauge to measure the heat flux at the CARS location. It was seen that for the motored engine, the high swirl configuration showed a lower overall temperature in the boundary layer than the low swirl configuration. This was attributed to a higher trapped mass in the high swirl configuration. For the motoring case, temperature by the CARS method was only obtained at TDC compression. It was shown that at this crank angle position, for both the low swirl and high swirl configurations, the thermal boundary layer thickness was about 2.5 mm. In the fired condition, measurement using the CARS method was done at four crank angles, close to, but after compression TDC. After start of combustion, the low swirl and high swirl configurations showed strikingly similar thermal boundary layers, meaning that the thermal boundary layer development during combustion is independent of the swirl condition.

From the measurement of boundary layer temperature using the CARS method, Lucht et al. [51] estimated the gas-wall heat flux which compared well with that obtained from a Fourier spectral analysis on the surface temperature data obtained from the erodible K-type thermocouple.

2.1.9 Concluding Remarks on In-Cylinder Heat Transfer Literature

Having presented some of the significant literature on model development, experimental results, as well as peculiarities of heat transfer recorded in internal combustion engines, it is evident that this subject is a very challenging one. This results from several factors, including mainly: spatially different flow behaviours, complex chamber designs, thermal capacitance and pressure work in the boundary layer, radiation effects, different fuels and gas compositions, and surface thermometry limitations. The latter is indeed a problem on its own, posing its own inaccuracies and limitations on the measurements.

In the following section, a closer look will be given to the problem of surface thermometry – a factor which was, and perhaps still is, the main cause for limiting heat flux research. Several aspects of surface thermometry will be looked at, including sensor choice, materials making up the sensor, fitment considerations, sensor testing and characterisation.

2.2 Literature Review on Surface Thermocouples

Surface temperature measurement has been one of the long persisting problems in several important researches, such as internal combustion engine in-cylinder heat transfer, gun barrel temperature measurements, shock wave measurements and more. In some of the cases highlighted, the inability to obtain good and reliable surface temperature data prevents from having further advancements in the research field. Stemming from this appreciation, this part of the literature review aims to outline the prior and existing measuring art, together with the salient points which need to be approached carefully when using surface thermometers for reliable heat flux determination. In its majority, the following literature review revolves mainly around the use of thermocouples for the measurement of surface temperature; however occasional reference is also made to other types of surface thermometers.

2.2.1 Fundamentals of thermocouples

Prior focusing the attention to surface thermocouples, it is thought to be of benefit to highlight first an important literature by Moffat [52] [53] [54] which discusses the fundamentals of thermocouple physics. In its most basic explanation the thermocouple consists of two dissimilar metals, joined at one end forming a junction. A wide-spread misunderstanding of the thermocouple phenomenon is that this junction generates a thermoelectric voltage proportional to the temperature. This is simply not true. The junction is a point of both thermal and electrical equilibrium. From this point onward, a temperature gradient is setup in each of the thermocouple materials. Since the two thermocouple elements are dissimilar, the temperature gradients setup in each of the two metals would be different. According to a research done by Thomas Seebeck in 1821, if two dissimilar metals are joined at one end, an emf proportional to the temperature at the junction would result at the other end. The emf was found to be also dependent on the metallic element pairs on which the experiment was carried out. From the foregoing consideration it results that any length of the thermocouple wire which is in an isothermal state would not be contributing to any of the Seebeck emf because throughout that length the temperature gradient is zero.

The terminology 'thermocouple calibration' is often iterated in literature [55] [56]. Unfortunately this terminology seems to have at least two different connotations. The most obvious use of the terminology 'thermocouple calibration' refers to the process of cross-checking whether the emf given by a thermocouple at a known temperature agrees with that given by the NBS tables, according to the dissimilar materials of the thermocouple. On the other hand, if the output of the thermocouple as a function of its construction, materials and mounting location is of interest, then the terminology 'thermocouple characterisation' is preferred to avoid the confusing connotation with 'calibration'. In this work, the importance of surface thermocouples 'characterisation' will be explained in detail. The forthcoming literature review will discuss mainly the use, construction, and integration of surface thermocouples to obtain a voltage output that is solely a function of the thermocouple materials and not the sensor body material or its mounting method.

Surface temperature can be classified into two main categories; time-invarying (steady-state) and time-varying (transient). The type of surface temperature being

measured therefore dictates the sensor construction and its response time, amongst other factors. For steady-state surface temperature measurements, the problem of obtaining a faithful thermocouple response is somewhat reduced in complexity due to the reduced complication of thermocouple time response. One popular thermocouple construction for this kind of temperature measurement is the Schmidt-Boelter gage, first introduced by Ernest Schmidt in 1924 [57], and later revised by Vatell in 2001 [58]. Another well-known construction is the Gardon gage [59]. Some other steady-state surface thermocouples include thin-film gages which are based on an adhesive backing.

In this doctoral work, the study is concerned mainly with transient heat flux, hence the bulk of the forthcoming discussion will be focused on thermocouples with microsecond response times that are able to keep up with the transient nature of surface temperature in an internal combustion engine.

2.2.2 Coaxial Surface Thermocouple (Thin Film Gauge)

Early IC engine heat transfer research was heavily limited by the lack of a technology that was able to measure the fast changing engine cylinder surface temperature. Bendersky [14] seems to be behind the introduction of the first fast-response thermocouple design. This design is nowadays still used and produced by MedTherm [60]. The Bulletin 500 by MedTherm states that this design was really first introduced by Hackemann in 1941, and is termed the 'thin-film' or 'Coaxial' surface thermocouple. The name is derived from its construction in which a solid rod of a thermocouple material is electrically insulated, usually by oxidising or anodising its circumference. The second thermocouple material is in the form of a tube which wraps around the first thermocouple rod material. The exposed end of the combination is ground flat and a thin film of conductive material is vapour deposited as shown in Figure 2.1. This creates a thin junction between the two thermocouple materials. Recently, Hennes et al. [40] detailed a process which they use for development of small co-axial thermocouples from regular, commercial, mineral insulated thermocouples. The same thermocouple design process was also used earlier by Hohenberg [5]. For heat flux studies in insulated combustion chambers, a modified version of the Bendersky [14] thermocouple was put forward by Assanis et

22

al. [61]. For this purpose the metallic surface of the thermocouple was coated by a layer of ceramic. The junction was then set up on the ceramic layer by thin film deposition. A similar construction to that put forward by Assanis et al. [61], was used more recently by Aoki et al. [62].
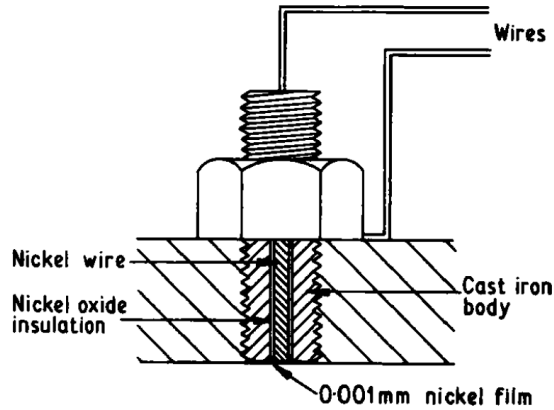
Figure 2.1. Coaxial surface thermocouple used by Bendersky [14].

Another type of thin film gauge temperature (TFG) sensor is that brought forward by Piccini et al. [63], shown in Figure 2.2. This sensor uses resistance as a thermometric property. In this variant of the TFG, a platinum thin film is sputtered over an insulating layer of polyimide. A constant current is sent through the platinum such that when the resistance of the metal changes in response to temperature, a change in voltage is recorded. To the other side of the polyimide a standard thermocouple is fitted. Therefore, the temperature difference across the combined 70 μm glue and polyamide layers allow the determination of the heat flux at the location of interest, if the thermal product of the TFG is found beforehand through appropriate tests of sensor characterisation. An evolution of this sensor design seems to have been used in internal combustion engine studies by Broakaert et al. [47] and Demuynck et al. [42] (mentioned in a previous section). Particular care should be given when using thermometers of this kind, especially in in-cylinder heat transfer. This is due to the fact that the use of an insulating material in the sensor construction makes them prone to reporting a higher average temperature and swing than the more conductive, undisturbed surface.
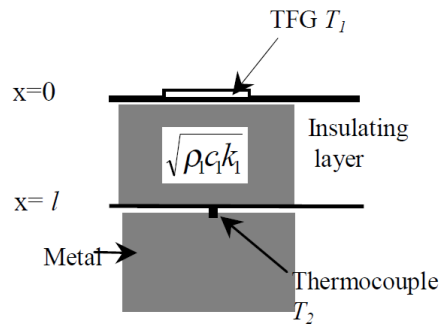
Figure 2.2. Thin-film gauge thermocouple as used by Piccini et al. [63].

2.2.3 The Eroding Surface Thermocouple

The design of the coaxial surface thermocouple explained in the previous section, by time seems to have evolved into an eroding type. The eroding type thermocouple, in present day construction consists of two thermocouple elements in a ribbon format, usually 25μm thick, separated from each other by a 5μm mica ribbon. The three ribbons are then sandwiched between a split-tapered pin, but insulated from it by two 5μm mica ribbons; one on each side. The sandwich is then pressed in a thin tube. The junction at the exposed surface is established by abrading the surface with an emery cloth, with which microscopic metallic slivers are carried from one metallic element to the other. This provides a thermal junction which has a very small mass, and therefore the heat capacity and consequently the response time is very small. The construction of the eroding thermocouple just described is supplied by Nanmac Corporations [64] and its schematic is shown in Figure 2.3. This design was used for in-cylinder heat flux measurements by several authors such as Nijeweme et al. [23], Wang et al. [41] and Torregrosa et al. [7]. It was also used successfully for exhaust heat flux measurements of a SI engine by Farrugia [65]. A slightly different kind of eroding thermocouple manufactured by ASEA was used by Lawton [22]. The design used by Lawton [22] is similar in construction to that of the coaxial thermocouple, however uses the technique of abrasion instead of vapour-deposition to establish a surface junction.
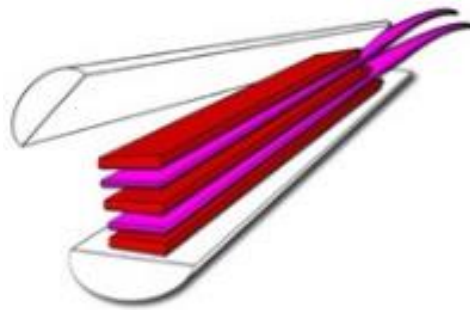
Figure 2.3. Eroding thermocouple construction as supplied by Nanmac [64].

With the surface junction requiring abrasion, the eroding surface thermocouple allows the flexibility of grinding the surface of the thermocouple to match the surface contour. This is a significant advantage as it ensures that the thermocouple does not perturb the velocity flow field of the gas. Perturbation of the temperature field is discussed in a forthcoming section.

The user manual made available by Nanmac [64] states that the procedure to establish a connection between the two dissimilar metal ribbons of the eroding thermocouple should first start by removing any connection between the two metallic elements. To open any existing connections, the sensor should be abraded by a #280 to #350 grit size paper in a directional parallel to the metallic ribbons. A resistance higher than 1000 Ω indicates an open connection. After the connection has been opened, the thermocouple surface is abraded in a direction of 45° to the ribbons with progressively coarser grit sizes until a resistance of around 10 Ω to 12 Ω is obtained. This procedure allows for the smallest possible sliver connecting the two thermocouple materials.

In a document by Nanmac [66], it is stated that the 'probe material' can be chosen amongst four standard availabilities, being Stainless Steel, Inconel, Copper and Tantalum. It is thought that 'probe material' in the document by Nanmac [66] refers to the outer tube of the eroding thermocouple, and not the split tapered pins. The split-tapered pins material seems to be dictated by whether the sensor is ordered as 'thermally grounded' or 'thermally ungrounded'. A thermally grounded sensor comes with split-tapered pins of a conductive material, such as Stainless Steel or Aluminium, whereas a 'thermally ungrounded' sensor comes with a thermally insulative material for the split-tapered pins, such as Zirconia. This gives some flexibility to the researcher in selecting a sensor material as close as possible to that

of the substrate material to be measured. Fortunately, the manufacturer also allows some limited customisation.

2.2.4 The Thermopile

In its broadest sense, a thermopile is a collection of thermocouples, usually electrically in series. The advantage of using a thermopile is primarily to obtain a higher signal voltage. Thermopiles that are configured electrically in parallel have also been reported [67] and their principal use is to obtain spatial temperature averaging.

The thermopile is usually known to be slightly bulky, hence its integration in several instances can prove to be challenging. Cornelis et al. [68] claims to have used successfully a thermopile supplied by Vatell [69] for internal combustion heat transfer research. The thermopile used by Cornelis et al. [68] was the HFM-7 and it was stated that a calibration equation was supplied with the sensor for the direct determination of heat flux from the acquired voltage. Such calibration is pertinent to temperatures at which it was conducted; hence a platinum resistance thermometer is fitted in the same sensor body to be able to conduct a temperature compensation for the calibration. Other Vatell surface thermometers employ a thin film thermocouple as a reference temperature.

2.2.5 Multi-Dimensional Heat Flux

The most popular constructions of surface thermocouples used in internal combustion engine in-cylinder heat transfer have been discussed in the previous sections and it was shown how each of these designs consist of a number of materials. If our attention is presently restricted to the eroding surface thermocouple, it is easy to see that at least four different materials make up this sensor.

In discussing the heat transfer through a typical eroding thermocouple, a useful property that describes the response of the materials to heat flux is the *thermal diffusivity*, $\alpha = \left(\frac{k}{\rho c}\right)$. The thermal diffusivity gives a measure of the ability of a material to conduct heat relative to its ability to store it. Materials with a large

thermal diffusivity respond quickly to changes in the thermal environment, whereas a material with a small thermal diffusivity responds sluggishly. Another important metric which will be used throughout this dissertation is the *thermal effusivity*, or sometimes called *thermal product*, and is described by $\sqrt{\rho c k}$. Thermal effusivity is defined as the rapidness of the material to exchange heat. This has a two-fold underlying mechanism; how efficiently the material can conduct heat and also how fast it can store or release its internal energy.

When a step heat flux is imposed on the surface of an eroding thermocouple, a temperature distribution is set up in the thermocouple, both axially (along its length) and also parallel to the sensor surface. The temperature distribution will depend on the thermal diffusivity and effusivity of the different materials making up the thermocouple. The temperature distribution parallel to the surface creates a potential for multi-dimensional heat flow in the sensor body, depending on which material retains the highest temperature and by how much, compared to the adjacent materials. To investigate this, Buttsworth [48] and Wang et al. [41] used a two-dimensional finite element analysis (FEA) with a step heat flux applied at the surface of the eroding thermocouple, whereas Grech et al. [70] imposed an impulse heat flux to the surface. The surface temperature that ensued after some time duration was examined. Buttsworth [48] and Wang et al. [41] both treated a thermocouple with Dural split-tapered pins, whereas Grech et al. [70] studied a thermocouple with Stainless Steel 304 as substrate material. These three literature contributions will be discussed in further detail in Chapter 5.

In experimental in-cylinder heat flux research, comments about observed peculiarities were made and presented in Section 2.1.6. These phenomena confused several researchers, in the sense that it was not easily determinable whether the observations made were truly present in the engine, or simply an artefact being falsely constructed by the experimental apparatus limitations. Wang et al. [41] reported that at least part of these observations are due to the false assumption taken by several, that the heat flux through the sensor flows in a one-dimensional manner. This was suggested also by Buttsworth [48]. The latter arrived to this conclusion after having imposed heat fluxes of a square and a sinusoidal nature on to the surface of the sensor in the FEA model, and the resulting temperature computed by the FEA

over the central mica was then used with a one-dimensional treatment using the thermo-physical properties of the sensor substrate (*i.e.* Dural). The result was an apparent heat flux (calculated from 1D) which showed a marked increase in the magnitude compared to the actual imposed heat flux (on the FEA). The apparent heat flux also showed negative values during the decay portion which were not synonymous to the imposed heat flux. Wang et al. [41] states that for a reliable determination of heat flux from eroding surface thermocouples, an impulse-response characterisation of the sensor that accounts for at least two-dimensional heat flow at the surface should be considered. The author does not rule out the possibility of having more than two-dimensions being prominent in the thermal environment, however no experimental evidence was presented.

2.2.6 Errors in Steady-State Component of Heat Flux

To obtain the total instantaneous heat flux, the transient component of heat flux determined from the temporal variation of surface temperature has to be added to the steady-state component of heat flux.

In Section 2.2.5, multi-dimensional heat flux affecting short time scales of interest which are responsible for errors in the transient component of heat flux were discussed. Unfortunately, multi-dimensional effects present errors not only in the transient component of the heat flux, but also in the steady-state component.

To obtain the steady-state component of heat flux, the mean surface temperature (obtained from the surface temperature swing) is not sufficient, but a constant temperature at some distance away from the surface is also required. This is usually obtained through a second thermocouple placed at a recessed distance from the surface, close to the axis of the surface thermocouple. Fourier's law of one-dimensional conduction is then used between the mean surface temperature and the recessed temperature. The distance at which the recessed junction should be located can be calculated by assuming a certain percentage of attenuation of the surface temperature swing. Farrugia [65] calculates the appropriate recessed depth for an attenuation by a factor of 200 using equation (2.5), where x is the recessed length, C is the attenuation factor, α is the thermal diffusivity of the material affected by the transfer of heat, and f is the frequency of the temperature cycle.

$$x = ln(C) \sqrt{\frac{2\alpha}{f}} \qquad \qquad \ldots (2.5)$$

Several authors, such as Hoag [36] explains how the use of a recessed thermocouple poses at least two problems on the determination of the steady-state component of heat flux. The first is that it is usually relatively difficult to ascertain the actual physical recessed depth with good accuracy. In fact, Alkidas [6] and Farrugia [65] used X-ray photography to determine with better accuracy the position of the recessed junction with respect to the surface.

The other problem revolves around the fact that the further the recessed thermocouple is situated from the surface, the larger is the error in the steady-state component of heat flux that results from the one-dimensional assumption. As can be noted from equation (2.5), the distance of the recessed thermocouple from the surface is dictated by the thermal diffusivity of the substrate material and the engine speed. This implies that for high diffusivity materials, such as Aluminium, at low engine speeds such as 1400 rpm, a recessed length of around 7 mm is required, which therefore creates a significant room for multi-dimensional heat transfer. This is considered a limitation in present day in-cylinder heat transfer research since current engine designs are in their majority made out of aluminium, unlike older engines made from cast iron on which the majority of the heat transfer research is based. Alkidas [34] reported a possible 20% error in the determined steady-state component of heat flux from eroding surface thermocouples due to the effect of multi-dimensional heat flux occurring between the surface junction and the recessed thermocouple junction at the chosen fitment location. It was found that the error in the steady-state component of heat flux was dependent on the spatial location of the sensor. For this reason, several authors used custom-made fittings engineered to limit two-dimensional heat flow between the surface junction and the recessed junction. Gilaber and Pinchon [29] used a ceramic circumferential insulator, whereas Jackson et al. [43] used an air layer at the periphery.

If the ultimate aim of the research work is not to obtain the steady-state component of heat flux, but rather the total instantaneous heat flux, the issues discussed above can somewhat be bypassed, with limitations. To reduce the possible errors associated with the measurement of the steady-state component of heat flux, Hoag [36]

determined the total instantaneous heat flux, without directly measuring the steady-state component of heat flux. The suggested method involved shifting the transient component of the heat flux in the y-axis (heat flux axis), such that at the end of exhaust stroke / beginning of intake stroke, when the wall temperature equals the bulk gas temperature, the heat flux is made to equal zero. The absolute values of the heat flux will then represent the total instantaneous heat flux. It is appreciated that while this method offers an acceptable approach for a comparative analysis of heat flux, its use to determine the true value of the total instantaneous heat flux is somewhat questionable. This is because with this approach, it is assumed that at the end of exhaust / beginning of intake, the problem of angular phase difference between the heat flux and bulk gas temperature is negligible. This might actually be not too bad of an assumption due to the fact that it is acknowledged from previous studies that the thermal boundary layer thickness (which is the prime factor that causes the phase shift) is small during the intake and exhaust strokes [50]. Cornelis et al. [68] also used a similar method to the one described to obtain the total heat flux from the transient heat flux component, without directly measuring the steady-state component of heat flux.

2.2.7 Effect of Sensor Body Material

It has been discussed that the effect of different materials in the thermocouple construction instigates multi-dimensional heat flow and associated errors in both the transient component of heat flux, and also in the steady-state component. The importance of the materials making up the sensor goes further than this. Using a sensor with a base material significantly different than the instrumented surface can result in a falsely measured surface temperature, and possibly heat flux, even if multi-dimensional effects do not exist, and a pure one-dimensional scenario is ficticiously considered. If the base material of the sensor is more insulative (or conductive) than the undisturbed surface, when the sensor is integrated in the engine it would act as a heat barrier (or a fin). This results in a measured surface temperature swing and mean which are a function of the thermocouple material, and not the instrumented surface. Such consideration is one of the main reasons why thin film gauges should be used with care [47]. Thin film gauges are usually based on an insulator substrate such as Macor [68] and Mullite [65], which are both insulative

compared to the usual metallic engine structure, hence act as a thermal insulator that hinder axial heat flow compared to the undisturbed instrumented surface. As a consequence, the measured temperature will be higher relative to the rest of the base material, leading to a false surface temperature measurement. An opposite scenario to this would be if a better conducting material is used for the sensor body. In such case the thermometer would conduct heat faster than the undisturbed instrumented surface, and hence a lower temperature swing and mean would be falsely measured. This would be the case if a standard Stainless Steel-based eroding thermocouple is used in an insulated (ceramic) engine. In fact this is why Assanis et al. [61] and Aoki et al. [62] revised the design of the co-axial thermocouple by Bendersky [14] for their application in insulated engines.

If the material for the sensor body is cautiously selected to be similar to the instrumented surface, care should still be taken as the thermocouple could still act as a fin and dissipate a higher heat flux than the undisturbed body would [65]. This happens if the thermocouple body physically increases the overall surface area affected by convective heat transfer, or somehow alters the fluid convection. In internal combustion engine heat flux measurements, this error is commonly found if the thermocouple body extends through the cooling jacket. Such phenomenon was termed by Farrugia [65] as the "Fin Effect", while apparently the same phenomenon is termed by Nanmac [71] as the "Stem Effect".

2.2.8 Surface Thermocouple Characterisation

Despite the knowledge of multi-dimensional effects present in surface temperature measurements, the most popular method of obtaining the transient surface heat flux component from the measured surface temperature swing is through the heat diffusion equation assuming a semi-infinite solid with a surface temperature being a harmonic function of time. This approach requires the surface temperature signal to be discretised into the frequency spectrum using the Fourier transform. Alkidas [6] and several other researchers made use of this method which assumes a one-dimensional heat flow through the sensor along the axial direction. Apart from neglecting the effects of multi-dimensional heat flux, this method presents another problem: determining which thermo-physical properties (ρ, c, k) should be used in

the heat diffusion equation, whether that of mica, the thermocouple elements, or the split-tapered insert material. In classical in-cylinder heat transfer work that made use of the Fourier 1D analysis, the thermo-physical properties used in the heat diffusion equation were those of the sensor body (split-tapered inserts) [6] [7].

Due to the above reason, characterisation of the surface thermocouples has been considered by several authors in ensuring sound surface temperature measurements [49] [65] [68] [72]. Different kinds of characterisation procedures were adopted. The main reasons of interest are mainly two; to assess which of the materials making up the thermocouple affects the heat flow (*i.e.* which thermo-physical properties to use in the heat diffusion equation), and to ensure adequate sensor rise time. In the following discussion, the different methods used for thermocouple characterisation are presented. The presented methods are split into two categories similar to how they are presented in literature; short timescales of interest (microseconds) and long timescales of interest ($\geq$ milliseconds).

2.2.8.1 Long timescales of interest

The methods presented for testing surface thermocouples at long timescales of interest are mostly used for the determination of the thermo-physical properties affecting the heat flux. Five different methods are presented.

In a study involving the use of eroding thermocouples in an extension of the exhaust port of a SI engine, Farrugia [65] characterised the E-type eroding thermocouples with Stainless Steel split-tapered inserts using a heat balancing technique. The eroding thermocouples used by Farrugia [65] had a factory-integrated recessed thermocouple for determination of the steady-state component of heat flux. The setup used to characterise the thermocouple in steady-state use is shown in Figure 2.4, reproduced from [65]. In this method, the eroding thermocouple assembly is fitted in series with a Stainless Steel (SS) calibrating section with two temperature measurements T_1 and T_2, a known distance apart. From these two temperature measurements the 'calibration' heat flux through the eroding thermocouple is found. Fourier's law of conduction is then used between the surface junction temperature and the recessed junction. The heat flux computed from the SS calibrating section and that through the eroding thermocouple should be equal, provided that heat flows

only from the 'calibrating section' towards the eroding thermocouple assembly. For this purpose two heaters are used to ensure that no heat flows from the stainless steel calibrating section towards the base. This is achieved if T_a and T_b are equal. Two dimensional heat flow was mitigated by insulating the setup with fibre sheets.

From this experiment, the thermal conductivity affecting the eroding thermocouple steady-state response could be found. Results acquired by Farrugia [65] showed that the material which affects the heat flux at steady-state was the body material of the sensor, *i.e.* the Stainless Steel split-tapered pins.
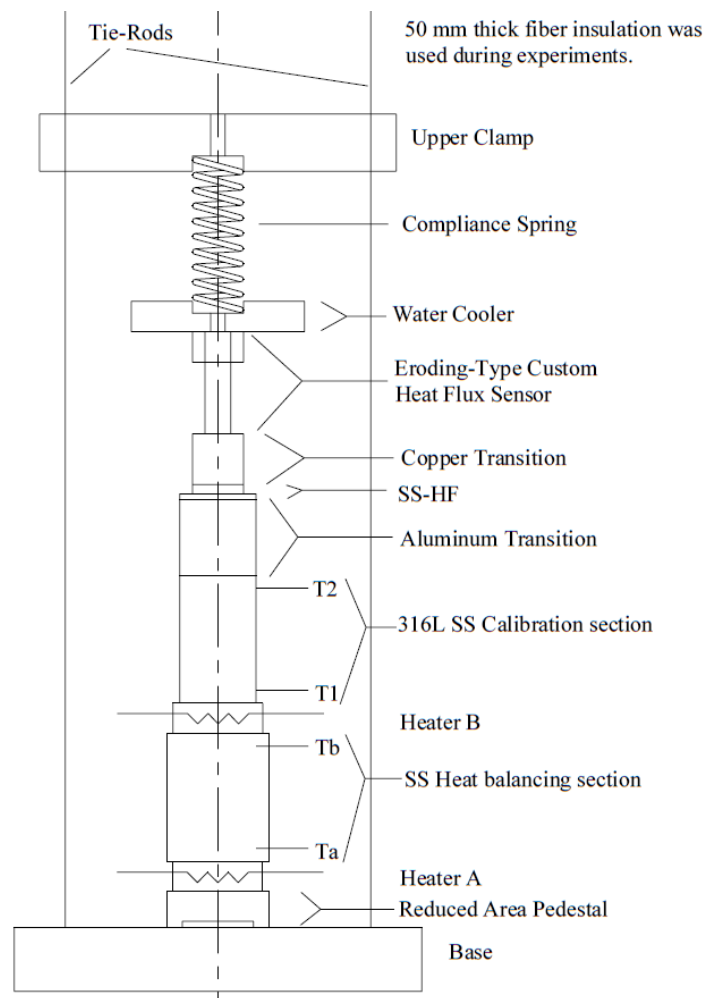
Figure 2.4. Setup used by Farrugia [65] to determine which of the sensor materials affect the steady-state component of heat flux.

A method used to test the thermocouple thermal response in the millisecond timescale utilises a water-droplet technique. This technique was presented by Buttsworth [49] in characterising an eroding thermocouple, but with a co-axial design (instead of the more common ribbon configuration). The apparatus used in

conducting the water droplet technique is reproduced from Buttsworth [49] and shown in Figure 2.5. In this setup, the thermocouple of interest is mounted through a block with their surfaces flush. The surfaces of the block and thermocouple are heated to a certain temperature (95℃ in the case of Buttsworth [49]). During heating of the block a nozzle vertically above the sensor surface is set up and a water droplet is prepared for free fall. During this process, a horizontal plate is placed between the nozzle and the heated block to avoid convection currents from the block heating the nozzle and water droplet. When the surface of the thermocouple reaches the prescribed temperature, the protecting horizontal plate is removed and the water droplet is released onto the sensor surface, creating a step change in temperature. Just before the droplet release, the temperature of the water droplet is measured by a thermocouple at the tip of the nozzle. This allows the evaluation of the thermal product of the water droplet to be used in equation (2.6), from which the effective thermal product of the sensor for the millisecond timescale can be determined.

$$\frac{T_{TC\,after\atop impact} - T_{TC\,inital\atop temp.}}{T_{water\atop initial\,temp.} - T_{TC\,inital\atop temp.}} = \frac{\left(\sqrt{\rho c k}\right)_{water}}{\left(\sqrt{\rho c k}\right)_{water} + \left(\sqrt{\rho c k}\right)_{TC}} \qquad \ldots (2.6)$$

From results reported by the author, it was noticed that for the water droplet technique, when a scalpel blade was used to set up the thermocouple junction and carried from the chromel to the alumel, the thermal product of the thermocouple $\left(\sqrt{\rho c k}\right)_{TC}$ from the measured heat flux coincided with that of the material on which the junction was set up, *i.e.* alumel. On the other hand, for tests in which the scalpel blade was carried from the alumel to the chromel, the thermal product calculated corresponded to that of the chromel. This observation was consistent throughout the several tests conducted by the author, which shows that establishing the junction with a scalpel blade gives a sensible level of confidence in which thermo-physical properties affect the millisecond timescale heat flux.

When the same experiment was done, but using a small area of abrasive grit carried over carefully from the chromel to the alumel, the thermal product of interest seemed to be much lower than that for alumel. It was proposed that since the grit produces scratches which are much finer than those created by the scalpel blade, it is probable that the junctions created with the grit reside very close to the insulation material,

while those created with the scalpel blade were found to reside around 30 μm away from the insulation. Hence, for junctions established with an abrasive grit, the insulation material ends up influencing the effective thermal product significantly.

In a separate scenario, when the surface of the thermocouple was abraded with an abrasive grit across the whole area, it was noted that the determined thermal product showed a relatively large variability between different tests. For the configuration of the discussed eroding thermocouple (co-axial), it is probable that when abrasion is created across the whole surface, multiple junctions are setup on both the chromel and the alumel with different and unknown quantities. This consequently results in a thermal product which is closer to the material on which the highest number of junctions are set up for the particular abrasion. Furthermore, it was also outlined that due to the fine scratches that result from the abrasive grit, the proximity of the junctions from the insulating material, which are different for each individual junction, and distinct between different abrasions also influence the effective thermal product, and hence could explain the noted variability.
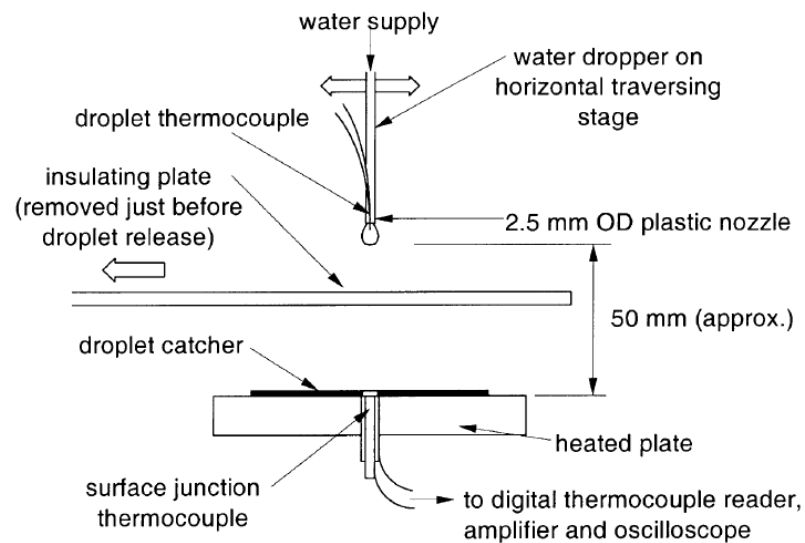
Figure 2.5. Water droplet setup used by Buttsworth [49] for evaluation of the effective thermal product.

Another technique used for thermocouple characterisation in the millisecond timescale uses a hot air gun. Cornelis et al. [68] used this method in two different configurations. In the first experiment, a shutter rig was used to expose the thermometer surface to a step heat flux from the hot gun. The second experiment

35

utilised a chopper rotating at a known frequency in between the hot gun and the sensor. This therefore allowed for a cyclic pulse train of heat flux to the sensor surface. Both experiments consisted of a hot gun mounted vertically below the sensor's instrumenting surface.

In the study by Cornelis et al. [68], the hot gun tests were not aimed to determine the thermal product, but to compare the rise times of different surface thermometers. In a similar study by Jackson et al. [43], a chopper experiment was also conducted for rise time evaluation, however instead of a hot gun, a 5 kW Tungsten lamp was used. In an earlier study by Gatowski et al. [72], the method of using a chopper for the determination of the rise time was not favoured as it was believed that the rise time of the heat flux arriving at the sensor surface with this method might not resemble a true step when compared to the expected rise time of the eroding thermocouple.

In the case of Cornelis et al. [68], three different surface thermometers were investigated, including a TFG as developed by University of Oxford, the HFM-7 by Vatell and an eroding thermocouple of the Nanmac type. From results published by the author, it was shown that from the shutter rig experiment, the rise times of the different sensors revealed to be in the range between 0.1 ms to 0.8 ms. The TFG sensor seemed to show the shortest rise time, followed by the thermopile HFM-7 and finally the eroding thermocouple. The heat flux calculated from the three sensors seemed to fall in the same range. The chopper and shutter experiments showed similar rise time results for both the TFG and the thermopile HFM-7, however for the eroding thermocouple, rise times obtained from the chopper experiment were smaller than the rise times obtained from the shutter experiment. This was attributed by Cornelis et al. [68] to be a result of the fact that with the chopper experiment, the temperature swing induced at the surface is superimposed to a relatively high steady-state temperature due to cumulative effect of the heat flux pulses. On the other hand for shutter rig measurements, the temperature swing is superimposed on a small mean surface temperature equal to room temperature.

Cornelis et al. [68] also mentioned that the eroding ribbon thermocouple required re-establishment of the junction several times during testing. From a relative error analysis done on the heat flux determined from the three types of sensors, it was

reported that the eroding thermocouple presents a relative error of 23%, which is the highest when compared to 13% for the TFG and 3% for the HFM-7.

Another method used for millisecond timescale characterisation involves a radiometric technique which uses a 500 W tungsten-halogen lamp with an ellipsoidal reflector. The thermometer is placed with the instrumenting surface facing the lamp, with both the lamp and thermometer setup on a rail to ensure the distance between the lamp and the probe is fixed and repeatable between different tests. To have consistent absorptivity between the different thermometers used, a uniform coating of soot is applied to the surface of each thermometer. Gatowski et al. [72] utilised this technique to determine the thermal product affecting the heat flux for four different types of surface thermometers. The thermometers tested in this work include an eroding thermocouple of the ribbon type, a resistance thermometer (TFG) based on Macor, a spot-welded surface thermocouple and a Bendersky-type co-axial thermocouple. It was shown that the thermal products that were obtained from experiment were lower than the thermal product of the 'typical' body material for each of the respective sensors, as assumed by several heat flux researchers [68] [35]. The only thermometer which showed a thermal product very close to that of the base material was the TFG sensor, based on Macor.

From tests done by the same author on a rapid compression machine (RCM), it was found that the different thermometers resulted in different measured surface temperature. The difference in the mean surface temperature between the eroding thermocouple and the TFG was around 40℃, with the TFG showing higher temperatures. This is understandable and expected due to the fact that each thermometer is based on different materials. With a one-dimensional treatment, the resulting heat flux as determined from the different thermometers revealed some differences as well. The TFG showed around 20% lower peak heat flux when compared to the heat flux from the eroding thermocouple. This discrepancy was attributed by Gatowski et al. [72] to the fact that the TFG was based on a ceramic (Macor), but fitted to an iron-based RCM. It was therefore argued that disturbance of the isotherms might have resulted due to the Macor, which hence led to the difference in the heat fluxes.

2.2.8.2 Microsecond timescales of interest

In this section, two different methods of characterisation of surface thermocouples at microsecond timescales of interest are presented. The first method is based on laser testing, whereas the other method involves shock wave experiments. Experiments done in the microsecond timescales are used for both thermo-physical properties characterisation, but also for rise time determination.

The laser pulse technique seems to be the most popular method for the timescale being discussed. This technique was used by Farrugia [65], Gatowski et al. [72] and Wang et al. [41]. Farrugia [65] used a pulsating laser setup at a frequency of 10 kHz. The copper vapour laser had a power rating of 15 W and was made to pulsate on the Stainless Steel-based eroding thermocouple surface. Temperature data was acquired with a sampling frequency of 100 kHz. From the results acquired by Farrugia [65], beating was noted and hence the data acquired could not be used for the determination of rise time, but was used to determine the thermo-physical properties pertinent to the microsecond timescale of operation. This was determined from the cooling part of the surface temperature trace by curve fitting the decay and comparing the trend line to the solution given by equation (2.7), which is the solution for the one-dimensional heat diffusion equation with the condition that a finite energy pulse hits the surface instantaneously. From curve fitting, the constant β in equation (2.7) could be found, which was then used in equation (2.8) with thermo-physical properties (α, ρ and c) pertaining to the different thermocouple materials. The resulting heat flux was compared against that imposed by the laser beam calculated from the laser power and frequency specifications.

$$T_s = \beta t^{-0.5} \qquad \qquad \text{...} (2.7)$$

$$Q'' = \beta \rho c \sqrt{\pi \alpha} \qquad \qquad \text{...} (2.8)$$

Through this procedure, Farrugia [65] concluded that the Mica is the material that mostly affects the heat flux at the high frequency of 10 kHz. Recall that in section 2.2.8.1, it was reported that the same author found that for steady-state operation, the sensor body material (*i.e.* Stainless Steel) was found to affect the heat flux. From testing conducted on the engine it was shown that the cut-off frequency between

using the Stainless Steel to that of using Mica thermo-physical properties is above the range of interest in internal combustion studies. Hence for the purpose of obtaining the transient component of heat flux in the extension of the exhaust port of a SI engine, the author made use of the Stainless Steel thermo-physical properties.

The laser pulse technique was chosen for the measurement of rise time by Gatowski et al. [72]. The author preferred this method over the previously explained hot gun – chopper method as it was argued that the very short rise time of the laser pulse ensures a step heat flux with a rise time much shorter than the expected response time of the surface thermometers. In this research, the laser pulse incident on the sensor was split using a beam splitter onto a photo-diode. This allowed the evaluation of the instant at which the beam hit the thermometer surface. From experiment results, it was shown that the rise time of the eroding thermocouple was around 20.8 μs, which according to Gatowski et al. [72] is much shorter than the timescales of interest in IC engine testing, which are typically measured in milliseconds. The use of the laser pulse method for characterisation of other surface thermometers investigated by Gatowski et al. [72] (TFG, Spot welded thermocouple and Co-axial thermocouple) was less satisfactory. This was due to the surface configuration of these thermometers, which required the whole sensing surface to be irradiated. Expanding the laser beam to cover the whole sensing surface resulted in small and undetectable heat flux levels.

The second method used for characterisation of thermocouples in microsecond timescales was that put forward by Buttsworth [49], and based on shock wave propagation. The experimental setup used is reproduced in Figure 2.6. This setup consists of a length of tube which is split at around the mid-section by cellophane diaphragms; separating a 'driver section' from the 'shock tube section'. The surface thermocouple of interest is fitted at the end wall of the shock tube section, opposite the cellophane diaphragms. Initially both sections of the tube are filled with air. The driver section is then pressurised with helium until the cellophane diaphragms rupture, which create a shock wave in the air inside the shock tube section. From two pressure transducers fitted along the shock tube length at some distance apart, together with several surface thermocouples, the shock wave propagation is identified.

Rise times for junctions formed with 400 grit or 1200 grit on a co-axial eroding thermocouple proved to be less than 1 μs. For grits of 120, the rise time was found to be around 1 μs. The thermal products affecting the heat flux at these time scales, with the junctions established using the abrasive grit showed significant variability with a standard deviation of around 9%. It was also noted that the thermal product for junctions established using the abrasive grit proved to be around 30% smaller than that obtained for the millisecond timescales from the water droplet experiment (described in section 2.2.8.1). This lower value of thermal product at the microsecond timescales is attributed by Buttsworth [49] to be an effect of the insulating material on the thermocouple junction. The effect of the insulation material was found to be higher if the abrasion is done with a finer grit, due to the fact that the junction will be created physically closer to the insulation material.

Shock wave experiments were also done with thermocouple junctions established using a scalpel blade. It was found that for junctions set up using this method, inconsistent results of rise time were obtained. This was attributed to the variability in the effective depth of the junction due to the fact that the scalpel blade scratch was drawn by hand.
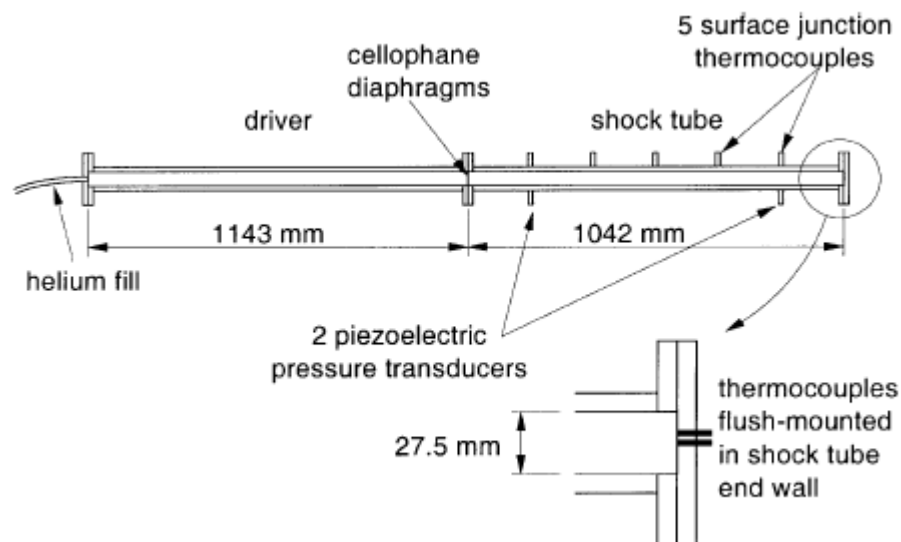
Figure 2.6. Shock tube setup used by Buttsworth [49] for evaluation of effective thermal product at microsecond timescales, and determination of the rise time.

Having looked at the different methods that are used for the purpose of thermocouple characterisation on both long and microsecond timescales, together with the results reported from several authors, it appears clear that the characterisation procedure is vital for reliable heat flux determination. From literature consulted, it was found that the rise times of surface thermometers vary significantly, even for the same type of thermocouple. The rise times reported for eroding surface thermocouples vary between < 1 μs to 0.35 ms. Even though the reported range seems very large, it is still found to be adequate for in-cylinder heat flux measurements, which is concerned with rise times on the order of 1 ms or larger [36] [43]. Whilst previous researchers have not flagged the rise times of the presented surface thermometers as an issue, characterisation experiments showed that large variances in the effective thermal product can be experienced, which was found to be at least frequency dependent and also reliant on the nature of the junction and its location. It was also found that it is highly unlikely that the effective thermal product resembles the thermal product of one material in the sensor, especially at the microsecond timescales.

2.2.9 Spatial Surface Temperatures

To investigate variations in heat flux due to the thermocouple mounting location, ideally several surface thermocouples would be fitted in the combustion chamber. This comes with the limitation that sound fitment of several thermocouples is often challenging due to complex cooling passages. Measurement of surface temperature at different locations allows for the determination of the parameters which drive different heat fluxes. Hohenberg [5] attributes spatial heat flux variation in motored engines to the fluid transport phenomena. Amongst the most popular literature of spatial heat transfer investigation, between two to five surface thermocouples were usually fitted simultaneously in the combustion chamber [7] [23] [34]. However, Hohenberg [5], from Daimler-Benz AG fitted seventy-two thermocouples in the cylinder head. Recently, Hennes et al. [40], also from Daimler AG, fitted twenty-six surface thermocouples in the piston and twelve in the cylinder head. It should be mentioned that both these authors made use of custom-made surface thermocouples of the co-axial configuration.

2.2.10 Other Considerations

The surface temperature swing of the combustion chamber is usually of the order of around 10 K to 20 K, even though both higher and also lower temperature swings have been occasionally observed [6] [40]. This means that for high fidelity of the thermocouple signal acquisition and processing, rigor should be practiced. One of the parasites in the acquisition of these sensitive signals is the electrical noise originating from the surroundings. Thermocouples usually have very small thermoelectric voltage response, for example the type-E thermocouple which has one of the highest voltage response, provides a thermoelectric voltage of around 59 μV/K. Due to this, an amplifier with a high gain has to be used to amplify the signal. Great care is required when amplifying these signals, especially due to the fact that if any electrical interference is present between the sensor and amplifier, this will also be amplified, resulting in a very noisy data. To minimise this problem, authors such as Wendland [18] and Nijeweme et al. [23] have adopted a method in which the surface thermocouple was connected to the recessed thermocouple such that the output voltage would be the difference between the two. This method has at least two advantages, but also a disadvantage to it.

The main advantage is that by considering the difference between the two signals, the amplification is performed on just the temperature swing, whereas if each thermocouple is amplified individually, the DC value of the thermocouple signal will be amplified together with the swing, which therefore reduces greatly the resolution of acquisition of the surface temperature swing. This method also removes the need for the cold-junction compensation.

This procedure, unfortunately, has an inherent error due to the fact that the thermoelectric voltage does not vary in a linear proportion with the temperature, but is usually represented by a polynomial with several high order terms. This implies that the temperature difference as obtained from a conversion of the potential difference between the surface and recessed thermocouples is not strictly the same as the actual temperature difference between the surface and the recessed location. It is understood however that the resulting discrepancy for the temperature difference expected between the surface and the recessed junction should be small; however when temperature swings are as small as 10 K, the slightest error needs to be

considered. To consider a practical example, if say the surface temperature is at an instantaneous temperature of 110℃ and the recessed temperature is 108℃, the corresponding millivolt reading from each individual thermocouple, assuming it being an E-type, is 6.998 mV and 6.862 mV respectively. If these two thermocouples are connected together such that the difference is 0.136 mV, this converts to a value of 2.3℃ according to the tables provided by the National Institute of Standards and Technology (NIST). This means that the temperature difference being obtained as a voltage difference overestimated the actual temperature difference by 0.3℃.

Another possible error in the determined heat flux from surface temperature measurement could be a result of pressure fluctuations in crevices. As mentioned in a previous section, and will be further explained in forthcoming chapters, the effect of the pressure work on the boundary layer results in a component of heat flux which leads the driving temperature [17] [18] [22]. Due to this, it is thought that the fitment of the surface thermocouple should be such that it does not promote any crevices. This is to prevent from having any pressure oscillations in that crevice region which might instigate an augmented heat flux measurement error due to the possibility of a small magnitude of pressure work in the crevice. To mitigate this, Farrugia [65] fitted the eroding surface thermocouples using an interference fit as this was believed to impose less crevice volumes when compared to a thread type fitment. This concern was also raised in [13] by Overbye et al. who carefully matched the screw-type thermocouple adaptors to the tapped hole in the cylinder head, to minimise as much as possible the crevice volume in the threads.

2.2.11 Conclusions on Surface Thermometry

Having outlined the existing surface thermometry technology, together with its limitations and precautious measures, it can be appreciated that sound practice in the choice, integration and use of the available technology is a strong limiting factor on reliable engine surface temperature measurements and heat flux determination. Although the majority of the mentioned problems/limitations had been known for several decades, one could very rarely find a heat flux study in the IC engine field which poses none of the above. This was better appreciated when the thermocouple probes in this study were procured, fitted and used in the engine considered in this

work. Due to this, it is re-iterated that for robust surface thermometry and heat flux measurements, the key concepts outlined are to be followed.

The next section presents a review of literature on the pressurised motored method. This test method was used throughout this dissertation for both mechanical friction and in-cylinder heat transfer measurements.

2.3 The Pressurised Motored Method

The Pressurised Motored method refers to the concept of driving an unfired engine with an electrical motor, whilst pressurising its intake manifold to simulate similar in-cylinder pressure loading conditions that the engine would see in fired conditions. Such method is not a new concept in the engine testing sector. It is reported by Mauke et al. [4] that the method was first developed by Ullmann [73] in 1939. Authors such as Dao et al. [25] and Pike and Spillman [74] had used this method in the mid-twentieth century namely to analyse engine mechanical friction and heat transfer from the cylinder. Nikanjam and Greif [75] utilised the method with a rapid compression machine for heat transfer measurements during the compression stroke. Lately, Torregrosa et al. [7] reported the use of this method for transient heat transfer measurements through the cylinder wall, whereas Allmaier et al. [76], Mauke et al. [4] and MAHLE [77] used the method for mechanical friction determination.

For testing purposes, motoring methods are usually preferred over fired ones. This is due to the elimination of the overpowering effect and variability induced by combustion in fired operation. Motoring also yields easier data acquisition and post-processing. However, it is well known that data obtained from conventional motored tests is sometimes far off from the actual operating conditions exhibited during firing; hence its use is sometimes limited. The Pressurised Motored method is favoured over conventional motoring for this reason. It provides a bridge between the conventional motored tests and the fired tests as it better simulates the pressure loading of a fired engine, without the presence of combustion.

Owing to the fact that combustion is not present, for a motored engine, the indicated mean effective pressure (IMEP) magnitudes are very small, in fact the IMEP computed over the whole cycle ($IMEP_{720}$) is known to be solely a function of heat

losses, blow-by losses and pumping losses. The $IMEP_{720}$ is obtained from integration on the indicator (p-V) diagram. The brake mean effective pressure (BMEP) is a measure of the total energy expenditure of the motored engine, and hence is a measure of the losses represented by the $IMEP_{720}$ along with mechanical frictional losses represented by the FMEP, and accessory losses (AMEP) if any. From this consideration, for a motored engine without any accessories, the FMEP can be simply obtained by a subtraction of the $IMEP_{720}$ from the BMEP.

For a fired engine, the $IMEP_{720}$ and BMEP are very large values when compared to the FMEP. Tests done in the author's Masters dissertation on a fired engine [78] [79] showed that at 2220 rpm and 151 kPa MAP, the $IMEP_{720}$ was 12.7 bar and the measured BMEP was 11.2 bar. This yields an FMEP of 1.5 bar. If the $IMEP_{720}$ is measured with an uncertainty of, say $\pm$ 2.5% (or $\pm$ 0.3 bar) and the uncertainty in the BMEP is $\pm$ 1.1% (or $\pm$ 0.1 bar), the uncertainty propagation yields a 21.6% uncertainty in the FMEP. This issue is reduced to a great extent when the FMEP is computed for a motored engine, since both $IMEP_{720}$ and BMEP are small and compare well in their magnitude to the FMEP. This leads to a more reliable FMEP value obtained from the experimental motored data. Similar to conventional motored engines, a pressurised motored engine also benefits from very small error propagation on the FMEP, since the $IMEP_{720}$ and BMEP of a pressurised motored engine are small and similar in magnitude to the FMEP. Hence the pressurised motored method offers the advantages of a conventionally motored setup, but with an additional benefit of a fired-representative in-cylinder pressure load.

The dependency of the uncertainties affecting the IMEP are discussed in great detail by Mauke et al. [4], who attributes them mainly to the thermal shock in the pressure transducer used for indicating measurements, and the angular phasing of the in-cylinder pressure data with the true TDC of the engine. It is reported by Mauke et al. [4] that the error originating from the thermal shock of the piezoelectric pressure sensor already adds up to more than $\pm$ 1.1% uncertainty in the IMEP. Pipitone et al. [80] reports that a pressure phasing error of 1 DegCA yields 10% error in the IMEP. Usually the pressure phasing done with a dedicated TDC capacitive probe can yield a maximum accuracy of 0.1 DegCA, hence if simple proportion is assumed, the error in the IMEP originating from the pressure phasing adds up to another $\pm$ 1% error in

the IMEP. This means that an error of around 2% in the IMEP is almost inevitable. One need not forget the error associated with the BMEP, which even though perhaps is lesser than that originating from the IMEP, if the engine torque measuring system is not well designed, then significant errors can result also in this quantity.

When compared to conventional fired tests, another advantage of the pressurised motored method is that the thermal loading on the engine is derived solely from gas compression, as dictated by the polytropic law. This shows that the in-cylinder gas temperature is (simplistically) dependent on just three parameters, being; the intake gas temperature, the polytropic exponent of compression and the cylinder volume ratio. Having outlined this, it should be clear that from a simplistic consideration, increasing the pressure loading by imparting higher manifold pressurisations theoretically leads to no effect on the in-cylinder bulk gas temperature. Similarly, changing the engine speed should theoretically result in no difference in the bulk gas temperature either. This quality is beneficial for friction measurements as it allows a direct correlation between pressure loading and engine friction, without variability induced by the thermal effect at different setpoints of engine speed and pressure load. One should however appreciate that practically some temperature variations with different engine speed and mechanical load (usually represented by peak in-cylinder pressure, PCP) will still be seen because of different heat transfer characteristics.

Having looked at the beneficial qualities of the pressurised motored method, one must note that this method still does not capture all the fired engine effects. On a typical motored engine, the peak in-cylinder pressure occurs at around 1 DegCA before top dead centre (BTDC), whereas for a typical working condition, a fired engine shows a peak in-cylinder pressure at around 10 DegCA after top dead centre (ATDC), depending on the start of combustion. This observation can be seen in Figure 2.7, reproduced from Mauke et al. [4]. At around the TDC location, the piston velocity is virtually zero and the connecting rod angle (normalised, β) is vertical. Such situation changes when the piston is at 10 DegCA ATDC (LPP at fired conditions). At this position, piston velocity is appreciable, and the force through the connecting rod has a component that forces the piston to the side wall of the cylinder (lateral thrust), creating a normal reaction for friction. Due to this condition, Mauke et al. [4] debates that the FMEP obtained from the pressurised motored method underestimates the actual friction in a fired engine running at a similar engine speed

and PCP setpoint. Allmaier et al. [76] does point out such observation however he states that the piston speed has minimal difference on friction determination between the two methods. Allmaier et al. [76] added that to make the pressurised motored engine more representative of the typical fired engine, the pressurised motored setup should be rotated faster to compensate for piston velocity.
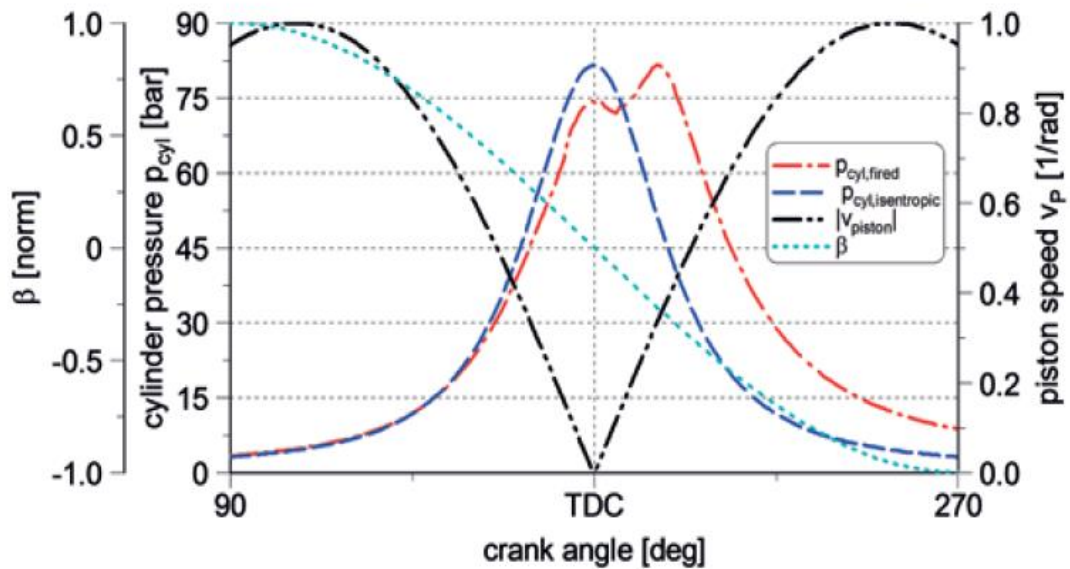
Figure 2.7. Comparison of in-cylinder pressure between pressurised motoring and firing [4].

Another difference evident between pressurised motored operation and fired operation can be noted if one compares the in-cylinder pressure traces shown in Figure 2.7 over the crank angle range between +90 DegCA and +180 DegCA. It can be seen that over this range, the pressure in the fired engine is much higher than that in the motored engine. This is mainly due to the fact that in fired engines the gas retains a significant portion of internal energy, even during the final phase of the expansion stroke. This is because combustion would have increased significantly the in-cylinder gas temperature. On the other hand, for a motored engine the gas at the end of the expansion stroke would be at a lower pressure than that at the symmetric crank angle in the compression stroke. This is because heat and blow-by losses would have decreased the internal energy of the gas.

Mauke et al. [4] also argues that the other main difference between pressurised motored tests and fired tests is the higher temperature induced by combustion in the firing scenario. It is said [4] that such temperature differences induce FMEP

discrepancies due to lubrication viscosities and thermal warpages. MAHLE [77] describes this thermal discrepancy as an advantage, since a comparison of FMEP obtained from pressurised motored testing and fired testing allows the understanding of the thermal effect on FMEP. More on this will be discussed after the presentation of results in Chapter 4.

Another difference between the pressurised motored method and the fired method is the gas mass ingested per cycle. It should be remembered that for pressurised motored operation, the high peak in-cylinder pressure obtained is a result of a higher manifold absolute pressure (MAP), and hence directly implies that a larger mass of gas per cycle is ingested when compared to a similar setpoint of engine speed and PCP in firing. Pressurising the intake manifold up to a pressure of 2.5 bar absolute implies that the engine accommodates more than twice the mass of air occupied at naturally aspirated, fired conditions. Such increase in mass of gas has to be expelled on the exhaust stroke from the same valve curtain area as that of the fired engine. Due to this, a recompression of the exhaust gases during the displacement phase of the exhaust stroke was found to occur during the course of this dissertation. This observation was made both experimentally and also from one-dimensional simulation (reported in section 4.3.2). Other authors using the pressurised motored method [9] [25] [75] did not report such anomaly.

2.3.1 FMEP studies using the Pressurised Motored Setup

Three comprehensive studies which present or promote the use of the pressurised motored setup were presented by MAHLE [77], Mauke et al. [4] and Allmaier et al. [76].

MAHLE [77] presents a study supplemented by results from Deuß [81]. The work by Deuß [81] was in the native language and could not be reviewed, but a comprehensive description of the results is given by MAHLE [77] and discussed here. The study analysed the effect of different parameters on FMEP, as determined from the fired engine and the pressurised motored engine, when run at similar conditions of speed and PCP. The parameters investigated were; the piston installation clearance, piston pin offset, the width of the first compression piston ring, the tangential force by the oil control ring, coating of the piston pin, engine oil

viscosity and piston skirt. Each of these parameters were varied individually and the corresponding total engine FMEP was measured from the two testing setups (pressurised motored and fired). The pressurised motored engine utilised air at a temperature of 25℃.

As a general observation from the results presented, it was noted that when each of the outlined parameters were varied individually, the magnitude difference incurred in the FMEP as a function of engine speed and PCP over the whole test matrix was similar between the fired and pressurised motored cases. On the other hand, however, the characteristic of variation of the FMEP with engine speed and PCP was different between the two setups.

Based on the data presented, MAHLE [77] suggests that the pressurised motored method is of limited use in engine optimisation for actual driving cycle, however the comparison between similar tests done on a fired engine and a similar pressurised motored engine allows for a better understanding of friction mechanisms. MAHLE [77] attributes this advantage to the fact that the pressurised motored engine decouples the contribution of pressure load from thermal load on the FMEP. Hence, since the mechanical load is "similar" between the two engines, whilst the thermal load is different, MAHLE attributed the FMEP difference between the two setups to be a result of the thermal differences, and its associated complications of thermal warpages and expansions. This is understood and appreciated, however upon review of this work, it was noted that no comparison was made in the light of the difference in FMEP that might be induced by the different angular phasing of in-cylinder pressure with crank angle between the fired and pressurised motored engine.

The effect of the different in-cylinder pressure angular phasing between fired and pressurised motored engine operation is outlined by Mauke et al. [4] in a report published by Kistler. Mauke et al. [4] highlights that the FMEP contribution by the crankshaft and valvetrain is not affected by the in-cylinder pressure angular phasing. The FMEP which is affected is that coming from the combination of piston, ring pack and liner. The author attributes this discrepancy in the piston-ring FMEP as a result of a different lateral thrust between the piston and the wall during the motored and fired cycles. The reason for this was already presented in section 2.3. To improve the pressurised motored method pressure load sensitivity on the FMEP due to the

different angular phasing of the pressure, Mauke et al. [4] suggests a method which gives the setpoint PCP that the pressurised motored engine should be run at to experience the same average friction work as that of the fired engine.

The method commences by geometrically deriving the lateral thrust for both the fired and pressurised motored engine, given by equation (2.9) and equation (2.10) respectively. The product of the lateral thrust, piston speed and coefficient of friction is then integrated over the crank angle duration of the closed part of the cycle. This gives the work done by piston-liner friction force, as shown by equation (2.11) and equation (2.12). This integration assumes that the coefficient of friction is constant throughout the cycle and similar for both the fired and pressurised motored engine. An equal energy balance is then conducted according to equation (2.13), where the constant C is included to take into consideration the differences in the FMEP induced between the fired and pressurised motored engine due to thermal warpage, thermal expansion and different lubricating conditions. According to the authors, the constant C should be calibrated for every engine – for their engine it was determined as 0.62. Once a value for C has been determined, the peak in-cylinder pressure required for the pressurised motored setup to yield a better representation of the FMEP of the fired engine is found from equation (2.13). With this method, therefore, it is not the peak in-cylinder pressure which is matched between the fired and pressurised motored method, but the work done by piston friction force (originating from piston lateral thrust). According to Mauke et al. [4], for the six cylinder engine used in their research, the PCP that needed to be set according to the lateral integral force method was between 3 bar smaller to 23 bar larger than that of the equivalent fired setpoint (assuming $C = 1$) throughout the test matrix. This variation of difference in PCP between the two methods was found to be significantly dependent on the location of the 50% mass fraction burn. When the combustion is retarded whilst retaining the same fired IMEP and engine speed, the PCP of the fired engine decreases, whereas the PCP required by the lateral integral force method has to increase to retain a similar work done by the piston frictional force. This can be understood by the fact that retarding the 50% mass fraction burn results in a fired PCP that occurs late in the cycle when the connecting rod angle is very large, hence very high lateral piston force, and consequently piston friction. For the pressurised motored engine to exhibit

the same piston friction work, the PCP has to be therefore set significantly higher than for the fired case for late combustion.

After having reviewed the lateral integral force method, a potential downside was identified. Since the two setups (fired and pressurised motored) are required to be run at different PCPs, the crankshaft bearings will be exposed to a disproportionately high loading in pressurised motoring if using the lateral integral force method. Hence, it is thought that while the method presented by Mauke et al. [4] has a valid use to better the FMEP contribution from the piston-liner of the pressurised motored engine, the FMEP contribution from the cranktrain will be probably made less representative.

$$F_{N,fired} = \left[\frac{(p(\theta) - p_{cc})A_p}{\cos\beta}\right] \sin\beta \qquad \ldots (2.9)$$

$$F_{N,motored} = \left[\frac{\left(p_0\left[\frac{V_{max}}{V(\theta)}\right]^\gamma - p_{cc}\right)A_p}{\cos\beta}\right] \sin\beta \qquad \ldots (2.10)$$

$$E_{FN,fired} = \int_0^{2\pi} F_{N,fired}(\theta) . v_p(\theta) . \mu \, d\alpha \qquad \ldots (2.11)$$

$$E_{FN,motored} = \int_0^{2\pi} F_{N,motored}(\theta) . v_p(\theta) . \mu \, d\alpha \qquad \ldots (2.12)$$

$$E_{FN,motored} = C . E_{FN,fired} \qquad \ldots (2.13)$$

In a study by Allmaier et al. [76], similar work to that done by MAHLE [77] was presented, where the author also measured the total engine FMEP and compared the results obtained from pressurised motoring to that from a similar fired engine run at the same PCP and engine speed. In a separate publication, Allmaier et al. [82] put forward an interesting approach for future FMEP studies involving the use of the pressurised motored engine.

In [82], a simulation of the cranktrain FMEP was conducted based on the software package, AVL Exite Power Unit ®. The simulation is capable of predicting the cranktrain FMEP (main and big-end bearings) as a function of the elastic properties of the involved bodies, the roughness of the surfaces involved and the complex

rheological properties of the lubricant. For simulation validation, numerous experiments using dedicated journal bearing test rigs were conducted at different crankshaft speeds, pressure loads and lubricants.

The simulated cranktrain FMEP is used together with valvetrain FMEP obtained experimentally from a dedicated test rig, and total engine FMEP obtained from the pressurised motored setup. This allows for a virtual engine strip-down which makes it possible to investigate the FMEP contribution of every sub-assembly in the engine. Consequently, the FMEP behaviour originating from the piston-ring sub-assembly can be investigated and compared to that of an equivalent fired engine. With this method, friction maps of sub-assemblies can be generated, which also gives the possibility of investigating optimisations of different parts for future engine designs.

Even though the studies presented by the above three authors seem similar in nature and strive towards the same aim, particular differences still emerge between the three works mentioned, some of which seem contradictory. Allmaier et al. [76] reported that the pressurised motored engine gives a higher FMEP in general, when compared to a fired engine. This was shown through experiments at 800 rpm, 1000 rpm and 1200 rpm at a PCP ranging from 30 bar to 180 bar on a large, heavy-duty, 13.0 L engine. Mauke et al. [4], on the other hand, for a 2.0 L engine showed that at engine speeds of 1500 rpm, 2400 rpm and 3000 rpm, the pressurised motored FMEP is either very similar, or less than that obtained from the fired engine.

Allmaier et al. [76] reports that the different location of peak pressure between firing and motoring should not result in a significant difference in the FMEP, since piston velocities are still small at crank angles synonymous to the firing location of peak in-cylinder pressure. The author suggests that the pressurised motored engine should be rotated faster to compensate for the discrepancy in the piston velocity at the location of peak in-cylinder pressure (LPP) motoring to LPP firing. In contrary, as described earlier, Mauke et al. [4] states that the in-cylinder pressure angular phasing is a major contributor to the difference in FMEP between the two methods.

The results by Allmaier et al. [76] show that the fired FMEP and pressurised motored FMEP are relatively close at very low PCPs (30 bar) and very high PCPs (180 bar), however at mid-range (120 bar), the FMEP from the two setups are different by around 0.25 bar, which is close to 25% of the average FMEP magnitude. The author

attributed the higher pressurised motored FMEP (than fired FMEP) at mid-range load to a higher liner and lubricant temperature in the fired engine. According to the author, this higher bulk gas temperature in the fired method decreased the viscosity of the lubricant and resulted in a drastic decrease in FMEP, which offset any increase in the FMEP due to pressure load. At higher pressure loadings however, the author explains that the fired FMEP and pressurised motored FMEP became similar again because the pressure load contribution on the FMEP offsets the negative thermal contribution on the FMEP in the fired engine.

2.3.2 Review of the research conducted in the previous project

This dissertation is a continuation of a previous research by the same author, started in the Masters dissertation [78]. In the previous project, a 2.0 HDi engine was tested first in the fired configuration on a water-brake dynamometer setup. FMEP testing was done using the Morse Test, Willan's Line and the Fired Indicating method. The engine was then transferred onto a newly built Pressurised Motored test rig and some preliminary tests were also done.

Outcomes from the Masters were mainly that the fired FMEP testing induces large uncertainties; both due to error propagation, but also due to a higher difficulty to maintain accurate setpoint stability of the engine and its environment (on the tested water brake dynamometer). With the pressurised motored method, a significant improvement was noticed as regards setpoint stability and ease of testing. Smaller data variability was also noted and FMEP uncertainty due to error propagation was drastically reduced. The shunt pipe idea, as proposed by Gilbert Sammut, a co-author in [79] and later first author in [83] [84], was also implemented to the pressurised motored setup, by which the intake manifold is shorted to the exhaust manifold such that the gas is re-circulated. With this configuration, the make-up gas flow required was shown to be minute as it is only required to supply the blow-by gases. In fact, it transpired that a conventional shop floor compressor is sufficient to supply a 2.0 L engine up to 3000 rpm with manifold pressures of up to 2.5 bar absolute. This allowed peak in-cylinder pressures of up to 120 bar to be achieved at minimum cost. For more information on this earlier work, the reader is referred to [78] and [79]. It was later found that the shunt pipe idea, even though not well communicated in

literature, was used in 1963 by Pike and Spillman [74]. In a later paper by Millington and Hartles [85], the review given by Holler from Caterpillar Tractor Company, states that for large engines, presumably without the use of a shunt pipe, the pressurised motored method was found to be severely taxing on the laboratory air supply, which led to the preclusion of its use at extreme test points. From an email communication with Allmaier et al. [76] during the duration of this dissertation, it was also confirmed that the idea of shunting the air from the exhaust to the intake side of the engine was also used in their research.

Although an FMEP testing session was conducted in the Masters dissertation on the pressurised motored setup, the main focus was the building of the setup, its functionality, together with setting up the associated LabVIEW scripts to control the engine, as well as to post-process the acquired data for FMEP determination. Furthermore, during the Masters research project, a sensor which provides appropriate angular phasing between the in-cylinder pressure trace and the crank angle was not available, hence the FMEP data acquired suffered significant errors due to uncertainties in the IMEP originating from this angular phasing.

3 ENGINE SETUP AND SINGLE CYLINDER MODIFICATION

In this chapter, an overview of the pressurised motored setup is given, together with modifications done to allow the engine to run (motored) on a gas other than air. Furthermore, engine geometry and cylinder head flow tests are detailed for later use in the one-dimensional models discussed in Chapter 6. The last part of this chapter deals with the conversion of a four cylinder engine to single cylinder operation, together with the associated balancing strategy. A detailed account is also given on the fitment of surface thermocouples in the cylinder head for a better understanding of the results of surface temperature and heat flux presented in Chapter 5.

3.1 Engine Test Setup

The pressurised motored setup as designed and manufactured in [78] consisted of the engine mounted on a test bed, and coupled to an 18 kW alternating current (AC) motor through a solid shaft between two Layrub 70+ 2/4 M14 flexible couplings. The AC motor was powered by a 47 kW Lenze ® variable frequency drive (VFD). The pressurised motored setup is shown in Figure 3.1.

A 3600 pulse per revolution (ppr) BEI® encoder was fitted to the crankshaft (auxiliary pulley side) using a custom-made, Kistler-type adaptor which was used as the timing signal for the data acquisition measurement system. The one pulse per revolution channel (Z-index) of the encoder was utilised as a phase-marker for post-processing of data. The data acquisition systems used were from National Instruments. The crank-angle resolved signals were acquired by: PCI 6251, USB 6341 and BNC USB 6363. The slow-speed steady-state signals were acquired through a PCI 6221. The software interface used for the data acquisition systems was LabVIEW. All LabVIEW virtual instruments for data acquisition and signal post-processing were developed either during this Doctoral work or in the Masters dissertation [78].

To determine the BMEP of the engine, the torque produced by the electric motor was measured. The method of torque measurement used is similar to the concept used on

electric brake dynamometers, where the casing of the AC motor was designed to swivel about its main shaft axis. The motor casing was constrained from rotating by attaching to it a moment arm, held by a perpendicular S-beam load cell. A 3D model showing the motor assembly is given in Figure 3.2. It should be noted that in the actual setup the load cell was held from the top of the structure and not from the bottom as shown in the image, such that during operation it is pulled in tension.
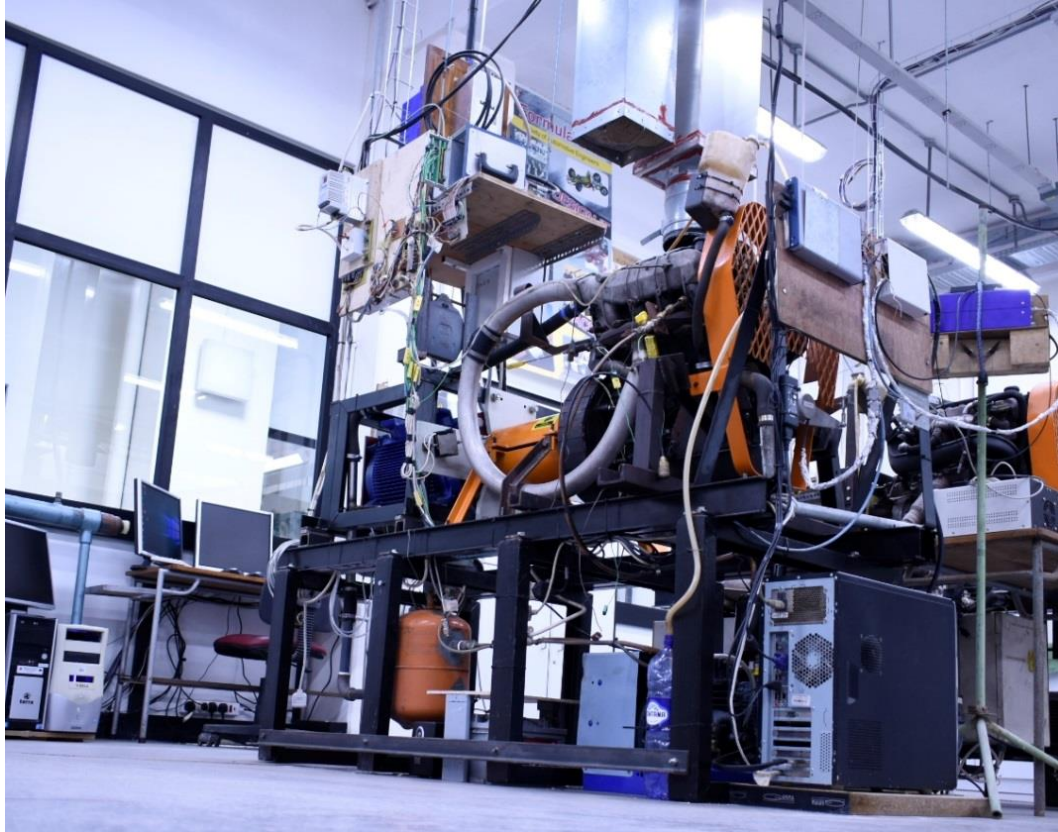
Figure 3.1. The pressurised motored setup.
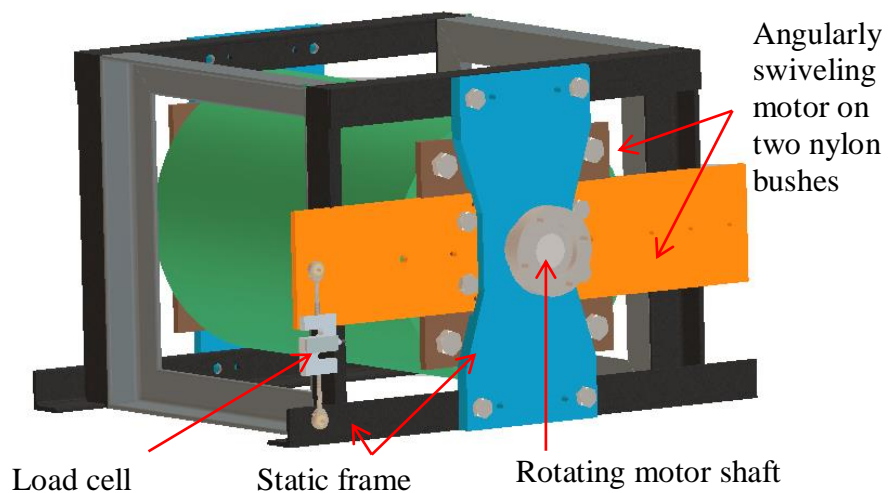
Figure 3.2. Motor assembled within the angle-iron frame.

Another method of torque measurement was used occasionally throughout this work where a full-bridge strain gauge system was installed on the rotating shaft, coupling the engine to the AC motor. This system allowed the determination of torque through the measurement of angular twist of the shaft. Initially a wireless transmitter-receiver, already available at University of Malta [86] was tested for data transmission between the rotating strain gauges and the computer receiving end. This system however proved to be not fit for this application since it showed data miss when configured to sample at more than half of its documented sampling rate capability. Battery lifetime was also relatively short. To resolve this issue, an Arduino UNO system was used in conjunction with a freeware sketch titled "Analog Bin Logger" available from the Arduino "SdFAT" library. This sketch makes use of the Arduino buffers and the data acquired is temporarily stored in the buffers until saturated. When this condition occurs, the data from the buffer is sent over to the SD card for permanent storage in a '.bin' file. Such methodology allowed a high sampling rate. The Arduino system was mounted directly to the drive shaft, close to the strain gauges and their amplifier. A Bluetooth module was also connected to the Arduino board in order to allow transfer of data from the SD card to a nearby computer or Android device, whenever data is not being acquired. Since the Arduino was a stand-alone data acquisition system, some sort of synchronisation was required between the Arduino data and the other data acquired through the National Instruments platform. To achieve this, an opaque disk with a large central hole (for the drive shaft to pass through) was constructed and mounted statically around, but not touching the drive shaft. A hole of 2 mm diameter was drilled into the opaque disk and made to coincide with a phototransistor (TCST2103) mounted to the drive shaft. The phototransistor was attached to the drive shaft using a custom-made aluminium clamp. The clamp was made as narrow as possible in order not to alter the elastic properties of the main shaft. Such system enabled the acquisition of a one pulse per revolution, which in this study was made to coincide with static TDC setting of pistons 1 and 4. The drive shaft torque measurement system provided a very clean torque measurement, however due to its dependability on batteries it was only used occasionally when its use was only crucial. For a greater detail on this system, the reader is referred to [87].

3.1.1 Modifications to the Pressurised Motored Setup

One of the main criticisms to the pressurised motored method revolves around the fact that the in-cylinder gas is at a much lower temperature when compared to that in a fired engine. This was already discussed in Chapter 2. Some authors [3] [4] [76] [77] have argued that this might result in a different FMEP footprint between pressurised motoring and firing, arising mainly from different lubrication conditions and thermal warpage of different components. To address this shortcoming, in this work, a study was conducted which investigates the effect of bulk gas temperatures on the FMEP and other engine metrics. For this purpose, gases with a high ratio of specific heats were used in place of air as the working gas. Through a simplified calculation assuming adiabatic compression without mass leakage, it can be shown that using Argon as the working gas allows peak in-cylinder temperatures in excess of 2000 K for an engine with a compression ratio of 18:1, and an intake temperature of 20℃. The peak bulk gas temperature that can be obtained with Argon is much higher when compared to a peak in-cylinder temperature of 900 K that can be achieved with air for the same setpoint conditions. This large difference between the two gases is a result of the high ratio of specific heats of Argon (γ: 1.67), when compared to that of air (γ: 1.4).

To implement this idea in practice, compressed Argon cylinders were used for gas supply to pressurise the engine. The recirculating shunt pipe put forward in [78], fitted to the pressurised motored engine proved to be of good utility to recirculate the rather expensive gas. With this scheme, after the initial pressurisation, the Argon cylinders are only required to make up for the blow-by losses which were vented to the atmosphere at the initial stages of the project. To further reduce the consumption of Argon, a blow-by recirculation system was also installed to the setup. The breather outlets on the HDi engine were all routed to the top cover in the OEM (original equipment manufacturer) setup, from which one collective outlet vents all the blow-by out of the engine. This outlet was connected to a buffer tank through a long stretch of pipe. The buffer tank allowed the settling of the pulsating flow induced by the reciprocating movement of the pistons. The outlet of the buffer tank was connected to the intake port of a positive displacement (refrigeration) compressor, driven with a 1 kW AC motor and powered through a dedicated variable frequency drive. The compressor pressurised the blow-by back to the shunt pipe through an oil

separator, where it was re-mixed with the intake gas. The compressor had to be powered through a VFD since blow-by flow-rates vary with both engine speed and in-cylinder pressure load, and hence the work by the compressor has to adapt according to the particular test point of the engine. A PID controller was set up to monitor the pressure in the crankcase and control the compressor speed appropriately to keep the crankcase pressure at 5 kPa above atmospheric conditions. The 5 kPa overpressure was set to ensure that if any of the engine gaskets allow any minute leaks, gas will flow out of the system and not diluting the system with inward flow of air. This 5 kPa overpressure slightly increases the ventilation losses when compared to the instance in which the crankcase is directly vented to atmosphere. With a 5 kPa overpressure, the mean effective pressure that results from the pumping of the crankcase gases is equal to $2.43x10^{-5}$ bar, whereas for the single cylinder engine, the same 5 kPa results in a MEP of $10.42x10^{-5}$ bar.

To ensure that the engine was truly operating on Argon, a UniNOx® sensor was installed in the buffer tank. The UniNOx® sensor measures both the nitrogen oxides concentration and also the oxygen concentration. In this application, only the oxygen concentration was of use and data collection started only when the oxygen concentration was reduced to zero through a purging process which utilised a small solenoid valve installed downstream of the blow-by compressor. A schematic of the system is shown in Figure 3.3.

The engine oil temperature was conditioned to 80℃ ± 1℃. For the four-cylinder engine, the oil temperature was conditioned by exchanging heat with the coolant through the engine structure, and OEM oil filter sandwich-type heat exchanger. The temperature of the coolant was in turn controlled by exchanging heat through a counterflow heat exchanger with laboratory fresh water. The flow rate of the fresh water was varied via a valve that was PID-controlled with a stepper motor. This control scheme had the disadvantage that to keep the oil temperature constant, the coolant temperature had to be varied between each setpoint, hence this might have induced some noise on the FMEP data. To better this control scheme, for the single cylinder engine, the oil temperature was conditioned independently from the coolant temperature which allowed both the coolant and oil to be set at a certain fixed temperature throughout the test matrix.

The engine oil used in this study was Shell Helix HX7 SAE 10W-40 API SN/CF, ACEA A3/B4 (Viscosity: 92.1cSt @ 40℃; 14.4cSt @ 100℃, both according to ASTM D445). The oil was aged for the FMEP tests, but new for the heat transfer testing in Chapter 5. The coolant used throughout the course of this study was fresh water.

Having given an overview of the main features of the pressurised motored setup, Figure 3.4 is presented which gives a simplified schematic of the experimental setup discussed in this chapter.
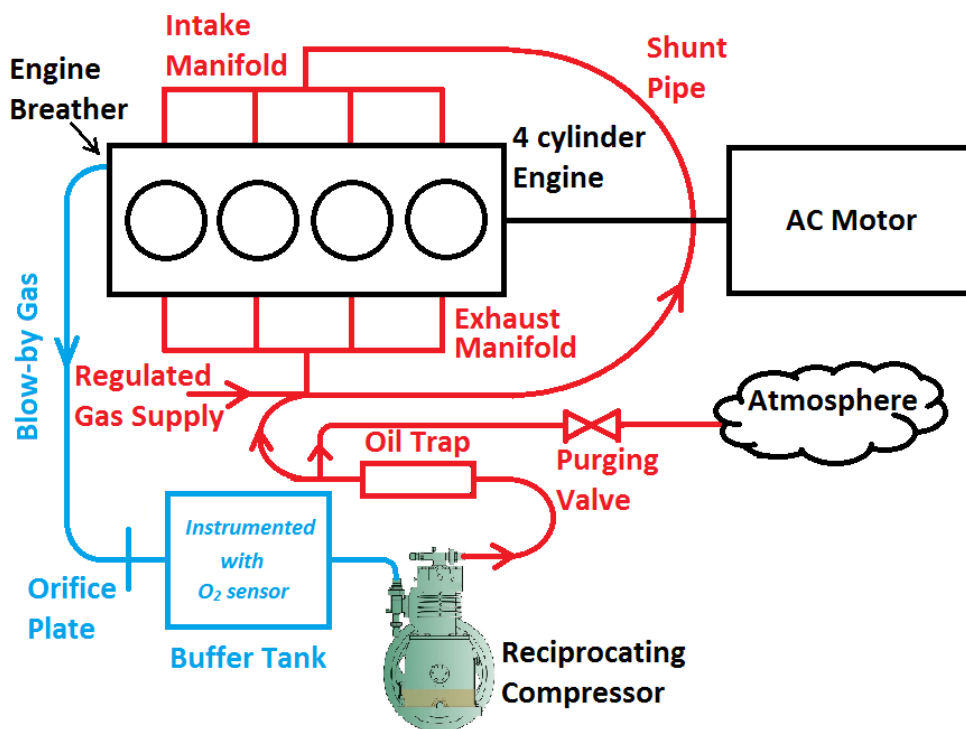
Figure 3.3. The Pressurised Motored Setup using the 4-cylinder 2.0 HDi engine.
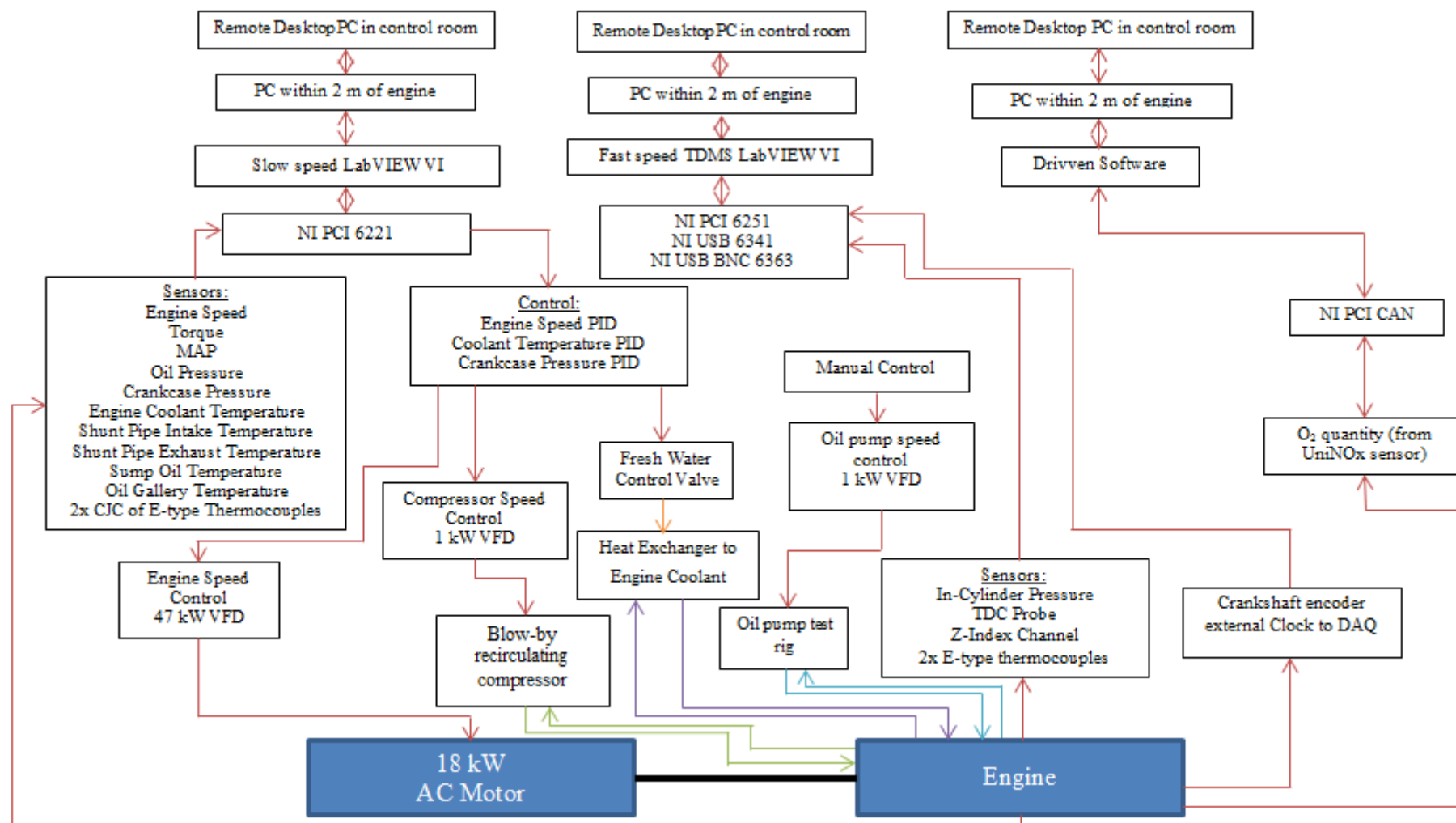
Figure 3.4. Schematic of the test setup used throughout this study.

3.2 Engine Geometry and Cylinder Head Flow Tests

The engine used for FMEP testing documented in the following chapter is a Peugeot 2.0 litre CI. The geometry data for the engine is given in Table 3.1.

The engine is under-square with the pistons having three rings. The pistons have a relatively deep bowl with a protruding sphere as shown in Figure 3.5, and are oil jet-cooled. The cylinder head chamber is flat with two valves per cylinder. The log-style intake manifold is shown in Figure 3.6, while the exhaust manifold is shown in Figure 3.7. Both figures give the relevant dimensions that might be required for engine modelling. The OEM exhaust manifold has an exhaust gas recirculation (EGR) port which in the pressurised motored configuration was used for regulated make-up gas supply. The intake manifold is made of cast aluminium, whereas the exhaust manifold is made of cast iron. The exhaust port has only an approximate 90° short bend. All intake ports and exhaust ports are identical. The exhaust manifold collector, which initially connected to the turbocharger, in the pressurised motored configuration was connected to one side of the shunt pipe. The other side of the shunt pipe connected to the intake manifold entry. The manufactured shunt pipe consisted of a 270 ° bend with a diameter of 60 cm, made up of two curved stainless steel pipes coupled together by a small rubber hose to allow for different thermal expansions, and for easier fabrication and installation. The internal diameter of the shunt pipe was 55 mm with a 2 mm stainless steel wall. Throughout the whole project, the shunt pipe was left unlagged.

Table 3.1. Engine Specifications

Make and Model	2000 Peugeot 2.0HDi
Number of Strokes	4
Number of Cylinders	4
Valvetrain	8 Valve, OHC
Compression Ratio	18:1
Engine Displacement [cc]	1997
Bore [mm] x Stroke [mm]	85 x 88
Connecting Rod Length [mm]	145
Intake Valve Diameter [mm]	35.6
Exhaust Valve Diameter [mm]	33.8
Intake Max. Valve Lift [mm]	9.6
Exhaust Max. Valve Lift [mm]	9.7

Piston Bowl: 23 cc
Piston Crown to Deck at TDC: 0.70 mm
Piston Crown Diameter: 84.32 mm
Piston Skirt Diameter: 84.91 mm
Piston Crown to first compression ring: 9 mm

Figure 3.5. The 2.0 HDi piston.
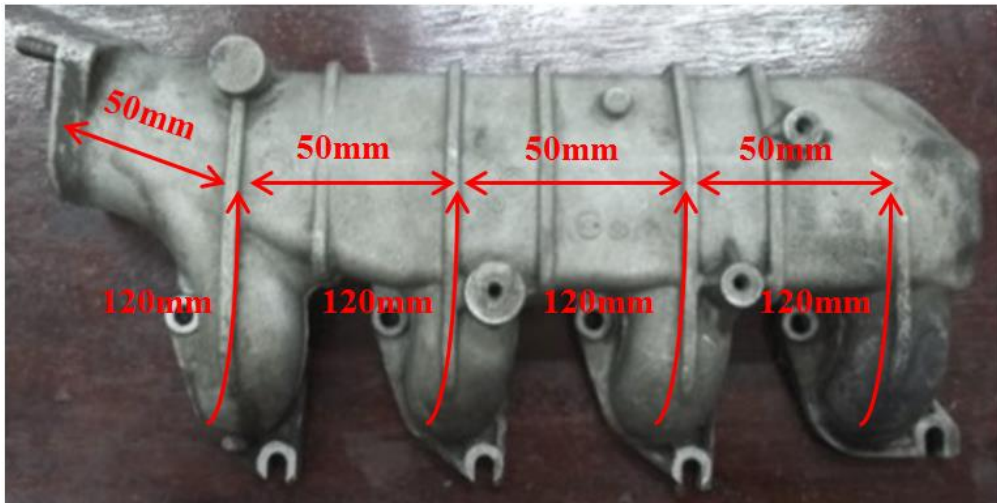
Intake Manifold:
Runner Diameter: 35mm
Plenum Cross-Sectional Area: 70mm x 50mm
Intake Manifold Entry Diameter: 40mm

Cylinder Head Intake Side:
Port Length: 120mm
Port Diameter: 35mm to 30mm

Figure 3.6. OEM intake manifold.

Figure 3.7. OEM exhaust manifold

3.2.1 Cylinder Head Geometry and Flow Characteristics

In obtaining the engine geometry, it was deemed important for later use to have the valve lift curves and discharge coefficients of the 2.0 HDi engine cylinder head. An experimental test session was performed on an in-house set-up flow-bench. The tests performed were similar to those explained in [88]. All tests carried out on the flow-bench were done at 28" of water (*i.e.* 7 kPa) below atmospheric conditions for pull through configuration (intake port to cylinder), and above atmospheric conditions for blow through configuration (cylinder to exhaust port). A temporary bell-mouth using modelling clay was manually formed at port entrance, as is common practice in flow bench testing.

When set up on the flow-bench, the cylinder head was in the condition as dismantled from a running fired engine, *i.e.* not cleaned. It was discovered that since the particular engine had an EGR system, the intake valves contained heavy soot deposits on their back face as seen in Figure 3.8. This might have been also a result of an EGR valve stuck open. It was noticed that the intake manifold was also heavily soiled. The cylinder head intake side was flow tested first in this condition and the flow coefficients were determined in this state. Later, the cylinder head was thoroughly cleaned and flow tested again. Figure 3.9 shows the mass flow

comparison between two clean intake valves and the same valves before cleaning. Mass flow rates are referenced to 1.01325 bar and 294.3 K. It is clearly visible that when clean, the two valves have relatively similar flow behaviours, whereas before cleaning, the flow was marginally lower for valve no. 3 and considerably lower for valve no. 2, dependent on the amount and shape of the deposited soot. It was found that the exhaust valves did not have excessive soot deposition, but normal to that usually found on exhaust valves. All exhaust valves were cleaned prior flow testing.

Figure 3.8: Soot present on intake valve, cylinder two.
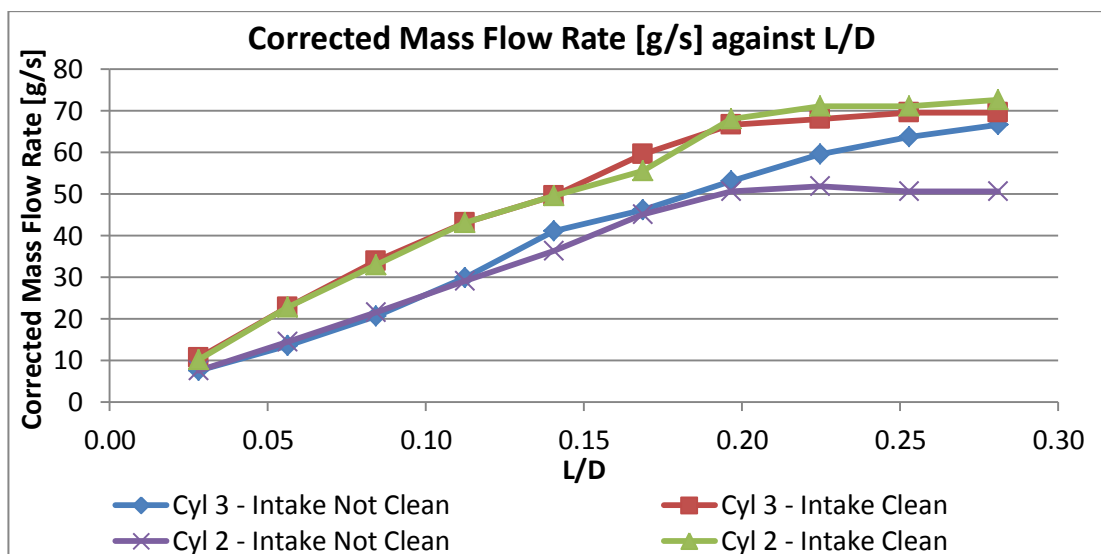
Figure 3.9: Corrected mass flow rate against L/D, showing difference between clean and sooted intake valves

The second aim of this flow testing session was to determine the restriction that both the intake and exhaust manifolds had on the mass flow. Figure 3.10 shows the intake and exhaust mass flow rates for cylinder 2 in cleaned condition. It is noted that the intake manifold was not a major restrictor at low lifts, but did restrict the flow at higher lift values. On the other hand, the exhaust manifold seems to have aided the flow through the exhaust valve at lower lifts but restricted it at higher lifts.
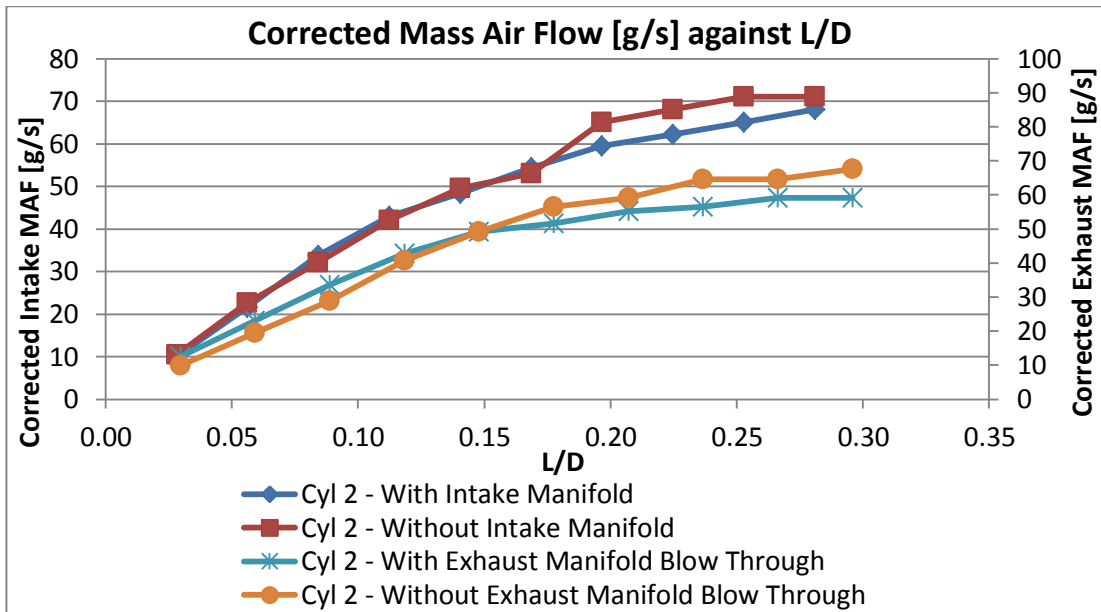
Figure 3.10: Corrected mass flow rate against L/D showing effect of manifolds

The 2.0 HDi cylinder head ports are relatively identical between cylinders. On the other hand however, the OEM exhaust manifold of the 2.0 HDi is known to be unsymmetrical with respect to the manifold outlet. Due to this, it was deemed necessary to flow test each port with the manifold attached to determine the flow characteristic of each runner. Figure 3.11 shows that the second exhaust runner, which is the shortest and straightest of the four, seems to flow in excess of 7 g/s more than the least flowing runner, *i.e.* that of cylinder 3.
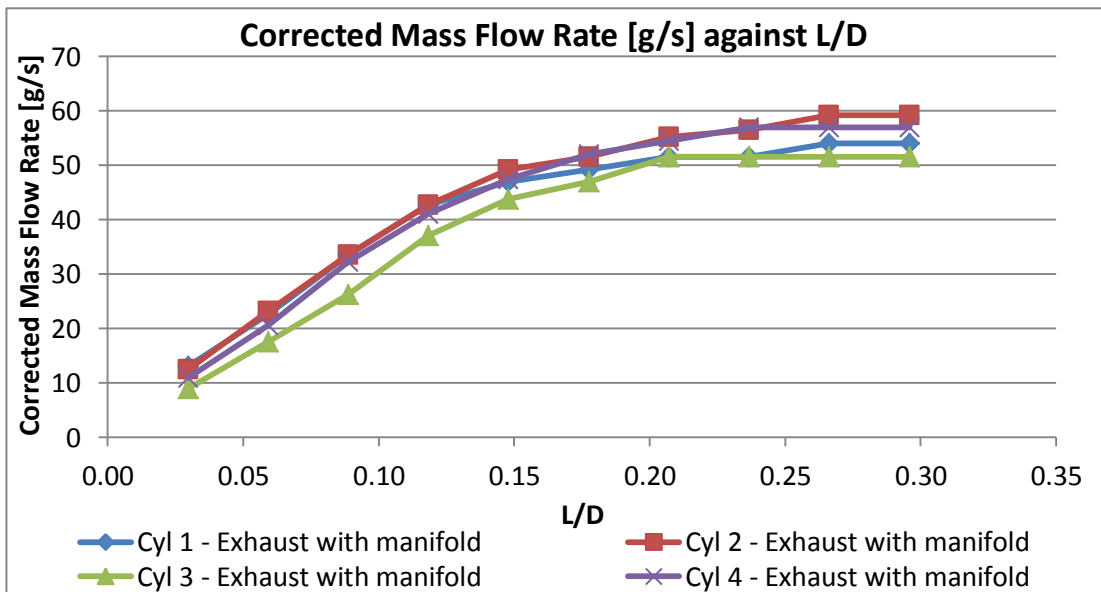
Figure 3.11: Corrected mass flow rate against L/D showing difference between each exhaust runner.

For the purpose of forthcoming Chapter 6 which deals with engine simulation, the valve flow coefficients as obtained from the results discussed above, together with valve lifts measured by Camilleri [89] are given in Figure 3.12 and Figure 3.13 respectively.
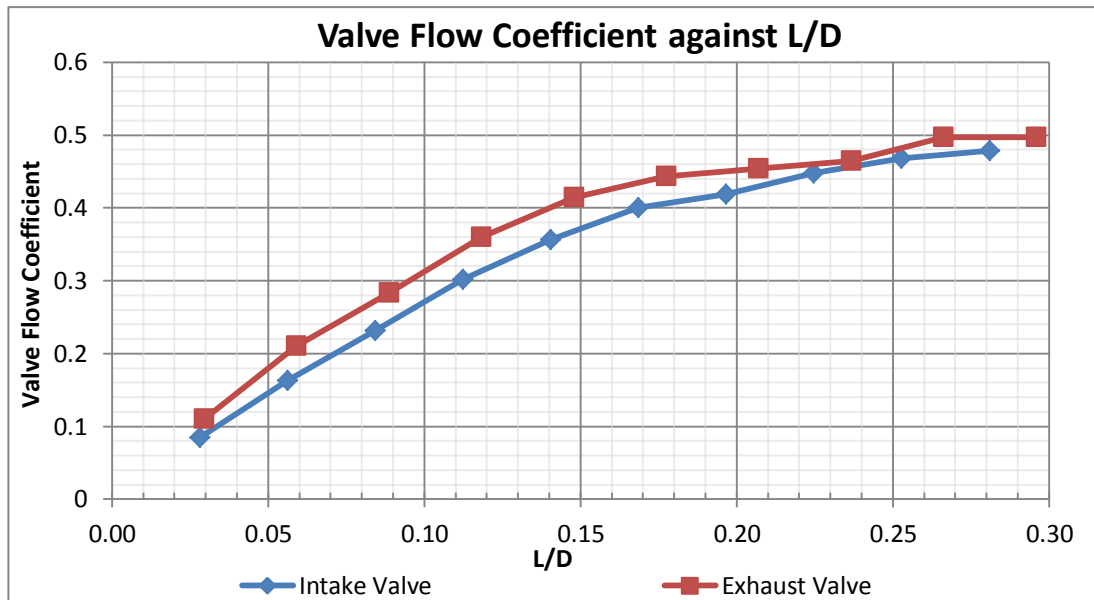
Figure 3.12. Valve flow coefficients for cylinder 1 (flywheel side).
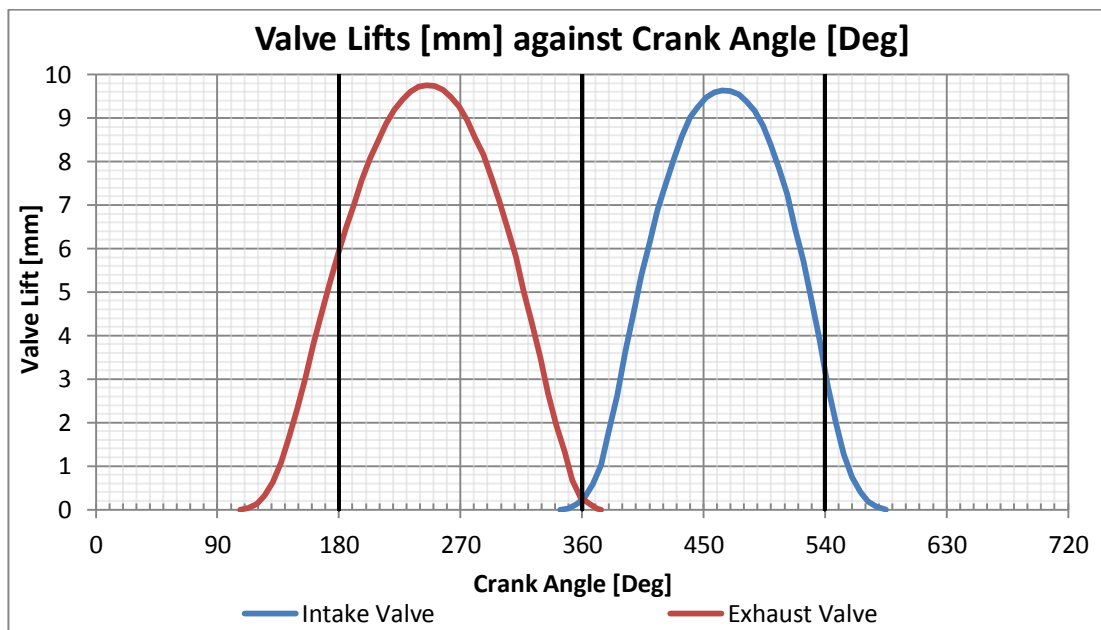
Figure 3.13. Valve lifts of the 2.0 HDi engine as measured by Camilleri [89].

3.3 Conversion of an Inline Four Cylinder Engine to Single Cylinder Operation

In preparation for the heat transfer research, a conversion was done whereby the four cylinder engine was converted to single cylinder to reduce the burden on the instrumentation required by the multi-cylinder engine. The main reason for preferring to convert a multi-cylinder to a single cylinder, instead of using a research or dedicated single cylinder engine is due to the fact that readily available single cylinder engines are either based on large and heavy duty structures for versatile research purposes, or based on very small utility-type (often air cooled) designs which are hardly representative of the actual commercial engine in question. Literature shows that the conversion from a multi-cylinder engine to single cylinder was done several times for different purposes [23] [34] [36] [40] [90] [91]. A detailed description of the single cylinder conversion conducted in this research is presented in [92]. A brief description is given below.

The conversion was done through the complete removal of the three unwanted pistons and connecting rods, leaving only the piston and corresponding connecting rod of the required active cylinder. The removal of the three pistons and connecting rods resulted in the need to rebalance the cranktrain, as well as modify the valvetrain and oil galleries. The engine which was used for this conversion was not the one tested previously on the same setup, but one having the same make and model, taken off a dynamometer test bed. It should be noted that according to literature [93] [94], balancing of an engine usually entails only mechanical considerations, (*i.e.* reciprocating and rotating masses) and do not take into consideration the effect of friction, cylinder-to-cylinder variations, and other occurrences which might still create small unbalances in the system. Timoshenko and Young [95] give a detailed derivation of the summation of forces on the cranktrain of a single cylinder engine. It is shown that the residual forces on the single cylinder engine foundations cannot be completely removed. Similarly, the residual moment about the crankshaft axis cannot be completely removed either. By designing the crankshaft counterweight to balance the moment of all the rotating mass, and a fraction of the reciprocating mass, one would be shifting the primary harmonic unbalance between the direction that is parallel to the cylinder (x-axis) and the direction perpendicular to it (y-axis), but not

eliminating the primary harmonic unbalance. Throughout the years, machinists developed the wisdom that the single cylinder crankshaft counterweight should balance the whole rotating mass and only around 50% to 60% of the reciprocating mass [96]. Millington and Hartles designed for 75% [85]. For a 50% reciprocating mass, the summation of forces in the *x* and *y* directions resolve as follows:

$$F_x = \frac{1}{2}m_{trec}r\dot{\emptyset}^2cos\emptyset + \; secondary \; and \; higher \; harmonics \qquad ...(3.1)$$

$$F_y = -\frac{1}{2}m_{trec}r\dot{\emptyset}^2sin\emptyset \qquad\qquad ...(3.2)$$

In the modification conducted in this dissertation the above result holds but with minor modifications. A four cylinder engine planar crankshaft is known to be fully balanced [97], except for the minor manufacturing inaccuracies. Adding only one piston and one connecting rod induces an unbalance in the system similar to that of the single cylinder engine, which requires counterweights to achieve partial balancing, as previously discussed. In the engine conversion considered, the balancing counterweights cannot originate from the four-cylinder crankshaft counterweight. Instead it has to originate from extra added bob-weights placed at appropriate locations on the crankshaft. Due to several practical reasons, these bob-weights could not be included in the same plane of the piston and connecting rod, but had to be placed on the flywheel, second crank pin and auxiliary pulley plane. Figure 3.14 shows a rendering of the assembled crankshaft with the flywheel mass and the added mass on the auxiliary pulley plane.
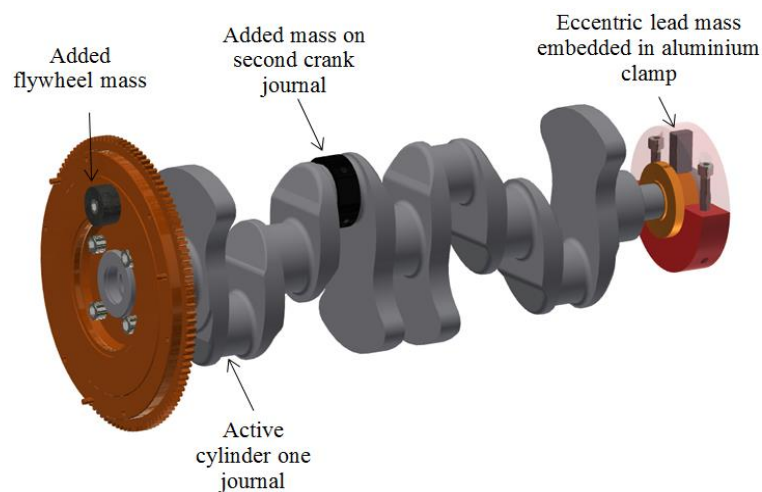
Figure 3.14. Crankshaft assembled with flywheel and counterweight masses used to rebalance the cranktrain.

The balancing counterweights fitted to the four cylinder crankshaft were found using the theory of shaft dynamic balancing, and designed to balance the full rotating mass and only 60% of the reciprocating mass. This reciprocating mass ratio was chosen based on experimental tests on the engine which through accelerometer results showed the smallest magnitudes of vibration. Table 3.2 gives the measured masses and the balancing counterweights for the chosen reciprocating mass ratio.

Table 3.2. Measured and calculated metrics. All masses are in grams, and lengths in millimeters.

Measured metrics		Calculated metrics	
Mass of connecting rod (including bolts, nuts, excluding big end shell bearings)	742.3	Reciprocating Mass Ratio	0.6
Mass of shell bearing (only one shell included)	21.8	Counterweight on flywheel plane	335.8
Mass of piston assembly (rings and circlips included, gudgeon pin excluded)	251.2	Counterweight on 2nd crankpin	355.6
Mass of gudgeon pin	251.2	Counterweight on auxiliary pulley plane	97.0
Length of connecting rod (centre-to-centre)	145.0		
Centre of mass of connecting rod from centre of big end	46.2		
Flywheel counterweight radial distance	100.0		
Auxiliary pulley plane radial distance	47.2		
Axial distance from flywheel to cyl 1	121.7		
Axial distance from flywheel to cyl 2	212.9		
Axial distance from flywheel to auxiliary	487.0		

3.4 Further Engine Modifications

Other modifications that had to be done as part of the single cylinder conversion include the oil passages and valvetrain. Due to the removal of the three connecting rods, the corresponding oil passages at the crank pins which conventionally were restricted from free flow by the tight clearances between the shell bearings and the crank journals, had to be closed. This was done by inserting a pressed fit plug into the crankshaft journal oil passage and securing it against pressure with a conventional jubilee clip. The supply ports in the engine block that mate with the cooling oil jets for the three deactivated pistons were also blanked off by custom machined plugs, utilising rubber O-rings.

As described in section 3.1.1, in this study the sump of the engine was pressurised to 5 kPa above atmospheric conditions during operation. The intake system was also pressurised to a maximum of 2.5 bar, but dependent on the particular test point. To avoid having a short between the two system pressures through the deactivated cylinders, the intake and exhaust valves on the three deactivated cylinders had to be closed off permanently. This is due to the fact that for the single cylinder engine, the same intake and exhaust manifolds of the four cylinder engine were used, and hence the manifolds runners for the deactivated cylinders were still supplied with the MAP pressure. For this reason, the valves of the deactivated cylinders were permanently closed by removing the hydraulic lifters and their respective rocker arms, which prevented the camshaft from mechanically opening the valves. To ensure that the spring-loaded valves do not open by the difference in pressure across them, the runners of the three deactivated cylinders were also blanked off by a thin aluminium gasket to isolate the ports of the deactivated cylinders from the MAP pressure.

As an improvement over the four-cylinder engine setup, it was thought that for the single cylinder engine, the oil pump should be driven externally to make sure that the FMEP determined is not biased by any accessory loss. The oil pump was the only accessory that remained driven by the engine in the four-cylinder setup and the reason was mainly that for it to be removed, the setup had to be extensively dismantled. To remove the oil pump from the single cylinder engine, the mating hole in the cylinder block to which the OEM pump used to supply oil had to be blocked in order not to drain the oil supply back to the sump. This was done by machining a plug with a rubber O-ring, which was also positively clamped against pressure.

The oil pump used externally was the one dismantled from the same engine. The pump was fitted on a small custom-made rig, driven by a 2800 rpm rated electric motor, which in turn was controlled through a variable frequency drive. The OEM oil pump has an internal pressure regulator which limits oil pressure to 4.5 bar, independently of the rotational speed of the pump. An adapter was machined and fitted at the inlet of the pump, which was gravity fed from a drilled hole in the engine sump. In the hose connecting the engine sump to the inlet of the oil pump, an inline washable strainer was fitted. The outlet of the oil pump was then fed to the engine through a custom-made sandwich plate fitted between the oil filter heat exchanger (of sandwich type) and the cylinder block. The constructed oil pump rig was also

made to have a considerably sized tank situated under the oil pump. The reason for the construction of the tank was that the oil pump shaft did not have an oil tight seal with the housing. This was acceptable in the original configuration of the engine since the pump was situated in the sump, and hence a small leak between the shaft and housing was not an issue. However, on the oil pump rig developed this created a problem since the oil tank constructed filled after about an hour of full load operation. To solve this issue, a level sensor based on a magnetic reed switch and a floater was fitted in the oil pump rig tank. This was made to switch on a positive displacement pump when the oil in the tank reached a certain level and was made to switch off after the level decreased by a certain quantity. The positive displacement pump scavenged the leaking oil from the oil pump on the rig and delivered it back to the sump.

To the oil gallery of the engine, a K-type thermocouple was fitted, as well as an electronic oil pressure sensor which was made to trigger an alarm in LabVIEW engine control interface if the oil pressure fell below a threshold value.

3.5 Fitment of Surface Thermocouples

It was shown by several researchers [43] [98] that the heat flux from the combustion chamber surface shows spatial variation. To study this effect, an attempt was made to fit multiple surface thermocouples in the experimental single cylinder engine. It transpired that due to the complex coolant jackets and irregularity of the top surface of the cylinder head, not more than two surface thermocouples could be fitted – one in place of the OEM fuel injector and another could be fitted by drilling through the cylinder head, perpendicular to the combustion chamber surface. Another surface thermocouple could be fitted in place of the glow plug, but this location was already occupied by the in-cylinder pressure sensor.

The two thermocouple locations in the engine cylinder head can be seen in Figure 3.15. The mating location on the piston at the two thermocouple locations can be seen in Figure 3.16. From these figures, it is identifiable that the custom thermocouple location is in the squish area, with a measured squish clearance of 0.7 mm. On the other hand, the injector location is almost at the centre of the combustion chamber, pointing towards the centre of the spherical dome located in the toroidal

piston bowl. This hints that the two surface thermocouples are exposed to significantly different flow regimes. It is thought, but also supported by literature [99] [100], that at crank angles close to TDC the custom thermocouple experiences high gas velocities, but with a defined radial direction towards the piston bowl and parallel to the cylinder head surface. The OEM injector location probably experiences a high degree of tumble imposed by the piston bowl and protruding sphere at the centre of the piston. This means that at the OEM injector location, the gas velocity is defined by the direction perpendicular to the cylinder head surface. In a research by Jackson et al. [43], the heat flux was studied at locations similar to that studied in this work, *i.e.* at the valve bridge and at the bore edge. It was reported that a spatial variation of the order of 350% was noted on the mean heat flow. The higher heat flux was reported at the valve bridge. As will be shown later in chapter 5, this was also the case in this Doctoral work.
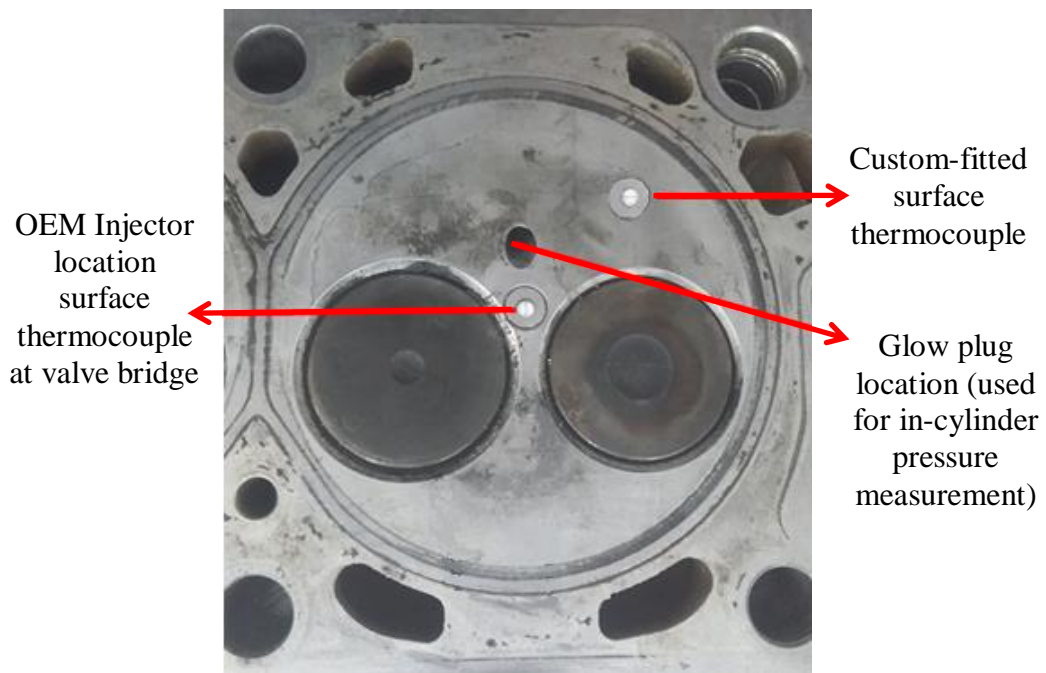
Figure 3.15. Photo showing the eroding thermocouples and pressure transducer location.
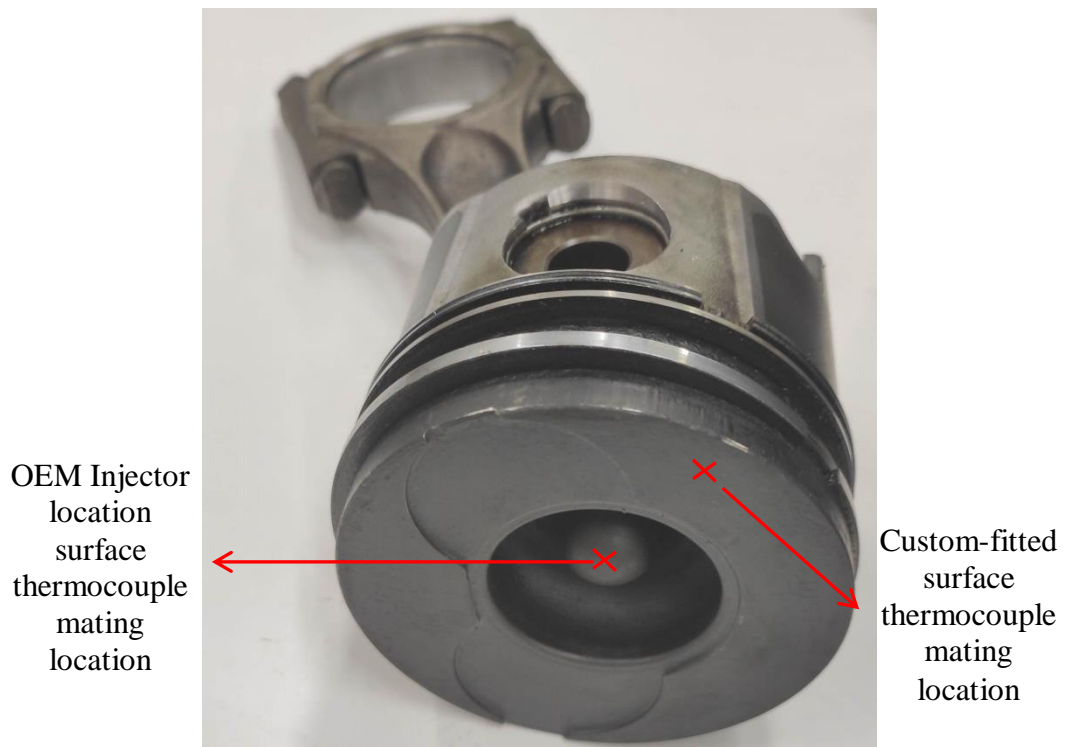
Figure 3.16. Photo showing the piston mating locations to the eroding thermocouples fitted in the cylinder head.

In this research, all surface thermocouples used were of the Nanmac eroding type. Three different versions of this thermocouple were procured, each with different substrate material, being: Aluminium, Stainless Steel and Zirconia. The Stainless-Steel and Aluminium thermocouples were composed of a total of four different materials, whereas the Zirconia thermocouple consisted of five different materials. These different materials belong to the thermocouple dissimilar ribbons, Mica insulator, split-tapered inserts and outer tube.

When fitting the surface thermocouples in the cylinder head, interference fitment was seriously considered as one of the fitment candidates of the thermocouples in the cylinder head. In general this type of fitment results in an easier gas pressure sealing, and hence permits a larger amount of surface thermocouples to be fitted in the combustion chamber, due to the fact that the thermocouple can be fitted without the need for a bulky adaptor (and/or compression fittings). Furthermore this fitment method was favoured since it eliminates any crevices in between the thermocouple body and the cylinder head as explained in Chapter 2. The reason why interference fitment was not used is because during preliminary heat flux testing, the eroding thermocouple junction opened several times at certain operating conditions. This

resulted in the need to remove the surface thermocouple from the cylinder head and renew the junction by abrasion. If the surface thermocouple is interference fit, renewal of the thermocouple junction would be only possible through the removal of the cylinder head, with its associated downtime and cost. As a result, in this research, both surface thermocouples were fitted in custom-made adaptors through the use of compression fittings.

The adaptor for the surface thermocouple at the OEM injector location is shown in Figure 3.17. This adaptor was machined from aluminium with a through hole to allow sliding fit of the eroding thermocouple. The thermocouple was secured to the adaptor with a compression fitting that was located around 10 cm from the heated surface. The adaptor was in turn placed in the OEM injector hole, and sealed against the combustion chamber pressure with a copper washer. Compression of the adaptor against the copper washer was achieved by the same clamping method that the OEM injectors use. Since the OEM injector hole has a slight inclination from the vertical, the heated surface of the adaptor had to be ground at an angle to match the inclination of the cylinder head surface.
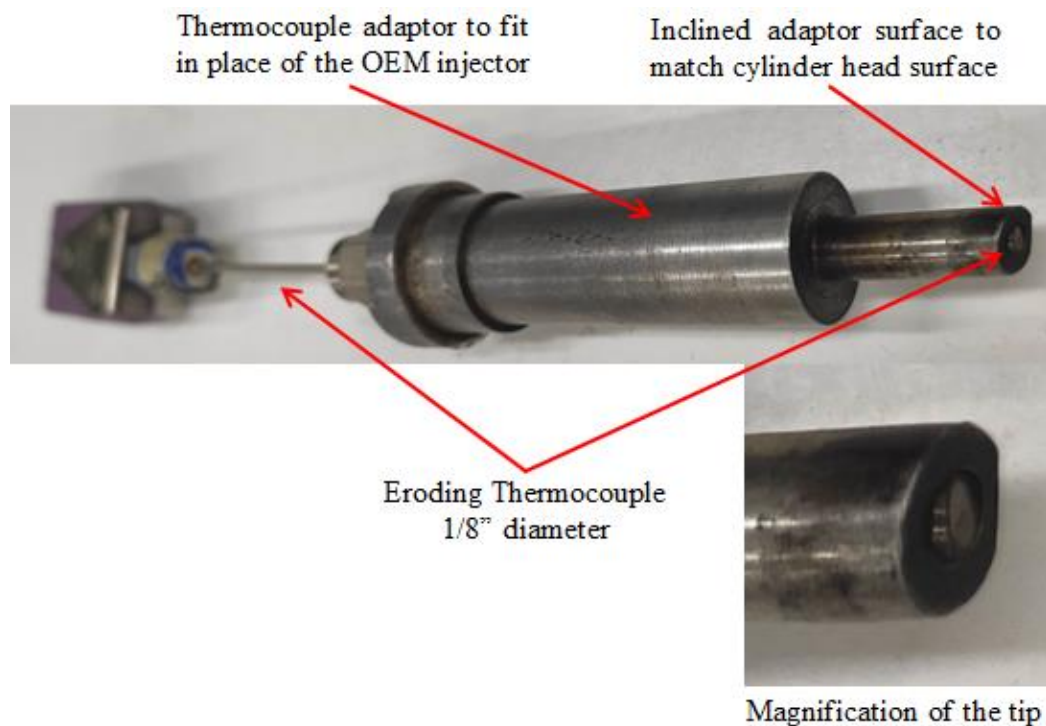
Figure 3.17. Surface thermocouple integrated in the custom-made adaptor for fitment at the OEM injector location.

Machining the cylinder head and the adaptor to fit the second surface thermocouple (*i.e.* the one that required drilling through the cylinder head) was not an easy task. Figure 3.18 shows a photo of the thermocouple assembly after few months of use. The photo is taken from an access hole at the side opening of the cylinder head which mates to an external coolant jacket. For clarity purposes Figure 3.19 shows a simplified schematic. An adaptor was machined out of aluminium to match the cylinder head material with two eccentric long holes (≈100 mm). One of the holes was through, and 1/8" in diameter to house the surface thermocouple. The other hole was 2 mm in diameter and penetrated up to a length of 12.4 mm from the heated surface to fit a recessed thermocouple for steady-state heat flux measurements. This recessed length was chosen according to a calculation which estimates an attenuation factor of 300 of the surface temperature fluctuation at 600 rpm.

The surface thermocouple was kept fixed in the adaptor by a custom-made compression fitting, utilising a grade 12.9 modified allen head M6 bolt which was drilled right through to accommodate the thermocouple. The ferrule was also custom made from aluminium to ensure that it does not damage the adaptor chamfered mating surface once compressed by the allen bolt. The adaptor sealed against compression pressure and coolant leaks to the combustion chamber using a copper washer against the inhouse machined surface of the coolant jacket. The surface of the coolant jacket was machined using an extra long end mill that had to go through the upper part of the cylinder head and through the coolant jacket. A positive compression on the adaptor and copper washer was achieved from two thread-locked grab screws which were threaded into an angle bracket bolted to the cylinder head. The grab screws were not made to compress against the adaptor itself due to it being made of aluminium. Instead, a steel cap was made to fit over the adaptor. To seal against coolant leaks from between the top surface of the cylinder-head and adaptor, a rubber O-ring was compressed between the aluminium adaptor and a machined chamfer in the top surface of the cylinder head, using a sleeve. The sleeve was compressed using a clamp (not shown in Figure 3.19, but shown in Figure 3.18). A slit had to be machined in the sleeve to mate with the side exit of the hole in the adaptor in order to accommodate the recessed thermocouple. Figure 3.20 shows a two-dimensional drawing of the adaptor.
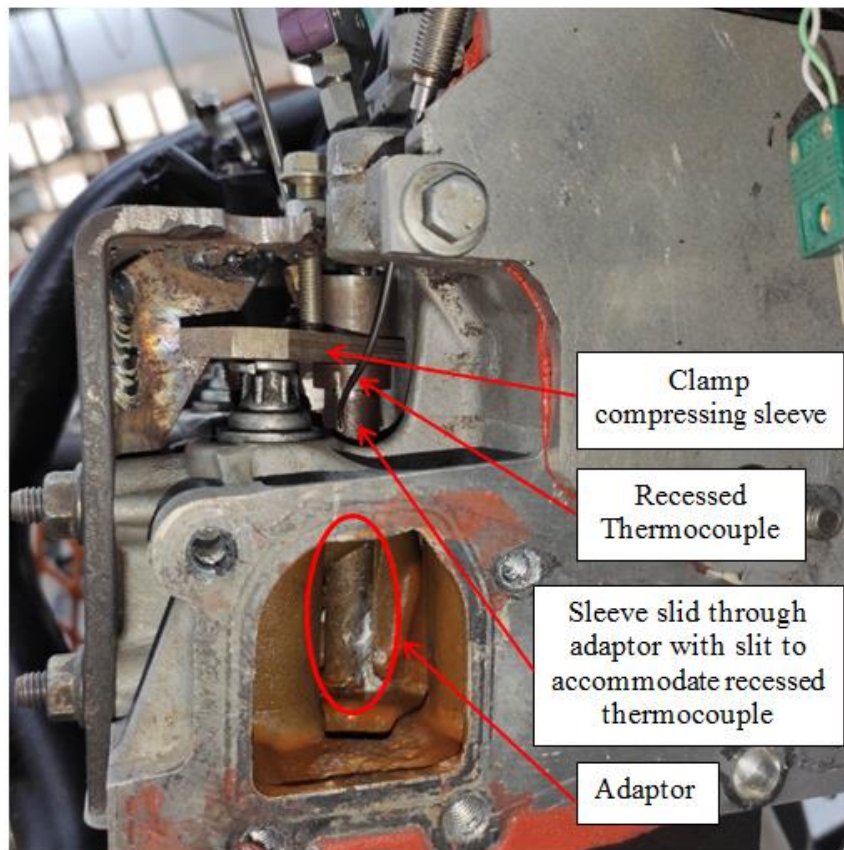
Figure 3.18. The custom-drilled thermocouple assembly after few months of use.

During machining of the adaptors for the two instrumented locations, it was made sure that the sliding fit of the sensor in the adaptor, and the sliding fit of the adaptor in the cylinder head were as tight as possible to limit the amount of periodic gas pressure fluctuation occurring in the two crevices.

To establish the thermocouple junction Nanmac [64] suggests the use of an emery cloth. Ideally the thermocouple junction is abraded with progressively coarser grit sizes until a resistance of between 2 Ω to 10 Ω is obtained. It is assumed that the coarser the sanding grit used, the slower will be the response time due to a thicker sliver junction. In this research, the thermocouples were first abraded with a #320 grit. During preliminary testing, this junction survived through testing with air, however it went open when testing with gases of higher ratios of specific heats. As a result coarser grits were used, down to #80 grit. Junctions established with #80 grit survived through long testing times; however occasional junction failure did occur.

Grade 12.9
Drilled M6 allen bolt used to
compress ferrule and secure
surface thermocouple to adaptor

M4 Grab screw

Surface
Thermocouple

Bracket bolted to
cylinder head

Surface and recessed
thermocouple adaptor

Cylinder Head
End View

Coolant jacket

Copper washer seal
Sliding fit
Flush mounted with
combustion chamber

Steel Cap

Aluminium
Ferrule

Irregular cylinder head top surface

Sleeve providing O-ring compression

Rubber O-ring compressed against machined
chamfered edge in cylinder head

Sleeve slit mating to side
hole in adaptor for recessed
thermocouple exit

Figure 3.19. Simplified schematic representation of the surface thermocouple assembly at the custom-drilled location.

78
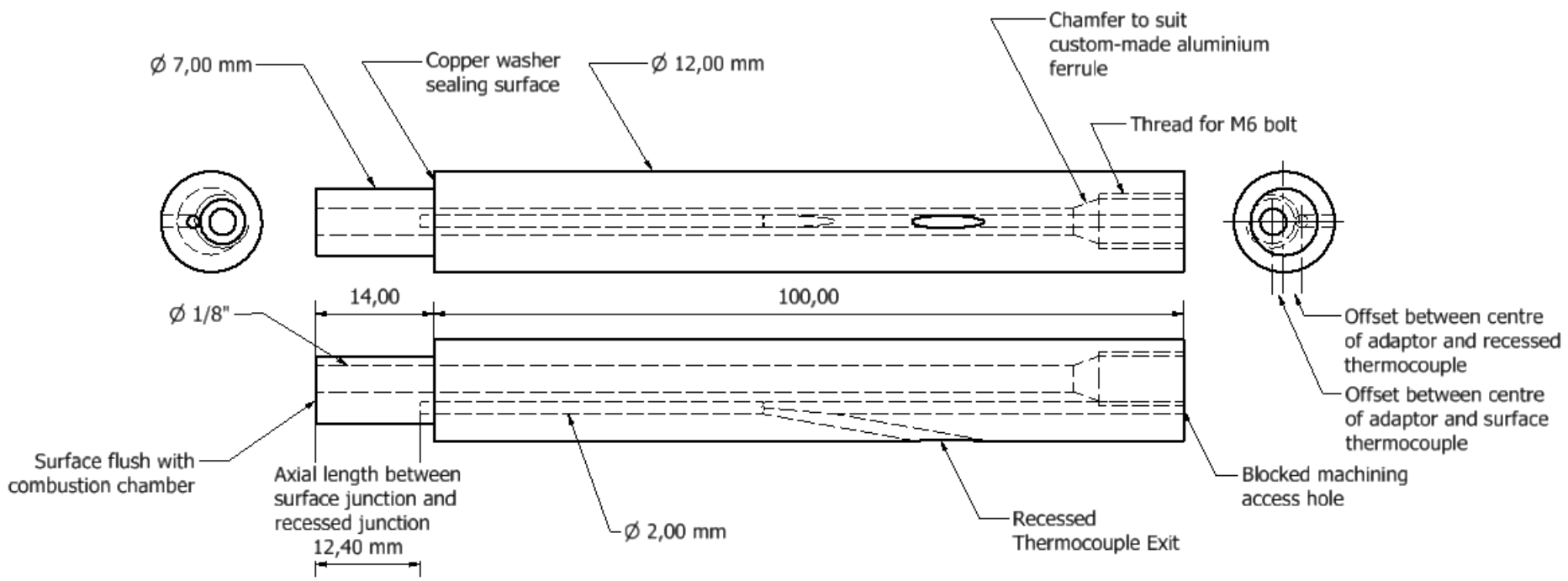
Figure 3.20. The thermocouple adaptor fitted at the custom-drilled location.

4   MECHANICAL FRICTION DETERMINATION AND OTHER METRICS

This chapter outlines the testing campaigns conducted on the pressurised motored setup developed at the Thermodynamics Laboratory, University of Malta for the purpose of determining the FMEP and other important engine metrics. The effect of bulk gas temperatures on the FMEP and other engine metrics was also investigated making use of the modified setup, described in Chapter 3, section 3.1.1, which allowed the recirculation of the exhaust gas and blow-by to the intake manifold.

4.1   Brief of FMEP Testing Campaigns

For the purpose of facilitating the interpretation of the results in this chapter, this section is dedicated at explaining the testing campaigns carried out for the purpose of engine mechanical friction measurements, and the rationale for each testing session conducted. The outline is being reported in a chronological order.

During the initial stages of this study, the testing matrix was defined by engine speed and mechanical (pressure) load. Initially, engine load was represented by the MAP. This practice was mainly derived from fired testing in previous projects.

The first test session conducted involved the engine running with air as the pressurisation gas, with the exhaust gas recirculated to the intake side via the shunt pipe. For this testing session, a wide range of engine speed and load was explored to aid in familiarising with the setup characteristics and determining the FMEP and other engine metrics dependency on engine speed and mechanical load. Table 4.1 shows the test points for the described testing session. Setpoints in the test matrix which were not tested are denoted by "N/A". Results from this test session were also published in [101].

Table 4.1. The test matrix for air testing.

Setpoints Tested		MAP [bar]						
		0.5	1.0	No Manifolds	1.5	2.0	2.5	3.0
Engine Speed [rpm]	1100	✓	N/A	✓	N/A	N/A	N/A	N/A
	1400	✓	✓	✓	✓	✓	✓	N/A
	1750	✓	✓	✓	✓	✓	✓	✓
	2000	✓	✓	✓	✓	✓	✓	N/A
	2250	✓	✓	✓	✓	✓	✓	N/A
	2500	✓	✓	✓	✓	✓	✓	N/A
	3000	✓	✓	✓	✓	✓	✓	N/A

Following this testing session, the setup was modified to allow the use of a substitute gas instead of air, with the aim of investigating the engine operating on Argon and its mixtures with air. After the modifications described in section 3.1.1 were done to the setup, a testing session was conducted using Argon as the pressurisation gas. In this testing campaign, the setpoint variables were still the engine speed and pressure load – represented by MAP. This testing session was not mainly targeted at obtaining data, but more to provide conclusions on whether the pressurised motored engine could be operated on Argon, and to allow the identification of any potential problems that could be posed in this kind of operation. Results of several metrics with Argon as the working gas obtained from this test matrix are presented in [101], but are not shown in this dissertation.

After having completed successfully the testing session using Argon, it was concluded that the engine could be run in the pressurised motored mode on Argon without any significant issues. As a result, another testing session was planned with the aim of investigating the effect of gradual increase in bulk gas temperatures on FMEP and other engine metrics. This was obtained by testing synthesised mixtures of gases with relative proportions of air and Argon. For this testing session to provide any meaningful results, the engine had to be tested at the same engine speeds and pressure loads for the different gas compositions. Due to this, the engine load parameter was represented by peak in-cylinder pressure as the control variable, instead of the MAP. The test points in this testing campaign are given in Table 4.2. Results from this test matrix are also published in [102] [103].

Table 4.2. The test matrix of gas mixtures.

Setpoints Tested		Engine Speed [rpm]			
Ratio of Specific Heats (γ)	PCP [bar]	1400	2000	2500	3000
1.40 *(air)*	84 bar	✓	✓	✓	✓
	103 bar	✓	✓	✓	✓
1.50 *(Mixture of air & Argon)*	84 bar	✓	✓	✓	✓
	103 bar	✓	✓	✓	✓
1.60 *(Mixture of air and Argon)*	84 bar	✓	✓	✓	✓
	103 bar	✓	✓	✓	✓
1.67 *(Argon)*	84 bar	✓	✓	✓	✓
	103 bar	✓	✓	✓	✓

The above presented test matrices were all conducted on the four cylinder engine. After the conversion from four cylinder to single cylinder was completed, another extensive test session was done on the single cylinder engine. In this test session, the engine speed was varied from 1400 rpm to 3000 rpm, at PCPs between 40 bar and 100 bar with gas compositions of γ between 1.40 and 1.67 (at room temperature). Coolant and oil temperatures between 60℃ and 95℃ were also tested. The main aim for this test session was to investigate the differences in the FMEP between the single cylinder engine and the four cylinder engine, but also to serve as a parametric test session for in-cylinder heat flux measurements. Apart from differences in FMEP arising from cylinder-to-cylinder variances on the four cylinder engine, it was expected that from this test matrix a difference in FMEP due to the oil pump would be also observed, which as stated in the previous chapter, was driven externally in the single cylinder setup. Furthermore, the independent oil and coolant temperature control used on the single cylinder was expected to eliminate any noise in the FMEP arising from different coolant temperatures suffered on the four cylinder engine setup. The full test matrix is not presented here, but will be presented later in Chapter 5.

In this chapter, results of PCPs and mean effective pressures are all reported as ensemble over 300 cycles except for the test matrix denoted by Table 4.2. For this test matrix, data is presented ensemble over 200 cycles only. The results obtained from the test matrix denoted by Table 4.2 also showed the highest magnitudes of standard deviations in the measured metrics when compared to the other test sessions. To have an indication of the standard deviations incurred in these metrics, the reader is referred to Appendix 8.1.

4.2 TDC Determination

For the computation of certain engine metrics, phasing of the in-cylinder pressure signal with respect to the angular position of the crankshaft (or linear position of the piston) is of fundamental importance. It is claimed by Pipitone and Beccari [104], Stas [105] and Nilsson and Eriksson [106], that 1 DegCA of phasing error between the in-cylinder pressure and crank angle position accounts to around 10% error in the fired IMEP and around 25% error in heat release. For the engine geometry used in this study, in the pressurised motored mode, 1 DegCA error in the pressure-to-crank angle phasing results in 42% error in the motored $IMEP_{720}$. This high error in the motored mode due to phasing is a result of the very narrow power (loss) p-V loop, compared to that of the fired engine. Consequently, in FMEP studies similar to that considered in this dissertation, phasing of in-cylinder pressure and volume is of utmost importance.

As noted in a previous chapter, the data acquisition was sampled according to a 3600 pulse per revolution (ppr) shaft encoder, which was attached to the crankshaft through a solid, custom-made aluminium coupling. The encoder mounting was designed to allow two degrees of freedom about two axes perpendicular to the crankshaft/encoder axis to take any misalignment in the two mating shafts (crankshaft and encoder shaft), without allowing the encoder to rotate about its shaft. The encoder mounting is shown in Figure 4.1.
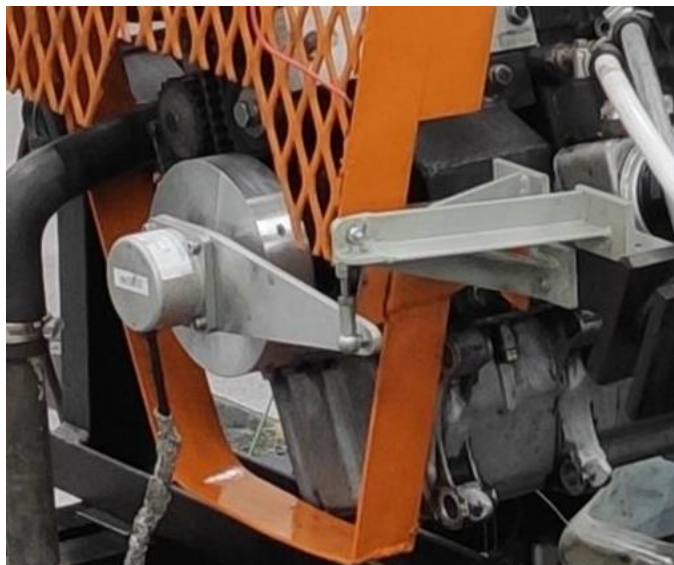
Figure 4.1. Crankshaft encoder coupling.

To achieve sound phasing between the in-cylinder pressure signal and the instantaneous cylinder volume, two methods can be used. The first and most reliable method is through the use of a TDC capacitive probe, which has the capability of sensing the proximity of the piston from a fixed point (cylinder head). The second, less preferred method is through the use of thermodynamic models which determine the thermodynamic loss angle (angle between peak in-cylinder pressure and minimum in-cylinder volume) through an estimation of heat losses and blow-by losses between the compression and expansion strokes. The larger the thermodynamic loss angle, the earlier the peak in-cylinder pressure occurs relative to the minimum cylinder volume location. In the Masters dissertation [78], a TDC probe was not available, hence FMEP data had to be analysed using thermodynamic models published in literature [104] [105]. It was found that employing these models is not simple and also very sensitive to compression ratio and in-cylinder pressure pegging – two quantities the accuracy of which is already questionable due to well-known limitations in the engine research sector [104] [107]. As a result, in this doctoral work, a TDC probe was used for the determination of the phasing between the in-cylinder pressure and volume. In order to prevent damage to the TDC probe, but also due to limited access holes in the cylinder head of the engine, the TDC probe was not mounted in the engine during actual FMEP testing. This practice is typical in engine testing due to the delicateness of the sensor, but also because it cannot withstand temperatures induced in fired testing (or extreme motored testing, as shown later in this chapter). Hence its use is only limited to conventional motored conditions.

Due to the reasons mentioned, in this project, prior to every FMEP/heat flux testing session the TDC probe was installed in place of the OEM injector and its signal was acquired together with the Z-index (1 ppr) of the shaft encoder, and in-cylinder pressure at least at three engine speeds and two PCPs. From this data, the angular position between the Z-index channel and dynamic TDC position could be found and used as a reference for the entire FMEP/heat flux test matrix, even though the TDC probe was removed during the actual FMEP/heat flux testing. This however assumes that throughout the whole FMEP/heat flux test matrix, no angular slip is incurred between the crankshaft and encoder shaft. To verify this, after each FMEP/heat flux test matrix, the TDC probe was re-installed and TDC testing at the same three engine

speeds and two PCPs was conducted once again. The angular difference between the Z-index and dynamic TDC is compared to that found prior the FMEP/heat flux test matrix to ensure that no angular shifts had been incurred between the shaft encoder and crankshaft during testing.

It is claimed by Knauder et al. [108] that dynamic TDC location is sensitive to several factors, such as engine speed, PCP and oil temperature. One hypothesis is that increasing the PCP could possibly cause the crankshaft to displace itself more in the oil film sustained between the shell bearings and crankshaft main journals. Hence a TDC shift might be incurred. To test these hypotheses, in this dissertation a study was conducted whereby the TDC signal was acquired at different engine speeds ranging from 1400 rpm to 3000 rpm, PCPs ranging between 40 bar and 100 bar, and oil gallery temperatures ranging between 40℃ and 70℃. It was noted that for all tests considered in this range, the angle between the Z-index and the dynamic location of TDC varied by no more than 0.1 DegCA, which is comparable to the absolute accuracy of the TDC probe.

Even though significant dynamic TDC shifts were not seen at the different engine speeds, PCPs and oil temperature, it was noted that the TDC signal shows slight magnitude variations at the different test conditions. Figure 4.2 shows the TDC signal at different engine speeds and constant PCP of 40 bar. It is evident that the peak signal occurring at compression TDC and exhaust TDC is the lowest at 1400 rpm, and highest at 3000 rpm. Since the voltage magnitude of the probe is a function of proximity, this hints that the piston tends to move closer to the cylinder head at TDC when the engine speed increases, but the angular position at which this occurs stays relatively constant. Figure 4.2 also shows that during the gas exchange TDC (~ 360 DegCA), the TDC signal peak is higher than that of the compression/expansion TDC. This is due to the pressure load difference on the piston at the two instances as shall be explained below.

In Figure 4.3 the peak TDC signal close to the PCP location shows that increasing the PCP from 40 bar to 100 bar resulted in a smaller TDC signal peak. This could be due to the fact that a higher pressure load forces the piston-connecting rod assembly, together with the cranktrain to displace downwards in the oil film, which hence decreases the proximity of the piston to the probe at TDC. It is interesting to note

however that during the low part of the compression (-30 DegCA) and expansion (+30 DegCA) strokes, the TDC signal is higher for the higher PCP and decreases for the lower PCPs. This trend changes at around ± 6 DegCA.
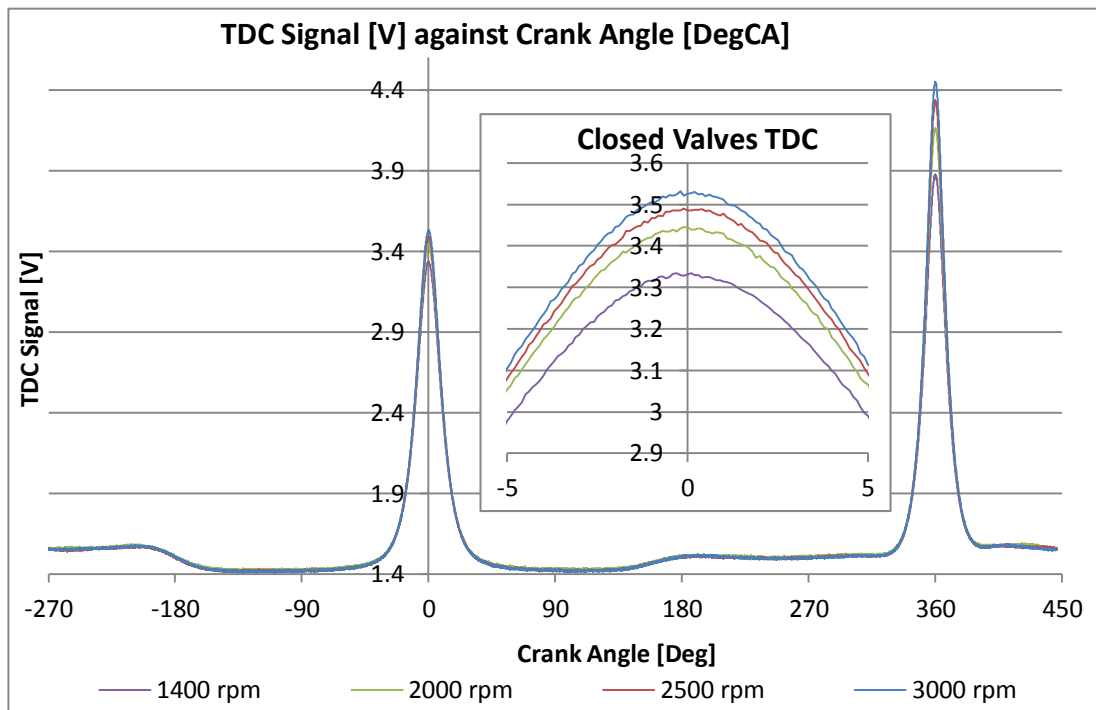
Figure 4.2. TDC signal at different engine speeds.
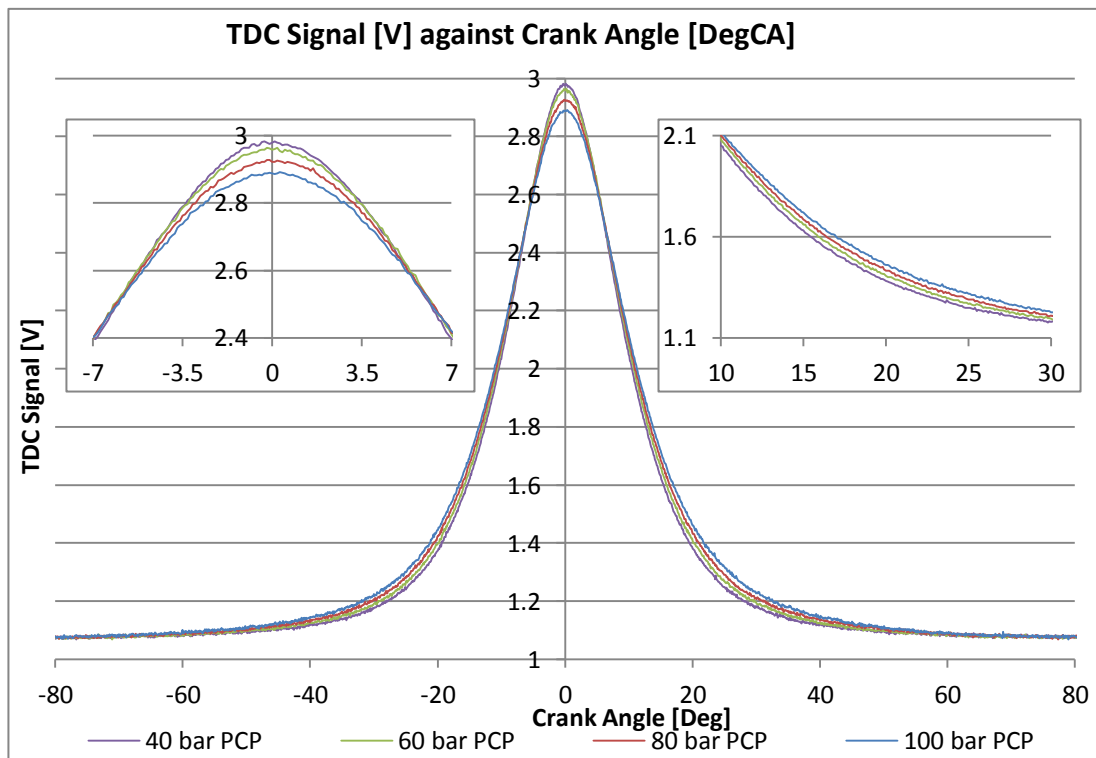
Figure 4.3. TDC signal at different PCPs (compression TDC).

86

4.3 Testing with Air as the Working Gas

The majority of the developed FMEP models rest on the assumption that the FMEP can be predicted only as a function of engine speed and PCP. Due to the importance of these two variables, a test session using air as the working gas was conducted to investigate their relationship with the FMEP of a pressurised motored engine. Additionally, this test session served to familiarise with the newly built pressurised motored setup, while answered some questions which remained pending from the previous project [78]. The test matrix for this experimental campaign is defined by Table 4.1 in section 4.1.

In conducting this test session, the manifolds and shunt pipe were pressurised using the laboratory air compressor, regulated through a single stage mechanical regulator. As outlined earlier, during this test session, engine load was represented by the MAP which consequently resulted in different PCPs at different engine speed conditions for the same MAP setting. The range of engine speeds tested was between 1100 rpm and 3000 rpm, whereas the range of PCPs was between 25 bar and 142 bar, for a MAP variation of between 0.5 bar and 2.5 bar. Apart from the in-cylinder pressure, crank angle and torque, other data was acquired to allow for an evaluation of when the engine reached steady-state. Amongst which is the engine speed, MAP, the shunt pipe temperatures at the intake and exhaust sides, coolant temperature and oil temperature. During this test session, the coolant was circulated with an electric pump rotating at a constant speed. The oil temperature measured at the sump was conditioned and kept at 80℃ ± 1℃, by heat transfer to (or from) the coolant through a cascade control procedure described earlier. This consequently resulted in coolant temperatures to vary according to the engine speed and pressure load setpoint.

4.3.1 Peak In-Cylinder Pressure

The acquired in-cylinder pressure was post-processed using a LabVIEW® virtual instrument which was specifically developed for use with the pressurised motored setup. The virtual instrument incorporated a check to make sure that 3600 data points are present in the data file between two successive pulses of the Z-index from the

crankshaft encoder. From the 3600 ppr channel, the in-cylinder volume could be determined.

The pegging procedure used for the processing of the in-cylinder pressure regarded the shifting of the in-cylinder pressure trace until the average in-cylinder pressure computed on 20 DegCA before and after BDC intake was made equal to the measured MAP. This given range of crank angles was chosen due to the low pressure variation noted in this region, and also because low mass flow rates are expected. This procedure was explained by Randolph [107], but also advocated by Pipitone [109] through a personal communication. The peak in-cylinder pressure was obtained from a quadratic fit on hundred data points (10 DegCA) around the peak in-cylinder pressure.

Figure 4.4 shows the PCP obtained at each setpoint of engine speed and MAP. It can be noted that the peak in-cylinder pressure shows a variation with engine speed, with a distinctively high magnitude at the 2000 rpm. Naturally, increasing the MAP resulted in larger PCPs. The observation of high PCP at 2000 rpm was also noted in [78], and it was hypothesised that the high peak in-cylinder pressure at this engine speed condition was the effect of the volumetric efficiency. A similar observation was also reported by Knauder et al. [110] for a similar engine. The volumetric efficiency as discussed here is defined as the ratio of mass of dry air ingested by the cylinder in one suction stroke, measured at inlet density, to the piston displacement of that cylinder [111]. In the testing session being reported here (defined by Table 4.1), additional test points were added around the 2000 rpm, at 1750 rpm and 2250 rpm, to have more data for testing the hypothesis. The *no manifolds* loading condition refers to the approximate 1.0 bar MAP, but having both manifolds and shunt pipe removed with the aim of reducing the effect of the volumetric efficiency.

It can be seen from Figure 4.4, that for the *no manifolds* condition, the average of the peak in-cylinder pressure over 300 cycles shows no evident peak at the 2000 rpm. This hints that the peaks over the 2000 rpm shown in Figure 4.4 are a result of the volumetric efficiency, however it should be stated that during the post processing of data, it was noted that for the case of the *no manifolds* condition, very large cycle-to-cycle deviations in the peak in-cylinder pressure emerged. At a particular engine speed of 1750 rpm, the deviation of the PCP over 300 cycles was noted to be around

$\pm$ 3 bar on a mean of 43 bar PCP. This kind of deviation was noted on all speeds for the *no manifolds condition*, except for 2000 rpm and 3000 rpm. It was also noted that at all speeds, for the *no manifolds condition*, a large pressure oscillation appeared on the intake and exhaust strokes.

The observation described is thought to have emerged as a consequence of the communication of the cylinder with an infinite ambient volume. The cycle-to-cycle deviations seen at this *no manifolds* condition raise doubts on whether the test of *no manifolds* is robust enough to conclude that the high peak in-cylinder pressure over the 2000 rpm is truly a result of the volumetric efficiency, however at this stage no other physical explanation was available.
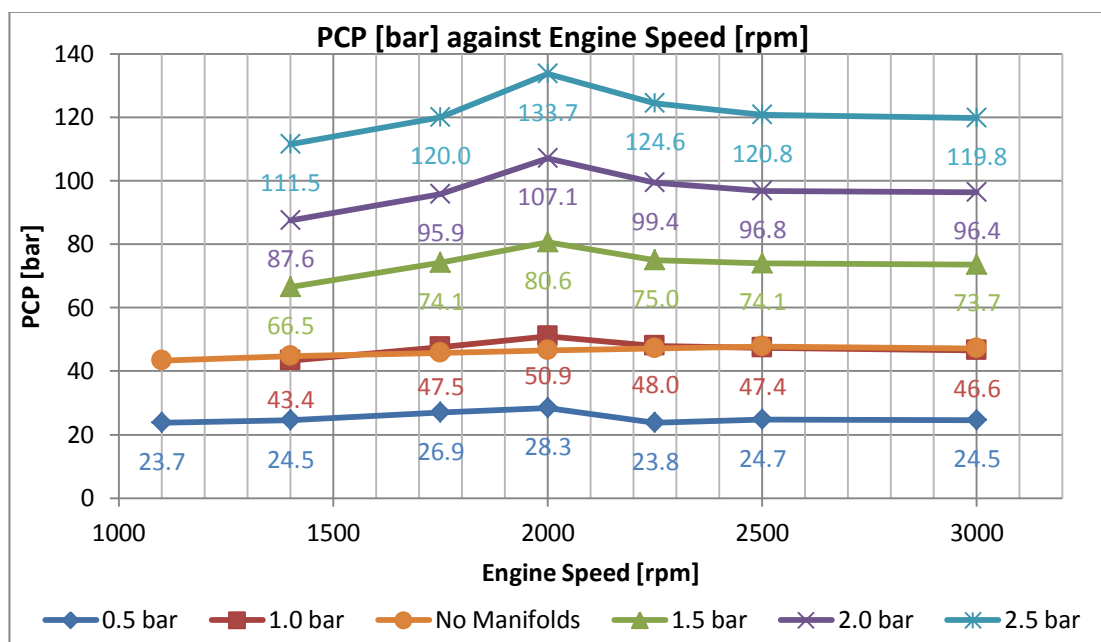
Figure 4.4. PCP against engine speed and MAP.

4.3.2 Shunt Pipe Gas Temperatures

The gas temperatures at the intake and exhaust sides of the shunt pipe were measured with 1.5 mm diameter, K-type, ungrounded and mineral insulated thermocouples extended up to around the centre of the shunt pipe cross-section. Figure 4.5 gives the recorded gas temperatures. It is noted that both the intake and exhaust shunt pipe gas temperatures increase with an increase in engine speed, and also with an increase in pressure load. A variation of the engine speed from 1750 rpm to 2250 rpm seems to show a small decrease in the temperatures at both sides of the shunt pipe.

Figure 4.5 shows that the exhaust side of the shunt pipe is distinctively hotter than the intake side, which initially might seem surprising for a motored engine. This is because, for a motored engine, it is expected that the in-cylinder pressure and temperature of the gas at the end of the expansion stroke are below those at the start of the compression stroke, as shown in Figure 4.6 and Figure 4.7. Note that in these figures, the x-axis angle for the expansion stroke should be positive, but it is plotted in this manner to facilitate comparison between compression and expansion. The lower in-cylinder pressure and temperature at the end of the expansion stroke is expected due to the energy lost from the system throughout the closed part of the cycle as heat and mass leakage (blow-by). In pressurised motoring the effect explained is obscured by the occurrence of another process that takes place during the exhaust stroke, which leads to the observation that exhaust gas temperature is higher than intake gas temperature, as shown in presented Figure 4.5.

It was seen that in pressurised motored operation high peak in-cylinder pressures, synonymous to fired operation are attainable. These high PCPs are a result of the quantity of trapped mass in the cylinder. The higher the trapped mass, the higher is the PCP expected. For instance, at the case of 2.5 bar MAP, around 2.5x the mass ingested at naturally aspirated conditions and same engine speed is expected. Due to the large amount of trapped mass, the exhaust valve curtain area ends up being a bottleneck to the exhaust flow, and as a result a recompression occurs in the cylinder during the displacement phase of the exhaust stroke. This experimentally observed recompression can be seen in Figure 4.8 at 3000 rpm, 84 bar. Figure 4.8 shows a rapid drop in the recompression pressure as soon as the intake valve opens, which creates another communication between the cylinder and the manifold/shunt pipe.

The recompression of the gas during the exhaust stroke results in an increase in the gas temperature of the cylinder to values above those at the start of compression. Hence, the higher exhaust gas temperatures noticed in Figure 4.5 are primarily due to two counteracting effects; a reduction due to energy losses during the closed part of cycle, and an increase due to recompression during the exhaust stroke. Secondary effects might have also contributed to this observation, for example heat transfer from the gas through the shunt pipe. The above explanation was first hypothesised from a physical understanding of the setup, but was later confirmed by a one-dimensional simulation study conducted by Sammut et al. [84] as a part of the same

project, where he changed the exhaust valve curtain area by different amounts and noticed the behaviour of the shunt pipe intake and exhaust temperatures. A reproduction of the result from the simulation is given in Figure 4.9.

A relatable observation from Figure 4.5 is that increasing the engine speed resulted in an increase in the temperature difference between the intake and exhaust sides at the same MAP condition. This is also explainable by the mechanism just described due to the fact that increasing the engine speed results in less time for the piston to exhaust the cylinder mass, hence the exhaust valve becomes an even worse bottle neck which results in a more pronounced recompression. The recompression effect is also worsened by an increase in the PCP, which results in a higher quantity of trapped mass.
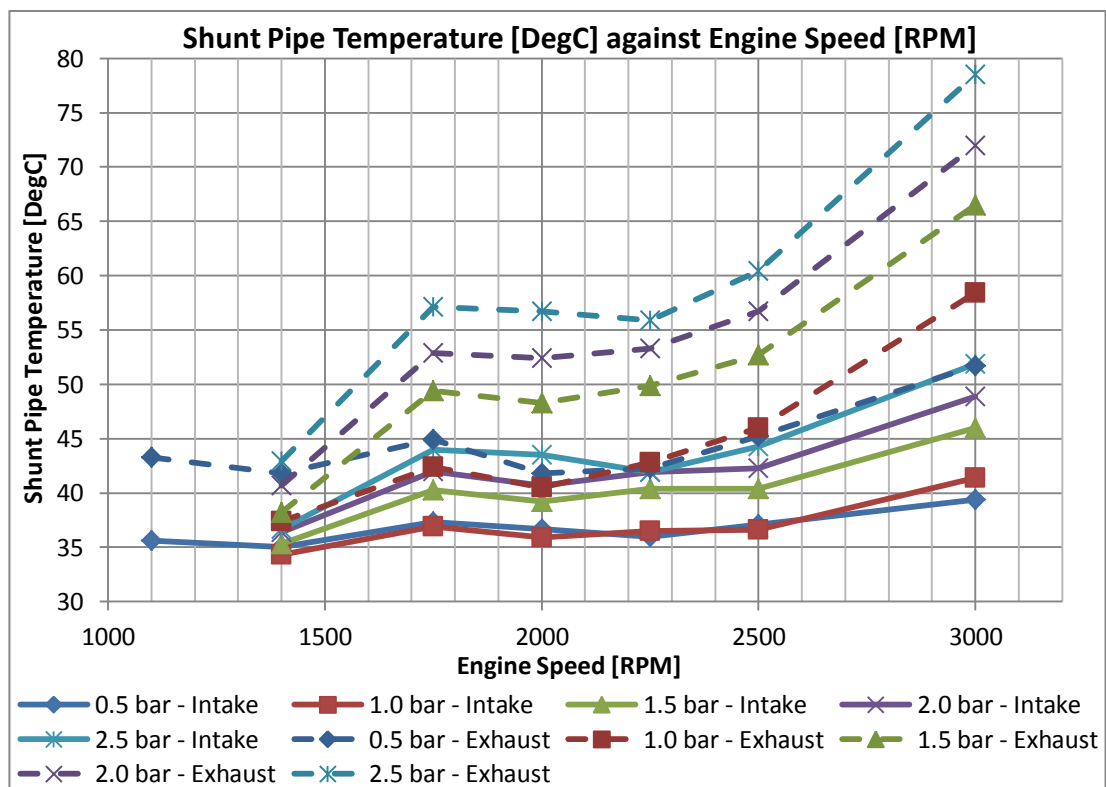
Figure 4.5. Shunt pipe gas temperature against engine speed and MAP.
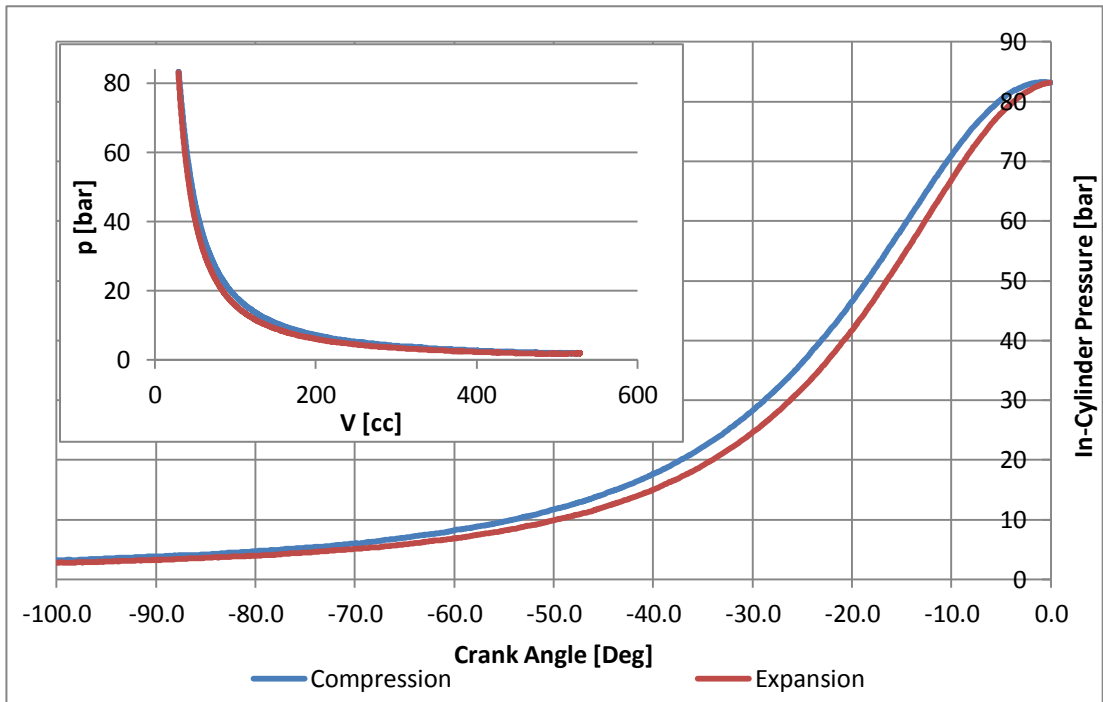
Figure 4.6. In-cylinder pressure against crank angle at 1400 rpm, 84 bar, with air as the working gas.
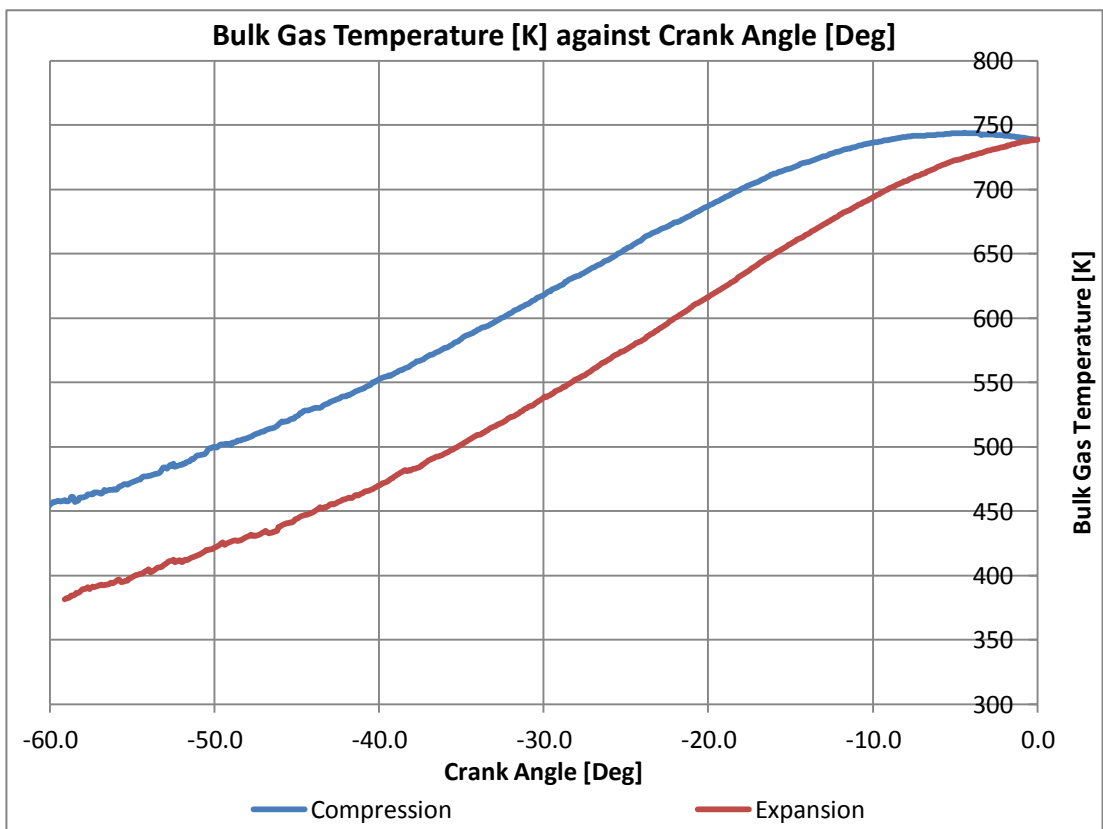
Figure 4.7. Bulk gas temperature against crank angle at 1400 rpm, 84 bar, with air as the working gas.
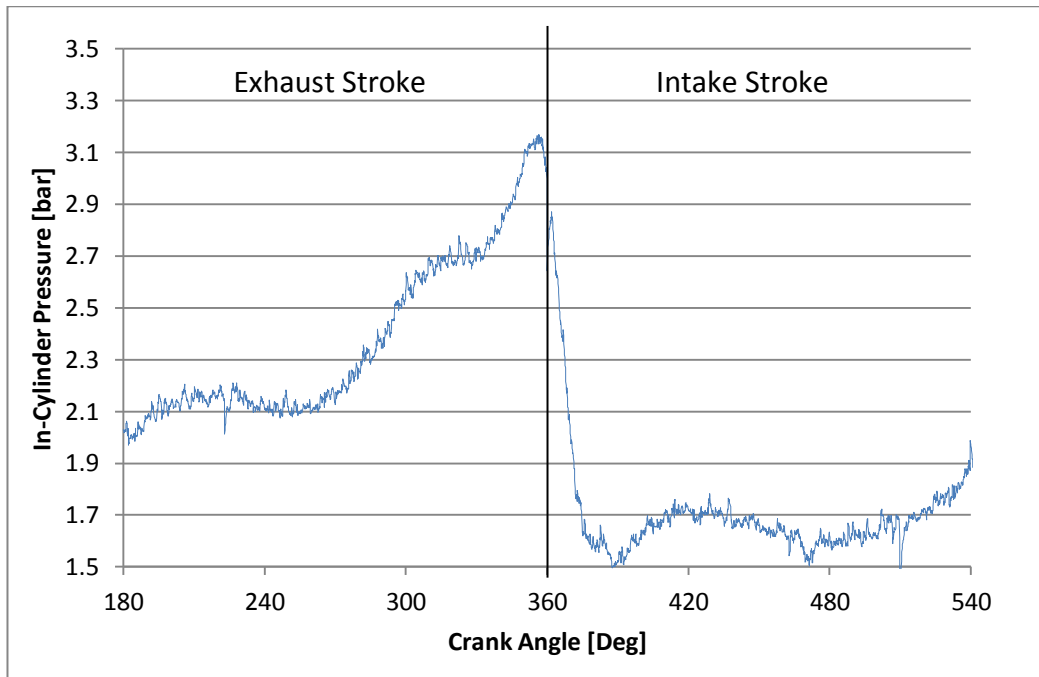
Figure 4.8. In-cylinder pressure at the exhaust and intake strokes at 3000 rpm, 84 bar (1.85 bar MAP).
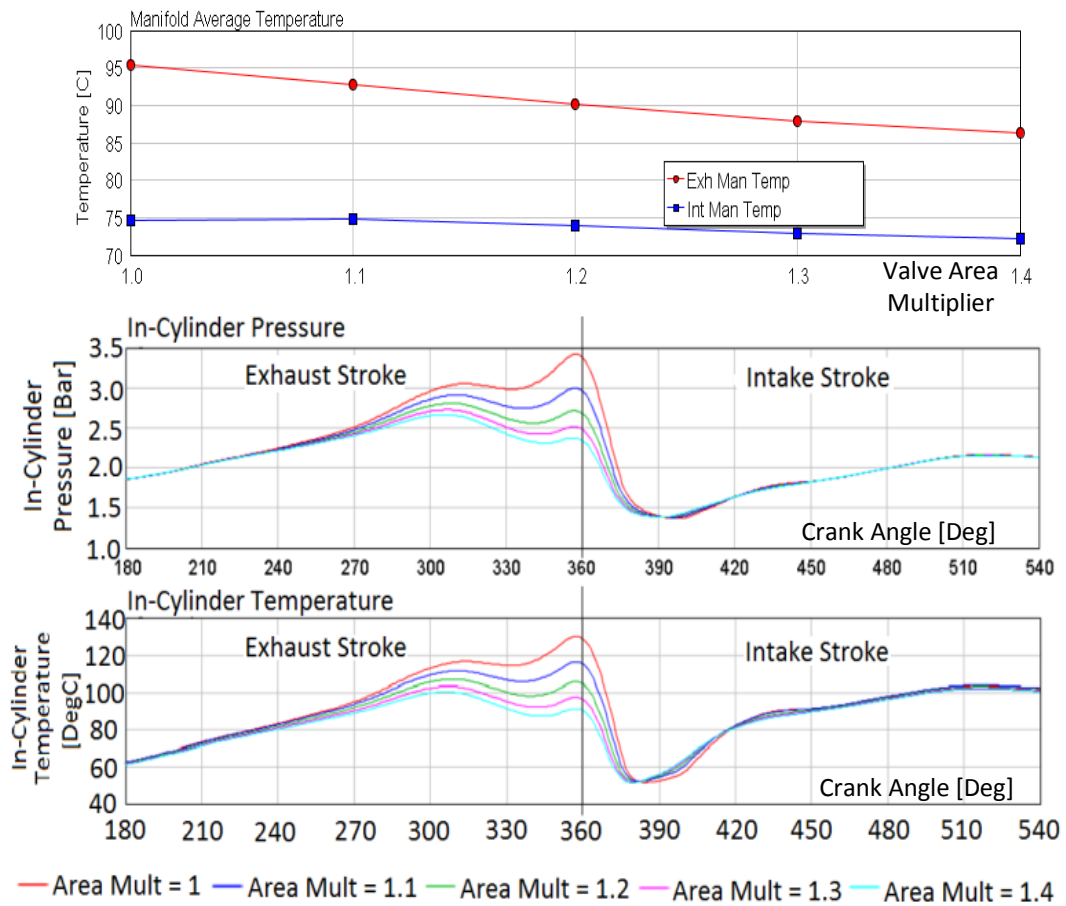
Figure 4.9. Simulated graphs of manifolds temperatures, in-cylinder pressure and bulk gas temperature during intake and exhaust strokes [84].

93

4.3.3 Coolant Temperature and Oil Temperature

As explained in section 4.1 in this test session, the oil temperature measured in the sump was controlled to 80℃ ±1℃ through the use of a cascade PID controller, which used the coolant temperature as the control variable. Even though it is thought that the oil temperature has a greater influence on the FMEP due to its direct contact between rubbing faces, however the coolant temperature should also be given its due importance, as it dictates the thermal expansions and warpages in the cooled cylinder liner and cylinder head. Hence it is expected that to some extent, the coolant temperature also inflicts its effect on the FMEP. It should also be mentioned that although the oil temperature was controlled to be 80℃ at the sump, at the hydrodynamic journal bearing surfaces and piston/ring-liner interface, the oil temperature is expected to be at a different (probably higher), unknown temperature. Figure 4.10 shows the coolant temperatures that were required during this test session in keeping the sump oil temperature at 80℃. The coolant temperature was measured in the coolant jacket, upstream of the thermostat location which in this engine is at the outlet of the cylinder head.

Not surprisingly, Figure 4.10 shows that increasing the engine speed and pressure load results in a decrease of the coolant temperature. One of the reasons for this relationship is that an increase in engine speed and pressure load shall result in an increase in the overall rubbing friction. The energy dissipated in friction is eventually rejected as heat to the oil between the two rubbing surfaces. Hence, to retain a constant oil temperature, the coolant must be able to absorb a higher amount of energy from the oil, which consequently requires a lower coolant temperature.

It can be noticed that to reach the oil setpoint temperature, at high engine speed and high pressure load setpoints, the coolant temperature had to be decreased to values of around 50℃. This is not something ideal in the case of FMEP testing due to the fact that such a low coolant temperature is not exactly representative of the operating conditions of a fired engine in service. Furthermore, having a varying coolant temperature between setpoints might have induced a bias factor in the FMEP values, which if used for theoretical model validation would need to be compensated for.
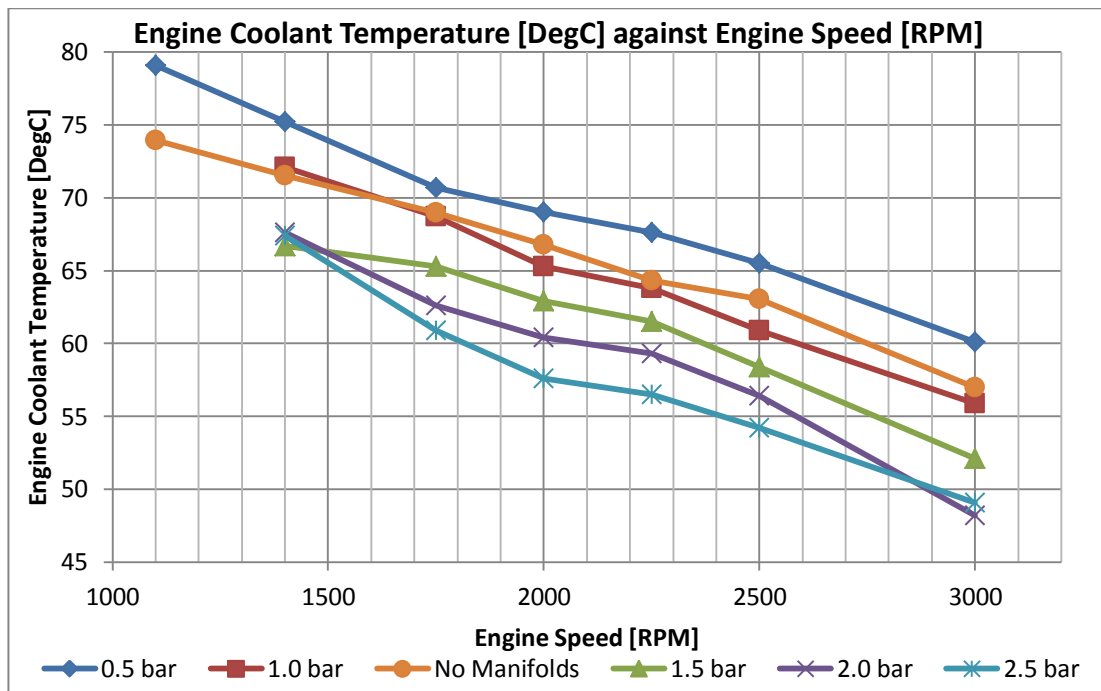
Figure 4.10. Coolant temperature against engine speed and MAP.

4.3.4 Thermodynamic Loss Angle

The thermodynamic loss angle is the angular difference between the location of peak in-cylinder pressure and location of minimum in-cylinder volume. To avoid confusion with similar metrics introduced later on in this dissertation, this will be termed the 'pressure loss angle', and experimentally obtained results are reported in Figure 4.11. For an ideal motored engine, the peak in-cylinder pressure and minimum cylinder volume coincide. The pressure loss angle is therefore a direct result of the heat and blow-by losses from the cylinder. This subject is explained in great detail by Pipitone et al. in [80] [104]. Figure 4.11 shows a decrease in the magnitude of the pressure loss angle with an increase in engine speed. The magnitude also decreases with an increase in the pressure load.

The decrease of the pressure loss angle magnitude with an increase in engine speed is explained by the time period associated with one complete cycle, which decreases with increasing the engine speed. Hence, less time is allowed for heat and blow-by to flow out of the cylinder, and consequently, the peak in-cylinder pressure occurs closer to TDC.

The relationship between pressure load (represented by MAP) and pressure loss angle magnitude can be understood by the following simplified explanation. An increase in MAP results in a higher trapped mass. According to a simple polytropic calculation on the compression stroke reveals that the in-cylinder peak temperature should not change with an increase in MAP. Consequently, for a higher trapped mass, a similar heat transfer should ensue, which therefore results in a lower energy loss per unit mass of the gas. This explanation is oversimplified; however for the present discussion it suffices for the understanding of the trend in Figure 4.11. In forthcoming chapters, it will become apparent why in-cylinder temperature is not exactly constant with differences in MAP, and why heat transfer is not necessarily equal with an increase in the trapped mass.
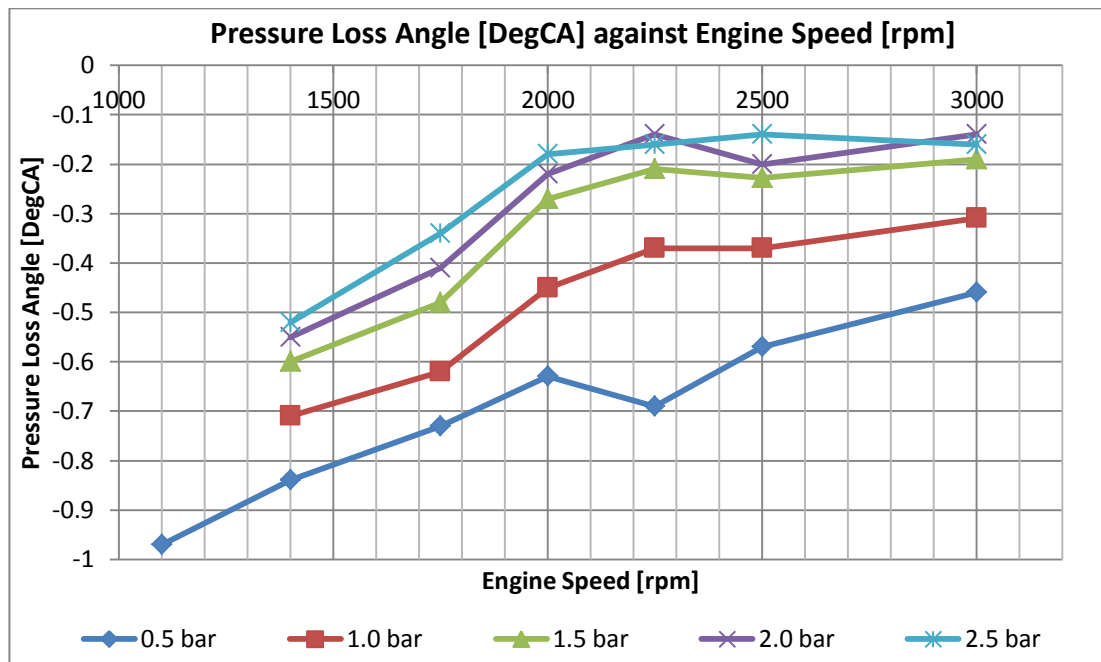
Figure 4.11. Thermodynamic loss angle against engine speed and MAP.

4.3.5 Mean Effective Pressures

In this section, the mean effective pressures that result in the FMEP determination are discussed. From the load cell measurement, the torque produced by the electric motor to drive the engine is obtained. This allows the evaluation of the BMEP, which for a motored engine represents a measure of the total losses.

An integration of the in-cylinder pressure curve with respect to the instantaneous volume over the closed portion of the cycle, for a motored engine gives the quantity of work by the electric motor that is lost as heat transfer and blow-by from the cylinder. This can be converted to a mean effective pressure, and for the purpose of reference, it will be called $IMEP_{360}$. On the other hand, if the integration of in-cylinder pressure and volume is determined over the gas exchange strokes, the work done due to gas pumping is obtained. From this, the pumping mean effective pressure (PMEP) can be determined. A summation of the $IMEP_{360}$ and PMEP results in the $IMEP_{720}$. It should be noted that throughout this research, only one piezoelectric in-cylinder pressure sensor was used. In the four cylinder engine, this was fitted in the OEM glow-plug hole of the fourth cylinder. The mean effective pressures reported for the four cylinder engine therefore do not take into consideration any cylinder-to-cylinder variations. A cylinder-to-cylinder variation analysis was done in [78] on the pressurised motored setup using the same four cylinder engine used in this research.

Since the BMEP, $IMEP_{360}$, PMEP and $IMEP_{720}$ represent only losses from the system, in the forthcoming discussions they will assume a negative value. If the engine is driven without any accessories, mechanical friction can be obtained through a subtraction of the $IMEP_{720}$ from the BMEP, as given by equation (4.1).

$$FMEP = BMEP - IMEP_{720} \qquad\qquad ...(4.1)$$

$$FMEP = BMEP - (IMEP_{360} + PMEP) \qquad\qquad ...(4.2)$$

Figure 4.12 shows the BMEP obtained at different engine speeds and pressure loads. It is noted that an increase in MAP shows a very clear increase in the BMEP magnitude, which represents an overall higher loss. The BMEP also shows an overall increase in the magnitude with an increase in speed, which is however superimposed by a peak at the 1750 rpm - 2000 rpm region. This originates due to the fact that the mechanical load is represented by the MAP and not the PCP, hence due to the dependency of volumetric efficiency on engine speed, at every engine speed condition for the same MAP, the PCP varies which results in a consequent variation in the losses. Essentially this means that the variation in the mean effective pressure (MEP) at a given MAP condition displayed in Figure 4.12, and forthcoming figures in this section do not represent the absolute variation with engine speed, but are

superimposed with an underlying inflicting effect of the non-uniform PCP. This should be kept in sight while observing the forthcoming figures which plot different metrics against engine speed.

In this test session, the highest BMEP magnitude was found to be at 1750 rpm and highest MAP condition of 2.5 bar. At this setpoint, the power dissipated by the motor to drive the engine was around 10.7 kW. At the highest engine speed and MAP condition, the power required was 17.7 kW, which means that the AC motor was practically reaching its maximum rated characteristics. At the lowest engine speed and MAP condition, the power requirement was almost 2 kW.
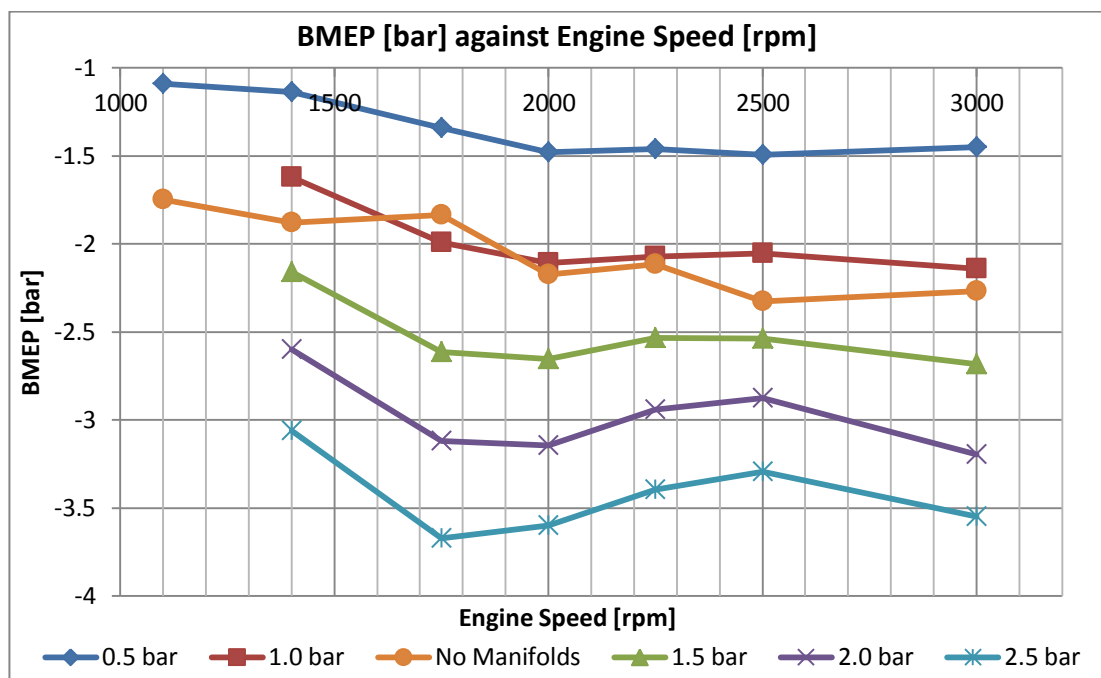
Figure 4.12. BMEP against engine speed and MAP.

The variation of $IMEP_{720}$ with engine speed and MAP is shown in Figure 4.13. It is noticed that the $IMEP_{720}$ shows a very similar trend to that reported in Figure 4.12 for the BMEP. Since the $IMEP_{720}$ includes the effect of three interacting variables, namely heat losses, blow-by and pumping losses, it is better understood if split into the two counterparts; $IMEP_{360}$ and PMEP. The $IMEP_{360}$ is shown in Figure 4.14 and Figure 4.15.
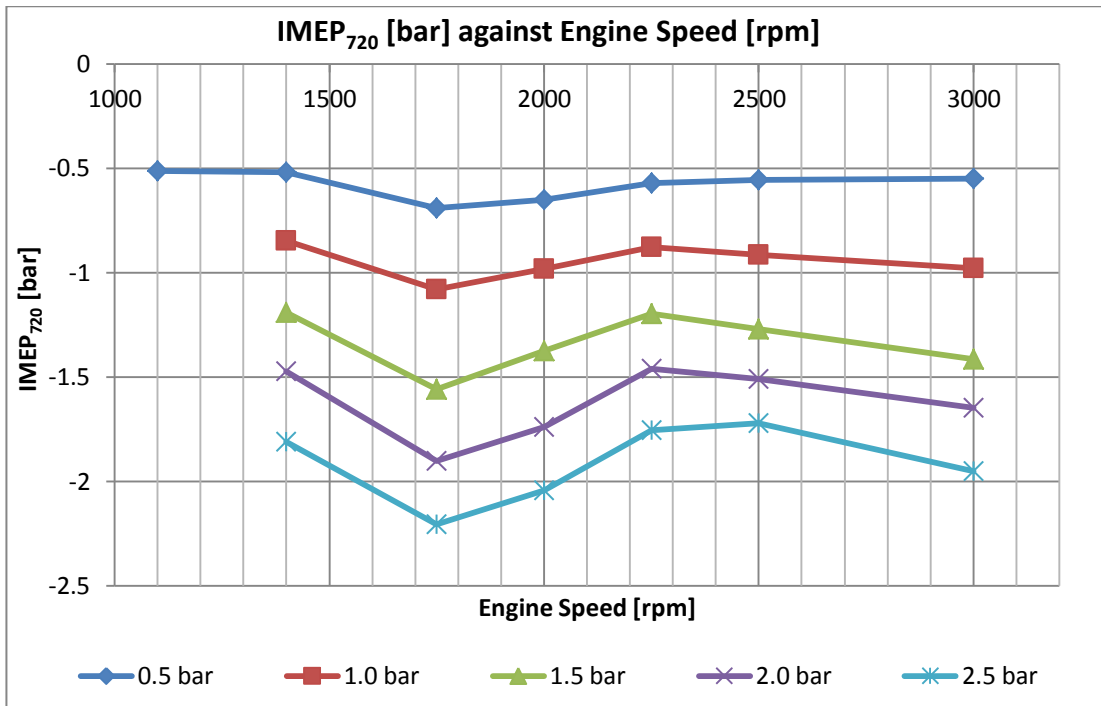
Figure 4.13. IMEP$_{720}$ against engine speed and MAP.
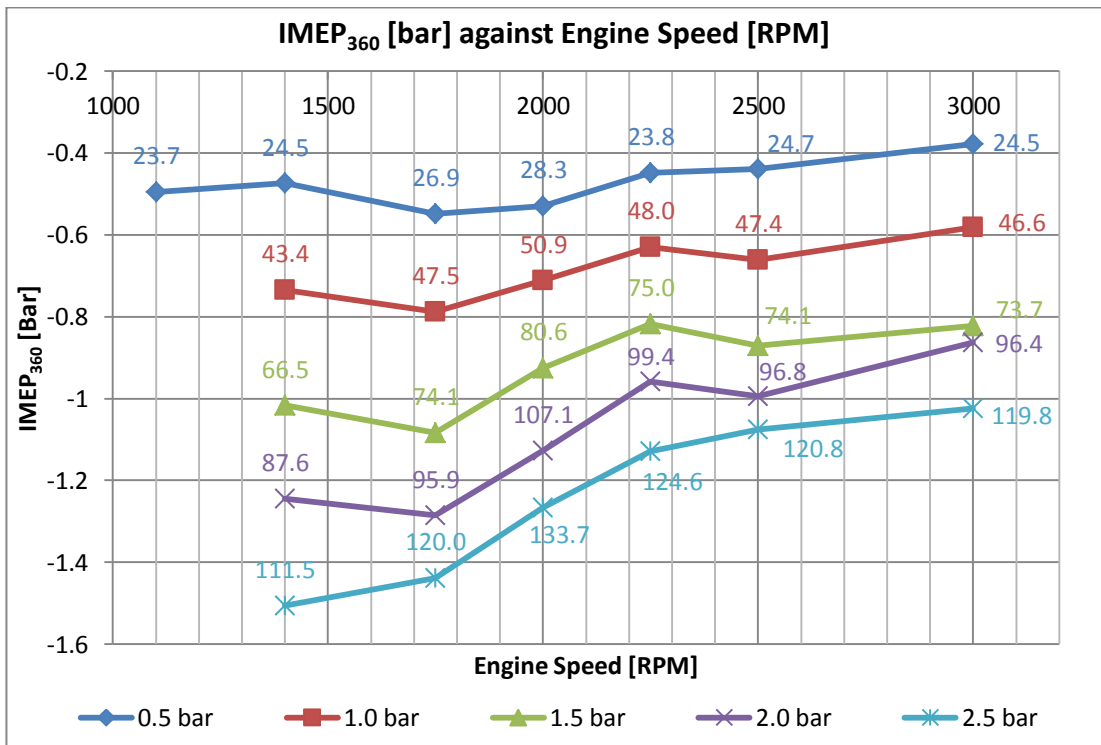
Figure 4.14. IMEP$_{360}$ against engine speed and MAP (PCP of each point included in data labels).
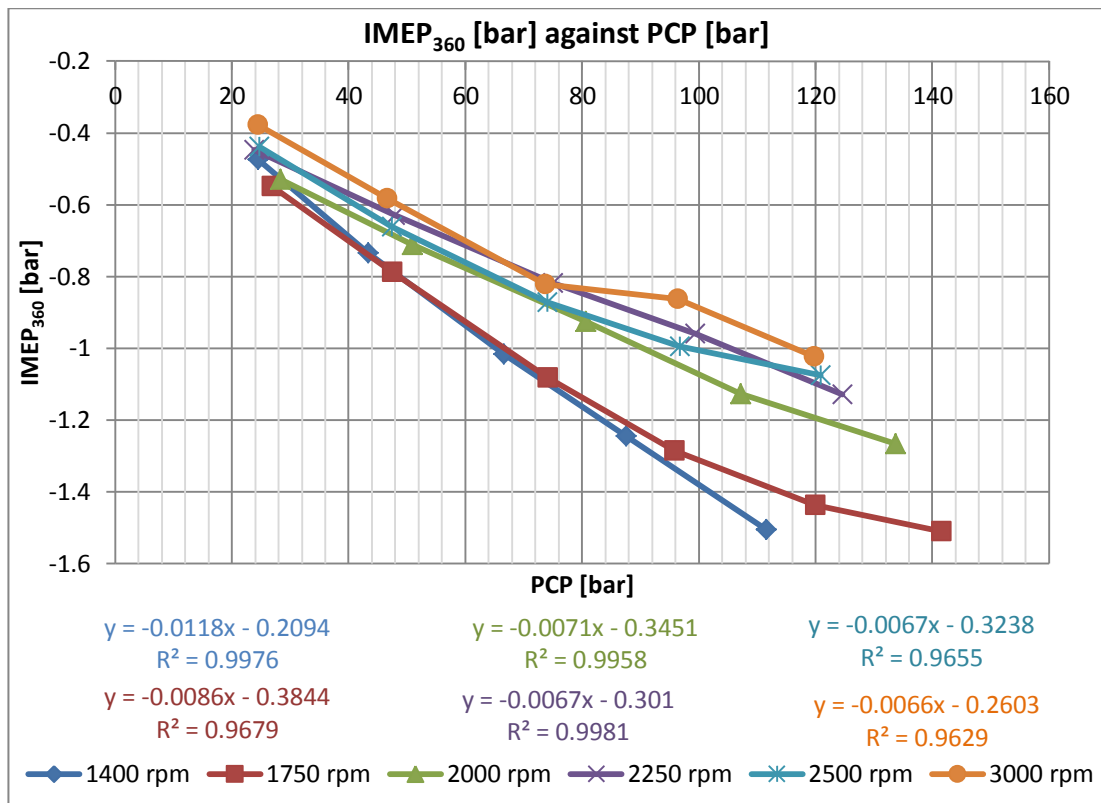
Figure 4.15. $IMEP_{360}$ against PCP and engine speed.

The $IMEP_{360}$ for a pressurised motored engine represents just the heat transfer and blow-by losses during the compression and expansion strokes. It can be noted from Figure 4.14 that the $IMEP_{360}$ shows a decreasing magnitude with an increase in engine speed (with irregularities due to variances in the PCPs at the same MAP). On the other hand, an increase in the magnitude of $IMEP_{360}$ is noted with an increase in the pressure load (or MAP). The relationship between $IMEP_{360}$ and pressure load is better shown in Figure 4.15, where the MAP values were converted to their corresponding PCPs according to the data presented earlier. It is interesting to note that the $IMEP_{360}$ relationship with PCP is adequately represented by a linear fitting. The gradient of this linear fitting seems dependent on engine speed and its magnitude consistently decreases with an increase in engine speed. To understand the physical reasons for the relationship between $IMEP_{360}$, engine speed and MAP, the reader is referred to the explanation of the variation of pressure loss angle in section 4.3.4, which is also a measure of heat and blow-by losses, and hence shares a similar physical explanation.

The PMEP variation with engine speed is shown in Figure 4.16, whereas the variation with PCP is shown in Figure 4.17. It is noted that the PMEP varies as a

linear function with PCP. On the other hand, the variation of PMEP with engine speed is not as straight forward. A distinctive peak is shown over the 1750 rpm - 2000 rpm range and has an underlying trend of increase in the PMEP magnitude with an increase in engine speed. The peak over the 1750 rpm and 2000 rpm is synonymous to that found in the $IMEP_{720}$, BMEP and shunt pipe temperatures. This comparison enables two conclusions.

The first conclusion is that the peaks shown in the $IMEP_{720}$, over the 1750 rpm and 2000 rpm originate principally from a distinctive increase in PMEP at these engine speed conditions. This conclusion can be made after having observed both the relationship of PMEP and $IMEP_{360}$ with engine speed. The $IMEP_{360}$ shows no distinctive peaks over this engine speed range, hence that seen on the $IMEP_{720}$ must have originated from the PMEP.

The second conclusion highlights the reason for the distinctively high PMEP at these two speeds. From Figure 4.4, it is noted that at the 2000 rpm range the highest PCP values were observed for each MAP condition. On the other hand, from Figure 4.5, a steep increase in the exhaust temperature was noted from 1400 rpm to 1750 rpm, which was sustained constant at the 2000 rpm. Both of these observations hint that the recompression effect on the exhaust stroke at 1750 rpm and 2000 rpm is appreciable and hence led to large PMEP at these two particular engine speed conditions. This was confirmed from an analysis of the in-cylinder pressure trace. A large recompression results in a wider pumping loop on the p-V indicator diagram, which consequently promotes a higher PMEP. From this observation, it could be noted that the severity of the recompression effect is a function of at least two variables, the quantity of trapped mass (determined from the MAP, or PCP), and the engine speed which dictates the rate of mass flow through the valve curtain area.
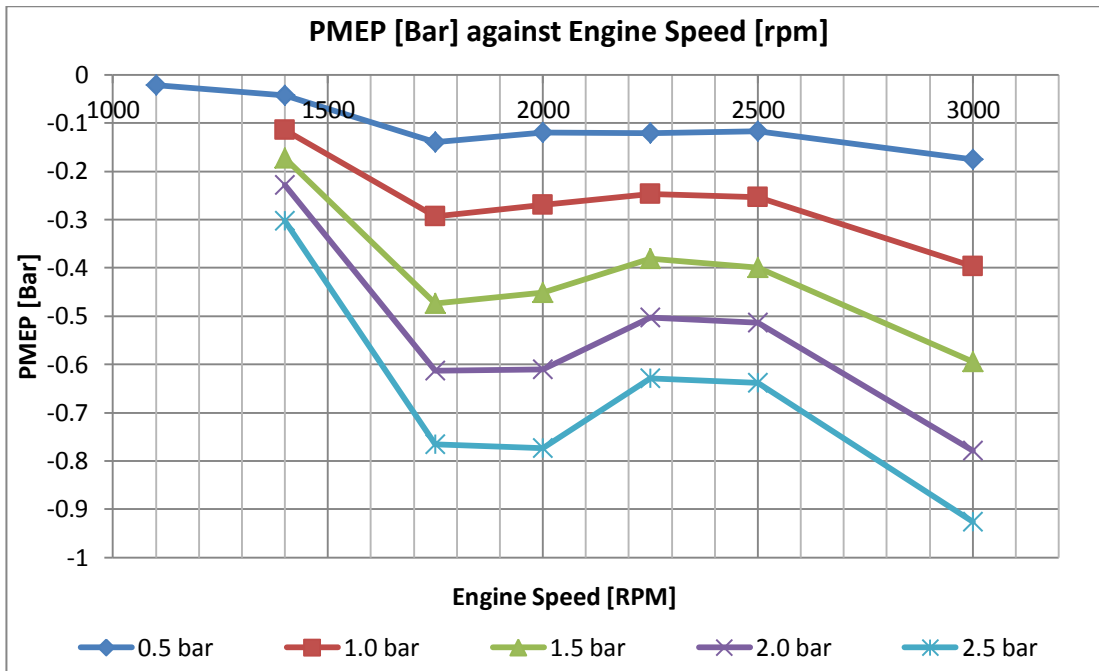
Figure 4.16. PMEP against engine speed and MAP
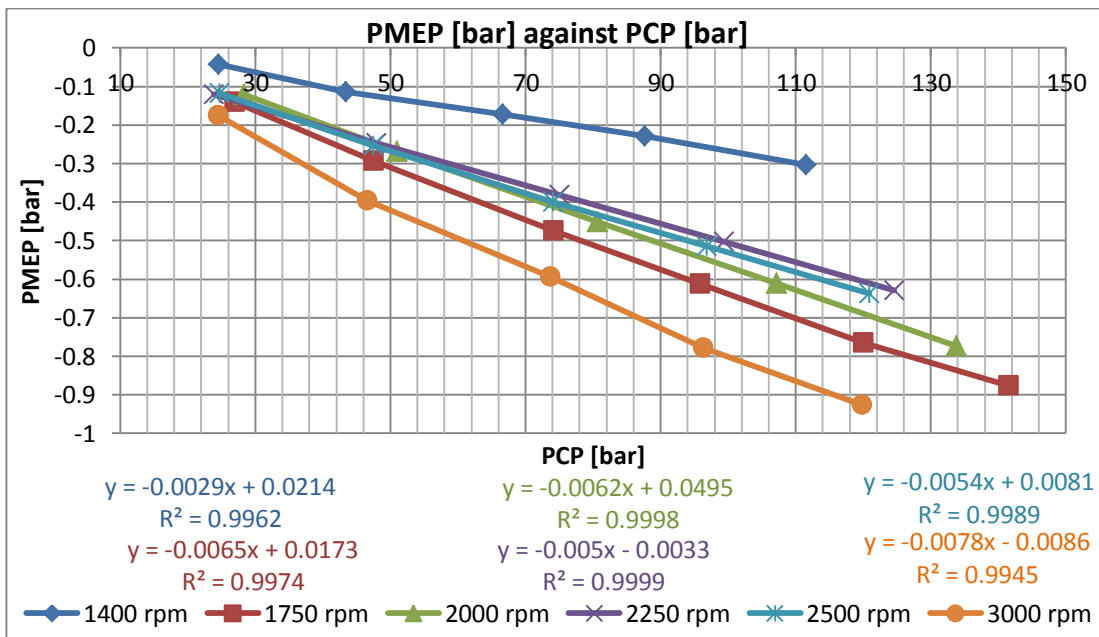
Figure 4.17. PMEP against PCP and engine speed.

Through a subtraction of the $IMEP_{720}$ from the BMEP, the FMEP was obtained and presented in Figure 4.18 and Figure 4.19. An increase in the FMEP magnitude can be seen with an increase in both engine speed and PCP. It is interesting to see that the FMEP for the pressurised motored engine varies in a linear relationship with PCP with a gradient that is similar for all engine speed conditions. This observation was also made by Allmaier et al. [76] for a much larger six-cylinder engine, tested on a

pressurised motored setup. The relationship of FMEP with engine speed shown in Figure 4.18 was not curve-fitted for the reason which was previously explained; that in this section the metrics plotted against engine speed have an underlying variation originating from different PCPs at the same MAP.

By observing Figure 4.18, Figure 4.12 and Figure 4.13, it can be identified that using the pressurised motored engine, the FMEP/BMEP and FMEP/IMEP$_{720}$ ratio can be as high as 62% and 170% respectively. This means that the FMEP magnitude is comparable to the magnitudes of both the BMEP and IMEP$_{720}$. This is thought to be the most powerful quality of the pressurised motored method for FMEP determination, since fired methods typically have FMEP/BMEP ratios of around 15%, which therefore makes the uncertainty propagation on the FMEP much larger than that obtained from a pressurised motored engine.

If a 2% uncertainty is assumed on the IMEP$_{720}$ and BMEP, as explained by Mauke et al. [4] and presented in chapter 2, the uncertainty propagation on the experimental FMEP presented in Figure 4.18 would be between 3.5% and 6% of the absolute value of the FMEP.
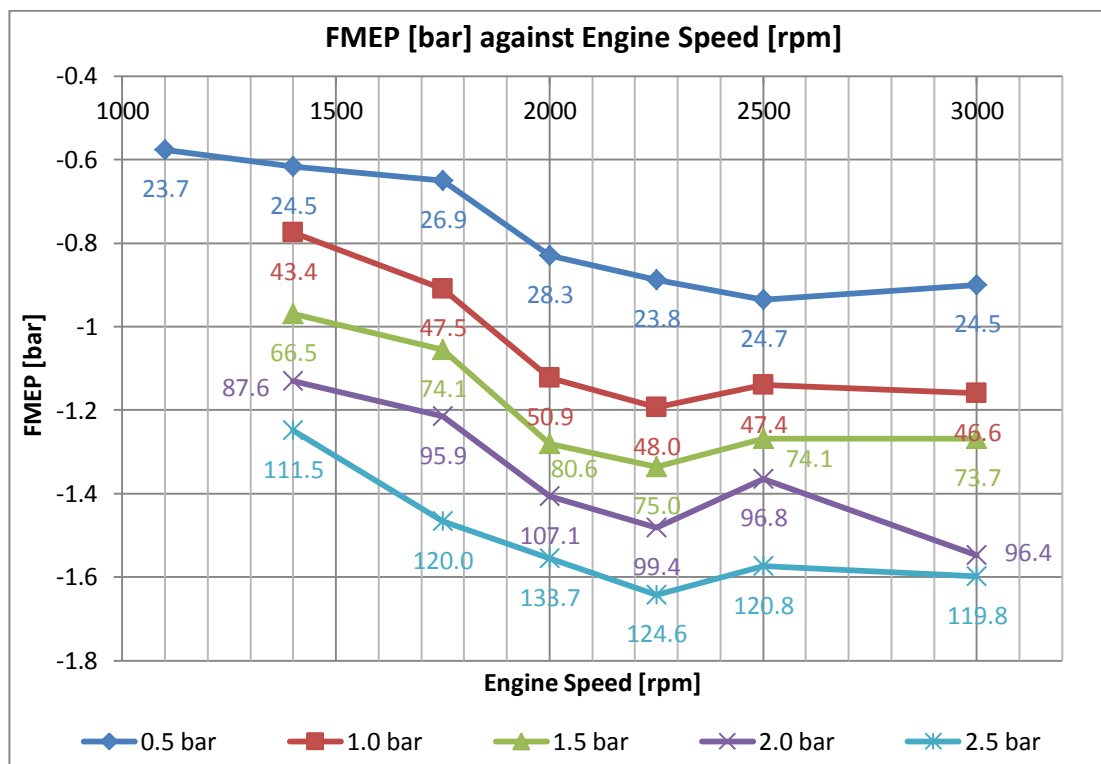
Figure 4.18. FMEP against engine speed and MAP (PCP in data labels).
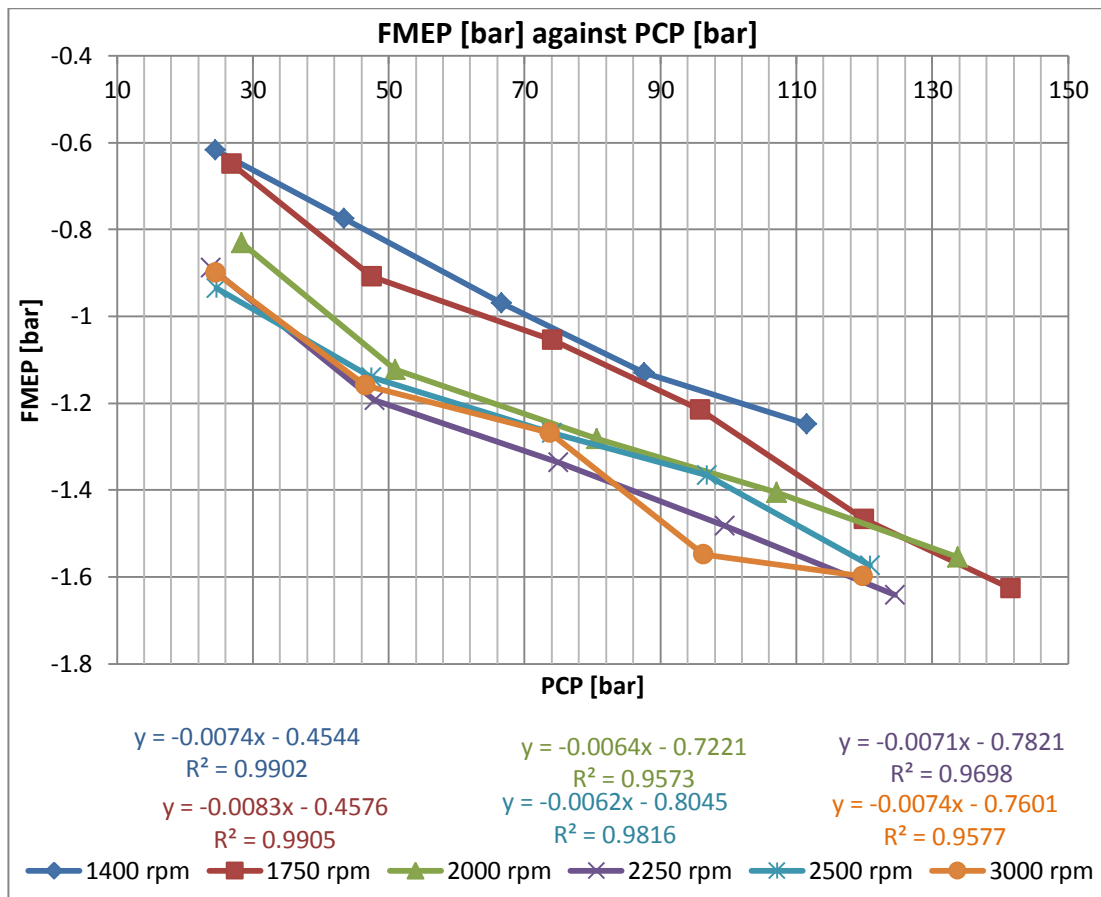
Figure 4.19. FMEP against PCP and engine speed.

4.3.6 Observations and Remarks

Having presented the FMEP, a reflection on the external factors which could have affected its determination is deemed fitting. Some compromises had to be made at the time that this test matrix was conducted, and as a result should this data be used for model calibration; some care has to be practiced.

To start off with the least affecting, as mentioned in the previous text, in this work the load parameter used was the MAP, which is incapable of fixing the PCP at a constant value at all engine speed conditions. At the same MAP condition, the PCP was found to vary by around 15% over the range of engine speed tested. This is expected to result in around 7% variation in the FMEP, based on the trend of FMEP with PCP presented in Figure 4.19. This however should not deter from using the data for model fitting, as the PCP at each setpoint condition was determined and hence could be accounted for. The reader just needs to observe the previously presented trends of engine speed with caution.

The second factor which was briefly mentioned at the beginning of section 4.3 is that the coolant temperatures were not constant at each setpoint, hence could have induced variances in FMEP due to different thermal expansions of the engine structure. The coolant temperatures were however measured and it was shown that the difference in the coolant temperatures between the two extreme setpoints is 30℃. The oil temperature, which is thought to be more directly related to mechanical friction was held constant at the sump, hence should not have induced variances in FMEP.

Two other external factors which surely affected the FMEP results are the power requirements of the OEM oil pump and vacuum pump, which for the test matrix described were the only two accessories still driven by the engine. In the original configuration of the 2.0 HDi engine, the oil pump is connected to the crankshaft, whereas the vacuum pump is directly driven by the camshaft. Even though the vacuum pump was retained connected to the engine camshaft, its suction port was blocked, and as a result its power requirement was drastically reduced.

To remove the oil pump, extensive dismantling of the setup was required, which at the time of testing was not deemed appropriate. This meant that the energy requirement to drive the oil pump was considered as part of the FMEP of the base engine. Since the OEM oil pump is driven through the crankshaft, the oil pressure is expected to have some characteristic with engine speed. Hence, it is also expected that the FMEP equivalent of the oil pump requirement also exhibits an increase with an increase in engine speed. Furthermore, a different lubrication pressure at the different engine speed conditions may have resulted in a different hydrodynamic lubrication condition at the journal bearing surfaces, and hence a variation in FMEP due to this is probable.

4.4 Testing with Argon and its Mixtures with Air

After having obtained the characteristics of the FMEP with engine speed and PCP, progression was made to tackle the main FMEP investigation concerning this study, *i.e.* the variation of FMEP and other metrics with different bulk gas temperatures. This was done mainly to provide a better emulation of the fired engine, while retaining the benefits of testing a motored engine. Furthermore, with the planned test

matrix evidence could be produced of the extent to which the differences seen in the FMEP between a fired and pressurised motored engine [77] are a result of the different bulk gas temperatures.

To conduct this investigation, at least two methods are available; either by heating the intake air to values around 400°C on the conventional pressurised motored setup, or use different gases of higher ratios of specific heats. In this study, the second method was preferred for various reasons, as will be outlined in the forthcoming text. It is known that at least three different authors made use of this method throughout the years, however the use of the different gases was not for FMEP determination, but for purposes of heat transfer measurements [24] [42] [75], and prevention of corrosive wear in an investigation of mechanical wear on the piston top ring [74].

In this study, different working gases were used such that the ratio of specific heats ($\gamma = c_p/c_v$, or *gamma*) was varied between 1.40 corresponding to that of air, to 1.67 corresponding to that of Argon (at room temperature). A gradual increase in the γ was obtained by synthesising two mixtures between air and Argon to obtain gases with a ratio of specific heats of 1.50 and 1.60 at room temperature. To synthesise these two mixtures, Argon concentrations of 57% and 87% by mass with air were employed, respectively. Air was also artificially synthesised from Oxygen and Nitrogen. The two mixtures tested were appropriately selected based on an adiabatic compression calculation to give an evenly distributed range of γ that is capable of inducing a linear increase in the peak bulk gas temperature for the same intake gas temperature and compression ratio (subject to the adiabatic assumption). Mixing of the gases could have been done in real time during testing through pressurised supplies of Air and Argon; however, in order to reduce testing complications and ensure a sound and consistent mixture, pre-mixed cylinders were used. The test matrix conducted consisted of 32 points involving four engine speeds, two PCPs and four different gases. The test matrix was presented in Table 4.2, section 4.1. To run the engine on a gas other than air, some modifications to the pressurised motored setup were required. These modifications were detailed in Chapter 3, section 3.1.1. Prior to testing the setpoints concerning this study, the engine was left to run for several minutes with Argon flowing from a 100 Nm^3 pressurised cylinder to the manifolds/shunt pipe system. During this time, the bleed valve was opened to purge the system with Argon. Evaluation of this purging procedure was possible through

the use of a UniNOx sensor, which provided a measurement of oxygen in the buffer tank.

In contrast to the previous testing session already documented, in this testing session done with mixtures, the mechanical load was represented by the peak in-cylinder pressure as the control variable, and not by the MAP. This change was not desired, as it was bound to create difficulty in comparing this data with that previously obtained. However, the manifold pressure could not be used as the control variable in the mixtures testing session due to the fact that a different ratio of specific heats produces a variation not only in the bulk in-cylinder temperature, but also in the in-cylinder pressure for the same MAP condition. Thus, if the manifold pressure was chosen as the control variable, the data would not have been fit to compare the FMEP between different bulk gas temperatures, as the pressure load on the piston assembly and cranktrain would have been different between the different gases. Additionally, using the PCP as the load parameter removes the underlying effect of volumetric efficiency from the engine metrics when plotted against engine speed, hence increases the experiment data quality. In this testing session, the PCPs that were initially intended to be tested were 80 bar and 100 bar, however since pegging could not be done in real time during data acquisition, the PCPs ended up being 84 bar and 103 bar with an average standard deviation of 0.5 bar and 1 bar respectively on the whole test matrix. Figure 4.20 shows the manifold absolute pressure recorded in obtaining both the 84 bar and 103 bar peak in-cylinder pressures. It is noted that the lowest manifold pressure was seen at 2000 rpm, which is consistent with observations done in the previously documented test sessions – showing that the engine has a higher volumetric efficiency at this engine speed, hence requires a lower manifold pressure.

An interesting observation is that with Argon as the working gas (γ: 1.67), a very low MAP setting of around 0.967 bar resulted in a peak in-cylinder pressure of 84 bar at 2000 rpm. This high PCP results from the same reason that the bulk in-cylinder temperature increases with the use of Argon, *i.e.* the high ratio of specific heats. Although the high bulk gas temperatures were the desired target in this investigation, it was found that using Argon (and its mixtures) reduced the range of PCPs that can be tested. The reason is that for the engine tested, the maximum PCP is limited to around 120 bar for reliability reasons, whereas the lower limit with

Argon was found to be around 80 bar due to the high γ. Decreasing further the MAP from the condition of 0.967 bar might result in the risk of diluting the closed Argon system with air. As a result the PCP was never set lower than 84 bar when using Argon mixtures.
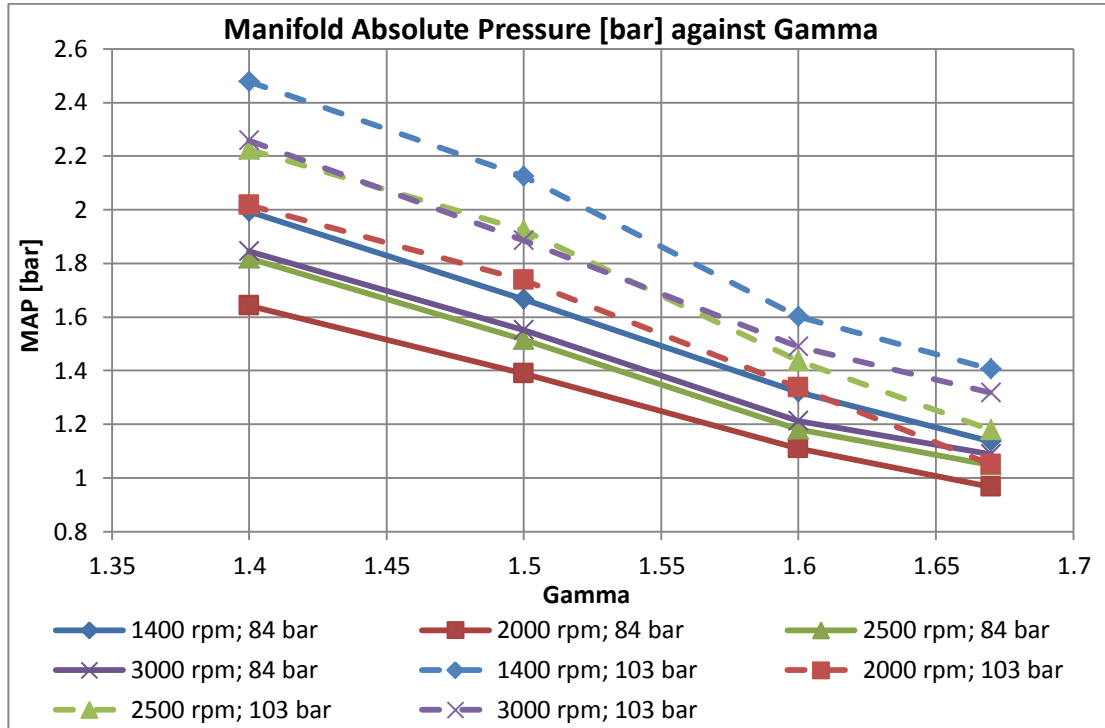
Figure 4.20. MAP against engine speed, PCP and projected γ.

4.4.1 The effect of Ratio of Specific Heats on Gas Temperatures

Figure 4.21 and Figure 4.22 show the intake-side and exhaust-side temperatures of the gas in the shunt pipe at 84 bar and 103 bar respectively. The pressurised motored setup was never fitted with a conditioning circuit for the intake air temperature. The system was left to reach thermal equilibrium with the ambient at every set point. This was a thought decision as conditioning the gas temperature would have required the use of a heat exchanger which would have complicated the installation, but mostly the heat exchanger was not fitted because if a one-dimensional model is set up to model the engine (as in section 6.1), the modelling of the heat exchanger would reduce greatly the simulation fidelity. Not fitting the heat exchanger had the consequence that at every engine speed and γ set point, the intake gas temperature reached at steady-state was different. It is however comforting to see from Figure 4.21 and Figure 4.22 that the only significant change in intake temperature was seen

with different engine speeds and not with different γ ratios. This means that at a given engine speed, for the range of γ tested in this work, the intake gas temperature showed minimal variation, hence the higher bulk gas temperature achieved with changing the gas and presented later on, can be attributed mainly to the change in γ, and not to a different intake temperature. From both figures, it can be noticed that the exhaust-side temperature is higher than that of the intake-side temperature. This observation is consistent with previously presented results for testing with air. This was attributed to the recompression effect that occurs during the exhaust stroke.
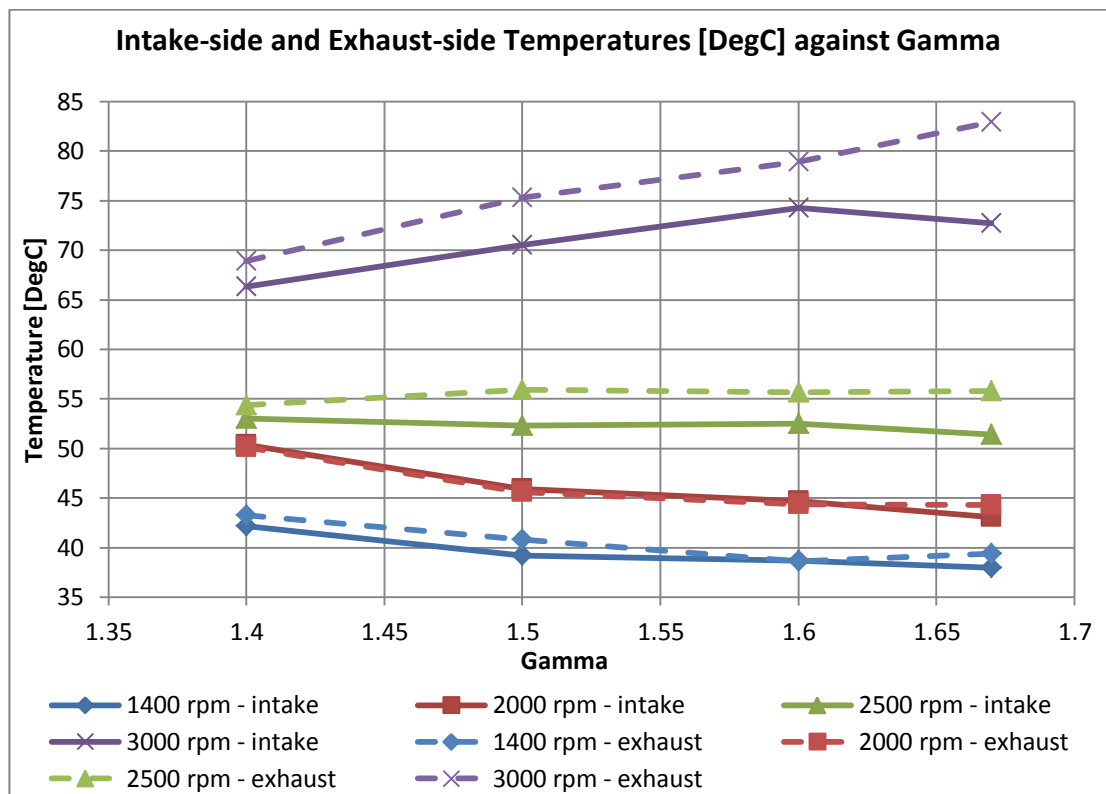
Figure 4.21. Shunt pipe gas temperatures against projected γ and engine speed at a PCP of 84 bar.
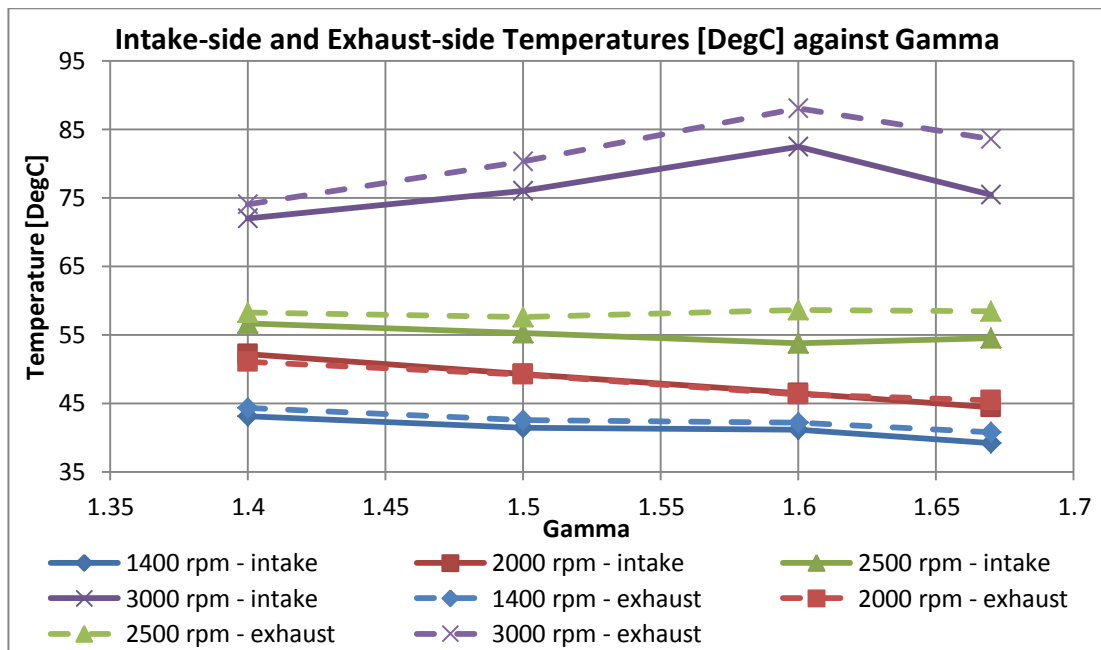
Figure 4.22. Shunt pipe gas temperatures against projected γ and engine speed at a PCP of 103 bar.

The in-cylinder bulk gas temperature was evaluated by making use of the ideal gas law, together with two simplifying assumptions: the in-cylinder gas mass was considered constant during the whole compression and expansion strokes, and the heat transfer during the intake process was considered negligible. The second of these assumptions allows for a simplification that the in-cylinder gas temperature at Inlet Valve Closure (IVC) can be assumed equal to the measured gas temperature in the intake manifold (reported in Figure 4.21 and Figure 4.22). Hence, for each crank angle θ, the bulk gas temperature $T(\theta)$ can be calculated as given by equation (4.3), where T_{IVC}, p_{IVC} and V_{IVC} are the gas temperature, the gas pressure and the in-cylinder volume at IVC. Not making use of the two simplifying assumptions would require a proper model supported by experimental identification to account for the heat transfer during the intake stroke and mass leakage during the compression and expansion strokes. It should be also mentioned that due to the large temperature fluctuation that the bulk gas experiences during the compression and expansion strokes, the variation of the ratio of specific heats with temperature becomes important and hence was taken into consideration when computing any inter-cycle calculations. The graphs presented in this chapter with the x-axis being γ refer to the ratio of specific heats that is expected at room temperature, here referred to as the "projected γ".

Figure 4.23 and Figure 4.24 show the peak of the bulk gas temperature as obtained from a curve fitting around the peak of the instnantaneous bulk gas temperature computed from equation (4.3). Both figures show similar trends with a gradual increase in peak bulk gas temperature for the different γ ratios, with the extremities being around 600°C apart. This graph proves the capability of the test to increase the peak bulk gas temperature of the pressurised motored engine to values synonymous with the fired engine [83]. Additionally, a comparison between the result of Figure 4.23 for the 84 bar PCP, to that of Figure 4.24 for the 103 bar PCP shows that the corresponding setpoints at the two PCP conditions experience virtually the same peak bulk gas temperature. This means that the method of gas mixtures in use with pressurised motored engine has the capability of controlling the peak bulk gas temperature (thermal load) independently from the PCP (pressure/mechanical load) of the engine. This therefore allows the experimentalist to study the effect of several engine metrics, including the FMEP, as a function of the bulk gas temperature decoupled from the effects of pressure load, or vice versa. This is something which cannot be easily acquired with fired FMEP testing, and hence opens a niche for the use of pressurised motoring.

The instantaneous bulk gas temperature as computed from the experimental in-cylinder pressure data using equation (4.3) for the 103 bar testing at 1400 rpm for the different γ ratios is given in Figure 4.25. It can be seen that all traces start from approximately the same gas temperature at IVC (according to the measured shunt pipe intake temperature in Figure 4.21 and Figure 4.22), however they quickly separate to give different bulk temperatures around TDC compression. At about 70 DegCA ATDC, the temperatures for each different γ ratio coincides back to the same value. After this point, the temperatures fall to different values, depending on their γ ratio. The gas with the highest γ reaches the lowest temperature near exhaust valve open (EVO), whereas the gas with the lowest γ retains the highest temperature near EVO. This shows that if all traces had similar temperatures at IVC, then increasing the γ resulted in a larger energy loss magnitude throughout the compression and expansion strokes, which is reflected in the respective temperature differences seen between IVC and EVO for each γ.

$$T(\theta) = T_{IVC} \left(\frac{p(\theta)}{p_{IVC}}\right)\left(\frac{V(\theta)}{V_{IVC}}\right) \qquad \ldots (4.3)$$

111

Apart from the difference in the magnitude seen between IVC and EVO on the bulk gas temperature, the heat loss and mass leakage from the cylinder also shifts the in-cylinder temperature trace to have an early peak with respect to TDC. This concept was clarified by Pipitone et al. [80], utilising a temperature-entropy diagram for the compression in a motored engine, where it is shown that the in-cylinder temperature peaks earlier than pressure, which in turn, is known to show a peak earlier than minimum volume. For the purpose of reference, in this work the angular shift between the in-cylinder peak bulk gas temperature and TDC will be called the 'temperature loss angle', whereas the shift between the peak in-cylinder pressure and TDC will continue to be referred to as the 'pressure loss angle'. Figure 4.26 and Figure 4.27 show the temperature and pressure loss angle for the testing sessions of 84 bar and 103 bar. It is shown that decreasing the engine speed increases the magnitude of both loss angles. This relationship of loss angle with engine speed was already explained in an earlier section by the fact that at higher engine speeds, less time is allowed for heat and mass to flow out of the cylinder. Using a gas with a higher ratio of specific heats also showed a significant increase in the loss angle magnitudes. This can be explained by the higher magnitude of heat losses owed to higher bulk gas temperatures. Figure 4.26 and Figure 4.27 also show that the temperature loss angle is between four to six times greater than the pressure loss angle. This is in line with the explanation by Pipitone et al. [80].

Due to the shift mentioned between temperature, pressure and volume, the polytropic relationships given in equation (4.4) and equation (4.5) require the prior knowledge of the pressure p^* and V^* at the crank angle at which the peak in-cylinder temperature occurs. Logically, these will be unknown at the point when the computed bulk gas temperature is not yet constructed, hence these relationships in the majority of the cases cannot be used to evaluate the peak in-cylinder temperature, but instead a stepwise computation using the previously given equation (4.3), should be utilised. Using equation (4.4) and equation (4.5), with the incorrect values of p^* and V^* (*i.e.* usually those at minimum volume, TDC) will result in errors of the order of 200℃ for the engine tested in this study.

$$T_{max} = T_{IVC} \left(\frac{p^*}{p_{IVC}}\right)^{\frac{n-1}{n}} \qquad \qquad \dots (4.4)$$

$$T_{max} = T_{IVC} \left(\frac{V_{IVC}}{V^*} \right)^{n-1} \qquad \qquad \dots (4.5)$$

Despite the ability of the proposed method to reach peak bulk gas temperatures synonymous to firing, it should be appreciated that the bulk gas temperature achieved in pressurised motoring still does not replicate completely the crank angle resolved temperature of the fired engine. This is due to the fact that in a fired engine, the temperature is low during compression but increases suddenly at the start of combustion. Furthermore, even though the combustion gases cool down rapidly after combustion, they still retain a significantly high temperature over the entire expansion stroke. On the other hand in the pressurised motored engine using gas mixtures, the bulk gas temperature is significantly higher than that of the fired engine throughout the compression stroke, but after compression TDC the bulk gas temperature decreases rapidly to a value significantly lower than that of the fired engine. This is better understood from Figure 4.28, which presents a result obtained from a one-dimensional simulation conducted as a part of this research project by Sammut et al. [84].

To have a more tangible indication of the increase of the in-cylinder thermal conditions with the use of gas mixtures, a 1/8" OMEGA K-type thermocouple was fitted at the OEM injector location. Due to the bulkiness of this thermocouple, only an average value of temperature could be obtained. It should also be mentioned that this thermocouple is electrically isolated and hence the junction is situated behind a thin stainless steel body and encapsulated in magnesium-oxide. The thermocouple protruded to around 1 mm from the piston crown, when at TDC. The temperature measured cannot be classified as either being that of the bulk gas temperature, or that of the wall temperature. Despite this, the readings given by this thermocouple can give a realistic comparative idea of the different thermal conditions imposed in the cylinder by Argon and its mixtures. Figure 4.29 shows the temperature as recorded by this thermocouple. It is seen that a near linear trend was achieved between the thermocouple reading and the γ variation. The temperature for the 103 bar PCP testing was very close to that of the 84 bar PCP, with that of the higher pressure loading showing slightly higher thermal conditions. The temperature also showed an overall increase with increasing engine speed, which is in line with theoretical explanation. One anomaly which is noted from Figure 4.29 is that the temperature for

the 2000 rpm testing is higher than that for the 2500 rpm. This was noted for all gases tested, at both PCPs.
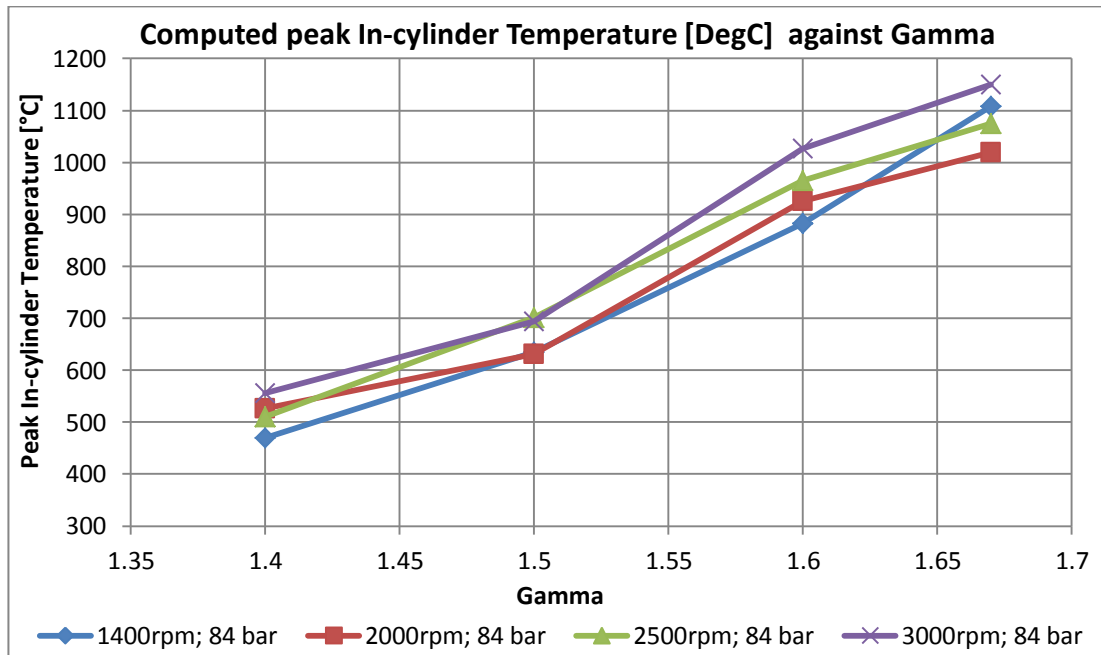
Figure 4.23. Computed peak bulk gas temperature against projected γ and engine speed at a PCP of 84 bar.
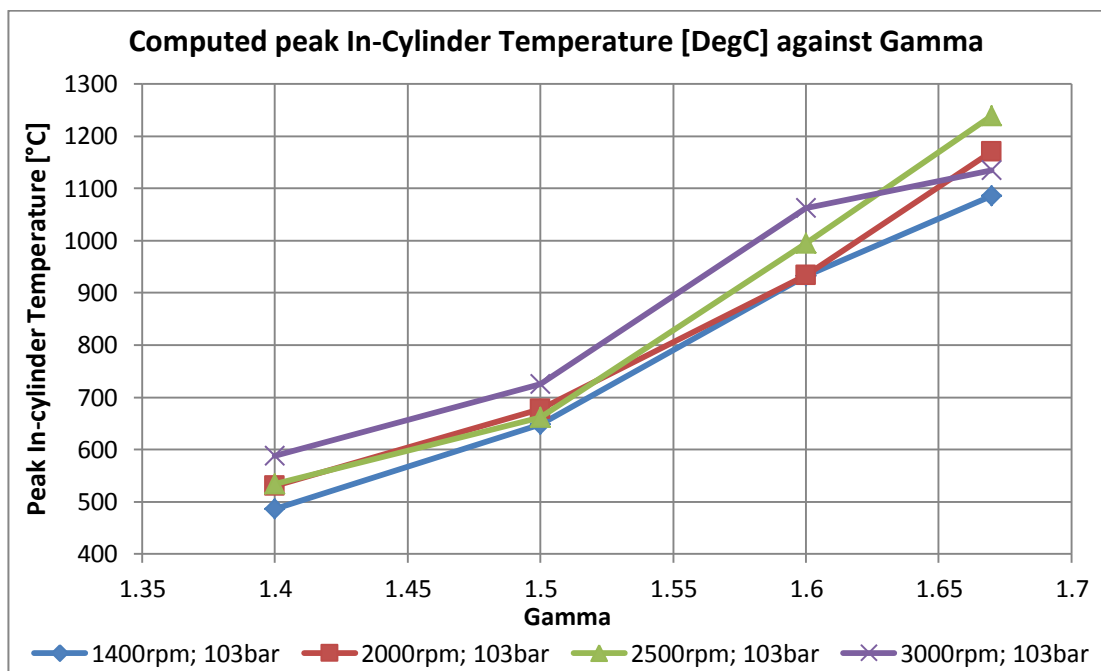
Figure 4.24. Computed peak bulk gas temperature against projected γ and engine speed at a PCP of 103 bar.
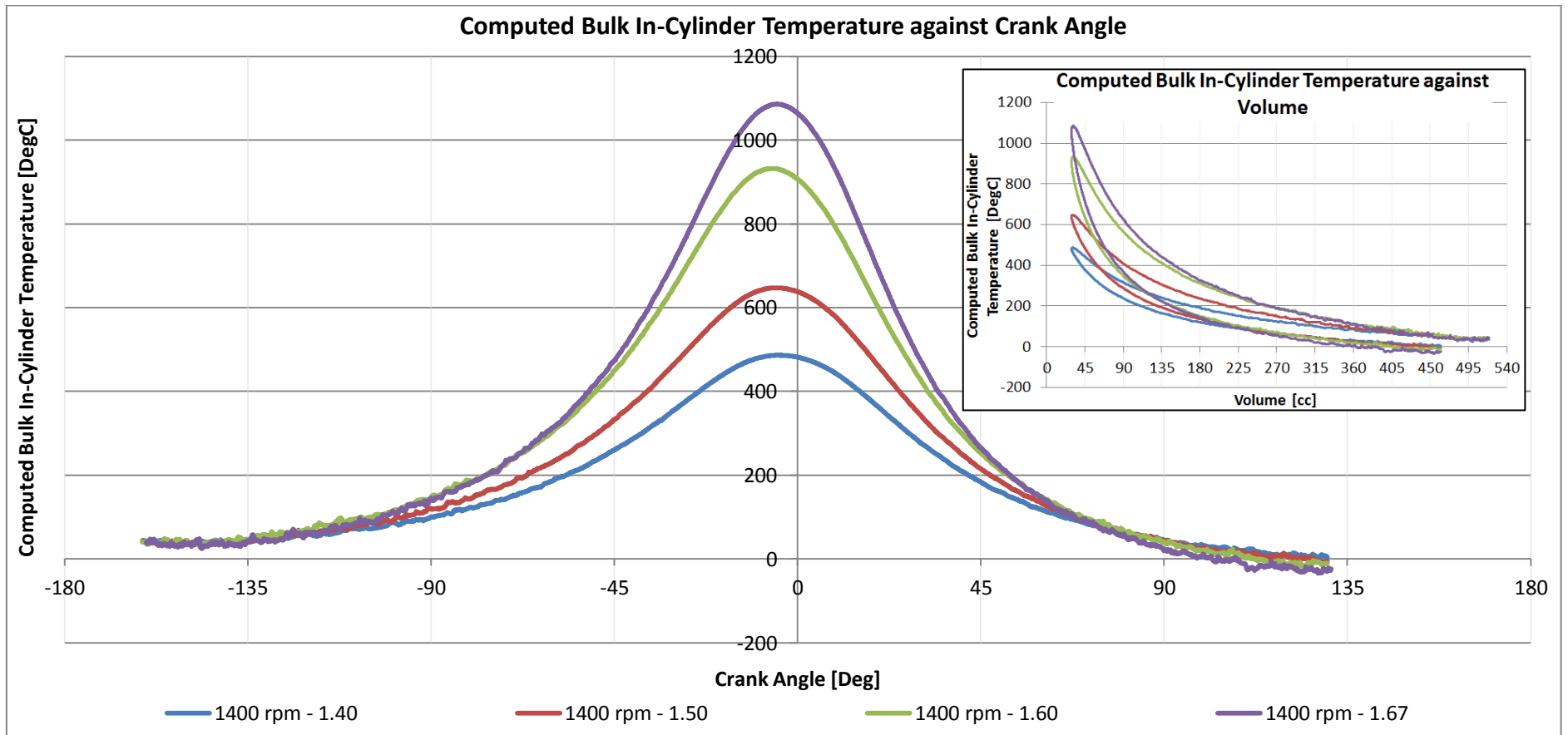
Figure 4.25. Computed bulk gas temperature against crank angle at different γ (at room temperature), 1400 rpm, 103 bar.
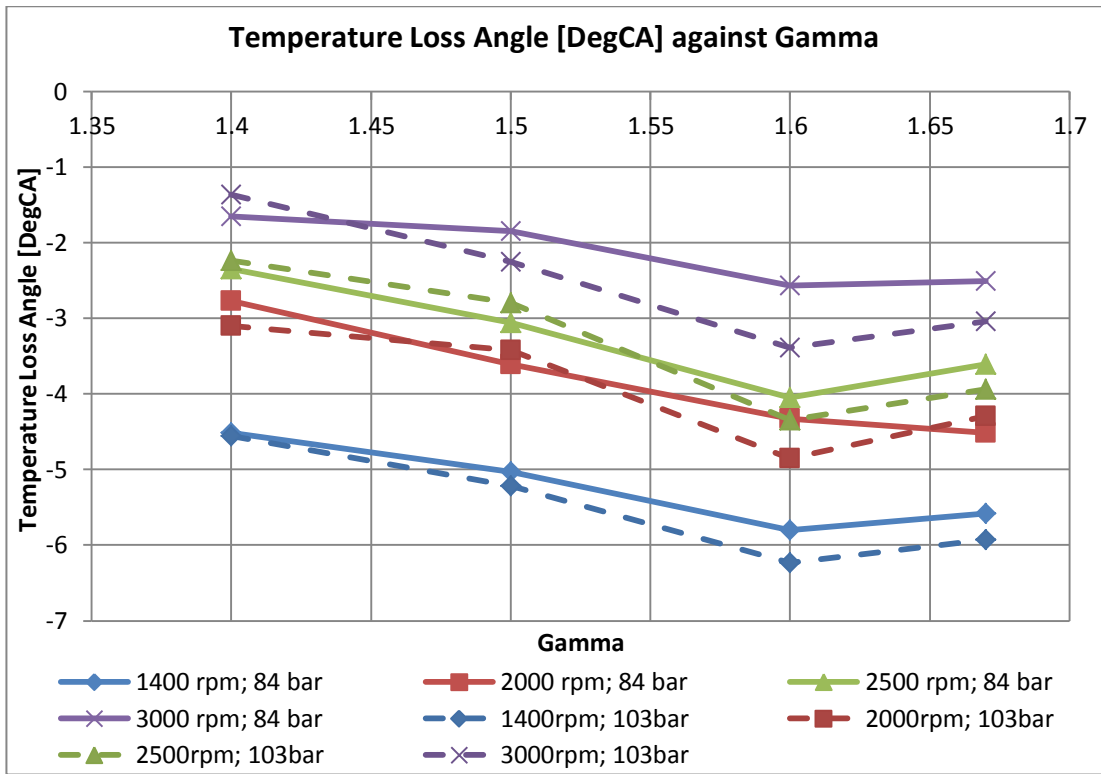
Figure 4.26. Temperature loss angle against projected γ, engine speed and PCP.
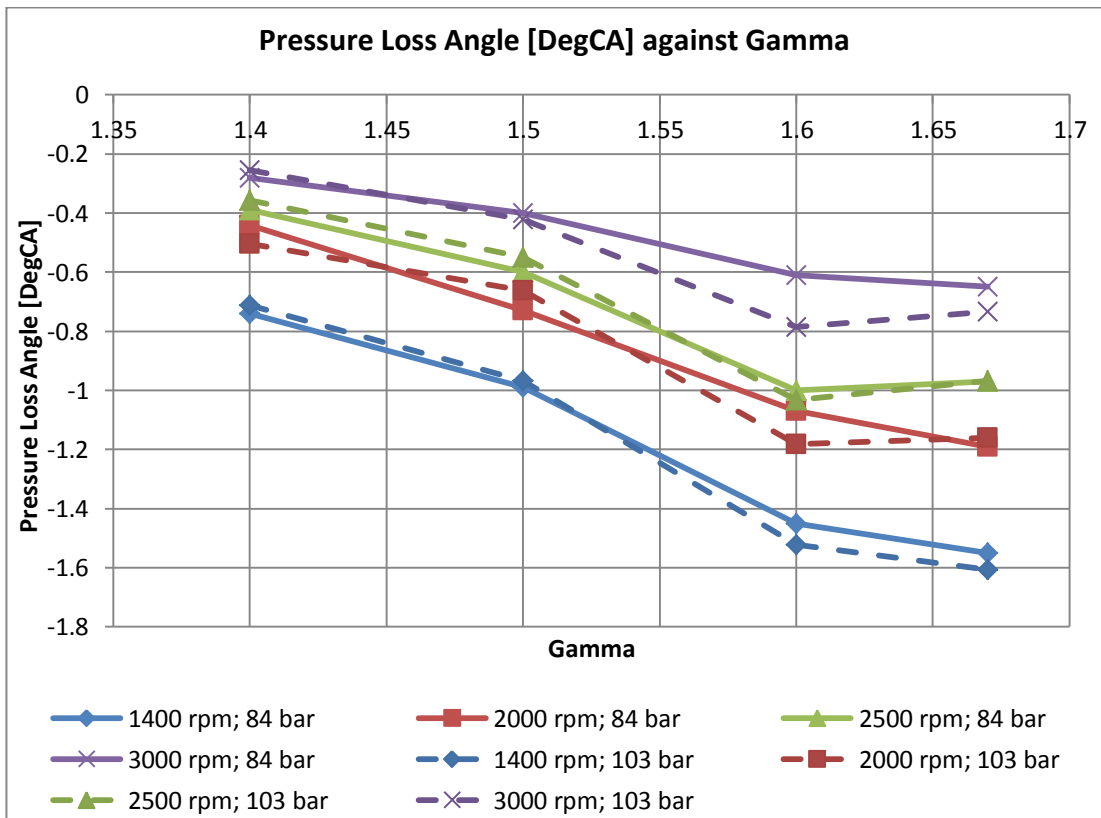
Figure 4.27. Pressure loss angle against projected γ, engine speed and PCP.
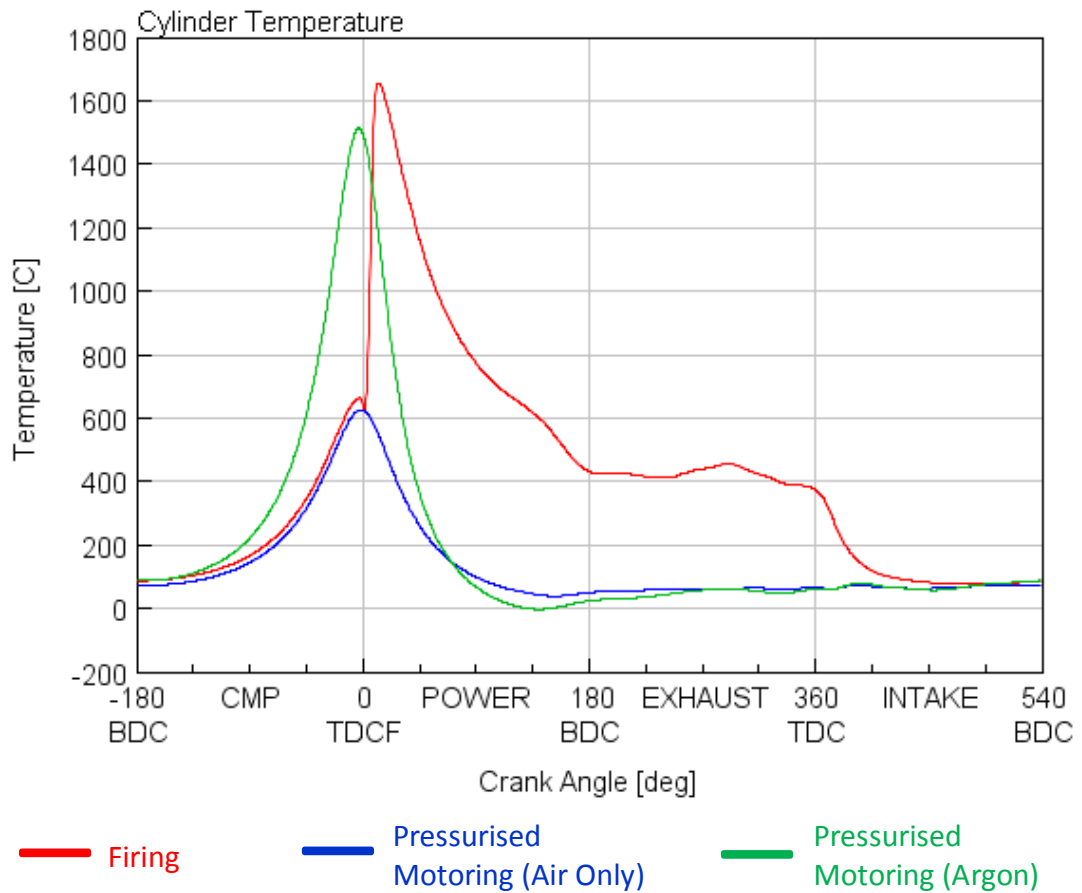
Figure 4.28. Simulated bulk gas temperature against crank angle for fired, pressurised motoring with air, and pressurised motoring with Argon [84].
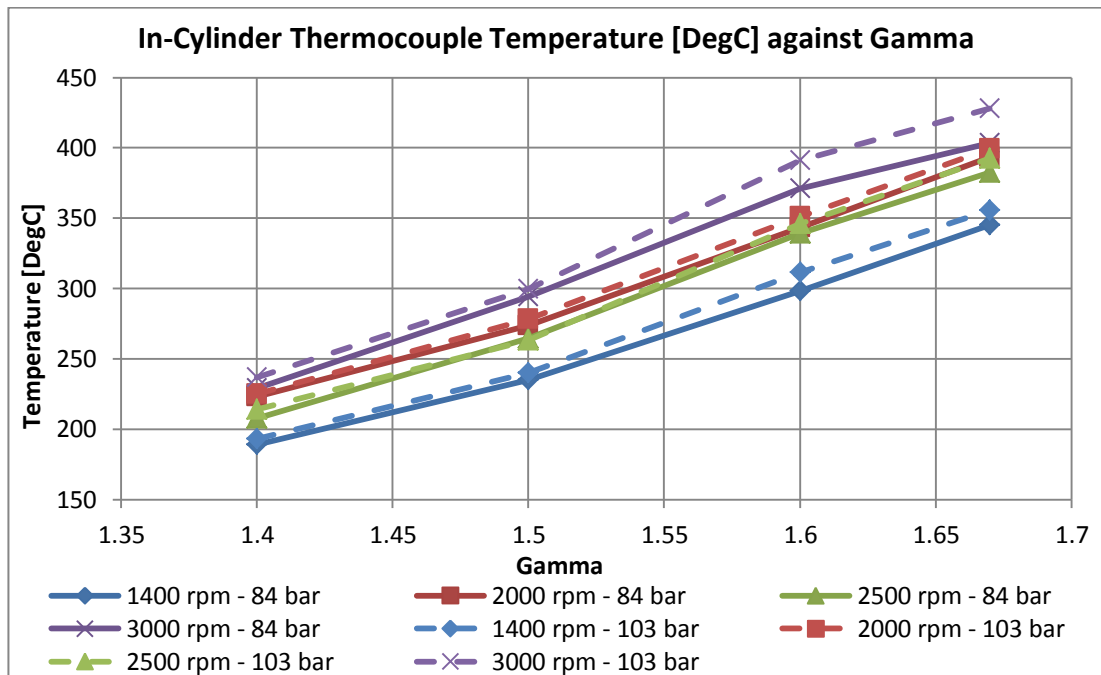
Figure 4.29. In-cylinder thermocouple temperature against projected *γ*, engine speed and PCP.

117

4.4.2 The effect of Bulk Gas Temperatures and Ratio of Specific Heats on Mean Effective Pressures

In this section, the mean effective pressure results will be presented and discussed. The discussion will first focus on the BMEP, representing the energy requirement to drive the motored engine – *i.e.* the summation of all the losses. To give a better understanding of the overlapping effects imposed on the BMEP, the mean effective pressures representing the individual losses are discussed seperately, and related to the observations made on the BMEP.

Figure 4.30 and Figure 4.31 show the BMEP recorded for the 84 bar testing, whereas Figure 4.32 and Figure 4.33 show the BMEP recorded for the 103 bar testing. It is evident that a similar trend is present at the two PCP conditions. The relationship of BMEP with engine speed is not easily identifiable. This is due to conflicting effects resulting from losses of different nature. The effect of the individual losses will become clearer once their mean effective pressures are presented. On the other hand, the increase in the BMEP losses with an increase in the ratios of specific heats is clearly identifiable. It should be remembered that the BMEP is a representation of the heat losses, mechanical friction losses, pumping losses and accessory losses. For this testing session, the only accessory loss was that of the OEM oil pump. The vacuum pump mentioned in a previous section, was mechanically disconnected for this testing session.

Figure 4.30 and Figure 4.32 show two characteristics which shall be discussed separately. The 'first characteristic' is that for both loadings a drastic increase in the overall losses was noted at the 3000 rpm, when compared to the smaller engine speeds. The 'second characteristic' is that at 3000 rpm, for both loadings, the losses at γ of 1.67 were smaller than the losses with γ of 1.60. Both of these characteristics are mirrored in the shunt pipe temperatures, represented previously in Figure 4.21 and Figure 4.22. To understand each of these two characteristics, whilst separating the contribution of each loss from the BMEP, the individual mean effective pressures shall be discussed separately.
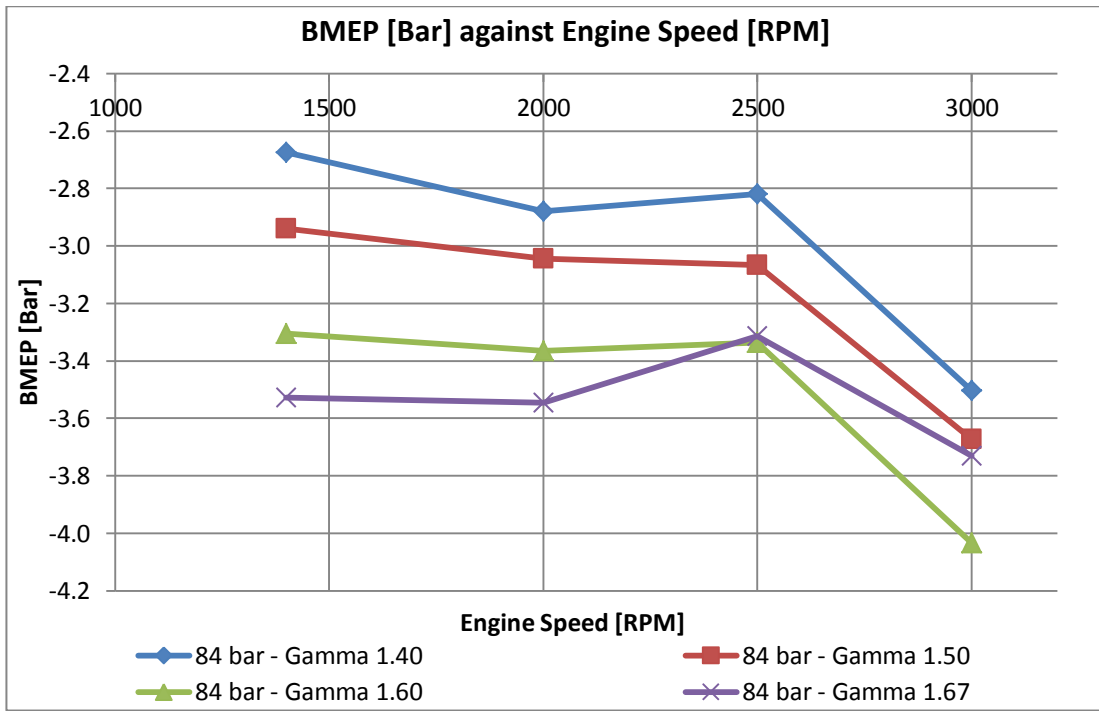
Figure 4.30. BMEP against engine speed and projected γ at 84 bar PCP.
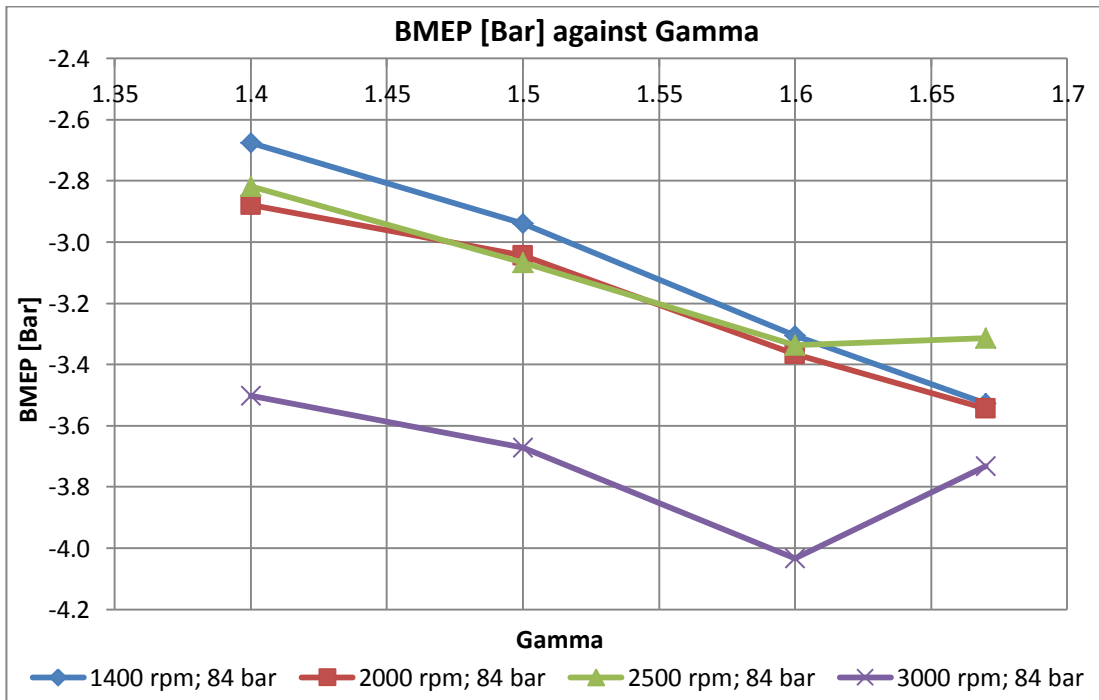
Figure 4.31. BMEP against projected γ and engine speed at 84 bar PCP.
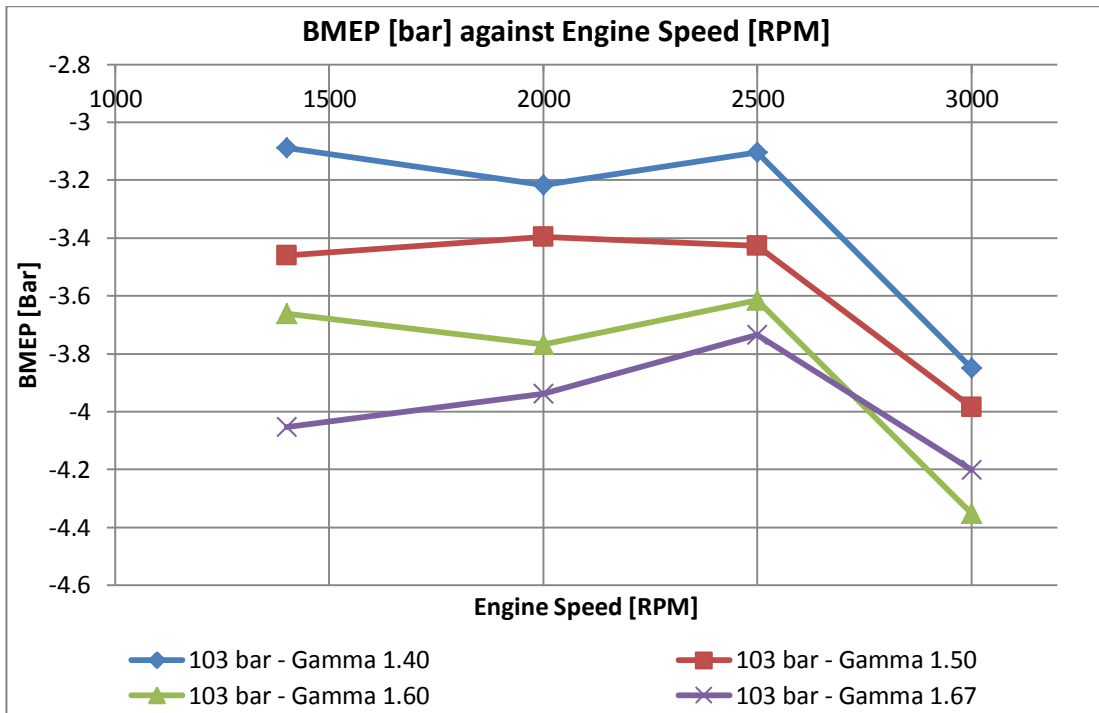
Figure 4.32. BMEP against engine speed and projected γ at 103 bar PCP.
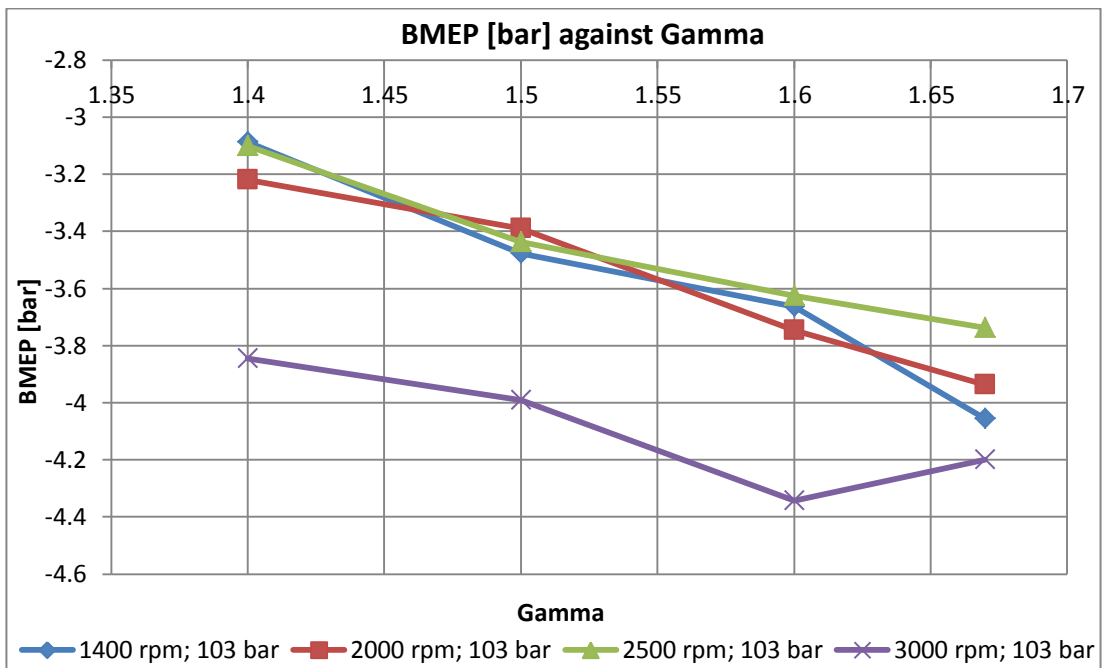
Figure 4.33. BMEP against projected γ and engine speed at 103 bar.

The $IMEP_{360}$ for the 84 bar and 103 bar PCPs are given in Figure 4.34 and Figure 4.35 respectively. Both figures show a quasi-linear trend with the ratio of specific heats. This hints that the likelihood of having interference from other uninvestigated variables on the relationships of $IMEP_{360}$ with γ is minimal. A collective increase in heat and blow-by losses is noted with an increase in γ, for both PCPs.

The relationship of $IMEP_{360}$ with γ is interesting for testing aimed at heat transfer, using the pressurised motored setup. From Figure 4.34 and Figure 4.35, it is evident that the $IMEP_{360}$ magnitude increased by around 75% with an increase in γ from 1.40 to 1.67. This is explained through the increase of bulk in-cylinder temperature; however one should not lose sight of other parameters which had to change as a consequence of changing γ. Some of these are the individual values of the specific heat capacities, the dynamic viscosity, and the density of the gas. Changing these parameters might have an effect on the heat transfer in the cylinder not only due to a larger change in temperature, but also due to difference in fluid flow and difference in the boundary layer behaviour. How these parameters have individually affected the heat transfer was not studied in this research, however a detailed account is given by Demuynck et al. [42]. The effect of changing the gas on in-cylinder heat transfer, with the consequence of changing all these mentioned parameters is reported later in Chapter 5.

In the previous test sessions, it was explained how the results of the relationship of $IMEP_{360}$ with engine speed was obscured by the underlying effect of a variation in PCP. Since in this test session the PCP was used as the control variable, the undisturbed variation of $IMEP_{360}$ with engine speed is now plotted at a constant PCP for the different gases, and shown in Figure 4.36 and Figure 4.37. Both figures show a gradual decrease in the $IMEP_{360}$ magnitude with an increase in engine speed. This means that the 'first characteristic' outlined earlier, as noted from the BMEP graphs did not originate from the $IMEP_{360}$. An interesting observation made on both figures is that for γ ratios between 1.40 and 1.60, the variation of $IMEP_{360}$ with engine speed seems to resemble a quadratic fit. On the other hand, for γ of 1.67, a linear function fits better the experimental data, especially in Figure 4.36. This observation resulted in the 'second characteristic' outlined earlier on the BMEP. Although no clear explanation is known for this observation, it is evident that it resulted from a decrease in the heat losses experienced at 3000 rpm and γ 1.67 compared to that experienced at 3000 rpm and γ 1.60, despite the higher bulk gas temperature attained by the former, compared to the latter. It should also be kept in sight that the $IMEP_{360}$ is also a representation of the mass leakage, and not just heat transfer losses, hence there is a possibility that the different blow-by mechanisms could have been the result behind the 'second characteristic'.
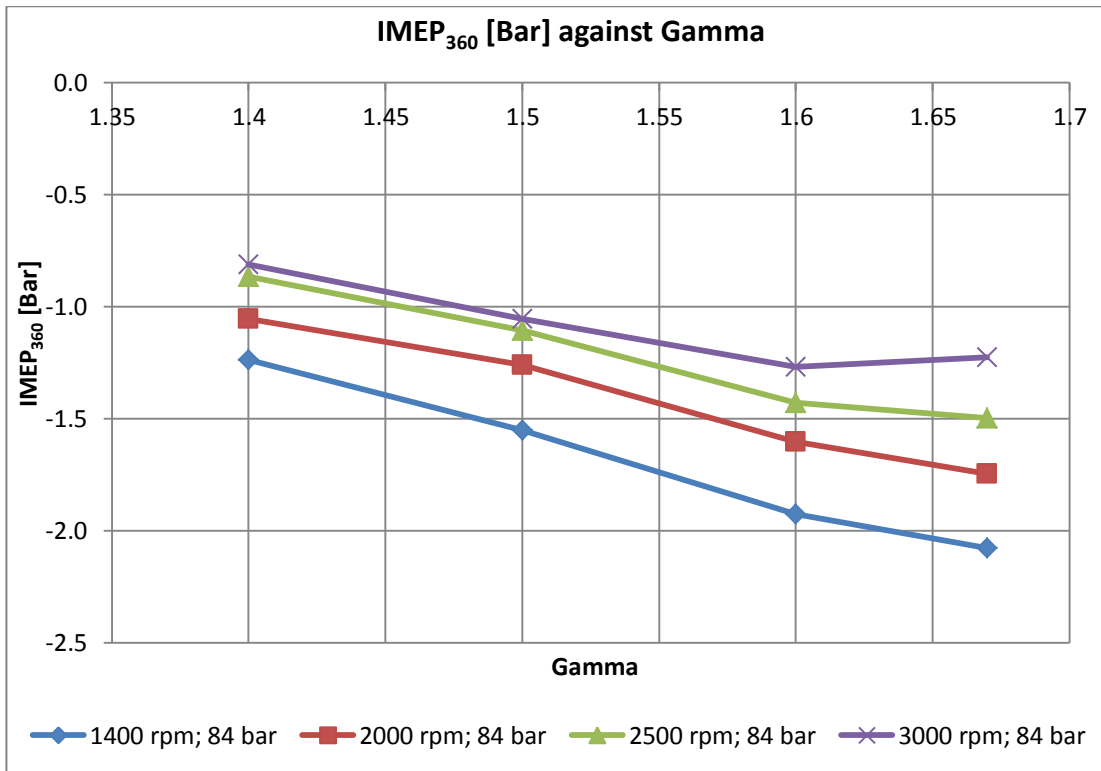
Figure 4.34. IMEP$_{360}$ against projected γ and engine speed at 84 bar PCP.
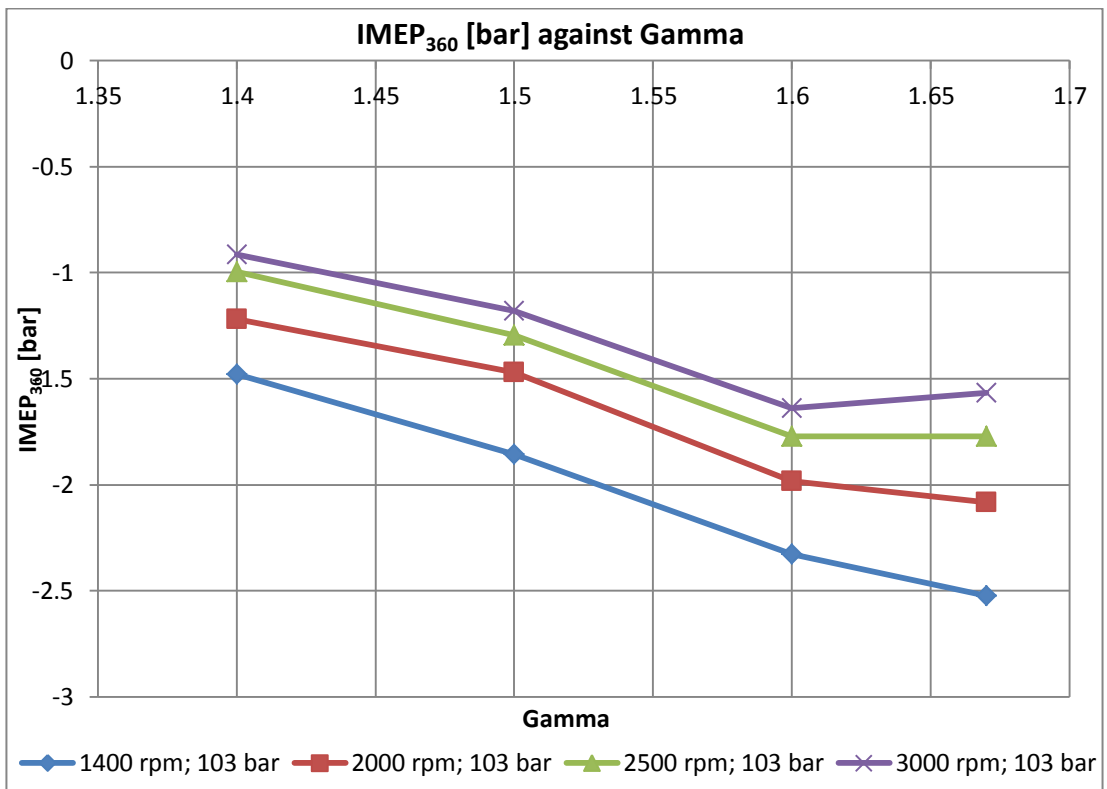
Figure 4.35. IMEP$_{360}$ against projected γ and engine speed at 103 bar PCP.
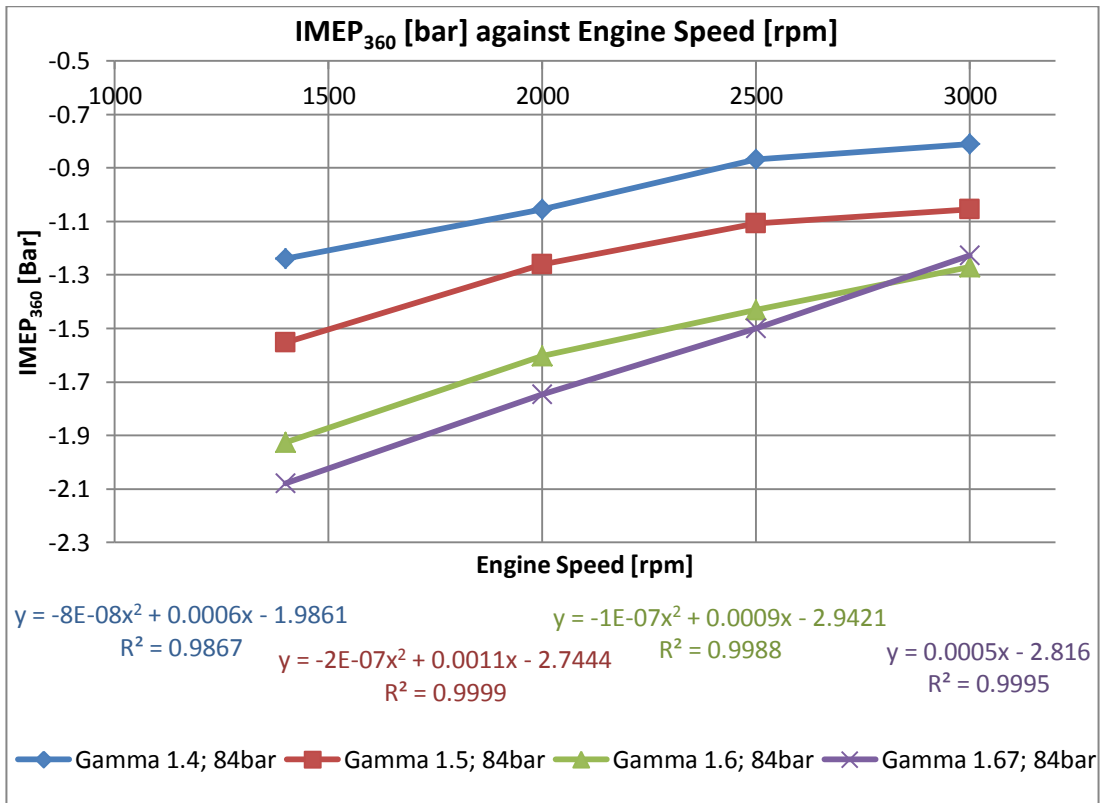
Figure 4.36. IMEP$_{360}$ against engine speed and projected γ at 84 bar PCP.
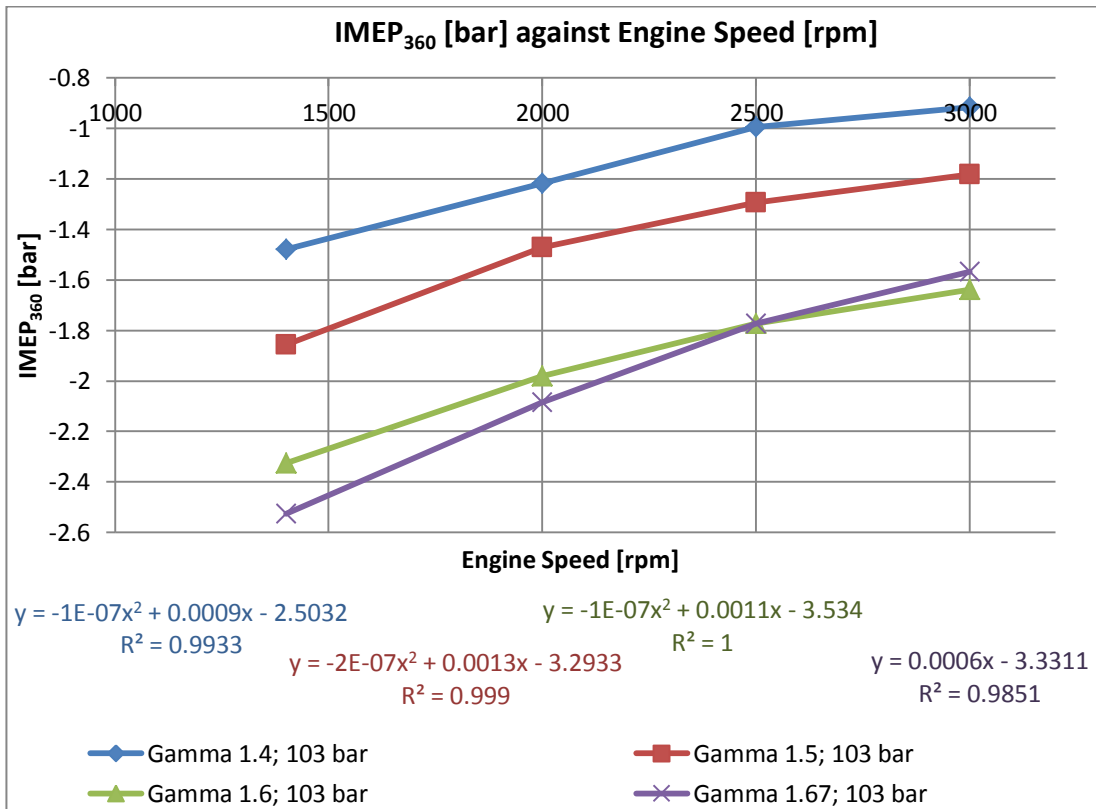
Figure 4.37. IMEP$_{360}$ against engine speed and projected γ at 103 bar PCP.

The relationship of PMEP with ratios of specific heat for the 84 bar and 103 bar PCP is shown in Figure 4.38 and Figure 4.39 respectively. Both pressure loadings show similar trends, with the 103 bar testing having a slightly higher pumping loss magnitude, as expected. It is noted from both figures that the pumping loss generally increases with increasing the speed, however the 2000 rpm range showed only a slightly smaller pumping loss when compared to the 2500 rpm. A gradual decrease in the pumping losses is shown with an increase in γ. This is consistent with the observation made in Figure 4.20, where it was shown that to achieve the same PCP, the MAP had to be decreased with an increase in γ. This is a result of a smaller trapped mass when using high γ gases, which consequently also leads to a smaller recompression effect on the exhaust stroke. This observation presents another advantage in using gases with high γ in the pressurised motored method, as opposed to the method of increasing the intake air temperature.

It was argued by Richardson [3] and Kovach et al. [112] that traditional pressurised motoring achieves fired-like peak in-cylinder pressures at an expense of an abnormal increase in PMEP. This results from a significantly larger trapped mass (and hence exhaust recompression), when the pressurised motored using air is compared to the same engine speed and pressure load setpoint for a fired engine. Using gases with higher γ proved that the PMEP can be decreased significantly, while still reaching the same PCP. This quality bridges further the gap between motored and fired testing. A quick verification was done by considering fired tests on the 2.0 HDi engine conducted in the Masters dissertation by the same author [78] [79].

For a fired test conducted at 3000 rpm and a peak fired in-cylinder pressure of 102 bar, the fired MAP was measured to be 1.60 bar, which for the displacement of the engine in question results in around 0.95 g of trapped mass. From the previously presented Figure 4.20, it shows that a PCP of 103 bar can be obtained from a motored MAP of 1.60 bar if the engine is operated with a gas having a γ ratio between 1.50 and 1.60. Considering the specific gas constant for the relevant gas mixture, the trapped mass would be around 1.19 g. This is 25% larger than that at the equivalent fired condition. On the other hand, if a conventional pressurised motored test using air is considered, a MAP of 2.26 bar would have to be set for the same PCP of 103 bar (see Figure 4.20) – meaning that the in-cylinder trapped mass would be around 1.35 g, hence 41% larger than the equivalent fired test.

To understand further this comparison, Figure 4.40 shows the pumping loops for operation with air and Argon at 3000 rpm, 84 bar PCP, plotted on a p-V diagram. It is shown that the pumping loop for the Argon case is much smaller than that for the air cycle. This therefore results in a larger PMEP magnitude for air testing. A similar observation was noted for the other engine speed setpoints.
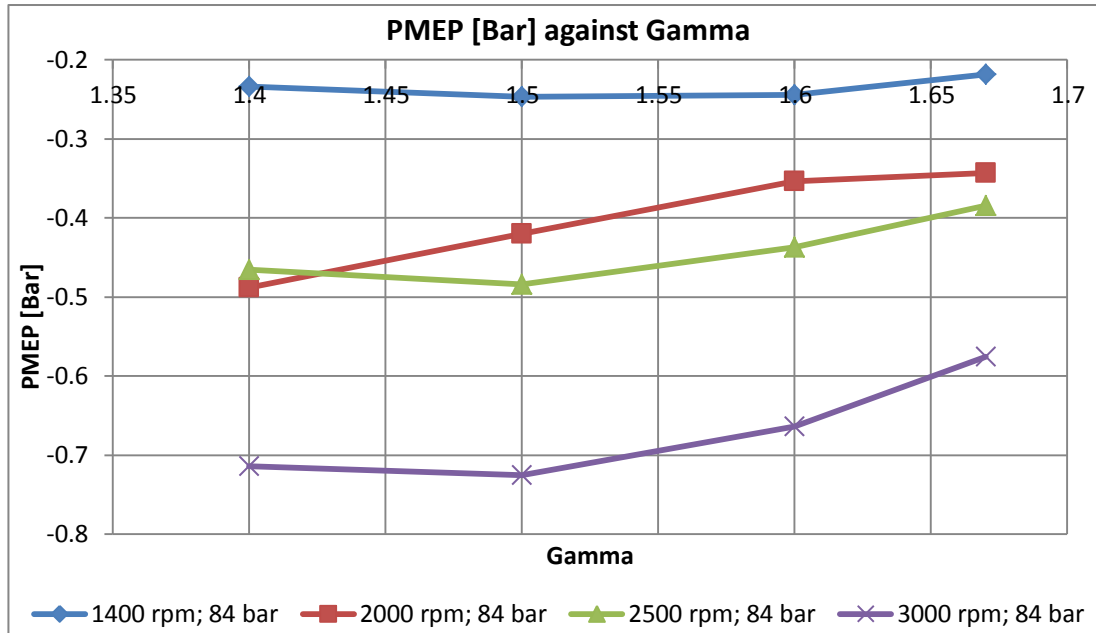
Figure 4.38. PMEP against projected γ and engine speed at 84 bar PCP.
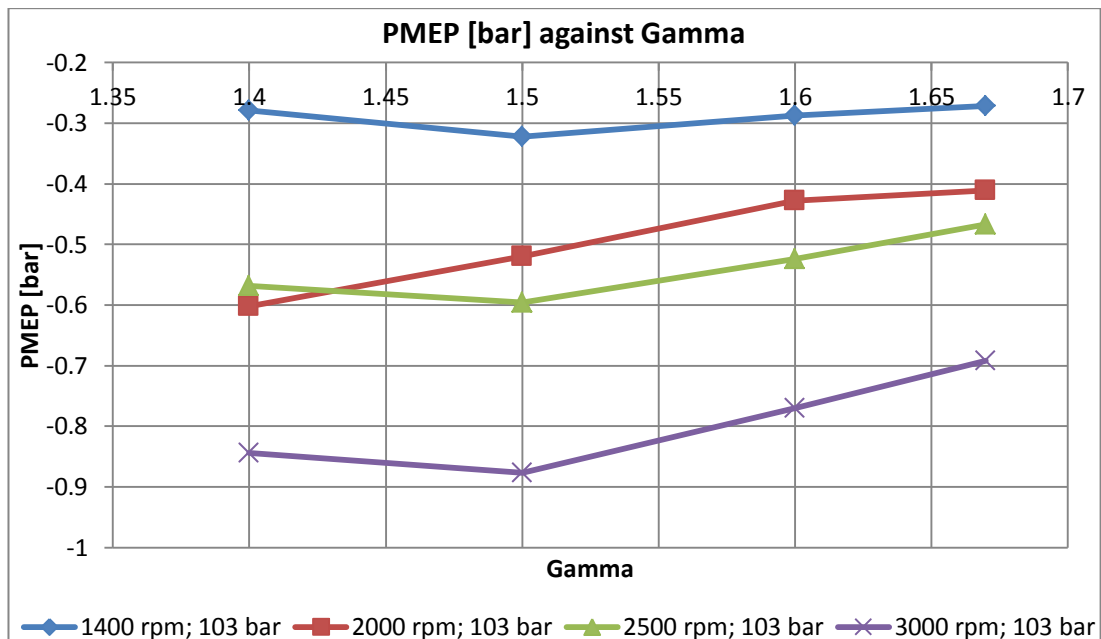
Figure 4.39. PMEP against projected γ and engine speed at 103 bar PCP.
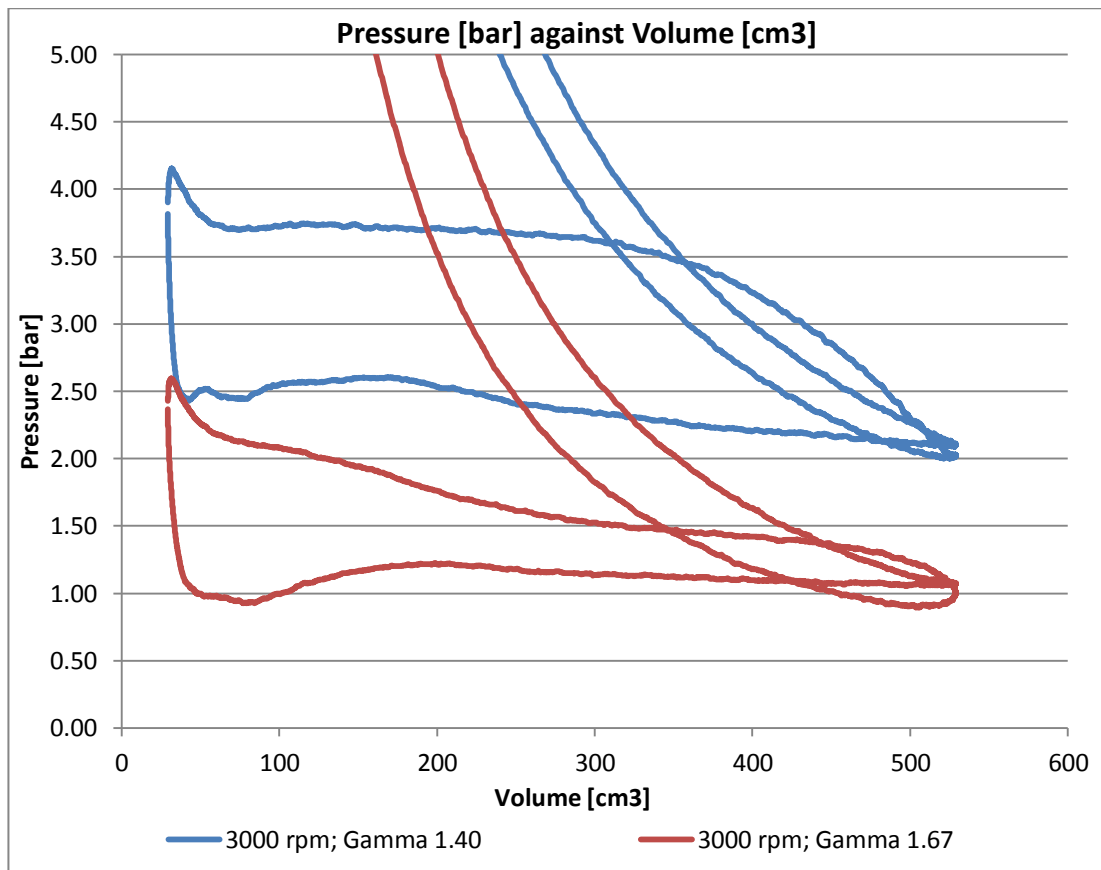
Figure 4.40. Pumping loops of air and argon at 3000 rpm and 84 bar PCP.

4.4.3 Effect of bulk gas temperature on FMEP

The FMEP as computed from the measured BMEP, $IMEP_{360}$ and PMEP is given in Figure 4.41 to Figure 4.44. Figure 4.41 and Figure 4.42 displays the general relationship of FMEP with engine speed, whereas Figure 4.43 and Figure 4.44 aim to show the dependency of FMEP on bulk gas temperature.

The first observation that is made from the first two figures is that the FMEP magnitude shows a clear increase with an increase in engine speed for all γ and PCP values. It is also evident that the increase in FMEP between the 2500 rpm and 3000 rpm is distinctively higher than the increase between each of the lower speeds. This is in line with the 'first characteristic' reported earlier for the BMEP – which up till now was shown that it is neither dependent on the $IMEP_{360}$, nor on the PMEP, hence it can be confidently concluded that such drastic increase in BMEP magnitude from 2500 rpm to 3000 rpm arises from a marked increase in FMEP at this engine speed condition.

The second observation is that the FMEP shows no appreciable variation with a change in the ratio of specific heats, or equivalently, no appreciable change with an increase of around 600°C in the in-cylinder peak bulk gas temperature. This shows that the FMEP in the pressurised motored engine tested in this project is insensitive to the bulk gas temperature at all speeds and PCPs considered.

The second observation might seem surprising initially due to the fact that intuitively one would relate temperature to the oil viscosity, and assume a lower friction footprint for a lower oil viscosity. This is not deniable; however one needs to consider the mechanism of mechanical friction to shed better light on these results. One possible reason why the FMEP did not show appreciable variation with higher bulk gas temperature is that the bulk gas temperature affects only one of the sub-assemblies responsible for rubbing FMEP, which is the piston-ring sub-assembly. This means that the FMEP contribution from the cranktrain and valvetrain are not affected by the higher bulk gas temperature. It is claimed that the piston and rings contribute to around 42% of the total mechanical friction in an IC engine [2]. This means that the bulk gas temperature difference induced is only expected to affect around half of the FMEP contribution. A study which can be related to this observation is that by MAHLE [77]. It was shown that changing the oil viscosity from SAE 10W60 to SAE 5W30 resulted in a maximum of 0.08 bar difference in the FMEP of the pressurised motored engine when run between extremities of 1000 rpm to 4000 rpm, and 20 bar to 180 bar PCP. Contrary to what has been explained above, the viscosity difference by changing the oil affects all lubricating surfaces, yet a very small difference was noted in the FMEP by MAHLE [77]. This means that any viscosity variation induced by a rise in the bulk gas temperature should logically have an even smaller effect than what is reported by MAHLE [77].

The relationship reported in Figure 4.43 and Figure 4.44 on FMEP with different bulk gas temperatures cannot be directly generalised also to fired engines, since friction mechanisms between the pressurised motored engine and the fired engine are not entirely similar. It should be remembered that the fired engine experiences the peak in-cylinder pressure at around 10 DegCA ATDC, whereas the pressurised motored engine experiences the peak in-cylinder pressure at around 1 DegCA BTDC. This difference in the peak pressure location leads to a different pressure load – to – thermal load phasing between the pressurised motored and the fired setup.

Hence, a possible reason why the fired engine and pressurised motored engine could show a difference in the FMEP dependence on bulk gas temperature is due to a different crank angle resolved interaction between pressure and bulk gas temperature.

This foregoing consideration should also be viewed in terms of the lubricant which experiences a change in its viscosity relative to its temperature. For the pressurised motored engine, the peak in-cylinder pressure is experienced at an instant when the piston is relatively stationary, and hence mixed boundary lubrication between the piston and liner is probable. On the other hand, at the peak in-cylinder pressure location for a fired engine, the piston would have gained an appreciable velocity and hence there is a higher probability that at peak in-cylinder pressure, the lubrication between the piston and the liner is mostly hydrodynamic and dependent on lubricant properties, and hence bulk gas temperature.

Furthermore, at the location of PCP, for a pressurised motored engine the connecting rod is virtually vertical. On the other hand, for a typical fired engine, peak pressure load occurs when the connecting rod has some inclination, which contributes to side loading between the piston and the wall.

The piston velocity and connecting rod angle both create a different friction dependency on the lubricating film, and consequently lubrication film temperature and bulk gas temperature. This means that although in the pressurised motored engine, FMEP is independent of bulk gas temperature, in the fired engine this might not be the case. Different engine geometries might also induce differences on the FMEP-to-temperature dependency due to piston pin offset and crank offset.

From the above presented results, it is shown that the method put forward succeeded in allowing the investigation of the dependency of FMEP and other engine metrics on bulk gas temperature, independently from the mechanical/pressure load. It was stated by Allmaier et al. [76] and MAHLE [77], and explained earlier, that the conventional pressurised motored method (using air) already has the advantage of decoupling the mechanical load from the thermal load. However, the thermal effect on the relevant engine metrics could not be previously studied without interaction from other variables due to the fact that in the fired engine the temperature and pressure are interlaced, whereas in the pressurised motored engine, a method to vary the bulk gas temperature was lacking.

Both Allmaier et al. [76] and MAHLE [77] attributed the differences in the FMEP between the pressurised motored engine and the fired engine due to the discrepancy in their bulk gas temperatures. However, from the results obtained in this Doctoral dissertation it was shown that a variation in the bulk gas temperature alone (independent of the pressure load) does not show a variation on the FMEP. Hence, it is probable that a better explanation to the differences noticed between the FMEP of a fired and pressurised motored engine is that these originate from their different pressure load – to – thermal load phasing. This latter hypothesis however needs to be backed up with further experimental evidence.

Based on the results obtained from Figure 4.43 and Figure 4.44, one could argue that the use of higher γ gases in a pressurised motored setup is not really worth considering, after having found that no FMEP variation is induced. It is the opinion of the author, from a general testing perspective, that even though there was no measurable difference in the FMEP, utilising gases which can induce bulk gas temperatures close to firing is still of benefit in at least two ways. The first benefit is that the heat transfer induced should be somewhat closer to that of a fired engine, hence any effects derived from this could be potentially captured. This was investigated in this work, and reported in the next chapter. The second advantage of using gases with high γ is that the PMEP that results from high γ testing is closer to that of an equivalent fired test. These two advantages have to be seen in the light of the expense incurred to run the engine with high γ gases. As documented in the experimental apparatus section, the extra setup required for this testing was not exhaustive. Also, the gas consumed during testing was found to be very low, and hence inexpensive. The control of the test engine was neither more complicated than when tested with air. It should also be noted that mixing of the gases was done in-house using a laboratory scale, and hence also an inexpensive procedure.

Having outlined the foregoing observations on the FMEP, it is natural to discuss further research which can be done to verify the hypothesis being made, *i.e.* that the FMEP does not depend on the thermal effects alone, but that it depends on the interaction of gas temperature and in-cylinder pressure curve shape. To further this study, a preliminary idea was brought forward as part of this research project, by Sammut et al. [83]. It is suggested that to test this hypothesis, instead of using gases with higher ratios of specific heat, the conventional pressurised motored method

(with air) should be *'partially'* fired through the use of very small fuel additions, while still retaining the recirculation via the shunt pipe and motoring with the AC motor driver. A short brief of this idea is documented in the forthcoming section 4.5.
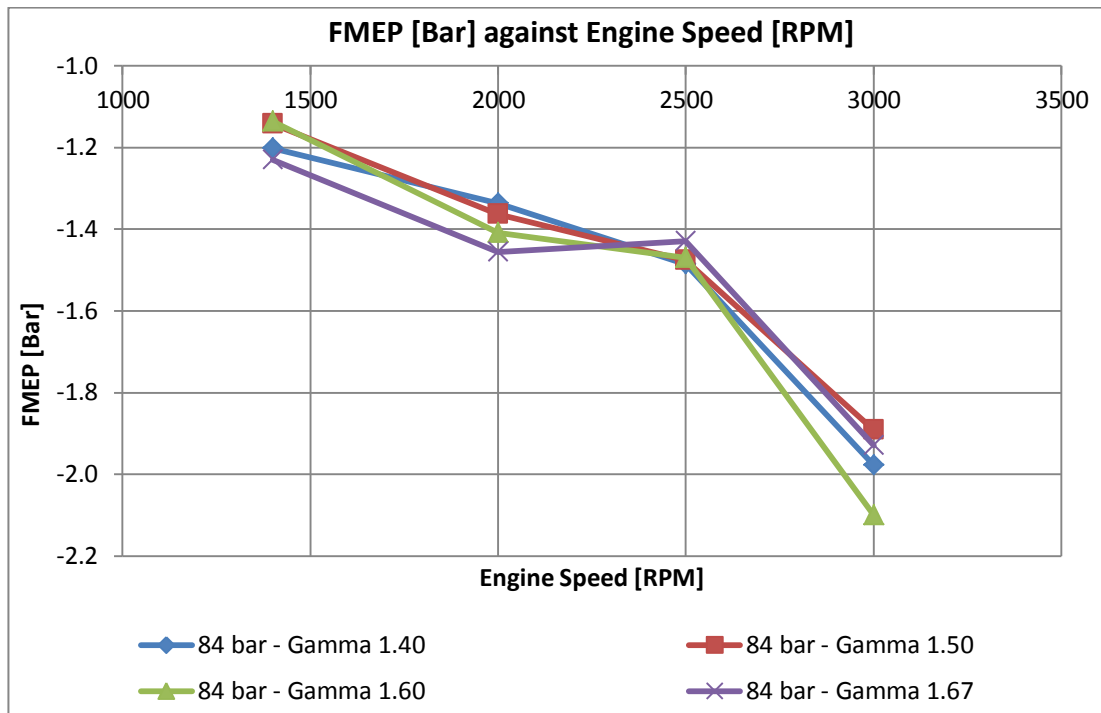
Figure 4.41. FMEP against engine speed and projected γ at 84 bar PCP.
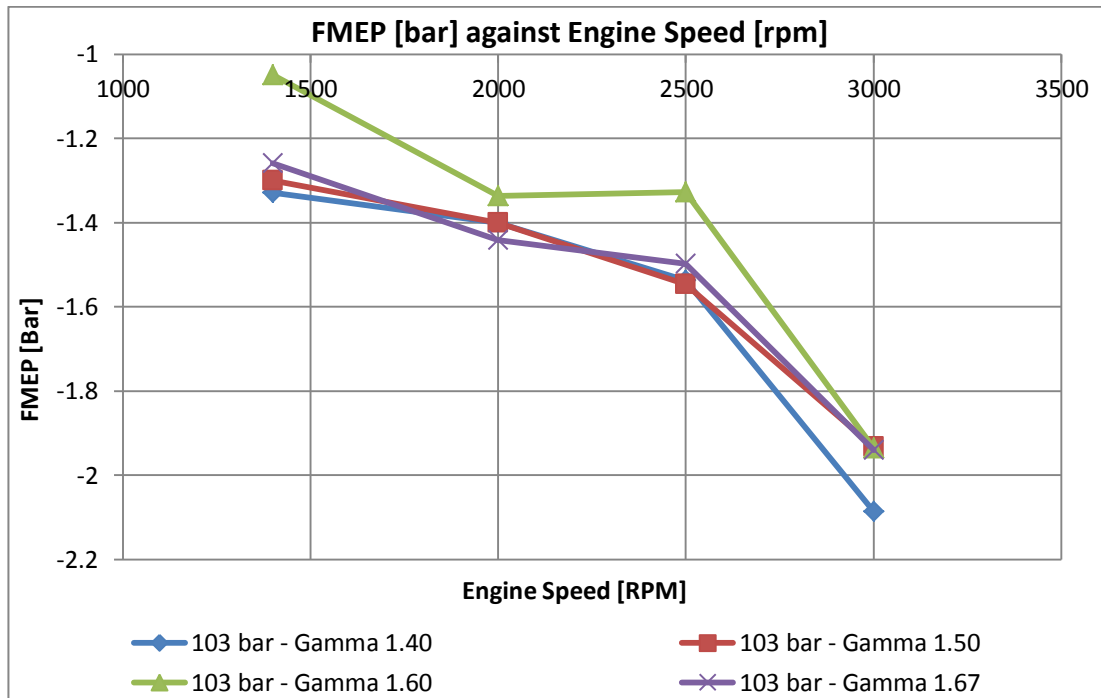
Figure 4.42. FMEP against engine speed and projected γ at 103 bar PCP.
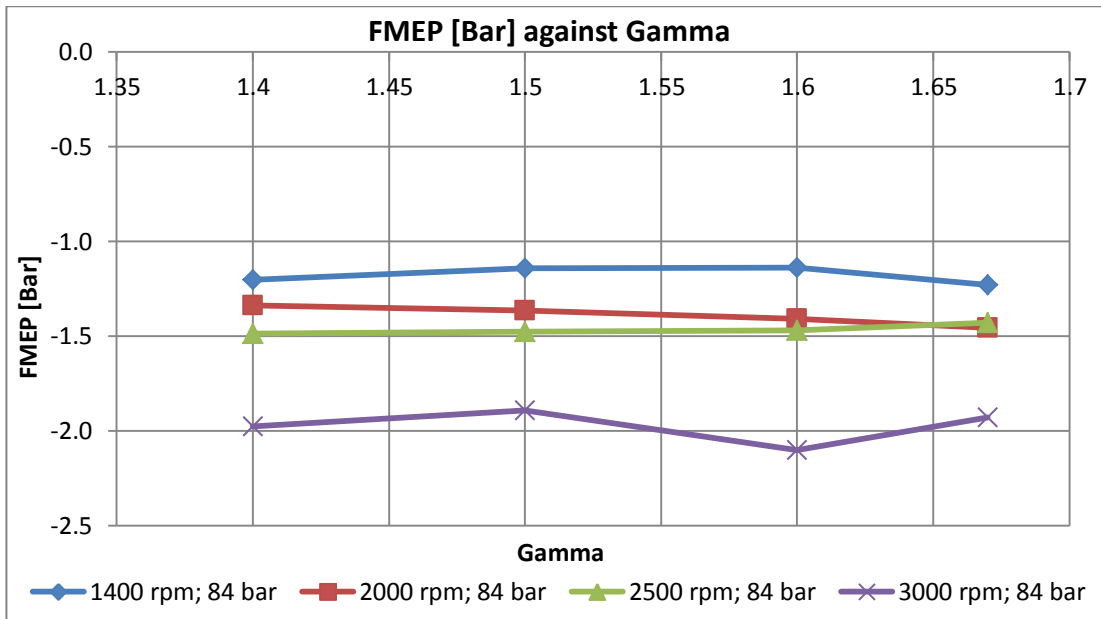
Figure 4.43. FMEP against projected γ and engine speed at 84 bar PCP.
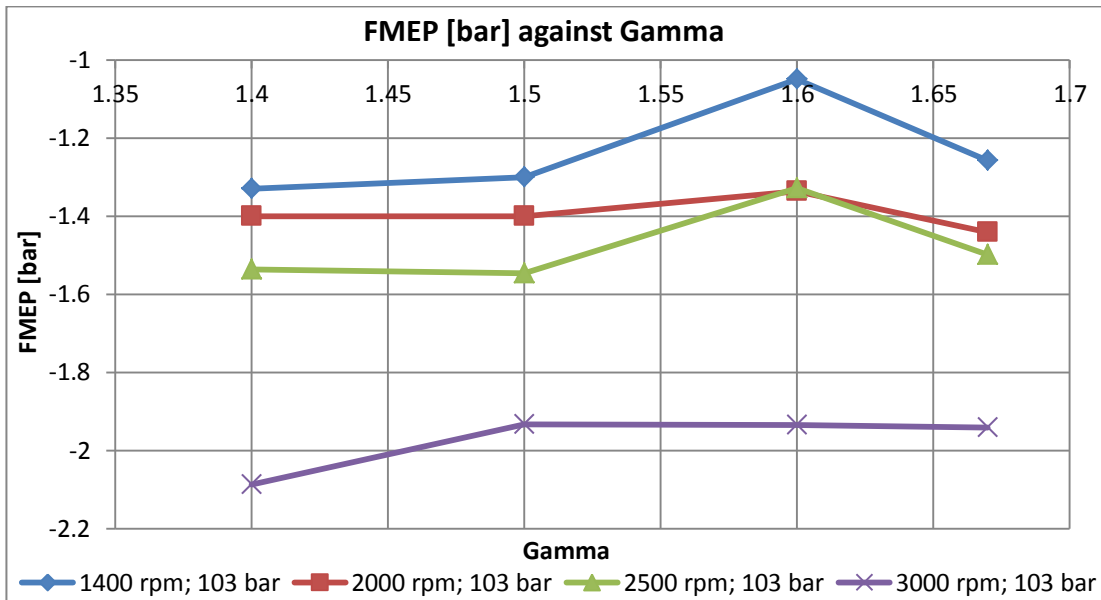
Figure 4.44. FMEP against projected γ and engine speed at 103 bar PCP.

4.4.4 Effect of working gas on blow-by

After having looked at the effect of different ratios of specific heat on bulk gas temperature and mean effective pressures, some few observations were made on the effect of the ratios of specific heat on the mass leakage out of the cylinder. To investigate this, the simple approach taken by Pipitone and Beccari [104] was considered whereby the mass leakage from the cylinder is modelled as gas flow

through a convergent-divergent nozzle. From a physical point of view, this is a very simplistic approach due to the fact that blow-by flow is usually complicated by the piston movement, as well as the piston ring dynamics during the whole 720 ° engine cycle. However, for the purpose of this evaluation it suffices to use the nozzle approach.

Based on a one-dimensional simulation study, documented later in Chapter 6, it was found that a 0.6 mm nozzle throat diameter per cylinder results in blow-by flow rates similar to those experimentally measured in the Masters dissertation [78] [79]. Equation (4.6) and equation (4.7) give the sub-critical and critical flow rates through a convergent-divergent nozzle respectively. For this analysis, the in-cylinder pressure measurements on both air and Argon testing at 2500 rpm and 103 bar PCP were used.

From this analysis, it was learnt that the use of Argon results in conflicting effects on the blow-by flow rate. In general, it was found that increasing the ratios of specific heats resulted in Argon having a smaller mass escaping from the cylinder per cycle. This however has to be seen in the light of two properties; the trapped mass and the flow rate.

For $\dfrac{p_{crank\ case}}{p(\theta)} > \left[\dfrac{p_{crank\ case}}{p(\theta)}\right]_{CR} \approx \left(\dfrac{2}{\gamma+1}\right)^{\frac{\gamma}{\gamma-1}}$

$$\dot{m} = A_{nozzle}\sqrt{\frac{2\gamma}{\gamma-1}\,m(\theta)\,\frac{p(\theta)}{V(\theta)}\left[\left(\frac{p_{crank\ case}}{p(\theta)}\right)^{\frac{2}{\gamma}} - \left(\frac{p_{crank\ case}}{p(\theta)}\right)^{\frac{\gamma+1}{\gamma}}\right]} \qquad \text{... (4.6)}$$

For $\dfrac{p_{crank\ case}}{p(\theta)} < \left[\dfrac{p_{crank\ case}}{p(\theta)}\right]_{CR} \approx \left(\dfrac{2}{\gamma+1}\right)^{\frac{\gamma}{\gamma-1}}$

$$\dot{m} = A_{nozzle}\sqrt{\gamma\,m(\theta)\,\frac{p(\theta)}{V(\theta)}\left(\frac{2}{\gamma+1}\right)^{\frac{\gamma+1}{\gamma-1}}} \qquad \text{... (4.7)}$$

Equation (4.6) and equation (4.7) show that increasing the ratios of specific heats yields an increase in the blow-by flow rate. Hence, Argon induces a higher blow-by flow rate than air. On the other hand, however, for a similar engine speed and peak in-cylinder pressure test, the crank-angle resolved in-cylinder pressure is lower for Argon than for air, except near TDC, when both reach the same peak. This implies

that Argon has a lower pressure difference throughout the whole engine cycle to drive the mass leakage through the convergent-divergent nozzle. This can be seen clearly in Figure 4.46, for the setpoint of 2500 rpm and 103 bar PCP. This result originates mainly from the fact which was explained earlier that the MAP required when using Argon to achieve the same peak in-cylinder pressure as that of air, is substantially lower. The combined conflicting effects of the γ and the pressure difference across the convergent-divergent nozzle yields a lower absolute mass leakage per cycle for Argon, when compared to air at a similar setpoint.

Due to the lower MAP required for Argon, the trapped mass per cycle is also smaller, when compared to that of air for a similar setpoint. Computing the ratio of the mass leakage per cycle to the trapped mass per cycle showed higher values for Argon than for air. This is shown in Figure 4.45 for the 103 bar PCP testing.
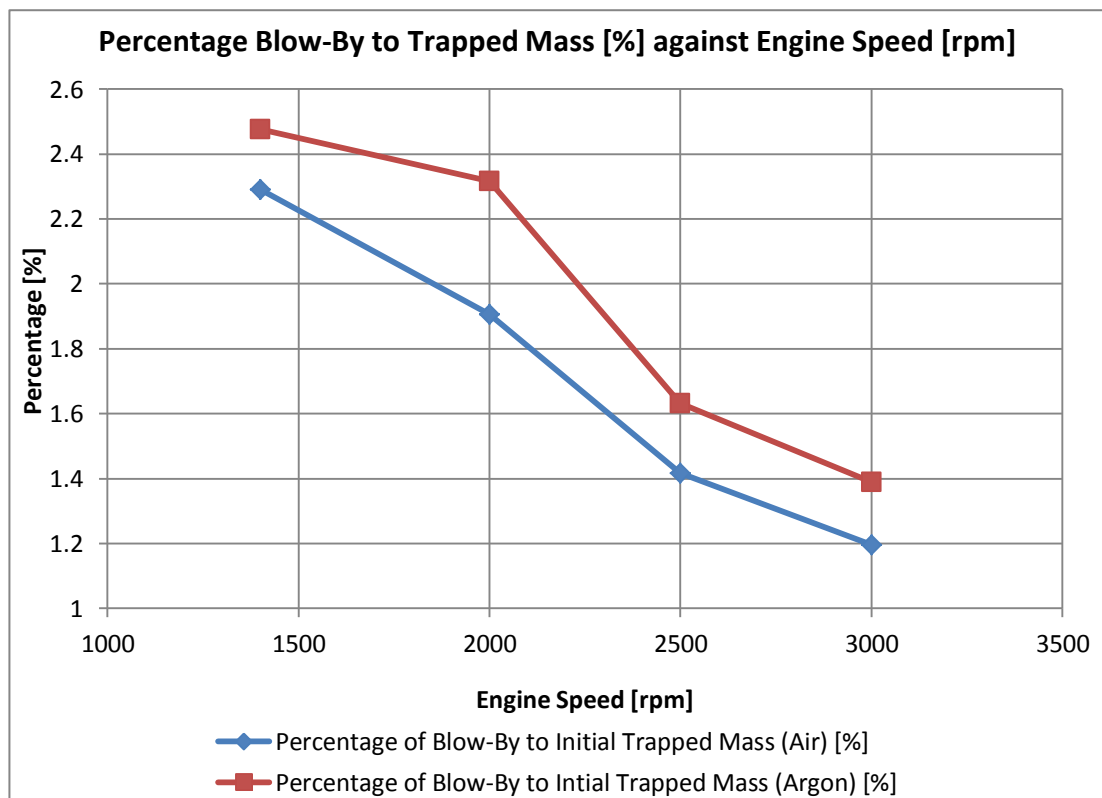
Figure 4.45. Percentage blow-by (720°) to trapped mass against engine speed at 103 bar PCP.
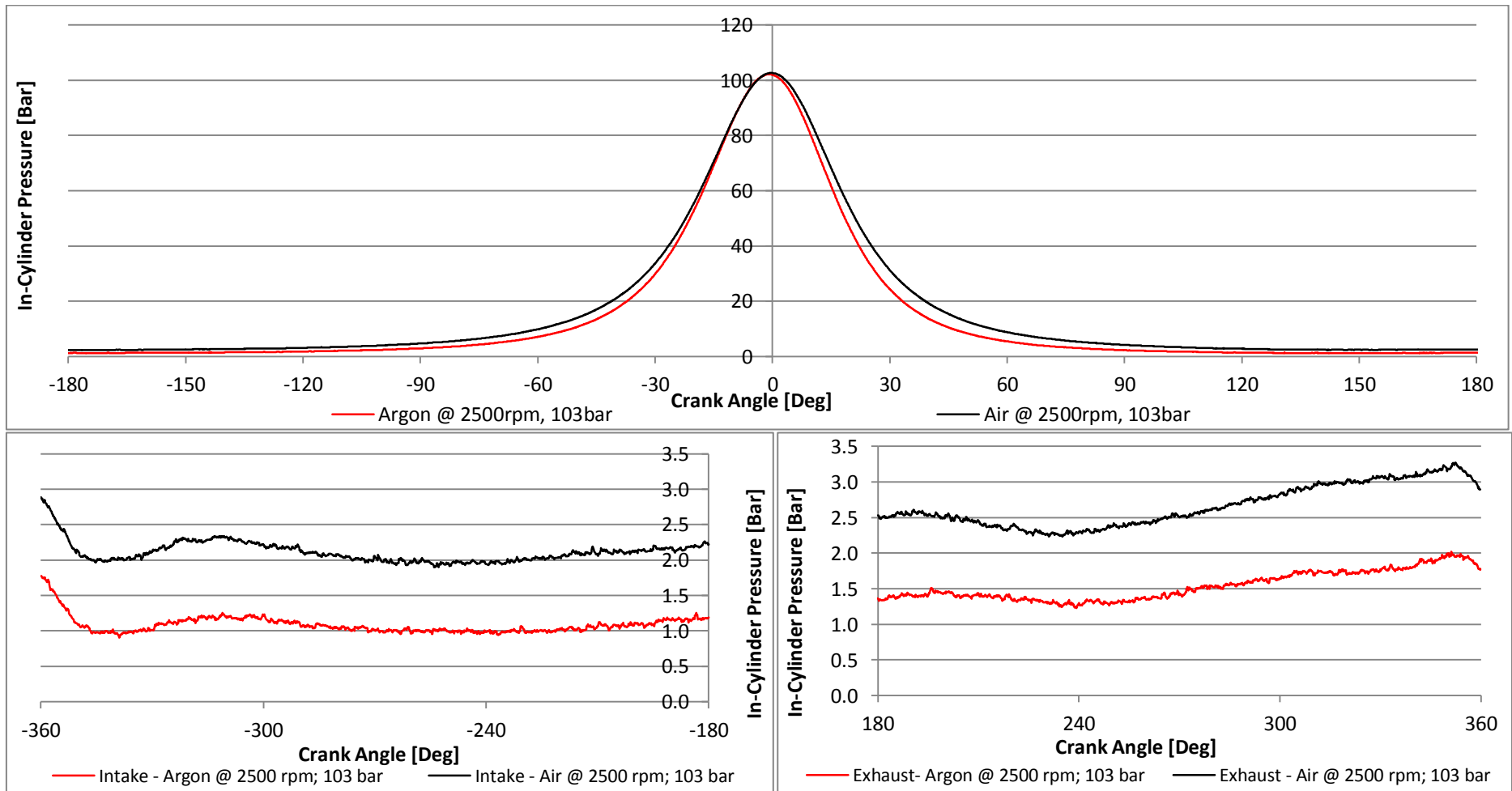
Figure 4.46. In-cylinder pressure against crank angle at 2500 rpm and 103 bar PCP.

4.4.5 Experimental Observations

Having presented the results obtained from this testing session, some pointers which were observed during testing and from the analysis of results are discussed here. It was earlier explained that for testing of each different gas, the engine was purged before the start of a test. The purging assessment was done through a UniNOx sensor that is capable of measuring the O_2 content. During purging, it was confirmed that the O_2 content for a given γ matched that given by the theoretical calculation. However, it was observed that after purging stopped, the O_2 content slowly fell down from the setpoint value. This observation was initially troublesome. It was also noted that this observation occurred only with γ of 1.50 and 1.60. It is hypothesised, and confirmed with a good degree of confidence that the very high bulk gas temperatures induced by changing γ was enabling oxidation of the reactive material, which slowly consumed the oxygen in the mixture. Since the engine was motored, 'lubricant oxidation' is a reasonable explanation for the observed phenomenon.

It can be safely assumed that the oxygen initially present converted to a mixture of CO_2, CO and H_2O. The ratio of specific heats for CO is equal to that of oxygen, whereas the ratio of specific heats for CO_2 and H_2O is 1.33. Therefore, this slow reduction of O_2 content might have reduced slightly the γ ratios of the mixtures initially intended, however from Figure 4.23 and Figure 4.24 it was still seen that the peak bulk gas temperature showed large changes from one γ ratio to another – which was the main aim of this testing session. In order to eliminate such 'lubricant oxidation', it is thought that one could make use of just Argon and Nitrogen to synthesise different γ ratios between 1.40 and 1.67. Since both Argon and Nitrogen are non-reactive gases, if proper purging is done, there would be no reactive gas which can be consumed by the high temperatures.

Another observation which was made after operating the engine with gases other than air was that a thick layer of soot deposited on the combustion chamber sensors. Figure 4.47 shows a photo of the in-cylinder pressure sensor (AVL pressure transducer GH14P, Serial No. 160506) evidently covered by soot. The in-cylinder pressure sensor was clean before the testing session. Initially, it was thought that this observation was related to the lubricant oxidation that was explained in the previous

paragraph. However it was later found that the problem of sooting occurred only when the engine was operated with γ of 1.67, *i.e.* pure Argon. This meant that the problem of sooting was not lubricant oxidation, but lubricant degradation in the absence of a reactive gas, such as oxygen. In fact, later on in this dissertation, a short test matrix was conducted using a gas of γ of 1.6 but synthesised by using just Argon and Nitrogen. This showed that even the gas mixture of γ 1.6 with the absence of oxygen results in sooting.

Figure 4.47. The in-cylinder pressure sensor showing signs of soot at the tip.

4.5 Discussion

The presented three testing sessions outline the characteristics of the pressurised motored method in its traditional form as used by [76] [77], and also with an added modification that uses different working gases to increase the bulk gas temperature. The use of different gases to raise the bulk gas temperature provided a solution to one of the frequently outlined criticisms of the pressurised motoring method [3] presented in the literature review chapter, *i.e.* the low bulk gas temperatures. It was also shown that with this method, despite that the bulk gas temperature peaks to values similar to a fired engine, the bulk gas temperature along the cycle is not identical, where pressurised motoring using Argon obtains bulk gas temperatures higher than firing during compression, whereas the fired engine has a higher bulk gas temperature during expansion and exhaust.

As a result of the high temperatures reached with Argon and its mixtures, an increase in heat transfer and mass leakage was noted, as represented by the $IMEP_{360}$. The pumping losses however decreased due to a smaller trapped mass, and a consequent decrease was also noted in the recompression effect during the exhaust stroke. The

mechanical friction was found to be independent of an increase of 600℃ in the peak bulk gas temperature. It was hypothesised that this independence of FMEP on bulk gas temperature might have resulted from the nature of the bulk gas temperature – to – pressure load phasing that is inherent in motored operation. This means that there is a significant possibility that the pressure phasing is a significant contributor to the FMEP, not just individually, but also through an interaction with the bulk gas temperature, and consequently oil film temperature. This hypothesis was drawn after comparing the results from the pressurised motored engine obtained from this work, to those obtained by Allmaier et al. [76] and MAHLE [77] for a pressurised motored engine using air, and a fired engine run at equivalent setpoints.

In support of this, the effect of the location of peak in-cylinder pressure on engine metrics was studied through a simulation study by Sammut et al. [83], as part of the same research project. The simulation investigated the possibility, viability and extent to which the motoring location of peak in-cylinder pressure can be varied, by introducing minor fuel quantities in the cylinder of the shunt pipe equipped, pressurised motored engine. Consequently, gas has to be bled off from the exhaust manifold in order to exhaust some of the burnt gases, whilst supplying fresh charge to the shunt pipe, using the make-up compressor. Figure 4.48 shows a schematic of the proposed setup for a single cylinder version of the 2.0 HDi engine.
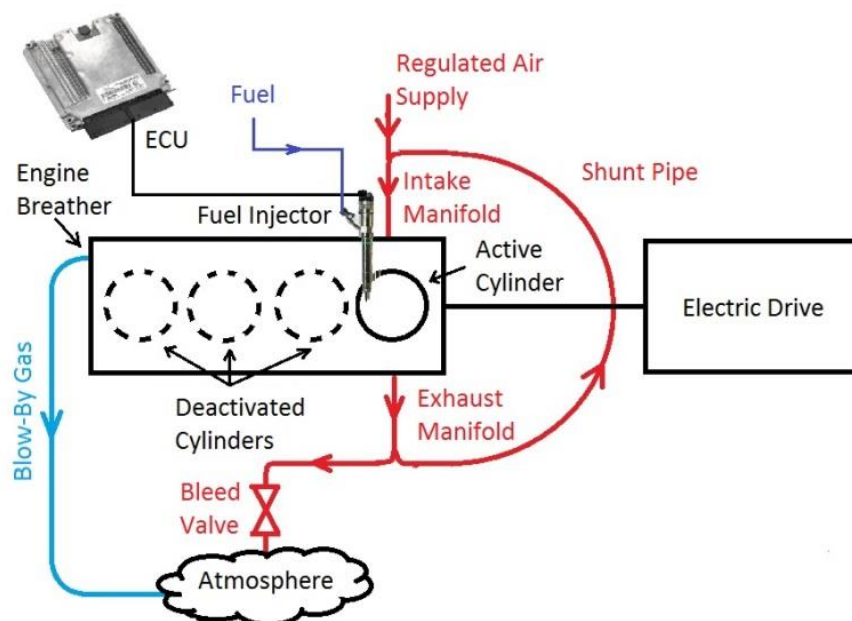
Figure 4.48. Schematic of the fuelled pressurised motored setup, proposed by Sammut et al. [83].

From initial simulation runs in [83], it was shown that shifting the motoring location of peak pressure is possible, even up to 10 DegCA ATDC, whilst the IMEP and BMEP could still be kept very low and comparable to the pressurised motored values. By running several simulation DOEs at different engine speeds and pressure loads, it transpired that achieving a certain LPP could be done by simply controlling the injected fuel quantity, point of injection, intake manifold pressure and bleed valve area. This simulation was mainly aimed at providing evidence, that a method can be devised which bridges to a greater extent the gap between fired and motored testing. It also provides a guide-through of what should be altered to the conventional pressurised motored method in order to adopt this strategy, together with useful control data that should be set in the event of experimental testing. For further information about the results obtained from this study, the reader is referred to [83].

The principal advantage of using the pressurised motored method was already outlined and explained in Chapter 2, where it was stated that the FMEP obtained from this method suffers from a far less uncertainty propagation than that suffered by the fired indicating method. Having obtained experimental data of FMEP from the same engine in the pressurised motored mode in this work, and fired mode in [78] [79], a comparison can be made on these grounds. Table 4.3 shows the PCP, BMEP, FMEP, their standard deviation on 300 cycles, and the ratio of FMEP/BMEP for the pressurised motored test with air and Argon, and a fired test at a similar setpoint obtained from [78] [79]. It shows that for a given setpoint of 3000 rpm, 102 - 103 bar PCP, the FMEPs are within 13% of each other. The difference lies in their standard deviations, and their FMEP/BMEP ratio, which are both an indicator of the robustness of the FMEP measurement of the test from which they were obtained. The FMEP/BMEP ratio is only 16% for the fired case, and around 46% to 55% for the pressurised motored cases. This shows that the pressurised motored method accentuates the friction portion from the total loss measurement (BMEP) by more than three-fold, hence guarantees a much more reliable FMEP measurement. Following from this, it could be noticed that the standard deviation surrounding the FMEP is around 28% for the fired case, and only 3.5% for the pressurised motored cases.

It is good to note that, due to the higher magnitude of the $IMEP_{360}$ for the pressurised motored engine with Argon operation compared to that with air, the FMEP/BMEP

ratio degraded by around 8% for Argon operation; however it is still appreciably larger than that of the fired operation.

Table 4.3. Comparison of FMEP/BMEP sensitivity between fired and motored testing (at 3000 rpm).

Method	PCP [bar]	Working Fluid	BMEP [bar]	FMEP [bar]	$\frac{FMEP}{BMEP} \, x \, 100$
Fired 1.6 bar MAP *	102.3	Air/Fuel	11.41 $\pm$ 0.25	1.83 $\pm$ 0.52	15.8%
Motored †	102.5 $\pm$ 0.4	Air	- 3.85 $\pm$ 0.03	2.09 $\pm$ 0.06	54.3%
Motored †	103.5 $\pm$ 0.2	Argon	- 4.20 $\pm$ 0.05	1.94 $\pm$ 0.07	46.2%
* Data published in [79]*, Table 4 based on work from* [78]*.* † *Data shown in* Figure 4.44 *in this Doctoral work.*					

With the advantages and disadvantages that are brought about with the use of the pressurised motored method for FMEP determination, at the present stage one has to consider that this method is in competition with tests such as the teardown, hot coasting, Morse test and fired indicating (IMEP) method. Based on a small number of visits to OEMs during the duration of this project, it was noticed that the teardown test is still one of the most popular methods of FMEP testing, despite its known limitations. It was shown by Richardson [3], but also explored in the Masters dissertation [78] that the above mentioned four methods have significant limitations, such as:

- Isolation of the FMEP from mechanical loading (*i.e.* assuming constant FMEP with PCP variation)
- FMEP not measured at thermal steady-state conditions
- Interaction of the FMEP of several components not taken into account
- Disadvantage of having to take apart the engine rather than testing it as a whole unit
- High magnitudes of numerical error propagation
- Anomalous interpretation of the PMEP as part of the FMEP

Accurate and physically representative friction models are required for the production engine. These friction models have uses, such as, for preliminary engine performance prediction, virtual torque estimation by the engine control unit (ECU),

vehicle level simulations for fuel economy and emissions optimisation, and for power split optimisation between the internal combustion engine and the electrical drive in a hybrid vehicle. A one-dimensional model can be tuned to results obtained from a pressurised motored engine, exploiting its accuracy and repeatability. The model will then have to bridge a smaller gap from the motored to the fired condition.

Engine friction models are often based on a teardown motoring test which have the necessary consistency and repeatability but lack the pressure and thermal load sensitivity [3]. On the other hand, engine friction models based on fired tests fall short on the consistency and repeatability, but allow the exploration of friction due to engine pressure load, superimposed by the thermal load. The pressurised motored test proposed in this study benefits from consistency, repeatability, pressure load sensitivity, and with the modification proposed – also the thermal load with the advantage of it being decoupled from the speed and pressure load. It is also worth mentioning that the limitation imposed by the peak in-cylinder pressure timing is opposed by the higher level of accuracy and repeatability of the pressurised motored method.

Pressurised motoring can be a viable, cheap, accurate and repeatable method for friction determination. It can provide an early indication of, among other things, anomalies in the rotating assembly without in-cylinder pressure indication measurement. If pressure indicating measurement is used, more detailed friction measurement can be obtained, but other vital health checks can be made for blow-by, theoretical versus dynamic compression ratio, and more. It is appreciated that this might require a break in the build phase of the prototype production engine. After the pressurised motored test and building the rest of the engine accessories, the engine would be ready for the more intensive and costly fired testing (*e.g.* fuel economy). The cost of the extra pressurised motoring test is expected to be outweighed by the savings from the more expensive fired test. The energy requirements and the associated hardware costs to motor the engine were shown to be quite low, even at rated peak in-cylinder pressures and temperatures.

4.6 Testing of the Single Cylinder Engine at different engine speeds, PCPs and gas compositions

After the pressurised motored setup was converted to single cylinder, a test session was planned, aimed at the FMEP determination of the single cylinder engine. With this setup, a better FMEP measurement was expected due to the decoupling of the oil pump energy requirement from the engine friction measurement. Furthermore, to remove any bias originating from the different coolant temperatures on the FMEP, for the single cylinder engine, the coolant and oil circuits were conditioned independently.

For this experimental test session, a 48 point test matrix was considered, as documented in later Table 5.4. This test matrix was planned to give adequate individual relationships of FMEP with engine speed, PCP, coolant temperature and in-cylinder gas temperature. The oil pressure was kept at a constant 4 bar throughout all setpoints tested, independent of the engine operating condition.

Following the processing of the data from the discussed test matrix, it was noted that the torque measured by the loadcell showed an anomalous relationship with speed and PCP. Even though not confirmed, it is thought that due to the greatly reduced overall loss of the single cylinder engine (compared to the four cylinder), the sensitivity of the floating motor torque measurement system was not sufficient. As a result for the single cylinder engine testing, the torque supplied by the motor was measured using the full-bridge strain gauge system mounted on the drive shaft, described in section 3.1 and published in [87]. Initial tests with the shaft-mounted measuring system gave a consistent torque measurement, with the resulting FMEP having an expected trend and magnitude, as shown in Figure 4.49. Unfortunately, during the initial phases of testing the 48 point test matrix, an issue related to the torque measurement system developed which could not be definitively traced in the available timeframe. As a result, from this testing session the BMEP and FMEP were not obtained, however metrics derived from the in-cylinder pressure measurements were still successfully obtained and presented in the forthcoming sections. The reason for presenting this data from the single cylinder engine is mainly due to the fact that it was acquired with a constant coolant temperature of 80℃, unlike that

obtained from the four-cylinder engine and reported earlier where the coolant temperature varied at each setpoint. Hence the data presented in this section is thought to have less influence from external factors originating from the different coolant temperatures. Discussion of results is limited since the majority of observations are similar to those made on the four-cylinder engine data, which were already explained in the previous sections.
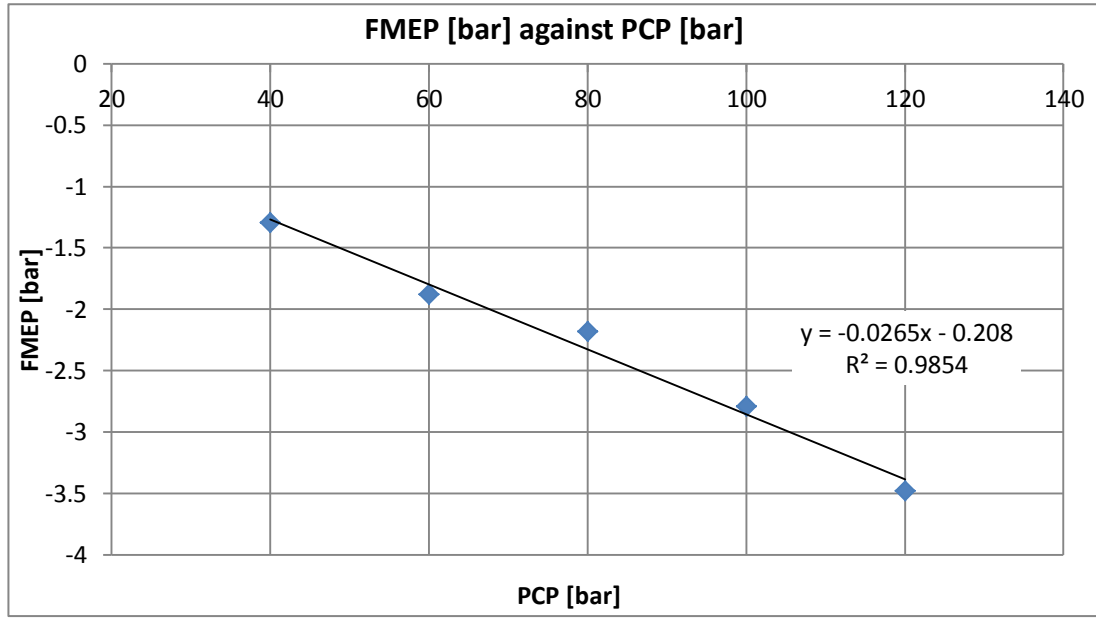
Figure 4.49. FMEP against PCP at 1400 rpm and air as the working gas for the single cylinder engine.

4.6.1 Variation of mean effective pressures with engine speed and PCP

Figure 4.50 shows the $IMEP_{360}$ plotted against engine speed, whereas Figure 4.51 shows the $IMEP_{360}$ against PCP. Both these figures are plotted for air as the working gas. It is noted that from the trends obtained, a decrease in the $IMEP_{360}$ magnitude is evident with an increase in engine speed. This is similar to that shown earlier for the four cylinder engine. However, it is noted that for the four cylinder engine, smaller $IMEP_{360}$ magnitudes were obtained (see Figure 4.36 and Figure 4.37 for 84 bar and 103 bar PCP respectively). Furthermore it is also observed that for the four cylinder engine, the gradient magnitude of the $IMEP_{360}$-engine speed graph decreases with an increase in engine speed. On the other hand, for the single cylinder engine in Figure 4.50, the gradient magnitude increases with an increase in engine speed.

Figure 4.51 shows that an increase in PCP results in a linear increase in the $IMEP_{360}$ magnitude. It is noted that for the single cylinder engine, the data of $IMEP_{360}$ against PCP is characterised by a higher gradient magnitude when compared to that of the four cylinder engine (see Figure 4.15).

The differences in the $IMEP_{360}$ magnitudes between both engines could potentially be attributed to the fact that on the four cylinder engine, the coolant temperature was set to be progressively cooler with an increase in engine speed (to condition the oil at 80°C), whereas for the single cylinder engine the coolant temperature was retained at a constant 80°C throughout. The different coolant temperatures between the two engines were however expected to yield a lower $IMEP_{360}$ magnitude for the single cylinder (compared to the four cylinder), and not vice versa. On the other hand, it should be appreciated that despite the fact that both the four cylinder engine and single cylinder engine are of similar base models, however differences could have originated from, for example, compression ratio variances between the two engines. Both engines were also previously used in road going vehicles before fitted on the pressurised motored setup, hence their wear states might have been different, for example due to different liner-rings conditions and valve-seat mating surfaces.
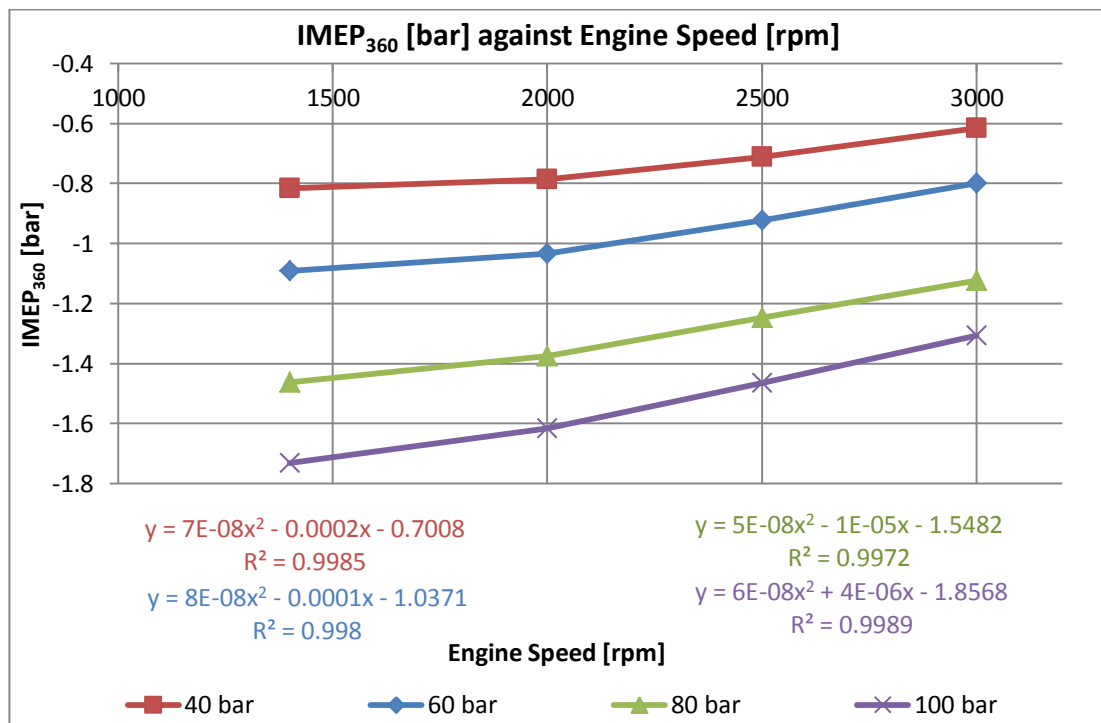
Figure 4.50. $IMEP_{360}$ against engine speed and PCP with air as the working gas for the single cylinder engine.

143
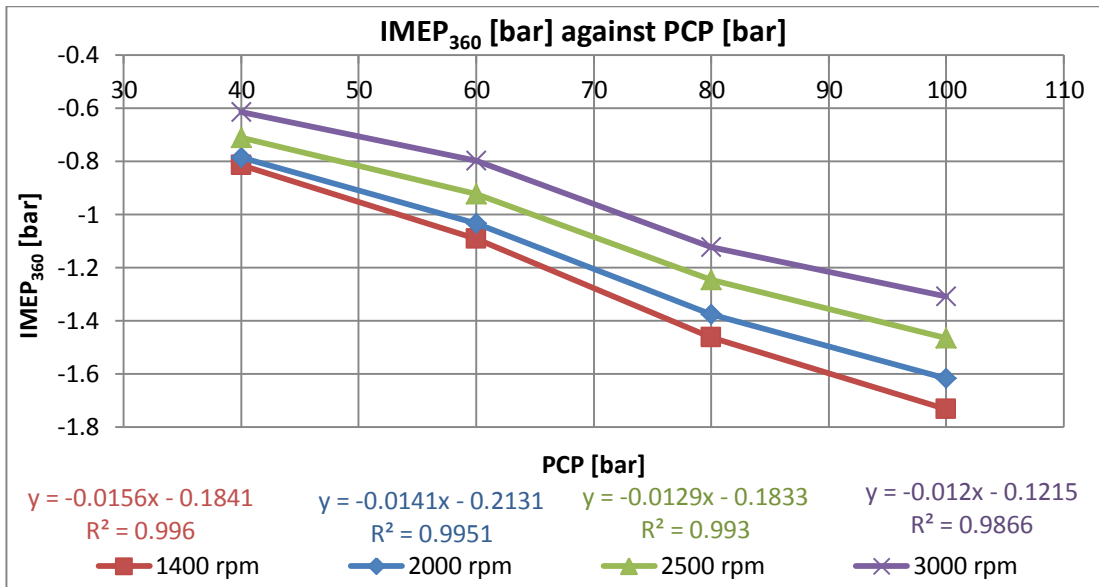
Figure 4.51. IMEP$_{360}$ against PCP and engine speed with air as the working gas for the single cylinder engine.

The PMEP is presented in Figure 4.52 and Figure 4.53. It is shown that an increase in pumping losses is evident with an increase in the engine speed. An abrupt increase in the gradient of the PMEP is shown at 2500 rpm. The extent of this change in gradient increases with an increase in PCP. This relationship can be explained by the exhaust stroke recompression effect occurring in the pressurised motored engine, which was dealt with in detail, previously in section 4.3.2. The relationship of PMEP with PCP is linear which shows an increase in losses with an increase in PCP. The PMEP magnitudes observed for the single cylinder engine are relatively similar to those obtained from the four cylinder engine (see Figure 4.38 and Figure 4.39).
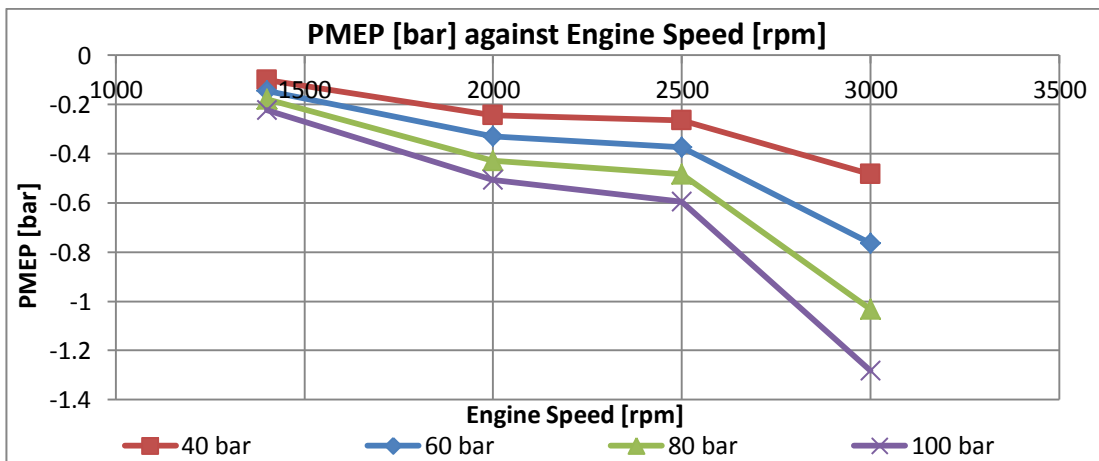
Figure 4.52. PMEP against engine speed and PCP with air as the working gas for the single cylinder engine.
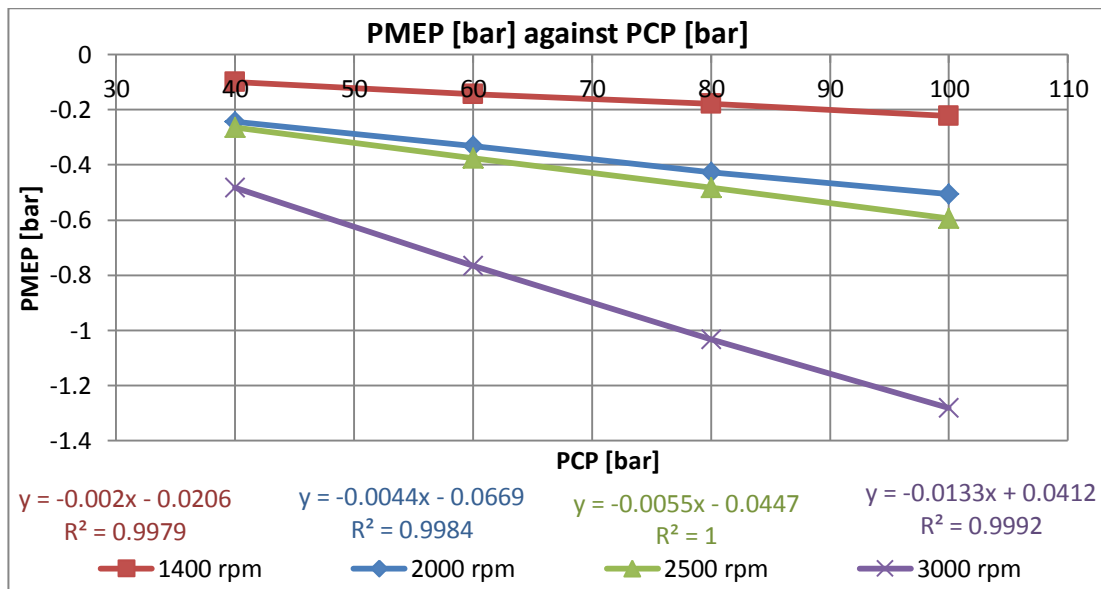
Figure 4.53. PMEP against PCP and engine speed with air as the working gas for the single cylinder engine.

4.6.2 Effect of Bulk Gas Temperature on Mean Effective Pressures

The graph of $IMEP_{360}$ for the different gas compositions is shown in Figure 4.54. For all gases and mixtures tested, an increase in the engine speed resulted in a decrease in the $IMEP_{360}$ magnitude. It is noted also that the $IMEP_{360}$ shows a similar relationship with engine speed for all gases tested, with minor differences being noticed for the gas with γ of 1.67. This figure can be compared to Figure 4.36 and Figure 4.37 for the four cylinder engine.

Since the single cylinder engine was instumented with combustion chamber surface thermocouples (for heat transfer measurements in chapter 5), the $IMEP_{360}$ obtained with different gases could be plotted against the average surface temperature. Figure 4.55 shows the variation of $IMEP_{360}$ with the cylinder head surface temperature. Similarly Figure 4.56 shows the $IMEP_{360}$ against the computed peak bulk gas temperature, and Figure 4.57 presents the $IMEP_{360}$ against the difference in temperature between the peak of the bulk gas and the surface temperature, which is referred to as ΔT_{G-W}. It is noted that the $IMEP_{360}$ shows a linear variation with ΔT_{G-W} for all engine speeds.
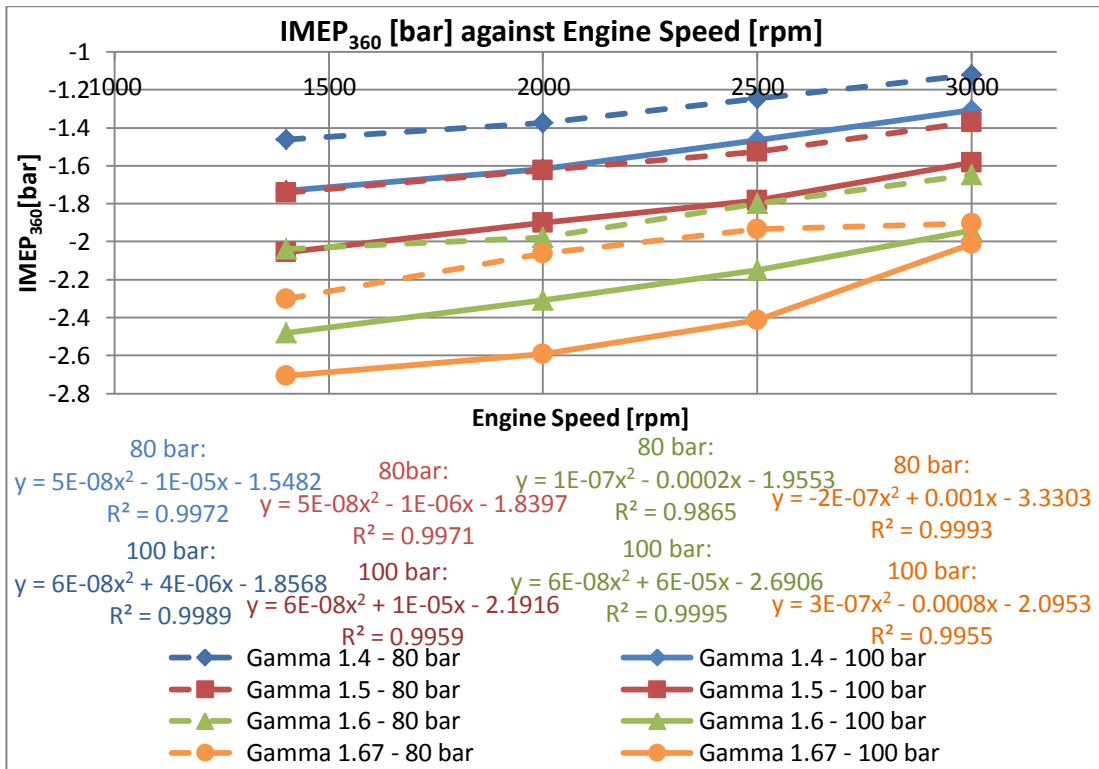
Figure 4.54. IMEP$_{360}$ against engine speed and PCP for different working gases for the single cylinder engine.
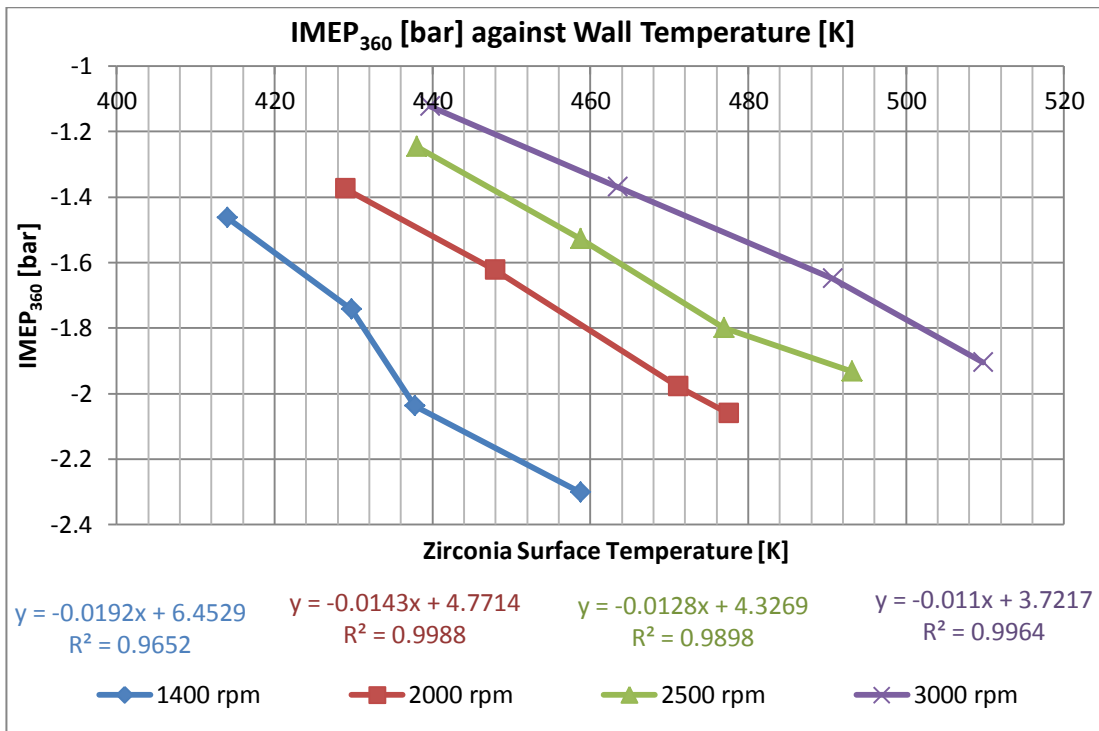
Figure 4.55. IMEP$_{360}$ against wall temperature at 80 bar PCP, measured by a Zirconia-based surface thermocouple at OEM injector location for the single cylinder engine.
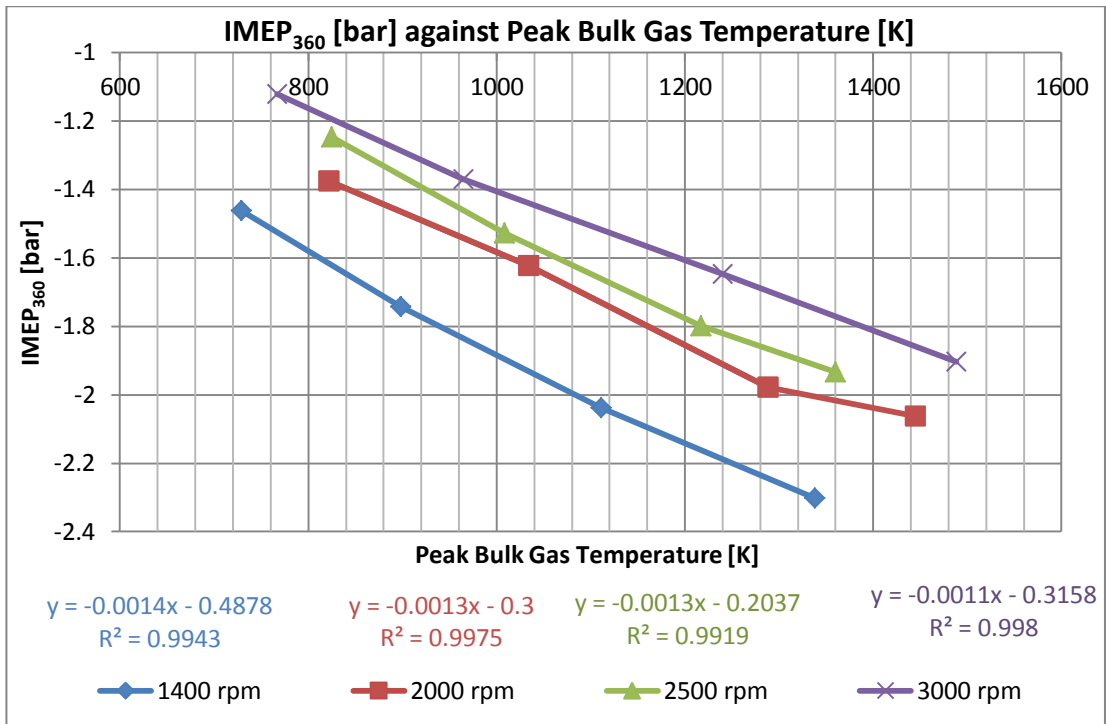
Figure 4.56. IMEP$_{360}$ against peak bulk gas temperature at 80 bar PCP for the single cylinder engine.
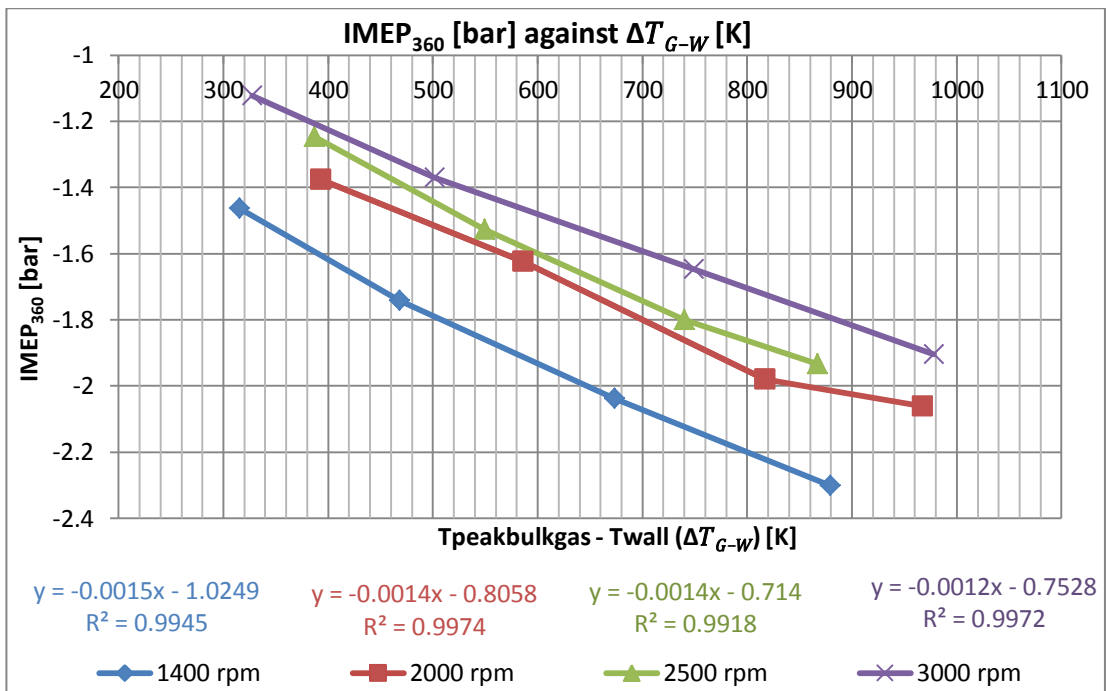
Figure 4.57. IMEP$_{360}$ against ΔT_{G-W} at 80 bar PCP for the single cylinder engine.

The pumping mean effective pressure is given in Figure 4.58 against engine speed. It is shown that the losses identified by the PMEP are very similar for all gases at 1400 rpm, but differ significantly as the engine speed increases, especially at 3000 rpm.

Air seems to show the largest loss compared to the other gases, at 3000 rpm. This relationship was already discussed for the four cylinder engine, and attributed to the recompression effect happening during the exhaust stroke. By increasing the ratio of specific heats of the gas, the same peak in-cylinder pressure can be attained by a smaller trapped mass, hence lower PMEP magnitude. Figure 4.59 shows that this advantage of a smaller PMEP is significant mostly at high engine speeds.
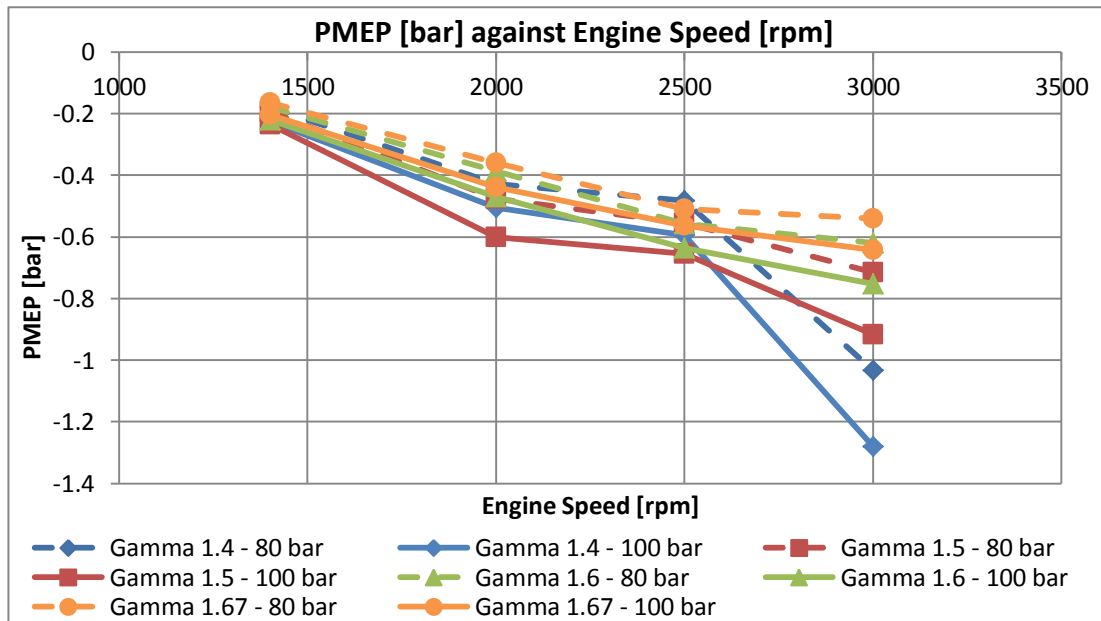
Figure 4.58. PMEP against engine speed for the single cylinder engine.
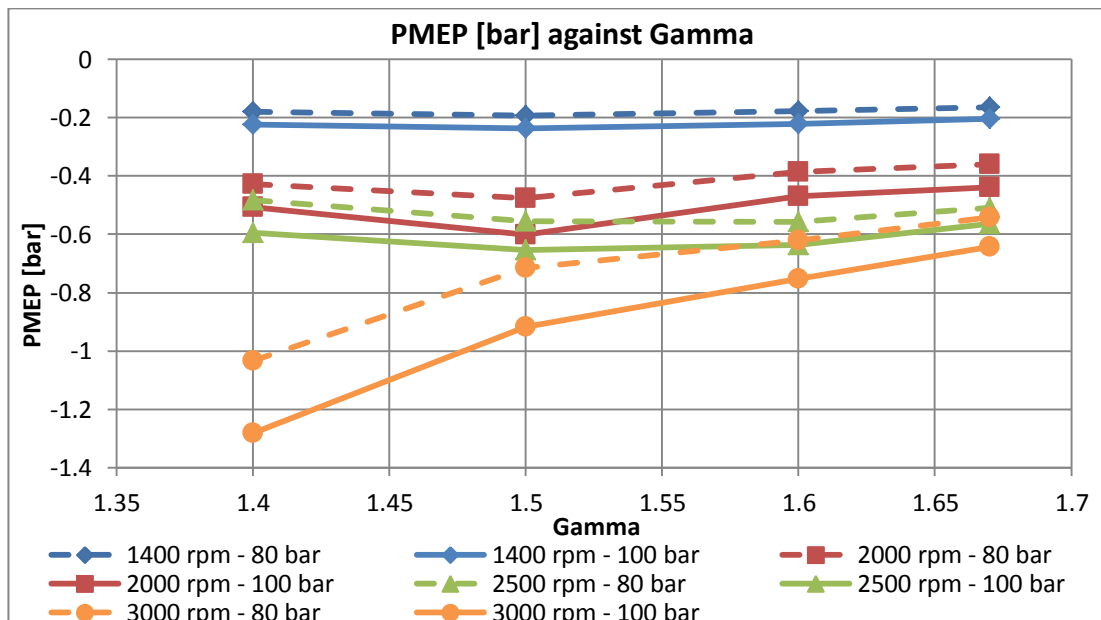
Figure 4.59. PMEP against projected gamma for the single cylinder engine.

4.6.3 Effect of Coolant and Oil Temperature on Mean Effective Pressures

The effect of coolant and oil temperature on engine losses could be studied on the single cylinder engine. Figure 4.60 shows the $IMEP_{360}$ at a PCP of 80 bar at three different coolant/oil temperatures and varying engine speed. Air was the working fluid. It is noted that at the three different coolant temperatures, a similar variation of $IMEP_{360}$ was found with engine speed. However, the variation of $IMEP_{360}$ with coolant/oil temperature is somewhat unclear, where it shows that the losses identified by the $IMEP_{360}$ increase by increasing the coolant/oil temperature from 60℃ to 80℃, but decrease from 80℃ to 95℃. Figure 4.61 shows that a change in the coolant/oil temperature renders negligible difference in the PMEP.
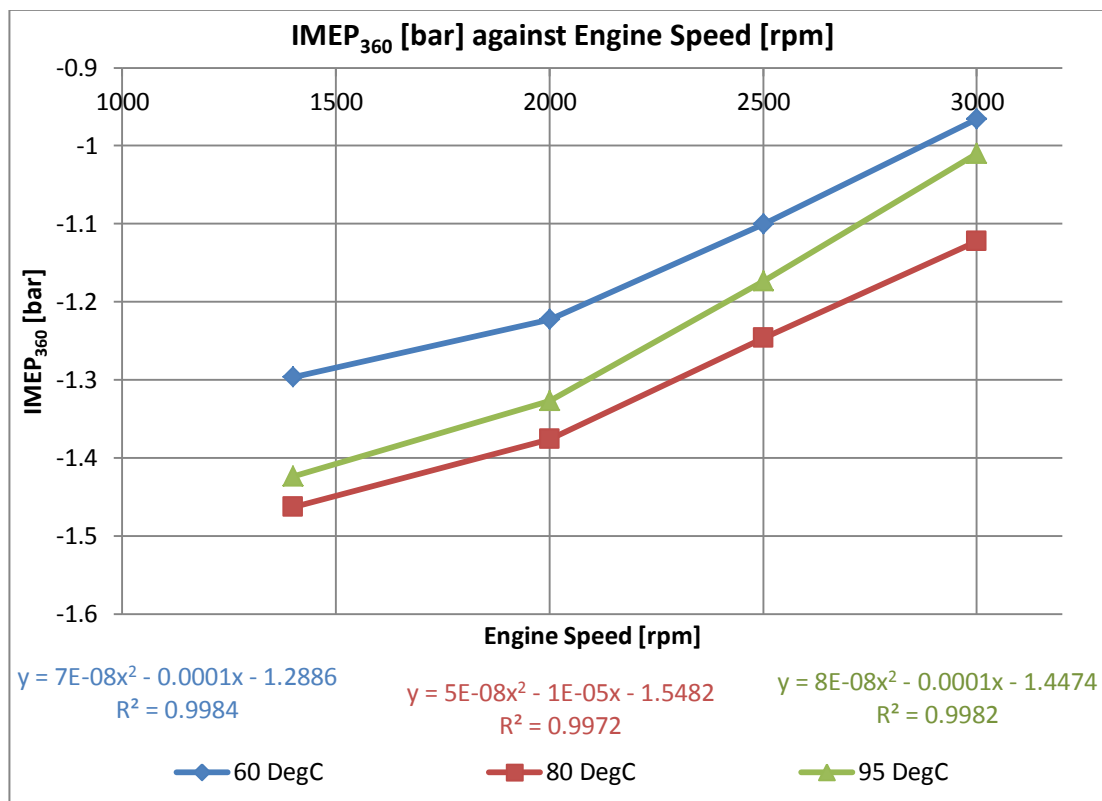
Figure 4.60. $IMEP_{360}$ against engine speed for different coolant temperatures for the single cylinder engine.
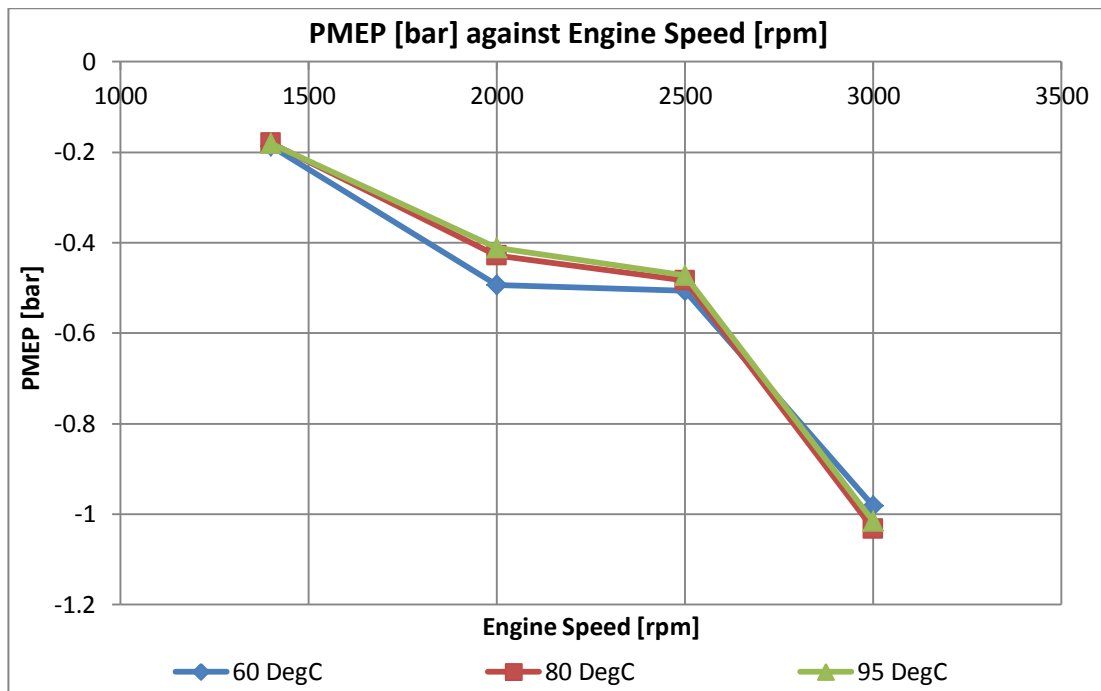
Figure 4.61. PMEP against engine speed for different coolant temperatures for the single cylinder engine.

4.6.4 Closing Remarks

As have been said before the presentation of results, the aim of the single cylinder testing was initially to obtain an FMEP measurement with a higher fidelity and to perform in-cylinder heat transfer measurements, documented later in chapter 5. Unfortunately FMEP testing was however disturbed by issues that cropped up in the torque measurement system. Despite this, the results that were obtained from the measurement of the in-cylinder pressure were still of benefit to obtain the variations of $IMEP_{360}$ and PMEP which are free from effects imposed by the coolant temperature.

The next chapter presents the experimental research conducted on the topic of in-cylinder heat transfer. The mean effective pressures presented for the single cylinder engine in the previous section of this chapter can be utilised to obtain a clearer understanding of the in-cylinder heat flux results presented in the next chapter.

5 SURFACE TEMPERATURE MEASUREMENTS AND HEAT FLUX DETERMINATION

The second aim of this doctoral work was to investigate the instantaneous heat flux from the combustion chamber of a pressurised motored engine. For this purpose, two locations at the cylinder head of the single cylinder engine were fitted with surface thermocouples of the eroding type, as explained in Chapter 3. In this chapter, a detailed account of the experimental campaigns for surface temperature measurements and heat flux determination will be given, but before, the theory surrounding the conversion of the surface temperature measurements to heat flux will be discussed.

5.1 Method used for Computation of Heat Flux from Surface Temperature

From a review of the existing literature, three methods had been found that are capable of converting the measured surface temperature to surface heat flux. These methods include the traditional and most popular spectral analysis using Fourier transform, a finite difference method, and the Impulse Response method which seems to be the new emerging method for this type of computation.

Out of the above mentioned methods, two were used in this work. The first method used was the one based on the Fast Fourier Transform [35] [7] [113], whereas the second method used is that which was put forward by Oldfield [114], known as the Impulse Response Method.

5.1.1 The Fourier Method

The Fourier method is the classical approach for the conversion of surface temperature swing to surface heat flux. This was used as early as 1961 by Overbye et al. [13], and has been in use ever since [7]. The temperature variation at the surface of the combustion chamber cannot be defined accurately by a simple function. The Fourier method builds on a harmonic analysis of the measured surface temperature,

which then allows its representation by the use of a finite number of terms in a series of sine and cosine terms. The temperature profile into the wall is obtained through the use of the reduced heat equation with the assumptions that the specific heat capacity and thermal conductivity of the surface material are constant, and heat flow is one-dimensional perpendicular to the surface.

For this method to be applied, the surface temperature has to be periodic. Equation (5.1) presents the solution of the heat diffusion equation through a semi-inifite solid when its surface temperature is a harmonic function of time. Equation (5.1) gives the temperature distribution through the semi-infinite solid from the surface (x = 0) to a certain distance from the surface (x = L) at which the temperature is assumed to be steady, A_{aj}. By evaluating the derivative of equation (5.1) at the ordinate x = 0 (heated surface), equation (5.2) is obtained. Applying equation (5.2) in Fourier's law of one-dimensional conduction allows the determination of the heat flux, as given by equation (5.3). This was adapted from Carslaw and Jaeger [115]. It is shown that the heat flux has two components; the steady-state component and the transient component at the surface of the heated solid. The steady-state component can be evaluated from the time-averaged wall temperature at the heated surface, A_{OW}, and the steady temperature at a distance L from the wall, A_{aj}. The temperature at x = L is usually measured by a thermocouple fitted at this recessed location. The transient component of heat flux requires the Fourier harmonic analysis, by which the coefficients of the cosine and sine terms, A_n and B_n respectively, can be determined.

$$T(x,t) = A_{OW} - \frac{(A_{ow} - A_{aj})x}{L}$$

$$+ \sum_{n=1}^{N} \left\{ \left[A_n cos\left(n\omega t - x\sqrt{\frac{n\omega}{2\alpha}} \right) + B_n sin\left(n\omega t - x\sqrt{\frac{n\omega}{2\alpha}} \right) \right] e^{-x\sqrt{\frac{n\omega}{2\alpha}}} \right\} \quad ...(5.1)$$

$$\frac{dT(x,t)}{dx}\bigg|_{x=0} = \frac{(A_{ow} - A_{aj})}{L} - \left(\sqrt{\frac{n\omega}{2\alpha}}\right) \sum_{n=1}^{N} [(B_n - A_n)\, sin(n\omega t) + (B_n + A_n)\, cos(n\omega t)]$$

$$...(5.2)$$

$$Q'' = -k \frac{dT(x,t)}{dx}\bigg|_{x=0}$$

$$= -\frac{(A_{ow} - A_{aj})k}{L} + k\left(\sqrt{\frac{n\omega}{2\alpha}}\right)\sum_{n=1}^{N}[(B_n - A_n)\,sin(n\omega t) + (B_n + A_n)\,cos(n\omega t)]$$

$$\dots (5.3)$$

For the application of the Fourier harmonic analysis, the Fast-Fourier Transform (FFT) is usually employed. For a successful application of the FFT, the temperature signal must fit in a 2^k array of ordinates. If the measured temperature signal from a single cycle, or ensemble average is smaller than the array, a padding scheme has to be employed. If for instance the measured surface temperature is sampled according to a 0.1 DegCA encoder, then for a full engine cycle (4-stroke) the surface temperature would have 7200 ordinates. This number of ordinates is not a factor of 2^k. As a result, a padding scheme must be employed to increase the number of ordinates to, for example, $2^{13} = 8192$.

The FFT algorithm assumes a continuous spectrum, meaning that the signal to be processed is one period of a periodic signal. Hence, the ordinates at the start and end of the analysed temperature cycle have to be at the same level. To ensure this, a windowing technique needs to be implemented [116]. The windowing technique multiplies the temperature signal cycle by a finite-length window with an amplitude that decays smoothly towards the edges.

An important consideration when applying the FFT algorithm is the number of harmonics used to represent the measured temperature signal. The maximum number of harmonics that can be used is equal to half the number of ordinates of the measured temperature array. For the most accurate representation of the measured temperature signal, all of these harmonics could be used; however this will result in serrations in the determined instantaneous heat flux which originate from the processing of electrical interference present at the higher end of the temperature frequency spectrum. As a result, in IC engine heat transfer research, a smaller number of harmonics are typically utilised. Decreasing the number of harmonics excessively results in the temperature signal being inadequately represented due to missing out of frequencies with important temperature information. In the work

presented by Overbye et al. [13] 72 harmonics were analysed. Both Farrugia [65] and Knight [117] also used a similar number of frequencies, whereas Hassan [118] used just 36 harmonics. Jackson et al. [43] used 180 harmonics. In this work, a quick analysis was made on the effect of the number of harmonics on the transient component of heat flux, starting from a large number of harmonics, down to 50. It was found that 70 harmonics presented a good representation of the heat flux as obtained with higher number of harmonics, however for the processing of the temperature signals using the FFT method, 100 harmonics were used.

5.1.2 Finite Difference Method

The finite difference computation is a discrete well-known mathematical method which approximates an exact solution of a differential equation, in this case the heat diffusion equation. This method was adopted by Nijeweme et al. [23]. To convert the surface temperature swing to instantaneous heat flux two boundary conditions have to be assigned, which are the measured temperatures at the surface and at the recessed location. An initial temperature distribution is then assumed between these two locations at the initial condition of time. A sensible initial temperature distribution can be a linear variation between the surface and the recessed location. By solving explicitly through the grid in both space and time, the temperature distribution in the space domain is obtained for the consecutive future time step using equation (5.6), derived from equation (5.5), which is a finite difference form of the one-dimensional heat diffusion equation (5.4). The temperature distribution at the end of the whole four stroke cycle is then compared to the initial condition for that cycle and if a large discrepancy is evident, the temperature distribution at the end of cycle P is used as a correction to the initial condition for cycle $P + 1$. This iteration scheme keeps on going until negligible differences in the temperature distribution are attained. After the iteration scheme converges, the surface instantaneous heat flux can be determined from Fourier's law of conduction.

An important consideration surrounding this method is the stability criteria, which is given by equation (5.7), adopted from Nijeweme et al. [23]. Since the computation makes use of the measured surface temperature, the time step size is usually dictated

by the resolution of the crankshaft encoder and the engine speed, which are responsible for the clock speed of the experimental data acquisition.

The main reason for preferring this scheme over the traditional Fourier spectral analysis is due to its simpler approach and ease of programming. It should be pointed out however that such numerical scheme is still based on the one-dimensional heat flow assumption, if derived from equation (5.4). Another inherent limitation of the method is that ultimately it provides an estimation to the exact value, however it was reported by Nijeweme et al. [23] that for the worst case, being the low engine speed of 120 rpm, the deviation of the approximate solution from the exact solution of instantaneous surface heat flux was always less than 1%.

$$\frac{\partial T}{\partial t} = \alpha \frac{\partial^2 T}{dx^2} \qquad \qquad \dots (5.4)$$

In a finite difference format:

$$\frac{1}{\Delta t}[T(t + \Delta t) - T(t)] = \frac{\alpha}{\Delta x^2}[T(x + \Delta x) - 2\,T(x) + T(x - \Delta x)] \qquad \dots (5.5)$$

$$T_{i,j+1} = T_{i,j} + \alpha \frac{\Delta t}{\Delta x^2}\left(T_{i+1,j} - 2.\,T_{i,j} + T_{i-1,j}\right) \qquad \dots (5.6)$$

$$0.5 > \alpha \frac{\Delta t}{\Delta x^2} > 0 \qquad \qquad \dots (5.7)$$

5.1.3 The Impulse Response Method

The Impulse Response method in the field of in-cylinder heat transfer knows its origins to Oldfield [114]. It makes use of discrete deconvolution of a pair of *'basis functions'* of temperature $T_1(t)$ and corresponding heat flux $q_1(t)$ to characterise the thermal behaviour of the system (eroding surface thermocouple). The heat flux imposed can be a step function. The resulting temperature from this step heat flux can be obtained in at least three ways; using the semi-infinite one-dimensional analytical solution, through a finite element analysis (numerical solution), or from thermocouple characterisation experiments that were presented in Chapter 2. In this research, to obtain the temperature response of the surface thermocouple to a step heat flux, the first two methods were utilised. Once the monotonically increasing

155

temperature resulting from the step heat flux is obtained for a given sampling frequency, a deconvolution algorithm between the imposed step heat flux and obtained temperature is used to obtain an *'Impulse Response Function'*, $h(t)$. The impulse response function describes the thermal behaviour of the eroding thermocouple.

The impulse response function can then be convoluted with the temperature signal measured by the eroding thermocouple in actual engine experiments to obtain the localised heat flux from the combustion chamber surface. It should be realised that an implicit assumption of the method is that, the functions $q(t)$ and $T(t)$ will follow the form of the basis functions $q_1(t)$ and $T_1(t)$.

In applying the impulse response method, the publications by Oldfield [114] [119] were consulted. A publication by Wang et al. [41] in which the impulse response method was applied on internal combustion engine surface temperature was also consulted.

The Impulse Response method is reported [114] to be applicable to any linear time invariant system where the signal to be processed is initially steady. The response of any linear time invariant system can be obtained through the convolution integral given in equation (5.8), where $h(t)$ is the impulse response function and τ is the dummy variable.

$$q(t) = h(t) * T(t) = \int_{-\infty}^{\infty} h(\tau)T(t - \tau)d\tau \qquad \text{... (5.8)}$$

It is reported by Oldfield [114] that this integral can be difficult to evaluate in the time domain and the impulse response function usually has singularities at the origin. In the discrete time domain, however, the surface temperature is sampled at a certain frequency and the convolution integral can be written in the discrete convolution sum as in equation (5.9). It should be remembered that in this study the sampling frequency is related to the engine speed since the surface temperature signal acquisition is sampled at every $1/10^{th}$ of a crank angle degree, according to the crankshaft encoder.

$$q[n] = h[n] * T[n] = \sum_{k=0}^{N-1} h[k]T[n - k] = \sum_{k=0}^{N-1} h[n - k]T[k] \qquad \text{... (5.9)}$$

The deconvolution of the basis functions to obtain the impulse response function $h[n]$ is most efficiently carried out by the Matlab function '*filter*', using the discrete impulse function $\delta[n]$=1, 0, 0, 0, … Taking z-transforms, the convolution operator * is replaced by multiplication.

$$Q_1 = H(z)\,T_1(z) \qquad\qquad \dots (5.10)$$

By convoluting the impulse response with an impulse function will, by definition, simply reproduce the impulse response, as in equation (5.11), where $\Delta(z)$ is the z-transform of δ[n].

$$H(z) = H(z)\Delta(z) = \frac{Q_1(z)}{T_1(z)}\Delta(z) \qquad\qquad \dots (5.11)$$

Thus, the required impulse response can be obtained by digitally filtering the impulse response function δ[n] by the infinite impulse response (IIR) filter whose coefficients are given by $\frac{Q_1(z)}{T_1(z)}$.

The one-dimensional heat flux assumption through the eroding surface thermocouple has been employed for several decades. This assumption is known to be not fully representative of the real heat flux through the sensor because of the different materials present in the construction of the eroding thermocouple. Due to this, the heat flux determination method based on FFT spectral analysis, using the semi-infinite solid solution of periodic heating at the surface has been criticised multiple times [19].

The impulse response method has the added advantage that if the eroding thermocouple is characterised by the basis functions, then each evaluation of heat flux making use of the obtained impulse response function and sampled surface temperature will yield the heat flux through the sensor in line with the assumptions taken in choosing the basis functions. This makes the impulse response method very versatile since it allows the user to account for multi-dimensional heat flow, or other physical characteristics of the thermocouple, if basis functions reflecting these factors are available.

Initially in this work, the impulse response method was employed making use of the basis function of temperature derived from the one-dimensional, semi-infinite solid

assumption in response to a step heat flux applied at the surface, given by equation (5.12). The one-dimensional assumption was chosen initially for two reasons; first to retain the problem simple during which confidence could be acquired in the impulse response method, and secondly to check the results obtained from the impulse response method with those obtained through the FFT method. Recall that the FFT method uses the same underlying assumption of a one-dimensional, semi-infinite solid conduction.

$$T_1(t) = \frac{2}{\sqrt{\rho c k}} \cdot \sqrt{\frac{t}{\pi}} \qquad \ldots (5.12)$$

After obtaining the impulse response function from the one-dimensional semi-infinite solid consideration, the surface temperatures measured from the eroding thermocouples fitted in the single cylinder engine were processed and the resulting heat flux could be compared with the heat flux computed from the FFT method. As presented later, the results from the FFT method and from a 1D consideration of the Impulse Response method matched, as expected.

Having outlined the Fast Fourier Transform method in the previous section, and introduced the Impulse Response method, it can be stated that the Impulse Response method offers the advantage of not requiring the zero padding scheme and more importantly also does not require the windowing technique that is essential for the FFT to ensure periodicity. This therefore makes the Impulse Response method slightly easier to implement.

When employing the impulse response method, a sufficiently long surface temperature signal must be convoluted, instead of an ensemble average temperature. The reason for this is that the method will induce a starting transient on the computed heat flux which will eventually settle after a few cycles, hence the very first few cycles of computed heat flux needs to be discarded and the remaining heat flux cycles can then be ensembled to yield one representative heat flux cycle of the tested setpoint. To understand better this starting transient phenomena, a test was done in which a 50 Hz sine wave with 32 identical cycles was constructed and used as the hypothetical sampled temperature signal. The resulting heat flux was obtained through the discrete convolution of this constructed temperature signal with the

impulse response determined from the 1D semi-infinite solid solution. The result consequently consisted of 32 heat flux cycles. In a separate run, a single 50 Hz sine wave temperature signal identical to that in the previous run, was processed using the FFT method. Figure 5.1 shows the heat fluxes of the first and last (32nd) cycles obtained from the impulse response method, and that obtained from the FFT method. It can be seen that the last cycle from the impulse response method matches exactly that obtained from the FFT method, however the first heat flux cycle from the impulse response method starts out distorted and settles later in the cycle. This demonstrates the starting transient induced by the impulse response. It must be said that from the third cycle onwards, the heat flux settles almost completely and hence only very few starting cycles need to be discarded.
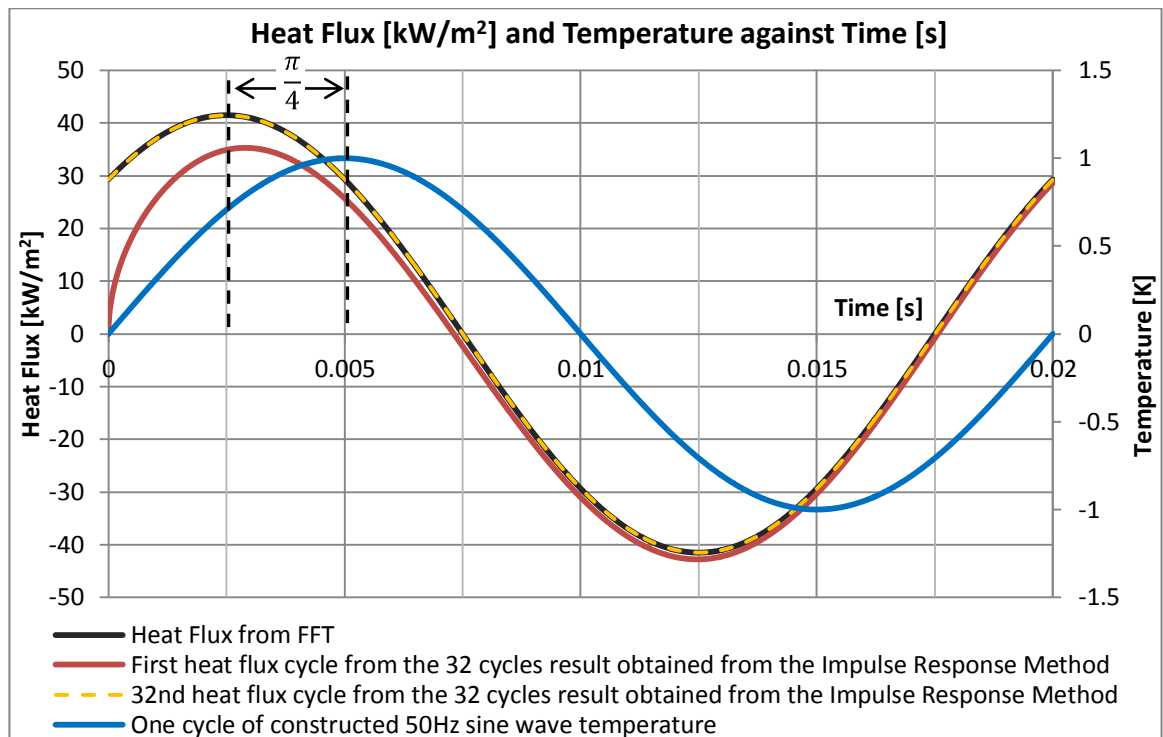
Figure 5.1. Heat flux against time which shows the starting transient of the Impulse Response Method.

To generate the data shown in Figure 5.1, a sinusoidal signal was chosen amongst others for two main purposes; to have a somewhat representative temperature of what would be recorded in an internal combustion engine, and to have a wave starting and ending with a zero temperature. Temperature recorded from an internal combustion engine would naturally not start at zero temperature, but would be relatively steady throughout the majority of the intake and exhaust strokes, and hence

for this matter, to employ the impulse response method, the recorded temperature signal has to be shifted by subtracting from it the initial temperature.

The requirement of the Impulse Response method to process a long stream of data yields itself time consuming initially when obtaining the impulse response function. This process would escalate greatly in the time duration if a two-dimensional heat flux approach is considered, as explained in a forthcoming section. After obtaining the impulse response, the method then becomes very computationally efficient since the obtained impulse response function can be convoluted with the sampled temperature over and over, as long as the sampling frequency for the given thermocouple is unchanged.

To reduce the computational time of the impulse response function, it was suggested by Oldfield [120] that the *decimate* function in Matlab is used to reduce the sample rate of the temperature signal by an integer factor of ten. This therefore meant that with the impulse response method, the heat flux was computed every one degree crank angle, as opposed to that computed from the FFT method, which had a resolution of $1/10^{th}$ of a crank angle degree.

One disadvantage underlying the impulse response method is the fact that the computed result is very sensitive to electrical noise interference in the sampled temperature signal. It is understood that this originates from the fact that the impulse response technique employs no filtering to the measured temperature signal. On the other hand, the more common FFT method requires from the user the number of harmonics by which the surface temperature is to be represented. In previous studies, the number of harmonics was usually set to around 72 [13] [117]. Limiting the number of harmonics indirectly means that the sampled temperature trace is filtered from the electrical noise present at the high frequency components of the signal. Hence, with the FFT method, the computed heat flux is less susceptible to serrations originating from the sampled surface temperature. While this seems to be a disadvantage to the impulse response method, one can always employ a frequency filtering scheme on the sampled temperature and then use its result in the convolution integral of the impulse response method.

5.1.4 Effect of Engine Speed Fluctuations

The three methods outlined that convert the surface temperature to heat flux assume a constant finite time interval between one ordinate and another. In internal combustion engine heat flux research, this criterion is not strictly followed due to the fact that the surface temperature signal is usually sampled according to a crankshaft encoder with a given number of pulses per revolution. If the engine is assumed to rotate with a constant angular velocity, then the condition of constant time interval is fully upheld. However, it is known that during a given cycle of an IC engine, the rotational speed varies between the different strokes due to the deceleration of the crankshaft on compression, and acceleration during expansion. The extent of this acceleration and deceleration might be even larger for single cylinder engines, which do not have other piston assemblies to counterbalance, as explained in Chapter 3. As a result, the assumption of constant finite time interval might be stretched for single cylinder engines.

To investigate the variation in the engine speed, the single cylinder engine was run at two engine speeds of 1400 rpm and 2000 rpm, and two different PCPs of 40 bar and 100 bar. The OEM crank sensor of the engine was used to read the 60-2 trigger wheel on the crank (60 teeth less 2 to provide a marker that engine will start another revolution). The crank signal was sampled by the internal clock of the data acquisition system (DAQ) with a fixed frequency of 200 kHz. The time duration of three teeth on the trigger wheel (18 DegCA) were measured at the middle of the intake stroke, the end of the compression stroke, beginning of expansion stroke, and middle of exhaust stroke.

It was found that at 1400 rpm, 40 bar PCP, the crankshaft slows down by an average of 55 μs (on 18 DegCA) at the end of the compression stroke, compared to the intake and exhaust stroke. This delay has to be seen in comparison to the time interval that is dictated by the crankshaft encoder when the engine is run at 1400 rpm, which is equal to 11.9 μs for 0.1 DegCA, and 119 μs for 1 DegCA. The delay of 55 μs is about 0.06% of the periodic time of the measured surface temperature cycle. If the engine rotates at exactly 1400 rpm, three teeth on the trigger wheel (18 DegCA) should take 2.14 ms, which is around 40x larger than the measured delay at this setpoint.

At the setpoint of 1400 rpm, 100 bar PCP, the crankshaft slows down further due to an increased compression load. In fact, at this condition, it was found that the crankshaft slows down an average of 195 μs (on 18 DegCA) at the end of the compression stroke, when compared to the intake and exhaust strokes. This is 0.14% of the surface temperature periodic time. Increasing the engine speed from 1400 rpm to 2000 rpm with a PCP of 100 bar, the deceleration on the compression stroke was found to decrease. At this higher engine speed, the crankshaft slows down by an average of 68 μs (on 18 DegCA) between the end of compression stroke and the exhaust/intake strokes. Working out this delay as a ratio of the surface temperature periodic time reveals a similar 0.11% to that found at 1400 rpm; 100 bar.

Although it is evident that the time interval between the measured temperature ordinates is not constant, the difference is found to be very small.. As a result, it could be reasonably assumed that the assumption of constant time interval is reasonable, even at the slowest engine speeds and most loaded conditions.

5.2 Two-Dimensional Finite Element Analysis of Eroding Thermocouple

The main reason why the impulse response method was sought in this study is because of its ability to use the characterisation of the actual construction of the eroding thermocouple, including any multi-dimensional heat flux that might occur within the sensor. For this to be possible, either a two-dimensional finite element model of the thermocouple, or alternatively results obtained from characterisation tests on the same thermocouple are required. The FEA method which provides the basis functions to the impulse response method was first communicated by Buttsworth [48] and later refined by Wang et al. [41]. Both of these authors utilised eroding surface thermocouples with the split-tapered inserts (substrate material) made out of Dural. In this Doctoral work, a transient, two-dimensional finite element analysis using Ansys 2019 R3 was carried out. The temperature at the surface of every material making up the 2D thermocouple model was evaluated for a step in heat flux of 1 MW/m^2 applied at the surface. The imposed step heat flux, and FEA-obtained temperature over the material of interest were then used as the basis functions in the impulse response method to obtain an impulse response function

which is thought to better characterise the heat flux process through the eroding thermocouple than the more common one-dimensional, semi-infinite solid analytical assumption. The obtained impulse response function could then be used with the sampled surface temperature obtained from engine testing to determine the transient component of surface heat flux.

When a one-dimensional, semi-infinite solution of heat flux is assumed through the sensor, the researcher has to choose a material, out of at least four different materials that make up the sensor, through which assumingly all of the heat flows irrespective of the time scales involved in the particular application. This has been the subject of several debates [49], and was explained thoroughly in Chapter 2.

The issue of choosing a representative material that affects the heat flow present in one-dimensional heat transfer assumption is partially resolved when the impulse response function used with the impulse response method is obtained through basis solutions that result from a two-dimensional FEA. It is fully resolved if the impulse response function is obtained from thermocouple characterisation experiments.

The 2D FEA simulation takes care of the heat flow through the composite body of the sensor made up of the different materials. As a result of the different materials, for a step heat flux of 1 MW/m^2 applied at the surface, the FEA simulation gives the temperature variation with time at the surface of each of the materials making up the thermocouple 2D model. Each material will have a different temporal variation of temperature, dependent on its thermo-physical properties. Consequently, with this method, even though the researcher is not required to choose which material affects the heat transfer, as in one-dimensional studies; knowledge of which material surface the physical thermocouple is measuring is still required. For a better understanding of the foregoing discussion, refer to Figure 5.2.

Figure 5.2 shows hypothetical temperatures at the surface of fictitious Material A (ρ: 2800 kg/m^3, c: 896 J/kgK, k: 190 W/mK) and ficticious Material B (2800 kg/m^3, c: 448 J/kgK, k: 50 W/mK), in response to two distinct step heat fluxes; one of 1 MW/m^2 and the other 2.5 MW/m^2. Assume that a hypothetical temperature measurement is made by a thermocouple made up of the two dissimilar materials; material A and material B. The applied heat flux to the thermocouple surface is unknown and needs to be determined. It is noted from the figure that the measured

surface temperature lies between the temperature response of material A at 2.5 MW/m², and that of material B at 1 MW/m². If it is known with certainty that the measured temperature is made on the surface of material A (*i.e.* thermocouple junction lies on material A), then the unknown heat flux applied to the sensor surface is 2.5 MW/m². On the other hand, if it is known with certainty that the measured surface temperature is representing material B (*i.e.* the thermocouple junction lies on material B), then the true heat flux applied to the sensor is 1.0 MW/m². This shows the importance of the knowledge of the location of the thermocouple junction for accurate two-dimensional heat flux determination.
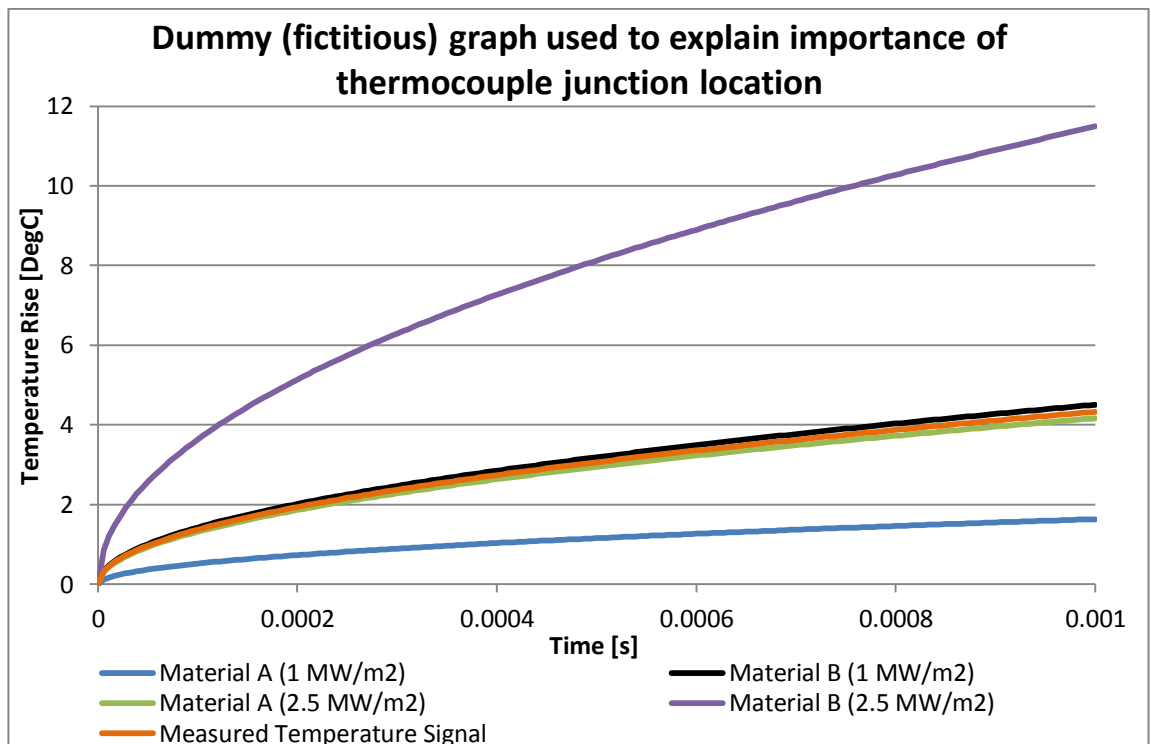
Figure 5.2. Dummy graph to show importance of knowledge of thermocouple junction location.

Naturally the determination of the location of temperature measurement coincides with the determination of where is the location of the thermocouple junction. Generally speaking, the junction is physically expected to reside on the thermocouple elements (Chromel or Constantan) since the abrasive grit deposits the sliver from one thermocouple ribbon to the other, however the thermocouple response might actually be affected by the proximity of the junctions to the central Mica, over which the slivers are bridged. To wrap up this discussion, it can be concluded that the two-dimensional heat flux determination method using FEA removes the need for the

assumption of which material mostly affects the heat flow (as is required with one-dimensional consideration). On the other hand however, knowledge of the thermocouple junction location is necessary. Physical understanding of the sensor construction yields the reasoning that the junction is most probably located at the thermocouple ribbons, or at most, the central Mica. Wang et al. [41] showed through laser impulse testing that the two-dimensional heat flux should be computed assuming that the junction lies on top of the central Mica. In this chapter, results obtained from the engine shows how the thermocouples used in this work seem to be better characterised with the assumption that the junctions lie on the constantan or chromel surfaces.

From the foregoing discussion, a better approach for obtaining the impulse response function other than using a 2D FEA is to perform experimental tests involving exposure of the thermocouple surface to a known step-heat flux. The known step heat flux and the recorded temperature will be the basis functions for the impulse response method. These basis functions will not only include the multi-dimensional characterisation of the thermocouple, but also the effect of location of the actual junctions. Furthermore it would also account for the thermal contact resistances between the different thermocouple materials, something that cannot be judged properly for implementation in the FEA.

In this project, three different eroding thermocouples were procured. All three thermocouples were chosen to be of type-E due to the high voltage gradient associated with this thermocouple type. The three different thermocouples were procured with different split-tapered insert materials made out of Zirconia, Aluminium and Stainless Steel.

The eroding thermocouples were used at engine speeds of 1400 rpm, 2000 rpm, 2500 rpm and 3000 rpm, hence the temperature data obtained through this testing campaign was sampled with four distinct sampling rates. The impulse response function used to determine the heat flux from a given sampled temperature needs to have the same amount of data points and the same sampling frequency. As a result, when the basis functions are evaluated from FEA two approaches can be taken. The first is that the finite element model is run four times, each time with a different time step such that each simulation run corresponds to a given sampling rate at a certain

engine speed. The second way is to run the simulation once with a time step pertaining to the highest engine speed (smallest time interval), and then curve fit the result to obtain the temperature basis functions at the other slower test sampling rates. The first method provides a better approach to reduce numerical errors associated with curve fitting; however a lengthier process is expected. The resulting time steps for the four engine speeds considered, with a resolution of 1 DegCA (using only a tenth of the sampling resolution with *decimate* function) are 119.05 μs, 83.33 μs, 66.67 μs and 55.56 μs for engine speeds of 1400 rpm, 2000 rpm, 2500 rpm and 3000 rpm respectively.

It was noted that for the very first few time increments of the finite-element analysis, a finer time step was required to reduce the numerical errors resulting from a very steep initial increase in the temperature at the surface. Hence, initially, a time step equivalent to 0.1 DegCA was imposed on the FEA.

According to the requirements of the Impulse Response method dictated previously, the basis functions (and hence impulse response function) should be of the same length of the measured surface temperature data. In this work, 300 consecutive engine cycles of surface temperature were analysed at each particular setpoint. This implied that the FEA model had to be run with heating times of 25.7 seconds corresponding to 1400 rpm, down to 12 seconds for the engine speed of 3000 rpm. Such long heating times at constant heat flux results in the penetration of the heat flux deep in the axial direction of the thermocouple. Since the model has a finite width and depth with insulated boundary conditions, when the axial heating penetration was sufficient, the insulated back face temperature increased from the initial value of 22°C. This consequently resulted in a rapid increase in the heated face temperature due to the incapability of the sink to keep diffusing the heat with the same effectiveness. This observation was also made by Buttsworth [48] and results in a falsely augmented temporal temperature variation at the heated surface. To prevent this, in this Doctoral work, the axial length of the sensor was modelled to be the smallest possible length such that the insulated back face remained at 22°C after the whole heating period. According to a heat penetration calculation, for the longest heating time corresponding to that of 300 cycles at 1400 rpm, the axial lengths required for the Zirconia, Stainless Steel and Aluminum thermocouples were assigned to be 25 mm, 70 mm and 175 mm respectively. The different lengths of the

2D model required by the different sensors reflect the different thermal diffusivities of the three materials, with the Aluminum having the highest diffusivity and the Zirconia having the lowest diffusivity. The length of the FEA model as conducted by Buttsworth [48] was only 1 mm for a heating time of 10 ms. Buttsworth [48] reports that the insulated boundary condition at the opposite end of the heating surface started affecting the model after 6.4 ms. The model used by Buttsworth [48] also made use of symmetry and assumed that the two thermocouple materials had the same thermo-physical properties. The length of the FEA model as considered by Wang et al. [41] was 4.76 mm. The heating time is not explicitly stated in the publication by Wang et al. [41], however it is thought that a heating time of 100 ms was used, which according to his analysis seemed to have been the maximum heating time until the insulated boundary condition at the end opposite the heated surface started affecting the analysis. The short time length assigned by both Buttsworth [48] and Wang et al. [41] were possible due to the fact that they applied the Impulse Response Method on an ensemble surface temperature, instead of the full number of temperature cycles acquired from the thermocouple. This is generally not recommended due to the starting transient induced by the method, as explained earlier. Wang et al. [41] however avoided this starting transient error by padding the ensemble surface temperature and effectively increasing the data length. This was done such that any starting transient would affect only the padded length and not the actual 720 DegCA cycle. Due to the padding scheme added to the surface temperature, the impulse response obtained through the FEA by Wang et al. [41] was extrapolated with a power law beyond the 100 ms, and which matched the slope at this time.

The issue of an unrealistic temperature at the heated surface of the 2D model also occurs if heat flow parallel to the surface reaches the insulated sides of the model any time before the end of the heating duration. As a result, the thickness of the 2D split-tapered insert also has to have sufficient length to allow undisturbed heat diffusion in the second dimension (parallel to the heated surface). To prevent from having excessive computational times and large data files, while retaining a good mesh resolution; the thickness of the split-tapered material was limited to 0.25 mm for all the three sensors. This was expected to result in some deviation in the temperature response at the surface of the Central Mica and the other materials. To verify that this

deviation was not excessive, the one-dimensional responses (for the longest heating time of 25.7 s – 300 cycles @ 1400 rpm) of the split-tapered inserts were plotted against the 2D temperature response of the split-tapered insert at the node closest to the insulated side edge. Any deviation of the 2D response at this point from the 1D response means that the heat conduction parallel to the surface is suppressed by the side edge insulated boundary condition. It was noted that the deviation showed by the Aluminium thermocouple was equal to 4%, whereas that for the Stainless Steel thermocouple was equal to 1%. For the Zirconia thermocouple, a significant deviation of 25% was noted. While the deviations for the Aluminium and Stainless Steel thermocouples present an acceptable compromise, the deviation for the Zirconia thermocouple seemed high. To investigate further, the Zirconia thermocouple model was run with the Zirconia split-tapered inserts with a large thickness of 1 mm at the slowest engine speed (hence longest heating time). The temperature response of the central Mica from this model was compared to that of the 0.25 mm split-tapered insert thickness. It was noted that the temperature response at the node closest to the insulated Zirconia side boundary on the thicker model showed only a deviation of 7.5% compared to that of the 1D Zirconia temperature response. This however increased the computing time and data file size significantly compared to the 0.25 mm model.

The dimensions of the sensors as designed in the finite element model were taken to be similar to those reported in literature by [6] [55] for the same sensor construction, *i.e.* the three mica sheets being 5 μm thick and the two thermocouple ribbons having a thickness of 25 μm. The split-tapered inserts were modelled with a thickness of 250 μm. This dimension is not equal to the actual diameter of the split-tapered inserts, but this thickness as drawn in the model had to be reduced in order to decrease the overall computational time.

The long axial lengths assigned to the FEA models naturally resulted in a large number of elements, and hence a relatively long computational time. To reduce the computer processing as much as possible, the axial length of the materials were discretised with a smoothly increasing element length starting with 1 μm at the heated surface and increasing with length according to a bias factor, which was different for each FEA model. The lateral discretisation of each material varied depending on the material width. The discretisation was set to be fine at the material

boundaries and course at the centre of each material. It was made sure that the mesh was as regular as possible, also ensuring that the aspect ratio is reasonable. The thermal resistance at the materials interface was set to be negligible. This might be debatable, however it is noted that in the actual construction of the thermocouple, the split-tapered pins are forced into the tube and hence pressed considerably.

Table 5.1 gives the thermo-physical properties of the materials making up each of the three different eroding thermocouples used in this work. The last two columns give the diffusivity and effusivity of each material.

From a search on the web, it was noted that the thermal properties of Mica vary significantly. As pointed out by Farrugia [65] there exists at least two types of Mica; Muscovite and Phlogopite. The thermal conductivity is anisotropic and dependent on the cleavage planes in the material. It is reported that the thermal conductivity along the cleavage planes is ten times that perpendicular to the cleavage planes [121]. In all simulations carried out in this dissertation, the material properties of Mica were assigned to be those reported by Buttsworth [48] and Wang et al. [41], in which they assumed an isotropic behaviour of thermal conductivity synonymous to that parallel to the cleavage planes. A large uncertainty also surrounds the specific heat capacity of Mica. Buttsworth [48] and Wang et al. [41] report a specific heat capacity of 56.5 J/kgK. Touloukian et al. [122] reports a thermal diffusivity of 1.9×10^{-6} m^2/s along the cleavage planes of Phlogopite which yields a specific heat of around 280 J/kgK, and Farrugia [65] reports a value of 837 J/kgK, which seems to be the most commonly quoted value.

It is interesting to note that although Mica has the lowest thermal conductivity of all materials in Table 5.1 (both parallel and perpendicular to cleavage planes), its diffusivity is well comparable to that of the thermocouple ribbon materials (Chromel and Constantan) and Stainless Steel. This is mainly due to its lower density and specific heat capacity. The thermal effusivity of Mica is however by far the lowest of all the materials considered. On the other hand, Zirconia, whilst being similar in its conductivity to that of Mica, however its thermal diffusivity is significantly smaller than that of Mica, and two orders of magnitude smaller than that of Aluminium. This originates from the very high density and high thermal capacity of Zirconia. The

thermal effusivity of Zirconia seems to fall between that of Mica and the thermocouple ribbons.

This observation is made on Mica and Zirconia due to the fact that whilst they have similar heat conductivities, it seems that the two materials do not behave similarly in the way they absorb the thermal energy. All this has to be viewed in the light of the thermal property variation of Mica.

Table 5.1. Thermo-physical properties of the materials making up the eroding thermocouples used in this work.

	k [W/mK]	Density [kg/m^3]	Specific Heat Capacity [J/kgK]	Diffusivity [m^2/s]	Effusivity [J/m^{2}Ks$^{0.5}$]
*Zirconia	1.8	6090	427.0	7.076E-07	2187
**Mica	1.6	2800	56.5	9.999E-06	500
!!Chromel	19.2	8730	448.0	4.909E-06	8666
!!Constantan	21.2	8920	393.6	6.039E-06	8627
†Aluminium	190.0	2800	896.0	7.573E-05	21833
††Stainless Steel	15.1	7750	480.0	4.059E-06	7495

* Ansys 2019 R3, but also supplied by Nanmac (Eroding thermocouples manufacturer)
** Buttsworth [48] and Wang et al. [41]
!! Caldwell [123]
† Callister and Rethwisch [124]
†† Ansys 2019 R3

5.2.1 Microscope and X-ray Images of Eroding Thermocouples

To obtain a better understanding of the construction of the eroding thermocouples, microscope images of the thermocouple surface and X-ray images of the thermocouple body were taken. Figure 5.3 to Figure 5.5 give the microscope images, whereas Figure 5.6 to Figure 5.8 give the X-rays images. For a better correlation of the X-ray and microscope images, two photos of the eroding thermocouple are presented in Figure 5.9 and Figure 5.10.

The microscope images show clearly the split-tapered inserts surface, as well as the two thermocouple ribbons (Chromel and Constantan). The three Mica sheets are not visible, but they are expected to be located between the two split-tapered inserts and each of the thermocouple ribbons, and another between the two thermocouple

ribbons. The outer tube, surrounding the split-tapered inserts is visible in all three images, particularly in that of the Zirconia thermocouple. It is noted that for this particular thermocouple, an unexplainable void is evident between the Zirconia split-tapered insert and the outer tube. It should be mentioned that this was the case for all the other procured Zirconia thermocouples. For the case of the Stainless Steel and Aluminium thermocouples, the interface between the split-tapered inserts and the outer tube is quite hard to see, and is shown by a very fine line.

The microscope images for both Stainless Steel and Aluminium show the abraded surfaces as dispatched by Nanmac with the junction established. It is noted that the abrasion lines make an angle of around 45 degrees with the thermocouple ribbons, as suggested in the maintenance manual [64]. The Zirconia thermocouple, on the other hand shows an open junction with abrasive lines almost parallel to the thermocouple ribbons. The open junction can supposedly be identified by the fine black line separating the two thermocouple ribbons.

Lateral to the thermocouple ribbons sandwich, on both sides, some void is noticeable in all three microscope images. If this space is truly unoccupied by any material, it could be said that three dimensional heat flow in the sensor is, to some extent, obstructed by the insulation of the void.

The X-ray image in Figure 5.6 shows an oblique view of the Zirconia thermocouple tip. From this figure, the outer tube material can be seen surrounding the less visible split-tapered inserts, which in turn sandwich the two thermocouple ribbons. A very fine line with a different contrast to the thermocouple ribbons is visible in between them. This is thought to correspond to the central Mica material separating the two thermocouple ribbons. Figure 5.7 for the Stainless Steel thermocouple shows the axial length to which the split-tapered inserts penetrate. The figure also shows a significant gap between the back surface of the split-tapered inserts and the thermocouple stem which is overlapping the surface thermocouple body. The two thermocouple wires seem to exit from the thermocouple stem and enter between the two split-tapered inserts. In the gap between the back surface of the split-tapered inserts and the thermocouple stem, the two thermocouple wires transition into a ribbon format. This is better shown in Figure 5.8.

Table 5.2 gives an indication of the lengths of the split-tapered inserts, and the void between the back surface of the split-tapered inserts and the thermocouple stem. These lengths were measured from the X-ray photographs. Although little can be done with these presented lengths, having an idea of the length of the split-tapered inserts helps in visualising the heat flow phenomena probably occurring in the sensor body. Since the split-tapered inserts have only a finite length, it is expected that the heat flow through the body is first conducted axially from the surface through the split-tapered inserts, thermocouple ribbons, Mica and Stainless Steel tube. As the heat approaches the back surface of the split-tapered inserts, conduction has to continue only through the Stainless-Steel tube and thermocouple ribbons.
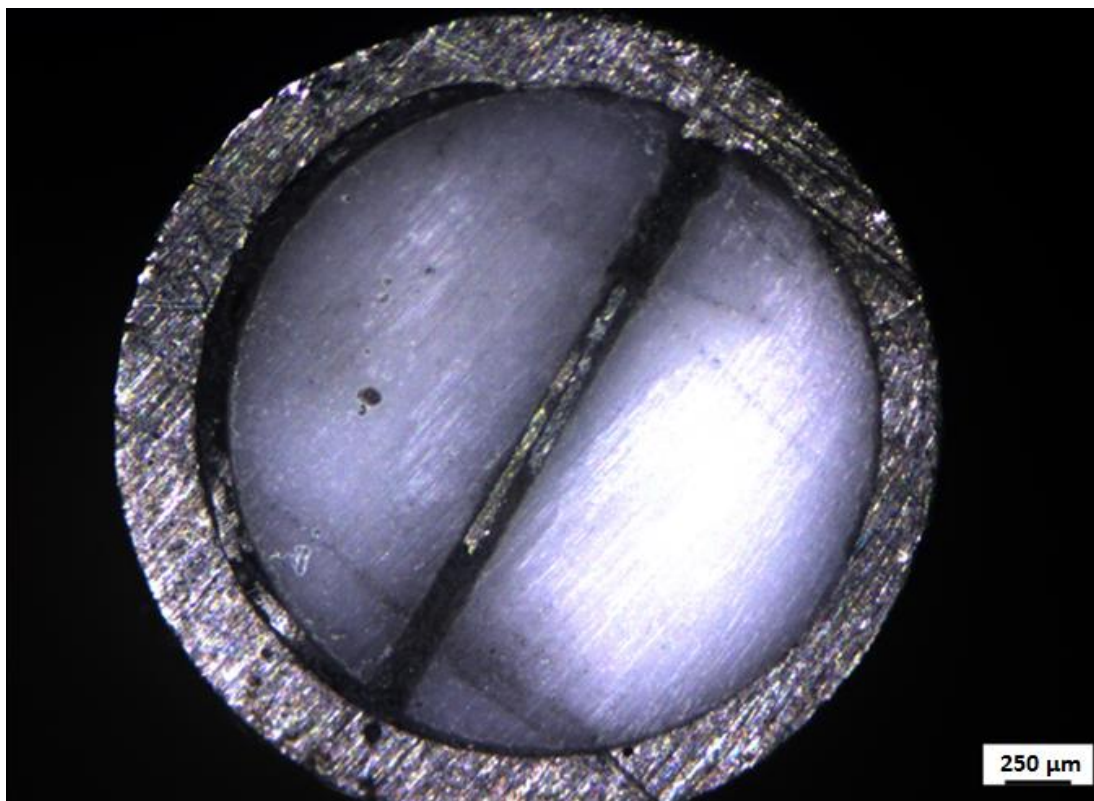
Figure 5.3. Microscope image of Zirconia eroding thermocouple (open junction).
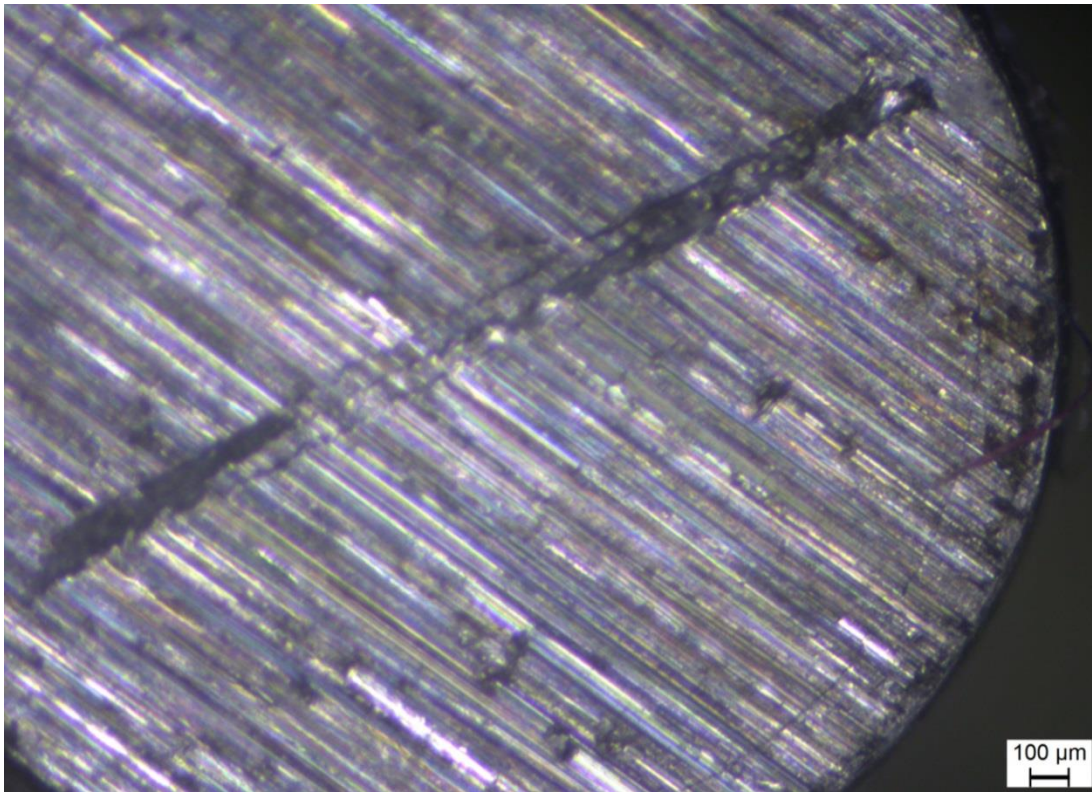
Figure 5.4. Microscope image of the Stainless Steel eroding thermocouple.
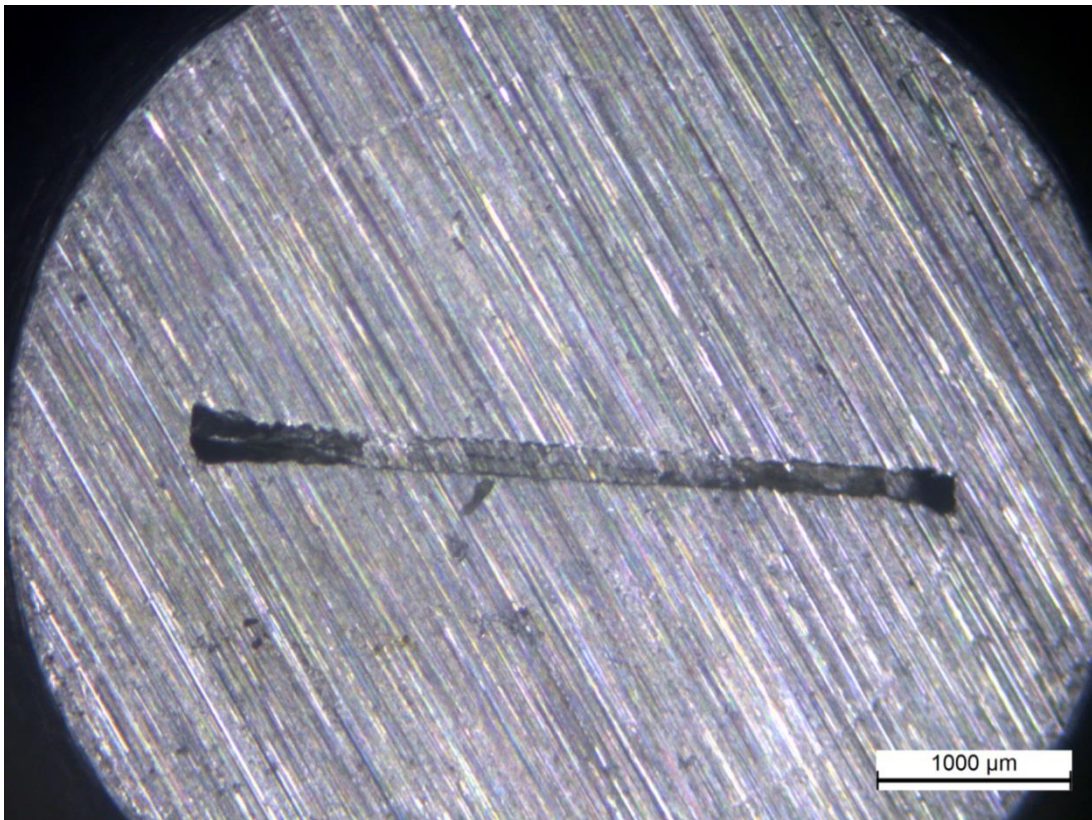
Figure 5.5. Microscope image of the Aluminium eroding thermocouple.

173
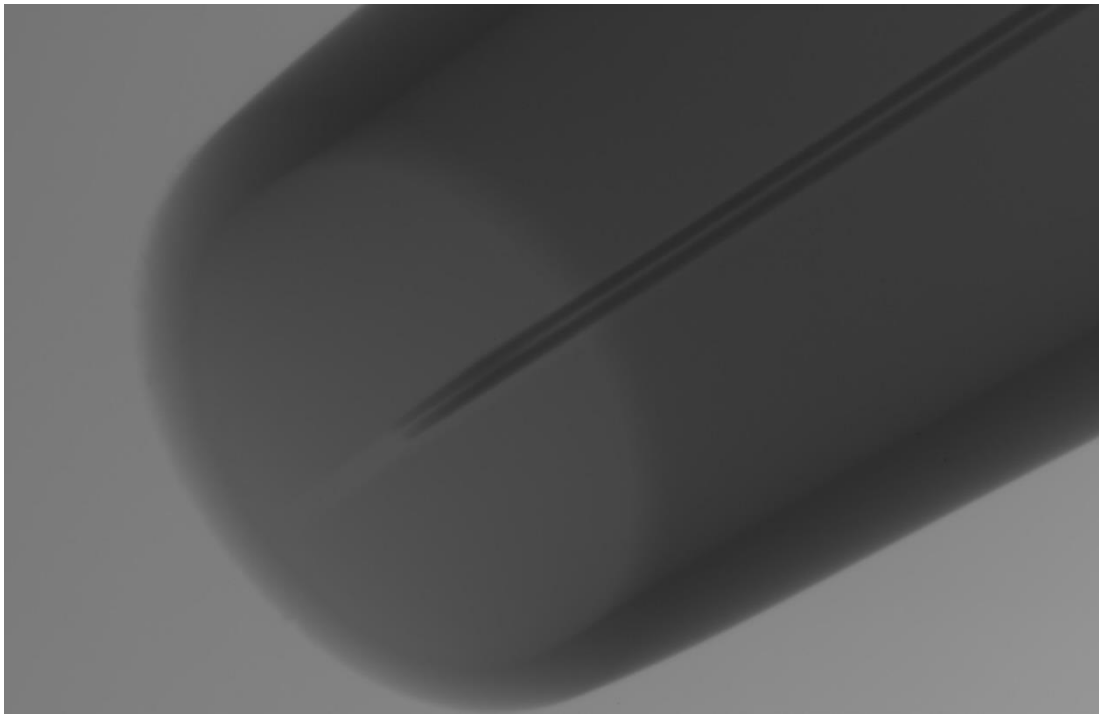
Figure 5.6. X-ray image of the Zirconia eroding thermocouple showing the two distinct thermocouple ribbons separated by the central Mica ribbon. The image was taken at 140 kV and 1.6 W.
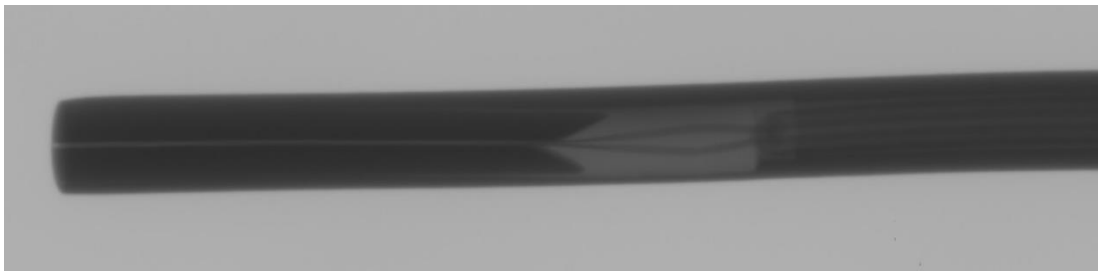
Figure 5.7. X-ray image of the Stainless Steel eroding thermocouple showing the split-tapered inserts and the gap existing from its back surface to the thermocouple stem. The image was taken at 140 kV and 1.6 W.
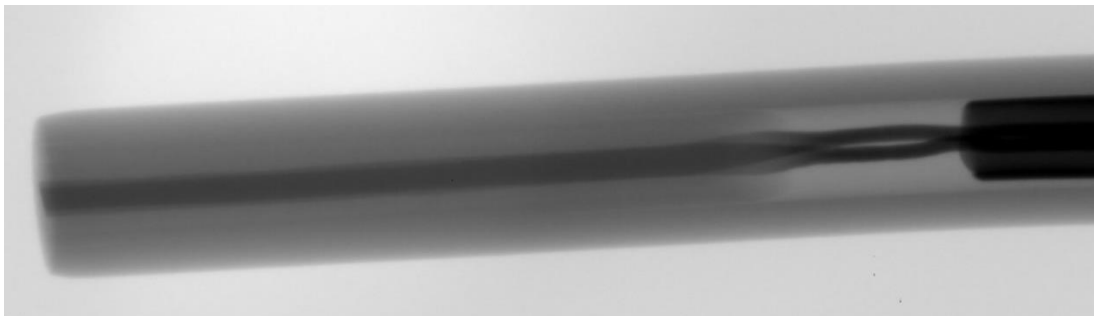
Figure 5.8. X-ray image of the Aluminium eroding thermocouple showing the length of the split-tapered inserts, the gap separating them from the thermocouple stem, and the transition of the thermocouple elements from a wire format to ribbon format. The image was taken at 125 kV and 1.3 W.

Figure 5.9. The Zirconia eroding thermocouple.

Figure 5.10. The surface of the Aluminium eroding thermocouple.

Table 5.2. The length of the split-tapered inserts and the gap between their back surface to the thermocouple stem, measured from the X-ray images.

	Length of Split-Tapered Insert [mm]	Length of Gap [mm]
Zirconia-based Thermocouple	16.8	6.5
Stainless Steel-based Thermocouple	16.8	6.4
Aluminium-based Thermocouple	24.8	10.0

5.2.2 Two-Dimensional Temperature Response using FEA model

Figure 5.12, Figure 5.13 and Figure 5.14 show the temperature responses at the heated surface of the Aluminium, Stainless Steel and Zirconia thermocouples respectively for a heating time of 1 ms, as obtained from the Finite Element Model for a step heat flux of 1 MW/m^2. Each of the graphs shows the two-dimensional temperature response at the surface of the central Mica sheet, each of the thermocouple ribbons (Chromel and Constantan), and the split-tapered substrate material. Two probing points were assigned on the split-tapered insert; one very close to the Mica separating the split-tapered insert from the thermocouple ribbon,

and one at the centre of the split-tapered insert surface. These surface probing points are shown in Figure 5.11 (points A to G). The one-dimensional surface temperature response, assuming the thermo-physical properties of Chromel, Mica and the split-tapered insert material are also drawn on each of Figure 5.12 to Figure 5.14 for comparison purposes.
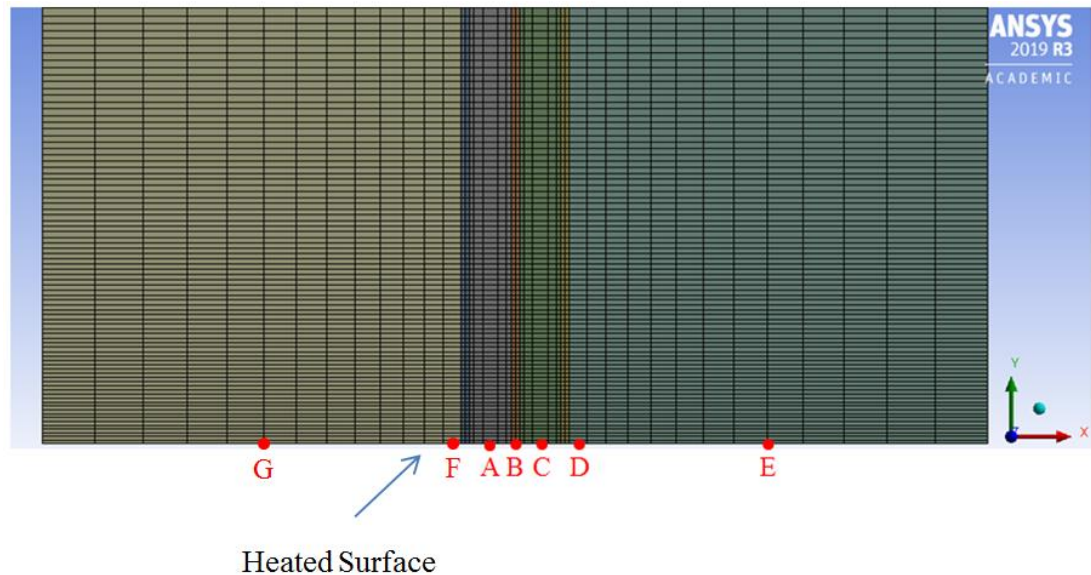
Figure 5.11. The finite element model. A: Constantan, B: Central Mica, C: Chromel, D E F G: Split-tapered insert.

Aluminium-based Surface Thermocouple

The temperature response for the Aluminium-based thermocouple in Figure 5.12 shows that the temperature response of the 2D central Mica rises much more rapidly compared to the 2D temperature response of all other materials in the sensor. This is due to the much lower thermal conductivity of the Mica compared to the other materials. It is shown that the 2D Mica response is significantly different than the 1D Mica response from a very early time. This is attributed to the two dimensional heat flow occurring from the Mica to the two thermocouple ribbons (Chromel and Constantan). The temperature response of the 2D Chromel and 2D Constantan also separate from that of the 1D Chromel at around 0.05 ms. This is due to lateral heat flow from the two ribbons to the aluminium split tapered inserts, which act as a heat sink to the two thermocouple ribbons. As a result of this heat flow from the thermocouple ribbons to the aluminium, the temperature of the aluminium close to the Mica material (Edge AL) separating each thermocouple ribbon from the split-

176

tapered insert increases slightly above that of the 1D Aluminium response. On the other hand however, at a significant lateral distance from the Mica edge, into the aluminium, the temperature of the aluminium (Central AL) is identical to that of the 1D aluminium response.

It is interesting to note that both the temperature responses of the 2D Chromel and 2D Constantan are very similar. This reflects in the temperature responses of the 2D aluminium at the Chromel and Constantan sides, showing an almost thermally symmetric scenario, about the central Mica.

Stainless Steel-based Surface Thermocouple

Figure 5.13 gives the temperature response of the Stainless Steel-based (SS) thermocouple. It is noted that the two-dimensional responses of the metallic elements in the thermocouple (SS, Chromel and Constanan) are very similar. The only different temperature response is that originating from the central Mica. This means that the high temperature retained at the central Mica surface distributes heat to the surrounding thermocouple ribbons and consequently into the stainless steel split-tapered inserts. Due to this flow of heat parallel to the surface, the temperature response of the 2D Mica is less than that expected from the 1D response of Mica. This is because of the lateral cooling to the metallic elements. Consequently, the 2D responses of the Constantan and Chromel elements are higher than the 1D response of Chromel. Figure 5.13 also shows that the 2D temperature response of the SS material, close to the side-Mica interface is higher than that of the SS away from the Mica interface. This is understandable due to its proximity to Mica. On the other hand, the temperature response of the SS material away from the interface traces exactly the temperature response of the 1D SS.

Zirconia-based Surface Thermocouple

The temperature response of the Zirconia-based sensor shows the largest deviations between every different material making up the sensor. It is shown that after around 0.02 ms, the 2D Zirconia away from the Mica interface (Central Zirconia) obtains the highest temperature, which is identical to the 1D temperature response of Zirconia. This means that after 0.02 ms, the Zirconia material provides lateral heat conduction

to the Mica, and from the Mica to the thermocouple ribbons. This is evidently shown by the fact that just below the 2D Zirconia temperature response, one finds the temperature response of the Zirconia at the Mica interface (Edge Zirconia), then the Central Mica, and the lowest temperature is attributed to the thermocouple elements. The two-dimensional heat flow is very clearly shown by the fact that the 2D temperature responses of Chromel and Constantan are much higher than what would be expected if one-dimensional conditions prevailed (shown by 1D Chromel).

Interestingly, below 0.005 ms, the central Mica material seems to be at a higher temperature than the Zirconia, but quickly cools off to the surrounding thermocouple elements. The rapid increase in the temperature of Mica above that of the Zirconia material results mainly from the very low specific heat capacity and low density of Mica.

5.2.3 Summary of FEA model results

From the two-dimensional analysis carried out in this work, on three variants of the eroding thermocouple, it was shown that the thermocouple ribbon materials (Chromel and Constantan) at which the junctions are to be expected have a relatively different temperature response than the split-tapered inserts. Central Mica, which is the material over which the sliver junctions bridge also shows a significantly different temperature response than that of the split-tapered insert material. These differences are noticeably large for the case of the Aluminium-based and Zirconia-based thermocouples. A similar observation to this was made by Wang et al. [41] for a Dural-based eroding thermocouple. Wang et al. [41] had also shown experimentally that when the surface of the eroding thermocouple (based on Dural) was exposed to a step heat flux from an Nd-YAG laser, the temperature recorded was very close to that of the central Mica, as obtained from the two-dimensional simulation. This is due to the fact that the sliver physically bridges over the central Mica, but is actually set up on either of the thermocouple ribbons.

The above observation creates some unrest, since in the majority of the classical research carried out in the past using the eroding thermocouples, researchers made use of a one-dimensional heat flow assumption, using the thermal properties of the split-tapered inserts. From this two-dimensional FEA analysis, it is however shown

178

that the 1D approach using split-tapered inserts thermo-physical properties is questionable. Having said this, however, it should also be mentioned that in the classical heat transfer works, [19] [35] to name a few, the base engine was made out of cast iron, and consequently the thermocouples used were also probably based on iron split-tapered inserts. The thermo-physical properties of cast iron lie somewhere between that of Stainless Steel, and Aluminum; however closer to that of Stainless Steel. This means that while two-dimensional errors were surely incurred with the assumption of a one-dimensional heat flux, the extent of the error was probably much less than that incurred in present studies which involve either engines based on Aluminium (highly conductive), or insulated engines based on materials such as Zirconia (highly insulative). This is due to the fact, that the one-dimensional assumption for the Zirconia and Aluminium thermocouples is far worse than that of Stainless Steel (and presumably cast iron).

To show the temperature gradients parallel to the surface set up in the respective materials for each of the three sensors, Figure 5.15 to Figure 5.17 give the surface temperature distributions at different heating times for the three sensors. In all these three figures, x = 0 corresponds to the centre of the central Mica ribbon. The boundary of the Central Mica – Chromel is at $2.5 \mu m$, the boundary of the Chromel – Side Mica is at $27.5 \mu m$, and the boundary of the Side Mica – Split tapered insert is at $32.5 \mu m$. As noted from these three figures, the temperature gradient at the insulated side of the thermocouple (*i.e.* approx. $265 \mu m$ from the central axis) at the maximum heating time of 25.7 seconds is zero for both the Stainless-Steel and Aluminium thermocouples. This shows that the thicknesses modelled in the FEA for these two thermocouples were sufficient. On the other hand, for the Zirconia thermocouple, it is shown that a significant temperature gradient was still evident at $300 \mu m$ away from the central axis for the same timescale of 25.7 seconds. Increasing the thickness of the Zirconia split-tapered inserts to around 1 mm was found to be sufficient to decrease the lateral temperature gradient close to zero at the insulated side (see graph inset).
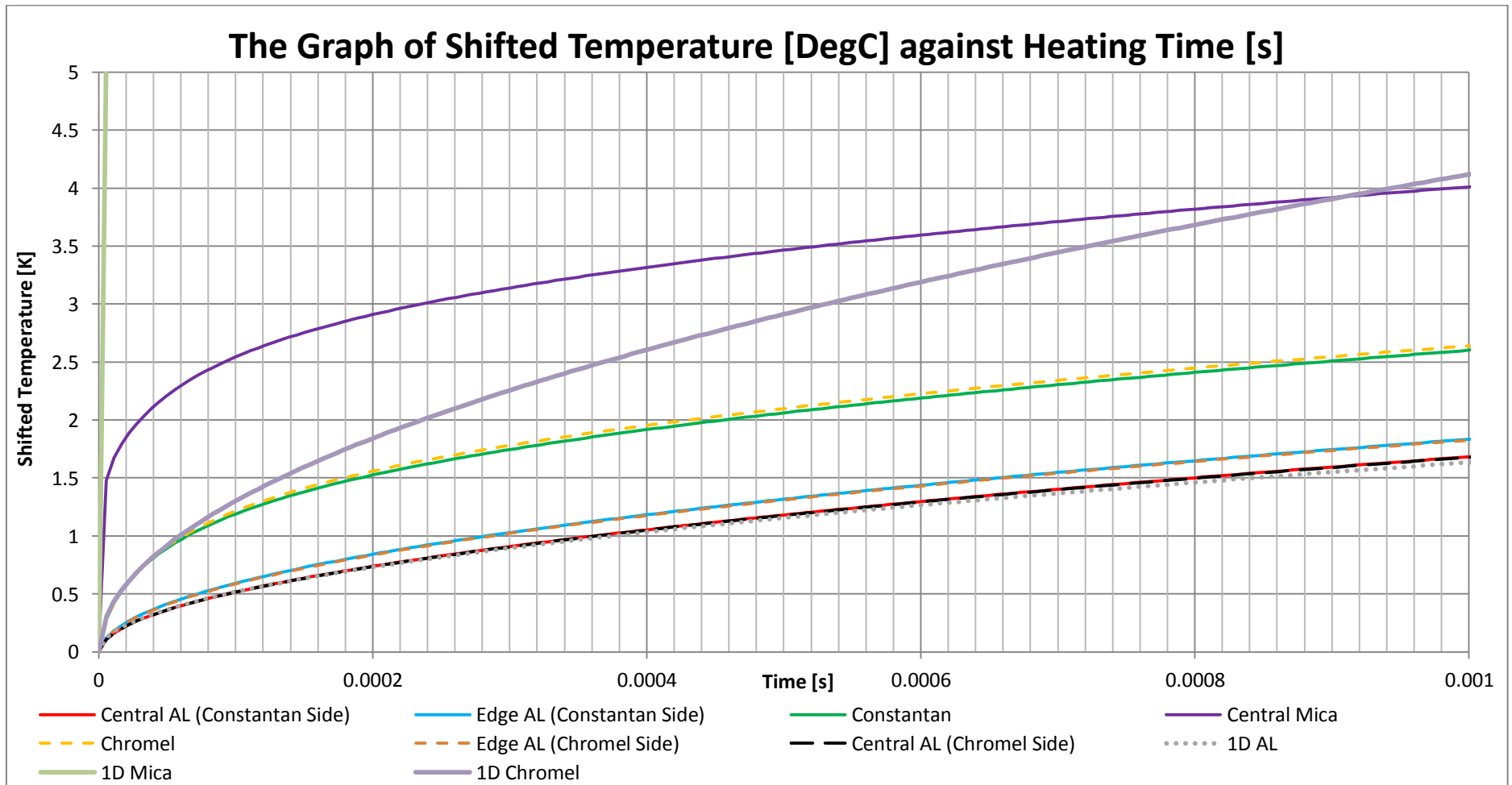
Figure 5.12. The temperature response of the Aluminium eroding thermocouple for a 1 MW/m^2 step heat flux at the surface, obtained from 2D FEA.
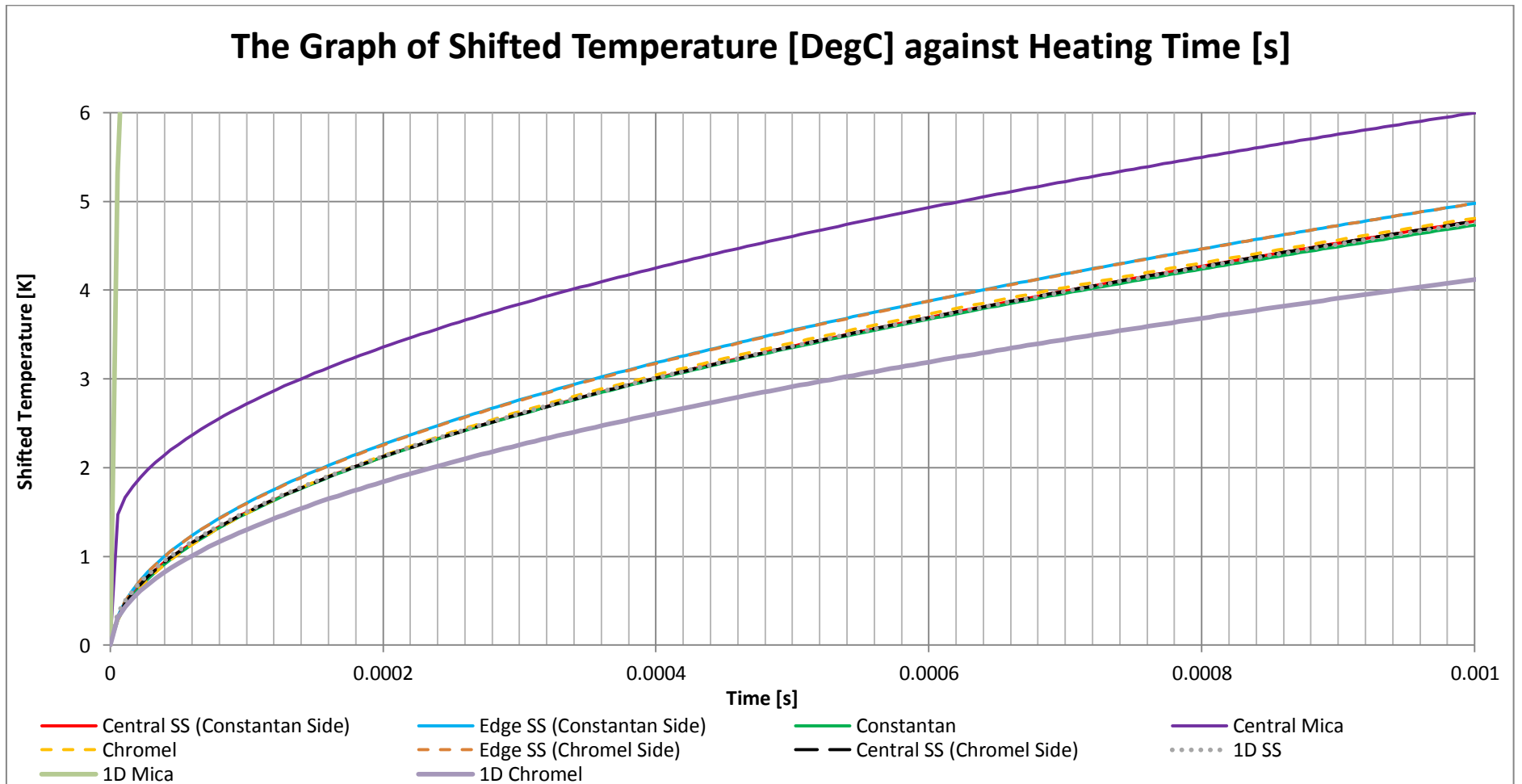
Figure 5.13. The temperature response of the Stainless Steel eroding thermocouple for a 1 MW/m^2 step heat flux at the surface, obtained from 2D FEA.
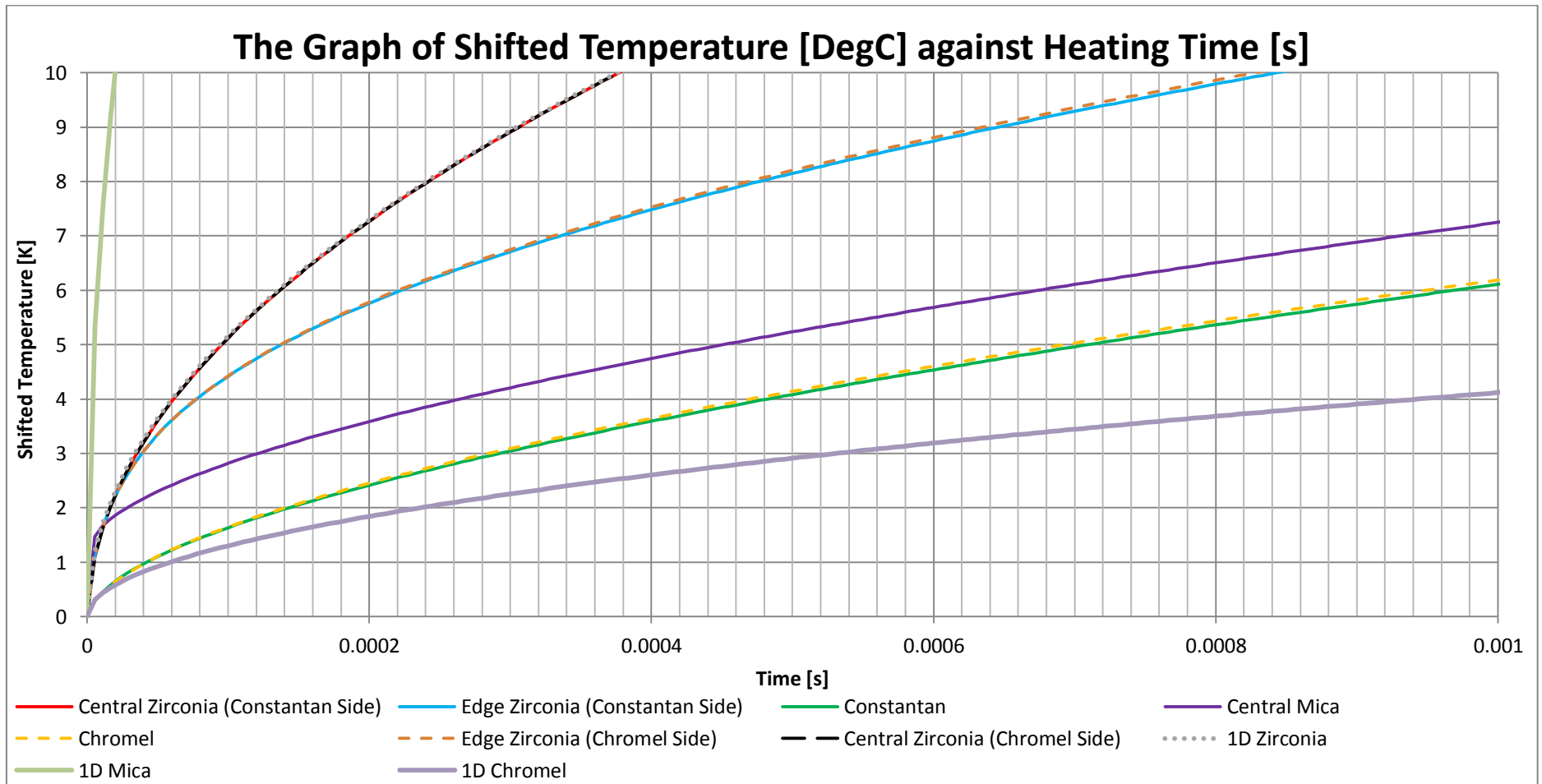
Figure 5.14. The temperature response of the Zirconia eroding thermocouple for a 1 MW/m^2 step heat flux at the surface, obtained from 2D FEA.
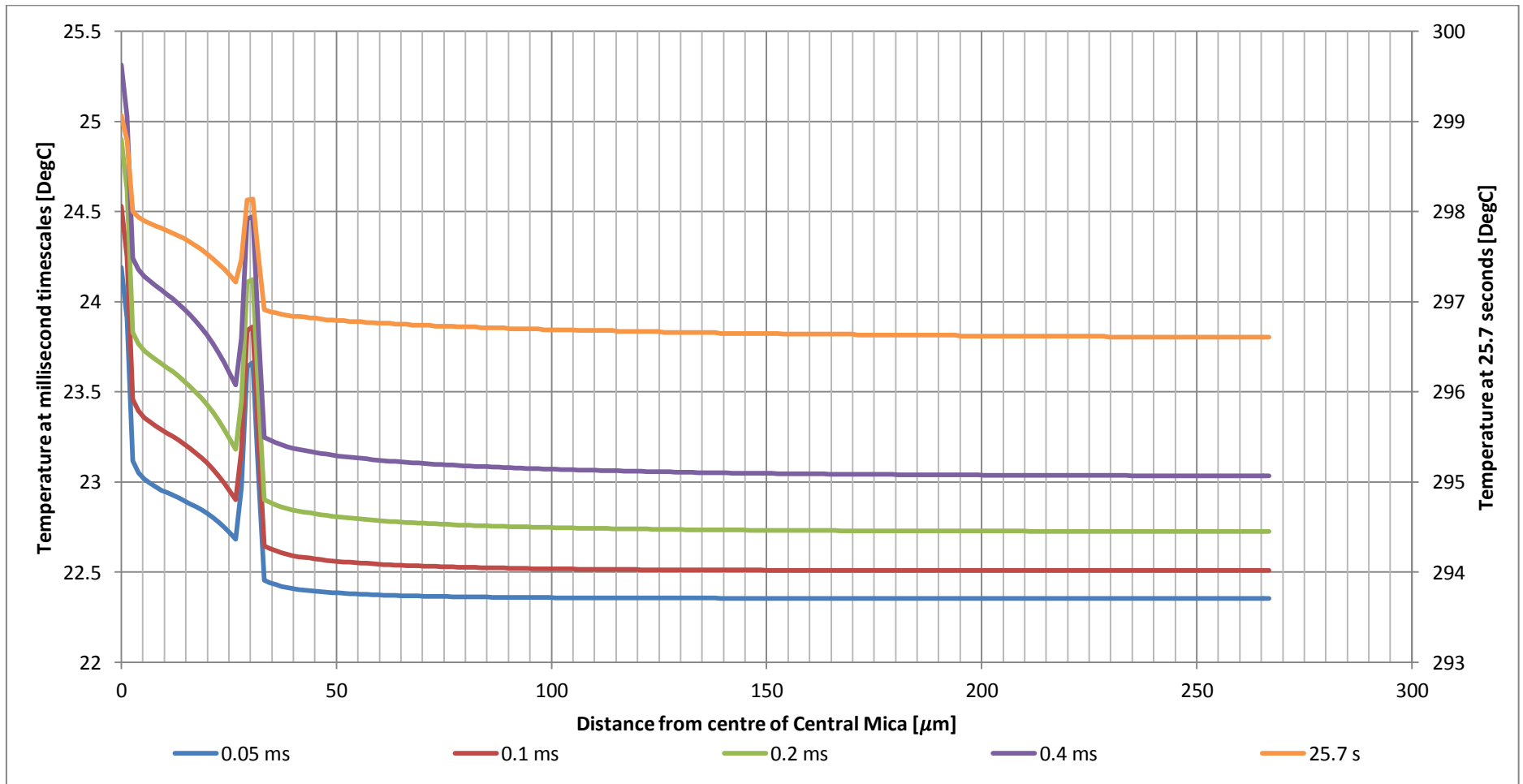
Figure 5.15. The surface temperature distribution of the Aluminium eroding thermocouple for a 1 MW/m^2 step heat flux at the surface, obtained from 2D FEA.
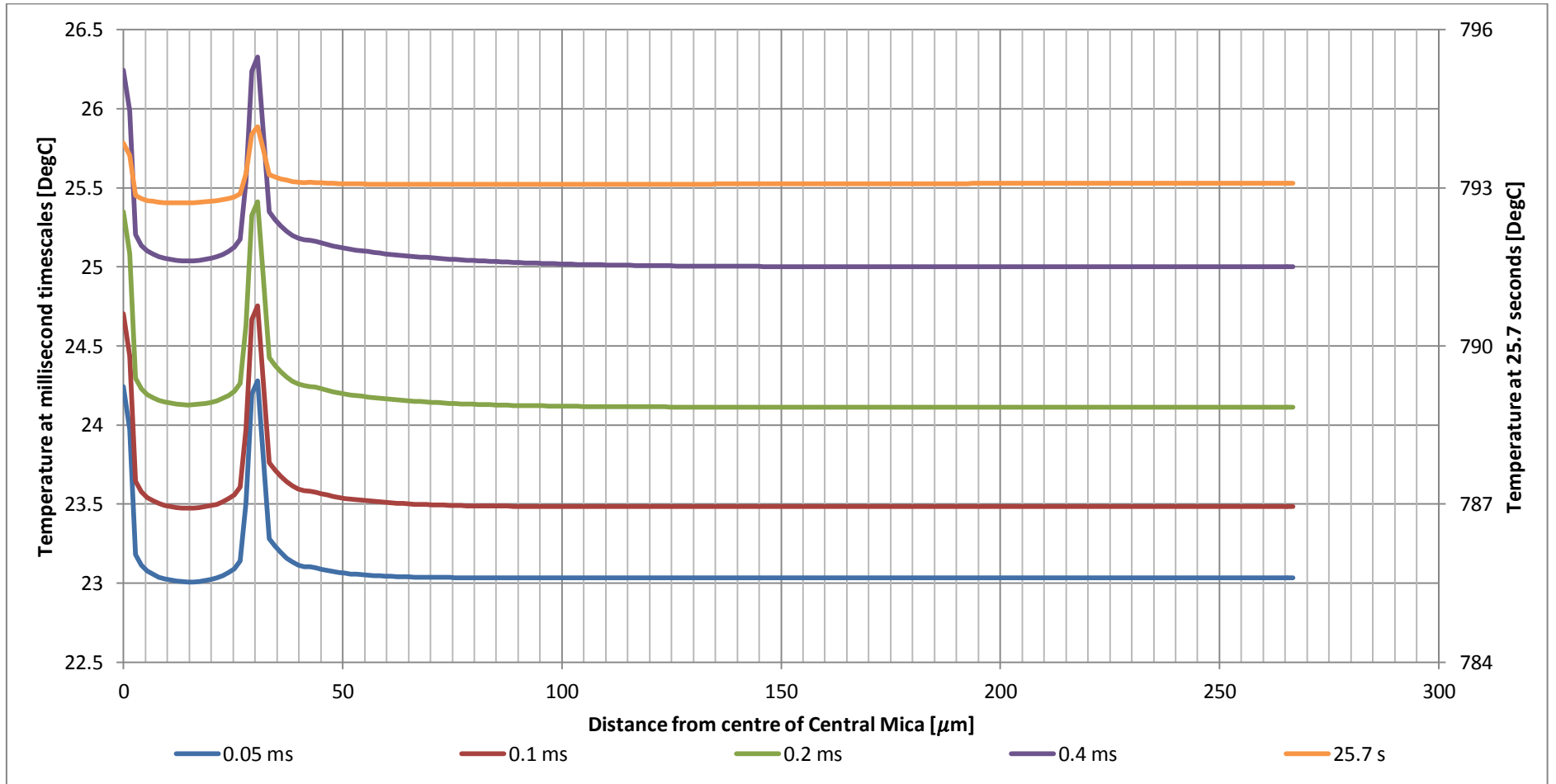
Figure 5.16. The surface temperature distribution of the Stainless Steel eroding thermocouple for a 1 MW/m^2 step heat flux at the surface, obtained from 2D FEA.
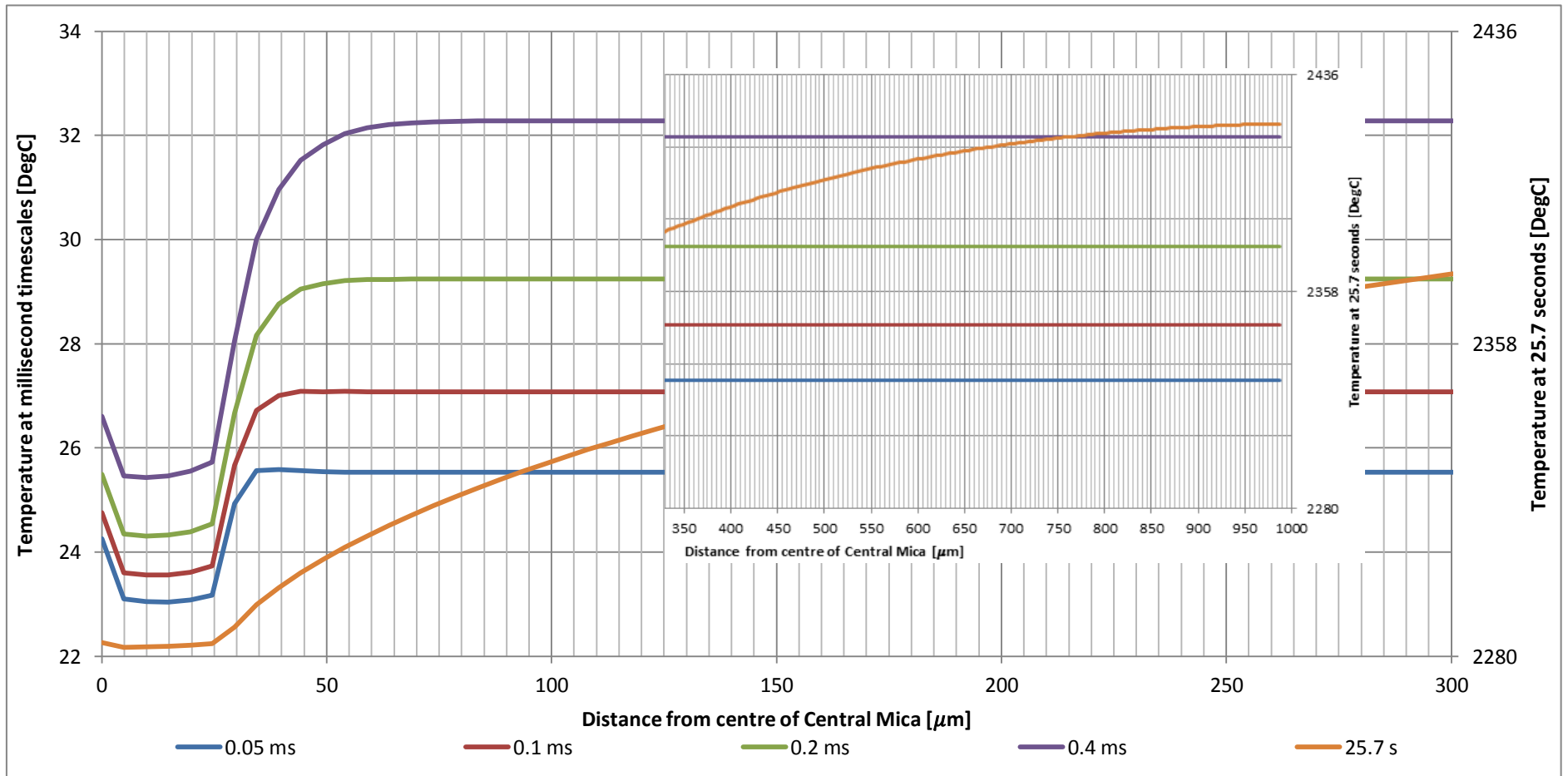
Figure 5.17. The surface temperature distribution of the Zirconia eroding thermocouple for a 1 MW/m^2 step heat flux at the surface, obtained from 2D FEA. Inset shows the temperature distribution towards the insulated side of the Zirconia split-tapered insert.

5.3 Thermocouple Considerations

In this section, results from thermocouple checks are presented which validate the use of the eroding thermocouples for engine heat flux testing reported in a forthcoming section.

5.3.1 Thermocouple Rise Time Testing

Prior to starting the actual heat transfer testing, some effort was spent in trying to set up a method by which the response time of the thermocouple could be quickly checked prior and after a test session. Initially, a light chopper was used, together with a 12 V, 60 W halogen lamp and a converging lens. This setup showed only very small increase in the surface temperature of the thermocouple, and hence was discarded. The method which was found to work involved the use of a photography camera speedlight flash (Meike MK-300). The speedlight was directed towards the exposed surface of the thermocouple and flashed manually (*i.e.* without the use of a camera), with the speedlight being around 7 cm away from the thermocouple surface. A photodiode (OP999) was used to record the rise time of the speedlight in order to be compared to the response time of the thermocouple. The surface thermocouples were flashed before and after each test matrix to ensure that the fast response times were maintained throughout the whole testing matrix. The electrical resistance across the thermocouple elements was also measured and recorded, together with the rise time. It was noticed that the electrical resistance across the thermocouple materials was a very good indication of the rise time of the thermocouple. A slight increase in the resistance of the thermocouple indicated that the rise time became faster, whereas a decrease in the resistance of the thermocouple indicated that the rise time became slower.

Figure 5.18 shows the temperature rise of the five different surface thermocouples procured in this doctoral study, together with the output from the photodiode. The temperature measurements in Figure 5.18 were taken with the junctions being setup by Nanmac, except for the custom Zirconia thermocouple which was abraded with a #150 grit. To allow for an easy comparison between the different traces, the temperatures in Figure 5.18 are normalised. With the setup used in this study, even

186

though three thermocouples could be flashed simultaneously, the light intensity reaching the surface of one thermocouple was not necessarily equal in magnitude to the light intensity reaching the other thermocouples. As a result, the absolute magnitude of the temperature, as well as the ensuing heat flux between the different thermocouples exposed to the same flash cannot be faithfully compared with this setup. On the other hand, however, it provided a very convenient way to compare the rise time of the sensors.

Figure 5.18 shows that even though the five surface thermocouples under test utilise different split-tapered insert materials, their response times are virtually identical and equal to between 0.4 ms - 0.5 ms. This rise time seems to be similar to that recorded by Cornelis et al. [68], obtained from two distinct setups; a heat gun chopper rig and a heat gun shutter rig. Nanmac [64] states that using a #80 grit can result in rise times being in the range of 10 ms, however smaller rise times can be obtained using progressively smaller grits. Other authors [72] who made use of eroding thermocouples in the past have reported rise times as small as 20.8 μs.

According to the photodiode output, the speedlight flash used in this study had a rise time of no more than 50 μs, *i.e.* ten times faster than the recorded thermocouples rise times. One surprising observation from Figure 5.18 is that the thermocouples started cooling off before the photodiode showed a significant drop in light intensity. This observation was consistent throughout all testing done with the Meike speedlight. It is hypothesised that even though the light intensity seems to remain high for about 2 ms, the time duration during which the light energy was sufficient to produce significant heating at the thermocouples surfaces is shorter. This is better understood after zooming in on the negative slope of the seemingly horizontal high portion of the photodiode signal (see figure inset).

Figure 5.18 shows that after the peak temperature was reached, the custom Zirconia thermocouple was the slowest in conducting heat away from the junction. On the other hand, the Aluminium thermocouple was the fastest in cooling. The two Stainless Steel thermocouples show very similar cooling down traces, both of which falling between the custom Zirconia and Aluminium thermocouples. The injector Zirconia thermocouple proved to be slightly slower in its rise time than the rest of the

thermocouples and surprisingly had a cooling characteristic similar to the Stainless Steel thermocouples.
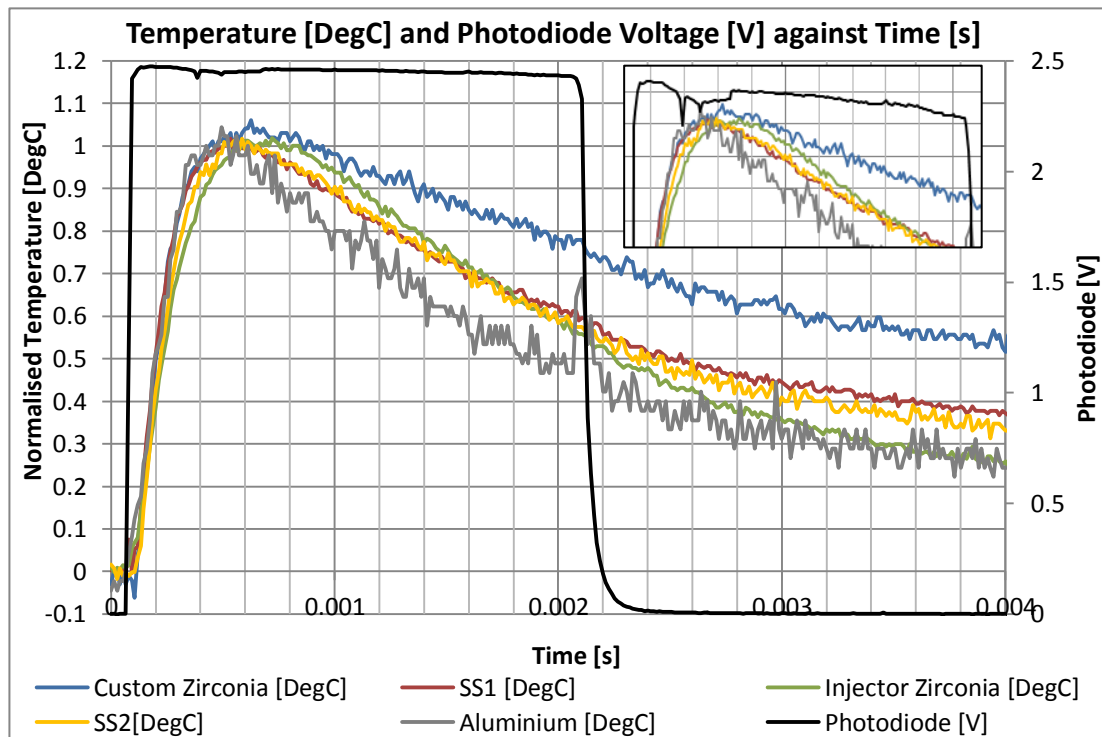
Figure 5.18. The thermocouples rise time in response to the same flash, and the photodiode signal.

In an investigation on the eroding thermocouple rise times, Cornelis et al. [68] found that with a heat gun shutter rig, the rise time of the eroding thermocouple was around 0.75 ms, whereas when the same eroding thermocouple was tested using the heat gun chopper rig, rise times of about 0.3 ms were obtained. Cornelis et al. [68] suggests that this discrepancy in the two rise times results from the fact that on the chopper rig, the eroding thermocouple surface experiences a temperature build-up due to the multiple consecutive heating pulses given by the chopper. On the other hand, on the shutter rig, the temperature swing induced by a single heat flux pulse is on a thermocouple surface at room temperature. To investigate this, some tests were done with the speedlight, on a hot thermocouple surface by constantly heating it using a heat gun prior to (but not during) the speedlight flash test. Figure 5.19 shows the Stainless Steel-based thermocouple response for two tests with the speedlight; one with pre-heating to around 97°C and one with the eroding thermocouple initially at room temperature. As can be seen from this figure no real difference is evident in the rise time for the two instances. If for the purpose of measurement, the two traces are

compared up to the same temperature rise of say 5°C, a difference in the rise time of 30 μs is noted, but actually showing that the cool temperature response is the fastest, hence in contradiction to what was reported by Cornelis et al. [68]. It is thought that the small difference being noted both in this study and also in the study by Cornelis et al. [68], should not affect the temperature measurement in internal combustion engine study which is known to have timescales of interest well in the milliseconds range. According to the work presented by Hoag [36] and Jackson et al. [43], the combustion chamber surface temperature rise time should be 1 ms or longer. Hence, from the temperature response by using the speedlight, it is shown that the rise time of the combined temperature measuring system, including the latency of the thermocouple itself, but also of the amplifier and DAQ, is at least two times faster than the temperature rise time expected for the most demanding setpoints in internal combustion engine study.
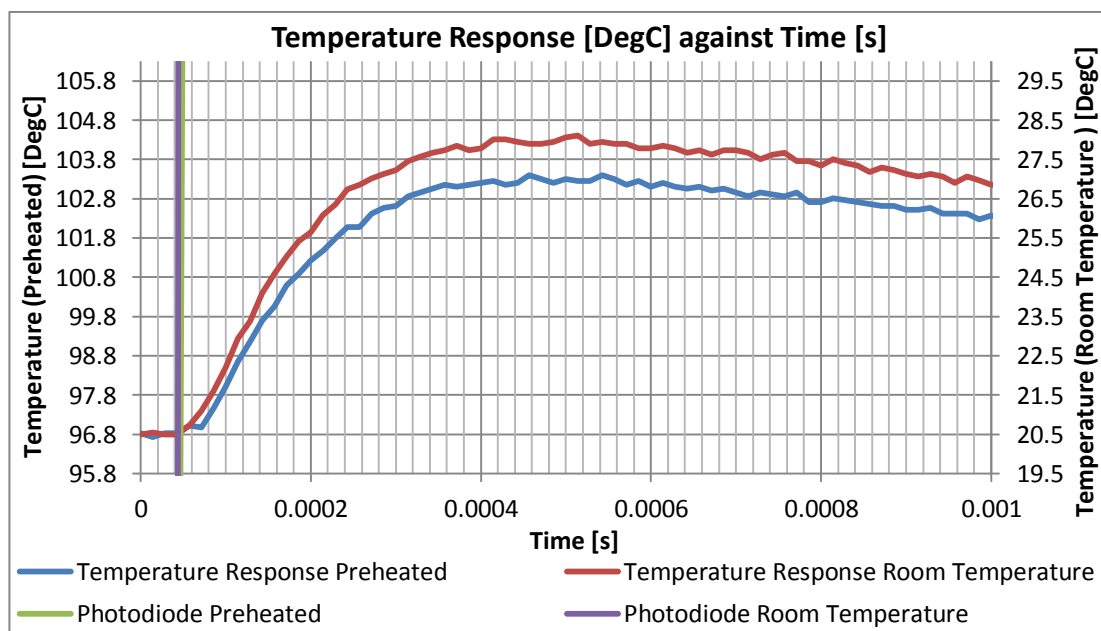
Figure 5.19. The rise times of the Stainless Steel thermocouple with preheating compared to that of the same thermocouple but without preheating. The photodiode rising edge is also given for both tests.

5.3.2 Temperature Signal Amplification

In this study, the amplifier used for temperature signals amplification was based on the dual op-amp by Burr Brown, OPA2277. This op-amp is popular due to its very low voltage offset. The gain-bandwidth product of this op-amp is 1 MHz, with a

slew-rate of 0.8 V/μs. The amplifier circuit was first constructed on a veroboard with a single amplifier for use with the Zirconia thermocouple fitted in the OEM injector location of the four-cylinder engine for the preliminary heat flux testing. The voltage gain was set to be equal to 101. After some confidence was acquired in the amplifier, a surface mount circuit with two OPA2277 op-amps was constructed on a prototyping board, manufactured by the Electronic Systems Engineering Department at the Faculty of Engineering, University of Malta. A schematic of the surface mount circuit is shown in Figure 5.20 which is adapted from the OPA2277 datasheet, whereas a photo of the prototyped circuit is shown in Figure 5.21.

The op-amp circuit was powered by two 9 V cells for supply of the positive and negative rails. Batteries were preferred over transformer-based power supplies to make sure that the amplifier is decoupled from any electrical noise associated with the laboratory electrical supply. Shielded BNC-terminated cables were used on the output signals. The amplifier circuit together with the batteries were enclosed in a custom-made 3D printed enclosure, which was covered with aluminium foil for electrical interference shielding. The female E-type thermocouple connectors were directly mounted to the amplifier enclosure (as shown in Figure 5.22), with the cold-junction compensation (CJC) K-type thermocouples embedded in the female E-type connectors, where the amplifier input signal copper wires connect to the E-type thermocouple materials.
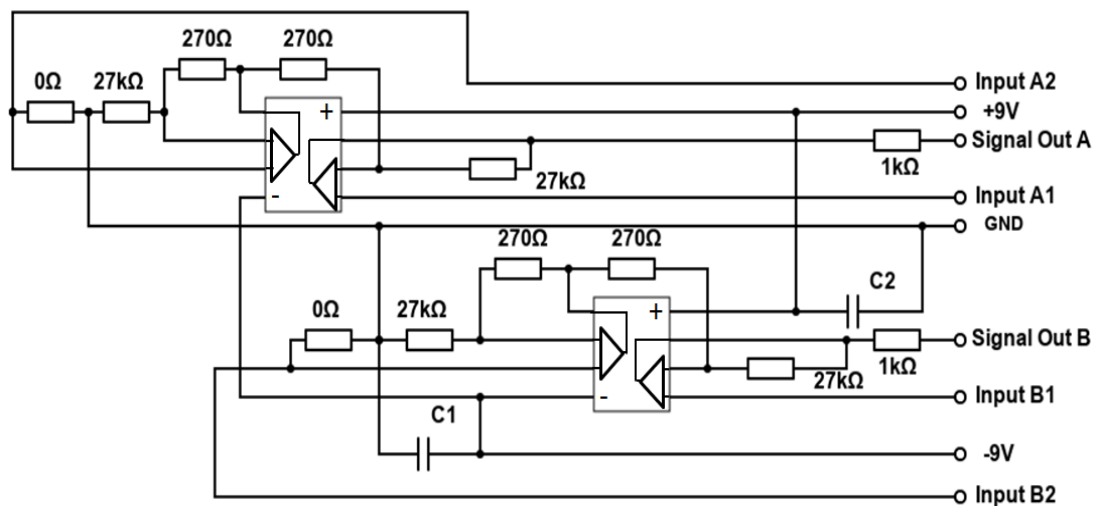
Figure 5.20. The thermocouples amplifier circuit.

190
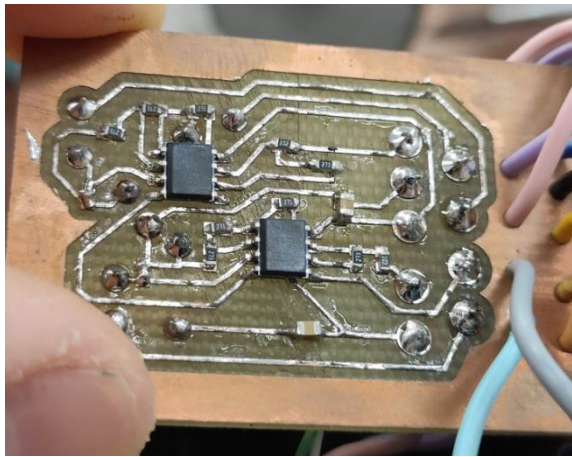
Figure 5.21. The developed PCB with two Op-Amps.
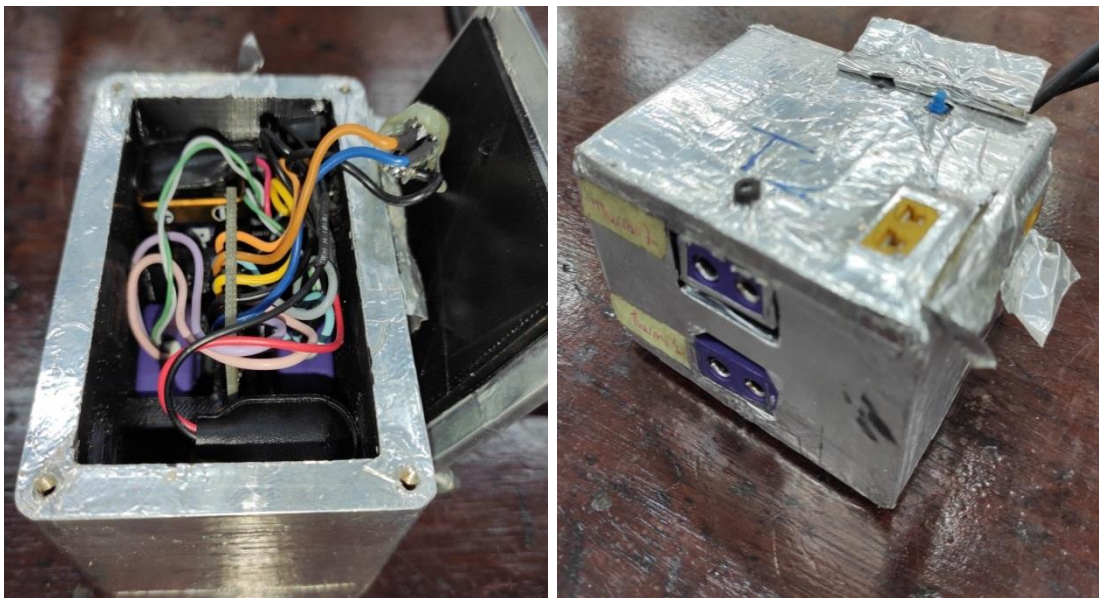
Figure 5.22. Photos showing the eroding thermocouples amplifier enclosure.

When considering temperature signals with rise times smaller than millisecond timescales, it is imperative to verify that for the timescales of interest, the temperature amplifier would not be attenuating the magnitude or shifting the signal. This was especially important when testing the thermocouples with the speedlight flash, since according to the photodiode, the speedlight imposed rise times of around 50 μs (20 kHz). The OPA2277 op-amp with the configured gain of 101, yields a frequency response of $\frac{1\,MHZ}{101} = 9.9\,kHz$, which is around 400 times the fundamental frequency of the temperature measurement at 3000 rpm. Figure 5.23 and Figure 5.24 show experimentally obtained graphs of the amplitude and phase against the frequency response of the amplifier based on OPA2277 with voltage gain of 101.
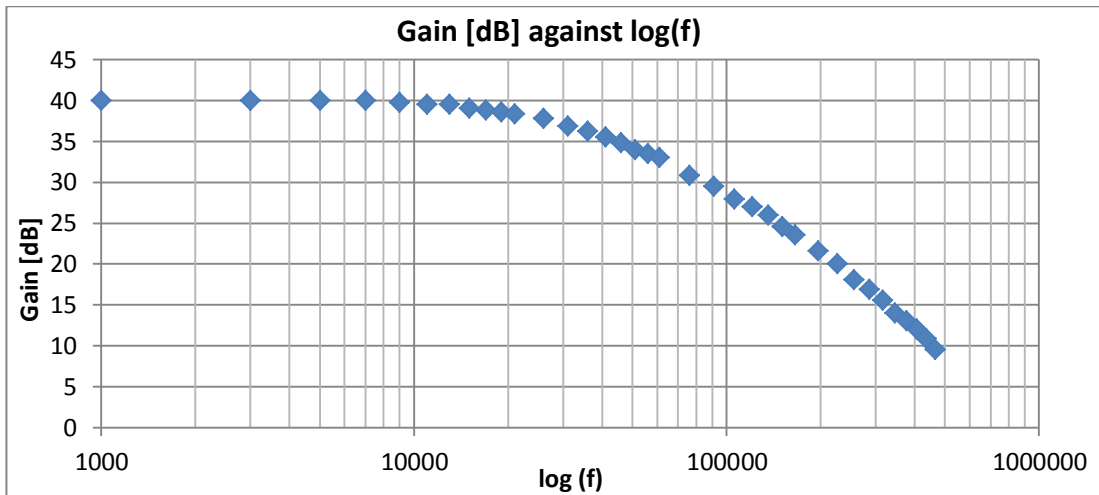
Figure 5.23. Amplitude of frequency response of OPA2277 thermocouple amplifier.
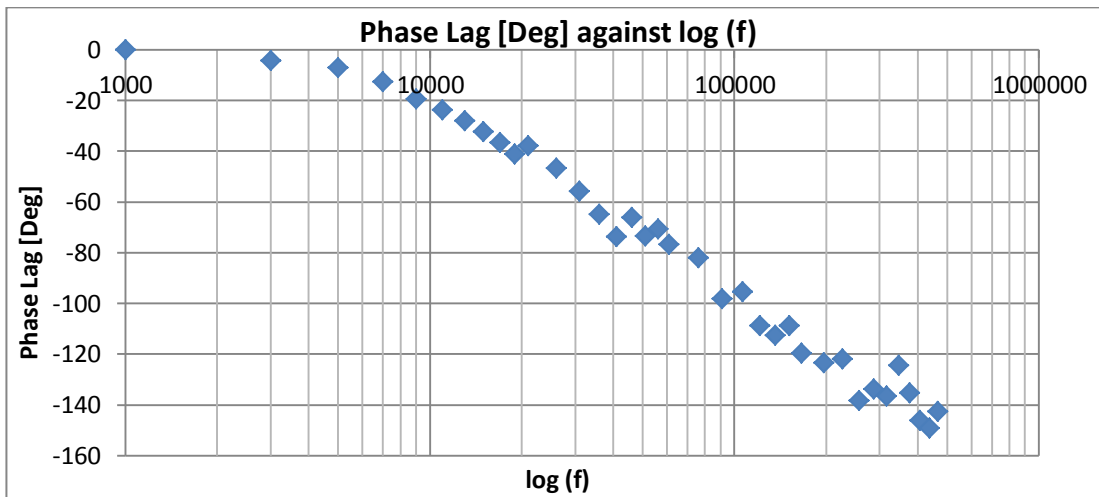
Figure 5.24. Phase of frequency response of the OPA2277 thermocouple amplifier.

Whilst the frequency response of OPA2277 with the set voltage gain is adequate for typical engine surface temperature measurements, it is slightly low for the speedlight flash testing. Due to this, another dual op-amp with better gain-bandwidth product was researched. It was found that LT1213 has a gain-bandwidth product of 28 MHz and a slew rate of 12 V/μs. This means that the LT1213 op-amp with the configured gain of 101, yields a frequency response of $\frac{28\ MHZ}{101} = 277\ kHz$, hence more than adequate for both speedlight flash testing, and also engine studies. The experimentally obtained amplitude and phase against frequency response of the amplifier based on LT1213 with a voltage gain of 101 is shown in Figure 5.25 and Figure 5.26. The pin configuration of this op-amp coincides with that of the OPA2277, and hence could be swapped without any changes in the circuit wiring.
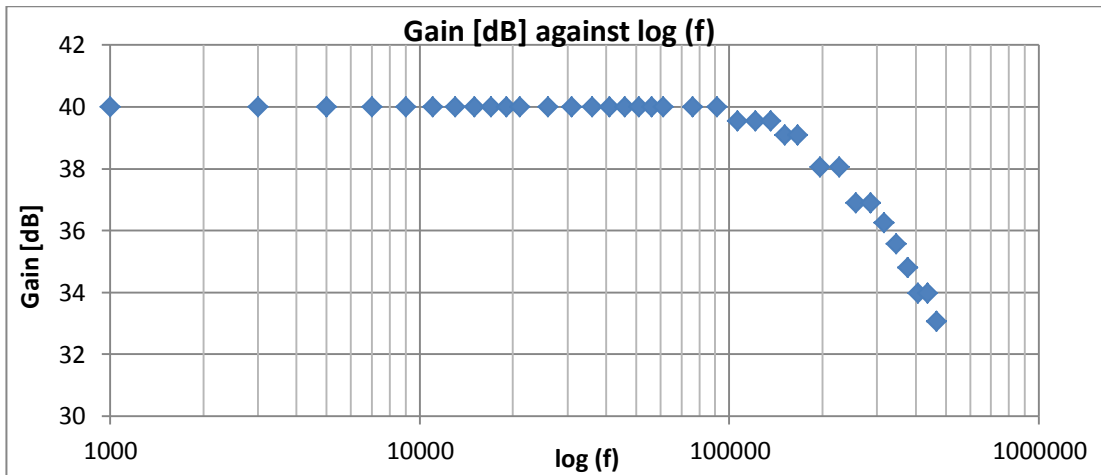
Figure 5.25. Amplitude of frequency response of LT1213 thermocouple amplifier.
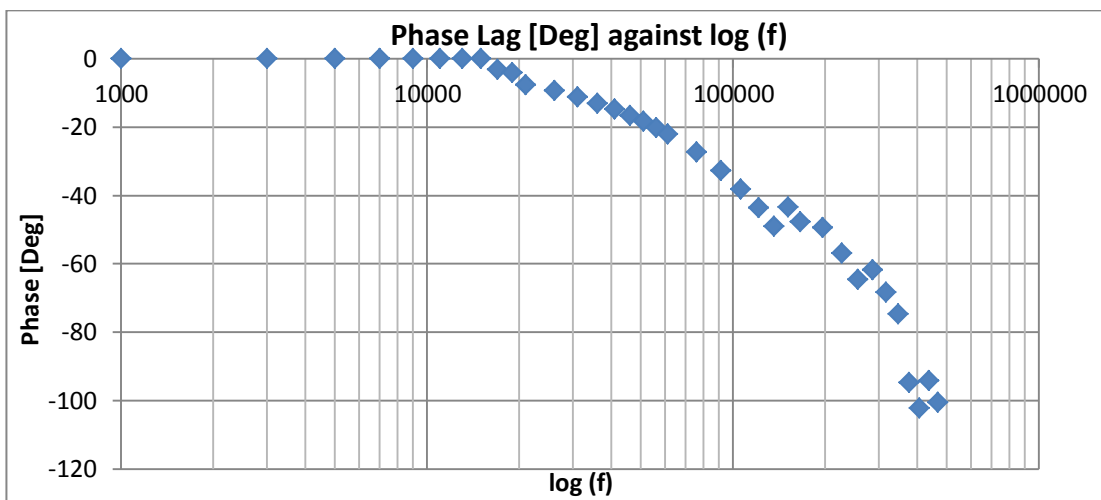
Figure 5.26. Phase of the frequency response of the LT1213 thermocouple amplifier.

Figure 5.27 shows the temperature response of the Stainless Steel thermocouple when exposed to the speedlight flash. A comparison is made between the temperature response measured with the OPA2277 and LT1213. No significant difference in the rise times is noted. This test was repeated on the different thermocouples tested in this work, with both cool surface temperature and also pre-heated to 100℃. No significant variations were seen between the response of the thermocouples using the OPA2277 and LT1213. This shows that whilst OPA2277 with the configured voltage gain is slightly slower than it should ideally be for speedlight flash testing, however the rise time limiting factor was the thermocouple, not the op-amp. Throughout the engine heat flux testing and speedlight flash testing OPA2277 was used due to its lower input offset voltage. The lower frequency range of the OPA2277 acts as an in-built low pass filter to prevent aliasing.
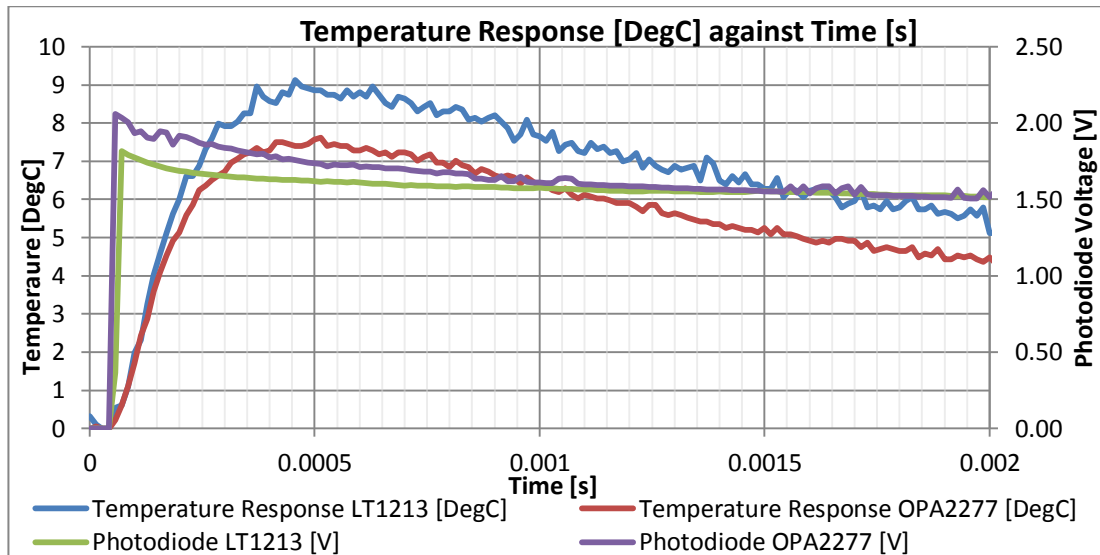
Figure 5.27. Stainless steel thermocouple response time with the LT1213 and OPA2277 op-amps.

5.4 Heat Flux Testing

For the purpose of surface temperature measurements and heat flux determination two test matrices were conducted, both using the single cylinder converted engine. The two extensive test matrices were conducted with the aim of obtaining enough data to support the development/verification of heat transfer models, as well as contribute to the general research of in-cylinder heat transfer. The setpoints tested in the first test matrix (Test Matrix A) are detailed in Table 5.3. In this testing session, the main aim was to investigate the differences that result in the acquired surface temperature and heat flux from the use of surface thermocouples with similar constructions, but different base materials. For this purpose each thermocouple was tested at eight different setpoints. Since the test matrix was diversified between engine speed, PCP and gas composition, some evaluation of the effect of these parameters on the surface temperature and heat flux could also be made from this test matrix. Test Matrix A is split into five sub-matrices as denoted in Table 5.3, which discretise the tests done on five different days using different thermocouples fitted at the OEM injector location. Throughout the five sub-matrices, a Zirconia-based eroding thermocouple was fitted at the custom drilled location. As can be noted in the first three sub-matrices, *i.e.* sub-matrix A1 to sub-matrix A3, the custom-drilled thermocouple was sooted due to previous preliminary tests which are not reported here. Before conducting each of the sub-matrices A4 and A5, the thermocouple at the

194

custom-drilled location was re-abraded (hence cleaned). The thermocouples tested at the OEM injector location were re-abraded prior every sub-matrix. The eroding thermocouple at the OEM injector location was inspected after conducting every sub-matrix to ensure that the thermocouple remained clean throughout the testing session. This inspection was also carried out on the Zirconia thermocouple at the custom drilled location, but only after testing sub-matrix A4 and sub-matrix A5.

The second test matrix conducted on the single cylinder engine was primarily targeted at FMEP determination of the single cylinder engine, however surface thermocouples were also fitted and care was taken during testing to ensure that the data acquired from these thermocouples could be used for heat flux determination. The setpoints tested in this testing session (Test Matrix B) are shown in Table 5.4. As can be noted, this test matrix diversifies between engine speed, PCP, gas composition and oil/coolant temperature. The size of this test matrix was designed such that it could allow a parametric investigation on surface temperature and heat flux. The results of the setpoints tested at γ of 1.67 shown in Table 5.4 are not presented in this dissertation due to thermocouple sooting issues which the Argon gas presented. This will be explained further in the respective section later in this report. For the whole duration of the test session presented by Table 5.4, the thermocouple fitted in the OEM injector location was the one based on Aluminium, while the thermocouple fitted at the custom drilled location was based on Zirconia. For a better understanding of the control variables tested in Test Matrix B, Table 5.4 is split into three sub-matrices; sub-matrix B1 describes the variation of PCP (Table 5.5), sub-matrix B2 describes the variation of the working gas (Table 5.6), and sub-matrix B3 describes the variation of the coolant/oil temperature (Table 5.7).

Table 5.3. Setpoints tested with different eroding thermocouples. Five testing events, two gases, two PCPs, two engine speeds, total 40 setpoints; Test Matrix A.

Setpoints Tested		*Sub-Matrix A1* SS$_{injec}$ Clean Zirc$_{Custom}$ Sooted		*Sub-Matrix A2* Zirc$_{injec}$ Clean Zirc$_{Custom}$ Sooted		*Sub-Matrix A3* AL$_{injec}$ Clean Zirc$_{Custom}$ Sooted		*Sub-Matrix A4* AL$_{injec}$ Clean Zirc$_{Custom}$ Clean		*Sub-Matrix A5* SS$_{injec}$ Clean Zirc$_{Custom}$ Clean	
Ratio of Specific Heats	PCP [bar]	Engine Speed [rpm]									
		1400	3000	1400	3000	1400	3000	1400	3000	1400	3000
1.4	80	✓	✓	✓	✓	✓	✓	✓	✓	✓	✓
	100	✓	✓	✓	✓	✓	✓	✓	✓	✓	✓
1.6	80	✓	✓	✓	✓	✓	✓	✓	✓	✓	✓
	100	✓	✓	✓	✓	✓	✓	✓	✓	✓	✓

SS$_{injec}$: Stainless Steel thermocouple fitted at OEM injector location
Zirc$_{injec}$: Zirconia thermocouple fitted at OEM injector location
AL$_{injec}$: Aluminium thermocouple fitted at OEM injector location
Zirc$_{Custom}$: Zirconia thermocouple fitted at custom drilled location
Clean: No traces of soot were observed on the thermocouple surface after the test session
Sooted: Traces of soot were observed on the thermocouple surface after the test session

Table 5.4. Setpoints tested with Aluminium thermocouple in OEM injector location and Zirconia thermocouple in custom-drilled location. Four gases, four PCPs, three coolant/oil temperatures and four speeds, total 48 setpoints; Test Matrix B.

Setpoints Tested			Engine Speed [rpm]			
Ratio of Specific Heats	PCP [bar]	Coolant & Oil Temperature [DegC]	1400	2000	2500	3000
1.40	40	80	✓	✓	✓	✓
	60	80	✓	✓	✓	✓
	80	60	✓	✓	✓	✓
		80	✓	✓	✓	✓
		95	✓	✓	✓	✓
	100	80	✓	✓	✓	✓
1.50	80	80	✓	✓	✓	✓
	100		✓	✓	✓	✓
1.60	80	80	✓	✓	✓	✓
	100		✓	✓	✓	✓
1.67	80	80	✓	✓	✓	✓
	100		✓	✓	✓	✓

Table 5.5. Sub-matrix of Table 5.4 which presents the setpoints tested investigating mainly different PCPs.

Sub-Matrix B1 @ 80°C Oil/Coolant, using only air		Engine Speed [rpm]			
		1400	2000	2500	3000
PCP [bar]	40	✓	✓	✓	✓
	60	✓	✓	✓	✓
	80	✓	✓	✓	✓
	100	✓	✓	✓	✓

Table 5.6. Sub-matrix of Table 5.4 which presents the setpoints investigating mainly the different gas compositions.

Sub-Matrix B2 @ 80°C Oil/Coolant		Engine Speed [rpm]			
γ	PCP [bar]	1400	2000	2500	3000
1.40	80	✓	✓	✓	✓
	100	✓	✓	✓	✓
1.50	80	✓	✓	✓	✓
	100	✓	✓	✓	✓
1.60	80	✓	✓	✓	✓
	100	✓	✓	✓	✓
1.67	80	✓	✓	✓	✓
	100	✓	✓	✓	✓

Table 5.7. Sub-matrix of Table 5.4 which presents the setpoints tested investigating mainly different oil and coolant temperatures.

Sub-Matrix B3 @ 80 bar PCP using only air		Engine Speed [rpm]			
		1400	2000	2500	3000
Oil and Coolant Temperature [DegC]	60	✓	✓	✓	✓
	80	✓	✓	✓	✓
	95	✓	✓	✓	✓

5.4.1 Repeatability Tests

To have an indication of the degree of repeatability associated with surface temperature and heat flux measurements, whilst ensuring that the thermocouple characteristics did not change during testing, a repeatability measure was conducted. This was done by running a setpoint twice; at the start and at the end of the test matrix. The setpoint considered for repeatability tests was 1400 rpm, 80 bar using air as the working gas.

Figure 5.28 and Figure 5.29 show the ensemble surface temperature and transient component of heat flux respectively, as recorded by the custom-fitted Zirconia thermocouple, comparing two tests conducted at the start and end of a particular test matrix. Figure 5.30 and Figure 5.31 show the ensemble surface temperature and transient component of heat flux for the Stainless Steel thermocouple fitted at the OEM injector location, during the same test runs. It should be mentioned that these figures were taken with the same abrasions on the thermocouple, and for both cases the thermocouples were clean. Throughout all instances of repeatability checking, it was noted that the average value of the ensemble temperature varied up to a maximum of 5°C. The temperature swing was very repeatable with minimal variations. As a result, the ensuing heat flux also showed very good repeatability, with variations occurring only around the peak, as shown in Figure 5.29 and Figure 5.31. The steady-state temperature values of the coolant, shunt pipe and oil gallery are also given in Table 5.8, to allow assessment of the setpoint reproducibility.

Table 5.8. The steady-state measurements for the two setpoints used for repeatability evaluation.

	Before Test Matrix	After Test Matrix
Manifold Gauge Pressure [bar]	0.999	0.999
Shunt Intake Temperature [DegC]	20.9	27.2
Sump Oil Temperature [DegC]	38.9	46.9
Oil Gallery Temperature [DegC]	38.9	45.9
Coolant Temperature [DegC]	29.7	33.5
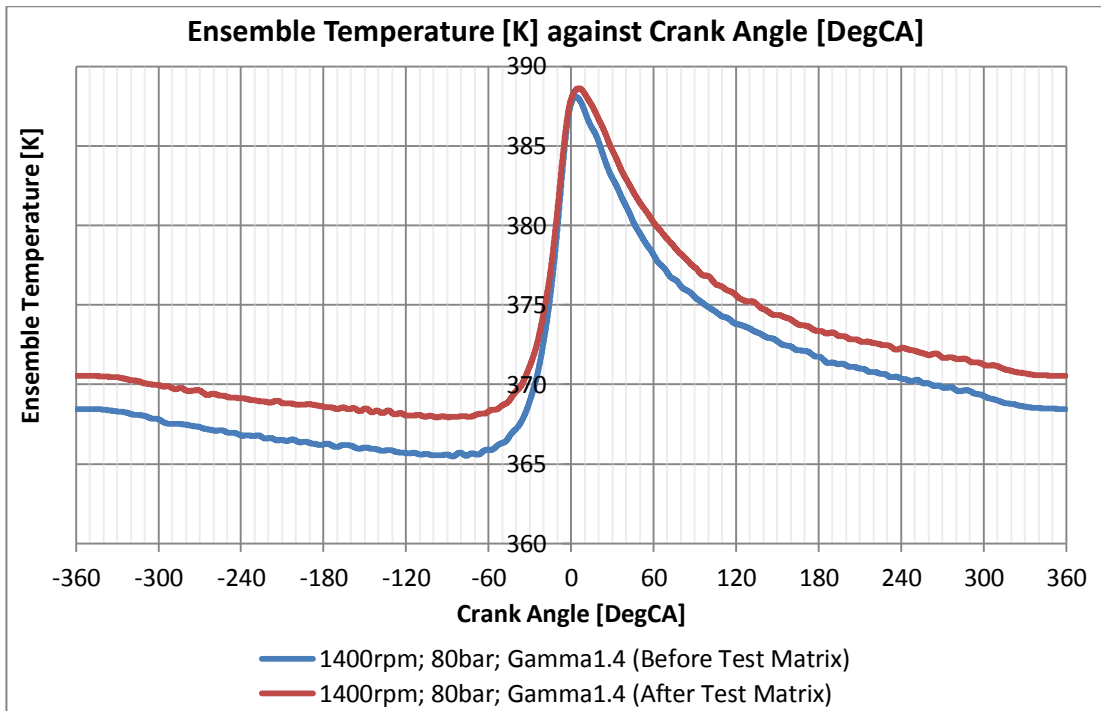
Figure 5.28. Ensemble temperatures taken at the two setpoints used for repeatability evaluation. These temperatures were recorded by the Zirconia thermocouple fitted at the custom-drilled location.
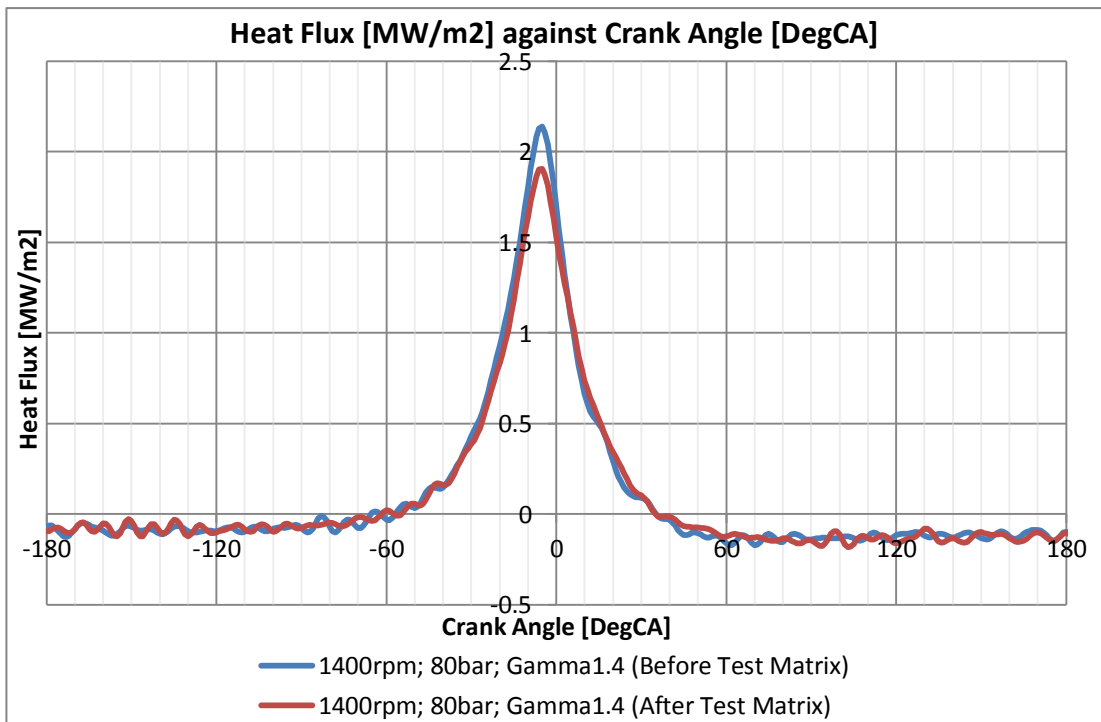
Figure 5.29. Transient component of heat flux obtained from the 2D response of Chromel (Impulse Response) IR analysis and using the temperature data reported in Figure 5.28.

200
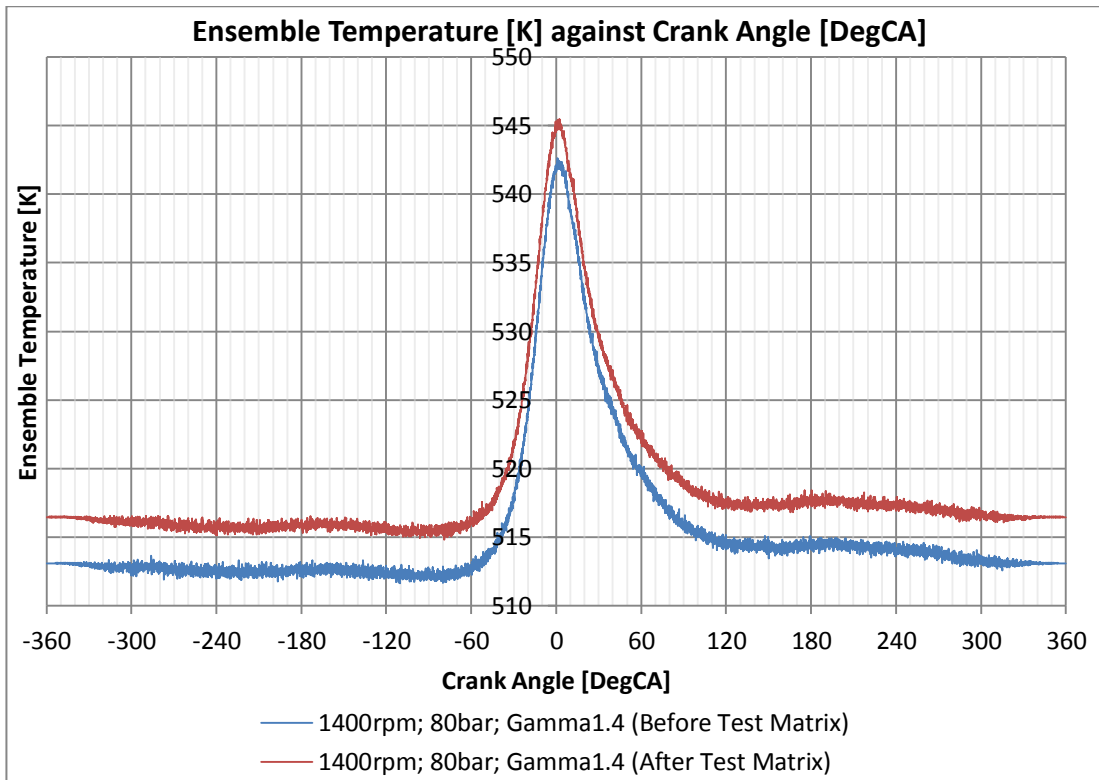
Figure 5.30. Ensemble temperatures taken at the two setpoints used for repeatability evaluation. These temperatures were recorded by the SS thermocouple fitted at the OEM injector location.
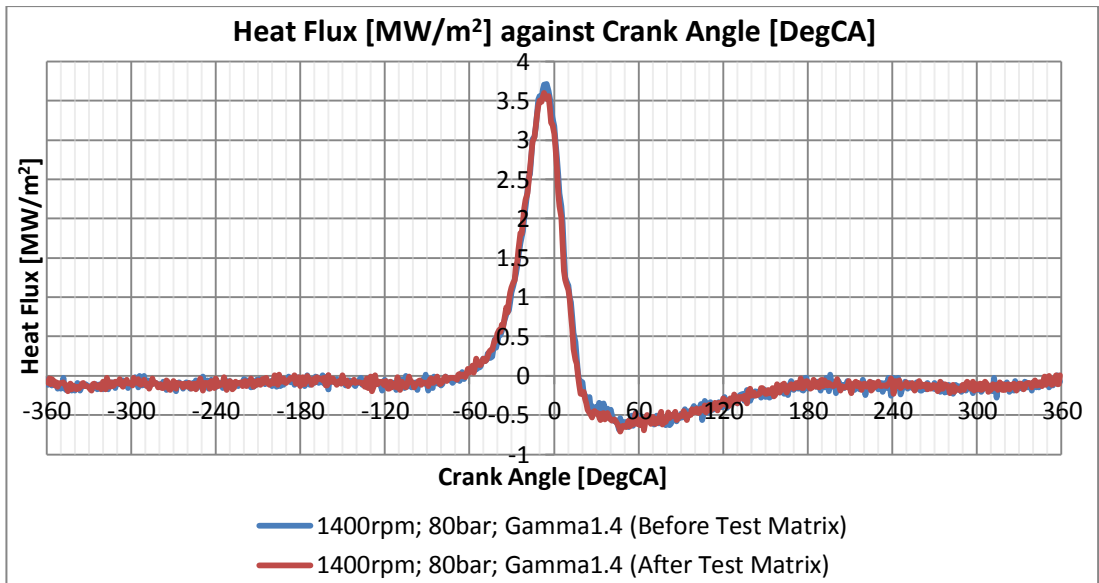
Figure 5.31. Transient component of heat flux obtained from the 2D response of Chromel IR analysis, and using the temperature data reported in Figure 5.30.

Repeatability evaluations of surface temperature and heat flux were also done on test matrices acquired on different days with different thermocouple abrasions. It is noted that in this case, the average value of temperature still showed differences of up to

around 5℃, however the temperature swing showed slightly larger differences than what was shown in Figure 5.28 and Figure 5.30. It should be said however that differences in heat flux were small and mainly concentrated around the peak. This observation was consistent on the whole matrix of eight setpoints. Figure 5.32 and Figure 5.33 show the ensemble surface temperature recorded by the custom-fitted Zirconia thermocouple, and resulting transient component of heat flux at 1400 rpm; 80 bar using air as the working gas. Coolant, oil and shunt pipe temperatures are given in Table 5.9 to indicate the setpoint reproducibility, from which it is noted that differences were minimal.

Table 5.9. The steady-state temperatures recorded at the two setpoints (from Test Matrix A) used for repeatability evaluation.

	Sub-Matrix A4	Sub-Matrix A5
Shunt Intake Temperature [DegC]	20.3	20.9
Shunt Exhaust Temperature [DegC]	17.3	18.4
Coolant Temperature [DegC]	28.6	29.8
Oil Gallery Temperature [DegC]	37.9	38.9
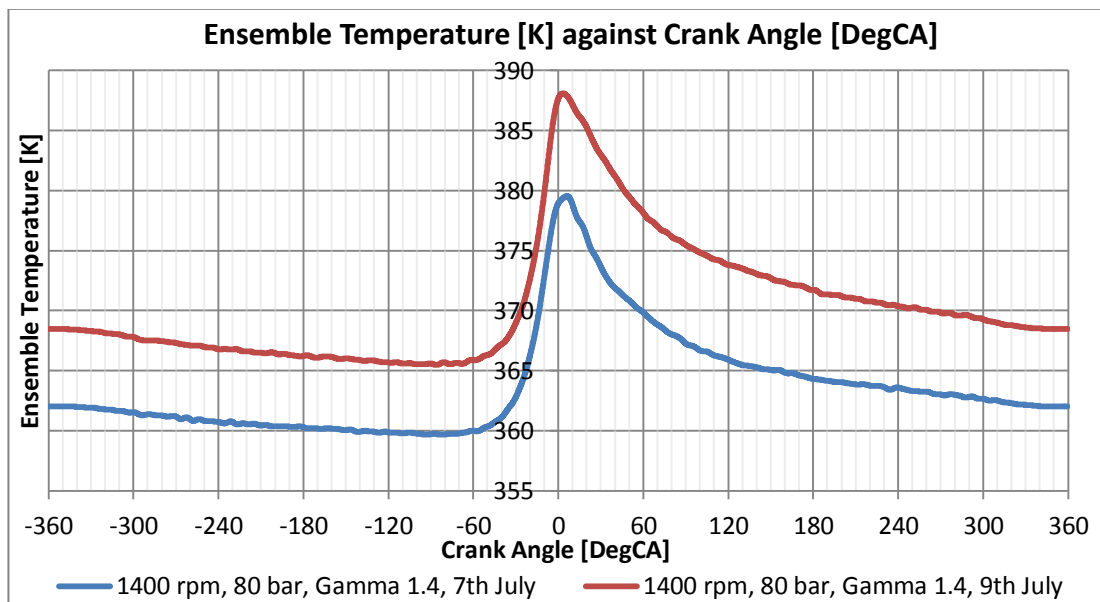
Figure 5.32. Ensemble surface temperatures taken by the Zirconia thermocouple at the custom-drilled location.
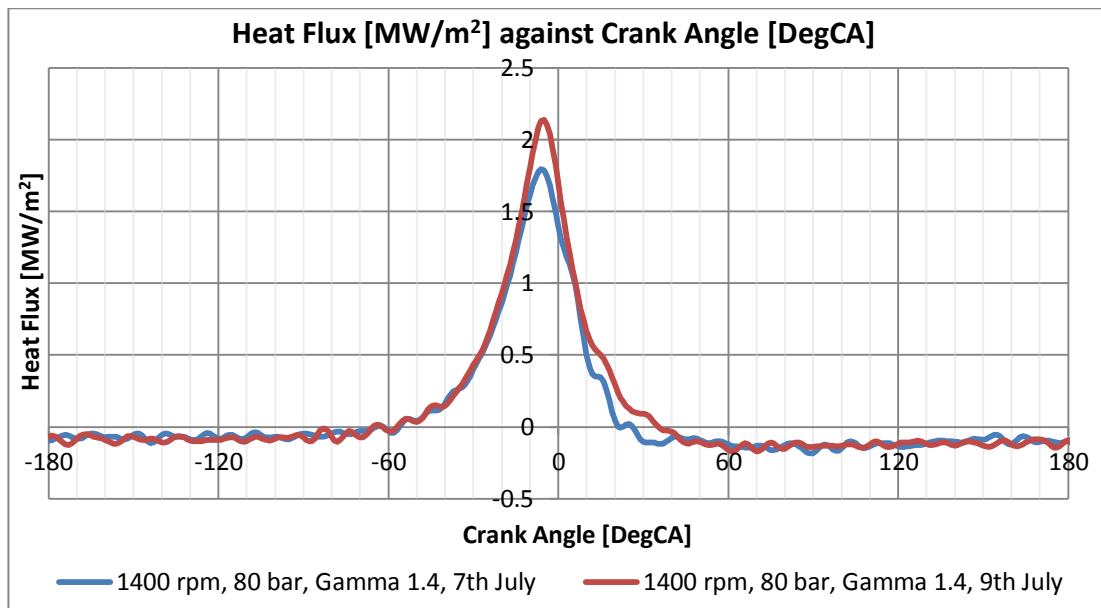
Figure 5.33. Transient component of heat flux obtained from the 2D response of Chromel IR analysis and using the temperature data reported in Figure 5.32.

As noted from the above, in the case where repeatability was tested for with the same thermocouple junction (same sub-matrix), repeatability ranked higher than when repeatability was tested for with a different junction (different day/ different sub-matrix). This observation was noted repeatedly. As a result, the differences seen in the ensemble surface temperature and heat flux reported above, even though may have partially resulted from slightly different setpoint reproducibility, it could be that the most significant contributor is the thermocouple junction (not necessarily the mass of junction, but also distribution of junction locations and their proximity to Mica). It should be mentioned that whilst the above graphs suggest that retaining the same junction abrasion gives better repeatable measurements, in certain instances it was noted that operating the engine for long times and using gases with high ratios of specific heats resulted in an increase in the junction resistance with time. In some instances this resulted in a consequent decrease in the sensor rise time when tested with the speedlight flash. The decrease in the rise time was never more than 100 μs, and possibly attributed to oxidation of the junction. This observation is being presented to convey the message that ideally heat flux measurements should always be accompanied by a characterisation of the sensor rise time and a complementary thermocouple resistance log sheet for meaningful conclusions to be made.

5.5 Computation of the steady-state component of heat flux

The Aluminium eroding surface thermocouple was custom-made and had to be ordered with a minimum diameter of 1/4" (*i.e.* double that of the Zirconia and SS thermocouples). Furthermore, the joint between the 1/4" Aluminium outer tube and the 1/8" Stainless Steel thermocouple stem could not be brazed as is usual practice, but had to be done using a high temperature (230℃ max.) epoxy. The initial plan was to fit the Aluminium thermocouple in the custom-drilled location. This strategy was planned due to the fact that the custom-drilled location was engineered with the purpose of having a tight fit between the thermocouple and the cylinder head, whilst having the thermocouple perfectly flush mounted and perpendicular to the cylinder head surface. Furthermore a recessed thermocouple at some distance from the cylinder head surface was also prepared at this location to allow for the measurement of the steady-state component of heat flux. Unfortunately due to space constraints at the custom-drilled location, the 1/4" aluminium thermocouple could not be fitted at this location, and hence one of the 1/8" eroding thermocouples had to be fitted instead. The thermocouple fitted at the custom-drilled location was the one based on Zirconia.

According to Alkidas [6], if a recessed thermocouple is used for the determination of the steady-state component of heat flux, it should be placed at a recessed depth at which no temperature swings are recorded. According to an estimation of heat penetration at 600 rpm, assuming an attenuation factor of 0.3%, the recessed thermocouple should be at 1.2 mm away from the cylinder head surface if fitted in the Zirconia material. This was also confirmed by Huang and Borman [37] in a study concerning insulated engines using Zirconia. A recessed depth of around 12 mm is required if fitted in the aluminium adaptor. Due to the construction of the eroding thermocouple, placing the recessed thermocouple in the Zirconia split-tapered insert is a very complex task. On the other hand, the approach to fit the recessed thermocouple in the aluminium adaptor is expected to yield large effects of multi-dimensional heat transfer due to the long depth of recess required [6]. This is further amplified by the fact that 12 mm of recess distance coincides with the thickness of the cylinder head deck from the combustion chamber surface to the inner coolant jacket surface. This means that fitting the recessed thermocouple at 12 mm away

from the heated surface results in it being exposed to the coolant temperature, rather than the metal temperature. A further complication is due to the fact that the average value of the surface temperature measurement is a function of the thermocouple substrate material, hence the change in between the mean surface temperature and the recessed temperature will be biased if the surface thermocouple used has a substrate material different than that of the instrumented surface.

Due to the foregoing consideration, although a recessed thermocouple was still fitted in the adaptor at the custom-drilled location, the steady-state heat flux component calculated from the fitted recessed thermocouple was not added to the transient component of heat flux to avoid large errors due to the above-mentioned. As a result all the forthcoming experimental heat flux results presented in figures show only the transient component, and not the total. The steady-state component of heat flux calculated from the recessed thermocouple measurements fitted at the custom-drilled location for the setpoints concerning the test matrix defined by Table 5.3 (Test Matrix A), are presented in Table 5.10. It should be remembered that these values are presented for the sake of understanding the large errors discussed above, and not to be used with the transient data presented in forthcoming sections.

To have a more robust estimate of the steady-component of heat flux, a computation involving equation (5.15), derived from the 1st law of thermodynamics (equation (5.13)) was conducted on the measured instantaneous in-cylinder pressure data, for the closed part of the cycle. Equation (5.15) gives a zero-dimensional estimation of the total instantaneous heat flux based on the deviation of the rate of change of in-cylinder pressure from the isentropic compression assumption, which results from heat transfer and blow-by. In using equation (5.15), the value of γ at different crank angles was taken to be function of the bulk gas temperature. In equation (5.15), the term $\frac{dQ}{dt}$ represents heat transferred in Watts (W), p is the instantaneous in-cylinder pressure, V is the instantaneous cylinder volume, and m is the instantaneous trapped mass (decreased every crank angle due to blow-by).

Equation (5.15), suggested by Pipitone and Beccari [104], is an improvement of equation (5.14). Equation (5.14) does not have a term specifically associated to energy loss due to blow-by. As a result, since the measured motored in-cylinder pressure has a reduction effect due to blow-by, on application of equation (5.14), this

reduction will be falsely interpreted as an added heat transfer. To correct for this, Pipitone and Beccari [104] added the extra term in equation (5.15) to separate the energy lost due to blow-by from the term $\frac{dQ}{dt}$ which is the true representation of heat transfer. As can be noticed from equation (5.15), an estimate of the blow-by flow rate and instantaneous trapped mass is required. Although it is difficult to know the true quantity of mass flowing out of the system, an estimate can be made from equation (4.6) and equation (4.7), presented previously in Chapter 4, which are based on the flow through a convergent-divergent nozzle with a throat diameter of 0.6 mm [104]. Table 5.11 gives the average value of the total heat flux pertaining to the test matrix defined by Table 5.3 (Test Matrix A). As will be observed in the forthcoming section, the steady-state component of the heat flux is relatively small compared to the swing of the transient component presented from the experimental results.

To have an estimation of the total heat flux, the experimentally obtained transient components of heat flux given in graphs in the following section can be added to the steady-state component of heat flux obtained from the zero-dimensional consideration using the 1st law of thermodynamics on the closed part of the cycle. The steady-state component can be obtained by averaging the instantaneous heat flux obtained from equation (5.15). It should be noted that since the results from equation (5.15) are computed with a zero-dimensional approach, had the steady-state component been obtained experimentally at different locations, it might have shown spatial differences. This could not be captured with the substitute zero-dimensional approach adopted. In the forthcoming section, in each experimental heat flux diagram, along with the experimentally obtained transient component of heat flux, the steady-state component of heat flux (over compression and expansion strokes only) obtained from equation (5.15) is given.

$$-\frac{dQ}{dt} = p\frac{dV}{dt} + \frac{dU}{dt} \qquad \dots (5.13)$$

$$-\frac{dQ}{dt} = \frac{\gamma}{\gamma - 1}p\frac{dV}{dt} + \frac{1}{\gamma - 1}V\frac{dP}{dt} \qquad \dots (5.14)$$

$$-\frac{dQ}{dt} = \frac{\gamma}{\gamma - 1}p\frac{dV}{dt} + \frac{1}{\gamma - 1}V\frac{dP}{dt} - \frac{\gamma}{\gamma - 1}\frac{pV}{m}\frac{dm}{dt} \qquad \dots (5.15)$$

Table 5.10. The steady-state component of the total heat flux computed from the average of the surface temperature at the custom-drilled location, and the recessed thermocouple, using Aluminium thermo-physical properties. Test matrix defined by Table 5.3 (Zirconia run 3rd July, Aluminium run 7th July and SS run 9th July).

Steady-State Component of Heat Flux at the custom-drilled location with Zirconia thermocouple fitted [MW/m^2]			c_p/c_v					
			1.4	1.6	1.4	1.6	1.4	1.6
			Aluminium Thermocouple run		Stainless Steel Thermocouple run		Zirconia Thermocouple run	
Engine Speed [rpm]	1400 rpm	80 bar	0.852	1.154	0.937	1.300	0.710	0.896
		100 bar	0.963	1.317	1.055	1.457	0.791	1.012
	3000 rpm	80 bar	1.238	1.726	1.334	1.861	0.978	1.511
		100 bar	1.400	1.968	1.527	2.108	1.098	1.709

Table 5.11. The steady-state component of heat flux computed from the 1st Law on the experimental in-cylinder pressure, with blow-by compensation. Test matrix defined by Table 5.3 (Zirconia run 3rd July, Aluminium run 7th July and SS run 9th July).

Steady-State Component of Heat Flux [MW/m^2]			c_p/c_v					
			1.4	1.6	1.4	1.6	1.4	1.6
			Aluminium Thermocouple run		Stainless Steel Thermocouple run		Zirconia Thermocouple run	
Engine Speed [rpm]	1400 rpm	80 bar	0.1721	0.2346	0.1754	0.2250	0.1718	0.2330
		100 bar	0.1987	0.2769	0.2027	0.2703	0.1926	0.2690
	3000 rpm	80 bar	0.3083	0.4152	0.2938	0.4020	0.2957	0.3911
		100 bar	0.3648	0.4765	0.3450	0.4549	0.3369	0.4583

5.6 Impulse Response Heat Flux on different Eroding Thermocouple Base Materials

As documented in a previous section, to compute the transient component of heat flux from surface temperature measurements, the Impulse Response method was used. In section 5.2.2, the temperature response for a step heat flux of 1 MW/m^2 at the thermocouple surface was presented for each thermocouple used in this research.

After having obtained the surface temperature signals from each different thermocouple placed at the OEM injector location, the temperature signals were processed with the impulse response technique using the impulse response function *h(t)*, obtained from the basis functions of the two dimensional FEA study. The surface temperature signal acquired from each engine test point was processed to heat flux seven times, using the impulse response function of the 2D response of both thermocouple materials (Chromel and Constantan), the 2D response of the central Mica, and the 2D response of the split-tapered insert material (close to the Mica boundary, and mid-way through the material surface). The heat flux was also computed using the FFT 1D method with the thermo-physical properties of the split-tapered insert material and using the one-dimensional impulse response method with the thermo-physical properties of the split-tapered insert material. Refer to Figure 5.11 in section 5.2.2 for a visual identification of surface temperature probing points assigned on the FEA model.

As shown by Table 5.3 (Test Matrix A) in section 5.4, each of the different thermocouples tested in this study were placed in the OEM injector location and tested at eight setpoints consisting of two engine speeds (1400 rpm and 3000 rpm), two PCPs (80 bar and 100 bar) and two gas compositions (Air and γ: 1.6). The acquired surface temperature data and processed transient component of heat flux are presented for each thermocouple in Figure 5.34 to Figure 5.36. For the purpose of presentation, only the results of the setpoint 1400 rpm, 80 bar, air are being shown. The observations made on this setpoint are common to setpoints involving other engine speeds, PCPs and gases. The next section discusses at length the observations made on Figure 5.34 to Figure 5.36.
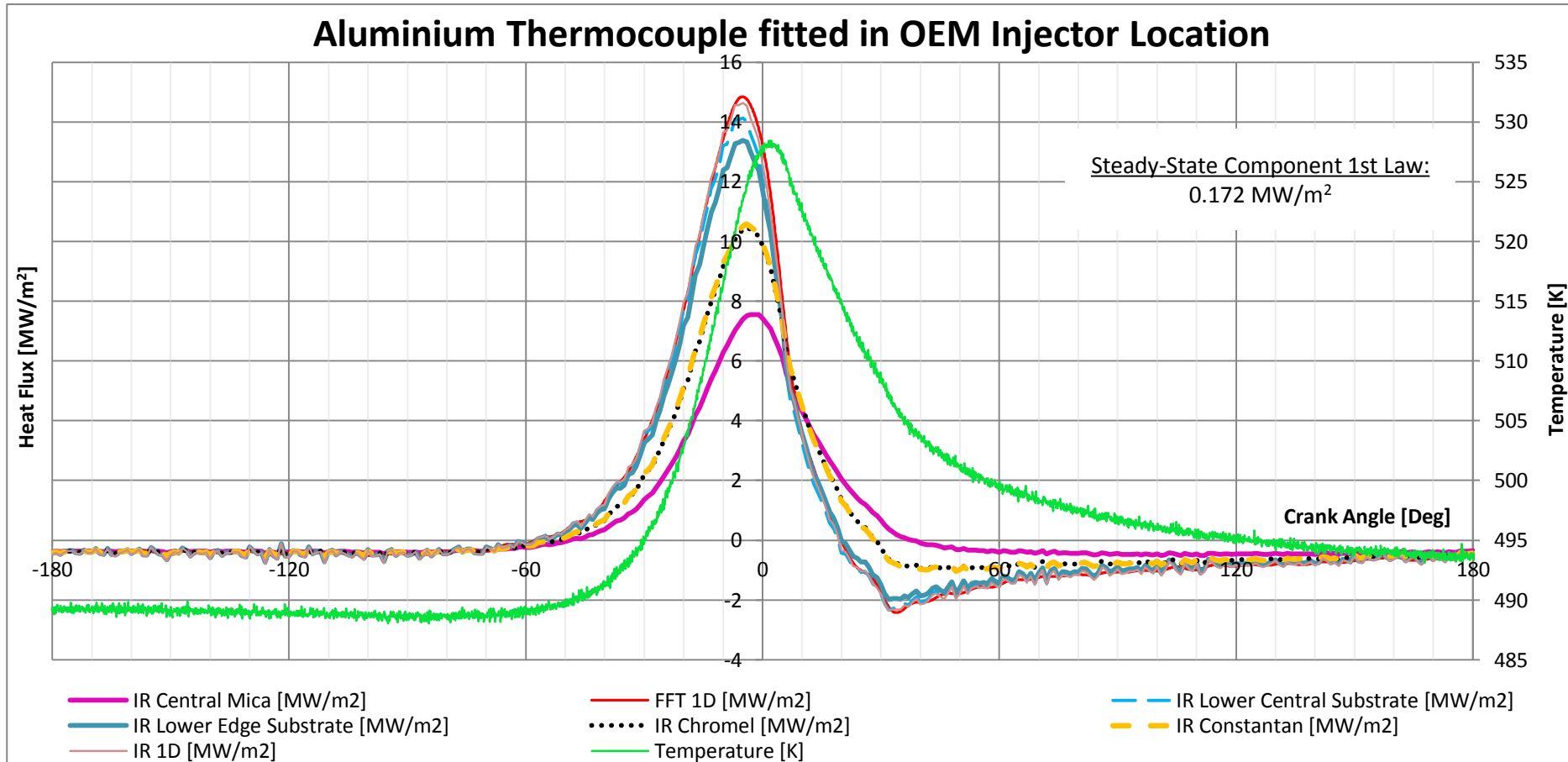
Figure 5.34. Transient component of heat flux and ensemble surface temperature recorded by the Aluminium thermocouple fitted at the OEM injector location, at 1400 rpm, 80 bar PCP using air as the working gas. Sub-Matrix A4.
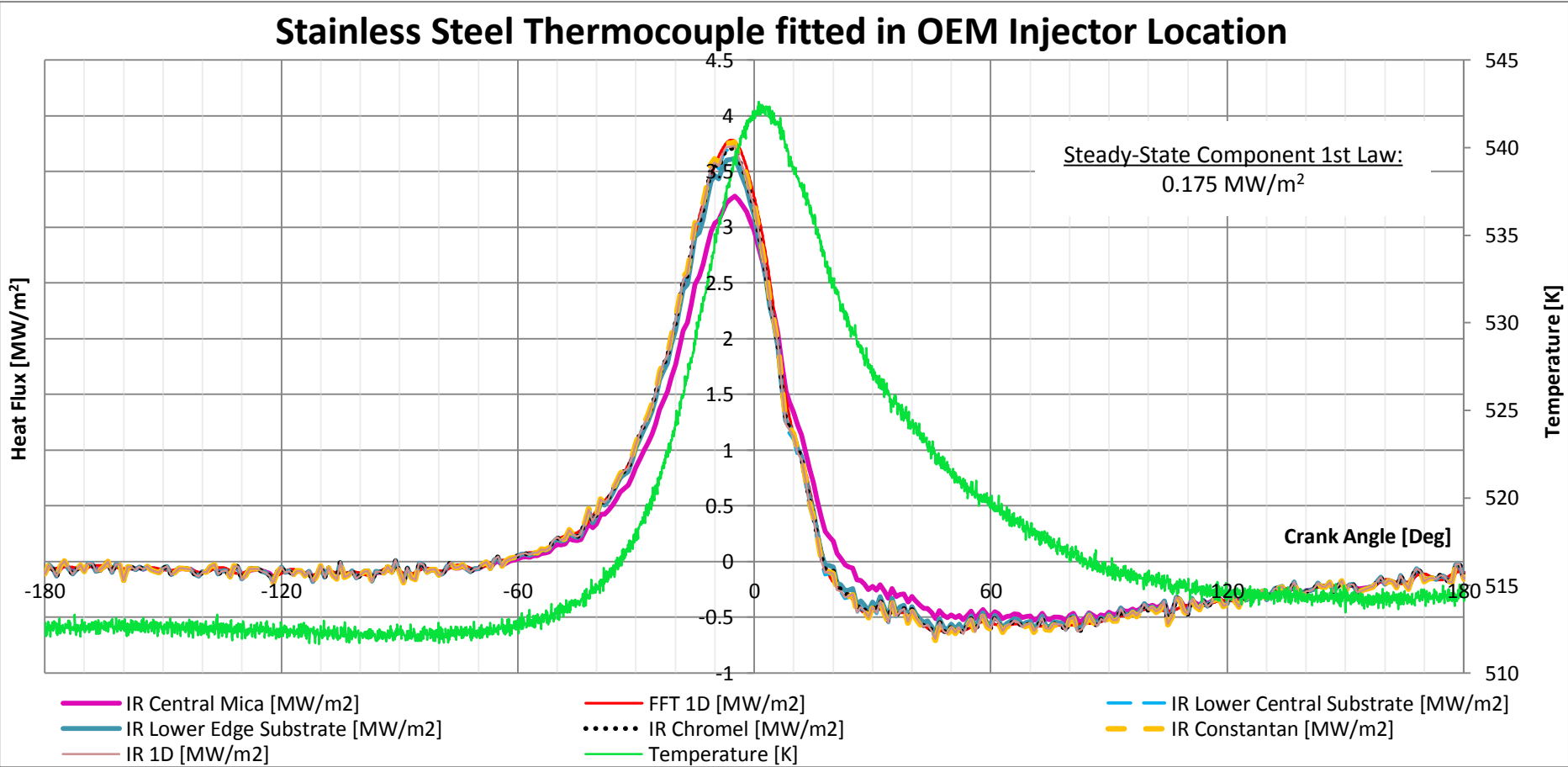
Figure 5.35. Transient component of heat flux and ensemble surface temperature recorded by the SS thermocouple fitted at the OEM injector location, at 1400 rpm, 80 bar PCP using air as the working gas. Sub-Matrix A5.
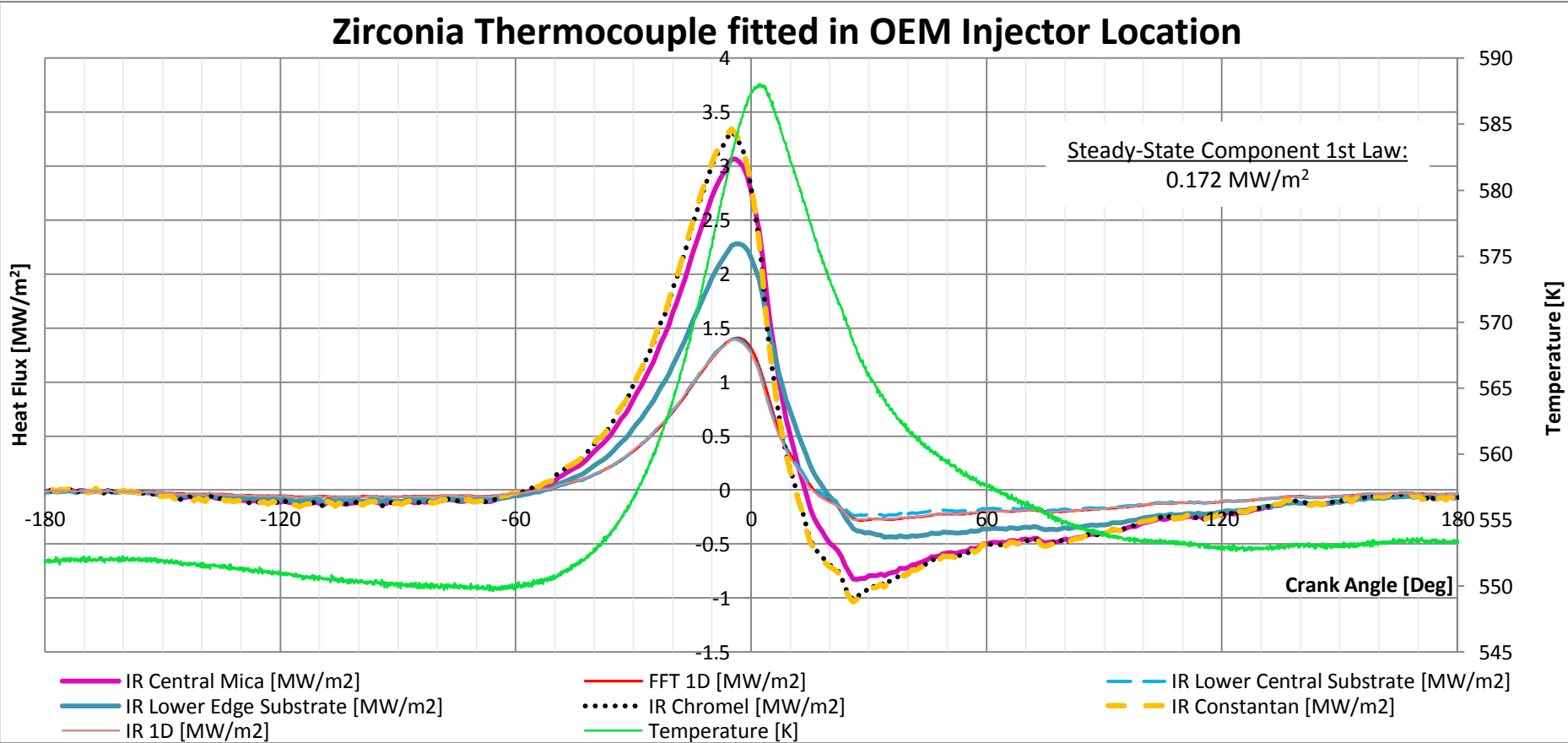
Figure 5.36. Transient component of heat flux and ensemble surface temperature recorded by the Zirconia thermocouple fitted at the OEM injector location, at 1400 rpm, 80 bar PCP using air as the working gas. Sub-Matrix A2.

5.6.1 Two-Dimensional versus One-Dimensional Heat Flux Assumption

Having computed the heat flux for each eroding thermocouple using the one-dimensional semi-infinite solid assumption, as well as using two-dimensional consideration, some comments can be made on the differences in the reported heat fluxes. As can be seen from Figure 5.34 to Figure 5.36, it is evident that differences in the reported heat fluxes are evident between the one-dimensional consideration using thermo-physical properties of the split-tapered insert material and the two-dimensional heat flux consideration.

Starting out by observing the heat fluxes reported for the Aluminium thermocouple (Figure 5.34), it is shown that the one-dimensional heat flux assumption using the substrate (or split-tapered pins) material yields heat flux magnitudes twice as high as that shown for the two-dimensional consideration assuming the junction to be set up over the central Mica. This discrepancy between the two heat flux traces is shown around the high flux duration. The heat flux reported by the two-dimensional analysis, but assuming that the junction is set up on thermocouple ribbon materials shows heat flux magnitudes which fall between the 1D-substrate heat flux and the 2D-Central-Mica heat flux. These observations made on the Aluminium thermocouple are fully consistent with observations made by Wang et al. [41] using a Dural-based eroding thermocouple, with thermo-physical properties similar to those of the Aluminium-based thermocouple used in this work.

Contrary to the above observation on the Aluminium thermocouple, Figure 5.36 shows that the one-dimensional analysis on the Zirconia thermocouple results in almost half the heat flux magnitude reported by the two-dimensional consideration using the assumption that the junction is set up either on the thermocouple ribbon surfaces, or on the central Mica. These two different observations made on the Aluminium and Zirconia thermocouples are physically understandable. To appreciate these results, the reader is referred to Table 5.1 in section 5.2, which gives the thermo-physical properties of the different materials making up the two thermocouples.

If the Aluminium thermocouple is considered, it can be identified that the effusivity of Aluminium is more than twice that of Chromel and Constantan, and almost forty-

three times that of Mica. With a one-dimensional heat flux consideration using the thermo-physical properties of Aluminium, it is assumed that all the heat flux transferred from the gas layer to the surface flows perpendicular to the cylinder head surface through one homogenous sensor made completely from Aluminium, with its associated very high effusivity – and hence efficient flow of heat. This situation is not a true representation of the real situation. In the real situation, the heat flux transferred by the gas results in different surface temperatures on each of the different materials making up the thermocouple. In the case of the Aluminium thermocouple, Mica would have the highest surface temperature, followed by the thermocouple elements, whilst the Aluminium split-tapered pins will have the lowest surface temperature in response to the heat flux transferred by the gas. Due to this non-uniform surface temperature, heat will not travel only perpendicular to the cylinder head surface, but also parallel to it from the Mica to the thermocouple ribbons, and then to the aluminium split-tapered pins. Whilst one-dimensional heat transfer assumes all the heat to be transferred through a very conductive Aluminium material, in the more realistic two-dimensional approach heat is transferred partially by the Aluminium material, but more immediate to the junction by the less heat conductive Mica and thermocouple ribbons. As a result, the reported two-dimensional heat flux will be lower than that assumed by a one-dimensional consideration using Aluminium thermo-physical properties.

If the Zirconia thermocouple is considered, one would realise that there is the exact opposite situation. Zirconia has a thermal effusivity four times smaller than that of the thermocouple ribbons (Chromel and Constantan), but four times higher that of Mica. This means that if a one-dimensional heat flux is considered, it is assumed that all heat is transferred perpendicular to the cylinder head surface through very insulative Zirconia. In reality however, the temperature gradient at the surface and parallel to it sets up two dimensional heat flux, with only a fraction of the heat being transported away by the insulative Zirconia, and the rest being conducted by the relatively conductive Chromel/Constantan, and some small portion by the insulative Mica. As a result, mainly due to the action of the Chromel/Constantan, the actual heat flux if considering two-dimensional effects is higher than that if considering a homogeneous, one-dimensional Zirconia thermocouple.

Through observation of Figure 5.35, it is evidently shown that for the setpoint tested with the Stainless Steel thermocouple, the two-dimensional heat flux is very similar to the one-dimensional heat flux using the Stainless Steel thermo-physical properties. This is of no surprise and can be understood by looking at Table 5.1, which shows that the thermocouple ribbons have very similar thermo-physical properties to that of the split-tapered insert material, being Stainless Steel. Hence, in this regard two dimensional effects are somewhat less than that in the other two sensors. It should be however noted that the Mica elements in the Stainless Steel thermocouple is still significantly different in their thermo-physical properties compared to the other materials making up the sensor. As a result, some two-dimensional effects will still be present due to the higher surface temperature set up over the Mica.

For the above two-dimensional explanation to be better understood, the reader is referred to Figure 5.37, which shows the FEA simulated temperature response on the surface of the central Mica for the three different thermocouples. As can be seen in this figure, the temperature response of the central Mica for the Aluminium-based thermocouple shows the smallest magnitudes. This is in line with the above explanation, and is a result of strong two-dimensional heat transfer away from the Mica material towards the more conductive substrate (aluminium). As a result the Mica material is cooled the most efficiently in this thermocouple. The central Mica of the Zirconia-based thermocouple is the one which has the highest temperature magnitude response. This is because the central Mica is surrounded by the Zirconia substrate which is nearly as insulative as Mica itself. In fact, according to the impulse response presented in Figure 5.17 in section 5.2.2, Zirconia acts to heat up Mica, rather than cool it. Figure 5.37 shows that the central Mica of the Stainless Steel-based thermocouple has a temperature response which falls between that of the other two thermocouples. This is understandable because in the Stainless Steel thermocouple Mica is the most insulative material, and hence both thermocouple ribbons, as well as the substrate material (SS) act to remove heat from the central Mica. Since all metallic materials in this sensor are much less conductive than, for example Aluminium, the temperature at the Mica surface will still be slightly higher than that displayed by the central Mica of the Aluminium-based thermocouple.
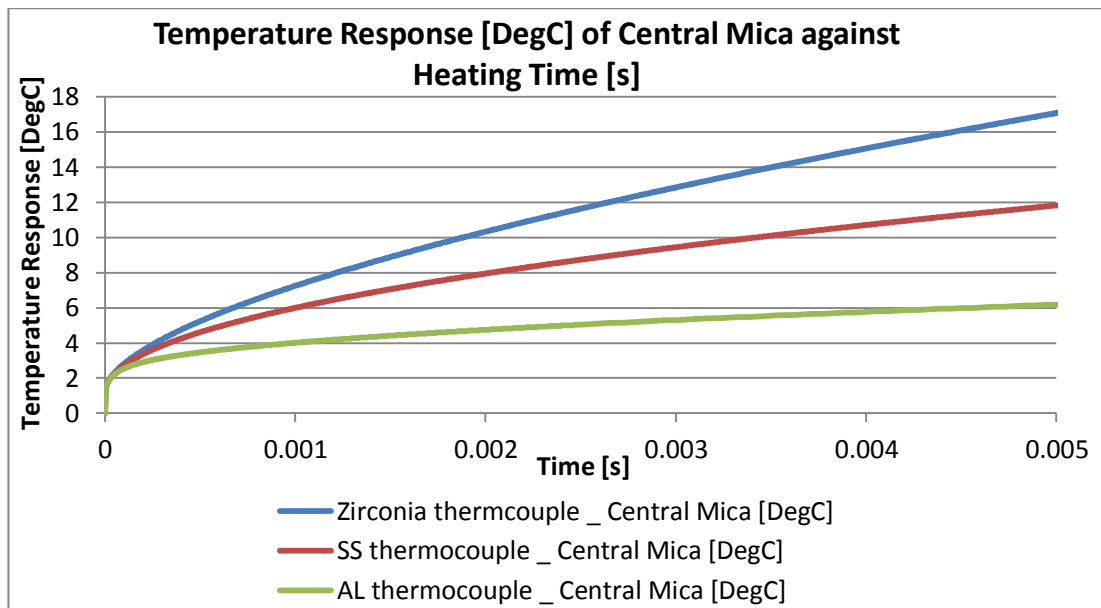
Figure 5.37. Temperature response of central mica of the different thermocouples subjected to a step heat flux of 1 MW/m^2 at the surface.

An interesting observation made from Figure 5.34 on the Aluminium-based thermocouple is that whilst the heat flux computed using the 1D analysis showed a significant negative heat flux after TDC, the heat flux reported using the 2D-Mica consideration showed only very small negative heat flux, very late in the expansion stroke, at around +40 DegCA for the 1400 rpm setpoint. This was also observed by Wang et al. [41], actually to a more significant extent, such that the heat flux barely showed any negative portions. In the classical heat flux research [7] [18], the majority of the studies showed that the heat flux drops to negative values by a significant amount. This was shown to be a result of the combined effect of heat capacity and pressure work in the boundary layer, as documented in Chapter 2. Unfortunately, the majority of the classical heat flux researches were all based on a one-dimensional heat flux assumption, which even back then was known to be inaccurate. As a result, Wang et al. [41] comments that the negative heat flux shown in the classical heat flux research could have been an artefact of the one-dimensional heat flux assumption. One would expect the two-dimensional transient component of heat flux computed in this dissertation to shift further in the positive heat flux axis, by an amount equivalent to that of the steady-state component of heat flux, hence resulting in an even more positive (less negative) total heat flux during the expansion stroke.

215

Whilst two-dimensional heat flux computation on the Aluminium thermocouple showed minimal, or close to no negative heat flux magnitude, the Stainless Steel and the Zirconia thermocouples fitted in the same OEM injector location showed considerable negative heat flux during the expansion stroke, even with two-dimensional consideration. Although the steady-state component of heat flux was not added in Figure 5.34 to Figure 5.36, it is notable that for the Zirconia thermocouple, considering two-dimensional effects resulted in an even higher negative heat flux magnitude to that which resulted from the one-dimensional consideration using Zirconia thermo-physical properties.

Judging by the results obtained from Figure 5.34 to Figure 5.36 and compared to the results of the speedlight testing in Figure 5.18, a modest, but reasonable explanation to the negative heat flux is suggested by the following. Figure 5.18 from speedlight testing shows that in a natural convective environment, the aluminium-based thermocouple cools down the fastest, followed by the Stainless Steel thermocouple, and the Zirconia thermocouple. This means that upon heating to a certain temperature, the Zirconia thermocouple retains the temperature for longer. Keeping this in sight when looking at Figure 5.34 to Figure 5.36, it is observed, that if say the 2D response of the central mica is considered compared to the respective 1D heat flux of the same thermocouple, the Zirconia thermocouple shows the largest negative heat flux magnitude, followed by Stainless Steel and Aluminium. It can therefore be hypothesised that the negative heat flux magnitude is a function of the duration of retainment of the peak surface temperature at the thermocouple surface. This hypothesis is further strengthened by the fact that if the thermocouple surface is retained at a higher temperature for longer, in the meantime, the boundary layer temperatures start dropping significantly (during expansion – as shown later in Chapter 6), which therefore provides a more effective cooling (larger magnitude of negative heat flux) to the still hot thermocouple surface.

5.6.2 Choice of Heat Flux

As noted from Figure 5.34 to Figure 5.36, for each sensor the one-dimensional heat flux reported by the FFT computation is virtually identical to the one-dimensional heat flux reported by the impulse response method. This is understood and expected due to the fact that both computations are based on the semi-infinite solid theory as documented in section 5.1. Both one-dimensional computations were also done with the same split-tapered insert thermo-physical material properties.

The two-dimensional heat flux reported in each of the presented figures depends on the location of the thermocouple junction. This was also reported by Wang et al. [41]. At this point, the researcher is faced with the dilemma of choosing on which material is the thermocouple junction likely situated. According to the previous text, Wang et al. [41] chose the central Mica due to the fact that with the thermocouple tested in his work, the response of the central Mica was close to the thermocouple ribbon materials. He then verified his choice by physically impulse testing the thermocouple using a Quanta-Ray GCR4 Nd:YAG laser system. In this Doctoral work, laser testing could not be carried out. As explained by the physical construction of the eroding thermocouple, the most plausible location of the thermocouple junction should be either on the chromel or the constantan ribbons. This was also explained by Buttsworth [49]. An observation which strengthens this choice can be noted if the heat fluxes reported by the Zirconia thermocouple (fitted in the OEM injector location; Figure 5.36) are compared with the equivalent setpoint reported by the Stainless Steel thermocouple fitted at the same location (Figure 5.35). It is evident that the peak heat fluxes of both sensors reported by the assumption that the junctions lie at the constantan and chromel surfaces match to within 13.6%. This observation was made on all setpoints considered, and it was noted that the deviation of the peak heat fluxes from the two sensors varied between 9.5% and 16.4% across all setpoints tested. A better agreement is seen if the peak heat fluxes from the two sensors are compared on the assumption that the junction lies on the central mica, with deviations between 5.3% and 8.3% across all setpoints tested. Figure 5.38 shows the heat flux at 1400 rpm and 80 bar for the Stainless Steel and Zirconia thermocouples plotted on the same diagram and both are computed based on the assumption that the thermocouple junctions lie at the chromel surface. As can be

seen from this figure, the heat flux reported by the two thermocouples are virtually identical not just at the peak, but throughout the whole cycle, with minor differences only visible at the location of maximum heat transfer from the wall to the gas (*i.e.* at peak negative heat flux). This difference noted at the maximum negative heat flux is greatly reduced at the high engine speed conditions, as shown in Figure 5.39 for 3000 rpm. Based on this deduction, it is concluded that for the 2D heat flux evaluation using the impulse response method, the responses of either the central Mica or Constantan/Chromel should be used. In all the forthcoming analysis, whenever the experimental transient component of heat flux is presented for both the OEM injector location and custom-drilled location, reference would be made to the heat fluxes obtained assuming the 2D Chromel response using the Impulse Response method. The 2D chromel was chosen above the 2D central Mica due to the physical explanation that the junction should reside over the thermocouple element.

Unfortunately, the surface temperature data obtained at the custom-drilled location suffered high magnitudes of electrical noise interference. Since the impulse response method does not have the capability of filtering out the high noise frequency, the 2D Chromel response using the Impulse Response method resulted in large serrations in the computed heat fluxes when the measured temperature was directly processed. Due to this, it was deemed unfit to present these graphs with the large magnitudes of noise interference. Hence, a procedure was adopted whereby the surface temperature measured at the custom-drilled location was first filtered using an FFT scheme which retained only the first 100 harmonics, and the filtered temperature was then processed with the impulse response method using the 2D response of Chromel. This allowed the presentation of a noise-free heat flux, whilst still ensuring that the reported heat flux is not heavily filtered.
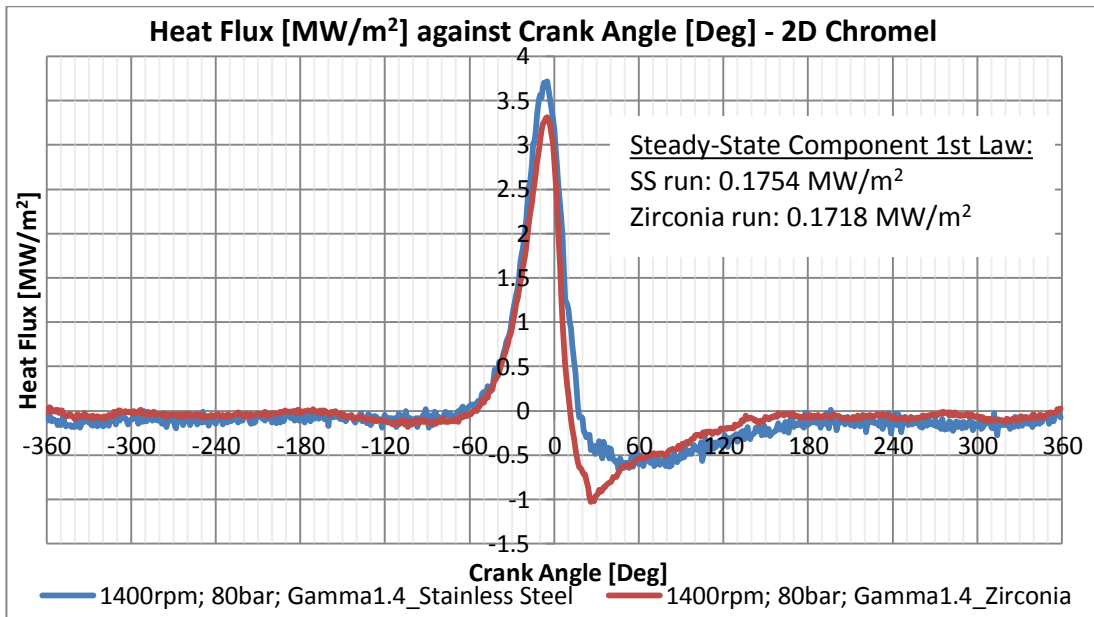
Figure 5.38. Transient component of heat flux acquired from the surface temperatures measured by the SS (Sub-Matrix A5) and Zirconia (Sub-Matrix A2) thermocouples fitted at the OEM injector location, computed using the 2D response of chromel at 1400 rpm, 80 bar.
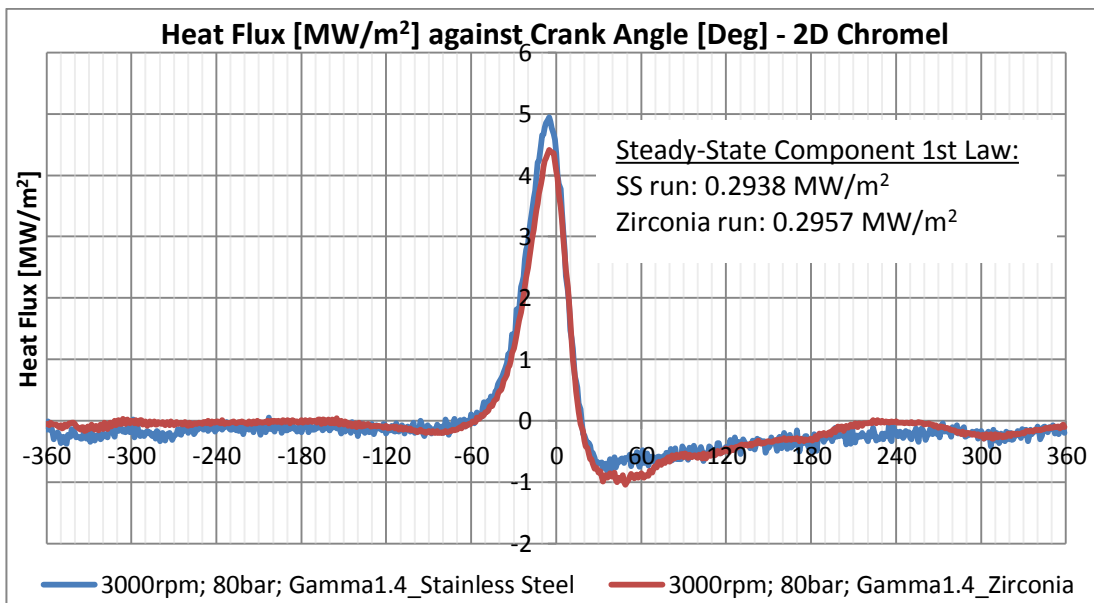
Figure 5.39. Transient component of heat flux acquired from the surface temperatures measured by the SS (Sub-Matrix A5) and Zirconia (Sub-Matrix A2) thermocouples fitted at the OEM injector location, computed using the 2D response of chromel at 3000 rpm, 80 bar.

An interesting, yet not completely understandable observation made from Figure 5.34 to Figure 5.36, is that the transient component of heat fluxes reported by the Aluminium thermocouple seems to be considerably higher than those reported by the Stainless Steel and Zirconia thermocouples fitted at the same OEM injector location.

The heat fluxes reported by the Aluminium thermocouple seem to lie in ranges which are synonymous to fired CI engine operation [36] [72], or possibly even higher. Considering the construction and fitment of this thermocouple compared to the Zirconia and Stainless Steel, it should be said that the Aluminium thermocouple was fitted in a dedicated adaptor, different than that used by the other two thermocouples. Whilst the Aluminium thermocouple used a separate adaptor, the design of the adaptor was virtually identical to that for the Zirconia and SS thermocouple adaptor. The only difference was in the bore diameter, which was made to accommodate the 1/4" size of the Aluminium thermocouple. Due to design constraints, the Aluminium thermocouple had to be mounted with an annular gap of 0.5 mm between its circumference and the cylinder head injector hole wall for an axial length of approximately 20 mm. Whilst no evidence is available in this work, it might be possible that the periodic pressure fluctuation of the gas in the described crevice might have, to some extent, augmented the heat flux recorded by the probe [18]. On the other hand, in the case of the Zirconia and Stainless Steel thermocouples the gap between the thermocouple and the injector hole wall was filled with an aluminium sleeve designed as part of the adapter, hence this problem was eliminated.

Another factor which could have augmented the heat flux reported by the Aluminium thermocouple is also traced down to the fitment of the thermocouple. As discussed in an earlier section, the thermocouples fitted in the OEM injector location were inclined at a small angle to the cylinder head surface, according to the OEM injector hole inclination. This meant that for the thermocouples at this location to be flush with the cylinder head surface, the thermocouple surface had to be ground at an angle. It is claimed by the manufacturer that such procedure is supported by the thermocouples used. Unfortunately, however, in preliminary work it was found that eroding the thermocouple by around 1 mm, resulted in a permanent open junction due to the fact that the ribbons deviated radially away from each other with axial length, as shown in the microscope image in Figure 5.40. This was probably a defect in the sensor assembly, however to prevent troubles arising from this situation, the thermocouples at the OEM injector location were not sanded flush with the cylinder head surface. Instead, the protruding length was minimised by distributing the protrusion to above and below the cylinder head surface (see Figure 3.17). With this method, the protrusion of the Stainless Steel and Zirconia thermocouples above the

surface was just 0.7 mm, due to their small 1/8" diameter. Since the Aluminium thermocouple had a larger diameter of 1/4", logically the protrusion above the surface was twice as big as that for SS and Zirconia. Hence, the 1.4 mm protrusion above the cylinder head surface of the Aluminium thermocouple could have disturbed the local gas flow conditions at the installation location.
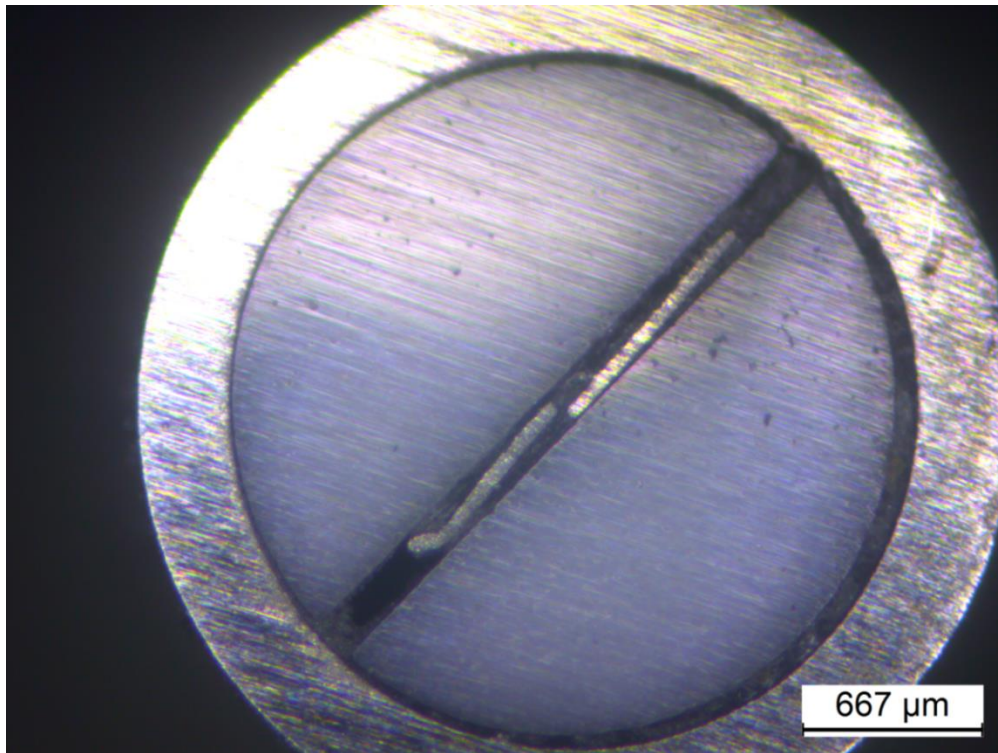
Figure 5.40. Microscope image showing the thermocouple ribbons separated radially.

5.6.3 Thermocouple material effect on the average surface temperature

Table 5.12 shows the mean surface temperature from the three tested thermocouples at the OEM injector location and the Zirconia thermocouple at the custom-drilled location. It is evident that some discrepancies arise between the three different OEM injector thermocouples. This is expected due to the fact that each thermocouple has different thermo-physical properties. By the foregoing explanation, it is therefore expected that the Aluminium thermocouple should give the most accurate representation of the surface temperature at the location of interest (OEM injector location). Table 5.12 shows that the Stainless Steel-based thermocouple reports a mean temperature of up to 7% higher than that reported by the Aluminium-based thermocouple. The Zirconia-based thermocouple fitted at the OEM injector location

reported an average surface temperature of up to 20% higher than the Aluminium-based thermocouple. It is also interesting to note that at the custom-drilled location using the Zirconia thermocouple, the temperature recorded is around 33% smaller than that measured by the Zirconia thermocouple at the OEM injector location. This discrepancy between the two measurements can be attributed to at least two factors; spatial differences (which are common and well observed in literature), and/or the possibility that the thermocouples at the OEM injector location are not truly measuring the surface temperature, but biased towards the boundary layer temperature due to their small protrusion above the cylinder head surface.

Table 5.12. Average of the measured surface temperatures.

Average of Measured Surface Temperatures [K]			PCP [bar]			
			80 bar		100 bar	
			γ			
			1.4	1.6	1.4	1.6
OEM injector Aluminium thermocouple	Engine Speed [rpm]	1400	493.9	616.2	507.1	642.0
		3000	542.1	727.0	563.0	767.0
OEM injector Zirconia thermocouple		1400	550.2	742.5	559.3	764.4
		3000	594.4	844.5	609.4	881.2
OEM injector Stainless Steel thermocouple		1400	515.5	661.2	526.5	682.1
		3000	554.9	741.5	571.6	765.8
Custom-Drilled Zirconia thermocouple		1400	370.6	399.8	379.8	411.5
		3000	402.2	443.4	417.8	461.0

5.7 Parametric Study Results

In this section, the results of a parametric study on heat flux and surface temperature are presented. The results were mainly acquired from a testing session described by the test matrix presented earlier by Table 5.4 (Test Matrix B) in section 5.4, and explained by Table 5.5 to Table 5.7. Throughout this test matrix, the Aluminium thermocouple was fitted at the OEM injector location and the Zirconia thermocouple was fitted at the custom-drilled location. Due to the high magnitudes of heat flux that resulted from the Aluminium thermocouple, it is advised that the results from this thermocouple should only be viewed in a comparative manner. In some cases where data was available, results acquired from the test matrix defined by Table 5.3 (Test Matrix A) are also presented from the Stainless Steel-based and Zirconia-based thermocouples at the OEM injector location.

5.7.1 Heat Flux Variation with Engine Speed

The dependence of ensemble surface temperature and heat flux on engine speed is important due to its direct relation with piston speed, and hence convective heat transfer coefficient. In this study, four engine speeds were tested ranging from 1400 rpm to 3000 rpm. In previous studies on motored engines, the general conclusion was that increasing the engine speed results in higher total heat flux. This was shown by Dao et al. [25] and Annand and Pinfold [125] in early heat transfer studies. On this observation, several quasi-steady heat transfer models [5] [11], including the one by Annand [8] [19] himself were formulated to give higher heat transfer rates with an increase in engine speed. In a recent study by Torregrosa et al. [7], even though the general trend agrees with that of the two previous authors; two particular engine speeds showed a trend in which heat flux stayed constant with an increase in engine speed. In another recent study by Hennes et al. [40] conducted on a fired CI engine, a definite and consistent relationship of decreasing heat flux magnitudes with an increase in engine speed was noted. A similar relationship was reported by Hoag [36].

In this study, the transient component of heat flux variation with engine speed was obtained from several separate test campaigns. The results presented and discussed in this section are those obtained from the test matrix defined by Table 5.4 (Test Matrix B - not considering Argon (γ 1.67), and tests with air at 60℃ and 95℃). Hence, eight testing campaigns were investigated for the transient component of heat flux variation with engine speed. Four test campaigns with air as the working gas, at four different PCPs (sub-matrix B1), and another four test campaigns with two different working gases γ 1.50 and γ 1.60, where each gas was tested at two different PCPs (sub-matrix B2).

Figure 5.41 and Figure 5.42 show the variation of ensemble temperature and transient component of heat flux with engine speed from sub-matrix B1, recorded by the Aluminium thermocouple fitted in the OEM injector location. Figure 5.43 and Figure 5.44 show the average surface temperature recorded by the Aluminium thermocouple (OEM injector location) and the Zirconia thermocouple (custom-drilled location) respectively, while Figure 5.45 gives the steady-state component of

heat flux from the 1st law at the same sub-matrix B1. The general engine average temperatures for the presented results of sub-matrix B1 are given in Table 5.13.

Figure 5.46 to Figure 5.48 show the ensemble temperature and transient component of heat flux recorded by the Zirconia thermocouple at the custom-drilled location recorded from sub-matrix B2. Table 5.14 gives the measurements of general engine average temperatures from this presented sub-matrix B2.

For these eight testing campaigns presented the same abrasion on both thermocouples was maintained throughout each individual engine speed test spectrum. The thermocouples abrasions were however renewed between each of the eight testing campaigns.

From the average value of surface temperature at different engine speeds presented in Figure 5.43, it is evident that an increase in engine speed results in shifting the average value of the ensemble surface temperature to higher magnitudes. The rate of increase in the surface temperature decreases with an increase in engine speed. This is physically understandable through the theory that increasing the engine speed results in less time for heat to flow out of the cylinder, which hence yields a higher surface temperature. Boundary layer phenomena are also expected to change with engine speed, particularly the fact that increasing the engine speed results in less time for the capacitive nature of the boundary layer to store heat from the bulk gas.

Unlike the average value of surface temperature, the surface temperature swings, do not show a consistently increasing trend with increasing engine speed. This is also reflected in the computed transient heat flux component. At the OEM injector location (Figure 5.41 and Figure 5.42), the temperature swing and transient component of heat flux were relatively insensitive to the variation in engine speed, with only small variations at the peak that were random. On the other hand, at the custom-drilled location a more identifiable trend was noted where the transient component of heat flux increases with engine speed, especially in Figure 5.47 and Figure 5.48.

The steady-state component of heat flux (computed from the 1st law analysis) reported in Figure 5.45 increases with an increase in engine speed. This is understandable and attributed to the fact that increasing the engine speed results in

higher convection due to the gas motion resulting from the piston velocity. The rate of increase of the steady-state component of heat flux seems to decrease with an increase in engine speed.

The above analysis of surface temperature and heat transfer with engine speed needs to be viewed in the context of the thermal condition of the engine. For this to be possible the reader is encouraged to analyse Table 5.13 and Table 5.14 which give the average temperature of the shunt pipe, coolant temperature, oil temperature and recessed temperature at the respective setpoints. It is noted that whilst the coolant and oil temperatures are constant with only very small setpoint deviations, the shunt pipe temperatures varied significantly between one engine speed setpoint and another. The variation in shunt pipe temperature shows a monotonic increase with an increase in engine speed. A higher shunt pipe temperature supposedly results in a higher gas temperature at intake BDC which consequently yields a higher gas temperature along the compression and expansion strokes, especially around TDC. This hints that an increase in shunt pipe temperature is expected to result in a higher wall temperature, and possibly a higher heat flux. Even though the effect of shunt pipe temperature on temperature swing and heat flux was not experimentally studied in this dissertation, it should be remembered that the experimental results shown at different engine speeds possibly have an underlying effect originating from the different shunt pipe temperatures.
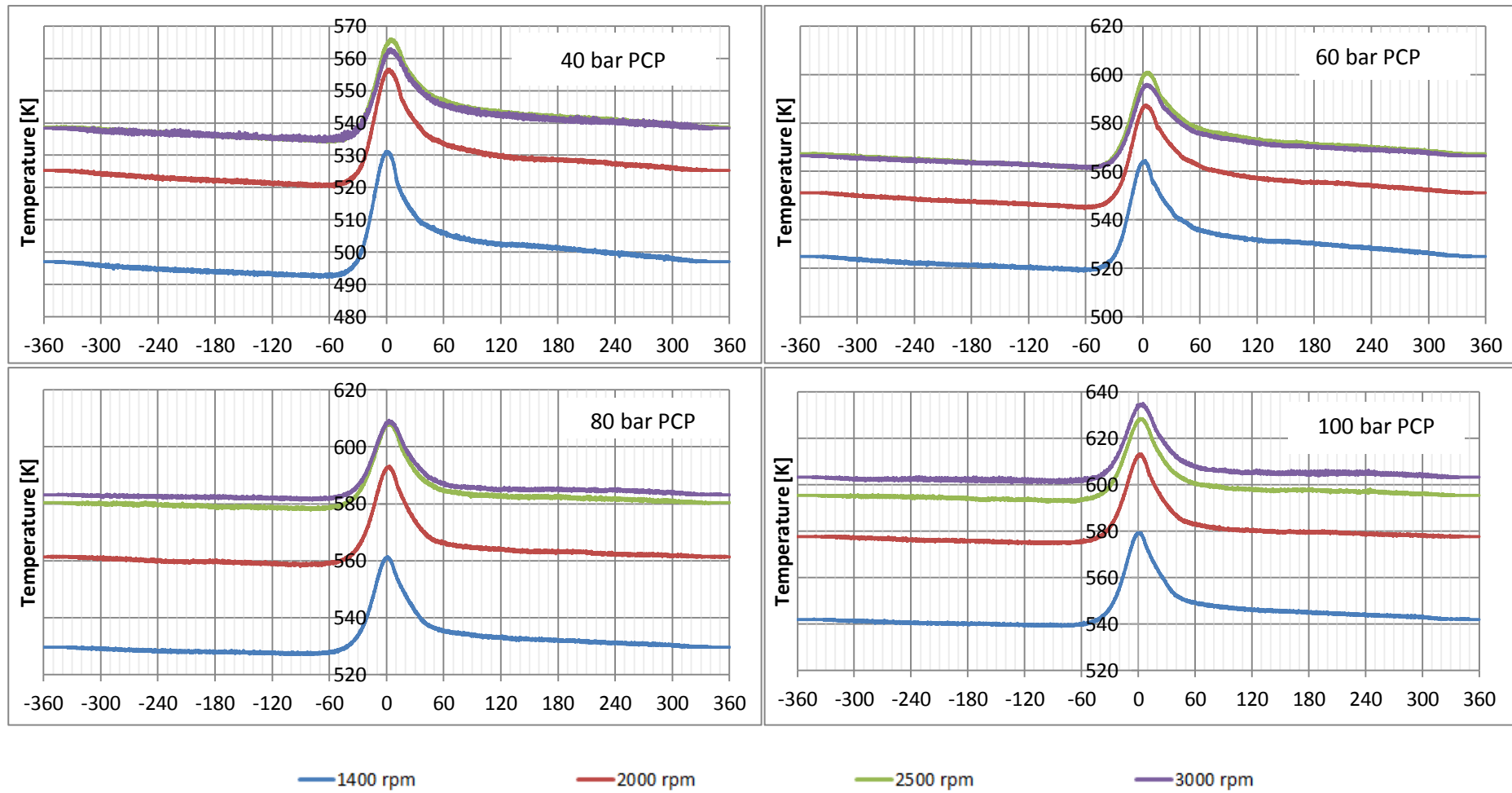
Figure 5.41. Ensemble surface temperature (K) recorded by the Aluminium eroding thermocouple at the OEM injector location against crank angle (Deg), with air as the working gas (Sub-Matrix B1). (see Table 5.13).
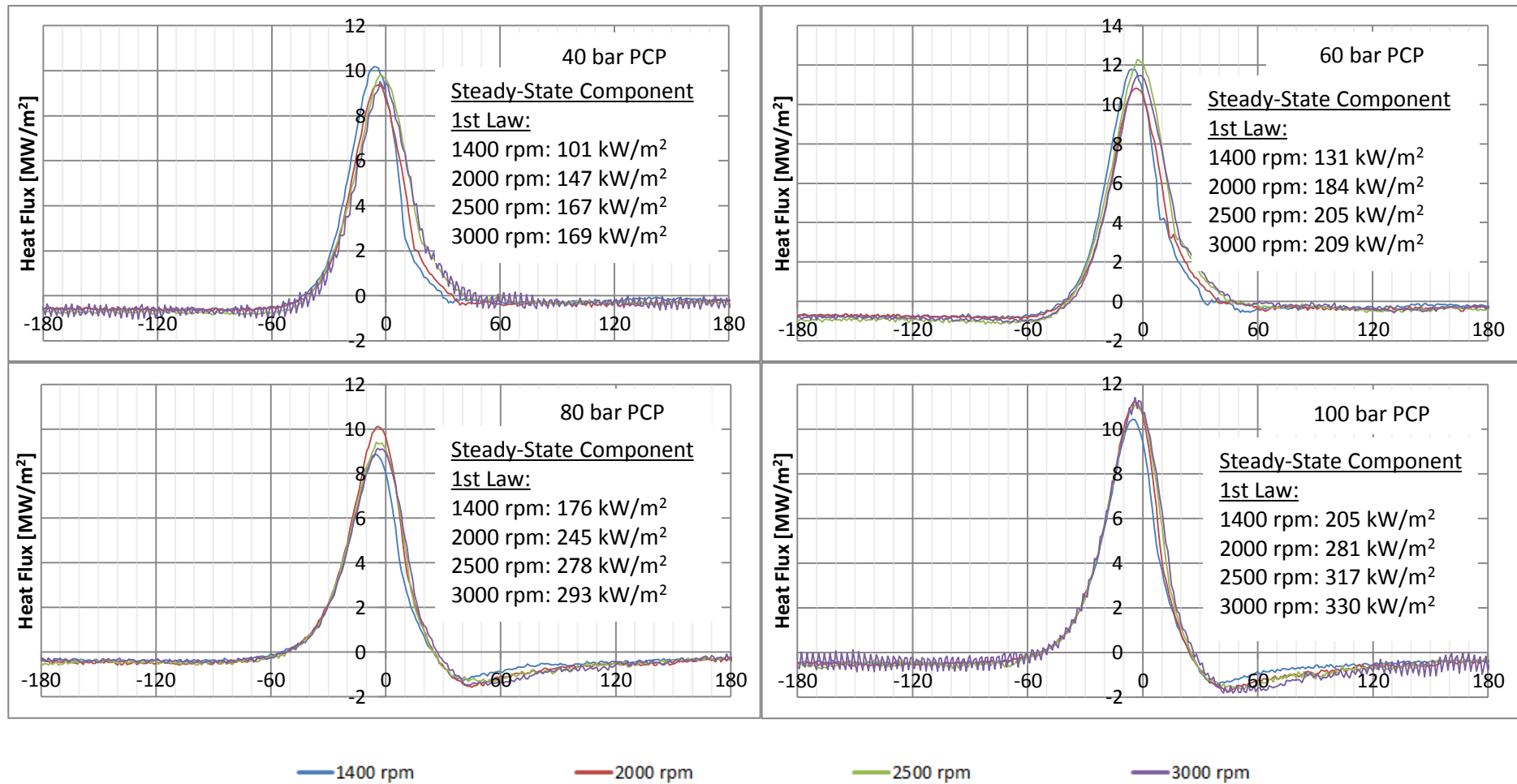
Figure 5.42. Transient component of heat flux (MW/m^2) recorded by the Aluminium eroding thermocouple at the OEM injector location against crank angle (Deg), with air as the working gas (Sub-Matrix B1). The heat flux is computed using 2D response of Chromel. (see Table 5.13).
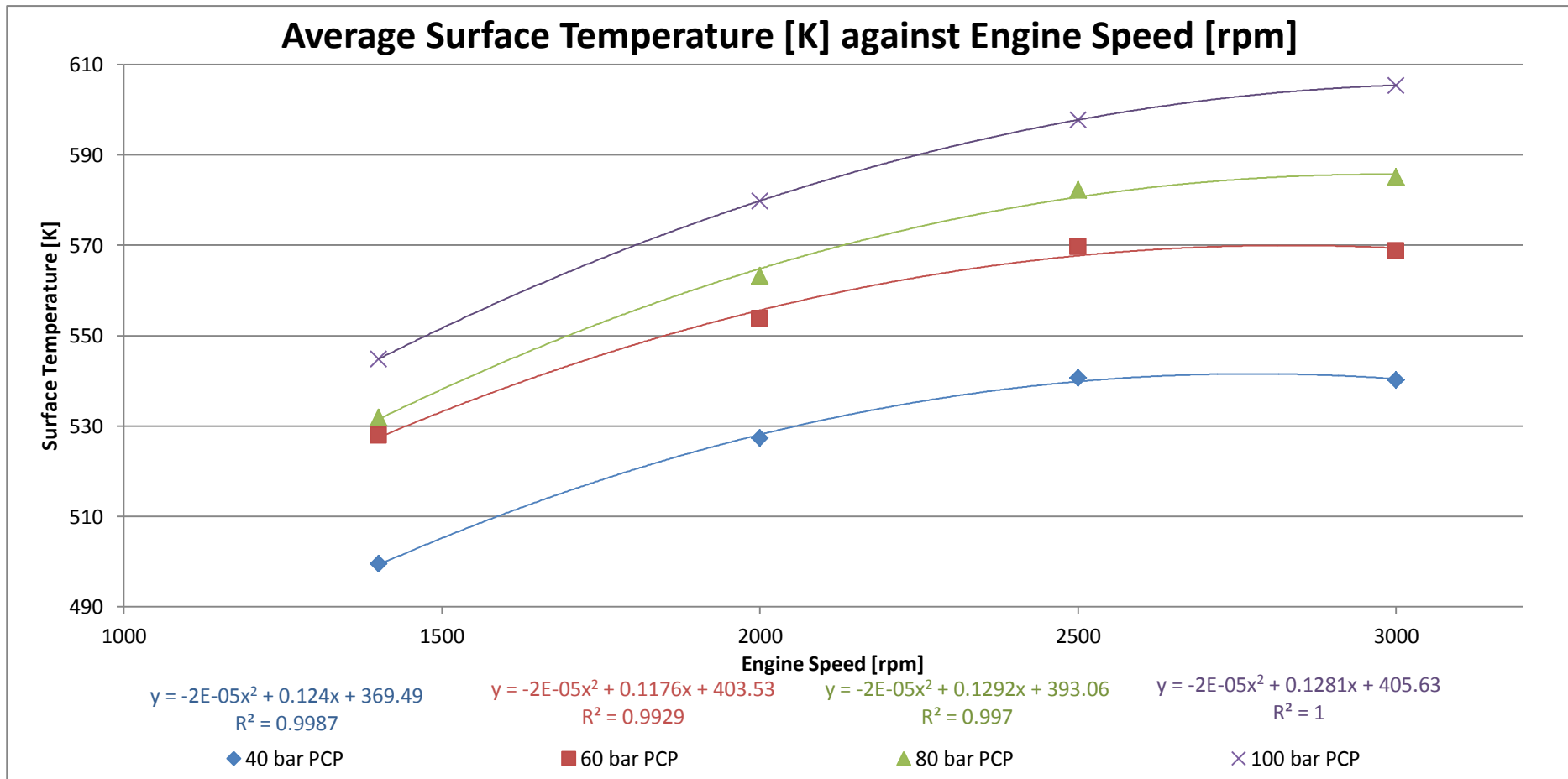
Figure 5.43. Average surface temperature measured by the Aluminium surface thermocouple at the OEM injector location at different engine speeds, with air as the working gas (Sub-Matrix B1).
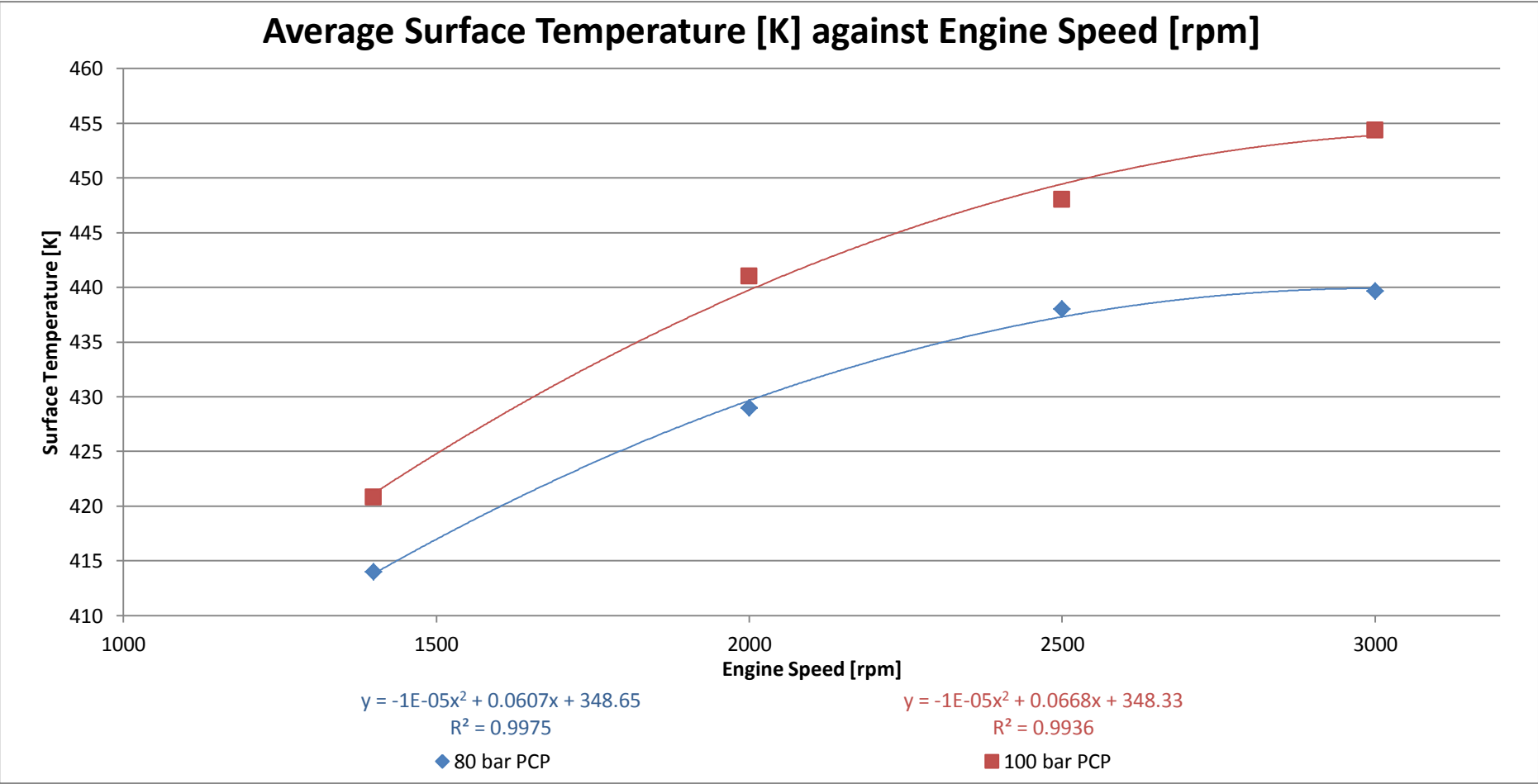
Figure 5.44. Average surface temperature measured by the Zirconia surface thermocouple at the custom-drilled location at different engine speeds, with air as the working gas (Sub-Matrix B1).
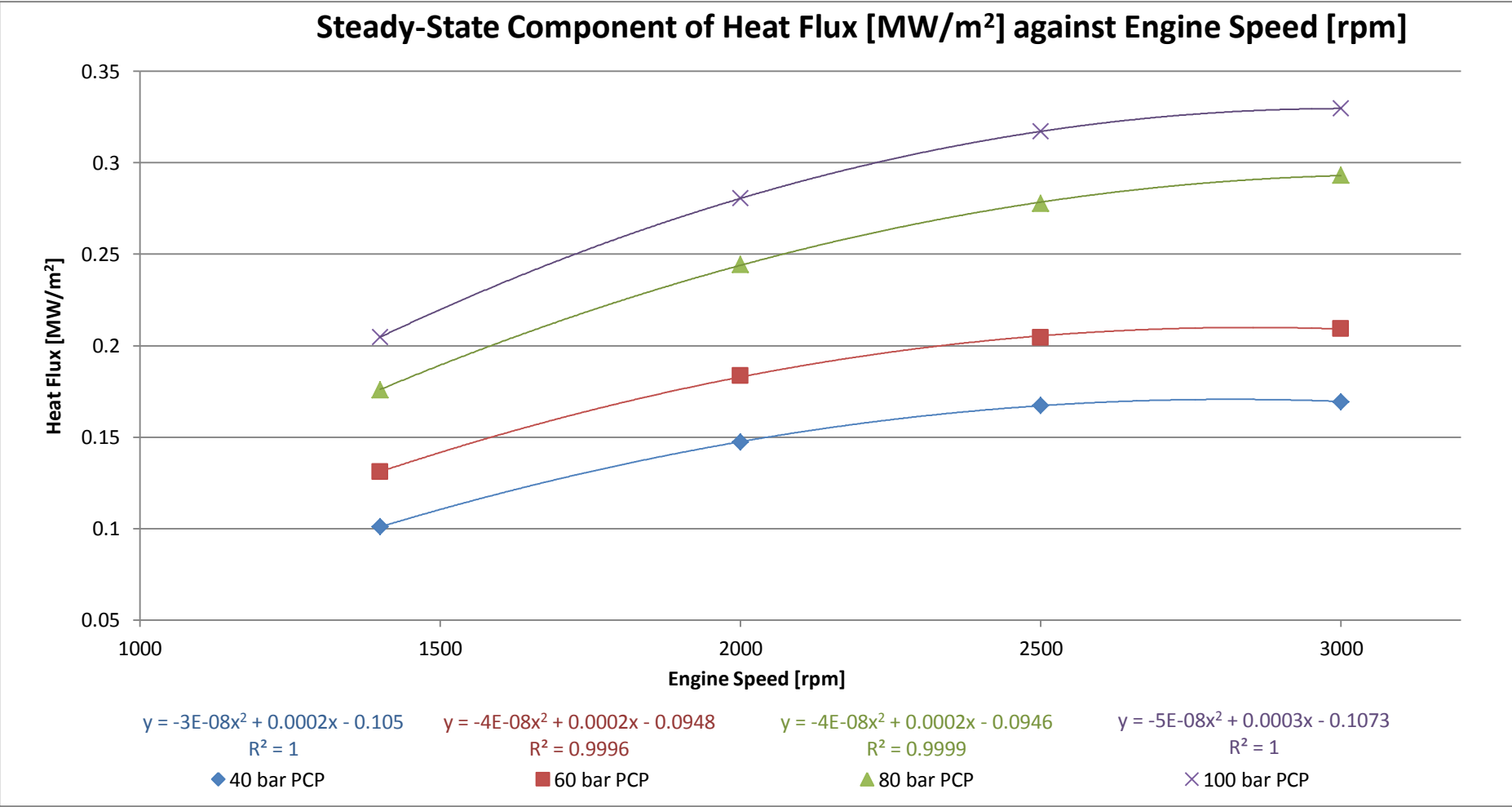
Figure 5.45. Steady-State component of heat flux as computed from the first law at different engine speeds (Sub-Matrix B1).

Table 5.13. Slow speed data for the ensemble temperatures and heat fluxes given in Figure 5.41 and Figure 5.42. (Sub-Matrix B1).

	PCP [bar]															
	40				60				80				100			
Engine Speed [rpm]	1400	2000	2500	3000	1400	2000	2500	3000	1400	2000	2500	3000	1400	2000	2500	3000
Shunt Intake Exposed Temperature	48.1	48.0	52.4	56.3	53.9	51.1	53.8	62.2	44.5	50.2	57.6	73.4	45.7	53.7	61.0	80.9
Shunt Exhaust Temperature [°C]	52.0	57.1	61.4	75.1	56.3	60.1	63.7	82.5	51.1	59.1	66.4	88.4	51.5	62.3	68.7	95.3
Coolant Temperature [°C]	79.8	80.6	78.8	80.4	80.4	78.6	79.6	80.6	80.4	79.7	80.6	77.9	78.5	81.2	79.2	78.7
Oil Gallery Temperature [°C]	78.8	80.2	80.8	82.6	81.4	81.9	81.4	82.2	79.3	81.5	81.2	81.0	79.1	79.7	80.4	80.7
Recessed Temperature [°C]	81.9	85.8	81.6	84.5	82.7	81.8	83.7	85.4	84.3	84.9	85.7	85.1	82.5	87.0	85.7	87.1
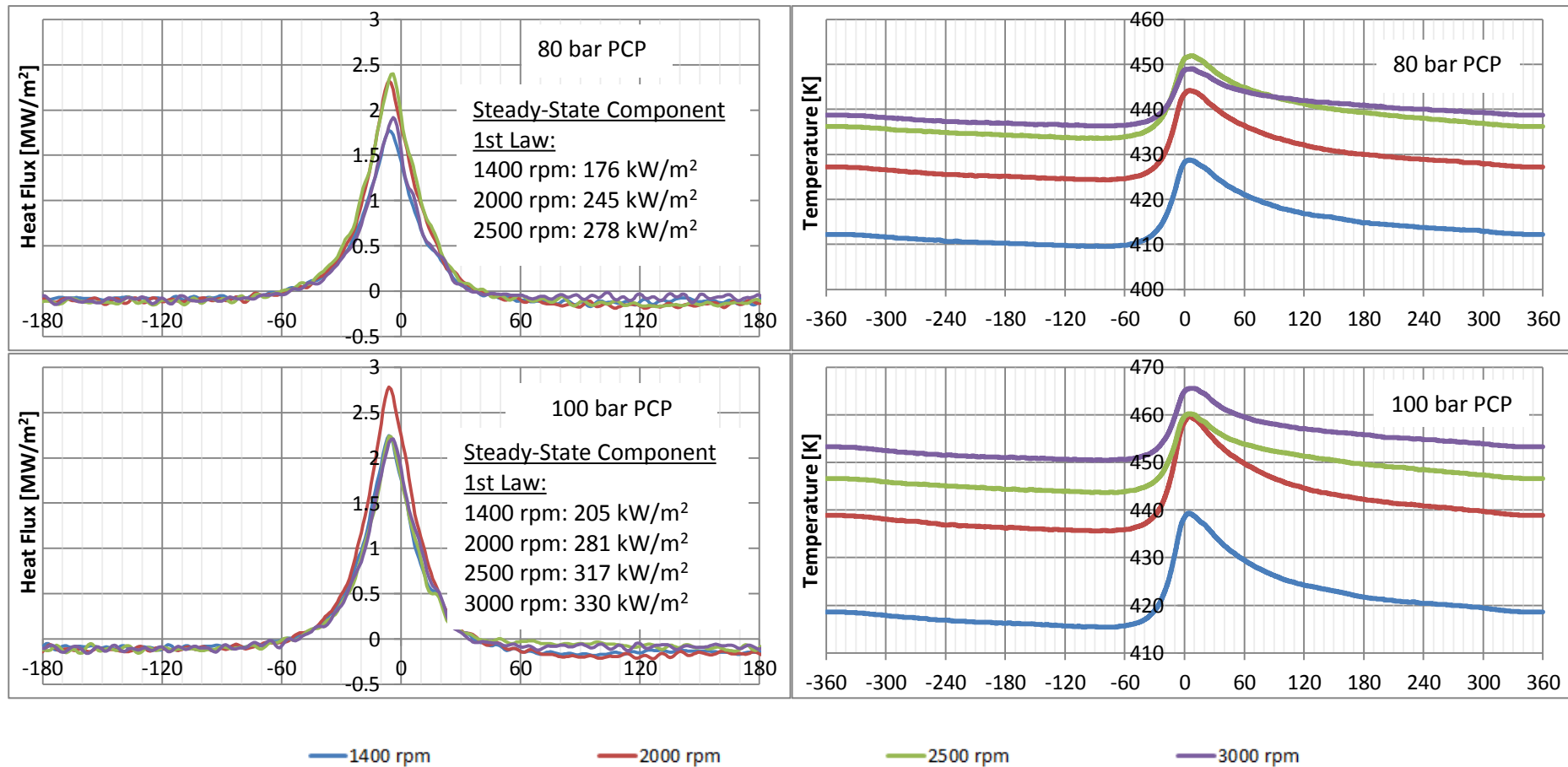
Figure 5.46. Transient component of heat flux (MW/m^2) and ensemble surface temperature (K) against crank angle (Deg), recorded by the Zirconia eroding thermocouple at the custom-drilled location with air as the working gas (Sub-Matrix B2). The heat flux is computed using 2D response of Chromel. See Table 5.14.
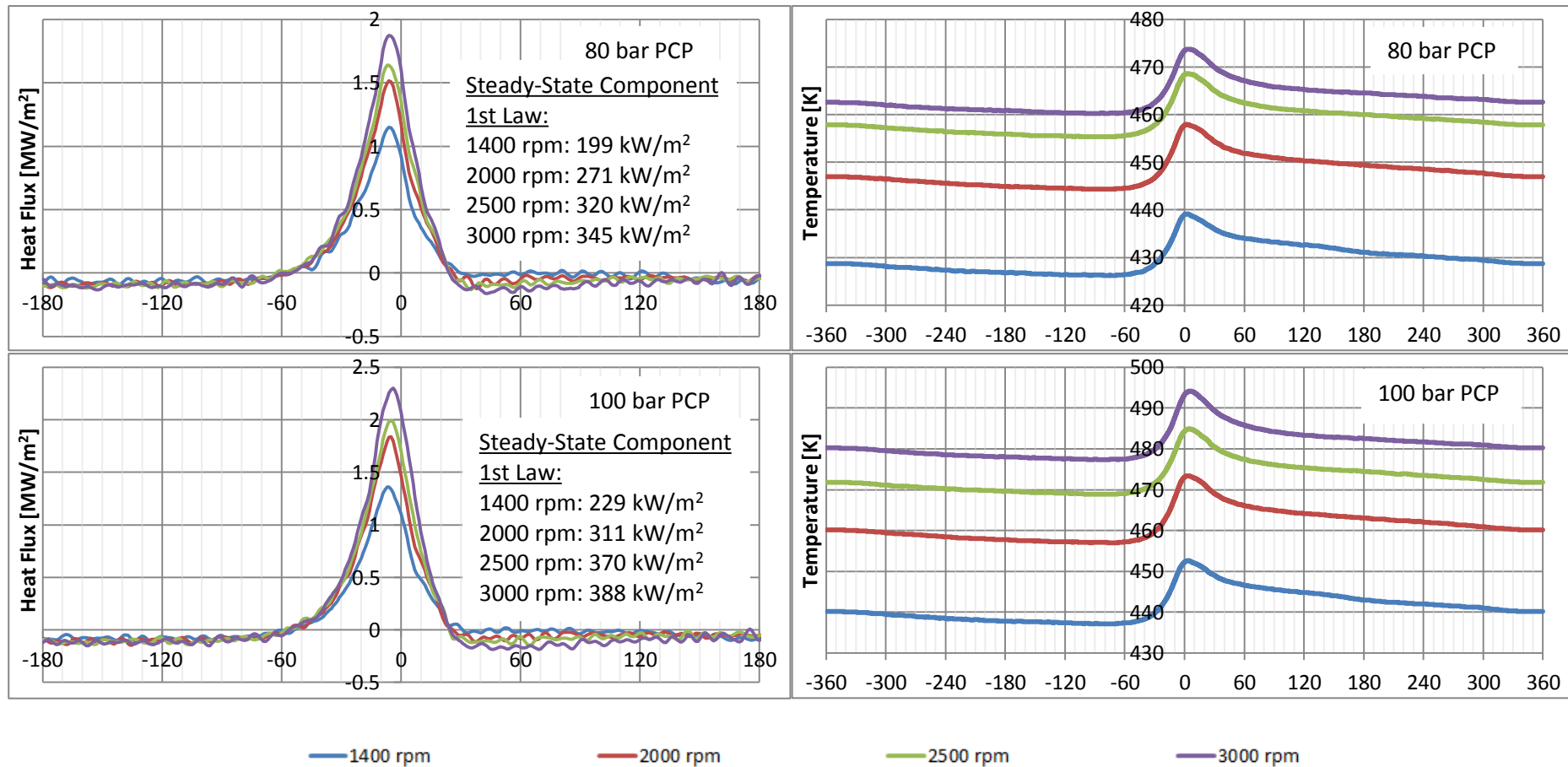
Figure 5.47. Transient component of heat flux (MW/m^2) and ensemble surface temperature (K) against crank angle (Deg), recorded by the Zirconia eroding thermocouple at the custom-drilled location, with working gas of γ: 1.5 (Sub-Matrix B2). The heat flux is computed using 2D response of Chromel. See Table 5.14.

233
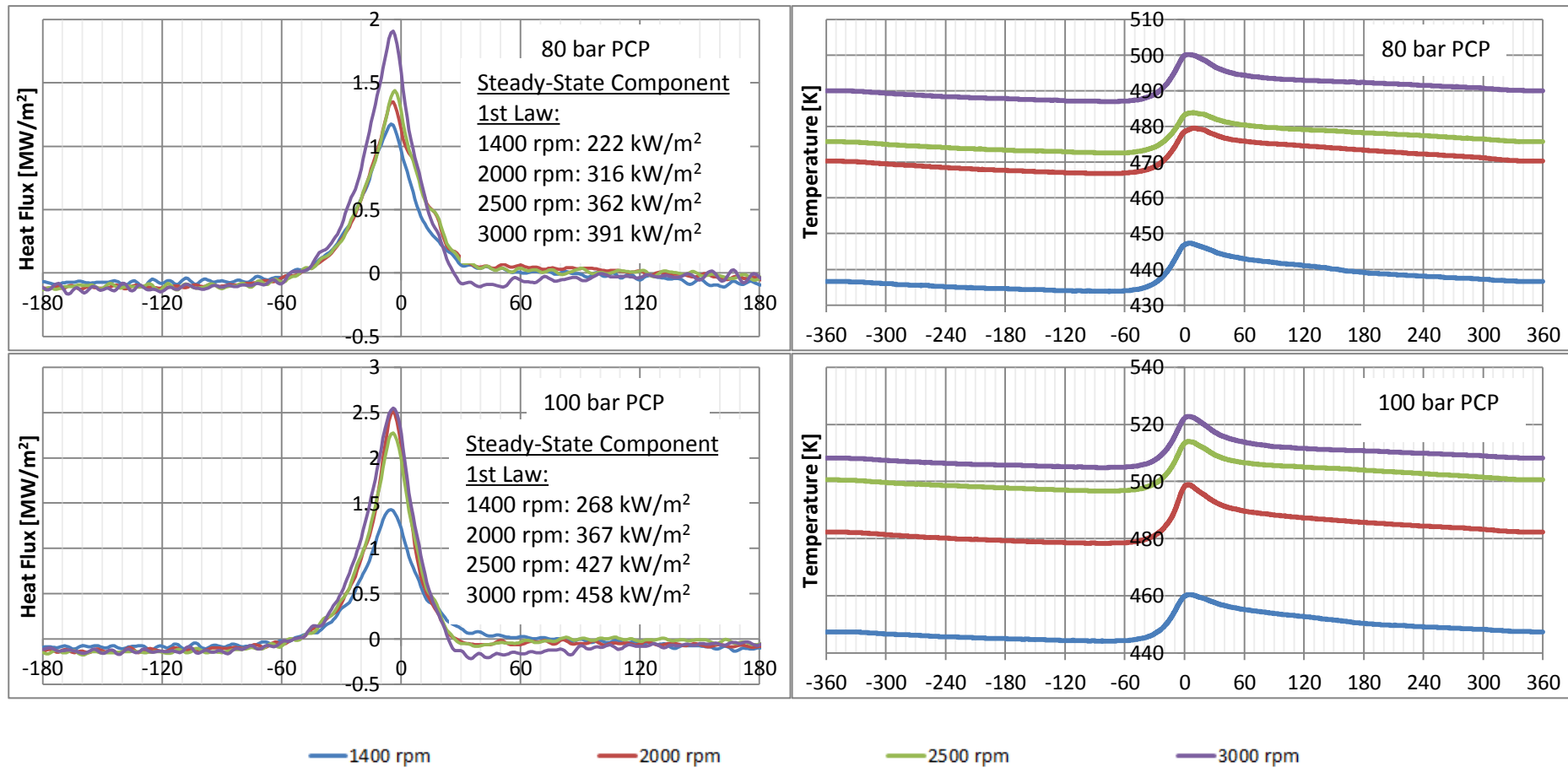
Figure 5.48. Transient component of heat flux (MW/m^2) and ensemble surface temperature (K) against crank angle (Deg), recorded by the Zirconia eroding thermocouple at the custom-drilled location, with working gas of γ: 1.6 (Sub-Matrix B2). The heat flux is computed using 2D response of Chromel. See Table 5.14.

234

Table 5.14. Slow speed data for the ensemble temperatures and heat fluxes given in Figure 5.46, Figure 5.47 and Figure 5.48. Sub-Matrix B2.

	Ratio of Specific Heats γ																								
	1.40								1.50								1.60							
	PCP [bar]																								
	80 bar				100 bar				80 bar				100 bar				80 bar				100 bar			
Engine Speed [rpm]	1400	2000	2500	3000	1400	2000	2500	3000	1400	2000	2500	3000	1400	2000	2500	3000	1400	2000	2500	3000	1400	2000	2500	3000
Shunt Intake Exposed Temperature [°C]	44.5	50.2	57.6	73.4	45.7	53.7	61.0	80.9	41.8	47.1	60.3	67.7	43.4	51.4	63.1	75.9	41.9	48.2	53.4	67.0	42.4	46.6	61.2	69.9
Shunt Exhaust Temperature [°C]	51.1	59.1	66.4	88.8	51.5	62.3	68.7	95.3	50.2	57.1	73.4	82.4	51.6	61.1	75.9	90.3	70.8	58.1	73.7	85.5	51.2	57.2	79.7	89.2
Coolant Temperature [°C]	80.4	79.7	80.6	77.9	78.5	81.2	79.2	78.7	81.9	79.9	81.2	79.9	81.9	79.5	81.7	80.1	81.4	83.5	81.7	79.5	78.5	80.8	79.6	79.7
Oil Gallery Temperature [°C]	79.3	81.5	81.2	81.0	79.1	79.7	80.4	80.7	79.5	79.6	80.0	80.8	80.9	80.2	79.5	81.3	79.7	81.4	81.5	80.9	80.7	79.7	80.9	81.2
Recessed Temperature [°C]	84.3	84.9	85.7	85.1	82.5	87.0	85.7	87.1	85.3	85.5	87.8	87.1	86.2	86.0	88.8	89.6	85.3	89.2	87.9	88.1	83.2	87.9	88.5	89.6

5.7.2 Heat Flux Variation with PCP

The surface temperature and heat flux variation with an increase in peak in-cylinder pressure is one of importance as it gives a measure of the thermal load variation with pressure load variation. In a previous study by Torregrosa et al. [7], in which the authors made use of pressurised motoring, it was reported that the average surface temperature, as well as total heat flux show a clear increase with an increase in PCP. This was also reported earlier by Overbye et al. [13] and Annand and Pinfold [125].

The surface temperature and heat flux variations with PCP were studied over the range from 60 bar to 100 bar at speeds varying from 1400 rpm to 3000 rpm. The temporal variations of surface temperature and transient component of heat flux recorded by the Aluminium thermocouple at the OEM injector location from sub-matrix B1 are given in Figure 5.49 and Figure 5.50, using air as the working gas. For the same setpoints, the average surface temperature recorded by the Aluminium thermocouple at the OEM injector location and the steady-state component of heat flux computed by the 1st law are given in Figure 5.51 and Figure 5.52 respectively.

Figure 5.50 shows that the transient components of heat flux are relatively identical throughout the whole cycle for different PCPs, except for a period at and around compression TDC, where the heat flux increases from 40 bar PCP to 60 bar PCP with roughly the same quantity as that from 80 bar PCP to 100 bar PCP. Oddly, the heat flux for the 80 bar falls below that of the 40 bar, and consequently the heat flux for the 100 bar falls below that of the 60 bar. This relationship might seem strange at first glance however it can be traced down to a physical reason. The tests at 80 bar and 100 bar were done on the 10th of July 2020, with the same thermocouple abrasion and junction resistance of 2.3 Ohms. The sensor showed a rise time of 0.56 ms. The 40 bar and 60 bar tests were done on the 20th of July 2020, sharing the same junction abrasion. The junction abrasion for the 40 bar and 60 bar was however different than that of the 80 bar and 100 bar testing. The junction resistance recorded at the 40 bar and 60 bar testing was 5.1 Ohms with a sensor rise time of 0.28 ms. The temperature response before and after each test matrix is given in Figure 5.53, where it is clearly shown that the junction set up for the 40 bar and 60 bar testing showed a faster thermocouple junction than that set up for the 80 bar and 100 bar. Although a

sensor rise time of 0.56 ms is still significantly faster than the rise times expected for engine operation, this change in rise time hints a strong possible difference between the two junctions (possible oxidation or difference in distribution and proximity to Mica). This observation in the junction rise times is consistent with the observation made on the two engine heat flux data sets in Figure 5.50. The 40 bar and 60 bar data seems to report an overall higher heat flux than the 80 bar and 100 bar data set, hence it is thought that the junction at the 80 bar and 100 bar testing might have attenuated the true temperature swing.

Looking at the data obtained with air as the working gas at 40 bar and 60 bar PCP, separately from that at 80 bar and 100 bar, it can be safely stated that the heat flux in pressurised motored operation increases with an increase in PCP. This statement is being made on evaluating also heat flux data with PCP variation using gases with ratios of specific heats of 1.50 and 1.60 (at room temperature), taken on different days and with different thermocouple abrasions than the two data sets discussed above. Figure 5.54 to Figure 5.61 show the surface temperature and heat flux variations with PCP taken with the Aluminium thermocouple at the OEM injector location, and with the Zirconia thermocouple at the custom-drilled location from sub-matrix B2. The same trend of increasing peak heat flux with increasing PCP was noted in two other test sessions and using the Zirconia and Stainless Steel thermocouples at the OEM injector location. These results are not shown here for the sake of limiting the number of presented graphs.

In analysing the presented ensemble temperature and heat flux, it is recommended that the reader also refers to the previously presented Table 5.13 and Table 5.14 for the corresponding temperatures of the shunt pipe, coolant and oil.

The compiled average surface temperature from Figure 5.49, presented in Figure 5.51 shows that the average surface temperature increases linearly with an increase in PCP. Similarly, the steady-state component of heat flux as computed from the first law and given in Figure 5.52 also shows a linear increase with an increase in PCP. This linear trend of the steady-state component of heat flux with PCP is synonymous to the trends of $IMEP_{360}$ with PCP presented in Chapter 4, in Figure 4.51.
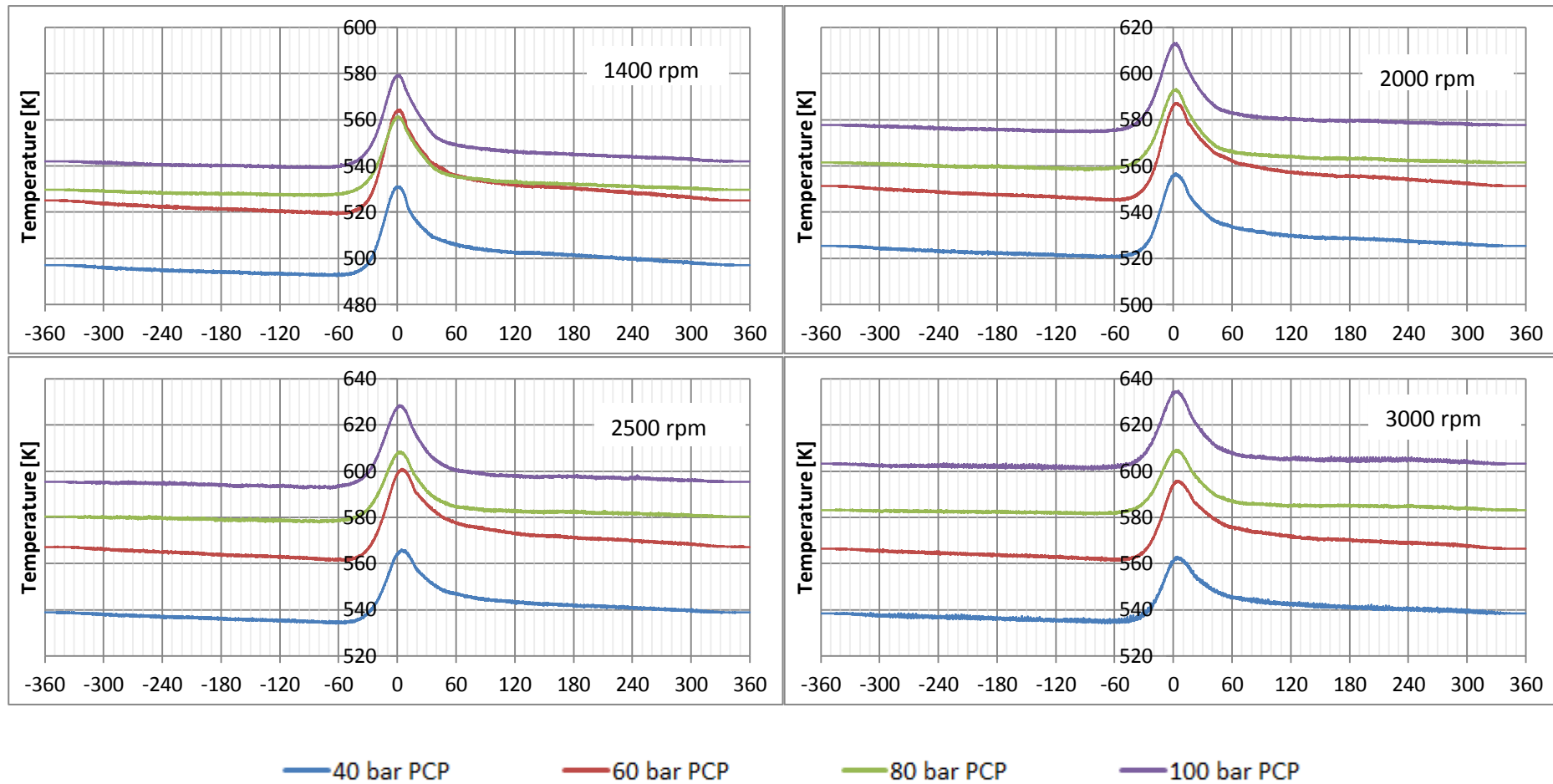
Figure 5.49. Ensemble surface temperature (K) against crank angle (Deg), recorded by the Aluminium eroding thermocouple at the OEM injector location, with air as the working gas (Sub-Matrix B1). Refer to Table 5.13 for the corresponding thermal condition of the engine.
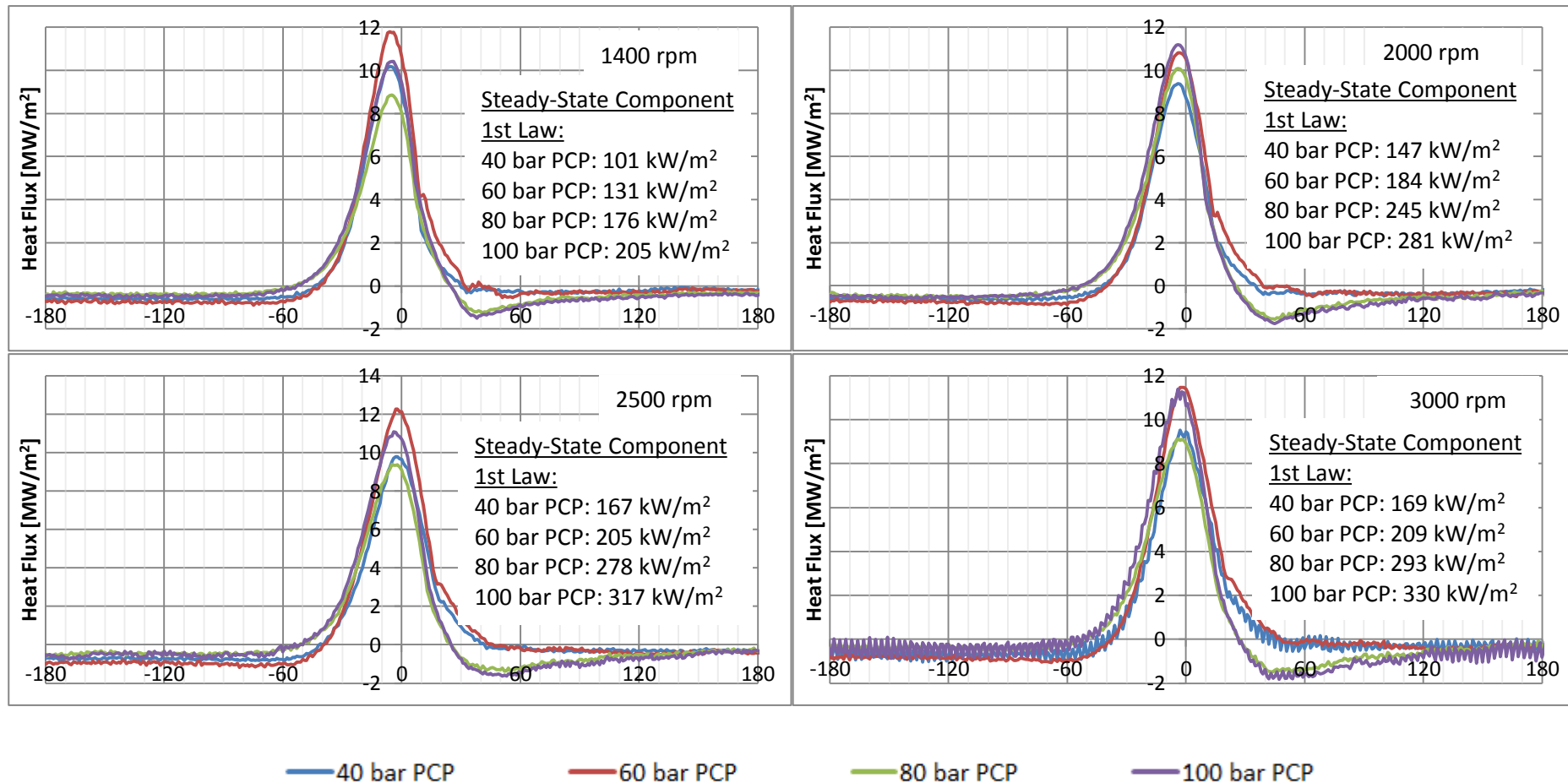
Figure 5.50. Transient component of heat flux (MW/m2) against crank angle (Deg), recorded by the Aluminium eroding thermocouple at the OEM injector location, with air as the working gas (Sub-Matrix B1). The heat flux is computed using 2D response of Chromel. Refer to Table 5.13 for the corresponding thermal conditions of the engine.
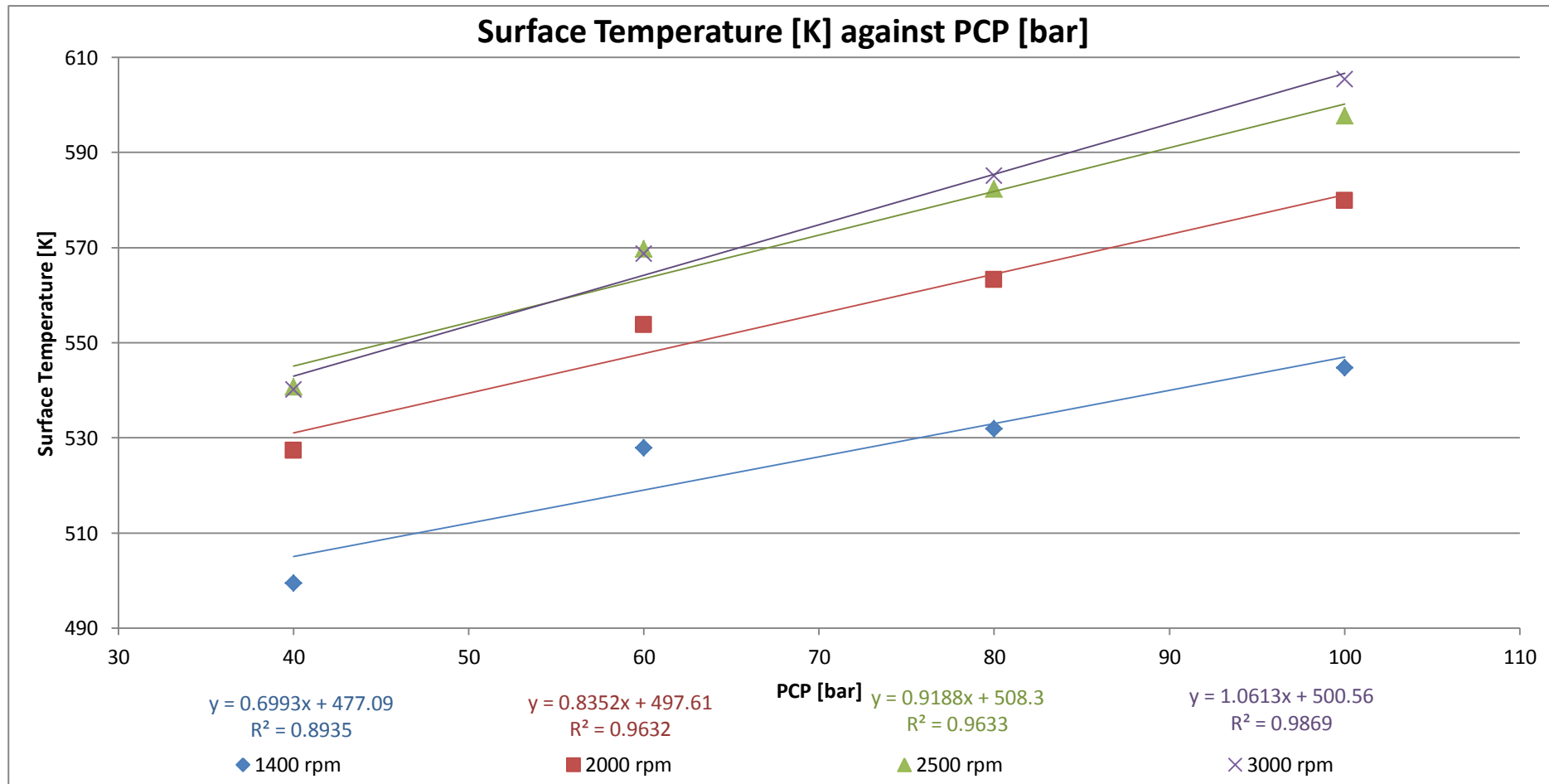
Figure 5.51. Average surface temperature measured by the Aluminium thermocouple fitted at the OEM injector location, against a variation in PCP (Sub-Matrix B1). Refer to Table 5.13 for the corresponding thermal condition of the engine.
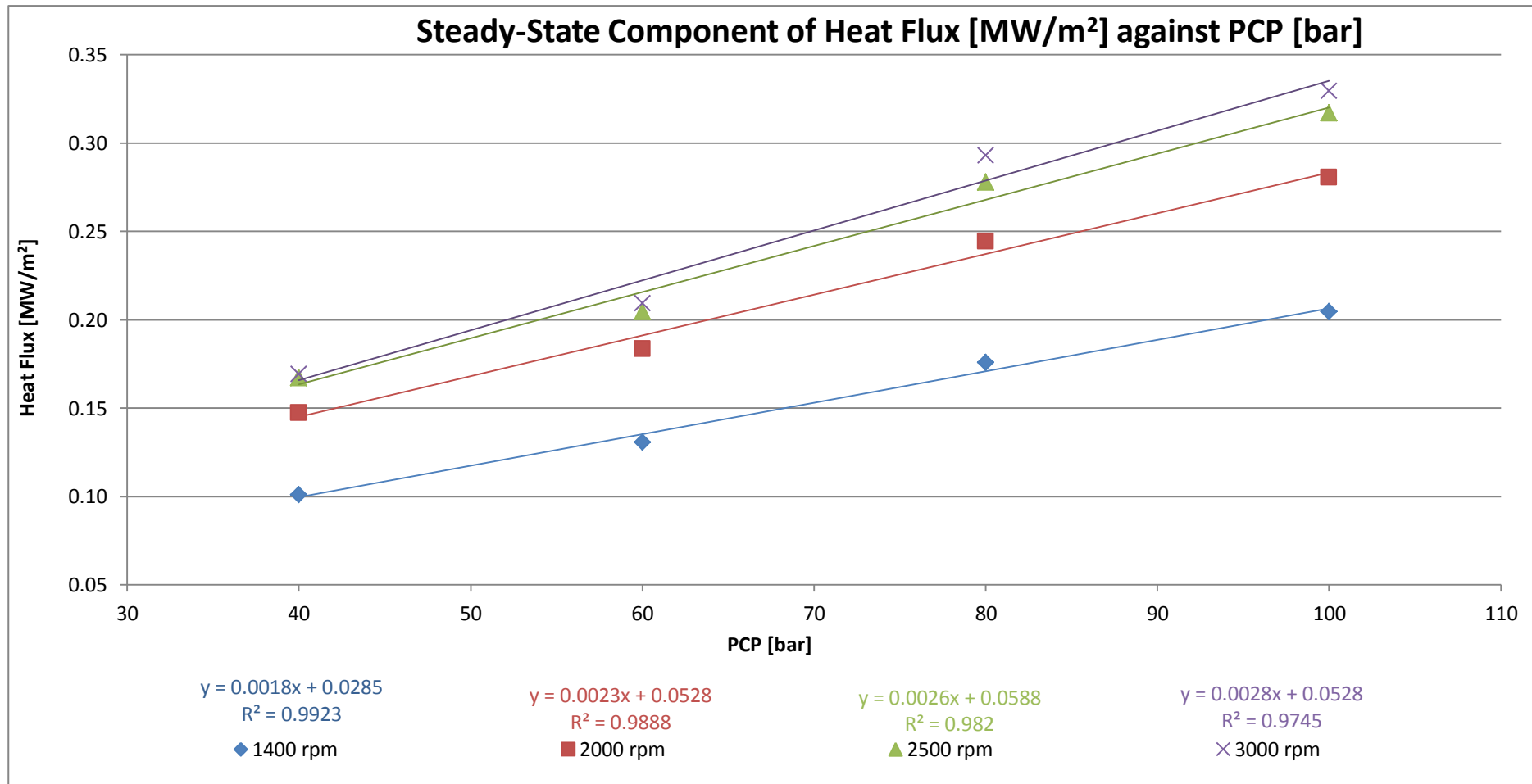
Figure 5.52. Steady-state component of heat flux as computed from the first law, against a variation in PCP (Sub-Matrix B1). Refer to Table 5.13 for the corresponding thermal condition of the engine.
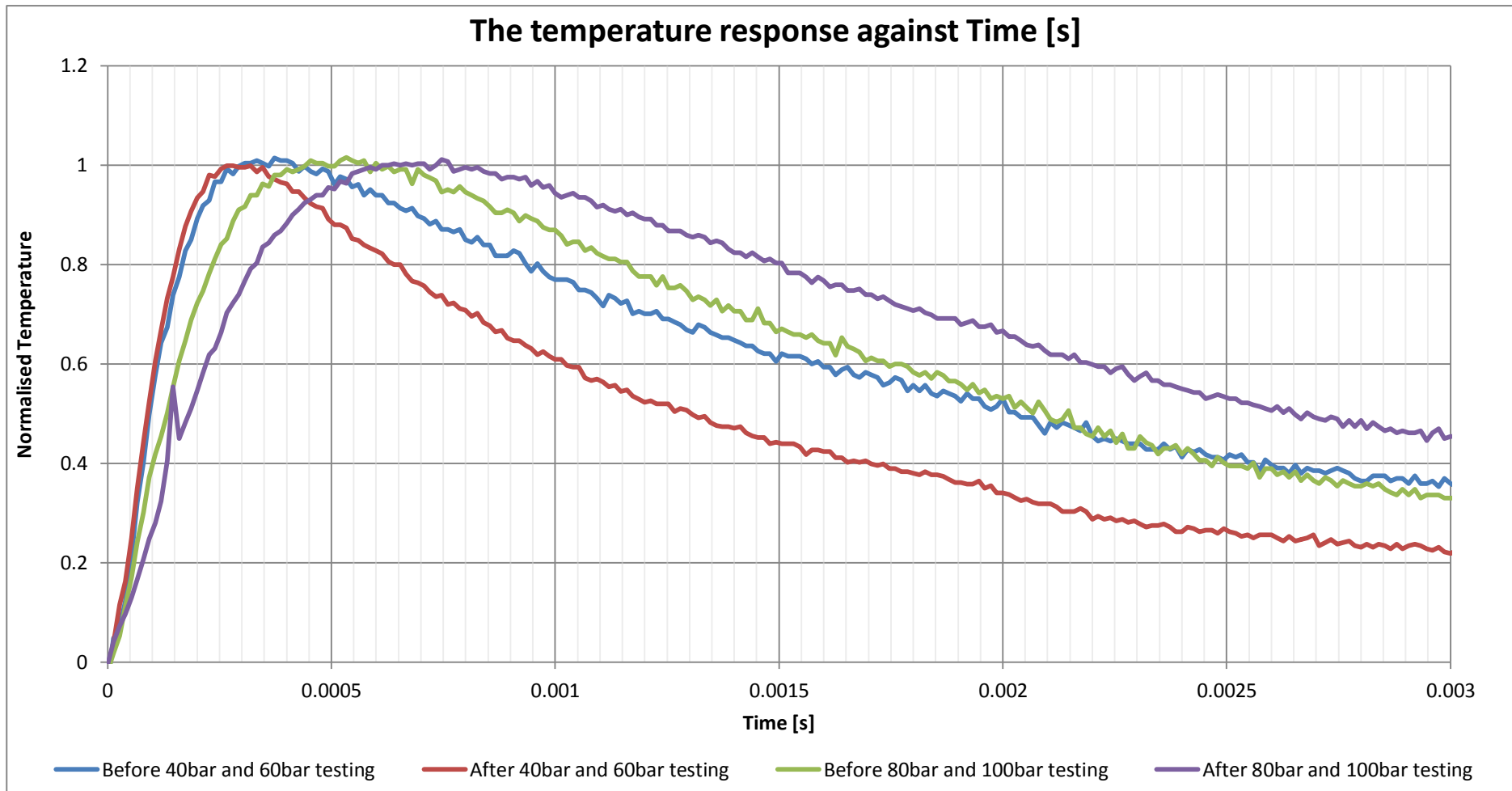
Figure 5.53. Temperature response of the Aluminium eroding thermocouple to the speedlight flash before and after PCP testing.
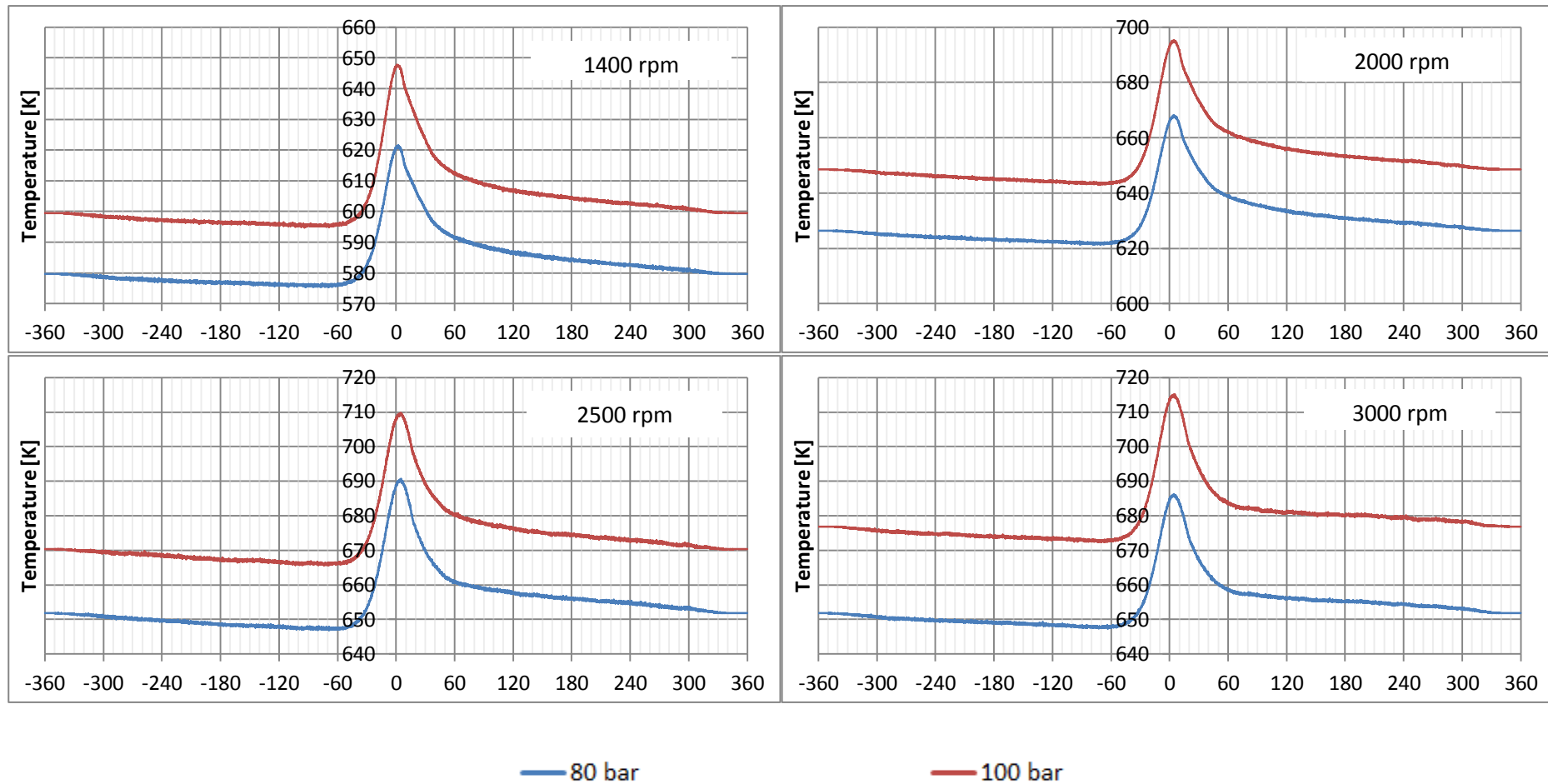
Figure 5.54. Ensemble surface temperature (K) against crank angle (Deg), recorded by the Aluminium eroding thermocouple at the OEM injector location, with working gas of γ: 1.5 (Sub-Matrix B2). Refer to Table 5.14 for the corresponding thermal condition of the engine.
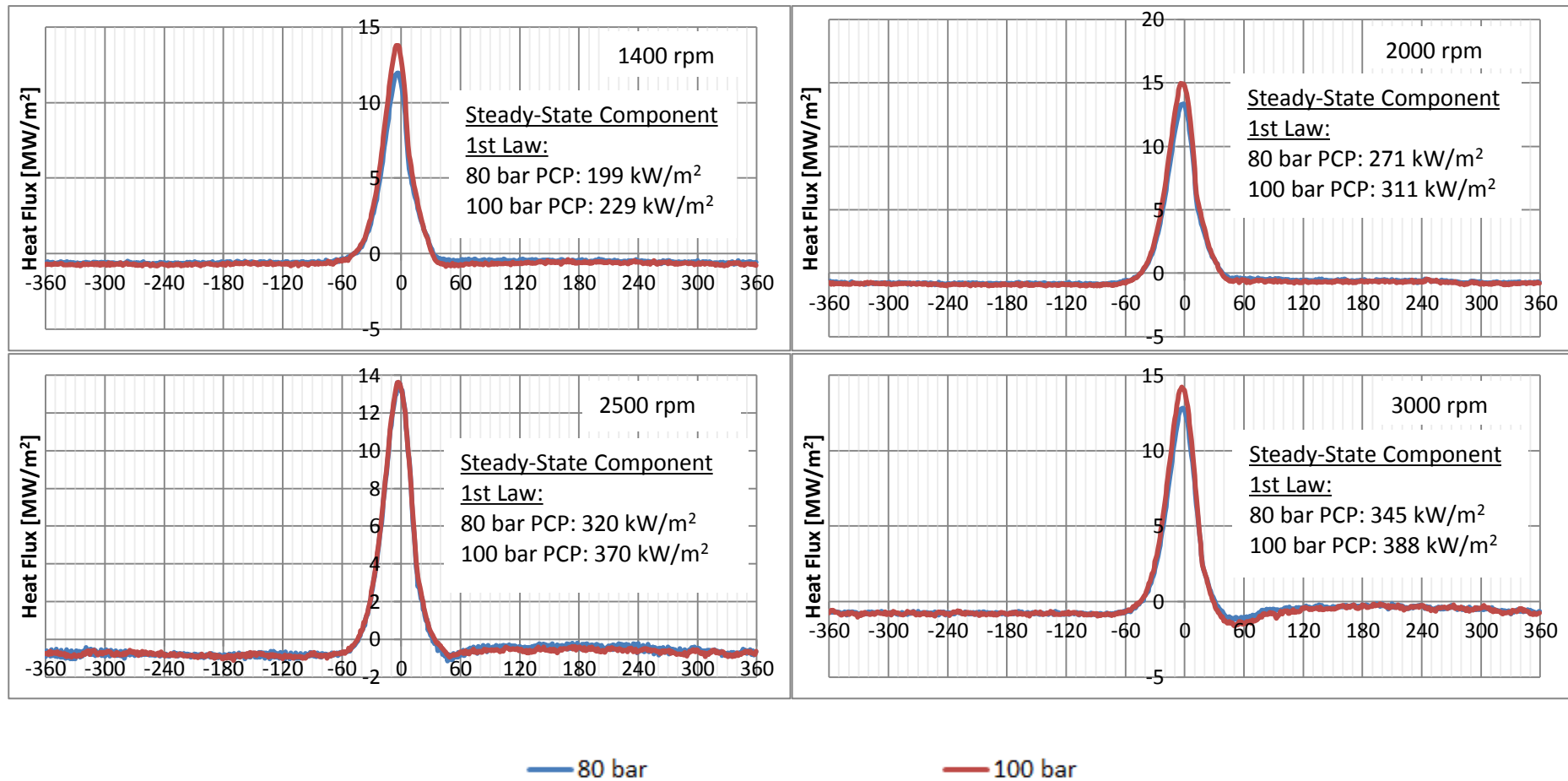
Figure 5.55. Transient component of heat flux (MW/m^2) against crank angle (Deg), recorded by the Aluminium eroding thermocouple at the OEM injector location, with working gas of γ: 1.5 (Sub-Matrix B2). The heat flux is computed using 2D response of Chromel. Refer to Table 5.14 for the corresponding thermal condition of the engine.
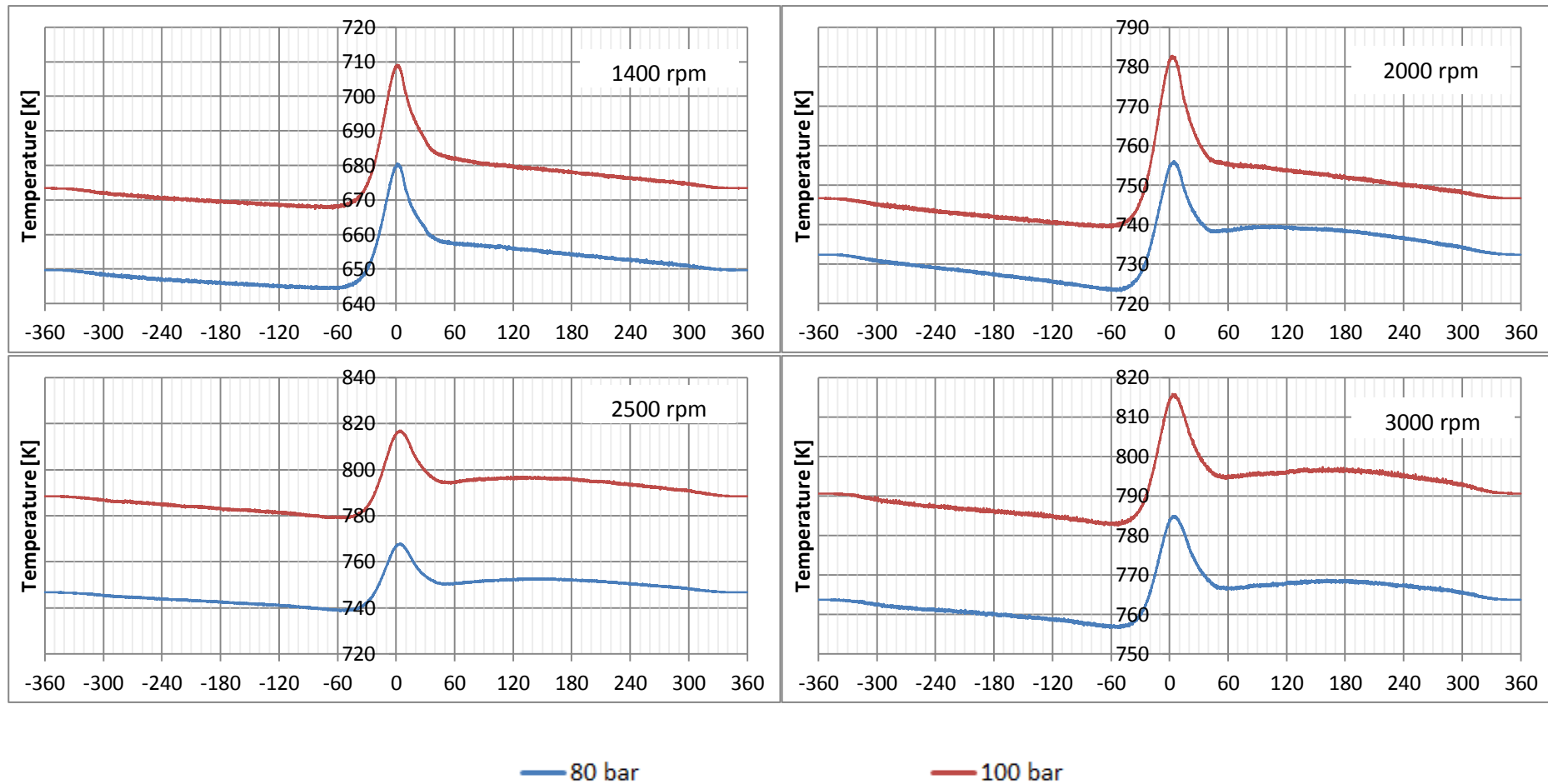
Figure 5.56. Ensemble surface temperature (K) against crank angle (Deg), recorded by the Aluminium eroding thermocouple at the OEM injector location, with working gas of γ: 1.6 (Sub-Matrix B2). Refer to Table 5.14 for the corresponding thermal condition of the engine.
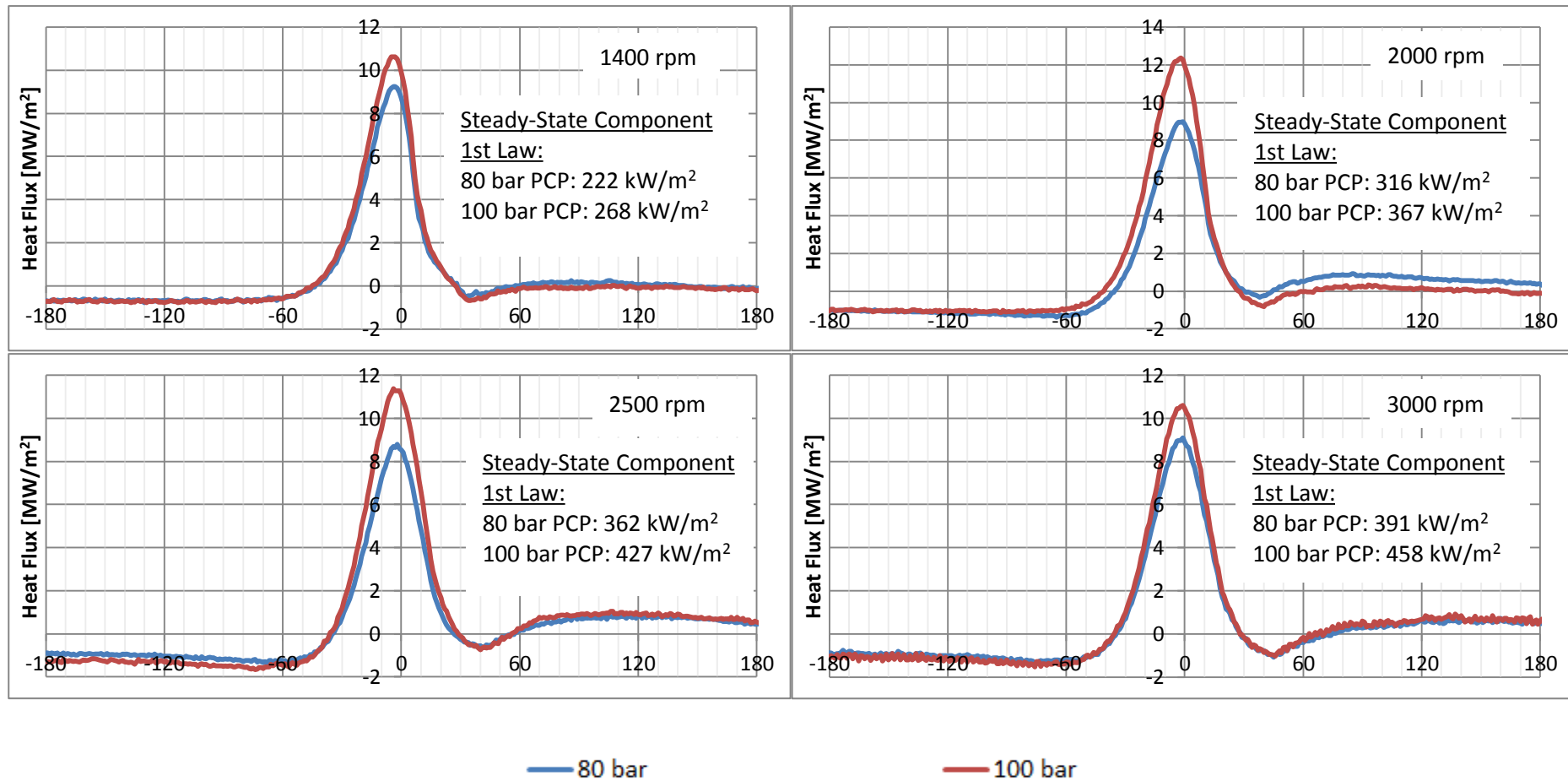
Figure 5.57. Transient component of heat flux (MW/m^2) against crank angle (Deg), recorded by the Aluminium eroding thermocouple at the OEM injector location, with working gas of γ: 1.6 (Sub-Matrix B2). The heat flux is computed using 2D response of Chromel. Refer to Table 5.14 for the corresponding thermal condition of the engine.
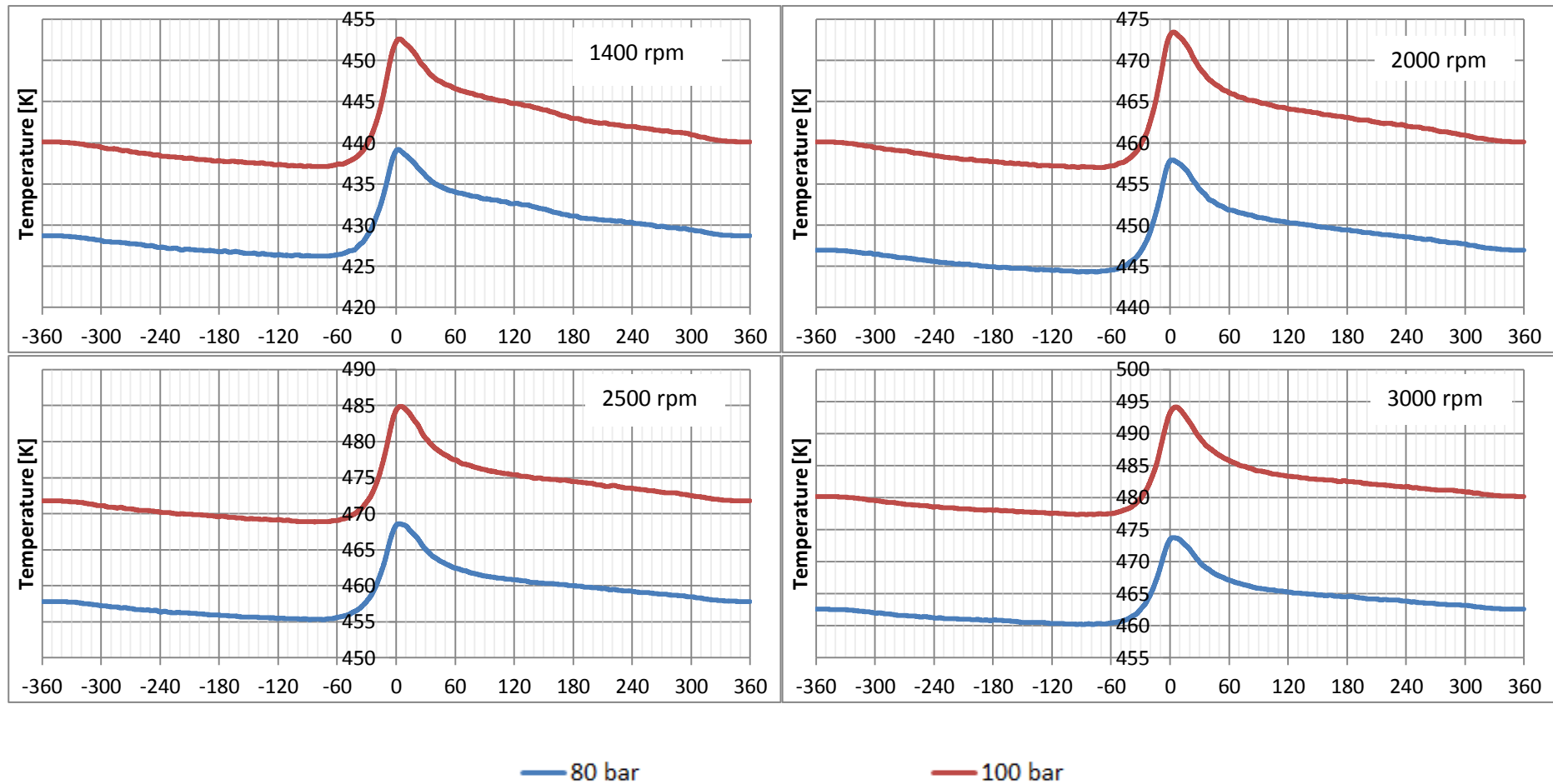
Figure 5.58. Ensemble surface temperature (K) against crank angle (Deg), recorded by the Zirconia eroding thermocouple at the custom-drilled location, with working gas of γ: 1.5 (Sub-Matrix B2). Refer to Table 5.14 for the corresponding thermal condition of the engine.
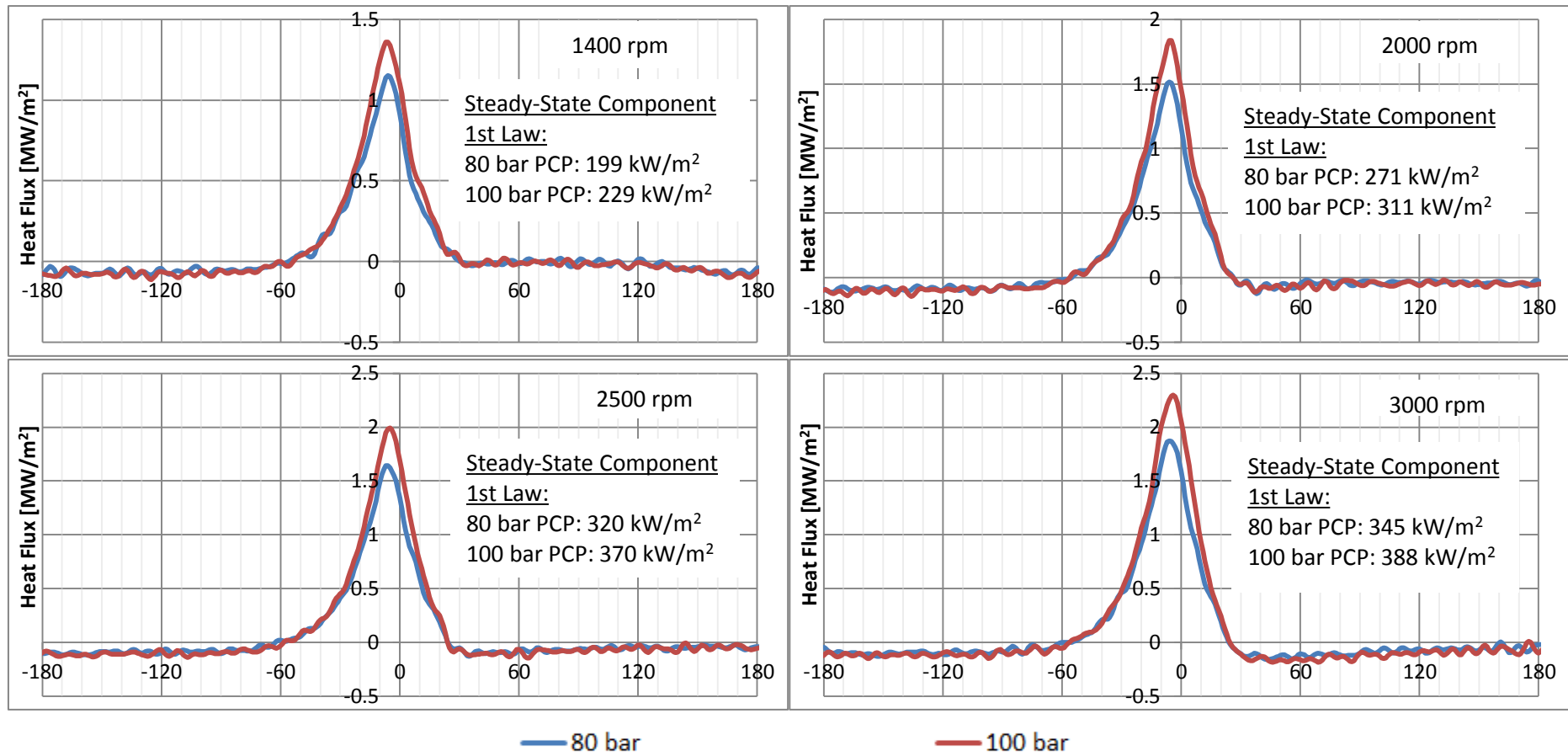
Figure 5.59. Transient component of heat flux (W/m^2) against crank angle (Deg), recorded by the Zirconia eroding thermocouple at the custom-drilled location, with working gas of γ: 1.5 (Sub-Matrix B2). The heat flux is computed using 2D response of Chromel. Refer to Table 5.14 for the corresponding thermal conditions of the engine.

248
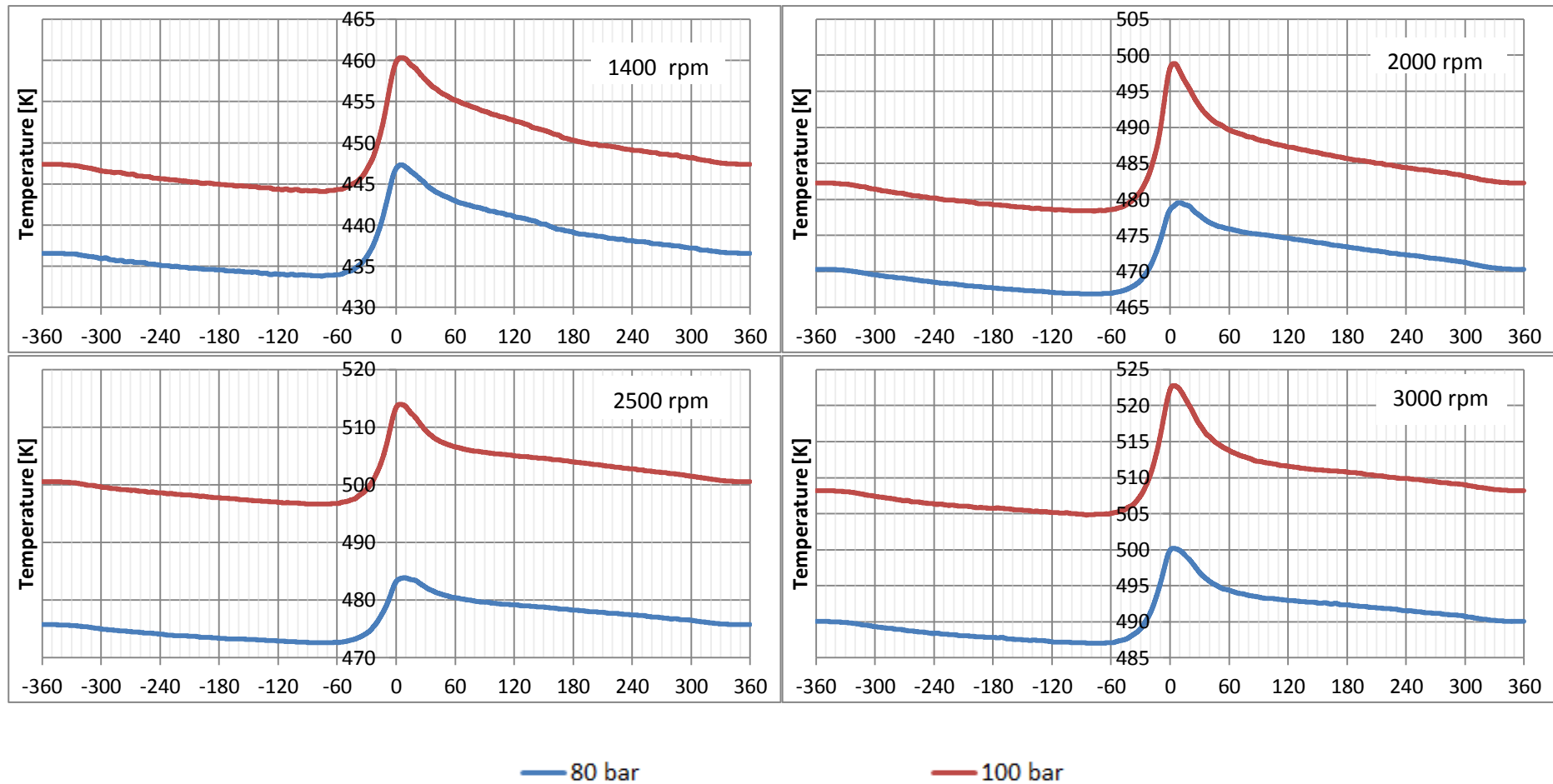
Figure 5.60. Ensemble surface temperature (K) against crank angle (Deg), recorded by the Zirconia eroding thermocouple at the custom-drilled location, with working gas of γ: 1.6 (Sub-Matrix B2). Refer to Table 5.14 for the corresponding thermal condition of the engine.
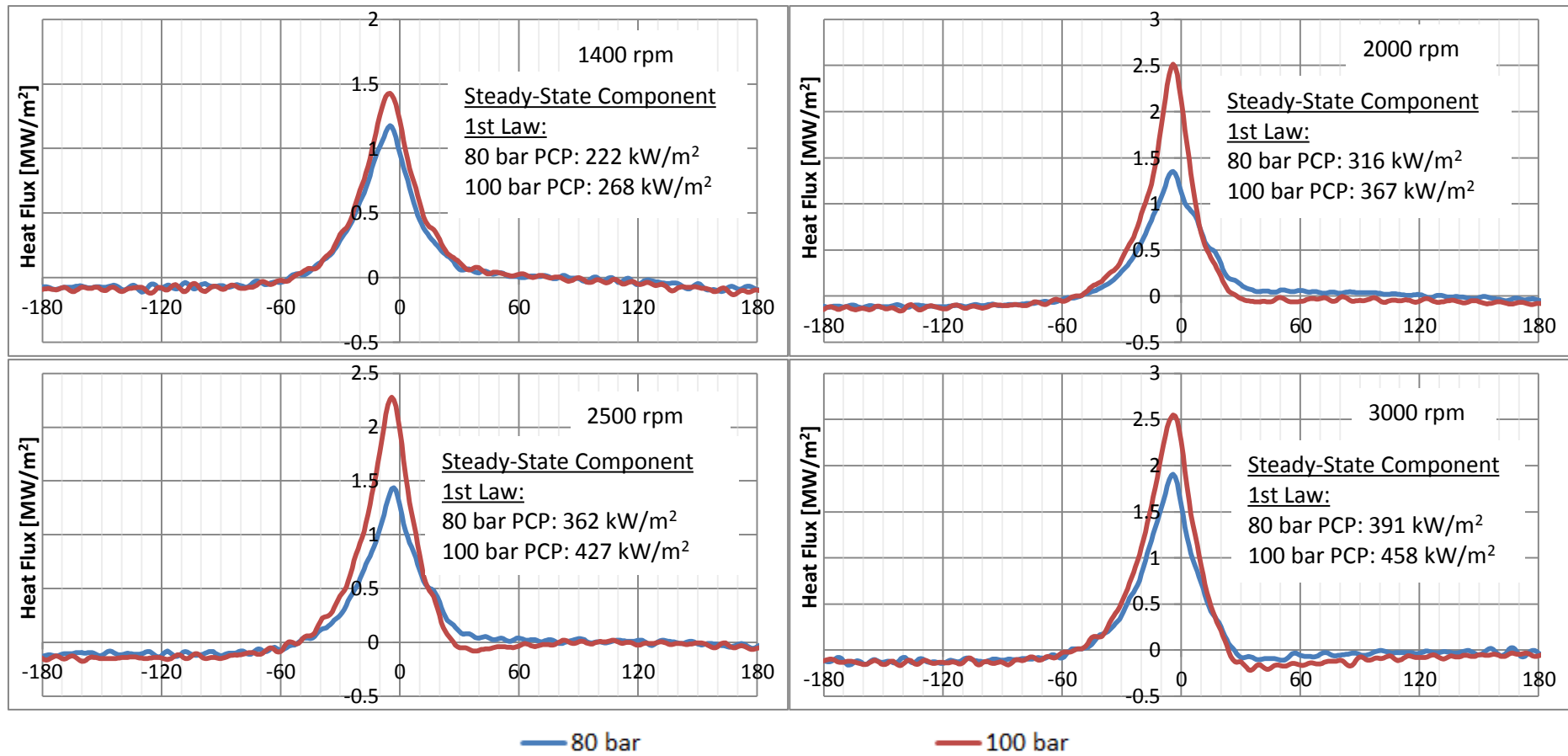
Figure 5.61. Transient component of heat flux (W/m^2) against crank angle (Deg), recorded by the Zirconia eroding thermocouple at the custom-drilled location, with working gas of γ: 1.6 (Sub-Matrix B2). The heat flux is computed using 2D response of Chromel. Refer to Table 5.14 for the corresponding thermal conditions of the engine.

5.7.3 Effect on Surface Temperature and Heat Flux by Soot Build-up

One of the comparison studies conducted in this project regards the soot build-up on the thermocouple surface. It was noted that through the use of Argon as the working gas, the high gas/surface temperatures promoted degradation of the oil layer deposited on the combustion chamber surface during motoring. As a result, after few minutes of operation with Argon, the surface thermocouples at both the injector and custom-drilled location got covered by a relatively thick layer of soot, as will be shown in a later figure. As a result, although heat flux testing with Argon was still done, results obtained are not given in this report due to their questionable nature. The method of operating the engine with gas mixtures allowed the ability to solve the problem of sooting by resorting to a gas with a ratio of specific heats slightly lower than that of Argon (1.67). Consequently, the highest specific heat capacity ratio presented in this report for the purpose of heat transfer measurements was γ: 1.60. The reason for limiting the ratio of specific heats below 1.67 were mainly two; to decrease the overall temperature reached by the gas on compression stroke, but mostly to have some dilution of oxygen in the gas mixture as a combustible component for the oil layer oxidation. This prevented any soot build-up on the sensor while still retained the possibility of having very high gas and wall temperatures in the cylinder during motoring.

Whilst soot build-up was not desired during the heat transfer testing (hence the solution to eliminate it), it was deemed interesting to investigate the effect of soot build-up on the thermocouple response, together with the surface temperature and ensuing transient component of heat flux. The setpoints tested for investigation of the soot build-up included two engine speeds (1400 rpm and 3000 rpm), two PCPs (80 bar and 100 bar) and two gas compositions (γ 1.40 and γ 1.60). These setpoints were tested two times; one conducted after the engine was operated for few minutes with pure Argon for soot build-up to occur, and the other was tested just after both thermocouples were thoroughly cleaned with alcohol and re-abraded with #80 grit. Results obtained from this testing session are shown in Figure 5.62 and Figure 5.63.

It is noted from Figure 5.62 that the ensemble surface temperature shows between 10 K to 20 K shift in the steady-state component, with the clean thermocouple

consistently showing a higher value than the thermocouple with the soot build-up. It is also evident that the swing of the clean thermocouple is significantly larger than that of the thermocouple with the soot build-up. As a result one expects a higher heat transfer rate through the clean surface. In fact, the heat flux reported in Figure 5.63 shows that at all tested conditions, the heat flux through the clean thermocouple shows a peak which is around five times higher than the peak heat flux reported by the thermocouple with soot build-up.

Another important observation noticed from Figure 5.62 is that the surface temperature also shows an angular shift in the location of peak surface temperature, where the thermocouple with soot build-up experiences the peak temperature 30 DegCA later than the clean thermocouple. Consequently, this resulted in around 5 DegCA delay in the peak of the transient component of heat flux where the thermocouple with soot build-up attains a peak just after TDC. This is anomalous and not conducive to the theoretical understanding of IC engine heat transfer. It is also evident that the angle at which the thermocouple with soot build-up shows the change in direction of heat flux, both at the compression and expansion strokes, is delayed when compared to that recorded by the clean thermocouple. This behaviour is a result of the fact that the junction of the thermocouple resides under microns of soot, which hence induces a phase lag in the temperature and heat flux swing.

To help in this analysis Figure 5.64 is presented, which gives the temperature response of the custom-fitted Zirconia thermocouple when flashed with the Meike speedlight. In Figure 5.64 three temperature responses are given; one after engine testing with soot build-up, one after the thermocouple was cleaned with alcohol – but retaining the same abrasion as with soot build-up, and another temperature response with the thermocouple re-abraded with #80 grit. Figure 5.65 shows the corresponding photographs of the sensor surface with soot build-up and after it was re-abraded.

It is clear from Figure 5.64 that similar to what was observed during engine testing, the thermocouple with soot build-up has a much slower response. In fact the newly abraded thermocouple showed a rise time smaller than that of the soot build-up by a factor of 10. Figure 5.64 shows that when the thermocouple was cleaned with alcohol but retaining the same junction, the rise time was around 0.25 ms, *i.e.* almost half that of the same thermocouple with a fresh #80 junction. Whilst it is ideal to have a

thermocouple with the fastest response possible, a reliable junction that could last possibly through the test matrix is required. This is mostly required when renewal of the thermocouple junction requires extensive dismantling of the setup. From several tests conducted on the engine, it was noted that when the rise time of the sensor came to be lower than the commonly obtained 0.45 ms, the thermocouple junction opened up sooner than usual, especially when using gases of high ratios of specific heats. Using an #80 grit emery cloth helped in sustaining a junction with a longer lifetime. The electrical resistance of the sensor was also measured prior flashing the thermocouple for the tests reported in Figure 5.64. It was noted that the electrical resistance of the thermocouple with soot build-up was 7 Ω. This resistance was retained even after cleaning the thermocouple surface with alcohol. Upon sanding the thermocouple with #80 grit, the electrical resistance dropped to 6 Ω. It is noted that the thermocouple resistances being given here and in other sections of this chapter were measured using a multimeter at the thermocouple male connector, and hence the reported resistances are not just a property of the sliver junction, but also of the length and gauge of the thermocouple wire. The length of the surface thermocouples was approximately 210 mm from surface to connector.

The presented results show that the soot acts as an attenuator to the temperature swing at the thermocouple surface, which then results in a significantly smaller and delayed peak of transient heat flux. This observation can be explained by the fact that the soot acts as an insulative cover which shields the surface from the heat transferred by/to the boundary layer.
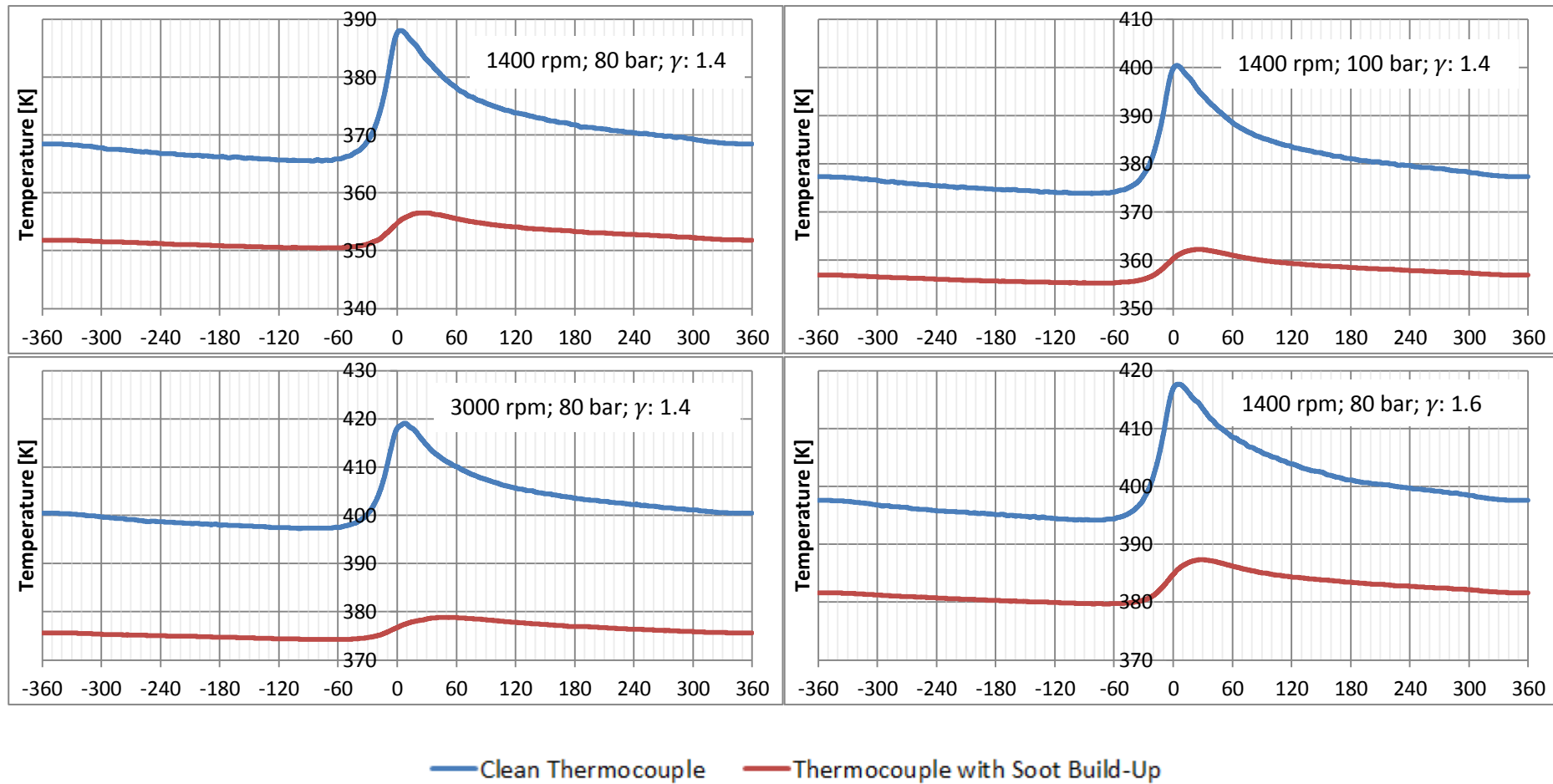
Figure 5.62. Ensemble surface temperature [K] with crank angle [Deg] recorded by the Zirconia thermocouple at the custom-drilled location, at different engine speeds, PCPs and gas compositions.
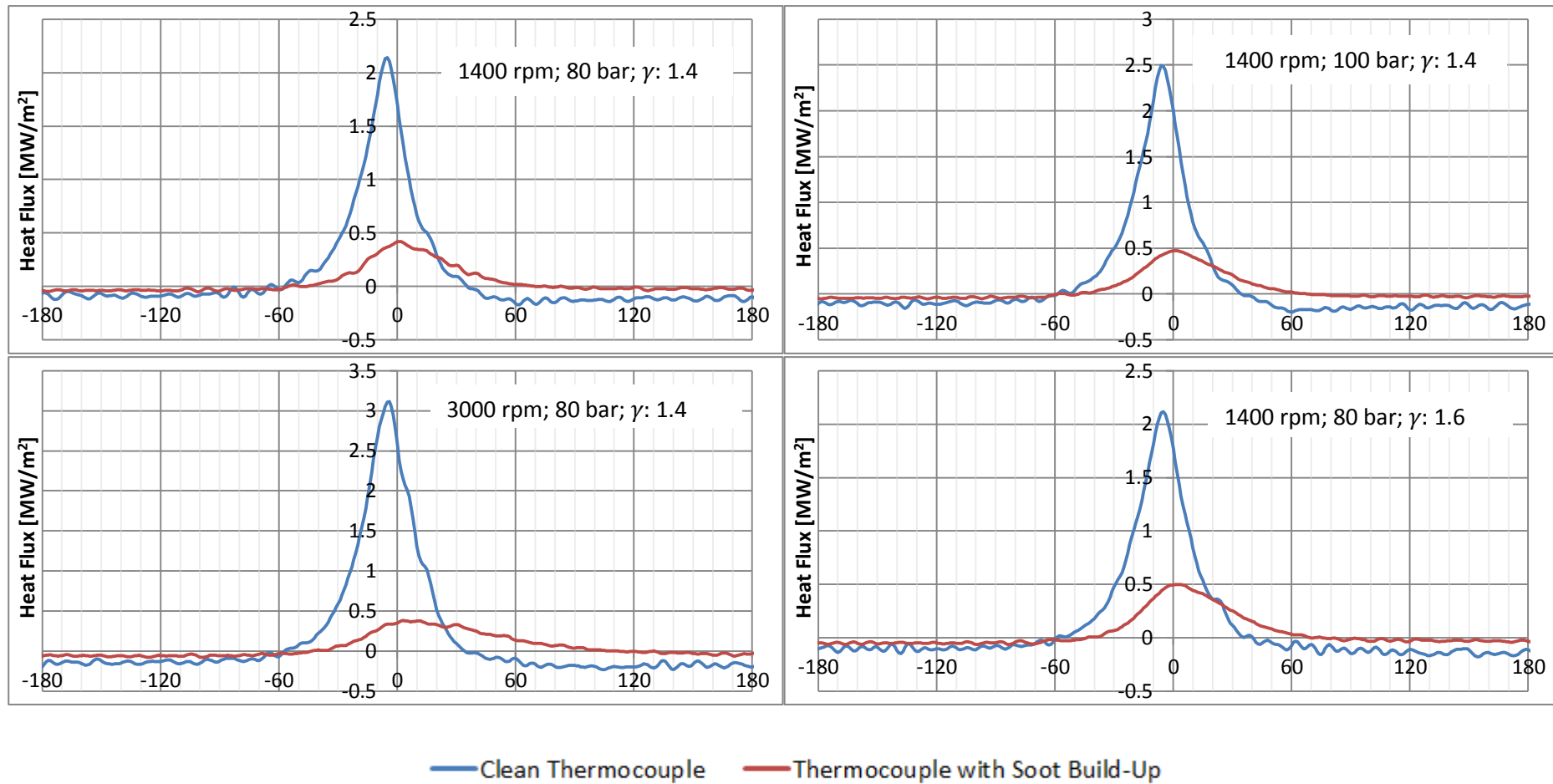
Figure 5.63. Transient component of heat flux [W/m^2] with crank angle [Deg] recorded by the Zirconia thermocouple at the custom-drilled location, at different engine speeds, PCPs and gas compositions. The heat flux is computed using 2D response of Chromel.
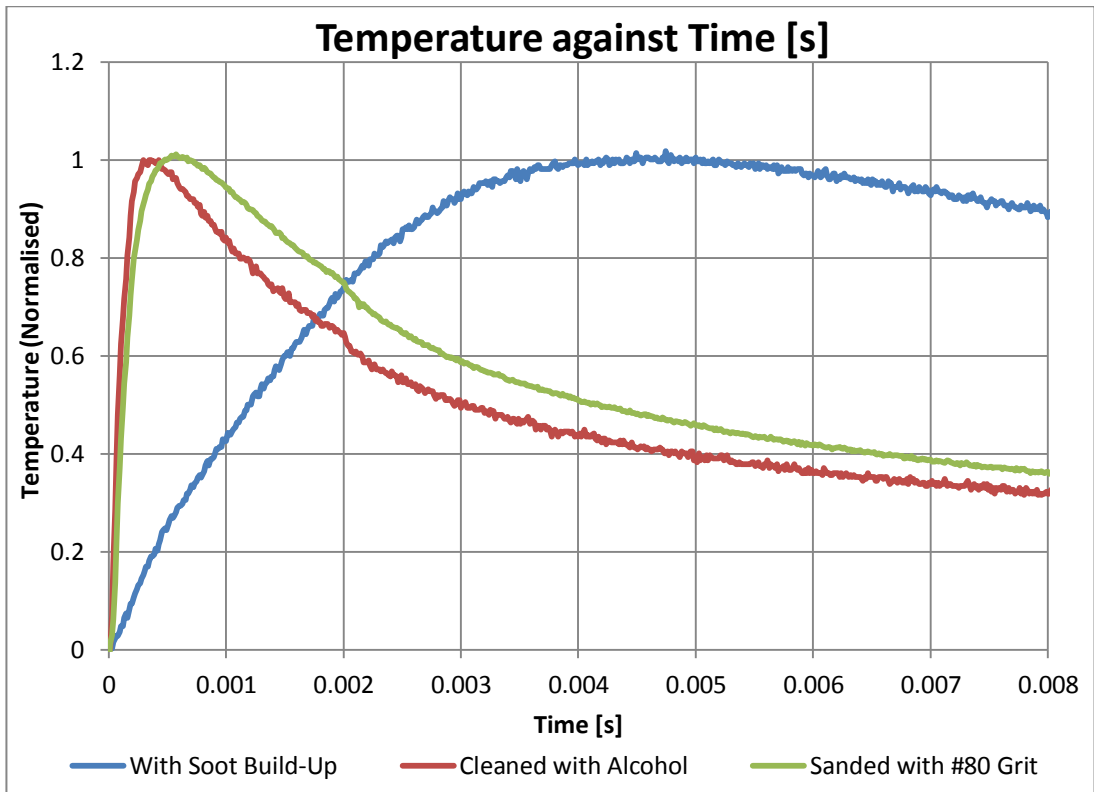
Figure 5.64. Temperature response of the Zirconia custom-fitted thermocouple when flashed with Meike speedlight.
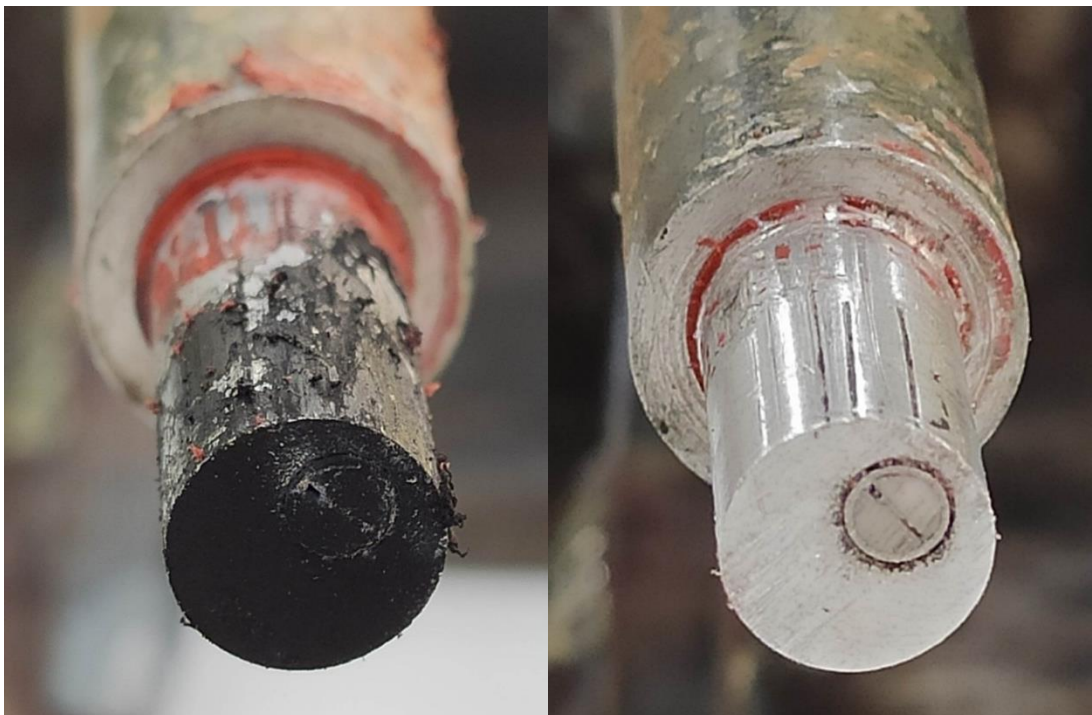
Figure 5.65. Photo showing the Zirconia thermocouple and its adaptor sooted and cleaned.

5.7.4 The effect of working gas on temperature swing and transient component of heat flux

The main novelty put forward in this doctoral work is the use of different gases in the pressurised motored engine. This was initially targeted to study the FMEP behaviour at different motoring in-cylinder gas temperatures; however it can also prove to be of good utility in heat transfer research. Studying the heat flux relationship with different gases could give information of how much the heat transfer could vary with drastic increases in the gas temperatures, but without the presence of the gas dynamics instigated by combustion. This therefore allows a partial decoupling of the thermal effect from the fluid dynamics effect on heat flux, which is not directly possible in conventional fired engine studies. Furthermore, the effect of different gas properties on heat flux may also be studied.

As mentioned in previous sections, in this study, the gases analysed ranged from Air (γ: 1.40) to Argon (γ: 1.67), with two synthesised mixtures in between having ratios of specific heats of 1.50 and 1.60. For FMEP studies the two gas mixtures (γ 1.50 and γ 1.60) were synthesised using Argon, Oxygen and Nitrogen. It was found that operating with just Argon resulted in soot build-up from oil degradation due to the very high gas temperature and no oxygen content. Due to this, for heat flux studies Argon (γ 1.67) was not used. Furthermore, the mixture of γ 1.60 used for heat flux testing was synthesised only from Argon and Oxygen (*i.e.* without Nitrogen). This was done to have adequate oxygen content such that if the temperature reached by the gas is high enough to promote lubricant degradation, there will be enough oxygen for the lubricant to react with, and hence prevents soot build-up. In fact it was found that with γ 1.60 using only Argon and Oxygen no sooting occured. The mixture of γ 1.50 was still synthesised with Oxygen, Nitrogen and Argon. In this mixture Nitrogen could be used since the temperatures reached were thought to be lower than those which promote lubricant degradation. Furthermore, if this gas ratio (γ 1.50) is synthesised with just Oxygen and Argon, a significantly high Oxygen quantity would be present in the mixture, which could potentially be highly combustable due to the presence of the lubricant and the high compression temperatures.

According to the previously presented Table 5.3 (Test Matrix A) and Table 5.4 (Test Matrix B) in section 5.4, in test matrix A the gases tested were air, and the

synthesised mixture with γ 1.60. On the other hand, in Table 5.4 (Test Matrix B), the gases tested were; air, synthesised mixture with γ: 1.50, and synthesised mixture with γ: 1.60 (see Sub-Matrix B2 in Table 5.6).

In conducting test matrix A, the thermocouple junctions (of the OEM injector location) were refreshed prior to testing of each of the five distinct thermocouple runs, and maintained throughout all eight setpoints corresponding to that thermocouple run (sub-matrix). The thermocouples were flash tested before and after each thermocouple run. Figure 5.66 to Figure 5.69 show the ensemble surface temperature and the computed transient component of heat flux acquired from the data taken during test matrix A at both locations. The general average temperatures of the engine during this test matrix are presented in Table 5.16 to Table 5.18.

From the analysis made on the data obtained from test matrix A, it was noted that the mean wall temperature measured by the Zirconia thermocouple, fitted at the custom-drilled location showed that testing with the gas of γ: 1.60 resulted in around 35℃ increase at 1400 rpm, and an increase of 40℃ at 3000 rpm (Figure 5.69). Surprisingly, negligible differences in the transient component of heat flux at this location were noted. The minute variations in the transient component of heat flux occurred only around the peak (close to, but before TDC), with very small variations in magnitude. The results obtained from test matrix B (sub-matrix B2) at the custom-drilled location show similar observations and are presented in Figure 5.70. From test matrix B, both gases of γ 1.50 and 1.60 show practically no difference in the transient component of heat flux when compared with air.

On the other hand, from the analysis made on test matrix A, but at the OEM injector location, the three different thermocouples (Zirconia, Aluminium and Stainless Steel), consistently showed that changing the working gas from air to the synthesised mixture with γ: 1.60 results in an increase in the transient component of heat flux around the peak, close to TDC. The temperature measured by the thermocouples placed in the injector location showed large positive shifts when changing the gas from air to that with γ: 1.60. The Zirconia thermocouple showed a maximum increase of 250℃, whereas the Stainless Steel and Aluminium thermocouples both showed a maximum increase of around 150℃ to 180℃. At the OEM injector location, no results are presented from test matrix B since they were obtained with the

Aluminium thermocouple which as highlighted in previous sections, showed abnormally large magnitudes. The observations reported above for different working gases at the two instrumented cylinder head locations result in two interesting conclusions.

The first observation is that the average surface temperature at the custom-drilled location rises only by a small quantity when testing with the higher γ gas, compared to air. This hints that this location is well quenched by the boundary layer, and hence the significantly higher average bulk gas temperature reached by the gas with γ: 1.60 results in only minute variations in the average temperature at the cylinder head surface. On the other hand, the observations made on the injector location thermocouple show that this location is heavily affected by the bulk gas, hinting therefore that the boundary layer is less effective in quenching the high bulk gas temperature. This observation was consistent for all the thermocouples investigated at this OEM injector location.

The second observation is that, surprisingly, at the custom-drilled location the transient component of heat flux experienced with the higher γ gases was practically the same as that experienced with air as the working gas. On the other hand, at the OEM injector location, a clear increase in the transient component of heat flux is visible with increasing the γ, however the increase was still not very large. In fact, at this OEM injector location, increasing the γ from 1.40 to 1.60 showed synonymous increase in transient component of heat flux to when the PCP was increased from 80 bar to 100 bar with air. The reasons for the negligible (or small) increase in heat flux with increasing γ could be several. Table 5.15 gives the thermal properties of air and Argon at two temperatures, which shows that although Argon (and its mixtures) promote higher bulk gas temperatures, the density, dynamic viscosity, specific heat capacities and thermal conductivity of Argon are significantly different than those for air. Hence, whilst the higher bulk gas temperature instigated by Argon (and its mixtures) might be acting to increase the heat flux, other gas properties might be acting to reduce it. Two parameters which hint this are the density and dynamic viscosity of Argon, which are both higher than those for air. This might consequently result in a decreased convective heat transfer coefficient for Argon and its mixtures, and hence the increase in heat flux promoted by the higher bulk gas temperature could be offset by the decrease in heat flux promoted by the density and dynamic

viscosity of the gas. Whilst this study was mostly concerned with the use of mixtures in relation to the bulk gas temperature that they induce, it is the author's opinion that investigation of the other mentioned parameters of the gas on heat flux should be made for a better analysis of the effect of the working gas on the transient component of heat flux. A study of this nature was already conducted by Demuynck et al. [42] and similarly concluded that the Argon gas, despite its ability to increase the instantaneous heat flux, the increase was less than initially expected.

Combining these two observations it can be deduced that whilst the higher γ gas contributed to a higher mean surface temperature (and probably steady-state heat flux had it been measured experimentally), the temperature swing was still not significantly higher than that of air, yielding a very similar transient component of heat flux.

Table 5.15. Properties of air and Argon at two different temperatures [42] [126].

		Density [kg/m^3]	γ	c_p [J/kg.K]	c_v [J/kg.K]	Dynamic viscosity [Pa.s]	Thermal Conductivity [W/m.K]
298 K	Air	1.184	1.40	1000	718	1.90e-5	0.026
	Argon	1.634	1.67	520	312	2.27e-5	0.018
900 K	Air	0.394	1.34	1100	834	3.90e-5	0.063
	Argon	0.541	1.67	520	312	5.17e-5	0.040
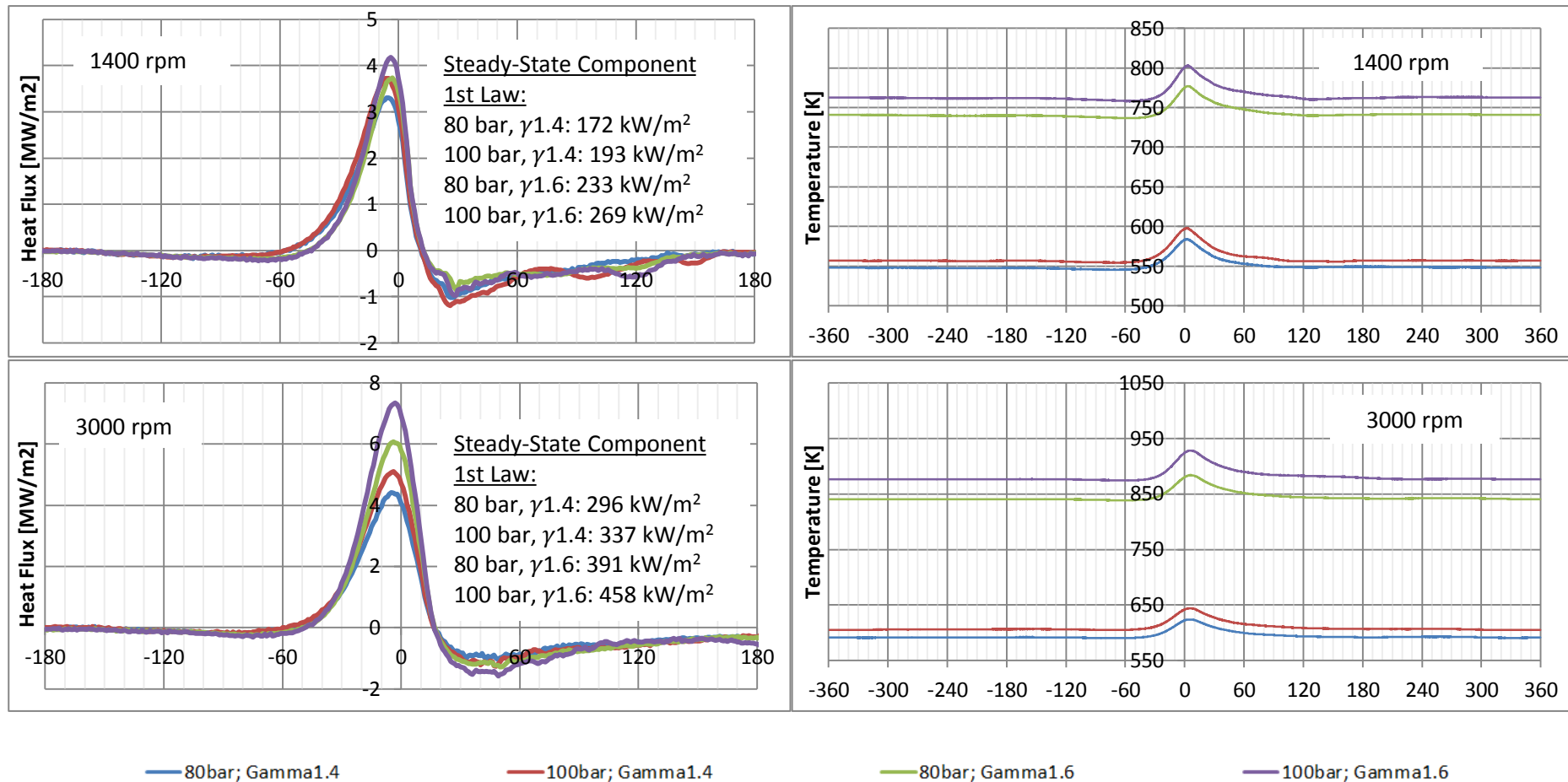
Figure 5.66. Ensemble surface temperature recorded by the Zirconia thermocouple fitted in the OEM injector location, and the calculated transient component of heat flux component from 'test matrix A'. The heat flux is computed using 2D response of Chromel. Data taken on 3rd July 2020. Refer to Table 5.16 for the corresponding thermal condition of the engine.

261

Figure 5.67. Ensemble surface temperature recorded by the Aluminium thermocouple fitted in the OEM injector location, and the calculated transient component of heat flux component from 'test matrix A'. The heat flux is computed using 2D response of Chromel. Data taken on 7th July 2020. Refer to Table 5.17 for the corresponding thermal condition of the engine.
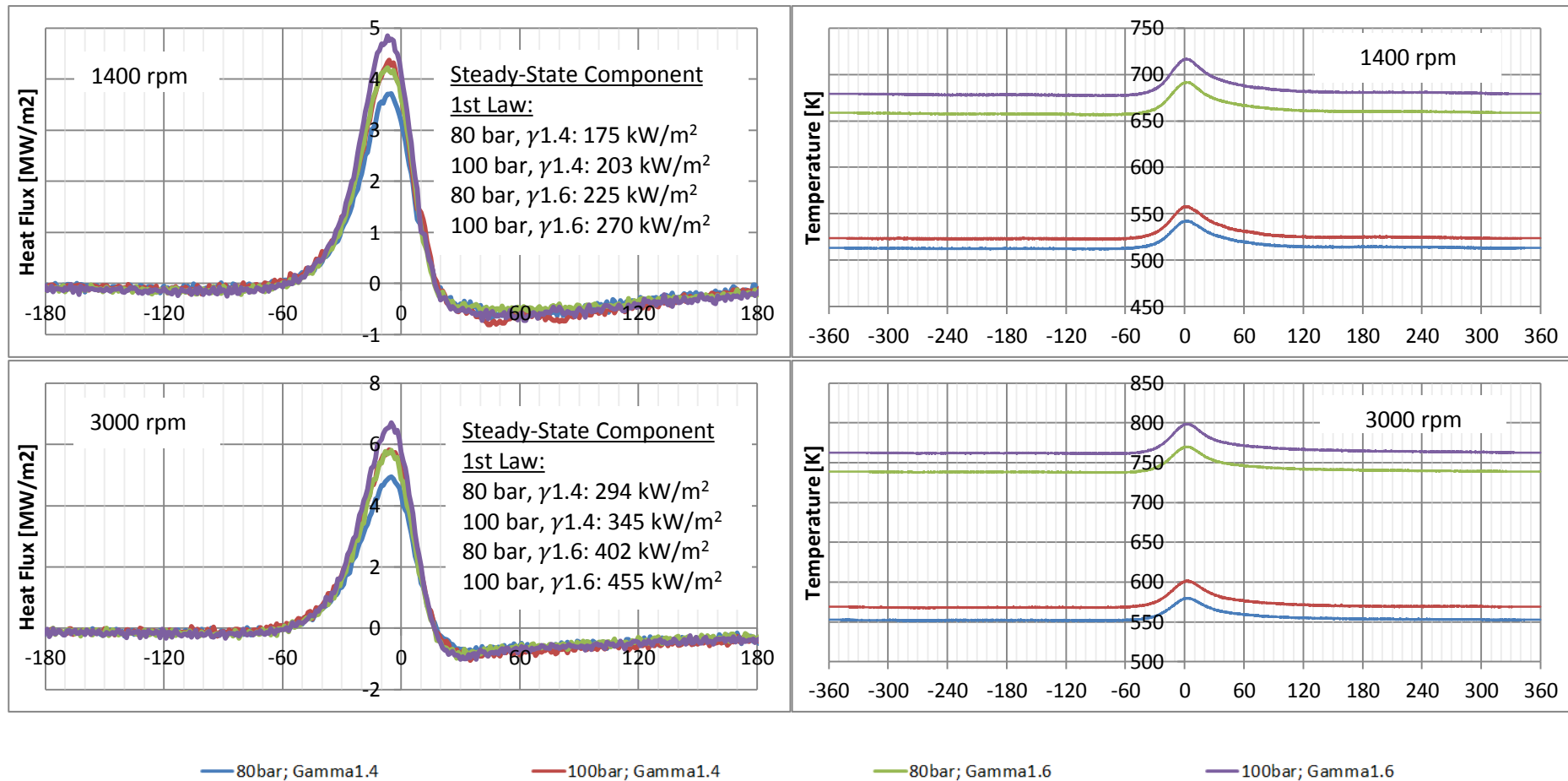
Figure 5.68. Ensemble surface temperature recorded by the Stainless Steel thermocouple fitted in the OEM injector location, and the calculated transient component of heat flux component from 'test matrix A'. The heat flux is computed using 2D response of Chromel. Data taken on 9th July 2020. Refer to Table 5.18 for the corresponding thermal condition of the engine.
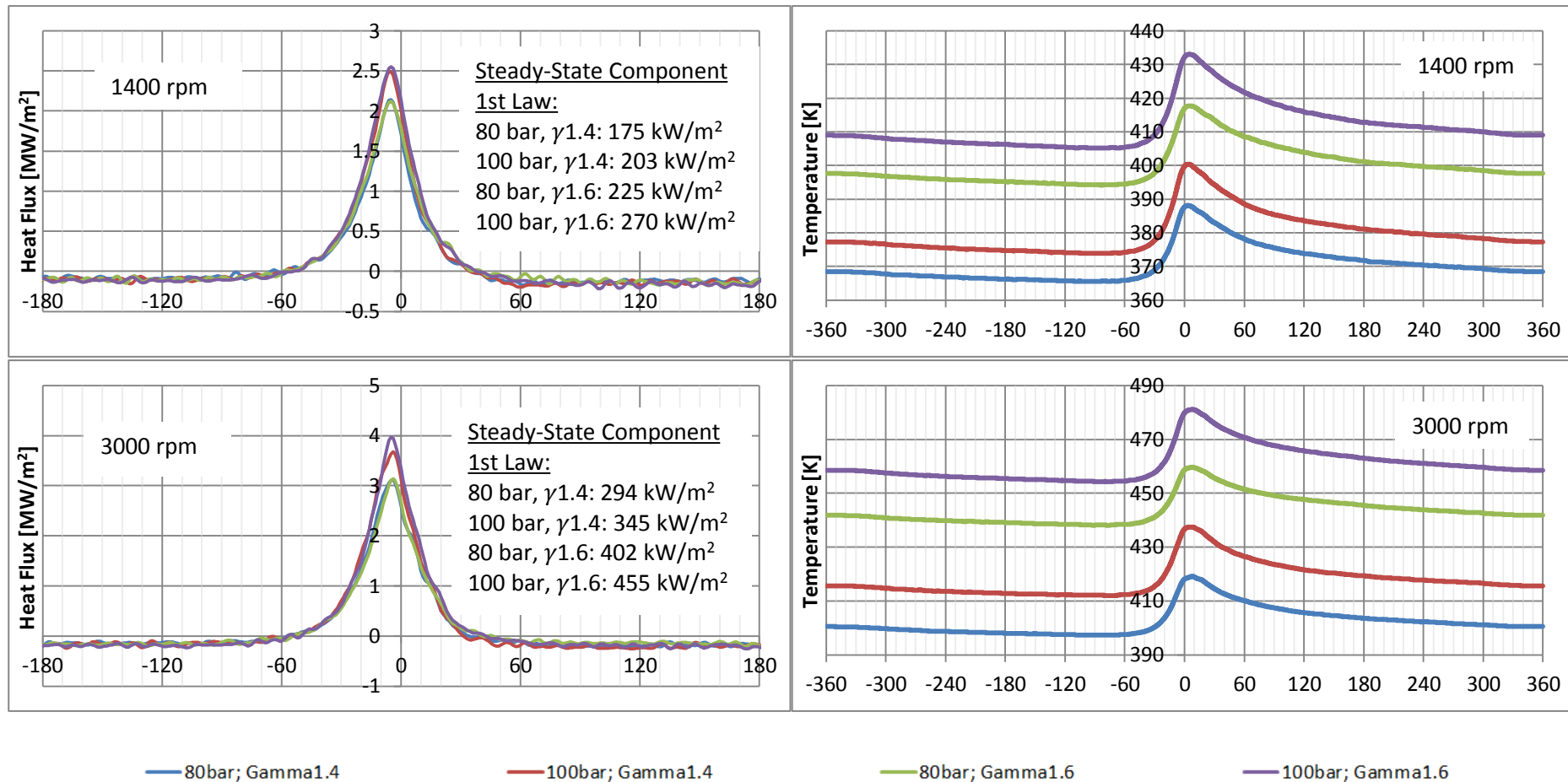
Figure 5.69. Ensemble surface temperature recorded by the Zirconia thermocouple fitted in the custom-drilled location, and the calculated transient component of heat flux component from 'test matrix A'. Data taken on 9th July 2020. The heat flux is computed using 2D response of Chromel. Refer to Table 5.18 for the corresponding thermal condition of the engine.

Table 5.16. Steady-state data for the testing session conducted on the 3rd of July (Test Matrix A).

	3rd July Testing							
	1400 rpm				3000 rpm			
	cp/cv							
	1.4		1.6		1.4		1.6	
	PCP [bar]							
	80	100	80	100	80	100	80	100
MAP [bar]	2.007	2.504	1.330	1.661	1.964	2.493	1.208	1.543
Shunt Intake Temperature [DegC]	26.9	26.2	23.3	23.8	37.4	47.0	45.3	49.8
Shunt Exhaust Temperature [DegC]	23.6	23.9	21.1	22.7	46.3	56.1	59.6	64.5
Engine Coolant Temperature [DegC]	33.5	33.4	31.9	32.5	33.5	34.1	33.9	34.6
Engine Oil Temperature [DegC]	45.6	45.4	43.1	43.8	49.0	52.1	51.9	53.6
Recessed Temperature [DegC]	36.6	37.0	35.9	37.1	38.8	40.3	40.6	42.5
1st Law Steady-State Heat Flux [MW/m^2]	0.1718	0.1926	0.2330	0.2690	0.2957	0.3369	0.3911	0.4583

Table 5.17. Steady-state data for the testing session conducted on the 7th of July (Test Matrix A).

	7th July Testing							
	1400 rpm				3000 rpm			
	cp/cv							
	1.4		1.6		1.4		1.6	
	PCP [bar]							
	80	100	80	100	80	100	80	100
MAP [bar]	2.029	2.440	1.351	1.678	1.964	2.499	1.238	1.540
Shunt Intake Temperature [DegC]	20.3	20.2	24.2	24.1	33.9	44.5	39.9	47.1
Shunt Exhaust Temperature [DegC]	17.3	17.9	21.3	22.4	42.0	52.5	55.4	62.6
Engine Coolant Temperature [DegC]	28.6	28.6	33.7	33.6	29.5	30.9	33.9	34.7
Engine Oil Temperature [DegC]	37.9	39.1	45.3	45.3	46.2	49.7	50.6	53.5
Recessed Temperature [DegC]	32.2	32.8	38.1	38.9	35.7	38.2	41.8	43.7
1st Law Steady-State Heat Flux [MW/m^2]	0.1721	0.1987	0.2346	0.2769	0.3083	0.3648	0.4152	0.4765

Table 5.18. Steady-state data for the testing session conducted on the 9th of July (Test Matrix A).

	9th July Testing							
	1400 rpm				3000 rpm			
	cp/cv							
	1.4		1.6		1.4		1.6	
	PCP [bar]							
	80	100	80	100	80	100	80	100
MAP [bar]	1.999	2.469	1.316	1.650	1.939	2.480	1.203	1.511
Shunt Intake Temperature [DegC]	20.9	21.2	26.1	25.8	34.3	46.0	47.8	44.7
Shunt Exhaust Temperature [DegC]	18.4	20.0	22.9	24.0	42.8	54.3	60.7	60.4
Engine Coolant Temperature [DegC]	29.8	30.2	33.0	33.0	31.3	32.6	34.8	34.1
Engine Oil Temperature [DegC]	38.9	40.1	45.0	45.0	47.0	51.0	54.7	52.1
Recessed Temperature [DegC]	33.0	34.1	37.3	38.1	37.3	39.6	42.2	42.8
1st Law Steady-State Heat Flux [MW/m^2]	0.1754	0.2027	0.2250	0.2703	0.2938	0.3450	0.4020	0.4549
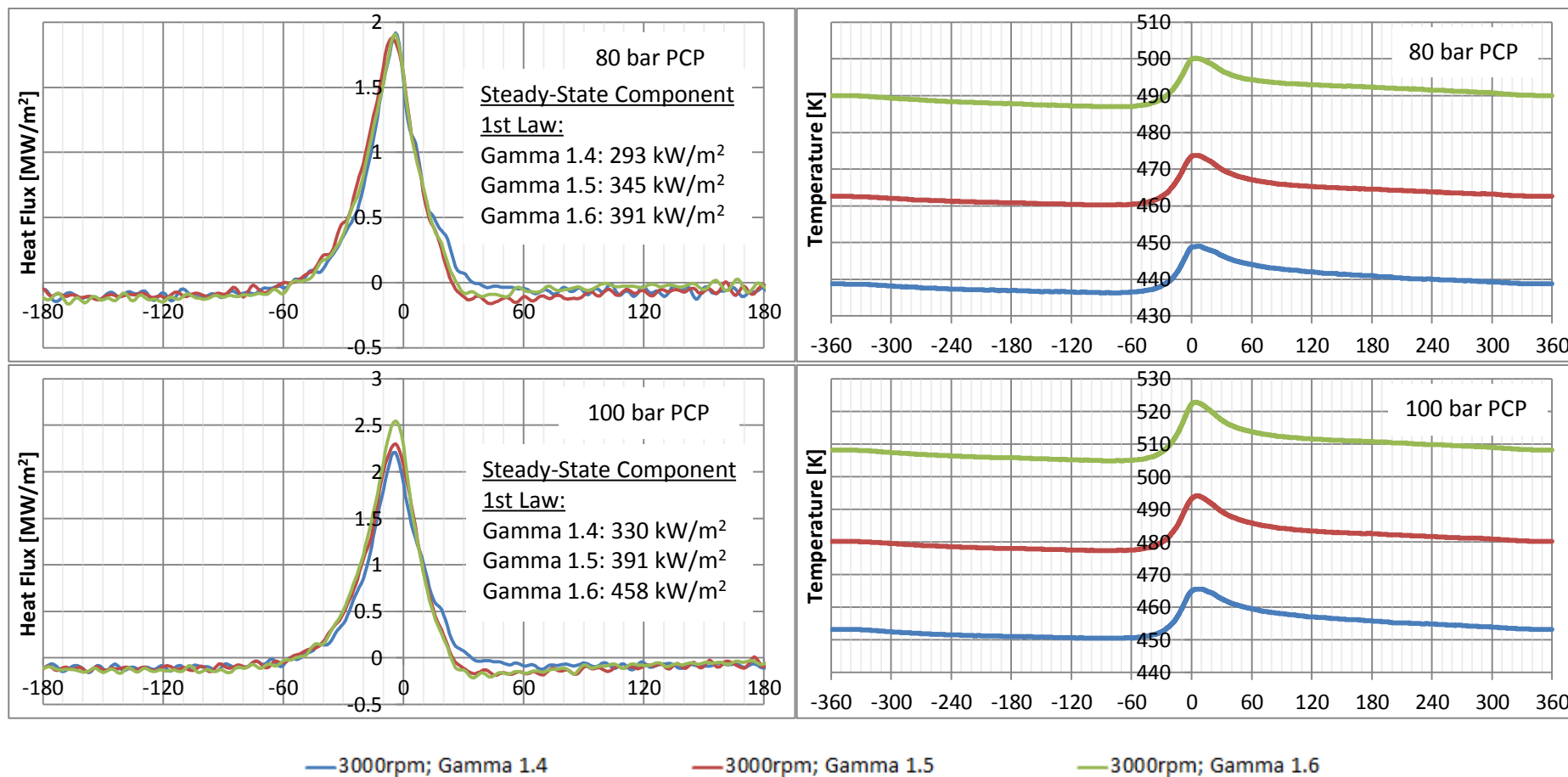
Figure 5.70. Ensemble surface temperature recorded by the Zirconia thermocouple fitted in the custom-drilled location, and the calculated transient component of heat flux component from test matrix B (Sub-Matrix B2). The heat flux is computed using 2D response of Chromel.

268

5.7.5 The effect of working gas on mean surface temperature and steady-state component of heat flux

In this section the mean of the surface temperature and steady-state component of heat flux obtained from the first law are presented with a variation of the working gas from test matrix B (sub-matrix B2).

Figure 5.71 and Figure 5.72 show the mean surface temperature obtained from the Zirconia thermocouple at the custom-drilled location and the Aluminium thermocouple at the OEM injector location for different gas compositions. A maximum of 11% increase in the mean surface temperature is noted between air and γ: 1.60 for the custom-drilled location, whereas 19% increase is noted if considering Argon (γ: 1.67). For the OEM injector Aluminium thermocouple, a maximum of 31% increase is noted between air and γ: 1.60, whereas a 47% increase is noted if considering pure Argon.
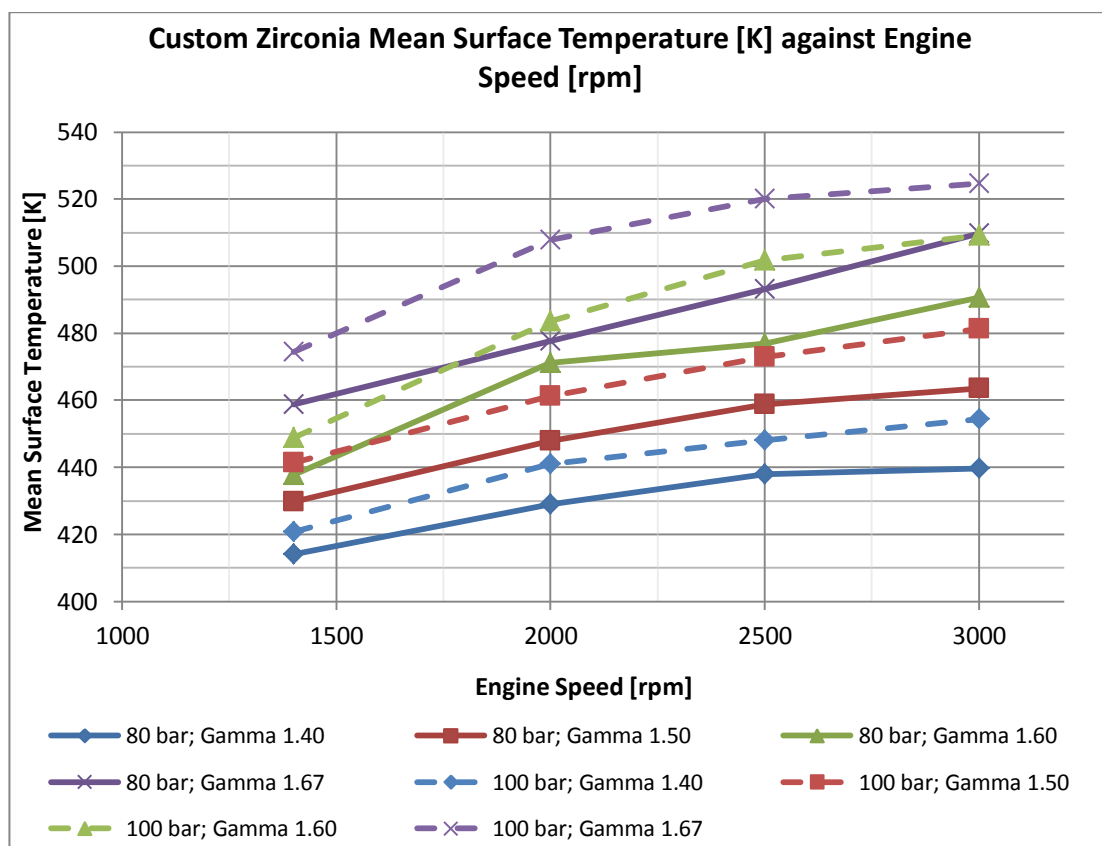
Figure 5.71. Mean surface temperature obtained at the custom-drilled location by the Zirconia eroding thermocouple.
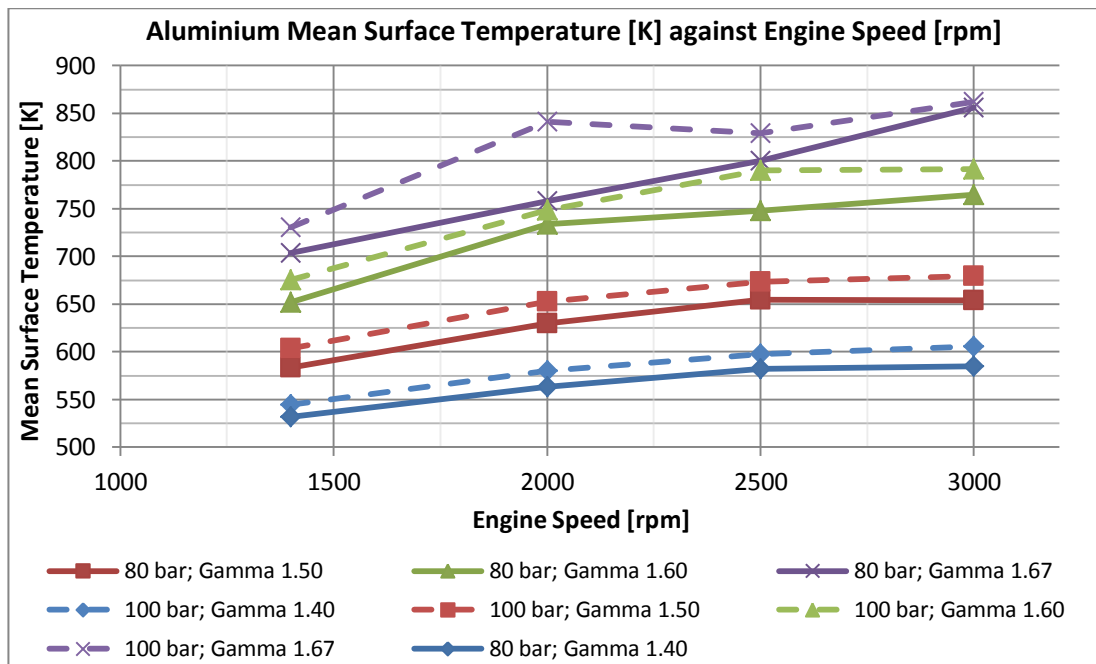
Figure 5.72. Mean surface temperature obtained at the OEM injector location by the Aluminium eroding thermocouple.

As explained in a previous section, the steady-state heat flux component was not obtained from recessed thermocouple measurements, however in Figure 5.73 and Figure 5.74 the steady-state component of heat flux computed from the 1st law analysis is given against gamma. It is noted that a linear trend prevails; dictating that a higher steady-state component of heat flux is expected when using gases of higher ratios of specific heats. This originates mainly from higher bulk gas temperatures which ensue with the use of high γ gases, and which was also previously noted to have a linear relationship between the peak of the bulk gas temperature and ratio of specific heats. In Figure 5.75, the steady-state component of heat flux for the 80 bar PCP condition is plotted against peak bulk gas temperature to distinguish the relationship of heat flux with gamma from that of heat flux with bulk gas temperature. Figure 5.75 also shows a linear trend.

As can be seen in all three figures, the steady-state component of heat flux was also computed for Argon, despite the fact that no experimentally measured transient heat flux was given in the relevant section. The steady-state component of heat flux for Argon could be given since its computation is dependent only on the measured in-cylinder pressure trace, and hence problems resulting from the sooting of the surface thermocouples were avoided.

In computing the steady-state component of heat flux from the 1st law of thermodynamics, the temperature dependence of the γ ratio had to be considered for each of the working gases. The variation of γ with temperature for each of the gas mixtures is given in Figure 5.76 fitted with a cubic polynomial. It is pointed out that for Argon, a constant γ was used, based on the derivation originating from the Kinetic Theory of Gases for a monoatomic molecule gas.
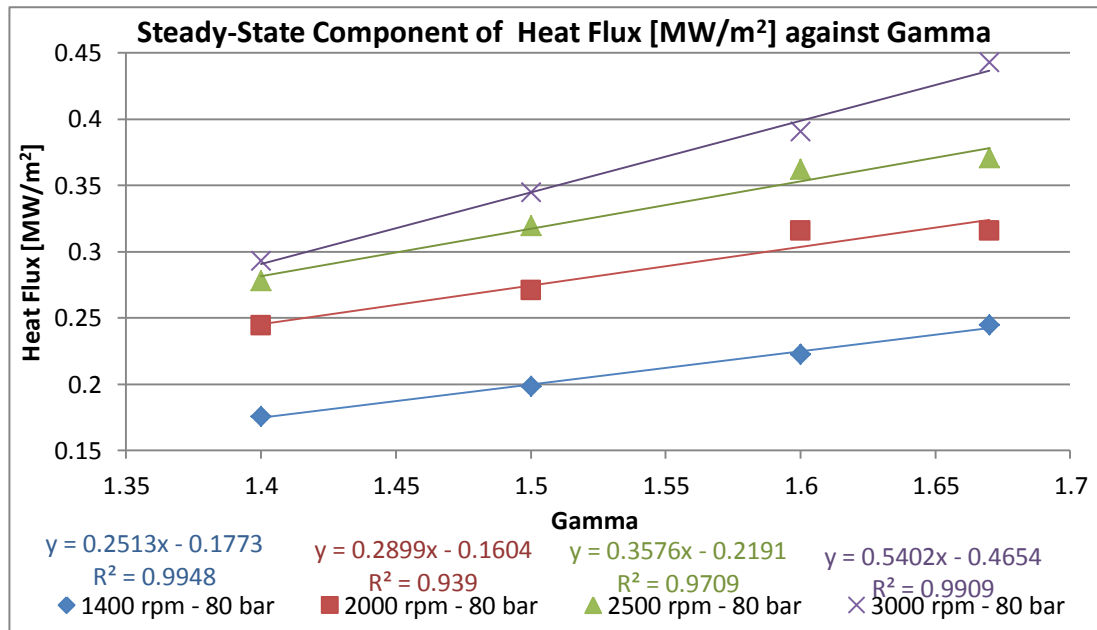
Figure 5.73. Steady-state component of heat flux obtained from the first law for the 80 bar PCP setpoints.
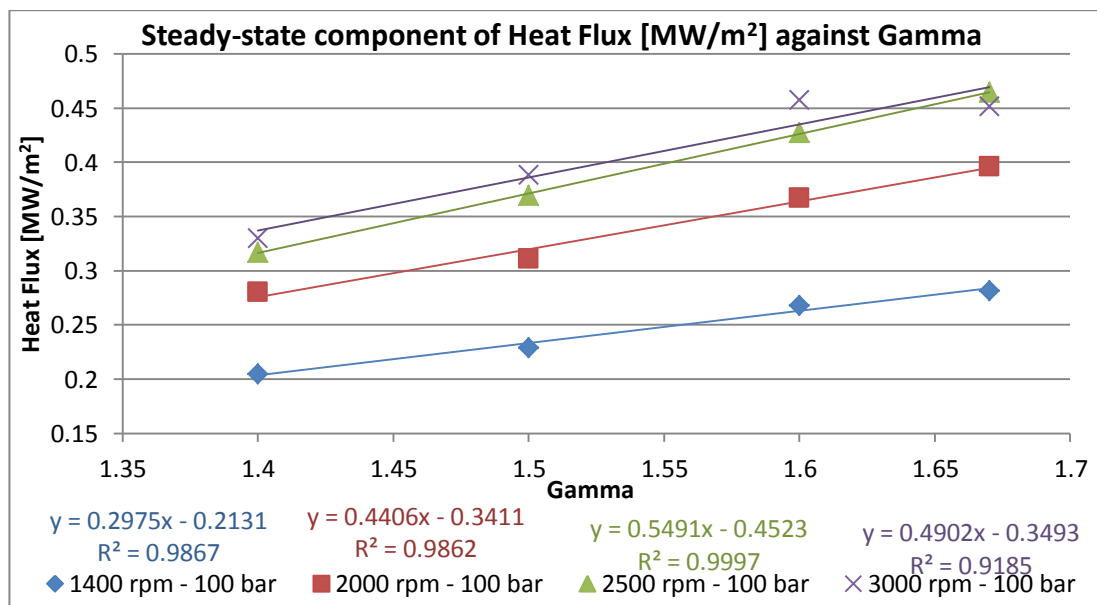
Figure 5.74. Steady-state component of heat flux obtained from the first law for the 100 bar PCP setpoints.

271
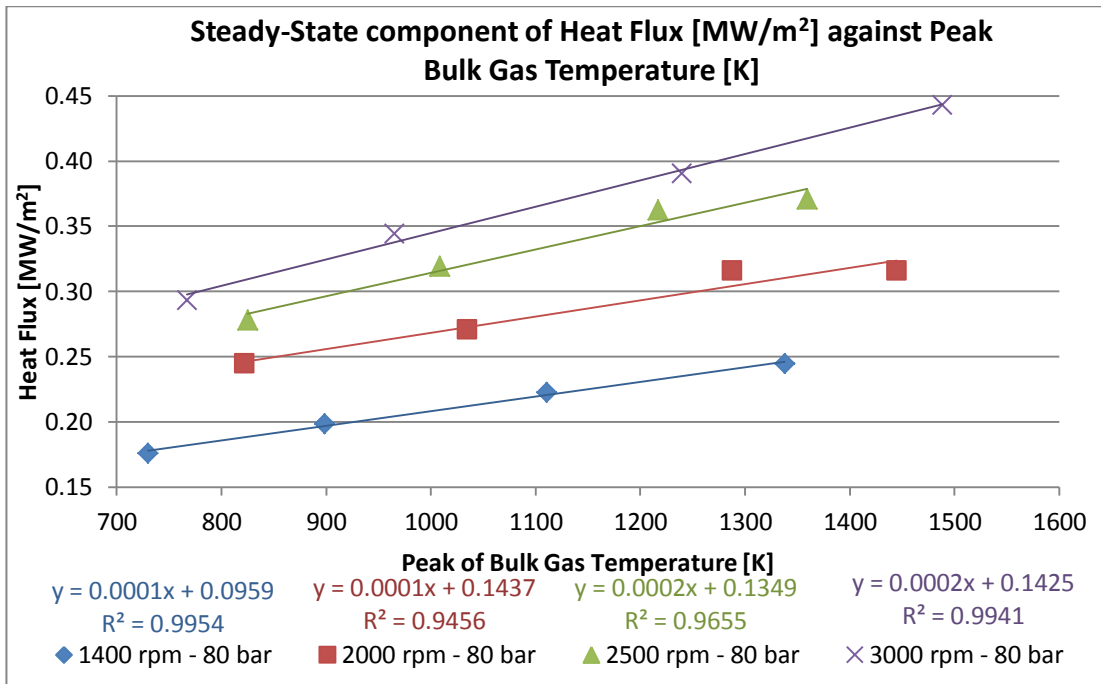
Figure 5.75. Steady-state component of heat flux obtained from the first law for the 80 bar PCP setpoints against the peak bulk gas temperature.
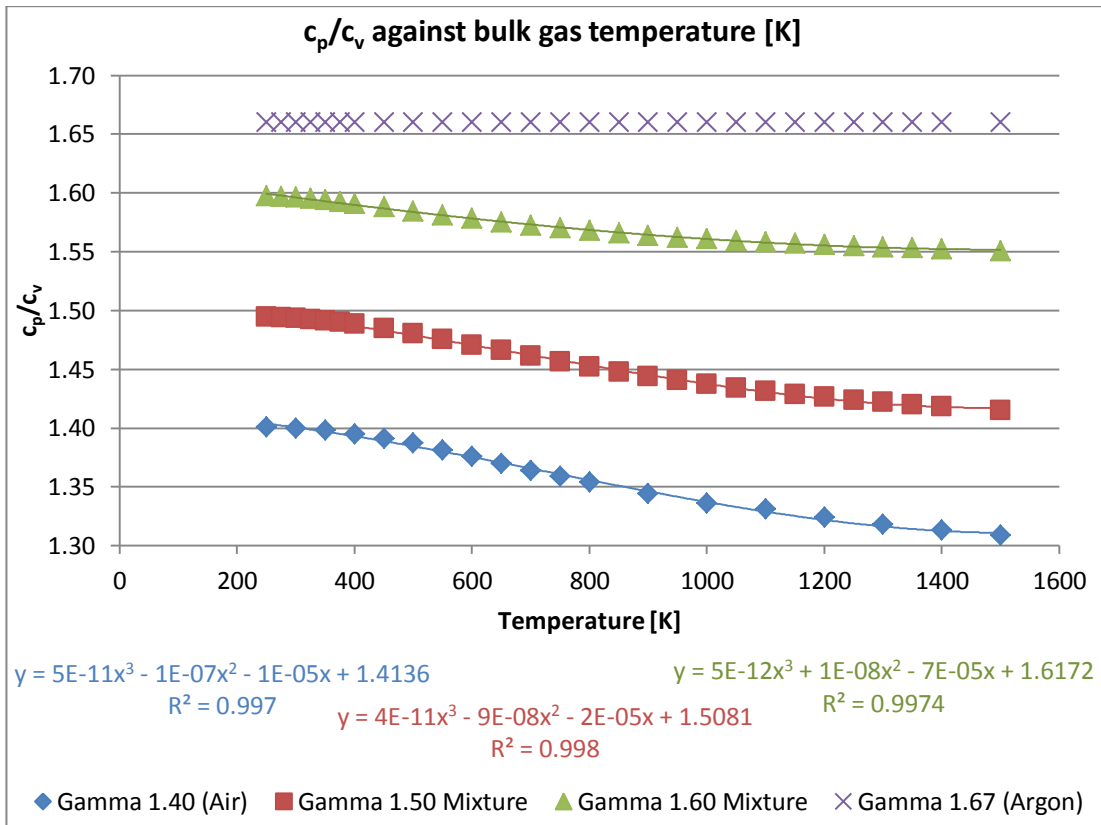
Figure 5.76. c_p/c_v against temperature. The relationship for air was obtained from [127], whereas for the other gases was calculated according to the relevant proportions of Oxygen, Nitrogen and Argon.

5.7.6 Coolant Temperature Effect on Surface Temperature and Heat Flux

The effect of oil and coolant temperature on the surface temperature and transient component of heat flux was observed in this study. The coolant used was 100% water and it was circulated with an independent electrical pump rotating at a fixed speed. Heating of the coolant was achieved through switchable heaters, whilst cooling was achieved through a heat exchanger. The oil was circulated using an external oil pump rotating at a fixed speed. The oil was heated naturally through heat exchange in the engine block, but a sandwich plate heat exchanger was also connected to a mixing valve between cool laboratory fresh water and heated water (returned from coolant heat exchanger outlet).

The oil and coolant temperatures tested in this study were 35℃, 60℃, 80℃ and 95℃. At each oil/coolant temperature, the engine speed was varied between 1400 rpm and 3000 rpm, whilst the PCP was kept at a constant 80 bar (see sub-matrix B3 in Table 5.7). It is noted that the 35℃ setpoints are not shown in Table 5.7, since these were tested in test matrix A, but only at two speeds (1400 rpm and 3000 rpm). Each oil/coolant temperature was tested on a separate day with the Aluminium thermocouple fitted at the OEM injector location. The thermocouple junction/abrasion used in this study was kept constant for the particular oil/coolant temperature tested, however the junction was renewed before every different oil/coolant temperature test session. Figure 5.77 shows the temperature responses before and after each oil/coolant temperature test for the Aluminium thermocouple. It is shown that the temperature response before each test matrix is fairly similar with a rise time of about 0.5 ms. The repeatability between the three 'before' tests is supposedly due to the fact that these temperature responses were taken just after the Aluminium thermocouple was freshly abraded with the #80 grit emery cloth. The temperature responses of the Aluminium thermocouple 'after' engine testing were not identical. It is noted that the temperature response after the 95℃ testing was the fastest at 0.275 ms, followed by that for the 60℃ oil/coolant at 0.45 ms and then by the 80℃ oil/coolant at 0.75 ms. This observation needs to be kept in sight when analysing the actual temperature data taken from the engine at the different oil/coolant temperatures.

Figure 5.78 shows the ensemble temperature taken by the Aluminium thermocouple at the OEM injector location, together with the transient component of the heat flux computed from the same temperature. It can be seen that in general increasing the coolant temperature showed an overall increase in the average surface temperature, better shown in Figure 5.79. The temperature swing from Figure 5.78 seems to increase in magnitude with an increase in the oil/coolant temperature. A noted anomaly shows that at the 80℃ oil/coolant, the temperature swing is the lowest and seems unfitting when compared to the rest of the traces for the other oil/coolant temperatures. If temporarily ignoring the 80℃ oil/coolant condition from the transient component of heat flux graphs, it can be seen that an increase in the transient component of heat flux magnitude at and around the peak (close to TDC) with an increase in the oil/coolant temperature is evident. As stated in an earlier section, since the results presented in Figure 5.78 are obtained from the Aluminium thermocouple, the absolute magnitude of heat flux should be noted with discretion. This figure is presented only to show a comparison between the different coolant/oil temperatures. Unfortunately data from other thermocouples (or locations) at different coolant/oil temperature is not available.

The thermocouple fitted at the OEM injector location used for this study was not in direct contact with the coolant. The aluminium adaptor of the thermocouple had a relatively large annular aluminium thickness around the thermocouple. The adaptor which was fitted at the OEM injector hole also had some annular gap between its circumference and the OEM injector hole which was made of a relatively thick aluminium casting.

Figure 5.80 shows the steady-state component of heat flux computed from the 1st law consideration against coolant temperature. It is shown that an increase in coolant and oil temperature from 35℃ to 60℃ showed a decrease in the steady-state component. This was followed by an increase in the steady-state component of heat flux from 60℃ to 80℃, and a decrease from 80℃ to 95℃. This trend was not totally understood, however considering the differences in magnitudes of the steady-state component between the four different coolant temperatures, it can be said that there was no appreciable variation for a coolant/oil temperature variation between 35℃ and 95℃.
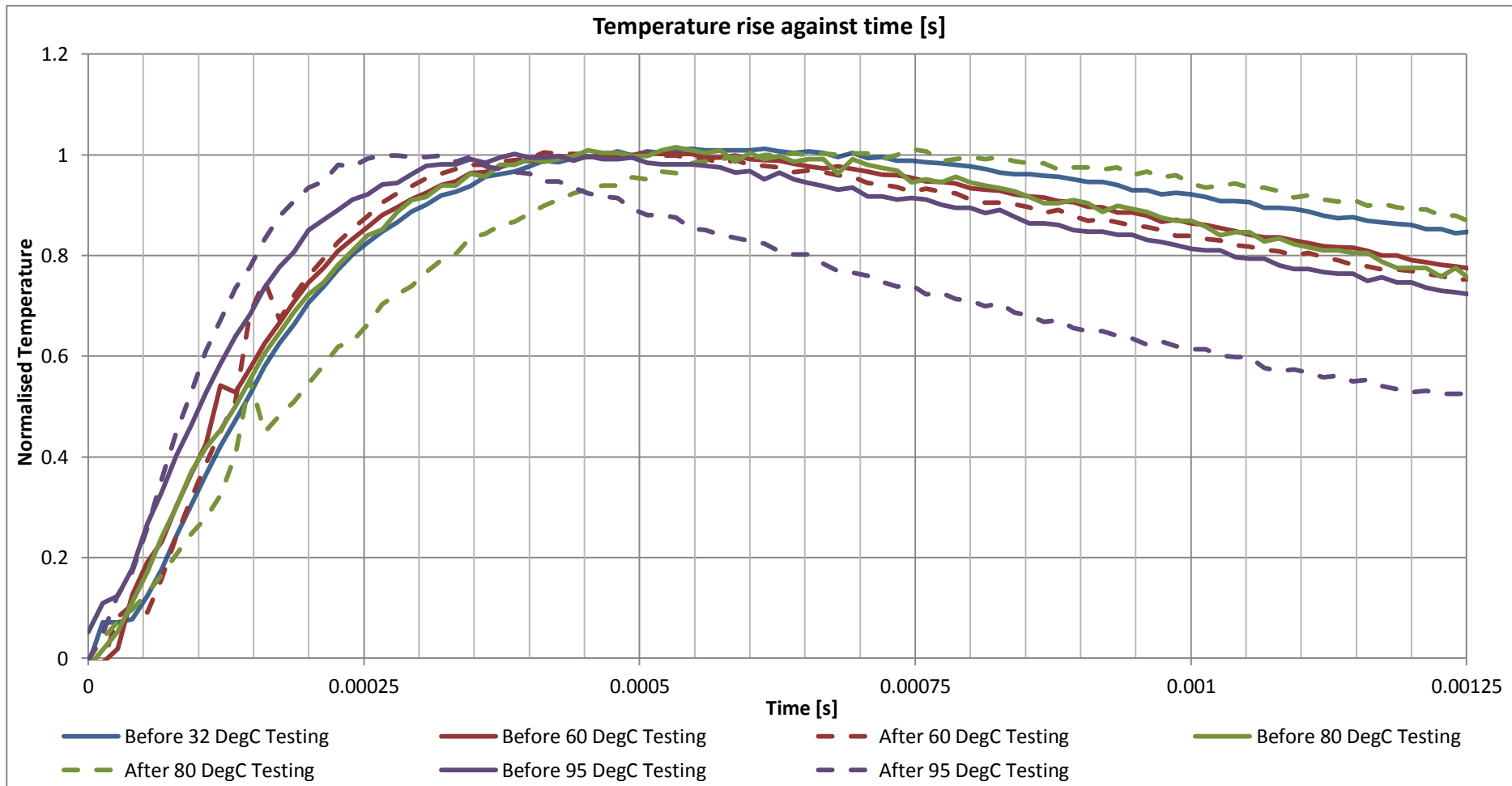
Figure 5.77. Thermocouples rise time when subjected to flash testing before and after testing of the parametric study involving different coolant/oil temperatures.
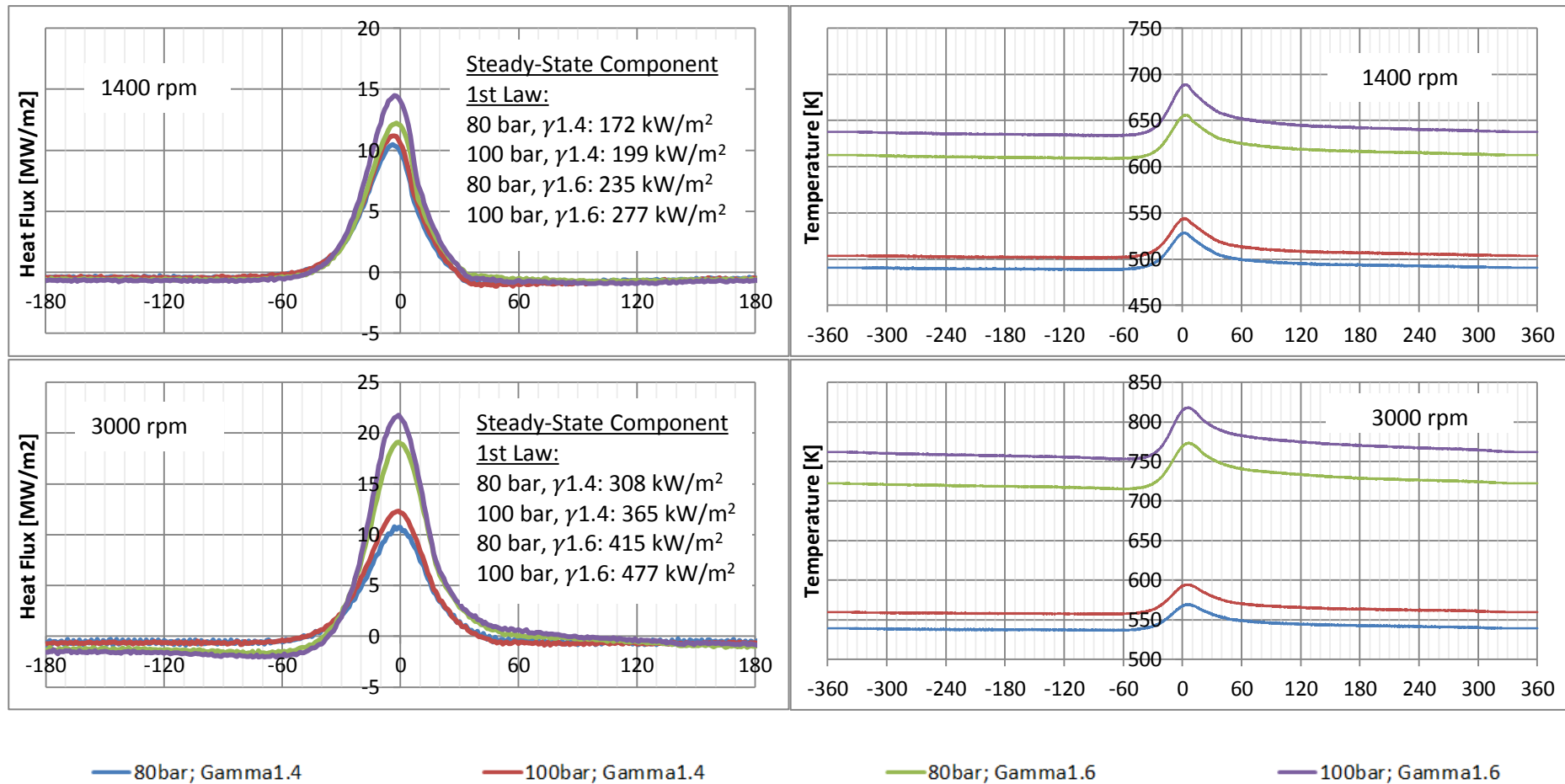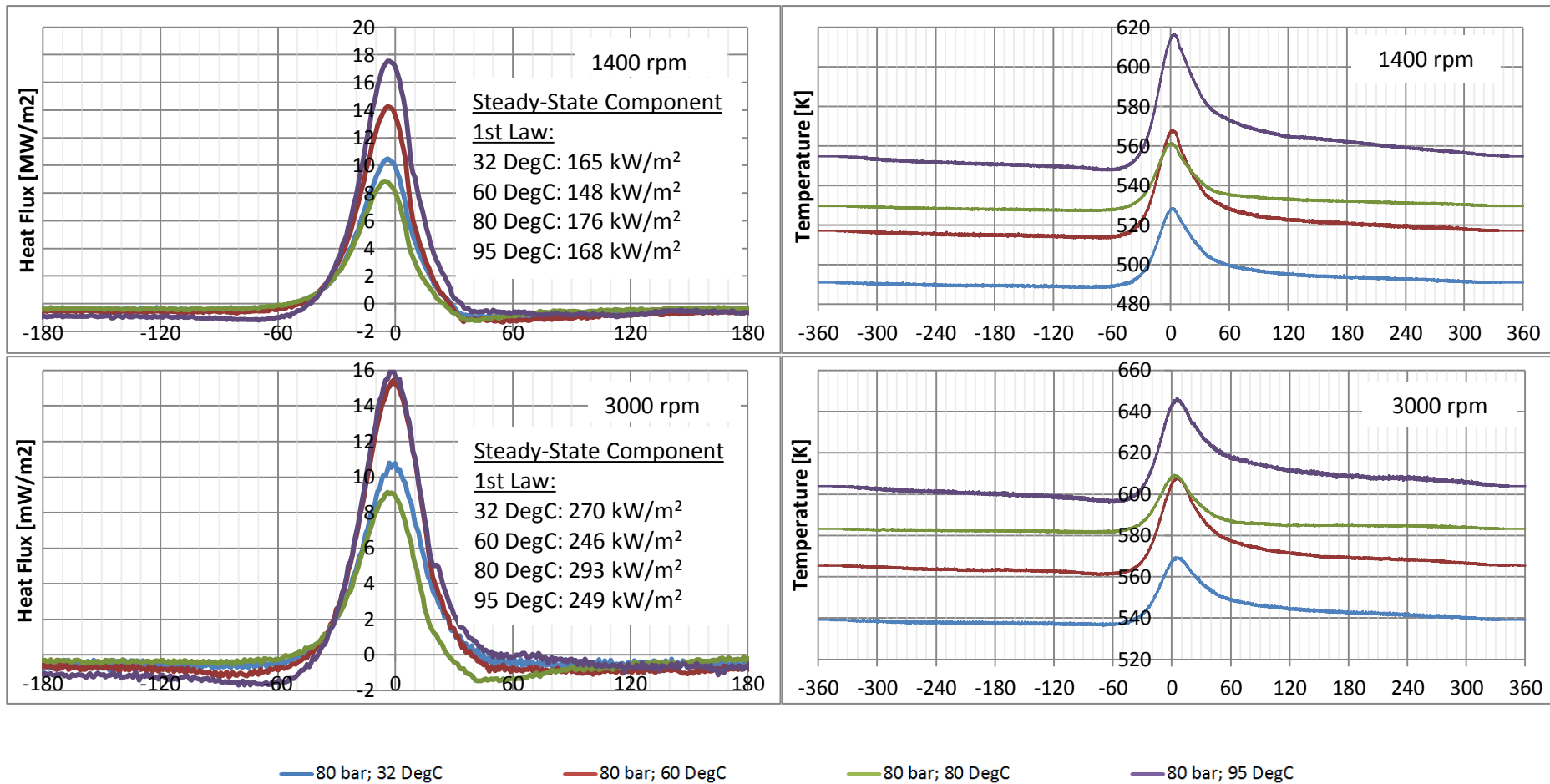
Figure 5.78. Ensemble surface temperature, measured by the Aluminium thermocouple at the OEM injector location, and the resulting transient component of heat flux at different oil and coolant temperatures. The heat flux is computed using 2D response of Chromel.
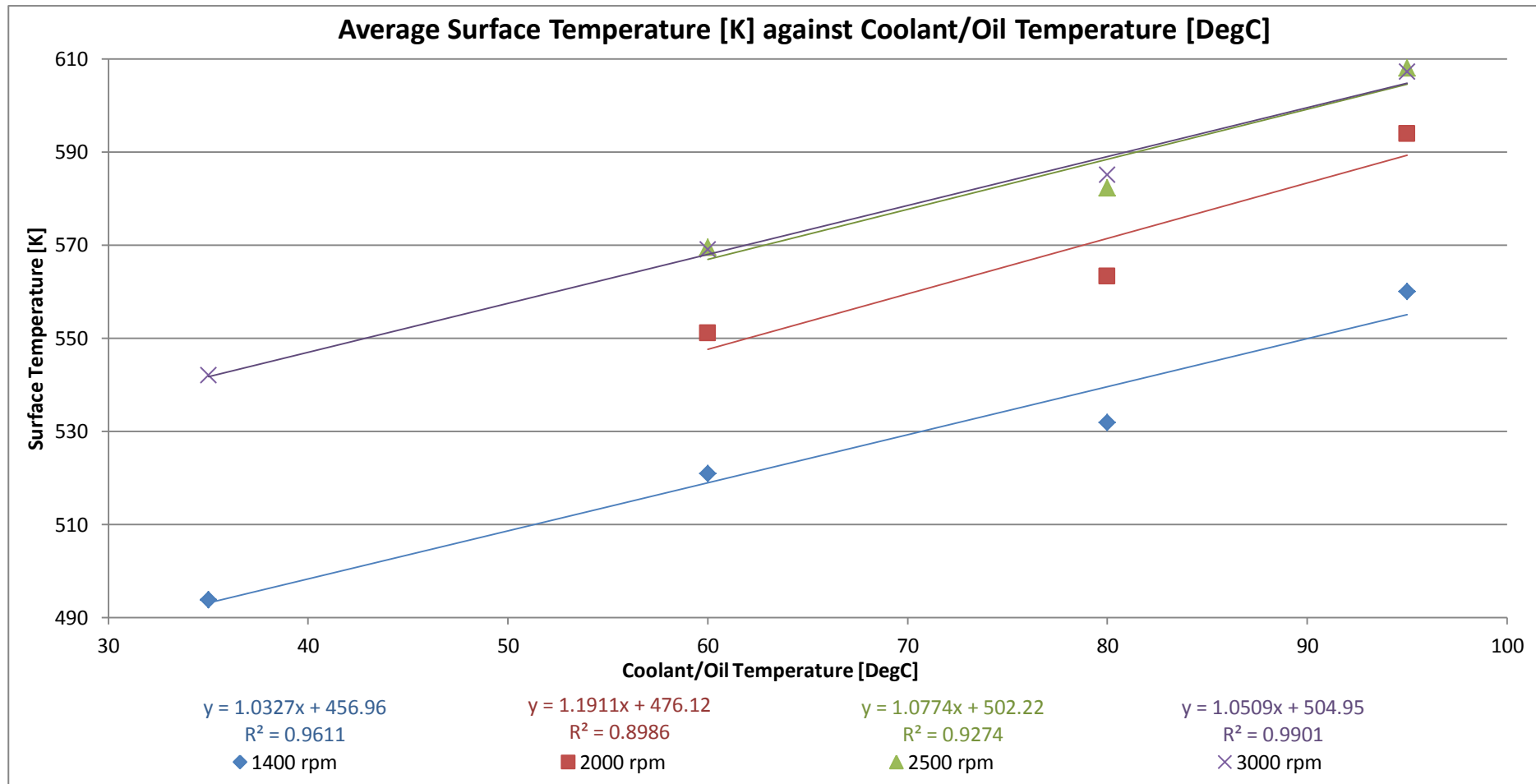
Figure 5.79. Average surface temperature measured by the Aluminium thermocouple at the OEM injector location with a variation in the coolant and oil temperatures.
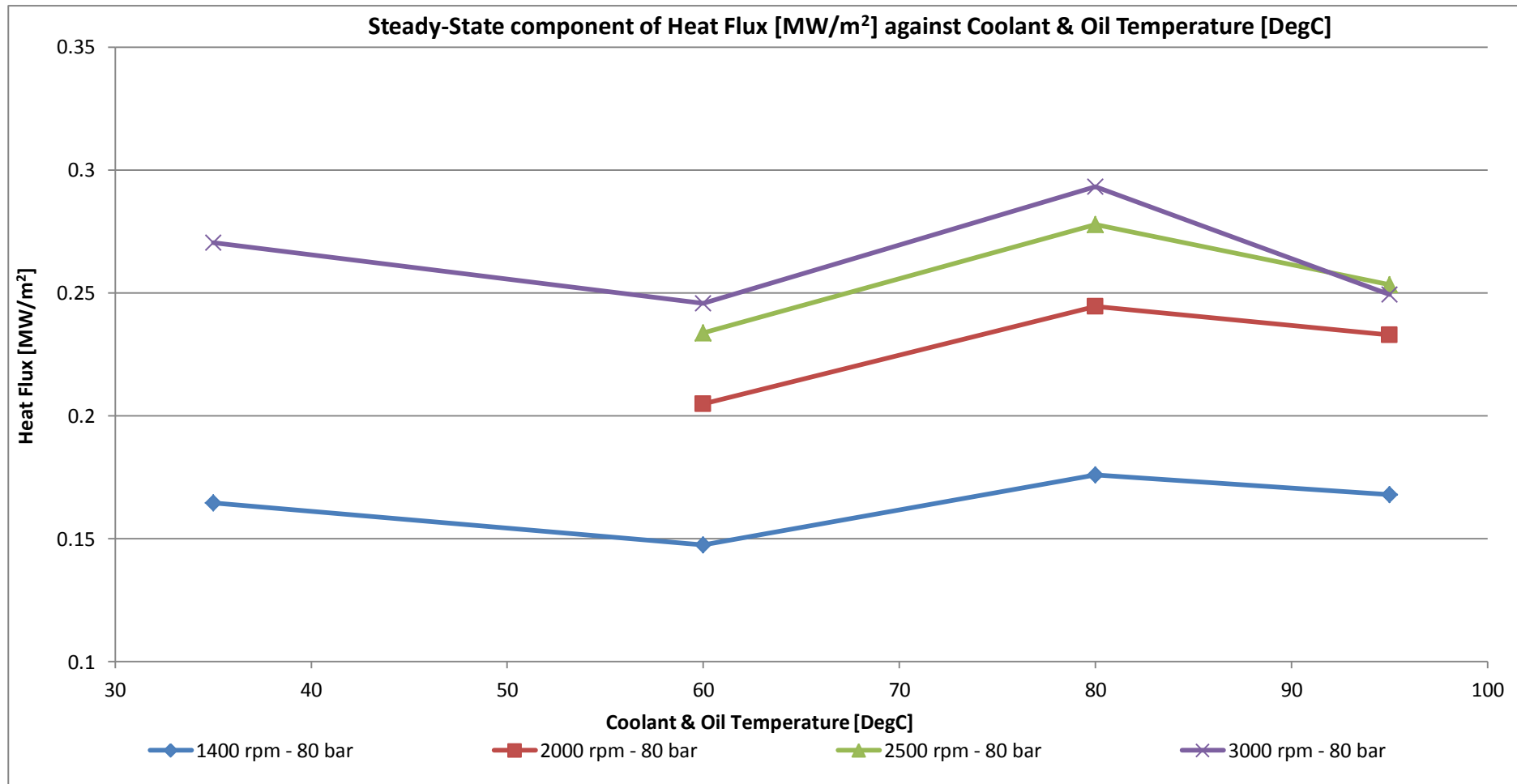
Figure 5.80. Steady-state component of heat flux obtained from the 1st law at different coolant/oil temperatures.

6 ZERO-DIMENSIONAL AND ONE-DIMENSIONAL MODELLING

The experimental results presented in Chapter 4 and Chapter 5 were aimed at contributing to the general knowledge of mechanical friction and heat flux studies. It would be beneficial if however engine models can be correlated to the experimentally obtained data for it to be of more significance to future studies. As a result this chapter involves the investigation of existing zero-dimensional and one-dimensional models mainly for FMEP and heat flux predictions.

6.1 Engine Simulation

Initially, a commercial software by Ricardo [128] was used for the development of a one-dimensional model of the pressurised motored engine. The simulation model was conducted for the four cylinder configuration. Figure 6.1 shows the canvas set up in Ricardo WAVE. Later in the project, another one-dimensional model of the 2.0 HDi engine was developed by Sammut et al. [83] using GT-Power to investigate a possible modification for future studies on the pressurised motored engine. This method was briefly described in an earlier chapter, but for the simulation results the reader is referred to [83] and [84]. In the forthcoming text, engine simulation conducted using Ricardo WAVE will be referred to as 'commercial one-dimensional model' to be clearly distinguished from one-dimensional heat flux models that will be introduced later in this chapter. Results from the commercial one-dimensional simulation are also published in [129].

In building the commercial one-dimensional model, all relevant lengths and diameters for the ports, manifolds and shunt pipe were entered as measured on the physical components presented earlier in Chapter 3. The cylinder head ports were assigned a discharge coefficient of unity. Their bend angle, as well as friction coefficient were switched off since their inefficiency was accounted for in the valve flow coefficients which were experimentally obtained, and presented earlier. Valve lift profiles were also measured and made available by Camilleri [89]. Experimental data for the manifold wall temperatures was not available; however experimental

coolant temperatures were measured and used in the model. The wall temperature for the manifolds was set to around 15℃ lower than that of the coolant for the particular setpoint considered.
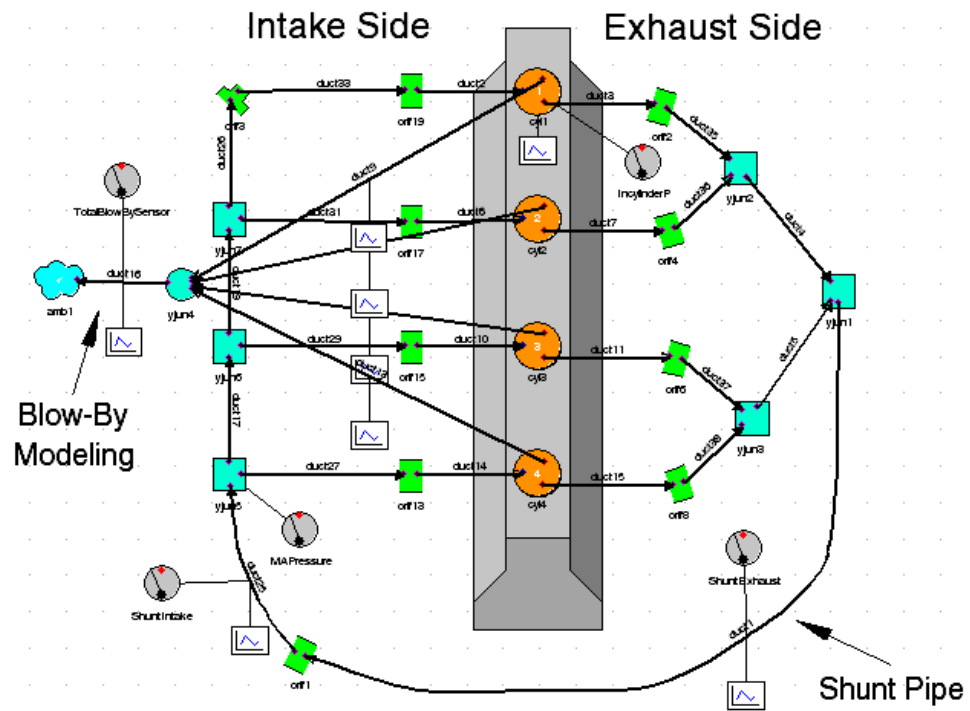
Figure 6.1. Ricardo WAVE simulation canvas.

The sub-models used in this commercial one-dimensional model were primarily two: for estimation of heat transfer and mechanical friction. For the prediction of heat flux, Ricardo WAVE presents three alternative sub-models: Annand's model [8], Woschni's model [11] and Colburn's model. Apart from these, WAVE provides the more advanced IRIS model and a user-defined heat transfer model. In this study, the model by Annand and Woschni were used separately as discussed in a later section. For the prediction of FMEP, WAVE supports only the Chen and Flynn correlation [130]. Additional sub-models like the conduction model and the thermocouple model were also considered and used, but preferred to turn them off for the final version of the model as their results were questionable.

Parameters like the thermodynamic loss angle are known to be sensitive to blow-by flow [104], even though its effect is small compared to heat transfer. Since experimental data for blow-by flow was available, a blow-by model was devised as suggested by WAVE knowledge centre [128]. The model consists of a third valve on each cylinder of the orifice type. Each of these valves were connected to a large

volume representing the crankcase. This large volume was connected to the atmosphere represented by an 'ambient element' to exhaust the blow-by. The diameter of the orifice valve was varied until the blow-by flow on each setpoint reasonably matched that obtained from the experimental sessions [79].

6.1.1 Model Correlation

In calibrating the pressurised motored commercial one-dimensional model, the experimental data presented in Chapter 4, section 4.4 was used. The test matrix for the experimental data entailed engine speeds of 1400 rpm, 2000 rpm, 2500 rpm and 3000 rpm with a peak in-cylinder pressure of 84 bar and 103 bar, and gas compositions of γ of 1.40, 1.50, 1.60 and 1.67. For the purpose of the commercial one-dimensional modelling conducted in this study, all setpoints related to air were considered successfully, however the simulation software used did not support Argon and hence experimental data for gamma of 1.50, 1.60 and 1.67 could not be modelled. These were however modelled later in the simulation study using GT-Power by Sammut et al. [84].

To calibrate the commercial one-dimensional model, certain data as obtained from experiments were input as constants for the different setpoints tested. Such information includes the engine speed, manifold absolute pressure, shunt pipe intake and exhaust temperatures, valve lifts, valve flow coefficients and other engine geometry. Results like PCP, $IMEP_{360}$, PMEP, $IMEP_{720}$ and FMEP were obtained from the simulation and compared to the experimentally obtained data. With such strategy meaningful results were obtained, however the discrepancies in the predicted metrics were still deemed too large for any qualitative deduction to be made.

The significant deviation from the commercial 1D model to the experimental data was traced down to the method by which the manifold pressure was being imposed in the model. Initially, the model was set up with an ambient element connected through an orifice to the y-junction at the exhaust collector upstream of the shunt pipe. This configuration was adopted to replicate the actual physical setup. The pressure and temperature of the ambient element were set to be equal to the MAP and shunt pipe intake temperature obtained experimentally. It was found that using an ambient element to impose the experimental MAP was acting as a strict boundary

condition, which resulted in the issues presented. This configuration of the model is not shown in this dissertation. Figure 6.1 presented earlier shows the modified version of the model.

To solve the discussed problem the ambient element was removed (as noted from Figure 6.1), and instead the manifold pressure was imposed as an initial pressure condition to the shunt pipe with an additional extra pressure required to fill all ducts with a pressure equal to that of the experimentally obtained MAP, whilst allowing also some flow as blow-by. The initial extra pressure in the shunt pipe was adjusted until the final condition in both manifolds and shunt pipe matched that obtained from the experimental MAP sensor to within ±0.001 bar. This scheme turned the shunt pipe into a sort of 'reservoir' which could provide a pressure condition in the ducts equal to the experimental MAP, while also supplying the blow-by flow. Although this strategy was found to work well, the tuning of the initial shunt pipe pressure was time consuming. Hence, such process was automated by using a PID controller responsible of varying the area of an orifice which connected an ambient element to the y-junction of the exhaust collector. With such configuration, better control of the MAP was obtained, whilst still retaining the system detached from the forced ambient element through the controlled orifice. The canvas for the improved model is shown in Figure 6.2.
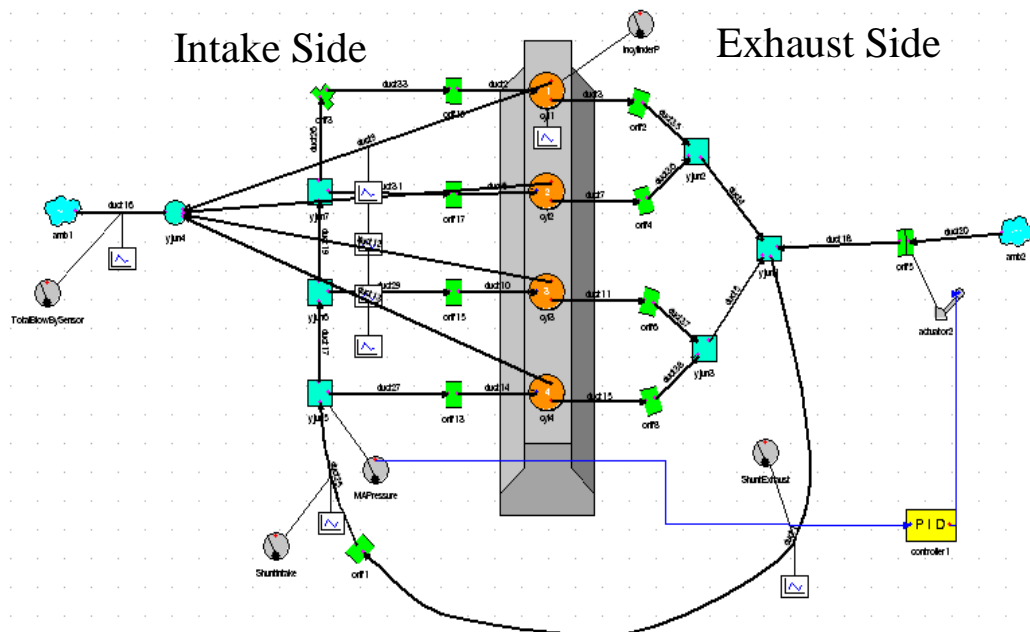
Figure 6.2. Ricardo WAVE improved canvas, including PID controller.

The in-cylinder pressure curve against crank angle was obtained from the commercial one-dimensional model for each setpoint and plotted against the relevant p-θ curve from the corresponding experimental data. To be able to compare the two traces, the experimental pressure curve was pegged on the intake stroke to the trace obtained from the commercial one-dimensional software. When pegging was attempted, it was seen that an acceptable match was evident between the wave nature of the simulation in-cylinder pressure intake stroke, and that obtained experimentally. Also, the simulation exhaust stroke in-cylinder pressure seemed to show well the recompression on the exhaust displacement phase visible in the experimental data. The phasing and magnitude of this recompression however were slightly different. To rectify the issue, an attempt was made to assign 0.3 mm of valve lash to each of the intake and exhaust valves. On this amendment, the in-cylinder pressure curve on the intake and exhaust strokes obtained from the simulation matched even better in its wave nature to that obtained from the experimental data. This was noted on all the setpoints tested and hence pegging could be now done not just at one crank angle, but on the whole intake stroke. Figure 6.3 shows the intake and exhaust stroke comparisons between that obtained from the simulation and the experimental data for two setpoints.

From this exercise it was appreciated that the simulation model gives the possibility of pegging the experimental data to the generated in-cylinder pressure. Randolph [107] explains that uncertainties in the metrics derived from experimental in-cylinder pressure processing originate mainly from uncertainties in the traditional methods of pegging. Pipitone and Beccari also explains this in [104]. In the publication by Randolph [107], 'method 8' suggests that pegging can be done to the pressure obtained from the ideal gas law equation, but stated that such method does not take into consideration the heat and blow-by losses. This issue is however catered for when pegging to the simulation in-cylinder pressure.
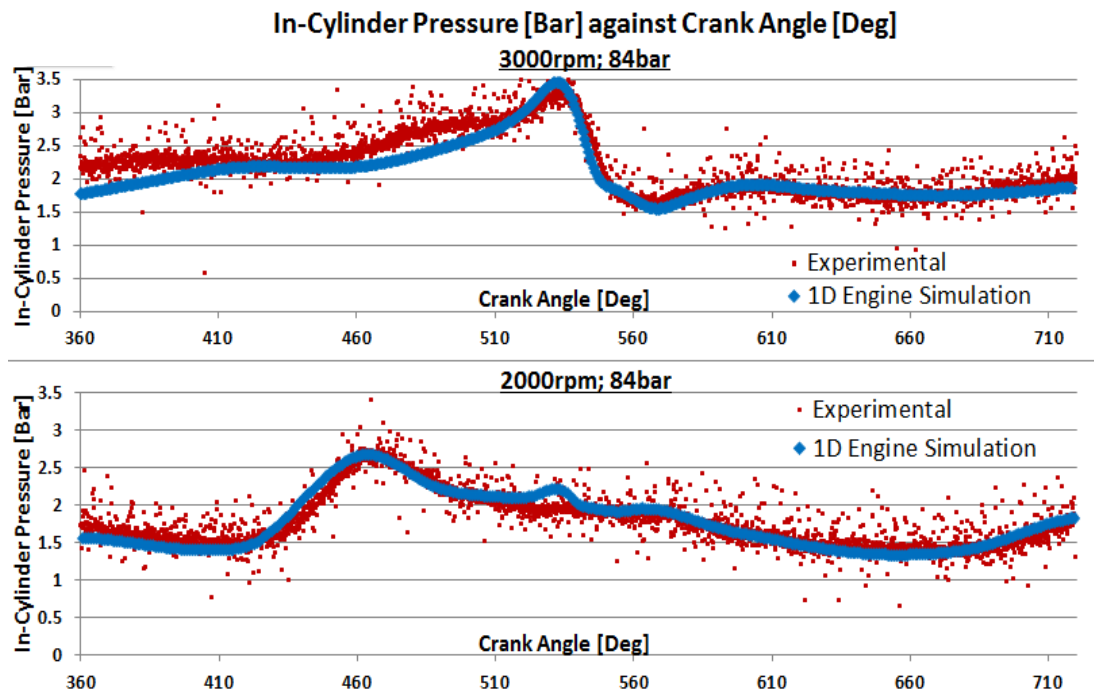
Figure 6.3. In-cylinder pressure against crank angle on the intake and exhaust strokes for two different setpoints.

After pegging the traces on the whole intake strokes, the full 720° simulation in-cylinder pressure cycle was compared to that from the corresponding experimental data. It was noted that some discrepancy on the peak in-cylinder pressure was evident. The heat transfer multiplier on closed valve for the heat transfer correlation was tweaked in the hope of getting a match on the peak in-cylinder pressure, however it was seen that when the peak pressure was successfully matched, the in-cylinder pressure during the compression stroke for the simulation fell below that of the experimental pressure trace by a significant amount as seen in Figure 6.4a. A similar observation was noted on the expansion stroke. Such discrepancy on the compression and expansion strokes led to a 38% discrepancy in the $IMEP_{360}$ on the setpoint of 3000 rpm; 84 bar between the simulation and experimental cases. To rectify this issue, the cylinder head, piston and liner temperatures were shifted to higher temperatures than the coolant temperature obtained experimentally by different amounts dependent on the engine speed setpoint, but not higher than the oil temperature of 80°C, as imposed experimentally. The higher the engine speed, the higher the temperature required due to a lesser time for heat to flow out of the system. Such amendment seemed to give a better all-around match between the simulation and experimental in-cylinder pressure traces as shown in Figure 6.4b.

Consequently the $IMEP_{360}$ showed a better match as well. Figure 6.5 shows the overall comparison between the simulation and experimental pressure traces on the same 3000 rpm; 84 bar. With such better comparison, the discrepancy in the $IMEP_{360}$ on the same setpoint of 3000 rpm; 84 bar was reduced to 9%.
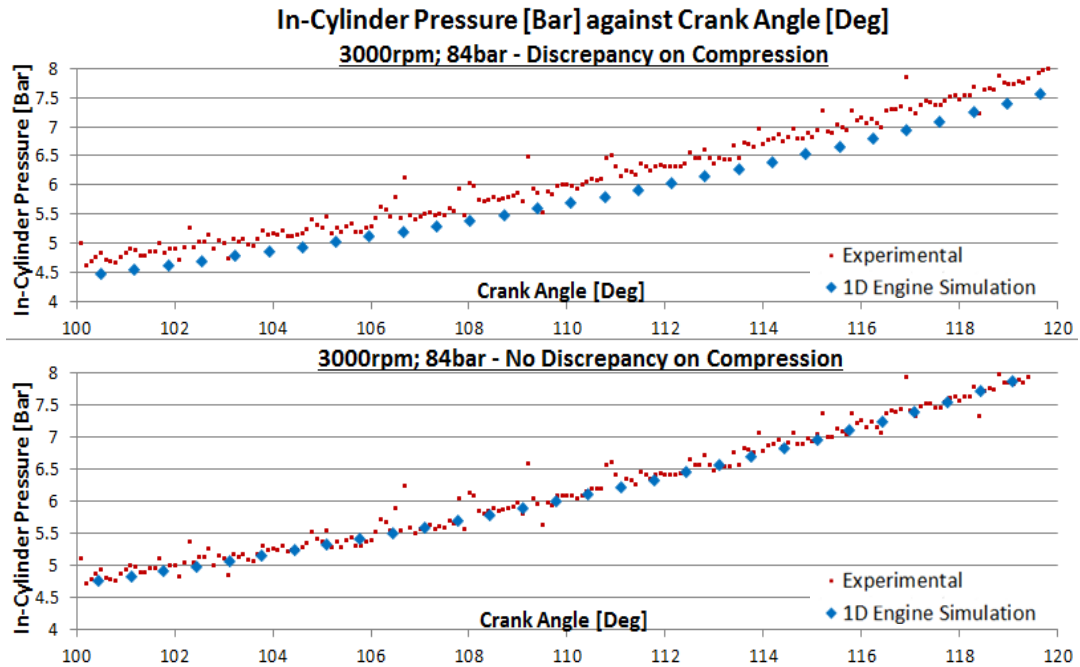
Figure 6.4. In-cylinder pressure against crank angle: a) Discrepancy on compression, b) No discrepancy on compression.
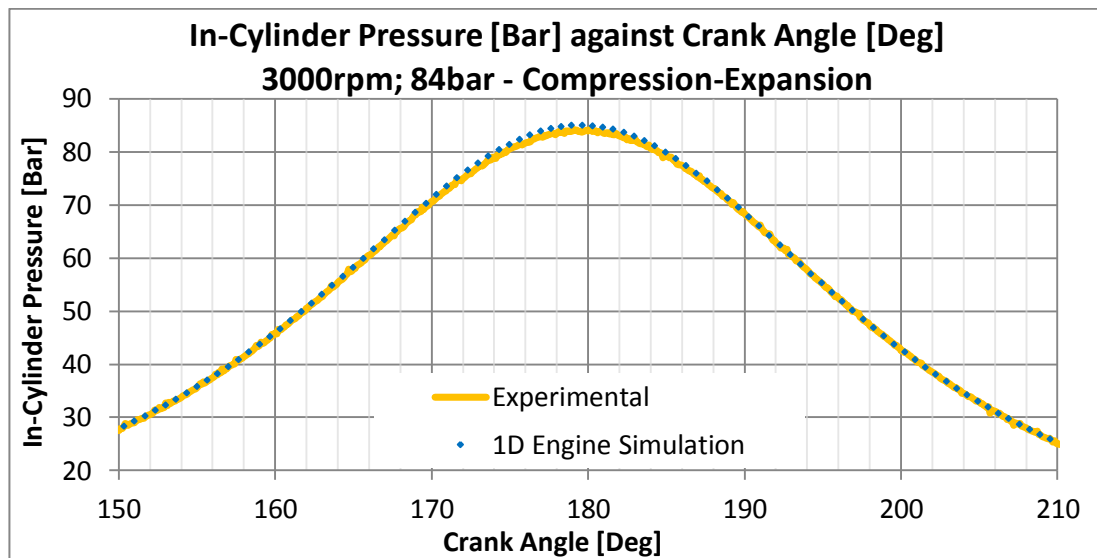
Figure 6.5. In-cylinder pressure against crank angle showing comparison between experiment and simulation data on the compression and expansion strokes.

6.1.2 Trapped Mass Estimation

To understand further the discrepancy between simulation and experimental results, the trapped mass at IVC obtained on each setpoint from the simulation was compared to that calculated using the ideal gas law equation on the respective experimental data. The trapped mass at IVC was matched to be within 10%; however it should be appreciated that several inaccuracies surround the calculation of the trapped mass on the experimental data. The trapped mass during the closed-valve period was calculated by decreasing the mass escaped as blow-by at each crank angle from the initial estimation of trapped mass at IVC using the ideal gas law, where the pressure is estimated equal to the measured MAP, and the temperature equal to the measured shunt pipe temperature at the intake side. It should be realised that both the MAP and the measured shunt pipe intake temperature are not accurate representations of the actual pressure and temperature in the cylinder at IVC. This is because of the intake valve inefficiency and the heating/cooling of the air from the measured point (shunt pipe intake throat) to the cylinder. As a result inaccuracies in the trapped mass calculated for the experimental data are unavoidable. The trapped mass during the gas-exchange strokes was calculated using a crank-angle resolved format of the ideal gas law, also utilising the shunt pipe temperatures and in-cylinder pressure. Figure 6.6 shows the trapped mass estimates at 3000 rpm and 84 bar.
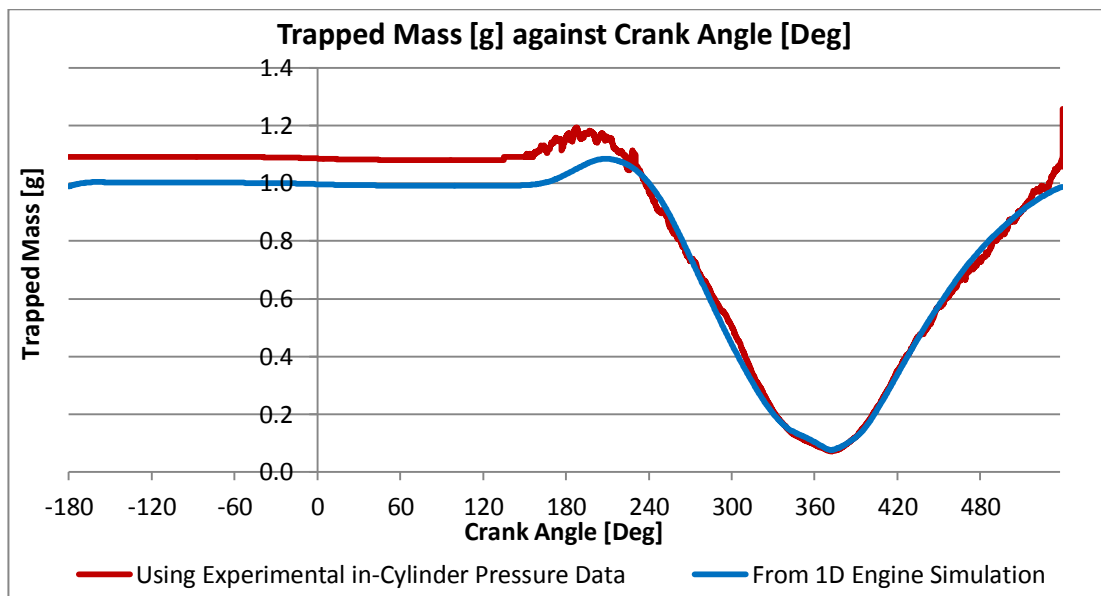
Figure 6.6. Trapped mass against crank angle for the 3000 rpm; 84 bar. (-180 DegCA to +180 DegCA represent the compression and expansion strokes)

6.1.3 Blow-by

As noted earlier from Figure 6.1 and Figure 6.2, a blow-by system was added to the model as a third valve on each cylinder, as suggested by WAVE knowledge centre [128]. The diameter of the assigned orifice valve was varied until a reasonable agreement on the cycle-average blow-by flow rate was obtained with that measured experimentally in [79] [78] at all setpoints. The orifice diameter which was found to give the best overall results was 0.6 mm on each cylinder. It was noted that the peak in-cylinder pressure obtained through the simulation model had a large effect on the relatively small blow-by flow rate, meaning that a small deviation of the peak in-cylinder pressure from the setpoint of 84 bar had a significant difference on the blow-by average value.

To have a rough comparison between the simulation-obtained crank-resolved blow-by flow-rate and that probably expected in the engine, the crank-resolved blow-by flow rate was calculated using the in-cylinder pressure and instantaneous trapped mass using the convergent-divergent nozzle equations, given by equation (4.6) and equation (4.7), presented earlier in Chapter 4. This calculation was adopted from [104]. Figure 6.7 shows the comparison of the crank-angle resolved blow-by flow rate between that obtained from simulation and that obtained using equation (4.6) and equation (4.7) on the experimental data, at 3000 rpm; 84 bar.
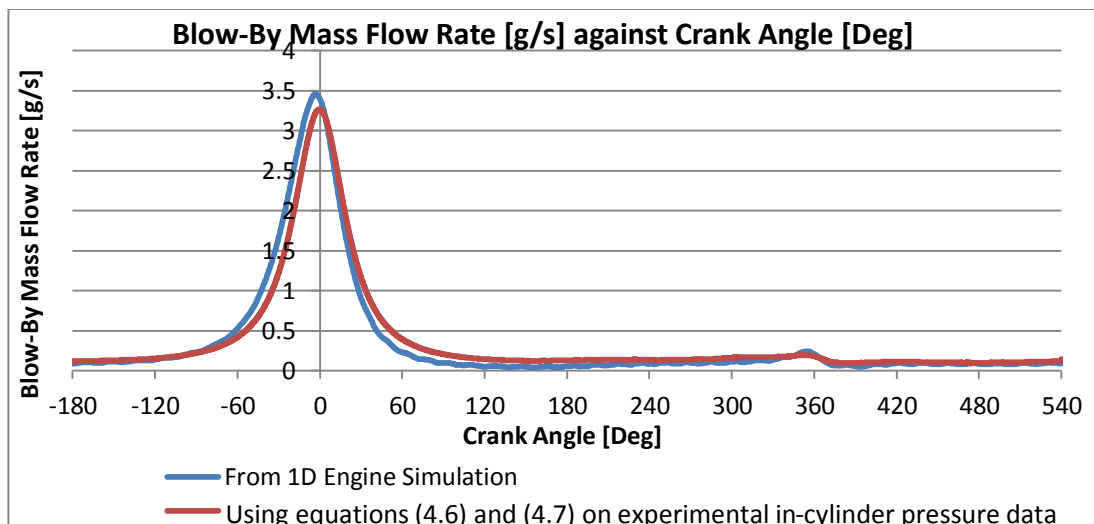
Figure 6.7. Blow-by flow rate of cylinder 1 obtained from simulation and using equations (4.6) and (4.7) on the experimental data at 3000 rpm; 84 bar PCP.

Figure 6.8 shows the simulation-obtained blow-by flow rate for just cylinder one, a summation of all four cylinders, a four cylinder cycle-averaged, and that measured experimentally in [79] [78] at 3000 rpm, 84 bar. It is noted from both Figure 6.7 and Figure 6.8 that the blow-by flow rate follows the in-cylinder pressure, resulting in a high blow-by flow rate around TDC compression, and a small peak at the exhaust stroke due to the exhaust recompression effect. From Figure 6.8, it is noted that the 0.6 mm orifice used to model blow-by in WAVE resulted in a good agreement with the measured cycle-average at the displayed setpoint of 3000 rpm, 84 bar, but also at the other setpoints considered.
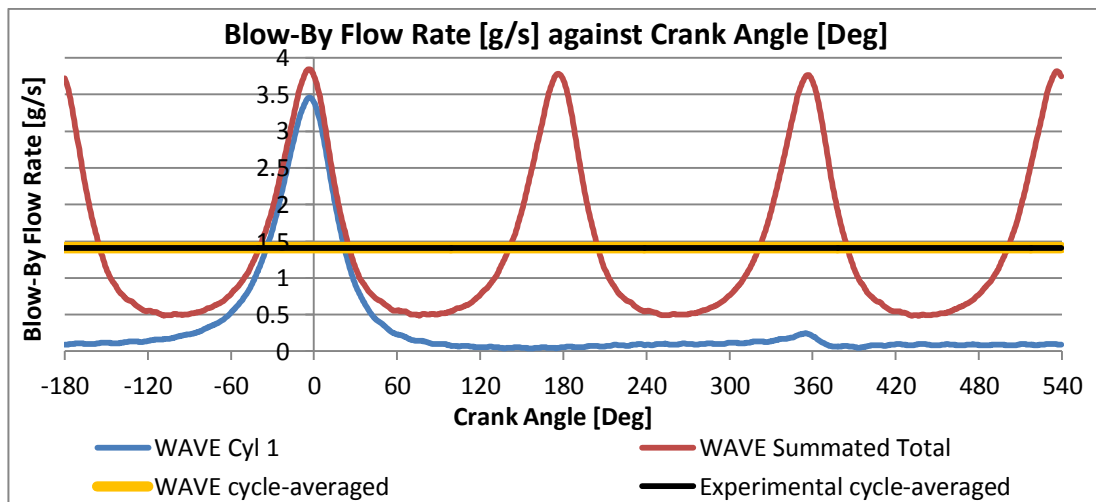
Figure 6.8. Blow-by flow rate against crank angle.

To investigate the effect of blow-by on the simulation results, the model was re-run with the blow-by system removed. It was noted that on the 3000 rpm, 84 bar the PCP increased from 84.5 bar to 85.5 bar. The $IMEP_{360}$ magnitude decreased from 0.862 bar to 0.777 bar. Such variations are consistent with theory, since blow-by acts to reduce the PCP through leakage, while increases the magnitude of the overall losses. With no blow-by, the LPP is also expected to be closer to TDC. During this study it was understood that Ricardo WAVE obtains the location of peak in-cylinder pressure by finding the point of $\frac{dP}{d\theta} = 0$ on the polynomial fitted to the generated in-cylinder pressure curve. The crank angle resolution of the generated p-θ curve in the commercial one-dimensional software was noted to vary with engine speed and was never better than 0.6 DegCA. This therefore implies that the LPP as obtained from the commercial one-dimensional software might be in disagreement with that obtained experimentally which had a resolution of 0.1 DegCA. At 3000 rpm and 84

bar with the blow-by model activated, the commercial one-dimensional model predicted a loss angle of -0.43 DegCA, whereas with the blow-by model de-activated, the loss angle was estimated as -0.37 DegCA. The experimental results gave a loss angle of -0.30 DegCA on the same setpoint.

6.1.4 Predicted Metrics

The $IMEP_{360}$, PMEP, BMEP and PCP obtained from simulation are compared to those obtained experimentally in Figure 6.9 to Figure 6.12. The figures show two results for the simulation; one corresponding to the simulation run using Annand's heat transfer model, and the other using Woschni's heat transfer model with intake scavenging. It is noted that the $IMEP_{360}$ compares well to the experimental values with maximum deviations of around 9%. Deviations in the $IMEP_{360}$ originate primarily from deficiencies in the heat transfer sub-models. The PMEP also shows relatively good comparison at 1400 rpm and 2000 rpm, but deviates to a maximum of 14% at the higher speed setpoints. This might be the result of the phase difference between the wave natures of the pressure on the exhaust stroke noted only at the higher speeds, as shown in Figure 6.3a. The comparison between the experimentally obtained BMEP and the results from the simulation show very good agreement, however it is the opinion of the author that the BMEP is not a good a metric to be used for calibration of the simulation to the experimental data. This is due to the fact that the BMEP from the commercial simulation incorporates the errors in the prediction of the $IMEP_{360}$, the PMEP, and most importantly the errors in predicting the FMEP, which might cancel each other (depending on the sign of the error) and result in a falsely interpreted good BMEP comparison.

The PCP comparison in Figure 6.12 shows that a good agreement of less than 1 bar was obtained at engine speeds equal to and higher than 2000 rpm. An over-prediction of the PCP was however noted at the 1400 rpm. Although the PCP error at this setpoint was more than what is ideally required, it was preferred to accept it rather than tune the simulation parameters for the individual setpoint. This is due to the fact that if the simulation is used to predict setpoints at which no experimental data is available, the simulation has to be capable of extrapolating based on a good average representation of all the experimentally tested setpoints of the engine.
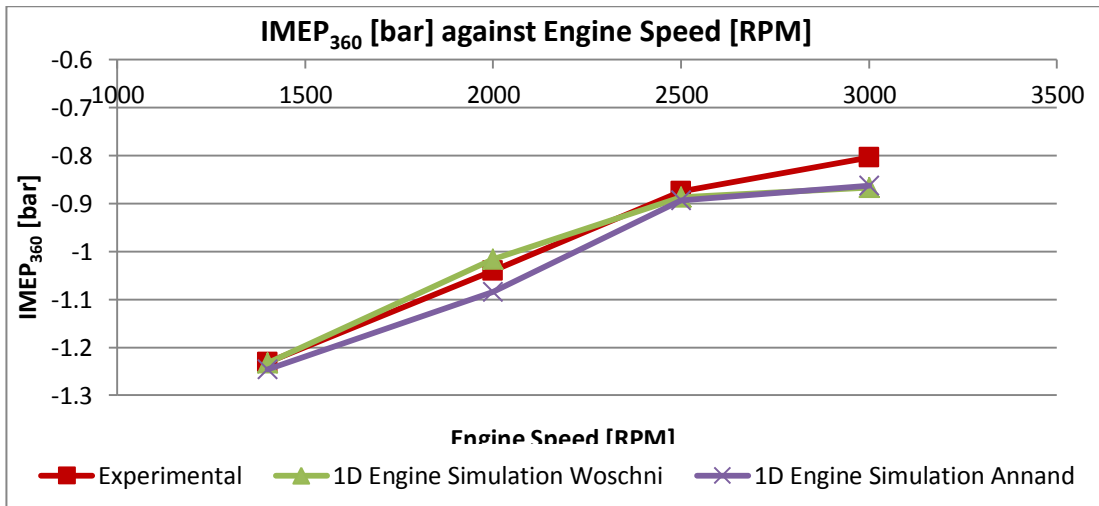
Figure 6.9. IMEP$_{360}$ graph comparing simulation and experimental results.
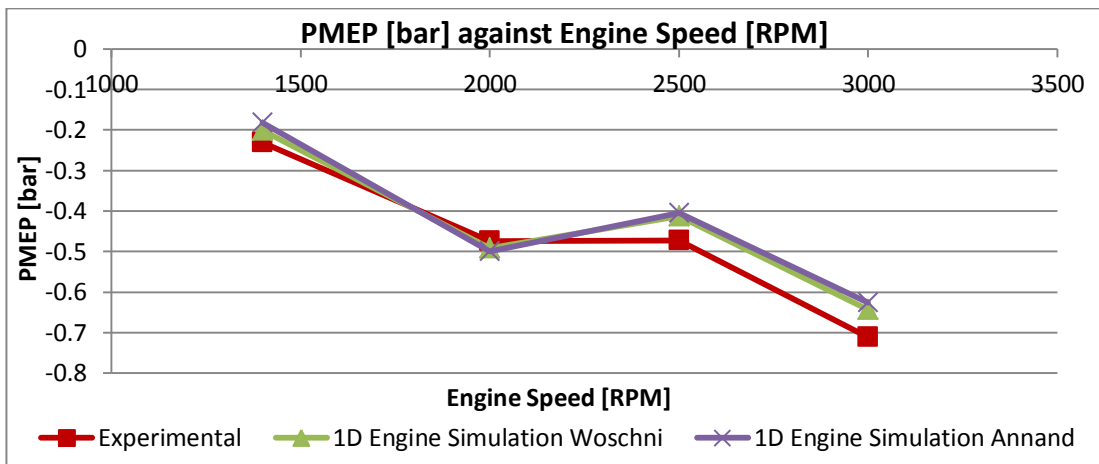
Figure 6.10. PMEP graph comparing simulation and experimental results.
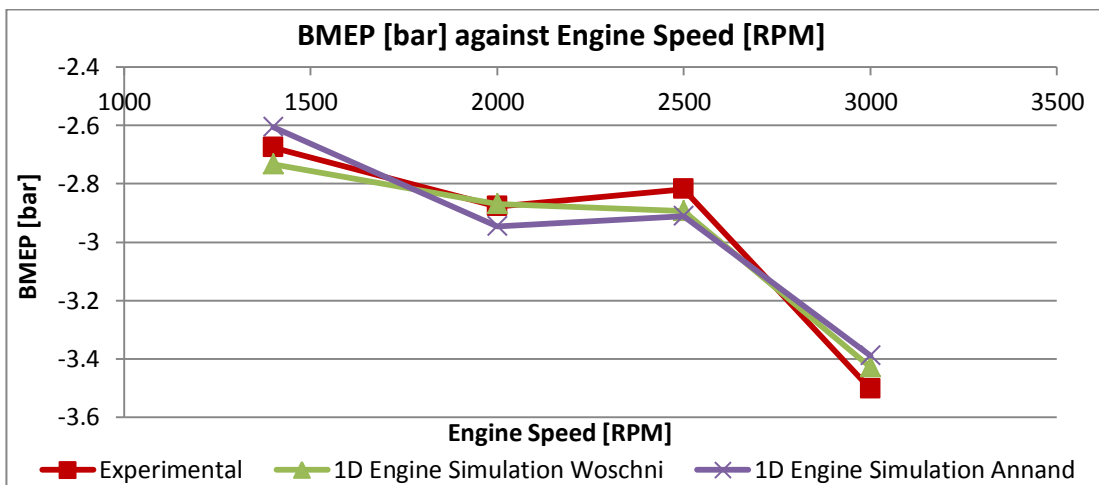
Figure 6.11. BMEP graph comparing simulation and experimental results.
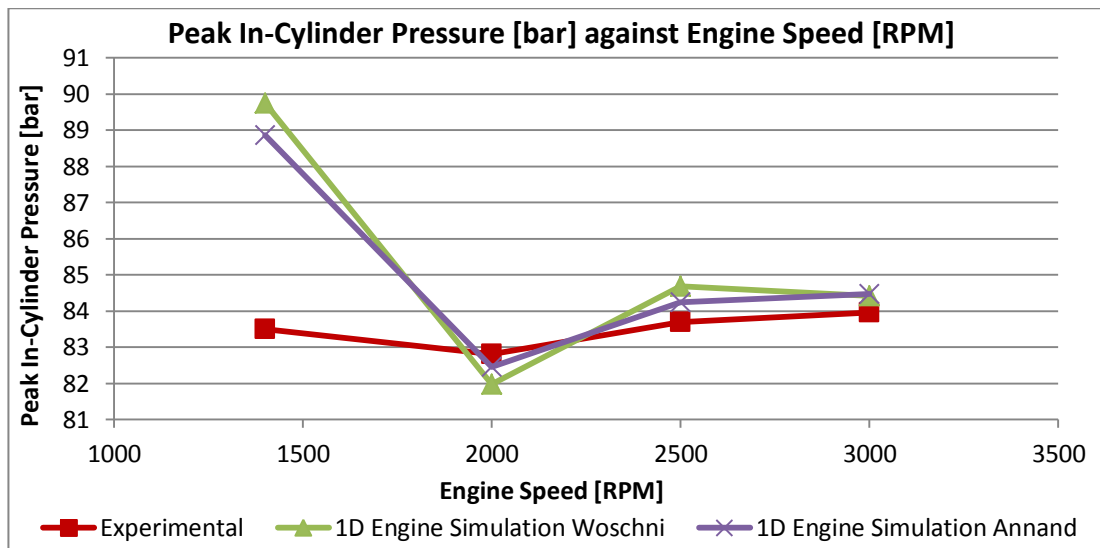
Figure 6.12. PCP graph comparing simulation and experimental results.

6.1.5 Zero-Dimensional (One-Zone) Heat Transfer Models

In this commercial one-dimensional simulation, the heat transfer sub-models used were those by Annand [8] and Woschni [11] which are of a zero-dimensional type. The 'multiplier on closed valve' which was found to give a sensible agreement between the simulated in-cylinder pressure and that obtained experimentally was around 0.42 for Annand's model. It should be noted that although the coefficient for Annand's model can be set between 0.25 and 0.80 according to WAVE knowledge centre [128], the value of 0.42 that was found optimal in this work is very close to that of 0.49 as proposed by Annand for an open-chamber DI engine in [8]. The 'multiplier on closed valve' for the Woschni model that was found to give optimal results is 1.20. Both the coefficients for Annand and Woschni models were chosen based on an evaluation of the agreement between the simulated in-cylinder pressure and that obtained experimentally on the whole test matrix. Figure 6.13 shows the in-cylinder temperature given by the simulation software and the heat transfer from the same cylinder as computed through Annand's and Woschni's models, for the setpoint of 3000 rpm; 84 bar.
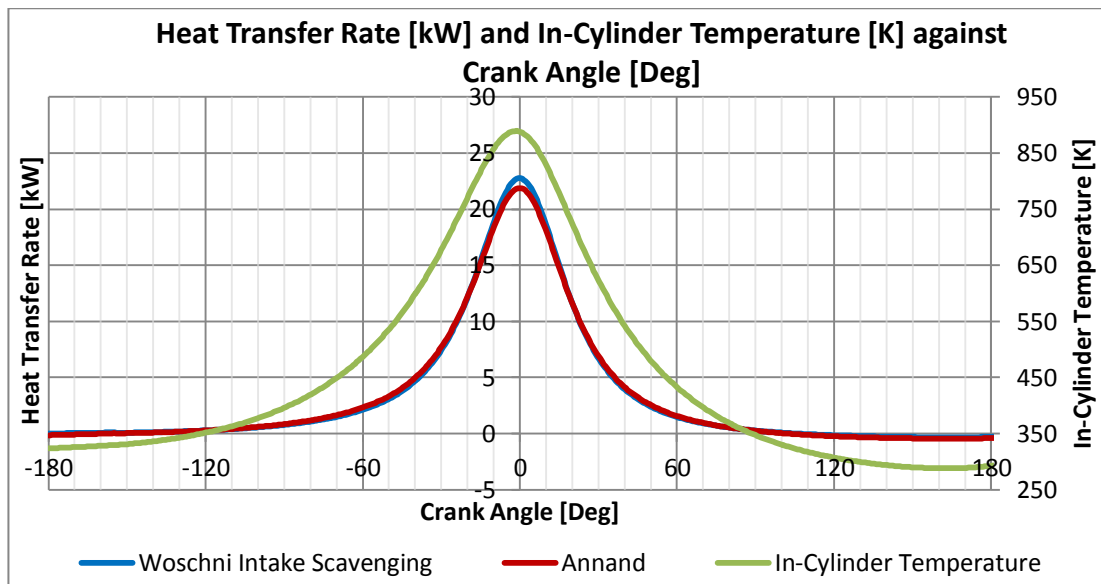
Figure 6.13. In-cylinder temperature and heat transfer rate obtained through Annand's and Woschni's correlation at 3000 rpm; 84 bar.

As explained in the literature review chapter, the models suggested by Annand and Woschni have their own shortcomings in predicting the heat flux of the combustion chamber surface due to the fact that they neglect important phenomena, such as the compression work in the boundary layer. In fact, an observation of Figure 6.13 reveals that the heat transfer is predicted to be centred and symmetric about TDC compression. Due to the inaccurate representation of the crank-angle resolved heat transfer, it cannot be expected that the simulated crank-angle resolved in-cylinder pressure will match exactly at each crank angle to that obtained experimentally. This means that if an attempt is made to match the predicted in-cylinder pressure to that experimentally obtained to a very high degree, the deficiencies in crank-angle resolved prediction of heat flux from these models might end up being 'falsely' compensated for by a compromise between other tuning parameters, such as cylinder head, piston and liner temperatures, compression ratio and trapped mass. In fact it was noted that the temperatures that had to be assigned to the cylinder head, piston and liner fell between those of the measured coolant and oil temperatures, hence were slightly cooler than what is expected from actual engine operation.

The compression ratio stated by the OEM for the engine tested and simulated is 18:1. This value was confirmed through a static compression ratio measurement using paraffin. It is however known that CR values do vary from that given in the engine manual [104] due to thermal expansions and gas pressure loading. The value of CR

which was found to give the best all round compromise in this simulation study was that of 17.3:1.

To have a better representation of the heat transfer, the thermodynamics first law as presented in Chapter 5, section 5.5 (equation (5.13)) was considered on the system for the closed-valve period, *i.e.* compression and expansion strokes, as suggested by Heywood [131]. Close examination of equation (5.14) reveals that with this approach, the heat transfer is computed from the rate of change of in-cylinder pressure, based on the conservation of energy principle. This is possible in the motored engine due to the fact that the deviation of the rate of change of pressure from an isentropic compression is solely due to the heat transfer from the cylinder walls, and blow-by flow.

It was explained in the previous chapter that since equation (5.14) does not have a term specifically representing the loss due to blow-by, the term $\frac{dQ}{dt}$ represents the total losses of heat and mass leakage. To correct this, Pipitone and Beccari [104] introduced a term in equation (5.14) which is the loss rate equivalent of blow-by. The modified version of equation (5.14) was given in the previous chapter by equation (5.15). Equation (5.14) was used on the ensemble average experimental in-cylinder pressure data and $\frac{dQ}{dt}$ is plotted in Figure 6.14 for the 3000 rpm; 84 bar. Figure 6.14 also shows the heat transfer corrected for blow-by obtained from equation (5.15) for the same setpoint. It can be noted that due to electrical noise interference present in the in-cylinder pressure data, the term $\frac{dP}{dt}$ in equation (5.14) and equation (5.15) is prone to serrations with large amplitudes. Due to this, a moving average filtering scheme was implemented both on the pressure trace and the heat transfer curve. It was also made sure that with this filtering scheme the shift in the pressure trace was not significant. This can be seen in Figure 6.15.

Figure 6.16 shows the crank angle resolved heat transfer obtained from Annand's and Woschni's models, together with the heat transfer obtained from the 1st law, compensated for blow-by. It is noted that the 1st law consideration shows a similar heat transfer to that obtained from experimental data in Chapter 5, where the heat transfer was seen to peak at crank angles before TDC compression, and to fall rapidly to negative values just after compression TDC. The positive peak in heat

transfer was calculated from the first law to be twice that from Annand's and Woschni's models. Although the crank angle resolved heat transfer from Annand and Woschni models seem significantly different from that obtained experimentally, and from the first law, their cycle-averaged values are similar. The cycle-average heat flux (computed over the closed part of the cycle) at 3000 rpm, 84 bar from Annand's model was found to be 3.322 kW, 3.348 kW from Woschni's model, and 4.038 kW from the 1st law using the experimentally obtained in-cylinder pressure.
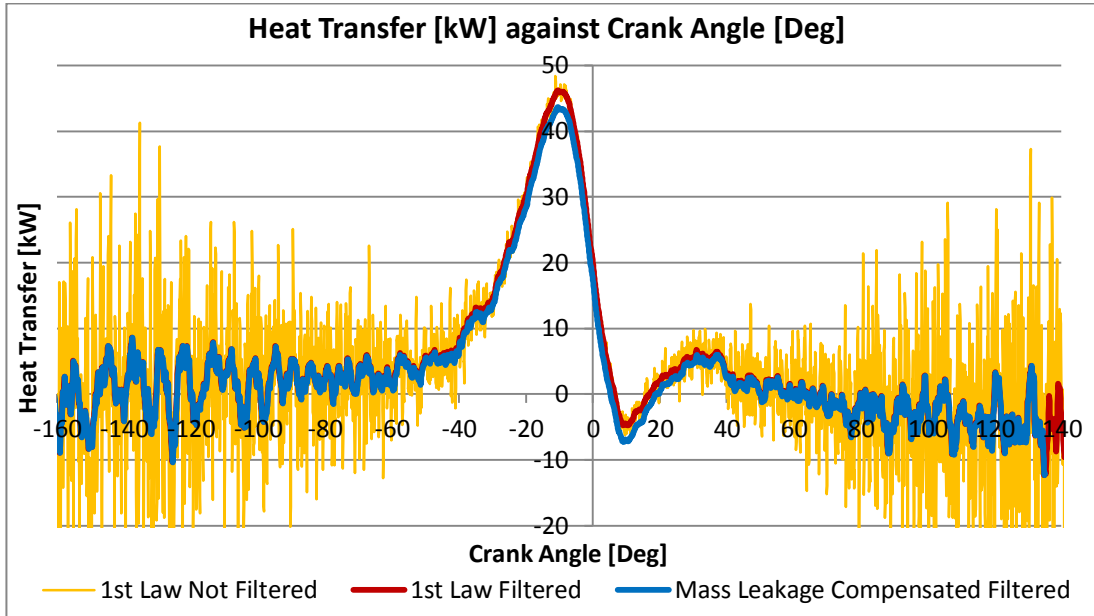
Figure 6.14. Heat transfer rate against crank angle at 3000 rpm; 84 bar.
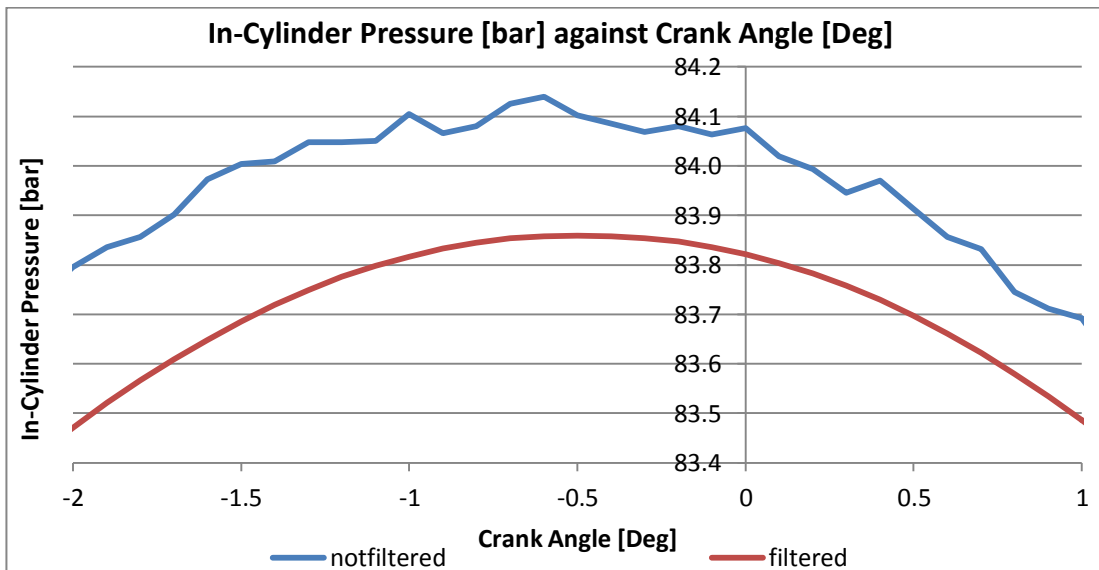
Figure 6.15. Comparison graph between filtered and unfiltered experimental in-cylinder pressure data at 3000 rpm and 84 bar PCP.
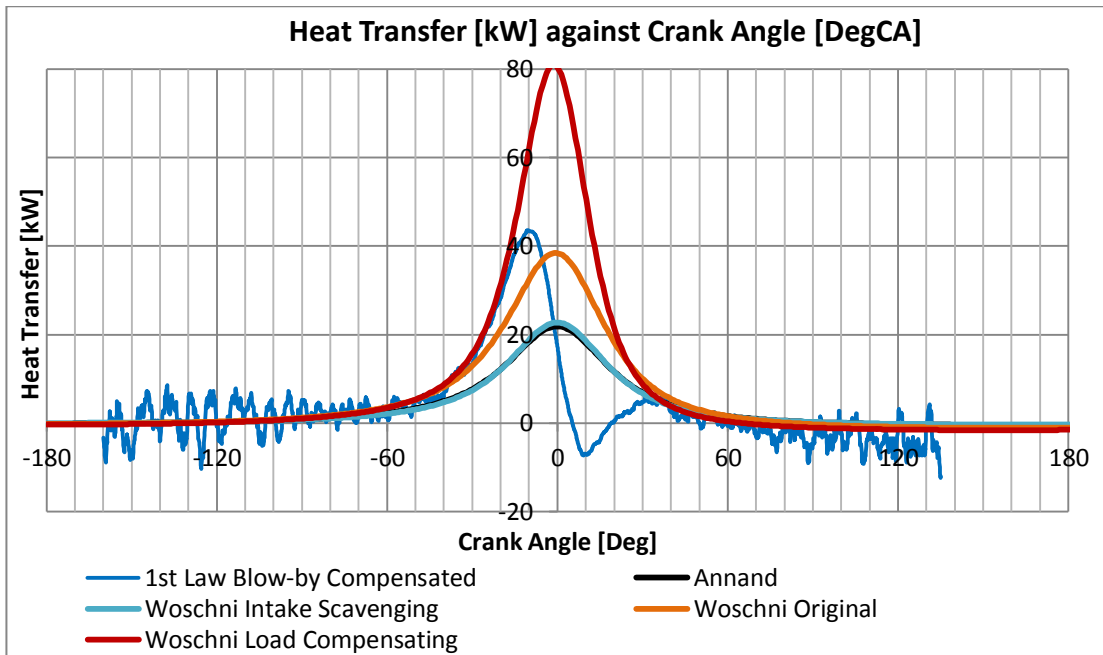
Figure 6.16.Heat transfer against crank angle, comparing different models to the calculated heat transfer at 3000 rpm and 84 bar PCP.

Equation (5.14) and equation (5.15) requires the knowledge of the ratio of specific heats for the working gas. It is known that the ratio of specific heats for air vary with temperature, and has a significant effect on the heat transfer obtained from both equations due to the high temperatures reached during compression. Figure 6.17 gives the ratio of specific heats during the closed valve period, as computed from a correlation of ratio of specific heats with temperature obtained from NBS data in [127]. It should be noted that any quantities obtained from the commercial 1D software utilise a similar variation of γ with temperature, as that shown in Figure 6.17.
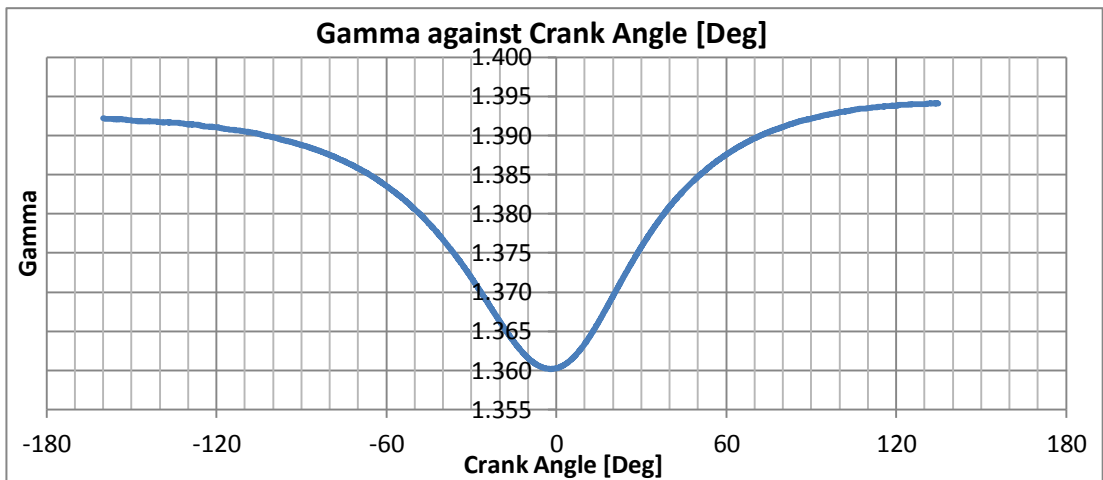
Figure 6.17. γ variation against crank angle at 3000 rpm and 84 bar PCP.

The determination of heat transfer from equation (5.14) and equation (5.15) requires the instantaneous in-cylinder volume and its rate of change. These in turn require knowledge of the compression ratio, which is usually only known from static compression ratio measurements. The true CR normally varies from that quoted by the OEM due to tolerances of manufacturing, thermal expansions and cyclic loadings in the engine structure. Pipitone and Beccari [104] reports that the true CR may vary by up to around $\pm 3\%$ from the OEM stated value.

The sensitivity of the heat transfer determined from equations (5.14) and (5.15) due to CR uncertainty was investigated. Figure 6.18 shows the heat transfer at 3000 rpm; 84 bar with a CR of 17.3:1. Variations of $\pm 5\%$ and $\pm 10\%$ from the CR of 17.3:1 were intentionally imposed. Results are also shown in Figure 6.18. It can be seen that for 5% variation on a CR of 17.3:1, an error of around 45 % in the peak heat transfer rate was incurred. A shift in the location of the peak heat transfer is also noted, where a mistakenly larger CR results in an earlier peak. Biasing the CR by 10% to either side resulted in the loss of the characteristics of the heat transfer curve. Although the curve nature of the heat transfer as determined from the 1st law analysis seems heavily dependent on the CR, the cycle-average heat transfer obtained from the same computation is relatively insensitive to the error in CR. The analysis was also extended up till $\pm$ 10% error of the true CR.

A sensitivity analysis on the heat transfer was also carried out as a function of the in-cylinder pressure pegging error. Figure 6.19 shows the heat transfer rates obtained from this study. It is observed that the shape of the heat transfer curve is not heavily distorted due to errors in pegging extending up to 10%. On the other hand however, it was noticed that the cycle-averaged heat flux suffers up to 5% error due to a 10% error in pegging.
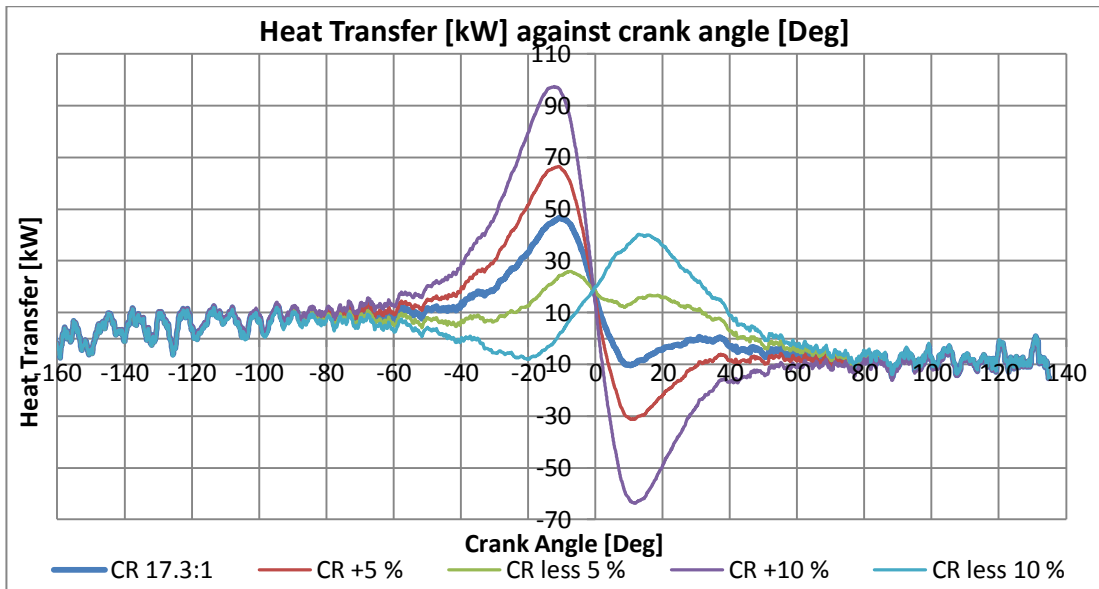
Figure 6.18. The effect of error in CR on the heat transfer as determined from the 1st law at 3000 rpm and 84 bar PCP.
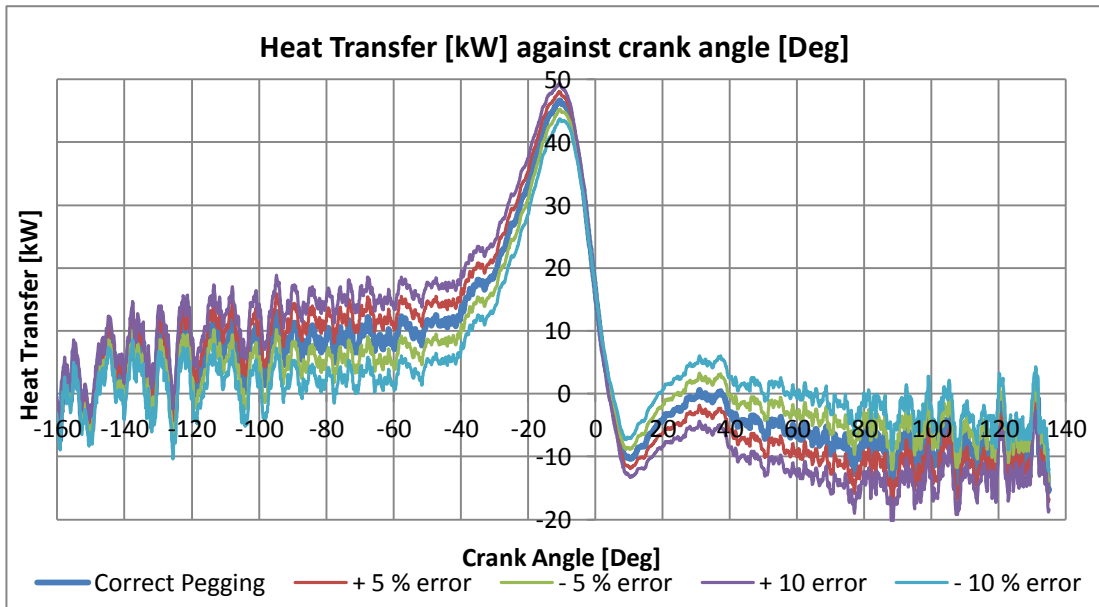
Figure 6.19. The effect of error due to pegging on heat transfer as obtained from the 1st law at 3000 rpm and 84 bar PCP.

6.1.6 One-Dimensional Heat Transfer Models

One-dimensional heat flux models proposed by Wendland [18] and Lawton [22] were considered in this study. Both models are based on a one-dimensional form of the unsteady energy equation applied at the boundary layer. Although both methods are based on the same fundamental theory, some distinctive differences arise

between them. The forthcoming text will first describe a qualitative explanation of heat transfer through the boundary layer as put forward by Wendland. Later, both Wendland's and Lawton's models are individually explained, and finally both methods are applied using the 2.0 HDi engine specifications. Comparison of the data obtained from the models with experimentally obtained data in this work is presented.

6.1.6.1   Understanding Heat Transfer through the Boundary Layer

During the development stage of the heat flux one-dimensional model, Wendland analysed the effects of different gas processes on the heat flux expected from the cylinder.

The first of these mechanisms is the heat capacity of the gas close to the wall. It was found that the heat capacity of the interface gas acts as a capacitive energy storage, meaning that a portion of the heat transferred by the gas core to the interface gas is not conducted to the cylinder head surface, but is instead stored in the boundary layer. When the gas core cools down, the boundary layer releases the energy previously stored.

The second phenomenon investigated by Wendland is the work done by the volume of gas near the wall. It was found that the work done represents an energy source or sink which results in the early peaking of the heat flux.

To qualitatively understand these two phenomena, let us consider a gas in the one-dimensional space, confined between a cylinder head surface and a bulk gas driver which is undergoing a periodic fluctuation of pressure and temperature. If the interface gas has no thermal capacity, its pressure is constant, but has a thermal conductivity, then it can be said that there is only a thermal resistance between the bulk gas driver and the wall. Due to this, the heat flux is expected to be in phase with the temperature of the bulk gas, *i.e.* $\approx$ 3 DegCA BTDC.

If for a more subtle representation we still consider an interface gas at constant pressure, but a thermal capacity is added to the interface gas (hence represented by a resistive and capacitive analogy), the heat flux will lag the temperature of the gas driver. This is because when the gas driver temperature increases, the boundary layer

absorbs a portion of the energy with the consequence of decreasing the net heat flux going to the surface. The boundary layer releases the stored energy afterwards when the gas driver temperature decreases. This results in a lag of the surface heat flux with respect to the bulk gas temperature.

If on the other hand, the interface gas has no thermal capacity, but its pressure varies with time, the pressure work in the boundary layer results in a heat flux to the surface which leads the temperature of the bulk gas.

This shows that the pressure work term and the heat capacity of the gas have opposing effects on the heat flux phase angle with respect to some datum, say the bulk gas temperature maximum. Therefore, the net phase angle between the surface heat flux and the bulk gas temperature maximum will depend on the relative proportions of the work term and capacitive energy storage. Since the experimental surface heat flux shows a peak before TDC, it can be safely stated that the pressure work has a larger effect than that of the gas thermal capacity. The next section details the model put forward by Wendland [18].
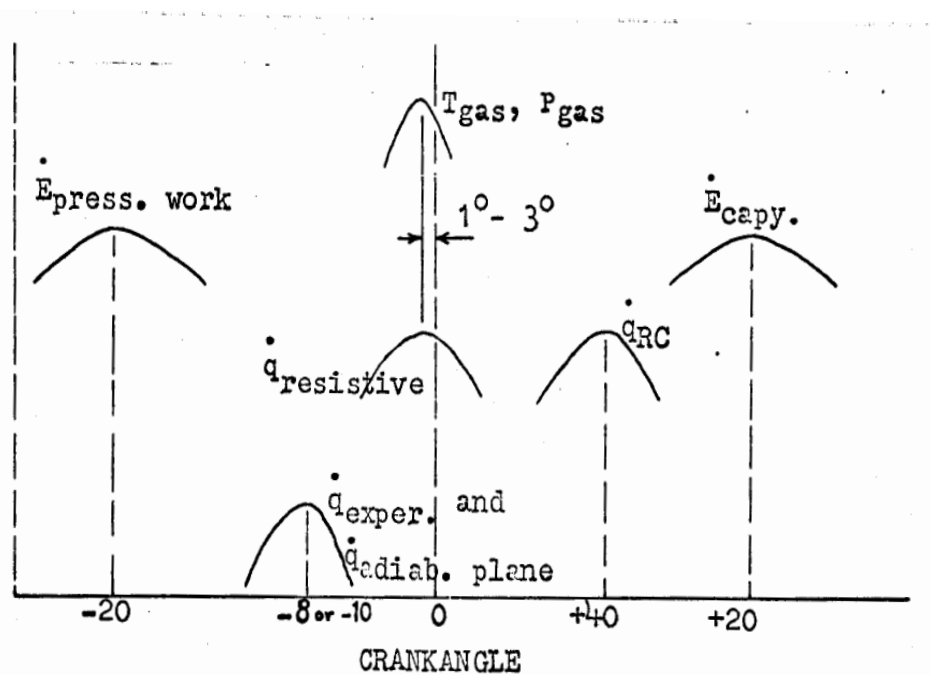
Figure 6.20. Phasor diagram reproduced from Wendland's report [18] showing the peak of the heat flux obtained with different analogies.

299

6.1.6.2 The Adiabatic Plane Model by Wendland [18]

Wendland [18] developed six theoretical models. The major distinctive model, termed the "Adiabatic Plane Model" was the only one reported in the available report [18]. It is however said that the other five secondary models were inferior to the Adiabatic Plane Model because they were based on the Eichelberg heat transfer correlation, which is known to be inadequate in properly simulating the experimental heat transfer curve. The Adiabatic Plane Model on the other hand was founded on basic thermodynamics and contains only simple assumptions in its development. In total, ten assumptions underlie the Adiabatic Plane Model, and these are:

1. The system is one-dimensional, normal to head and piston, *i.e.* ignores temperature gradients parallel to the surface, and heat transfer to the cylinder walls.
2. The head surface temperature is constant with time.
3. There is a plane midway between piston and head at which the temperature gradient is zero.
4. The fluid pressure is a function only of time.
5. The fluid, air, is a perfect gas.
6. The gas specific heat and thermal conductivities can be approximated by linear temperature functions.
7. No blow-by is considered, *i.e.* constant system mass.
8. Fluid is inviscid.
9. The fluid is not subjected to inertia forces.
10. There is no gravity field acting on the fluid.

From the outlined ten assumptions, in particular the first three need some clarification. The first assumption is the most significant, which assumes that the heat flux is one-dimensional. It is known from literature that temperature gradients parallel to the surface are not uncommon in IC engines. In fact it was also shown that heat flux at the surface is spatially sensitive [5]. However, for a flat combustion chamber it is expected that temperature gradients parallel to the surface are small, and hence the one-dimensional assumption is somewhat justified.

The second assumption is in fact a boundary condition which assumes that the surface temperature is constant with time. From experimental research it was found that the surface temperature swings are small compared to the gas temperature swings [6], hence this assumption is not expected to induce a large error in the model results. Nevertheless, the same model can be run with a varying wall temperature if this is known beforehand.

The adiabatic plane mentioned in the third assumption is set up to be at midway between the cylinder head and piston. Underlying this is the assumption that the piston and cylinder head are at the same temperature. It is known that this is untrue due to the fact that the cylinder head surface is in constant contact with the coolant jacket, whereas the piston can only reject heat through the piston rings-liner contact, and the oil splash/jet under the piston crown. Hence it is expected that the piston runs hotter than the cylinder head surface. For the numerical model this effectively means that the adiabatic plane should not be midway between the head surface and the piston, but slightly offset.

In the Adiabatic Plane Model, the space between the adiabatic plane and the head surface is split up into N laminae, each of constant mass, $1/N^{th}$ of the total mass. The first lamina communicates directly with the head surface, the Nth lamina communicates with the adiabatic plane, and the other N-2 laminae lie in between. Since each lamina occupies a constant mass of gas, no mass transport occurs across the boundaries of each lamina. However, heat is conducted from one lamina to the next. Each lamina is defined by the first law of thermodynamics for closed systems, given by equation (6.1), where m is the mass per unit area of lamina n, and V_n is the volume per unit area of lamina n. Therefore each term is expressed in terms of W/m^2.

$$q_{n_{in}} - q_{n_{out}} = mc_v\frac{dT_n}{dt} + P\frac{dV_n}{dt} \qquad\qquad ...(6.1)$$

Equation (6.1) can be converted into the form of equation (6.2) by expressing V_n in terms of the pressure and temperature of the lamina and applying partial differentiation. Equation (6.2) was converted by Wendland into a finite difference form and solved numerically according to the convergence and stability criteria.

$$\underbrace{q_{n_{in}} - q_{n_{out}}}_{heat\ flux} = \underbrace{mc_p \frac{dT_n}{dt}}_{enthalpy} - \underbrace{\frac{mRT_n}{P} \frac{dP}{dt}}_{pressure\ work} \qquad \ldots (6.2)$$

It is understood that the space domain is bounded by the cylinder head and the adiabatic plane, which moves according to the piston location at each crank angle. This therefore means that each lamina is displaced towards the cylinder head during compression and away from the cylinder head during expansion. Furthermore, if each lamina is defined by the ideal gas law equation $PV = mRT$, then since all lamina contain constant and equal mass, and share the same pressure (assumption no. 4), then it is expected that the volume of the laminae are different at one specific time, and dependent on the temperature of the lamina at that same time. The instantaneous volume between the cylinder head and the adiabatic plane is equal to the summation of the volumes of the individual laminae.

To commence with the calculation, the model requires two initial conditions. The required initial conditions are the in-cylinder pressure at t = 0 (IVC) and the initial guess of spatial temperature distribution at t = 0, which varies from the wall temperature at the 1st lamina to the temperature of the adiabatic gas core at IVC (which was taken to be equal to the measured shunt pipe temperature at the intake side). To be able to solve for the temperature at the immediate future time *(j+1)* at each lamina, the immediate future pressure *(j+1)* has to be known. This can be guessed through an adiabatic process assumption:

$$P(j+1) = P(j) \left[\frac{V(j)}{V(j+1)} \right]^{\gamma} \qquad \ldots (6.3)$$

From this guess and the initial conditions, the immediate future temperature $T_n(j+1)$ at all laminae can be found from the finite difference form of equation (6.2). From this found spatial temperature distribution $T_n(j+1)$, the previously guessed pressure can be corrected using a better guess computed from equation (6.4), which is consistent with the predicted spatial gas temperature distribution.

$$P_{\substack{better \\ guess}}(j+1) = \frac{mR}{V(j+1)} \sum_{n=1}^{N} T_n(j+1) \qquad \ldots (6.4)$$

302

If this better guess of pressure is different by more than 15 Pa compared to the previous guess, the better guess of pressure is used and the temperature at the same future time step $T_n(j+1)$ is recalculated for all laminae. This process continues until the specified convergence criterion is reached. Once this condition is satisfied, the spatial temperature distribution and pressure at that time step $(j+1)$ are known. The model then proceeds to calculate the pressure and spatial temperature distribution of the next time step, by again making a rough guess using equation (6.3).

The process repeats itself until the spatial temperature distribution has been found for all time steps throughout the closed part of the cycle. Once the temperature field and pressure is calculated around the cycle, Wendland suggests that the pressure at the cycle end (end of expansion, or EVO) is compared to the initial condition of pressure (beginning of compression, or IVC). If the two pressure values agree within 0.0069 bar, the model is said to be converged. If not, the spatial temperature distribution, and pressure at the end of the cycle are used as the initial conditions for the second iteration around the cycle. The above methodology repeats until the specified convergence criterion is satisfied.

Wendland showed that the Adiabatic Plane Model represented well the heat flux physical phenomena measured experimentally on the engine for moderate to high engine speeds. A comparison of the predicted and experimentally obtained heat flux histories were given by Wendland at 4000 rpm. It was found that the Adiabatic Plane Model showed a relatively good comparison as regards to the shape of the graph; however the predicted positive peak of heat flux was around 40% smaller than that obtained experimentally by the same author.

6.1.6.3   Lawton's Model

The one-dimensional model developed by Lawton [22] is also based on the first law of thermodynamics, however the system is assumed to be open, *i.e.* mass transport occurs past the boundaries of the control volume. A similar approach was taken by Nijeweme et al. [23], and shown in equation (6.5). In the development of equation (6.5), internal heat generation and viscous dissipation are neglected.

$$\underbrace{\rho c_p \frac{\partial T}{\partial t}}_{\substack{rate\ of\ change \\ of\ enthalpy}} + \underbrace{\rho u_x c_p \frac{\partial T}{\partial x}}_{convection} = \underbrace{\frac{\partial q_x}{\partial x}}_{heat\ flux} + \underbrace{\frac{dP}{dt}}_{pressure\ work} \qquad \text{... (6.5)}$$

Analysing equation (6.5) shows that the left most term represents the rate of change of enthalpy of the gas within the control volume. The second term represents the convection normal to the cylinder head surface due to the temperature gradient in the same direction. This term is present due to the fact that mass is transferred from one spatial element to another, resulting in energy advection. The third term signifies the heat diffusion, whereas the fourth term represents the pressure work.

The method put forward by Lawton is based on a spatial one-dimensional grid with equidistant nodes δx. The grid starts at the cylinder head surface and extends in the cylinder axial direction. The length of the grid is left at the choice of the user, but it is said that 15 mm grid length with 50 μm grid spacing is sufficient. The moving piston displaces mass from one spatial element to another when moving towards or away from the cylinder head. The time interval δt has to be chosen according to a certain stability criteria, which consequently often ends up being very small. This method also requires an initial spatial temperature distribution and pressure at t = 0, from which the calculation of the temperature array around the cycle can commence using a finite difference numerical scheme. In the work presented by Lawton [22], the equation used for the prediction of the spatial temperature distribution of the immediate future time step is derived from equation (6.5) previously presented. Below is a brief walkthrough of the derivation.

By the equation of continuity,

$$\frac{\partial \rho}{\partial t} + \frac{\partial}{\partial x}(\rho u_x) = 0 \qquad \text{... (6.6)}$$

Applying the partial differentiation results in:

$$\frac{\partial \rho}{\partial t} + \rho \frac{\partial u_x}{\partial x} + u_x \frac{\partial \rho}{\partial x} = 0 \qquad \text{... (6.7)}$$

By converting the second term on the right hand side of equation (6.5), the equation can be written as:

$$\rho c_p \frac{\partial T}{\partial t} + \rho u_x c_p \frac{\partial T}{\partial x} = \frac{\partial q_x}{\partial x} + R \frac{d(\rho T)}{dt} \qquad \ldots (6.8)$$

By partial differentiation, equation (6.8) can be written as:

$$\rho c_p \frac{\partial T}{\partial t} + \rho u_x c_p \frac{\partial T}{\partial x} = \frac{\partial q_x}{\partial x} + R \left[\rho \frac{\partial T}{\partial t} + T \frac{\partial \rho}{\partial t} \right] \qquad \ldots (6.9)$$

Substituting equation (6.7) in the third term on the right hand side of equation (6.9) for $\frac{d\rho}{dt}$ yields:

$$\rho c_p \frac{\partial T}{\partial t} + \rho u_x c_p \frac{\partial T}{\partial x} = \frac{\partial q_x}{\partial x} + R\rho \frac{\partial T}{\partial t} - RT \left\{ \rho \frac{\partial u_x}{\partial x} + u_x \frac{\partial \rho}{\partial x} \right\} \qquad \ldots (6.10)$$

The terms of $\frac{\partial T}{\partial t}$ can be grouped up using the relationship $R = c_p - c_v$. Also, the third term on the right hand side of equation (6.10) can be reduced using the ideal gas law equation, resulting in:

$$\rho c_v \frac{\partial T}{\partial t} + \rho u_x c_p \frac{\partial T}{\partial x} = \frac{\partial q_x}{\partial x} - P \frac{\partial u_x}{\partial x} - RT u_x \frac{\partial \rho}{\partial x} \qquad \ldots (6.11)$$

If the last term on the right hand side of equation (6.11) is expanded using the ideal gas law equation:

$$\rho c_v \frac{\partial T}{\partial t} + \rho u_x c_p \frac{\partial T}{\partial x} = \frac{\partial q_x}{\partial x} - P \frac{\partial u_x}{\partial x} - \frac{RT u_x}{R} \frac{\partial \left(\frac{P}{T} \right)}{\partial x} \qquad \ldots (6.12)$$

Through partial differentiation:

$$\rho c_v \frac{\partial T}{\partial t} + \rho u_x c_p \frac{\partial T}{\partial x} = \frac{\partial q_x}{\partial x} - P \frac{\partial u_x}{\partial x} - T u_x \left[\frac{1}{T} \frac{\partial P}{\partial x} - \frac{P}{T^2} \frac{\partial T}{\partial x} \right] \qquad \ldots (6.13)$$

By simplification, equation (6.13) can be represented as equation (6.14):

$$\rho c_v \frac{\partial T}{\partial t} + \rho u_x c_p \frac{\partial T}{\partial x} = \frac{\partial q_x}{\partial x} - P \frac{\partial u_x}{\partial x} - u_x \frac{\partial P}{\partial x} + \rho u_x R \frac{\partial T}{\partial x} \qquad \ldots (6.14)$$

Applying $R = c_p - c_v$ to the terms involving $\frac{\partial T}{\partial x}$ in equation (6.14):

$$\rho c_v \left[\frac{\partial T}{\partial t} + u_x \frac{\partial T}{\partial x} \right] + P \frac{\partial u_x}{\partial x} + u_x \frac{\partial P}{\partial x} = \frac{\partial q_x}{\partial x} \qquad \text{... (6.15)}$$

If no pressure gradients occur in the spatial domain, then the fourth term on the left hand side is equal to zero, and the equation simplifies to equation (6.16). This is the result as used by Lawton [22].

$$\rho c_v \left[\frac{\partial T}{\partial t} + u_x \frac{\partial T}{\partial x} \right] + P \frac{\partial u_x}{\partial x} = \frac{\partial q_x}{\partial x} \qquad \text{... (6.16)}$$

In the model put forward by Lawton [22], the piston and cylinder liner are considered to be thermally insulated. The temperature varies spatially from the wall to the bulk gas, through a boundary layer. The wall temperature is assumed to be constant with time. In-cylinder pressure is assumed to be spatially uniform but varying with time according to the piston motion. Temperature gradients perpendicular to the wall are only assumed negligible at regions far away from the wall (*i.e.* bulk gas). Velocities and temperature gradients in the radial and tangential directions are neglected, and the gas is assumed to be perfect.

Since the temperature far away from the wall is assumed to be spatially uniform, the density of the adiabatic gas core (far away from the wall) is also spatially constant. As a result, from continuity equation (6.6), it can be shown that the axial velocity of the gas varies linearly, and according to equation (6.17). The linear gas velocity variation ranges from zero at the cylinder head surface (x = 0), to the piston velocity at the piston surface.

$$u_x = \frac{1}{V} \left(\frac{dV}{dt} \right) x \qquad \text{... (6.17)}$$

If Fourier's law of thermal conduction is substituted in the term on the right hand side of equation (6.16), the following results:

$$\rho c_v \left[\frac{\partial T}{\partial t} + u_x \frac{\partial T}{\partial x} \right] + P \frac{\partial u_x}{\partial x} = -k \frac{\partial^2 T}{\partial x^2} \qquad \text{... (6.18)}$$

If equation (6.18) is applied at a distance far away from the wall, where the axial temperature gradient is negligible, the second and fourth terms become null. Applying $\rho = \frac{m}{V}$ and equation (6.17) in the remaining terms of equation (6.18) yields:

$$\frac{dT}{dt} = -\frac{(\gamma - 1)T}{V}\left(\frac{dV}{dt}\right) \qquad \qquad \text{... (6.19)}$$

Equation (6.19) has a solution of $\frac{T}{V^{1-\gamma}} = constant$, which shows that the energy equation given by equation (6.18), subject to the assumptions discussed above states that outside the boundary layer, the gas temperature follows an isentropic law.

In the boundary layer, from the previously derived equation (6.17), the axial gas velocity at the cylinder head surface is zero, $u_x = 0$. Hence, the second term in equation (6.18) reduces to zero. If the piston is assumed to be temporarily stationary, the third term of equation (6.18) resolves to zero as well. The thermal energy equation therefore becomes $\frac{\partial T}{\partial t} = \alpha \frac{d^2 T}{dx^2}$. This is the diffusion of thermal energy, and is used to describe the temperature distribution in the boundary layer.

Through the above two solutions, it is shown that the gas temperature is defined by the adiabatic law of compression outside the boundary layer, and with the heat diffusion equation within the boundary layer. It is said that at the interface between the boundary layer and the bulk gas is a region which neither solutions apply, and this is where odd effects arise [22]. Apart from Lawton, the above approach was also taken by Nijeweme et al. [23], Diana et al. [26], Han et al. [27] and Angelberger et al. [28].

Equation (6.18) can be solved with a numerical scheme in order to study the one-dimensional unsteady behaviour of the gas temperature distribution. Lawton [22] suggests two methods for this implementation; the forward Euler explicit finite difference, and the Crank-Nicolson finite difference scheme with Gauss-Seidel iteration. In this doctoral work, equation (6.18) was solved using the Euler explicit finite difference method.

For the purpose of implementation Lawton simplifies equation (6.18) on the grounds that the axial velocity is small in the boundary layer and near top dead centre. This, together with the assumption made previously that the temperature gradient is zero outside the boundary layer, led to the removal of the term $\rho c_v u_x \left(\frac{\partial T}{\partial x}\right)$ from equation (6.18). This therefore implies that convection normal to the wall as a result of the gas density variation is neglected. Han et al. [27] and Angelberger et al. [28], also took this approach. The importance of this term will be further discussed in the subsequent text.

6.1.6.4   <u>Comparison between the Adiabatic Plane Model and Lawton's Model</u>

As noted from the previous two sections, although both Lawton's and Wendland's models are founded on the same theory, the two models differ in the method of implementation. The differences outlined in these two methods are discussed below.

The major difference lies in the fact that Wendland assumes a closed system for every lamina which contains a constant mass of gas that is heated by conduction from the adjacent laminae, and compressed by the displacement of the adiabatic plane. On the other hand, Lawton's model is based on a fixed spatial grid in which each element is an open system that accommodates inward and outward flow of mass and heat. Additionally the gas is influenced by an isentropic compression/expansion process.

In both models, the term representing the heat flux can be opened up using Fourier's law of one-dimensional conduction, given by equation (6.20). Both authors assumed the thermal conductivity of the gas in Fourier's one-dimensional conduction law to be that for a laminar flow. It is understood that close to the cylinder head surface, a laminar regime dominates, however the further away from the wall, the higher is the degree of turbulence expected. In his work, Lawton [22] made use of the Boussinesq approximation and used a multiplier of 25 with the laminar heat conductivity to account for the increase in heat conductivity due to turbulence. On the other hand, Wendland [18] used a purely laminar thermal conductivity. Nijeweme et al. [23] did a more rigorous analysis and attributed the thermal conductivity to be a summation of the laminar thermal conductivity and the turbulent thermal conductivity. The turbulent thermal conductivity was used as a tuning variable until the computed heat

flux was made to match the measured surface heat flux of that location in the cylinder.

$$\frac{\partial q_x}{\partial x} = -k\frac{d^2T}{dx^2} \qquad\qquad \dots(6.20)$$

As described earlier, Lawton seems to have ignored the term involving the heat transfer by convection perpendicular to the cylinder head surface due to a varying density in the boundary layer. In Wendland's model a specific term representing heat transfer by convection is not present due to the condition that each lamina is a closed system, hence no mass transfer.

The last difference between the two models is in the iterative scheme implementation. In the method put forward by Wendland, an iteration scheme is implemented to ensure the spatial convergence of the model. On the other hand, in Lawton's model no iterations are done and the calculation proceeds from the assumed initial conditions of spatial temperature distribution and pressure for one time throughout the cycle and stops.

6.1.6.5 <u>Application of Models</u>

In this study, the above described two numerical one-dimensional heat flux models were written in Matlab R2017b. The method put forward by Wendland was represented by the finite difference form of equation (6.2), whereas that put forward by Lawton was represented by the finite difference form of equation (6.18). For the model of Lawton, initially the product $\rho c_v u_x \left(\frac{\partial T}{\partial x}\right)$ was ignored.

Prior to using the models with the HDi engine geometry studied in this work, both models were first run using the geometry and setpoint parameters of the engine on which they were developed, *i.e.* the data of the engine used by Wendland [18] and that used by Lawton [22]. The heat flux, together with the temperature spatial distribution within the boundary layer at various setpoints were compared to the graphs made available by Wendland in [18] and Lawton in [22]. This allowed acquiring some confidence in the models and served as a check on the Matlab code.

In applying Lawton's model, a constant spatial discretisation of 50 μm was used, similar to that reported by Lawton [22] with a time step equivalent to 0.01 DegCA. In conducting Wendland's model, the number of laminae used were around 71, as dictated by Wendland [18] with a timestep equivalent to 1 DegCA. The choice of timestep was determined by the stability criteria for both models, and also depended on the spatial discretisation chosen.

In applying Lawton's model with the 2.0 HDi engine geometry, a multiplier of 25 was assigned to the laminar thermal conductivity, as done by the same author [22]. On the other hand, the model derived from Wendland was assigned a multiplier of 4 to the laminar thermal conductivity which was found to be the best value for the predicted cycle in-cylinder pressure to match within reasonable limits to the experimental in-cylinder pressure at the same setpoint. For both models, the thermal conductivity of the gas was made to vary with respect to the spatial and temporal temperature distribution.

6.1.6.6 Results

Figure 6.21 and Figure 6.22 show the gas temperature distribution on the compression and expansion strokes respectively, obtained from Wendland's model applied to the 2.0 HDi engine at 1400 rpm, 80 bar PCP and using air as the working gas. These graphs show only the first 10 mm from the wall for clarity purposes. Figure 6.23 also shows temperature distributions obtained from the same model, but for crank angles at which peculiar observations are noticed. An explanation of the observed heat flux phenomena from these temperature distributions is given in the forthcoming text. Throughout the explanation, reference will be made to the quasi-steady heat flux assumption that was made by multiple authors, such as Annand [8] and Woschni [11], where it was assumed that the heat flux from the cylinder can be explained by equation (6.21), presented previously in Chapter 2. Figure 6.24 presents the heat transfer coefficient computed from equation (6.21) using the predicted heat flux and ΔT between the adiabatic plane temperature and the wall obtained from the results of Wendland's model applied to the 2.0 HDi engine.

$$q'' = h \left(T_{\substack{adiabatic \\ plane}} - T_{wall} \right) \qquad \ldots (6.21)$$

From an observation of Figure 6.21, it is understood that at the early stages of compression (-180 DegCA to -58 DegCA), the adiabatic plane temperature (away from the wall) is still lower than that of the wall. This follows from the fact that the intake gas is colder than the wall. Due to this interaction of the cold intake gas on the hot wall, heat flows from the wall to the gas. This is shown by the negative temperature gradient at the wall at -180 DegCA. This heat transfer from the wall to the gas follows for all temperature distributions up to around -64 DegCA, which are not shown due to clarity.

At -64 DegCA (refer to Figure 6.23), the wall temperature is still higher than that of the adiabatic plane, however at this crank angle the temperature gradient at the wall is effectively zero, meaning that heat flux has temporarily ceased. If this situation is understood from a steady-state consideration, the heat transfer coefficient would appear to be zero (refer to Figure 6.24).

Further on during the compression stroke, at -60 DegCA, the adiabatic plane temperature is still about 3 K below that of the wall, however the temperature gradient at the wall is now slightly positive, meaning that heat flux has changed direction and the core gas is heating the wall despite the fact that the core gas temperature is still below the temperature of the wall. This is evidence that the compression process has increased the temperature of the boundary layer above that of the wall, which therefore results in a heat flux from the gas to the wall. At this condition, the steady-state heat transfer coefficient assumes a small negative value (refer to Figure 6.24).

Progressing further into the compression stroke shows that the core gas temperature eventually reaches that of the wall. This happens at -58 DegCA (refer to Figure 6.23). At this crank angle heat flux is not zero, but flowing from the gas to the wall. This can be understood from the positive temperature gradient at the wall. If this is treated with a steady-state assumption, the heat transfer coefficient will appear to be $\pm\infty$ (refer to Figure 6.24). At crank angles closer to TDC compression, the core gas temperature increases above that of the wall and heat flux remains from the gas to the wall.

Through an observation of Figure 6.22 for the expansion stroke, it is shown that at around +24.3 DegCA ATDC, the core gas temperature is still around 220 K above that of the wall. Despite this however, the temperature gradient at the wall seems to be zero (refer to Figure 6.23), which means that the heat flux to the wall has temporarily ceased. If the problem is approached from a steady-state perspective, then this condition means that the heat transfer coefficient should effectively be zero (refer to Figure 6.24).

Progressing further through the expansion stroke, at +40 DegCA the core gas temperature is around 100 K above that of the wall. At the same condition, a large negative temperature gradient is shown at the wall, which means that despite the fact that the core gas temperature is higher than that of the wall, heat transfer is from the wall to the gas. From a steady-state perspective this would be interpreted by a negative heat transfer coefficient (refer to Figure 6.24).

At +57.2 DegCA the core gas temperature is effectively the same as that of the wall (refer to Figure 6.23). Despite this, the temperature gradient at the wall has an appreciable negative value which therefore shows that heat is transferred from the wall to the gas. With a steady-state assumption, this will show up as a $\pm\infty$ heat transfer coefficient (refer to Figure 6.24). At crank angles after +57.2 DegCA, the core gas temperature falls below that of the wall and heat transfer remains from the wall to the gas.
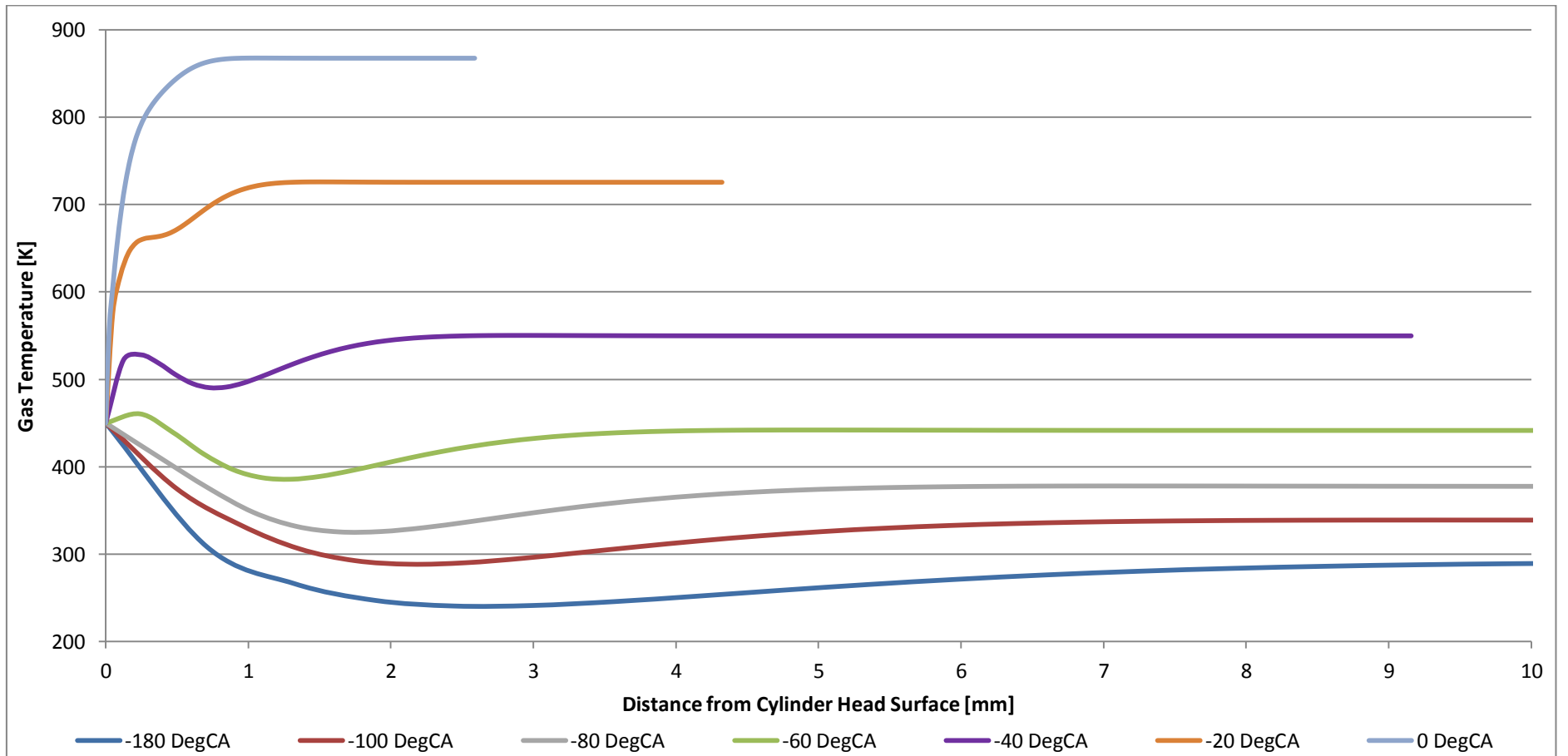
Figure 6.21. Spatial gas temperature distribution on compression stroke predicted using Wendland's model at 1400 rpm, 80 bar PCP.
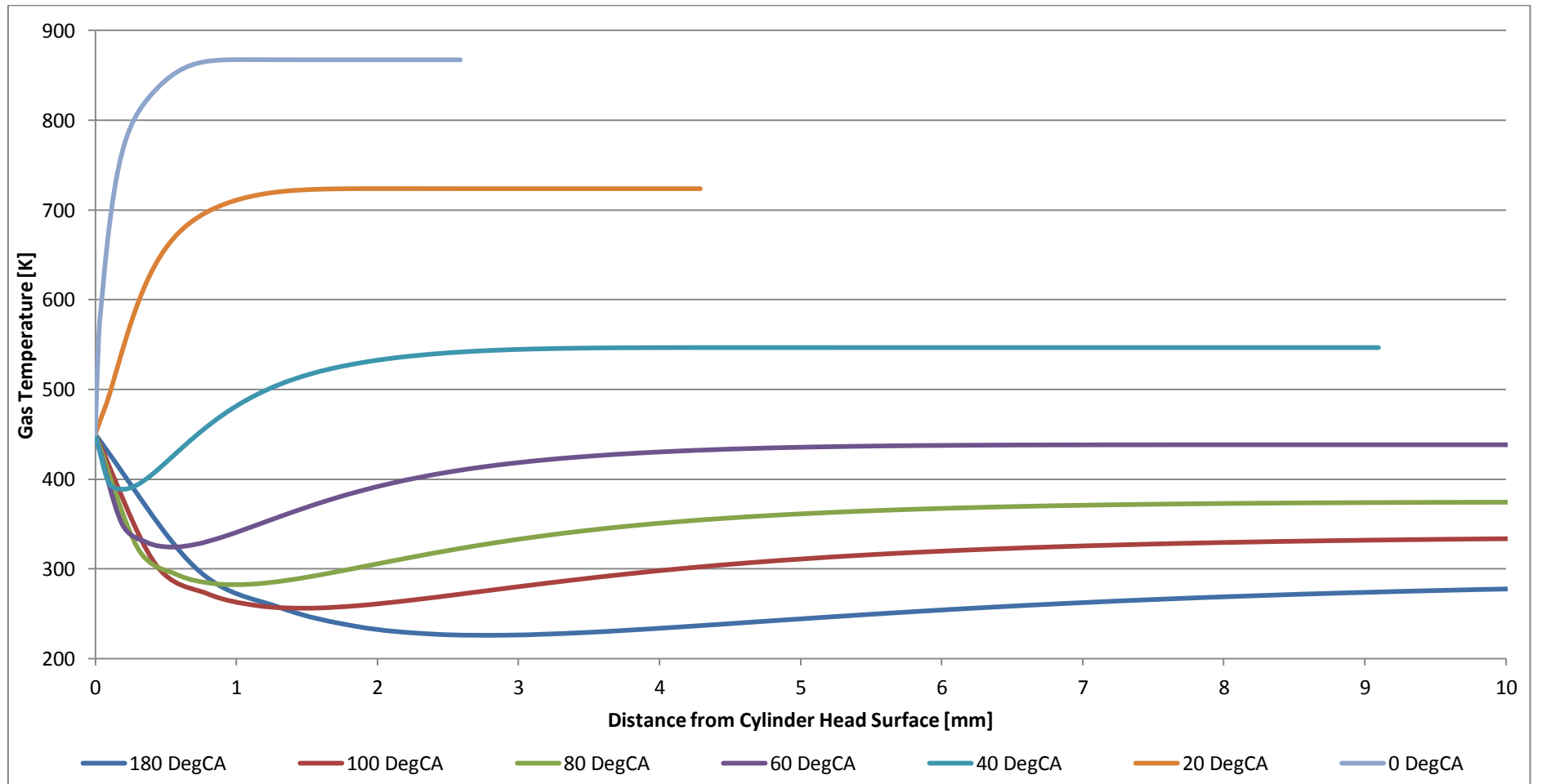
Figure 6.22. Spatial gas temperature distribution on expansion stroke predicted using Wendland's model at 1400 rpm, 80 bar PCP.
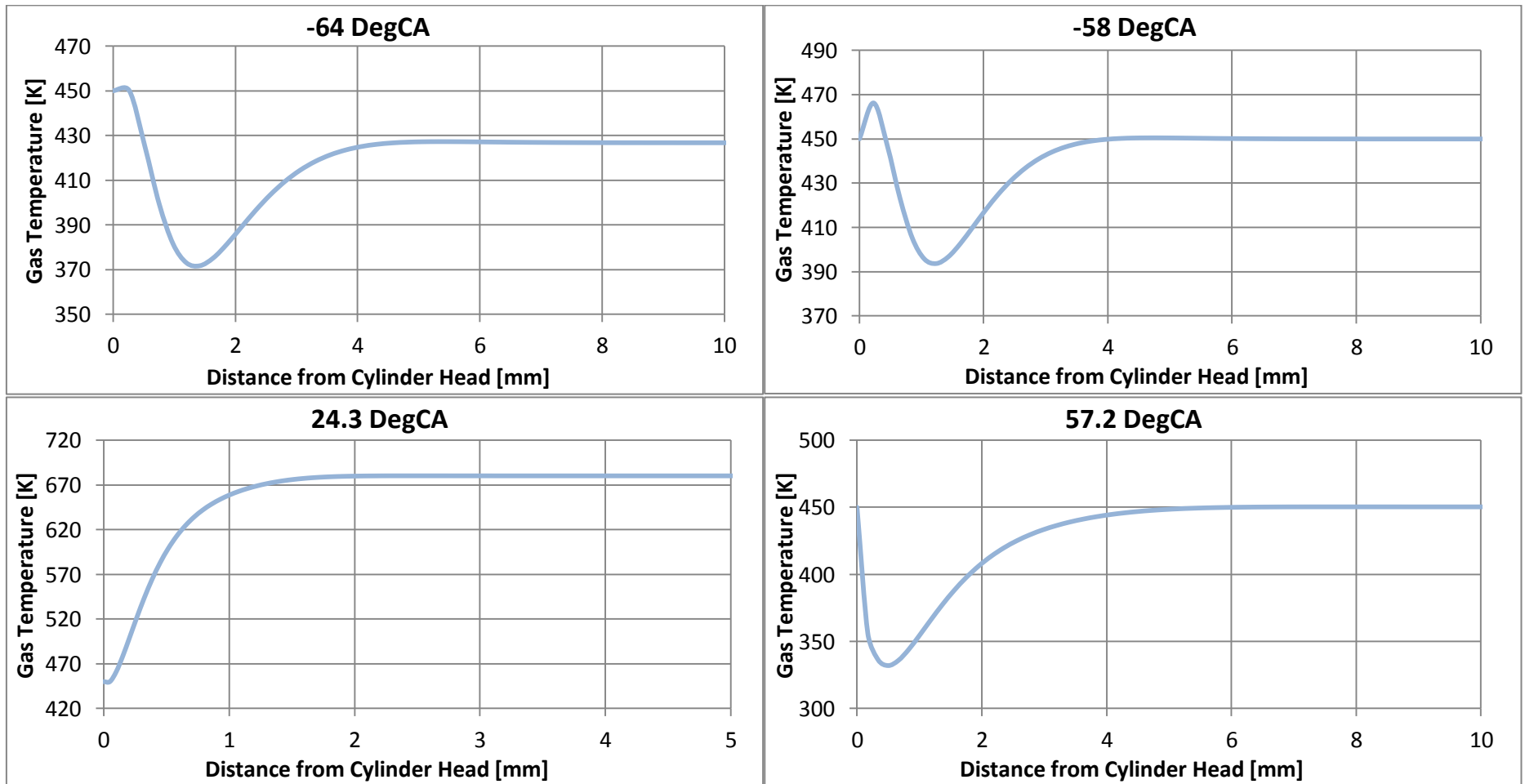
Figure 6.23. Spatial temperature distribution at crank angles where peculiar observations were made. These were obtained from Wendland's model run at 1400 rpm, 80 bar PCP.
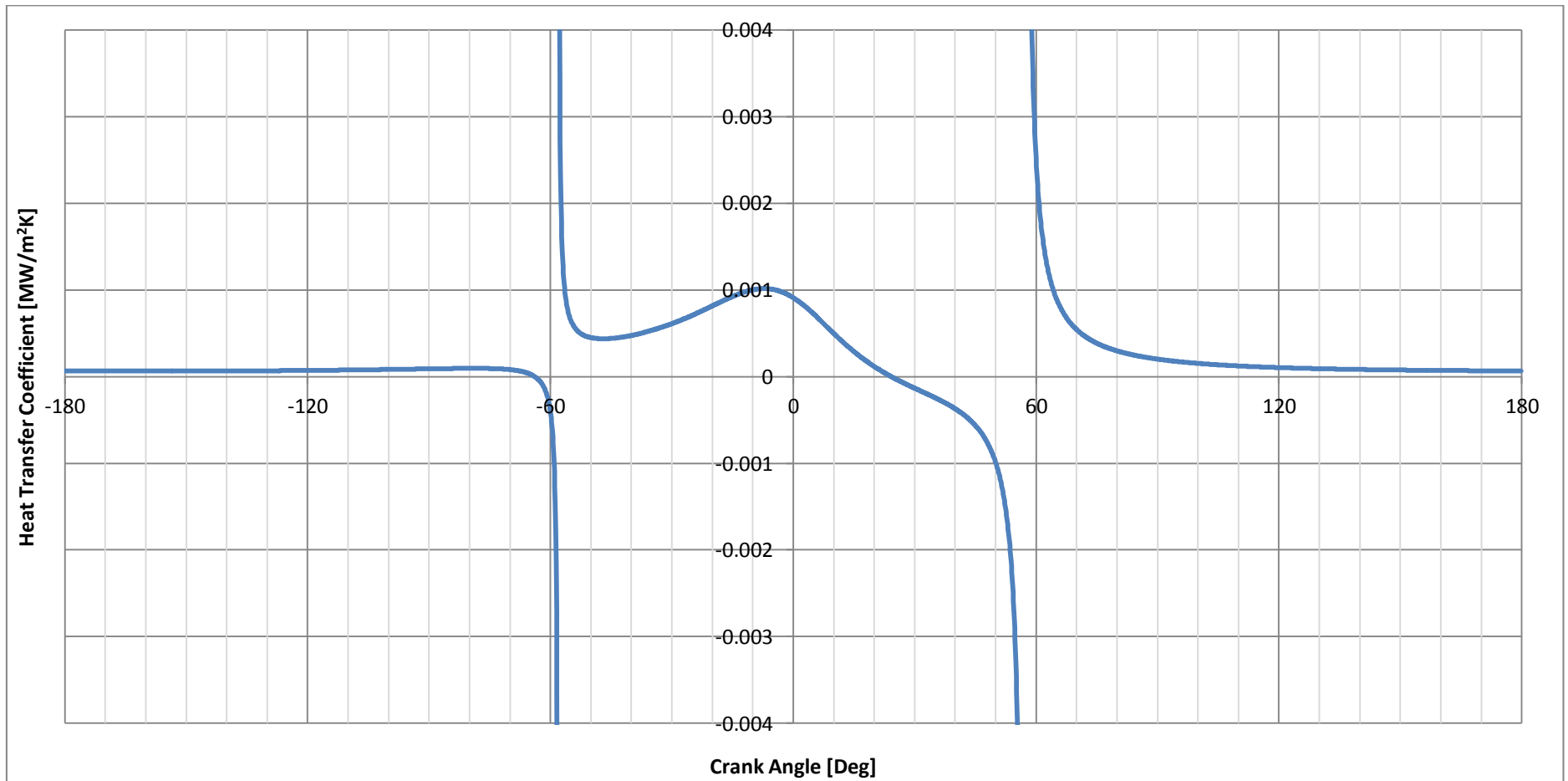
Figure 6.24. Heat transfer coefficient computed from a steady-state consideration using the heat flux and temperatures from Wendland's model at 1400 rpm and 80 bar PCP.

Figure 6.25 and Figure 6.26 show the spatial temperature distribution as obtained from Lawton's model applied to the 2.0 HDi engine. Figure 6.27 shows the temperature distributions for which peculiar observations were noted. It is reminded that in this model, the spatial grid is not resized at different crank angles to reflect the cylinder volume, hence a constant 15 mm grid is shown for every crank angle position. For an easier evaluation of the two figures, Figure 6.28 shows the steady-state heat transfer coefficient obtained from the heat flux and ΔT between the adiabatic core and the wall, as predicted from Lawton's model applied to the 2.0 HDi engine.

From an evaluation of the temperature distributions obtained from Lawton's, it is evident that similar observations are noted to those made on Wendland's temperature distributions. From Lawton's model, the heat flux seems to be from the wall to the gas up till -140 DegCA (refer to Figure 6.27). Up till this instant, the core gas temperature is still lower than the wall temperature. This occurrence is earlier than the prediction made from Wendland's model (-64 DegCA).

Moving further towards TDC, a heat flux from the gas to the wall occurs. At -85 DegCA, the bulk gas and wall reach the same temperature (refer to Figure 6.27) which results in $\pm\infty$ heat transfer coefficient (refer to Figure 6.28).

From -140 DegCA to +35 DegCA, a positive heat flux is noted with the adiabatic core temperature constantly above that of the wall. At +35 DegCA, a zero heat flux is noted despite the fact that the adiabatic core is still appreciably hotter than the wall (refer to Figure 6.27). This predicted duration is longer than that predicted by Wendland's which ranged from -64 DegCA to + 24.3 DegCA.

From +35 DegCA to around +85 DegCA, heat flux remained from the wall to the gas, while the temperature of the adiabatic core was still higher than that of the wall. At +85 DegCA, the adiabatic core reaches the same temperature as that of the wall (refer to Figure 6.27), and a $\pm\infty$ heat transfer coefficient is assumed if considering the problem with a steady-state assumption (refer to Figure 6.28).

Further on in the expansion stroke beyond +85 DegCA heat flux is from the wall to the gas when the core gas is cooler than the wall.

317
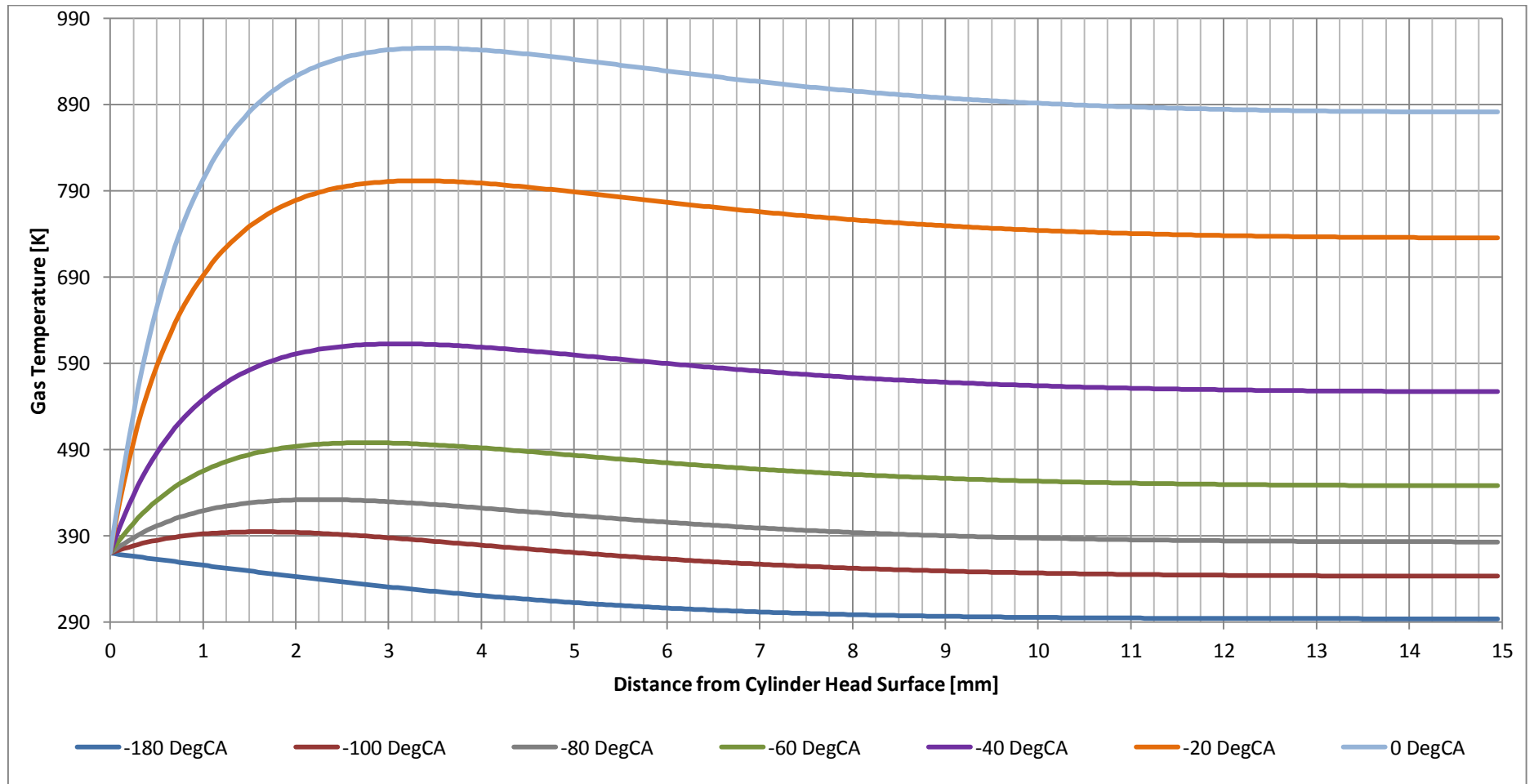
Figure 6.25. Spatial gas temperature distribution on compression stroke predicted using Lawton's model at 1400 rpm, 80 bar PCP.
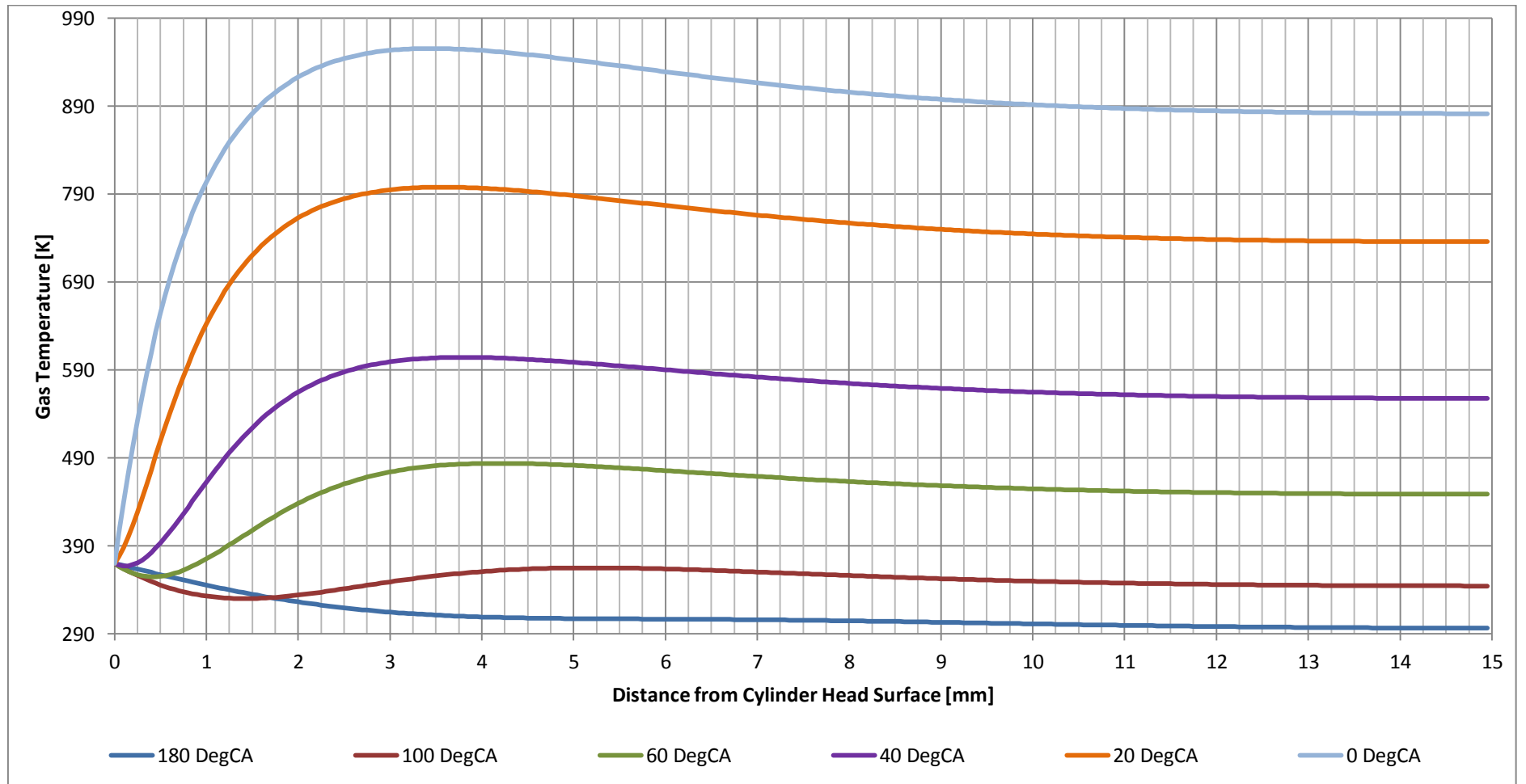
Figure 6.26. Spatial gas temperature distribution on expansion stroke predicted using Lawton's model at 1400 rpm, 80 bar PCP.
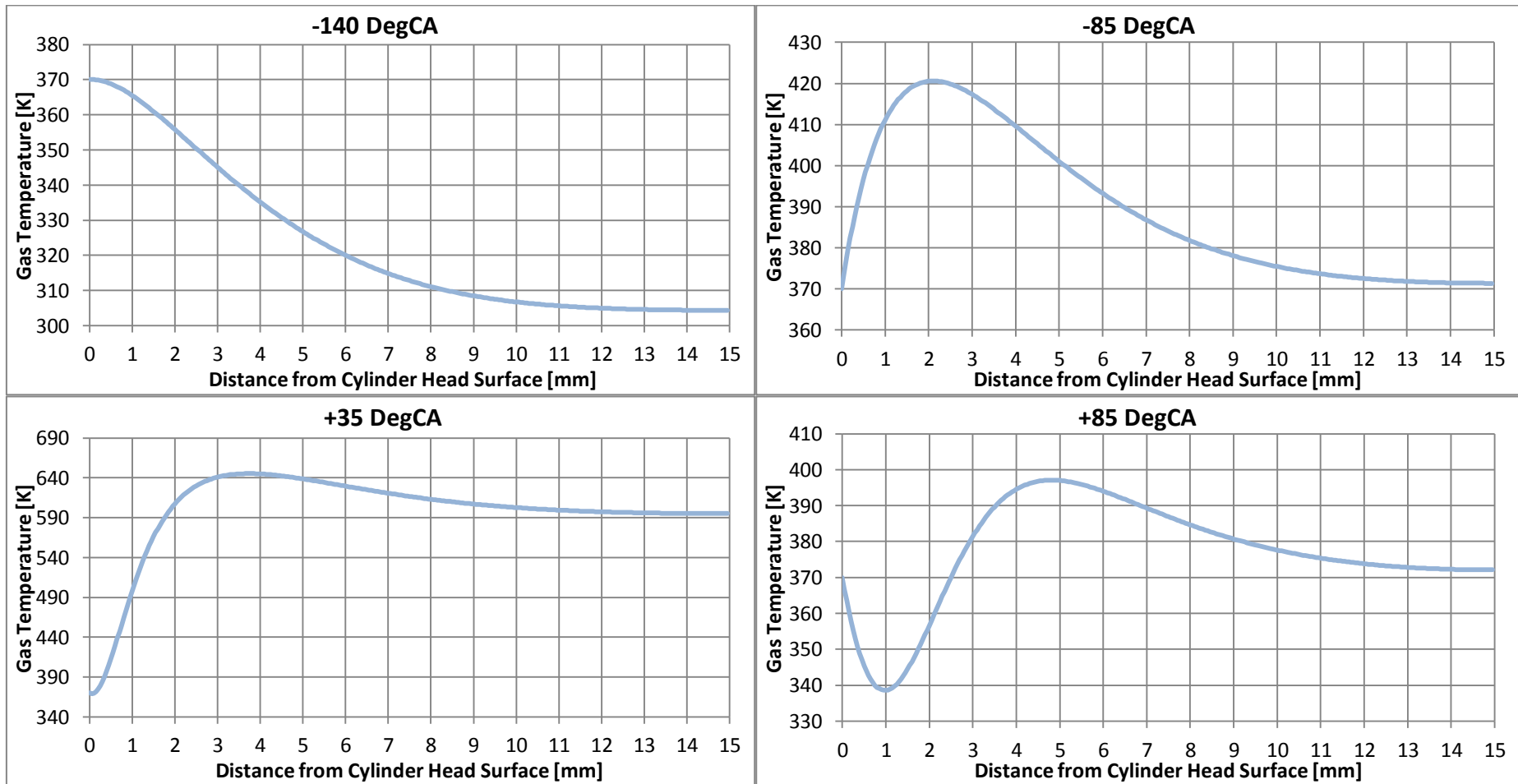
Figure 6.27. Spatial temperature distribution at crank angles where peculiar observations were made. These were obtained from Lawton's model run at 1400 rpm, 80 bar PCP.
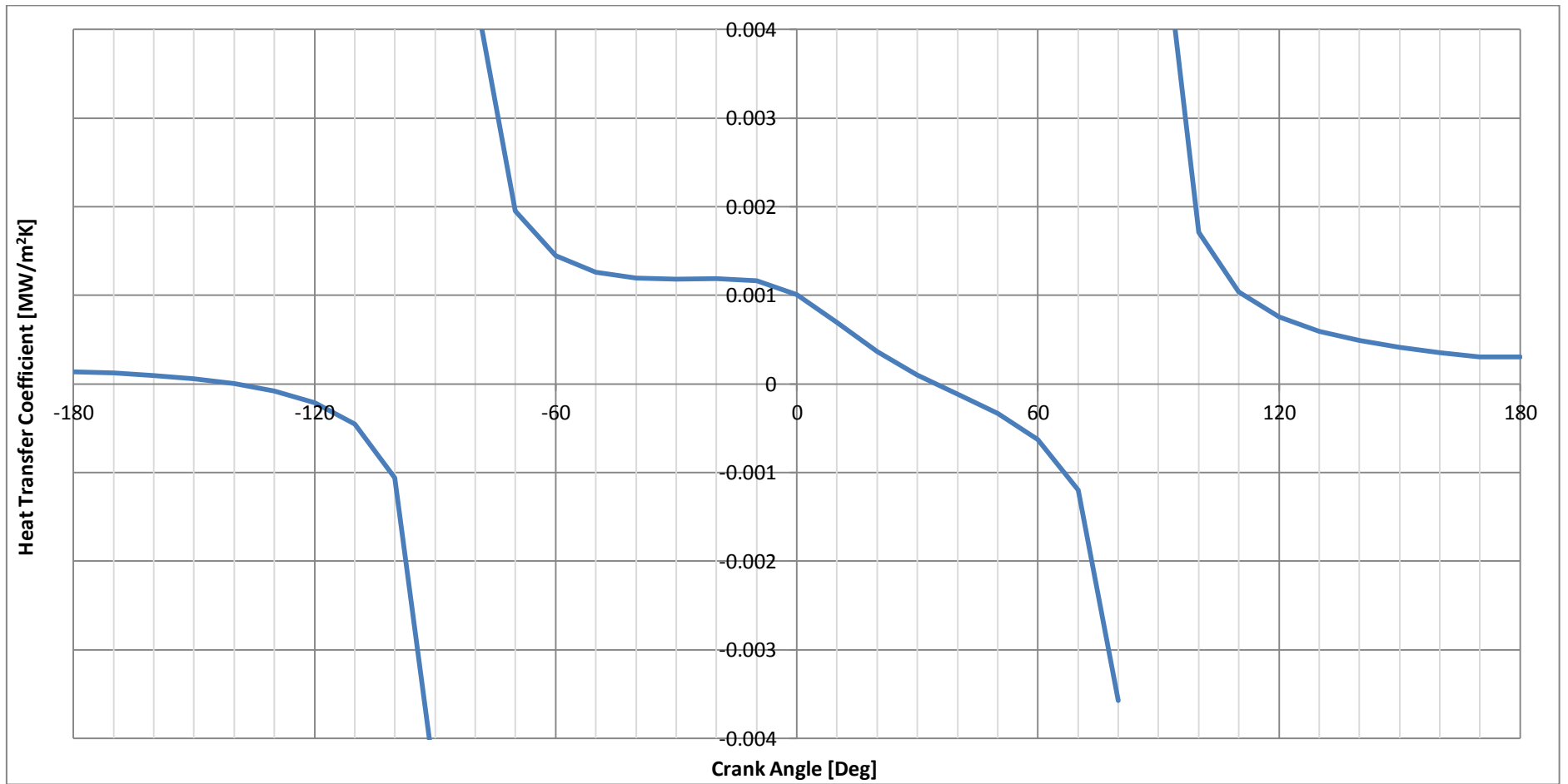
Figure 6.28. Heat transfer coefficient computed from a steady-state consideration using the heat flux and temperatures from Lawton's model at 1400 rpm and 80 bar PCP.

From the discussion of the temperature distributions obtained from Wendland's and Lawton's models, it is clear that the boundary layer plays a significant role in the mechanism of heat flux. As a result, a steady-state consideration utilising the bulk gas temperature (or adiabatic core temperature) and wall temperature cannot give an accurate prediction of the crank angle resolved heat flux. The section below details how both Wendland's and Lawton's models fair in their heat flux prediction when compared to the experimentally obtained heat fluxes presented earlier in Chapter 5.

Figure 6.29 shows the heat flux curves obtained experimentally from the Stainless Steel and Zirconia thermocouples fitted in the OEM injector location. On the other hand, Figure 6.30 shows the experimental heat flux curve at the same setpoint but obtained at the custom-drilled location. In both figures, heat flux curves estimated from Wendland's and Lawton's models are also presented. In evaluating the forthcoming heat flux curves, care must be exercised in the comparison between the experimentally obtained heat fluxes and the models-derived heat fluxes. This is because the experimentally obtained heat fluxes only show the transient component, and hence these graphs are expected to be shifted in the positive heat flux direction by some amount equal to the steady portion of heat flux. To have an indication of the magnitude shift expected in the experimental heat flux curves, the steady-state component of heat flux obtained from the first law of thermodynamics, and using the experimental pressure is given in Table 6.1 for the setpoint considered. Table 6.1 also gives other important parameters that were used in both models for the prediction of the heat fluxes in Figure 6.29 and Figure 6.30 at the particular setpoint.

Table 6.1. Steady-state values of pressure and temperature at
1400 rpm and 80 bar PCP.

Engine Speed [rpm]	1400
Peak In-Cylinder Pressure [bar]	83
MAP [bar]	1.999
Shunt Pipe Intake Temperature [K]	294
Average Wall Temperature - Measured [K]	370
Average Wall Temperature - Lawton [K]	370
Average Wall Temperature - Wendland [K]	450
Working Gas	Air
Steady-State Component of Heat Flux [MW/m^2]	0.1759

Figure 6.29 and Figure 6.30 show that both models predict to a very good extent the angular phasing of the peak heat flux. The negative portion of the heat flux is also captured in both models with Wendland's model performing very well when compared to the experimental data. At the custom-drilled location, the experimental data displays a change in the direction of heat flux around 20 DegCA later than that displayed at the OEM injector location. Since both models are only one-dimensional, the spatial difference shown between the experimental heat fluxes at the two locations could not be captured.

Despite the ability of both models to capture the phasing of the heat flux, magnitude comparability was found to be poor. For adequate graphical comparability of the angular phasing, the predicted heat fluxes in Figure 6.29 and Figure 6.30 were scaled by different quantities until their peaks matched those of the experimentally obtained heat fluxes. This 'scaling factor' is not to be confused with the multipliers assigned to the laminar thermal conductivity to account for turbulence phenomena as explained earlier. It has to be appreciated that the 'scaling factor' is simply used for ease of visual comparison, whereas the 'laminar thermal conductivity multiplier' alters the predicted heat flux due to a better heat conduction between each of the gas laminae.

With the assumed laminar thermal conductivity multiplier of 25, the peak heat flux predicted by Lawton's model was equal to 15% of that obtained experimentally at the OEM injector location and 25% that obtained experimentally at the custom-drilled location.

The peak heat flux predicted by Wendland's model was equal to 12% of that obtained experimentally at the OEM injector location, and 19% of that obtained experimentally at the custom-drilled location. The multiplier assigned to the laminar thermal conductivity in Wendland's model was equal to 4. This thermal conductivity multiplier was chosen based on a comparison of the predicted in-cylinder pressure from Wendland's model with that obtained experimentally at the same setpoint. Figure 6.31 shows the in-cylinder pressure trace as obtained from Wendland's model plotted against the experimental pressure trace. Figure 6.32 shows the difference between the two pressure traces crank-angle resolved.
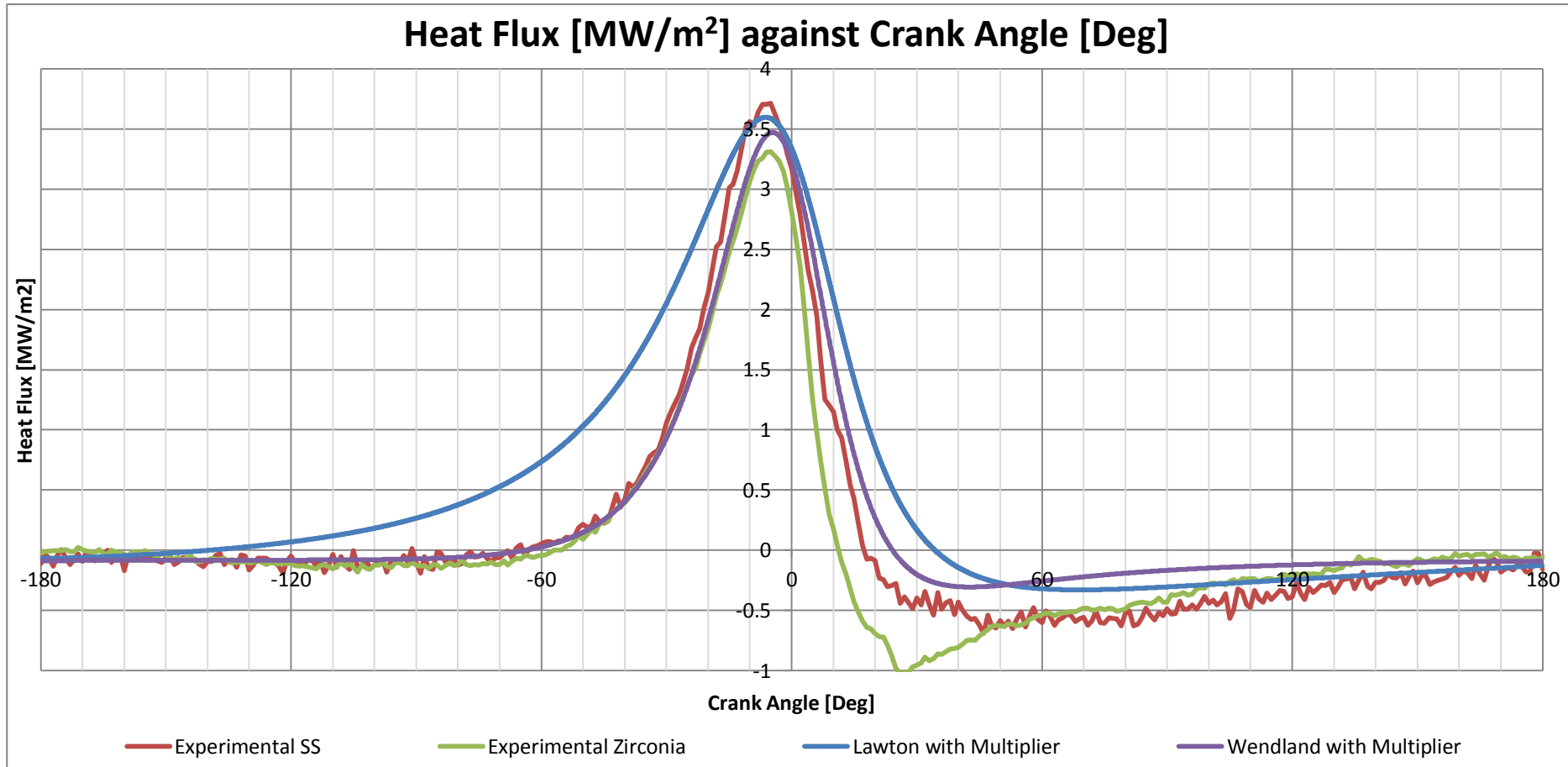
Figure 6.29. Heat flux at 1400 rpm and 80 bar PCP with air as the working gas, comparing the experimentally obtained heat flux from the Zirconia and Stainless Steel thermocouples fitted at the OEM injector location (Chromel 2D IR) to the result obtained from Lawton's and Wendland's models.
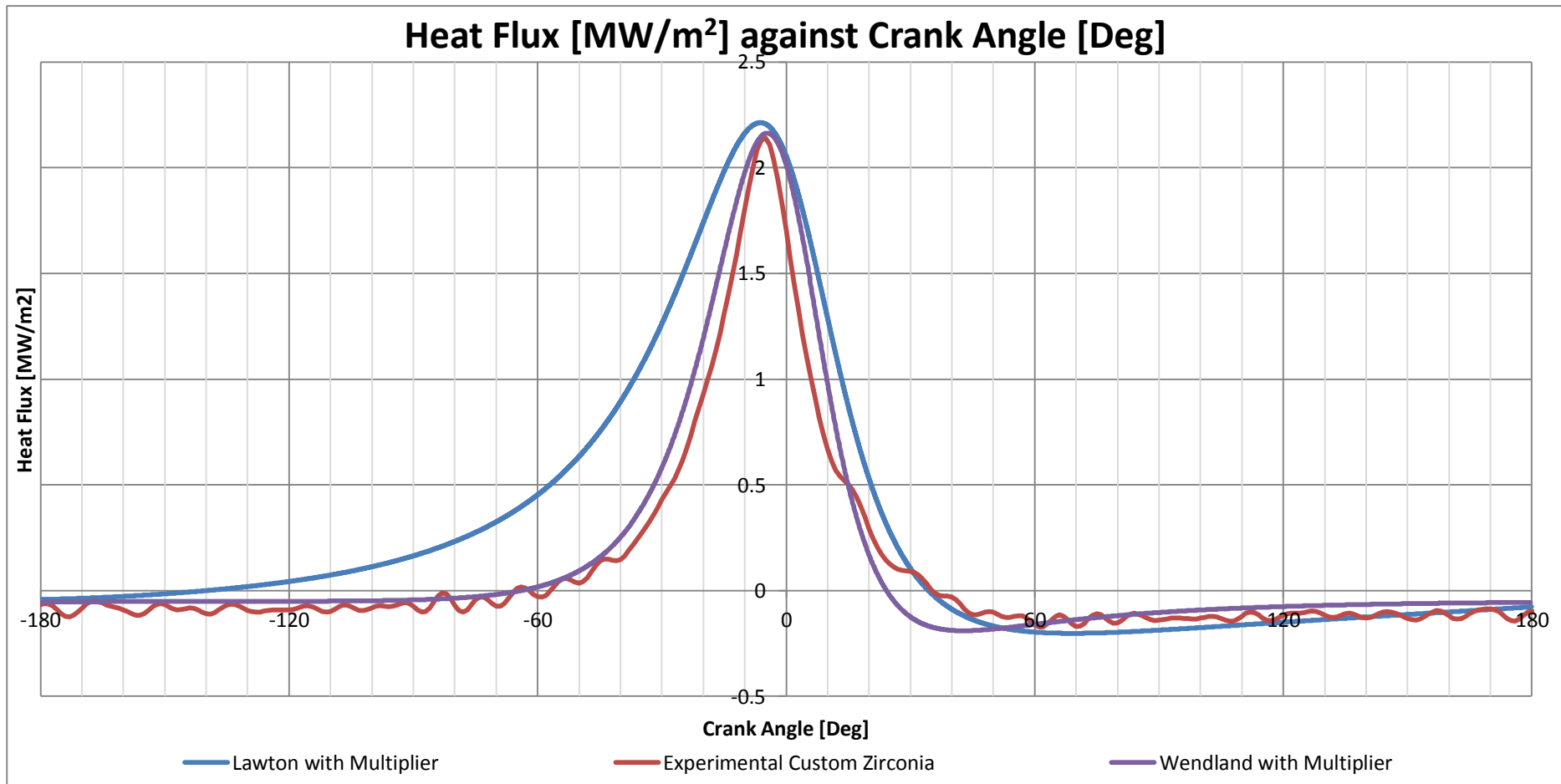
Figure 6.30. Heat flux at 1400 rpm and 80 bar PCP with air as the working gas, comparing the experimentally obtained heat flux from the Zirconia thermocouple fitted at the custom-drilled location (Chromel 2D IR) to the result obtained from Lawton's and Wendland's models.
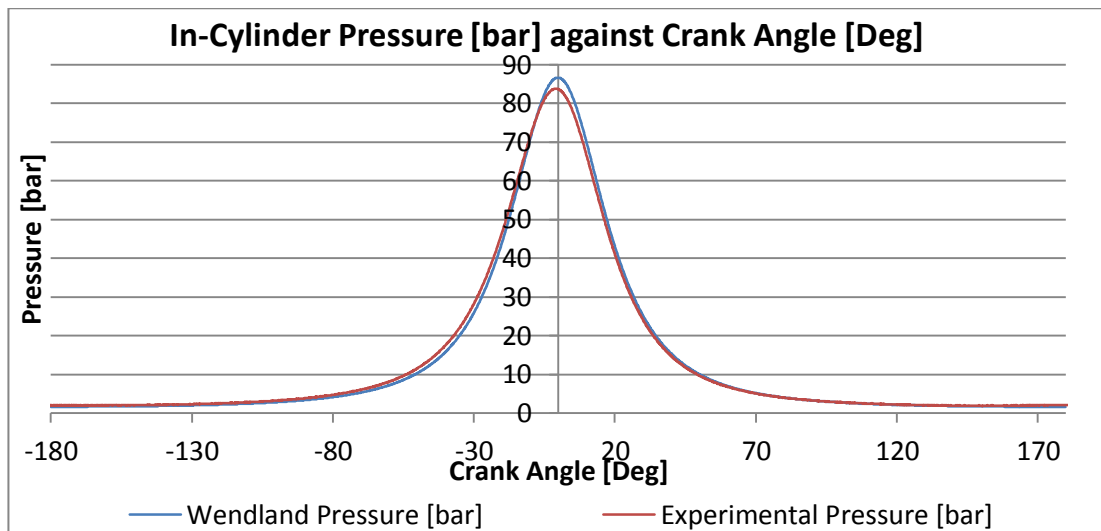
Figure 6.31. In-cylinder pressure obtained experimentally and predicted from Wendland's model at 1400 rpm and 80 bar PCP, using air as the working gas.
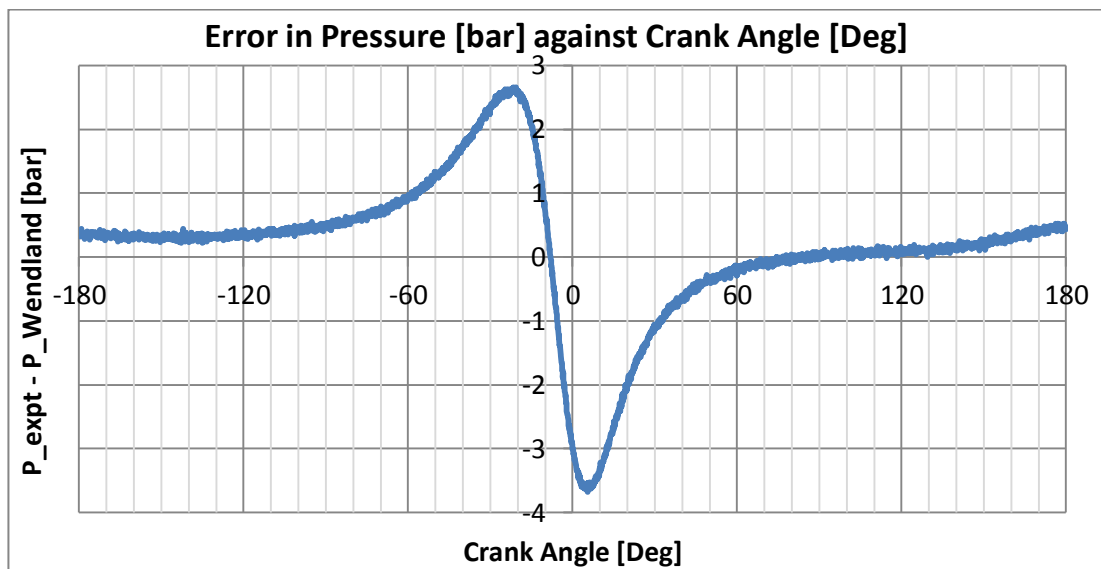
Figure 6.32. Difference between the experimental in-cylinder pressure and that predicted by Wendland's model at 1400 rpm, 80 bar PCP and air as the working gas.

The above analysis showed that both Lawton's and Wendland's models are adequate in predicting the phasing of the heat flux from a direct injection, modern diesel engine. On the other hand, magnitude prediction was poor. In fact it was shown that both models underestimate the heat flux even if a larger thermal conductivity is assigned to mimic the effect of gas turbulence.

In Lawton's work, using the laminar thermal conductivity multiplier of 25 showed a very good correlation of the heat flux magnitude. On the other hand, Wendland [18] also reported an underestimation of the peak heat flux from the model, despite the

efforts made to design an experimental setup which minimises both the temperature gradients parallel to the wall and gas turbulence. It should be said that in Wendland's work, the experimental heat flux at 4000 rpm for a 10:1 CR engine was found to be around 0.25 MW/m^2. In Lawton's work, for a 16:1 CR engine at 2395 rpm, the peak heat flux was found to be around 0.6 MW/m^2. Both of these are significantly smaller than the heat fluxes obtained in this work and presented earlier in Chapter 5.

In a study conducted by LeFeuvre et al. [9], the author made use of the adiabatic plane model put forward by Wendland [18]. LeFeuvre et al. [9] studied a 4-stroke, direct-injection, single cylinder diesel engine with a 4.5 inch bore and stroke. At first the adiabatic plane model was run assuming a laminar thermal conductivity throughout the laminae. The predicted heat flux from the model was between 17% to 25% of the experimentally obtained heat flux magnitude. To hope for a better correlation, LeFeuvre et al. [9] added a multiplier of 5x to the laminar thermal conductivity for all gas laminae, except at the wall surface. This seemed to have improved the magnitude prediction; however the peak heat flux was still underestimated by 33% to 50% of the experimental value.

In the application of the adiabatic plane model, LeFeuvre et al. [9] tried to impose a higher degree of experimental data input to the model. Instead of adopting the iteration approach put forward by Wendland [18] to generate the in-cylinder pressure cycle consistent with the boundary and initial conditions, LeFeuvre et al. [9] used the experimentally obtained in-cylinder pressure as the input to the model. This removed the need for the iteration, and it is expected that the yielded result should be more faithful to the engine considered. On the other hand, this somewhat defeats the purpose of the model as it removes the model's ability to predict the heat flux from virtually no experimental inputted data. LeFeuvre et al. [9] further explained how the choice of any reasonable initial temperature profile resulted in no significant differences in the predicted heat flux.

The observation of a lower heat flux magnitude prediction by the one-dimensional model of the thermal energy equation was also reported by Han et al. [27] and Nijeweme et al. [23] on a model similar to that put forward by Lawton [22]. They attributed this underestimation of magnitude to the fact that in the implementation of the model, the convective heat transfer due to the gas density variation, (*i.e.* term

$\rho c_v u_x \left(\frac{\partial T}{\partial x} \right)$ in equation (6.18)) was not considered. To try and investigate the effect of the convection term, a modification was done to the Matlab code of Lawton's model. In the modified version of the code, the term $\rho c_v u_x \left(\frac{\partial T}{\partial x} \right)$ was included to take into account effects of convective heat transfer. The laminar thermal conductivity was still scaled with a factor of 25 as considered by Lawton. The result showed that the magnitude of heat flux predicted was higher than that predicted without the convective term. The phasing of the heat flux was not affected. Even though the magnitude of the predicted heat flux improved with the addition of the convective term, however the predicted positive peak was still just 33% of that obtained experimentally at the OEM injector location, and 50% of that obtained experimentally at the custom drilled location (as opposed to 15% and 25% respectively without the convective term).

An interesting observation was made when comparing the spatial temperature distribution from Lawton's model with the convective term to Lawton's model without the convective term. From Figure 6.25 it was shown that from around -100 DegCA to 0 DegCA, the boundary layer exhibits a temperature higher than that of the wall. The distance from the cylinder head surface to the location of the temperature maxima was defined by Greif et al. [24] as being the boundary layer thickness. For the purpose of reference, in this text the same terminology will be used. It was noted that when Lawton's model was run without the convective heat transfer term, the locus of the thermal boundary layer thickness increased from some arbitrary value at around -100 DegCA until it reached an almost steady value close to compression TDC (0 DegCA). On the other hand, when the model was run including the convective term, $\rho c_v u_x \left(\frac{\partial T}{\partial x} \right)$ in the energy equation, the thermal boundary layer thickness increased from around -100 DegCA up to around -70 DegCA, but then slowly decreased towards compression TDC. These results are shown in Figure 6.33. Furthermore, it was also noticed that when the model was run with the convective heat transfer term, the thermal boundary layer thickness was smaller throughout the whole compression stroke. These same observations were also made by Greif et al. [24] in modelling gas compression with both air and Argon as the working fluids in a 4:1 CR single stroke compression machine.
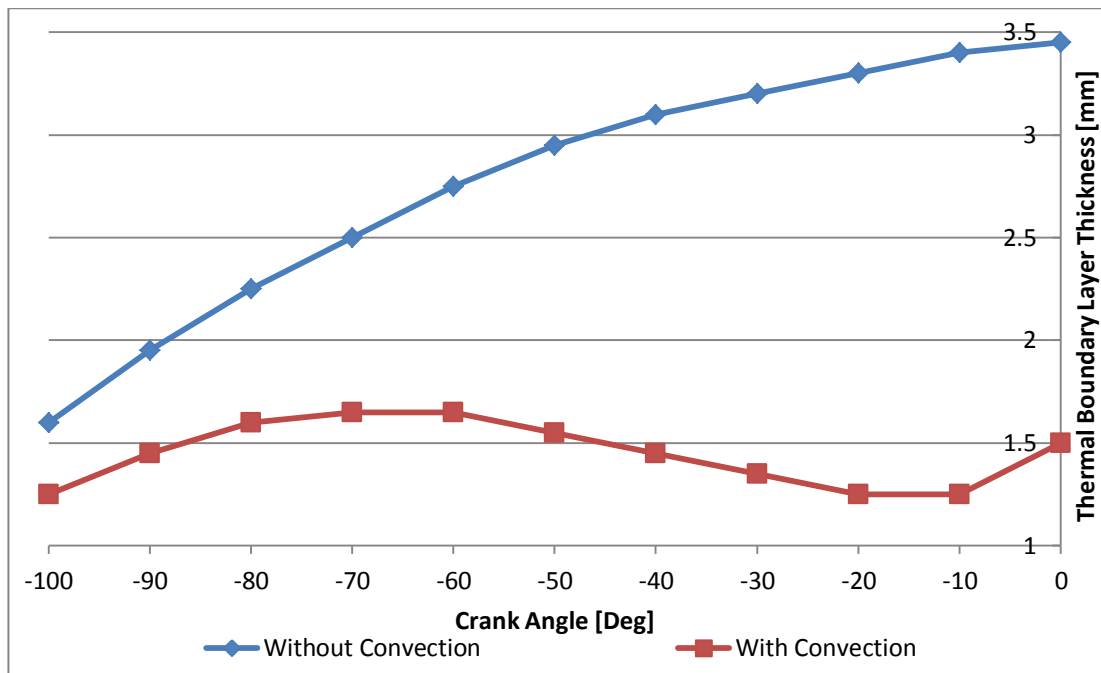
Figure 6.33. Locus of the temperature maxima experienced in the boundary layer during compression stroke using the results obtained from Lawton's model.

6.1.7 Applying One-Dimensional Heat Transfer Models on a Working Gas other than Air

In this work, the models by Lawton [22] and Wendland [18] were also applied with a working gas other than air. As presented in section 5.7.3, in the experimental campaign, testing with pure Argon resulted in the sooting of the eroding thermocouples at most of the setpoints tested. As a result, experimental data with pure Argon is very limited. Experimental tests carried out using gas mixtures were synthesised from Oxygen and Argon for γ 1.60, and from Oxygen, Argon and Nitrogen for γ 1.50. Having a gas mixture as the working gas makes the implementation of the one-dimensional heat flux models more involved and also prone to more errors. This is due to the fact that the thermal conductivities of gas mixtures at pressures synonymous to that experienced in an IC engine cannot be easily obtained from thermodynamic relationships. In fact, Poling et al. [132] state that experimental studies on this matter are very limited. While this is a problem in its own right, one must not lose sight of the limitation surrounding the model itself that the 'total apparent' thermal conductivity of the gas is taken as a simple multiplier of the laminar conductivity.

To have an idea of the performance of both models in their prediction of heat flux with gases other than air, the models were adjusted to work with the gas having γ 1.60. This particular mixture was chosen for two reasons; more experimental data was taken with this mixture, and the mixture is made up of only two components, being Argon and Oxygen (*i.e.* no Nitrogen was used). To obtain the variation of specific heats (c_p and c_v) of the mixture with temperature, the thermodynamic law of mixtures was used according to equation (6.22) and equation (6.23). The variation of c_p and c_v with temperature for Oxygen were obtained from [127].

$$c_{p_{mixture}} = \frac{\sum m_i c_{p_i}}{m_{mixture}} \qquad \ldots (6.22)$$

$$c_{v_{mixture}} = \frac{\sum m_i c_{v_i}}{m_{mixture}} \qquad \ldots (6.23)$$

The thermal conductivity of the mixture could not be easily obtained. A research paper by Barua and Mukhopadhyay [133] reported the experimentally obtained thermal conductivities of mixtures between Argon and Oxygen at different concentrations and different temperatures. The data revealed an almost linear relationship with temperature at the concentration pertaining to the mixture used experimentally in this work. This linear relationship was used in the Matlab code.

The specific heat capacities for the mixture of γ 1.60 are much lower in magnitude when compared to those for air. This means that air can effectively store more energy per unit mass, per unit temperature in the boundary layer than the gas mixture can. On the other hand, the thermal conductivities of air and mixture are similar. Figure 6.34 gives the temperature distribution at different crank angles, as predicted by Lawton's model. Figure 6.35 shows the heat transfer coefficient assuming a steady-state computation between heat flux and ΔT.
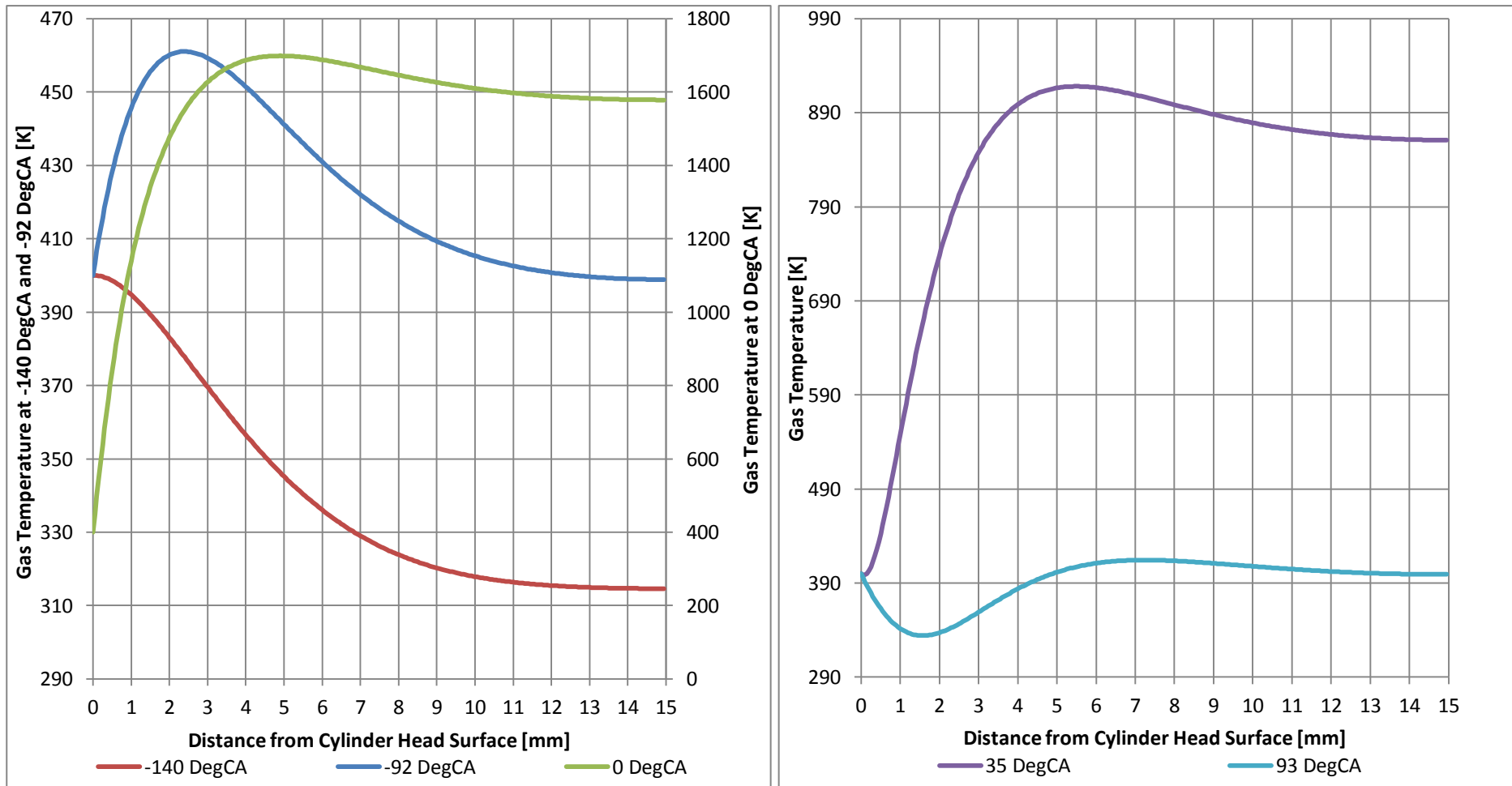
Figure 6.34. Predicted gas temperature distributions during the closed part of the cycle obtained at 1400 rpm, 84 bar with gamma 1.6 as the working gas, using Lawton's model.
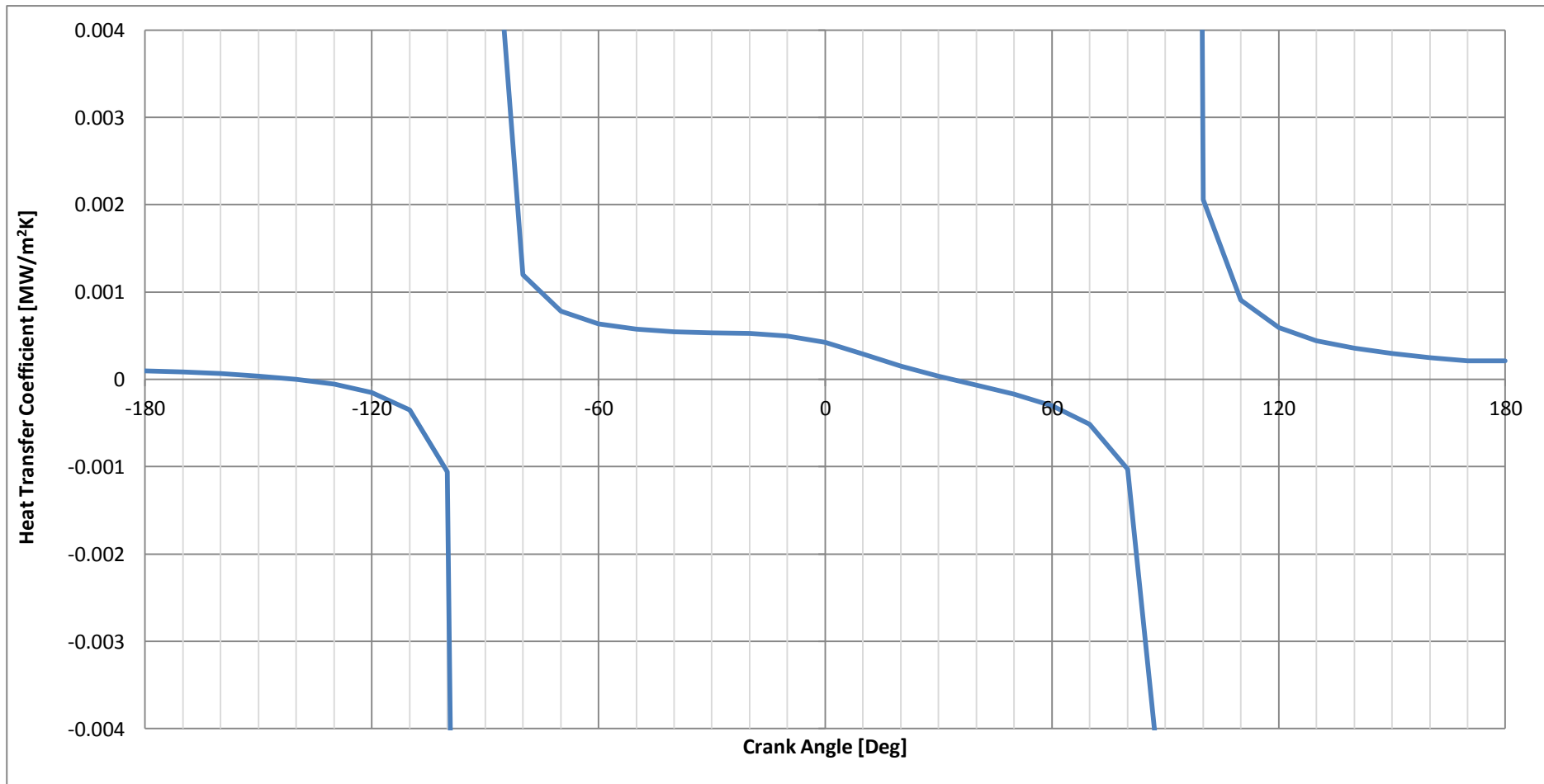
Figure 6.35. Heat transfer coefficient computed from a steady-state consideration using the heat flux and temperatures from Lawton's model at 1400 rpm, 80 bar PCP and gamma 1.6 as the working gas.

Figure 6.36 and Figure 6.37 show the comparison of heat flux obtained experimentally at the OEM injector location and custom-drilled location respectively with that predicted by the two models. Lawton's model was run neglecting the convective term. The setpoint considered was at 1400 rpm and 83 bar PCP. The data input to both models, as well as the steady-state component of heat flux obtained from the 1st law of thermodynamics using the experimental in-cylinder pressure are given in Table 6.2.

Table 6.2. Steady-state temperatures and pressures at the simulated setpoint.

Engine Speed [rpm]	1400
Peak In-Cylinder Pressure [bar]	83
MAP [bar]	1.316
Shunt Pipe Intake Temperature [K]	299
Average Wall Temperature - Measured [K]	400
Average Wall Temperature - Lawton [K]	400
Average Wall Temperature - Wendland [K]	450
Working Gas	Mixture with $\gamma = 1.6$
Steady-State Heat Flux [MW/m^2]	0.2224

It can be noticed from Figure 6.36 and Figure 6.37 that the peak heat flux location is well estimated by both Wendland's and Lawton's models. At the OEM injector location, Wendland's model seems to predict the expansion stroke of the experimentally obtained heat flux with good accuracy, while Lawton's model predicts the point of changing heat flux direction later than that reported experimentally. On the other hand, at the custom-drilled location, Lawton's model predicts better the phasing on the expansion stroke.

To allow easy visual comparison of angular phasing, the predicted heat fluxes in Figure 6.36 and Figure 6.37 are shown scaled such that their peaks are at the same level as that of the experimental traces. For the gas with γ 1.60, both models still showed an underestimation of the magnitude of heat flux. In fact Lawton's model run with a thermal conductivity of 25x the laminar value predicted a heat flux peak which is 15% that obtained experimentally at the OEM injector location, and 25% that obtained experimentally at the custom-drilled location. Wendland's model was run with no multiplier to the laminar thermal conductivity since this was found to

give the best reasonable match on the in-cylinder pressure between that obtained from the model and that recorded experimentally. The peak heat flux predicted was still 7% of that obtained experimentally at the OEM injector location and 13% of that obtained experimentally at the custom-drilled location.

Figure 6.38 shows the comparison of the in-cylinder pressure obtained from Wendland's model to that obtained experimentally, whereas Figure 6.39 shows the crank-angle resolved difference between the two pressures.
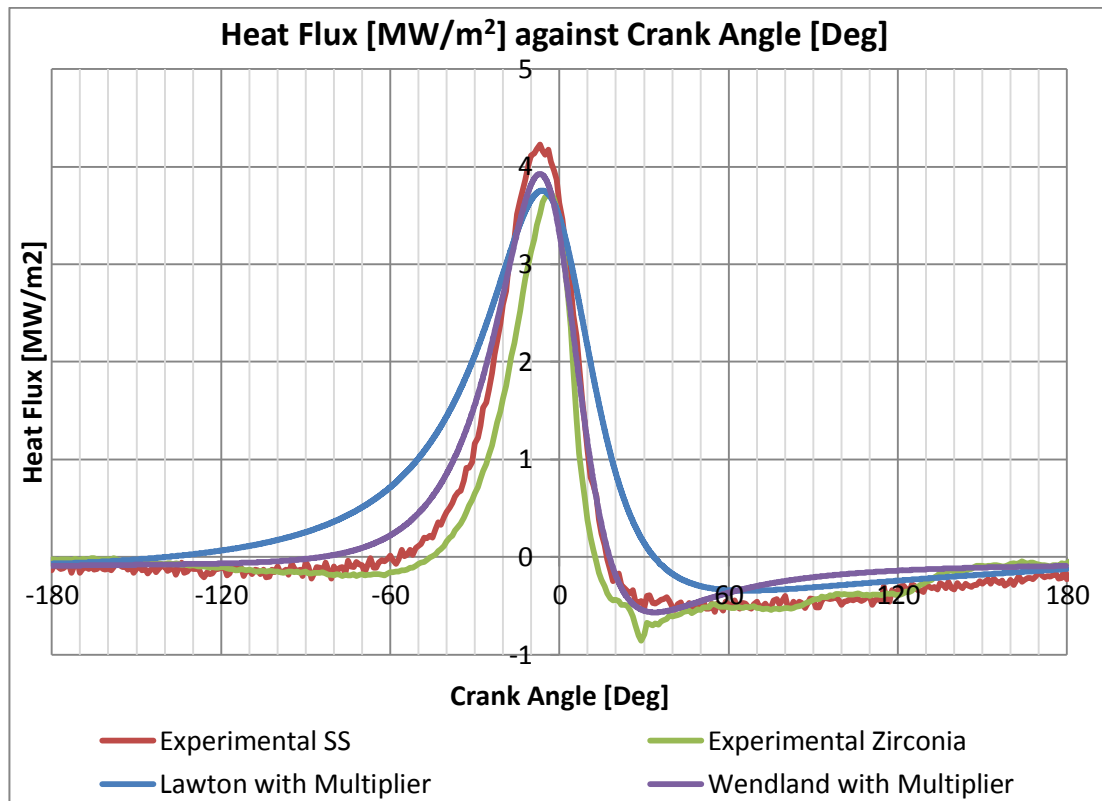
Figure 6.36. Heat flux obtained experimentally with the Zirconia and Stainless Steel thermocouples fitted at the OEM injector location (Chromel 2D IR), compared to that obtained from Wendland's and Lawton's models at 1400 rpm, 80 bar PCP and using gas of γ 1.6.
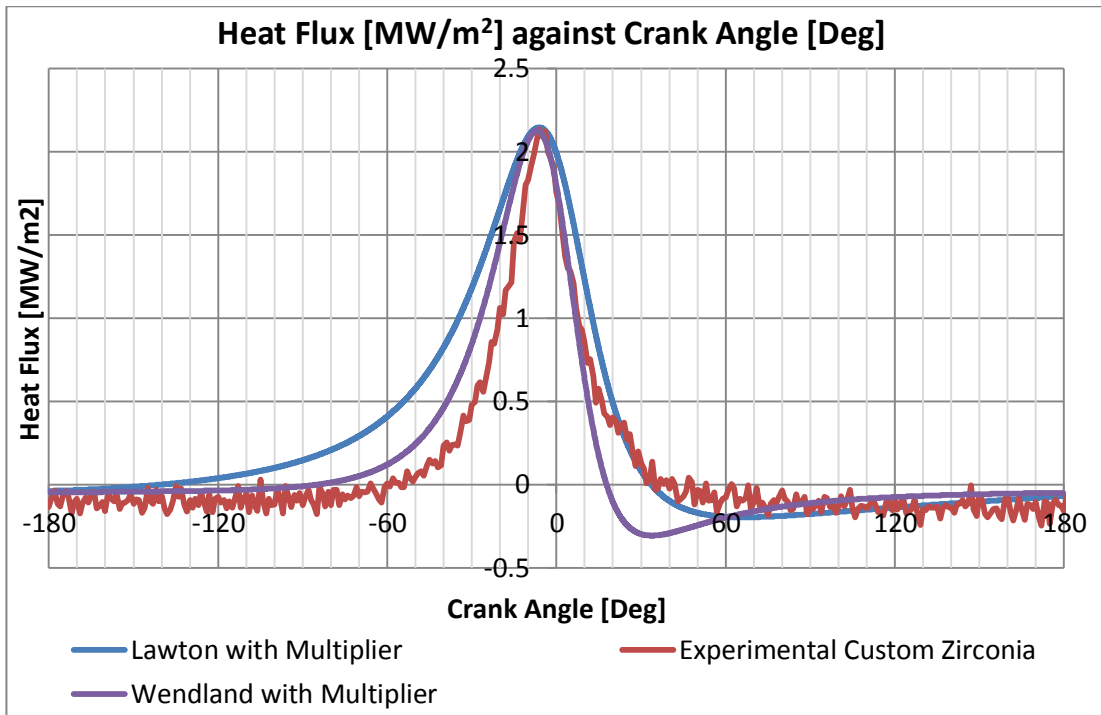
Figure 6.37. Heat flux obtained experimentally with the Zirconia thermocouple fitted at the custom-drilled location (Chromel 2D IR), compared to that obtained from Wendland's and Lawton's models at 1400 rpm, 80 bar PCP and using gas of γ 1.6.
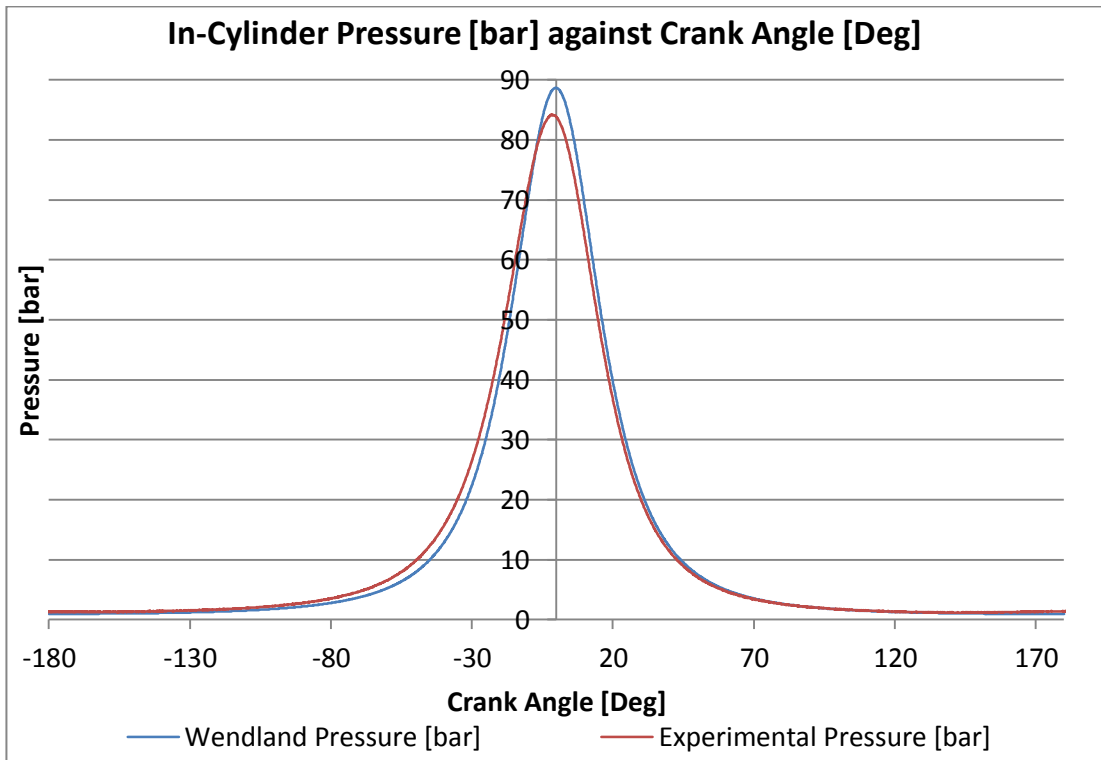
Figure 6.38. In-cylinder pressure obtained experimentally and predicted from Wendland's model at 1400 rpm and 80 bar PCP, using a gas of γ 1.6.

335
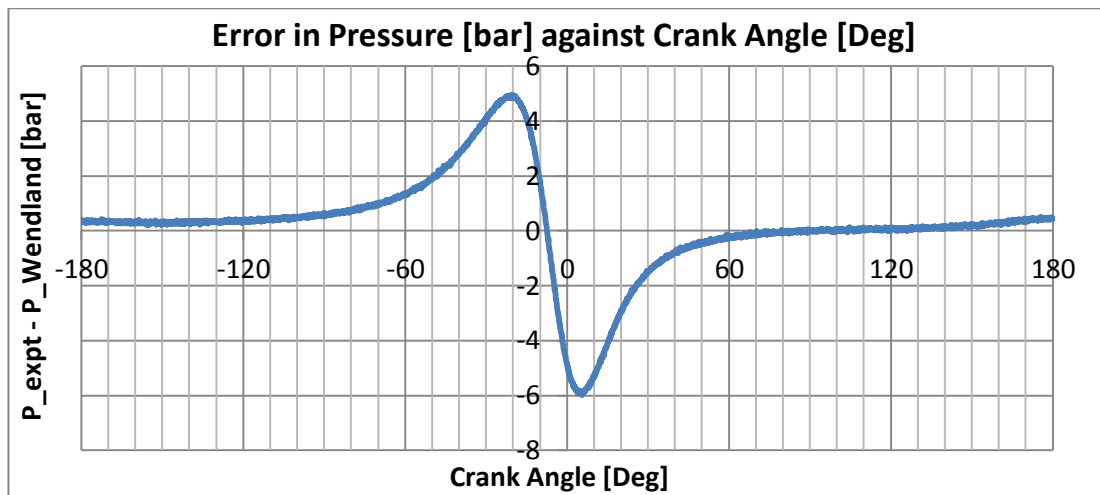
Figure 6.39. Difference between the experimental in-cylinder pressure and that predicted by Wendland's model at 1400 rpm, 80 bar PCP and gas with γ of 1.6.

6.1.8 Friction Mean Effective Pressure

At present, modelling of mechanical friction is possible at two extremes; through the use of empirical models which are essentially a regression analysis based on experimental data, or full three-dimensional hydrodynamic friction models which solve Reynolds-type lubrication equations for complex geometries like piston-liner interface, load-distortion of crankshaft journals and crankshaft-connecting rod bearings [134]. While the method of regression cannot always be extrapolated beyond conditions at which it was derived, phenomenological models are too involved to implement, especially at the early design stage when engine geometry is not yet fully defined. This leaves the engine modeller with only limited choice for FMEP prediction.

In this Doctoral work, some effort was made in trying to find an FMEP model which is independent of empirical correlations, but which still retains simplicity of application. The closest to the desired model was that by Patton et al. [135]. This model was developed on a SI engine, based on an FMEP teardown test. The total FMEP of the engine is predicted from a summation of individual FMEP predictions of several sub-assemblies. The FMEP of each sub-assembly is predicted from a theoretical evaluation of the possible lubrication phenomena. Each sub-assembly FMEP still requires a constant of proportionality, and hence the model is still reliant on experimental data correlation. On the other hand, however, it is understood that

since the total FMEP is split up into sub-assemblies, where some of which are expected to be relatively similar between one engine and another, their coefficients are not expected to vary by much. Table 6.3 outlines the FMEP terms of each sub-assembly of this model. Sandoval and Heywood [136], later revised this model and updated the coefficients given by Patton et al. [135] for more recent engine designs. Furthermore Sandoval and Heywood [136] also added a 'lubrication viscosity scaling factor' $\left(\frac{\mu(T)}{\mu_0(T_0)}\right)$ to the FMEP terms which represent hydrodynamic lubrication of the rubbing friction components. The constant μ_0 represents the lubricant viscosity of the relevant oil used in the engine for model calibration, whereas μ is the lubricant viscosity of the oil of the engine on which the model is being applied. In the original version of this model, Patton et al. [135] used SAE 10W30 oil in obtaining the calibration constants given in Table 6.3. Figure 6.40 shows the model with the coefficients as given by Patton et al. [135] applied to the 2.0 HDi engine geometry compared to the experimental FMEP data reported in earlier Figure 4.18. It is noted that a large standard error of 37% was incurred between the predicted and measured FMEP.

In another attempt, some effort was made in trying to correlate simple empirical models to the experimental data reported in Chapter 4. For the purpose of fitting an empirical model, two experimentally obtained FMEP data sets were available. The first FMEP data set was that obtained through the testing session represented by Table 4.1 (Figure 4.18). This FMEP data set was used as the 'training data' since it contained the largest number of setpoints. This allowed fitting of data with engine speed in the range between 1100 rpm and 3000 rpm, and PCP between 25 bar and 140 bar, on a total of 31 data points. The second FMEP data set available was that obtained through the testing session represented by Table 4.2 (Figure 4.43 and Figure 4.44). Only the data obtained with air as the working gas was used from this test matrix, since as reported in Chapter 4 it was found that the FMEP for a pressurised motored engine is insensitive to the bulk gas temperature. This FMEP data set was used as the 'validation data'.

For this regression analysis, the dependent variables investigated were: engine speed, PCP, LPP, coolant temperature, shunt intake temperature and IMEP$_{720}$. Table 6.4 gives the coefficients obtained through regression analysis for twelve different trials,

making up twelve different possible correlations. The adjusted R-squared value and standard error are given for each correlation type. Equation (6.25) gives the full version of the hypothetical model, however not all terms were used in each correlation type, as shown by Table 6.4. In correlating the model to the experimental data, the FMEP quantity was taken to be positive.

Some of the correlation types in Table 6.4 show negative coefficients for the intercept or A_{RPM}^2 coefficient. These correlation types are considered invalid due to the following two reasons. Firstly, in obtaining the FMEP 'training data' set, no accessories were fitted to the engine, apart from the oil pump and the vacuum pump. The vacuum pump had its intake port blanked off. Both of these accessories are expected to have a mean effective pressure which is either constant (positive) or increases in proportion to the engine speed. This contradicts the negative value of the intercept obtained with correlation type 2 and correlation type 4 in Table 6.4. Furthermore, it is also well known that a square increase in the engine speed usually results in an increase in the FMEP due to windage [128]. This contradicts the negative A_{RPM}^2 coefficient found in correlation type 2 and correlation type 8.

It should be noted that correlation types 1, 2, 7 and 8 are in fact an application of the classical Chen-Flynn model, which is a very popular model amongst commercial engine simulation software, such as Ricardo WAVE and GT Power. The Chen-Flynn model is given by equation (6.24), where A_{CF} represents the constant accessory friction, B_{CF} is the coefficient multiplied to the linear pressure load term (PCP), C_{CF} is the coefficient to the engine speed contribution, and Q_{CF} is the coefficient to the term representing the windage losses [128]. It is shown from Table 6.4 that applying the Chen-Flynn model to the training data set, correlation types 1 and 7 show a relatively good fit with a standard error of 7.2% and 8.6% respectively. In trying to obtain a better correlation, other dependent variables were considered as shown by correlation types 3, 4, 5, 6, 9, 10, 11 and 12.

$$FMEP = A_{CF} + \frac{1}{n_{cyl}} \sum_{i=1}^{n_{cyl}} \left[B_{CF} P_{max\,i} + C_{CF} \left(\frac{RPM \; x \; stroke}{2} \right) + Q_{CF} \left(\frac{RPM \; x \; stroke}{2} \right)^2 \right]$$

$$\ldots (6.24)$$

Correlation types 3 and 9 investigated the dependence of the FMEP on the location of peak in-cylinder pressure. For a motored engine the location of peak in-cylinder pressure occurs very close to TDC. As a result, its effect on the FMEP is expected to be small. However it is hypothesised that for fired engines which typically have LPPs equal to or higher than 10 DegCA, the LPP is potentially a representative variable which has underlying information of the FMEP dependence on the piston lateral thrust, as well as the interaction of the gas load and piston velocity (revisit section 2.3.1 in Chapter 2). This was in fact shown by Pipitone [137] for a fired SI engine, where it was found that the FMEP increased as a function of a 3rd order polynomial of the LPP, where an increase in LPP (after TDC) resulted in an increase in FMEP.

Correlation type 3 showed that adding the LPP variable improved the standard error to around 5.7%, however the intercept constant obtained was deemed to be high. Furthermore, for the same test, A_{LPP} was found to be positive. In this model, the LPP was input as a negative value (since for a motored engine LPP occurs BTDC), hence with the chosen LPP sign convention, a positive A_{LPP} means that advancing further the LPP from TDC results in a decrease in the FMEP, which is contradictory to what was found by Pipitone [137]. When the intercept was forced to zero, in correlation type 9, A_{LPP} changed sign to negative meaning that a higher FMEP is predicted with an LPP that is further away (advanced) from TDC, as expected. With this correlation type however, the standard error increased back to 8%, *i.e.* similar to that obtained from the traditional Chen-Flynn model (correlation types 1 and 7).

The other three dependable variables investigated were the coolant temperature, shunt pipe intake temperature and $IMEP_{720}$. It was found that both the coolant and shunt pipe intake temperature did not have any appreciable effect on the FMEP (correlation types 4, 5, 10, 11). Furthermore, their inclusion resulted in either a negative intercept or a positive A_{LPP}. Hence both these variables were discarded.

Introducing the $IMEP_{720}$ showed a relatively large intercept when unrestricted, together with a positive A_{LPP} (correlation type 6). When the intercept was restricted to zero (correlation type 12), a similar fit to that of correlation type 9 was noted.

From the aforementioned, the twelve regression tests conducted can be filtered down to four possibilities; correlation types 1, 7, 9 and 12. Correlation types 1 and 7 both

represent the traditional Chen-Flynn model without the windage term. Correlation type 7 does not include a constant term. Correlation type 9 represents the addition of the LPP term, whereas correlation type 12 represents the addition of the $IMEP_{720}$. It is noted that comparing correlation types 9 and 12 to the traditional Chen-Flynn model denoted by correlation types 1 and 7 showed no improvement in the standard error. When the short listed four versions of the FMEP model were compared to the validation data set, the best correlation was shown by type 12, *i.e.* with the inclusion of the LPP and $IMEP_{720}$ terms. This can be evaluated from the last column in Table 6.4. It is however noted that the inclusion of the $IMEP_{720}$ term showed negligible improvement in the FMEP prediction (*i.e.* when compared to correlation type 9). On the other hand, a small improvement in the FMEP prediction was noted with the addition of the LPP term (correlation type 9), when compared to the traditional Chen-Flynn model (represented by correlation types 1 and 7).

From the above analysis, it is thought that the model that constitutes the best representation of FMEP for the studied engine is that which includes a linear engine speed term, linear PCP term and linear LPP term (correlation type 9). Equation (6.26) in Figure 6.41 presents the proposed FMEP model. Figure 6.41 shows the experimental data from the training data compared to that predicted by the model. Figure 6.42 shows the predicted FMEP compared to the validation data set.

6.1.8.1 <u>Reflections</u>

Having made some attempts in correlating simple models to the experimentally obtained FMEP data, the limitations associated with FMEP modelling were identified. As highlighted from the experimental results in Chapter 4, it can be said with certainty that the pressurised motored engine FMEP is sensitive to engine speed and pressure load (represented by PCP). Throughout this work, and also from previous research by Mauke et al. [4] it was reasoned out that another possible variable which can be used to describe the FMEP in an engine is the angular phasing between the pressure load and the crank angle. This is due to it having an underlying effect of the lateral force between the piston and the liner, which gives rise to the rubbing friction component of the piston-liner assembly. A further hypothesis that was made in this work is that in an engine which has a pressure phasing (LPP) that is either heavily retarded, or heavily advanced with respect to TDC, bulk gas

temperature might show an effect on the FMEP due to a greater dependability of the FMEP of the piston on the hydrodynamic lubrication regime (when compared to the pressurised motored engine that has the LPP very close to TDC). Unfortunately, with the current experimental setup, this hypothesis could not be tested. A significant advancement in the field of FMEP modelling can be possibly made if experimental evidence is obtained that FMEP is truly dependent on the pressure phasing, without having any interference from other variables. As has been said in a previous paragraph, such study was already attempted by Pipitone [137] for a fired SI engine and showed that LPP was somewhat responsible for a variation in FMEP, however in the study by Pipitone, since the engine was fired the LPP was varied by varying the spark timing. Hence, it is possible that the relationship seen between FMEP and LPP could have been superimposed by effects due to different bulk gas temperatures at different spark timings.

Table 6.3. FMEP [kPa] terms of Patton's model. Calibration constants are those given by Patton et al..

Cranktrain Assembly	Valvetrain Assembly	Piston-Rings-Connecting Rod Assembly	Accessories
Crankshaft bearing seal $FMEP = (1.22x10^5)\dfrac{D_b}{B^2 S n_c}$	Camshaft bearing hydrodynamic friction $FMEP = (2.44x10^2)\left(\dfrac{N n_b}{B^2 S n_c}\right) + 4.12$	Reciprocating friction $FMEP = 294\left(\dfrac{S_p}{B}\right)$	General accessory term $FMEP = 6.23 + (5.22x10^{-3})N + (-1.79x10^{-7})N^2$
Crankshaft bearing hydrodynamic lubrication $FMEP = (3.03x10^{-4})\dfrac{N D_b{}^3 L_b n_b}{B^2 S n_c}$	Roller follower friction $FMEP = (0.0151)\dfrac{N n_v}{S n_c}$	Piston ring friction without gas $FMEP = 40600\left(1 + \dfrac{1000}{N}\right)\dfrac{1}{B^2}$	
Turbulent Dissipation $FMEP = (1.35x10^{-10})\dfrac{D_b{}^2 N^2 n_b}{n_c}$	Oscillating hydrodynamic $FMEP = 0.5\left(\dfrac{L_v{}^{1.5} N^{0.5} n_v}{B.S.n_c}\right)$	Gas Pressure Loading $FMEP = 6.89\dfrac{P_i}{P_a}\left(0.088 r_c + 0.182 r_c{}^{1.33 - K.S_p}\right)$	
	Oscillating Mixed $FMEP = 21.4\left(1 + \dfrac{1000}{N}\right)\dfrac{L_v n_v}{S n_c}$	Hydrodynamic journal bearing $FMEP = (3.03x10^{-4})\dfrac{N D_b{}^3 L_b n_b}{B^2 S n_c}$	
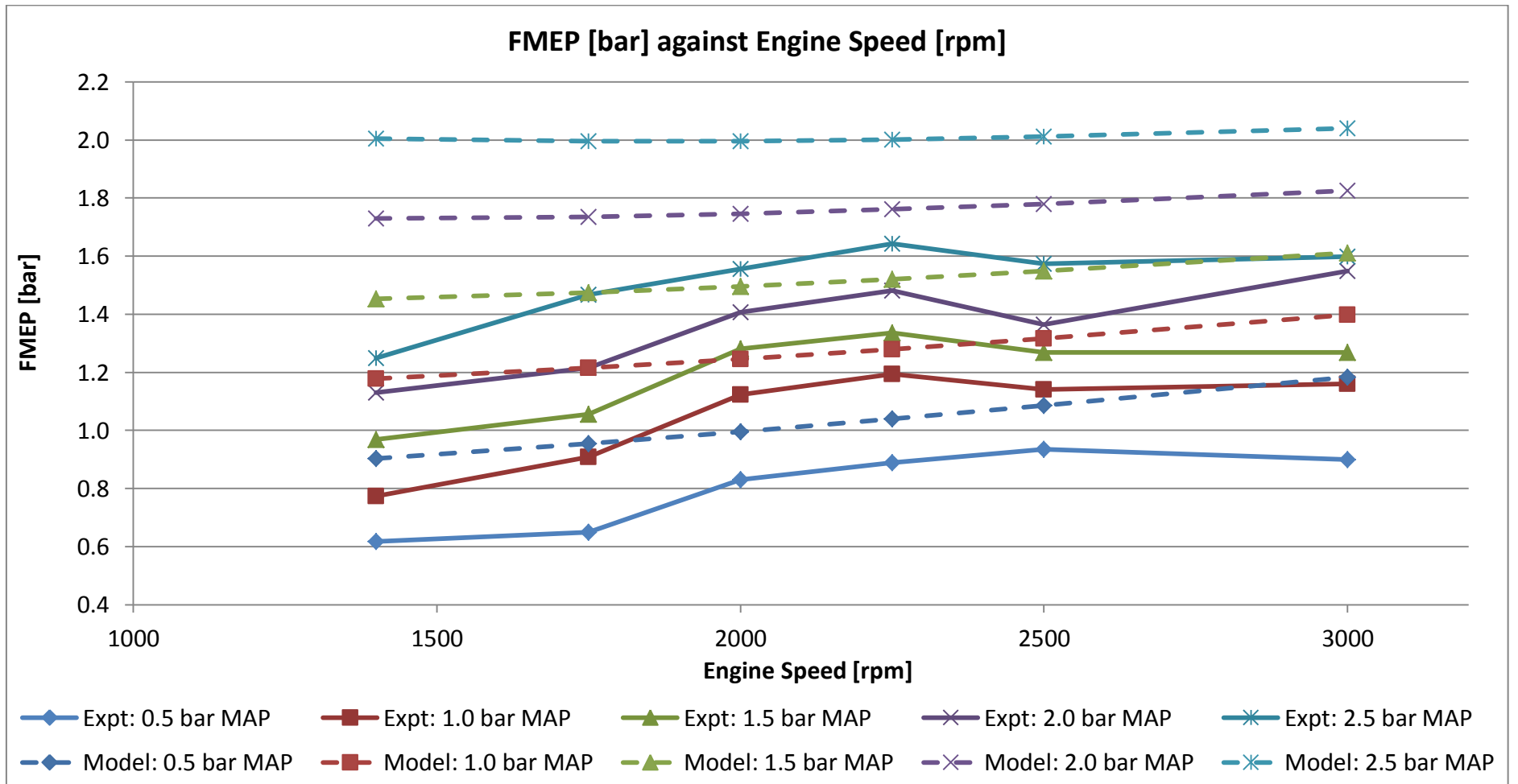
Figure 6.40. Comparison between the training FMEP data set and prediction from Patton's model.

Table 6.4. Coefficients of FMEP model and standard error from regression analysis.

Correlation Type	Intercept [bar]	A_RPM [bar.min]	A_RPM² [bar.min²]	A_PCP	A_LPP [bar/DegCA] Datum @ TDC	A_Coolant T [bar/K]	A_Intake T [bar/K]	A_IMEP720	Adjusted R-Squared	Standard Error	Standard Error
			Dependent Variables Coefficients						Compared to Training Data Set		Compared to Validation Data Set
Type 1	0.205	2.080E-04		0.00727					0.945	0.072	0.119
Type 2	-0.329	7.519E-04	-1.261E-07	0.00707					0.960	0.062	
Type 3	0.965	5.583E-05		0.00468	0.61				0.966	0.057	
Type 4	-2.076	1.348E-04		0.00550	0.63	0.008417			0.966	0.057	
Type 5	2.949	1.085E-04		0.00560	0.52		-0.0070		0.967	0.056	
Type 6	0.963	6.000E-05		0.00580	0.59			0.0743	0.966	0.057	
Type 7	0	2.827E-04		0.00778					0.962	0.086	0.136
Type 8	0	4.356E-04	-5.524E-08	0.00711					0.963	0.065	
Type 9	0	2.589E-04		0.00792	-0.12				0.961	0.080	0.099
Type 10	0	7.969E-05		0.00492	0.62	0.002688			0.962	0.056	
Type 11	0	3.842E-05		0.00437	0.62		0.0033		0.962	0.058	
Type 12	0	3.000E-04		0.00910	-0.14			0.0799	0.960	0.081	0.096

$$FMEP = Intercept + A_{RPM}(RPM) + A_{RPM^2}(RPM^2) + A_{PCP}(PCP) + A_{LPP}(LPP) + A_{Coolant\ T}(T_{Coolant}) + A_{Intake\ T}(T_{intake}) + A_{IMEP_{720}}(IMEP_{720})$$

... (6.25)
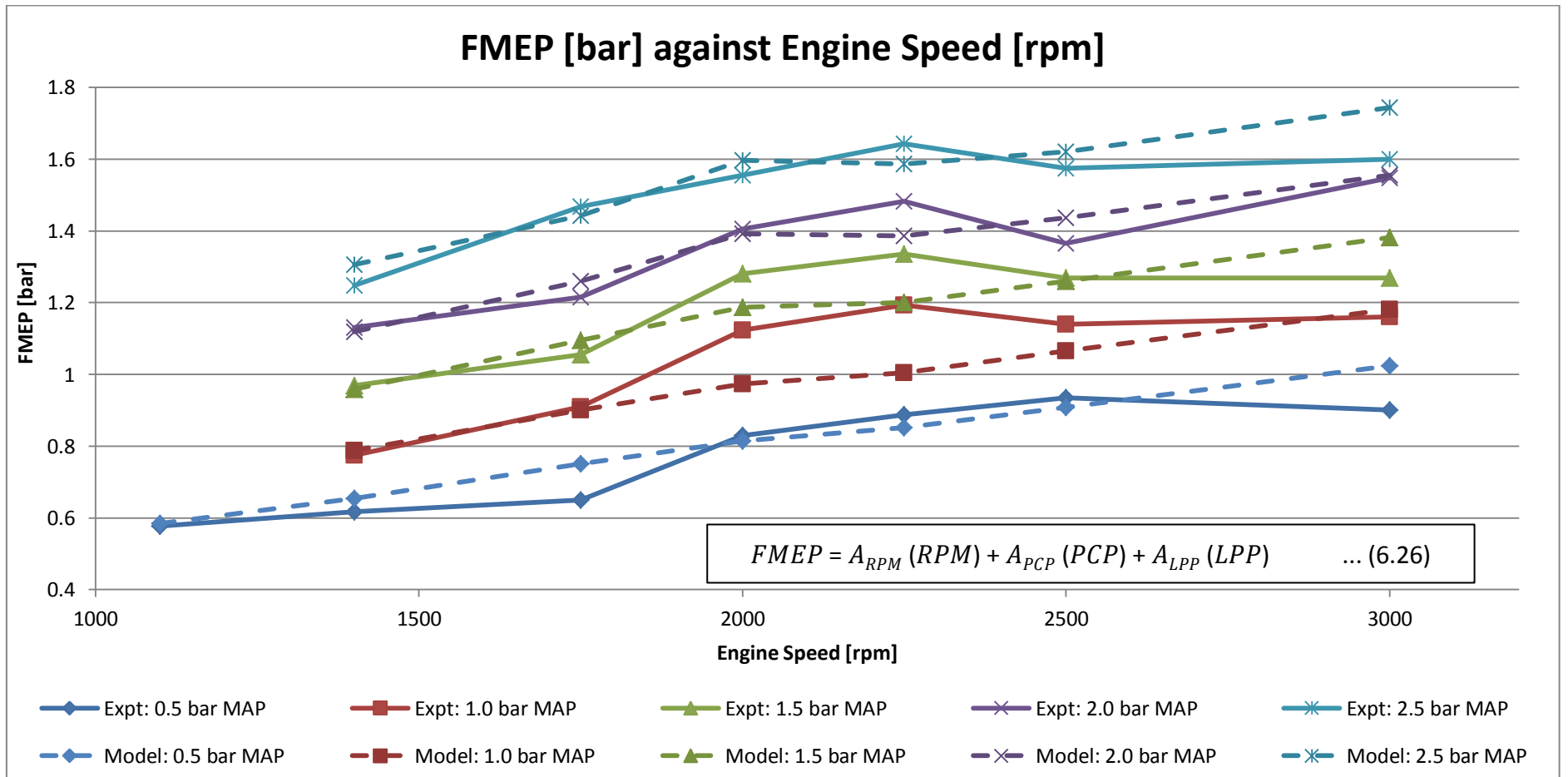
Figure 6.41. Comparison of FMEP between prediction from the proposed model (6.26) and the training data shown in Figure 4.18.

FMEP [bar] against Engine Speed [rpm]

$$FMEP = A_{RPM} \, (RPM) + A_{PCP} \, (PCP) + A_{LPP} \, (LPP) \qquad ... (6.26)$$

Legend: Expt: 84 bar PCP — Expt: 103 bar PCP — Model: 84 bar PCP — Model: 103 bar PCP
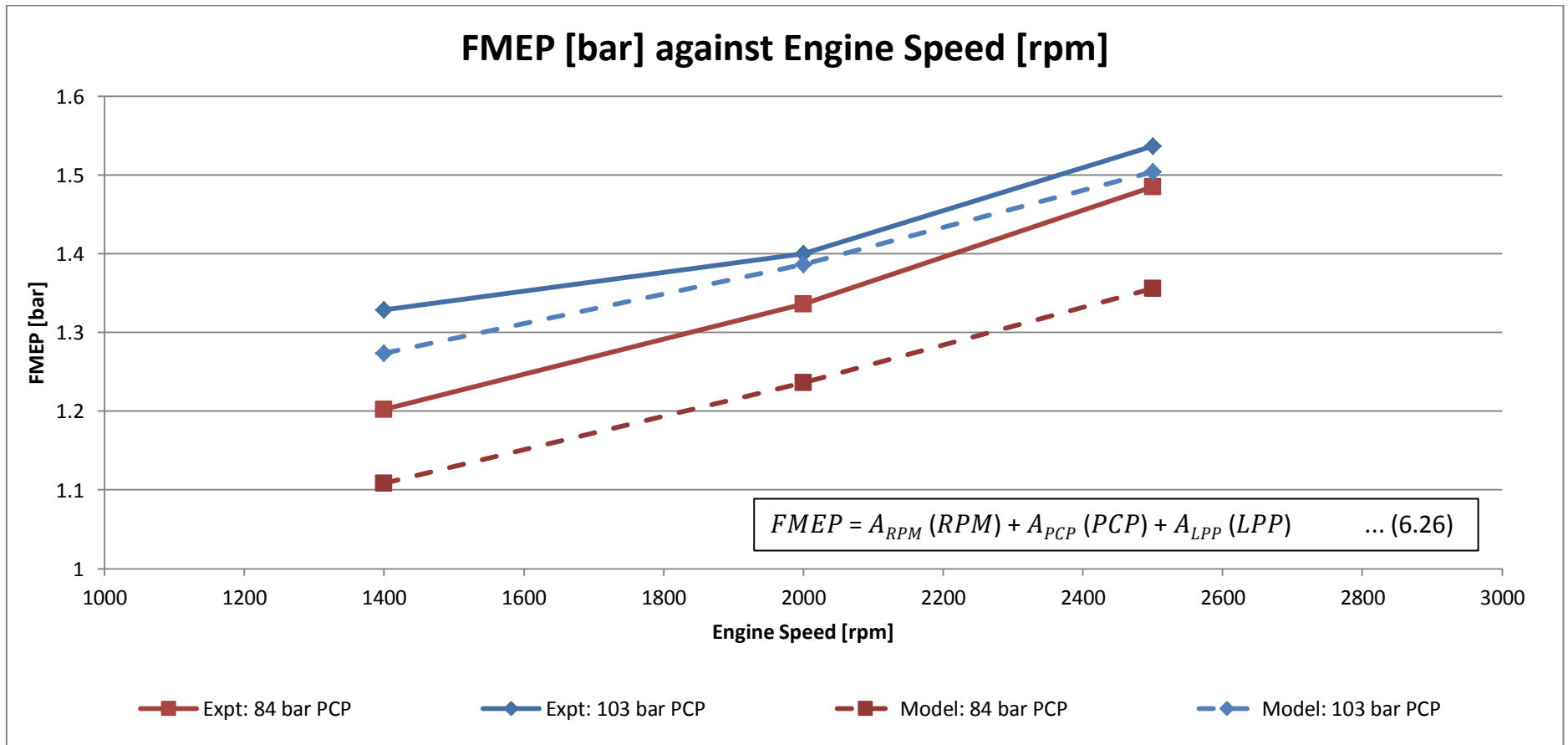
Figure 6.42. Comparison between predicted FMEP from (6.26) and the validation data shown in Figure 4.41 and Figure 4.42.

346

7 SUMMARY AND CONCLUSIONS

An experimental investigation was conducted in two main research areas; mechanical friction and in-cylinder heat transfer. The experimental data was obtained and analysed with the primary aim of furthering the knowledge in both research areas of interest. The research sought to improve the existing configuration of the pressurised motored method for the purpose of FMEP determination. Additionally, the present limitations in the determination of in-cylinder heat transfer through the method of surface temperature measurements were also evaluated. An attempt was also made to support recent research which promotes the use of a two-dimensional heat transfer evaluation at the surface of the eroding thermocouple, instead of the more common semi-infinite solid approach.

In the following text, two sections are presented with the summary and conclusions outlined from this project that involve the mechanical friction determination from the pressurised motored engine, and motored in-cylinder heat transfer.

7.1 Summary and Conclusions from FMEP Testing

The pressurised motored method in its conventional form was found to offer both the FMEP robustness and also a representative pressure load. With the modification proposed and conducted in this research utilising different working gases, the in-cylinder temperature can also be increased to values synonymous to the fired operation. The control of the in-cylinder gas temperature can be done independently from the control of the gas pressure load; a feature which cannot be easily obtained in fired testing. From the FMEP experimental investigation, the following conclusions were drawn:

1.   The pressurised motored method was found to offer high FMEP measurement robustness due to the fact that the FMEP has a magnitude which is comparable to the BMEP and $IMEP_{720}$. This quality of the pressurised motored method is one of the main reasons why this method of FMEP determination is preferred over conventional fired tests, in which the FMEP uncertainty is large due to a very small FMEP magnitude when compared to the magnitudes of the BMEP and $IMEP_{720}$.

2.   The method of using gases with high ratios of specific heats has been proposed and implemented. It was proved that the engine could be run for a long number of hours on a 100 Nm^3, 200 bar gas cylinder, if both the exhaust gas and blow-by are re-routed to the intake manifold.

3.   Running the engine with air, Argon, and mixtures using both constituents showed that the peak bulk gas temperatures can reach up to 1200℃, independent of the peak in-cylinder pressure setting. This conclusion answers the first research question.

4.   Using gas mixtures and Argon showed no particular difficulty in terms of engine control or setpoint stability. It was however found that at certain setpoints, running the engine with pure Argon results in sooting due to the degradation of the oil layer lubricating the cylinder wall. Furthermore, the use of a high γ gas was found to decrease the PCP testing range in a compromise to retain a well purged setup.

5.   It was shown that while the peak of the in-cylinder pressure and peak bulk gas temperature can be made equal to that in the fired engine, the method inherently lacks the fired peak pressure location emulation, and the emulation of bulk gas temperatures during part of the expansion stroke and the exhaust stroke.

6.   It was found that although in the pressurised motored engine the temperature at the end of the expansion stroke is lower than that at the beginning of the compression stroke due to heat and blow-by losses, the exhaust temperature is higher than the intake temperature. This was found to be a result of the recompression effect that occurs on the exhaust stroke. This effect was found to be accentuated at higher engine speeds, higher PCPs, and using a gas with a low γ.

7.   The magnitude of the IMEP$_{360}$ for the pressurised motored engine was found to decrease quadratically with an increase in engine speed at the same PCP condition. On the other hand, the magnitude of the IMEP$_{360}$ was found to increase as a linear function with PCP at any given engine speed. A linear increase in the IMEP$_{360}$ magnitude was found to occur with an increase in the γ, bulk gas temperature and wall temperature.

8.   A theoretical calculation on the experimentally obtained in-cylinder pressure with air and Argon showed that the use of Argon results in a smaller blow-by mass

escaping from the cylinder per cycle. This was found to be a result of two conflicting properties. Using a gas of higher ratio of specific heats results in higher mass flow rates, but the crank angle resolved in-cylinder pressure is lower for a high γ gas than that of air, if the PCP is the same for both tests.

9.   The magnitude of the PMEP of the pressurised motored engine was found to show an increase with an increase in engine speed for a constant PCP. The shape and rate of increase of the PMEP with engine speed is found to be dependent on the PCP and gas used. The PMEP magnitude was found to be highly dependent on the extent of the exhaust recompression; hence conditions of PCP and gas which promote a high exhaust recompression experience a drastic increase in the PMEP magnitude. This showed that running the engine with gases of higher γ benefit the data quality due to a more fired-like PMEP magnitude.

10.   It was shown that the FMEP of the pressurised motored engine exhibits an increase with an increase in engine speed, at all PCPs and gases tested in this work. It was also found that the FMEP shows a linear increase with an increase in PCP at all engine speeds and for all gases tested.

11.   Testing of the pressurised motored engine at peak bulk gas temperatures of around 600 DegC higher than that reached with air as the working gas showed no measureable variation in the FMEP. This conclusion answers part of the second research question. It is hypothesised that the reason why the FMEP showed to be independent of an increase in the bulk gas temperature is due to the phasing of in-cylinder pressure and bulk gas temperature with piston trajectory of the pressurised motored engine. This hypothesis, however, could not be tested with the setup used in this research.

12.   It was found that running the engine with gases of high γ resulted in a slight decrease in the ratio of FMEP/BMEP, which is a measure of the FMEP determination robustness. The decrease in the FMEP/BMEP with high γ gases is because the BMEP increases due to an increase in the heat losses attributed to the higher bulk gas temperatures. The FMEP/BMEP ratio of the pressurised motored engine running on Argon was still found to be much larger than that for a fired engine.

13.   A regression analysis performed on the experimentally acquired FMEP data showed that the FMEP for the four cylinder pressurised motored engine used in this research can be explained by the correlation defined by equation (6.26). This correlation was obtained from experimental data ranging between engine speeds of 1100 rpm and 3000 rpm, and PCPs between 25 bar and 140 bar. The LPP for this test range was found to vary between 0.15 DegCA BTDC and 1 DegCA BTDC.

$$FMEP = A_{RPM} \, (RPM) + A_{PCP} \, (PCP) + A_{LPP} \, (LPP) \qquad \dots (6.26)$$

7.2 Summary and Conclusions from Heat Transfer Testing

The cylinder head of the single cylinder engine was fitted with surface thermocouples of the eroding type at two locations; at the OEM injector location that is close to the central axis of the cylinder, and at a custom-drilled location close to the periphery of the cylinder, which is in the squish region. The transient component of heat flux was determined from the traditional Fourier's spectral analysis with the semi-infinite solid assumption, and also using the newer Impulse Response Method. The impulse response method was coupled to the results obtained from two-dimensional finite element models of the eroding thermocouples to account for the two-dimensional heat flow that is known to occur with these kind of surface thermocouples. Three eroding surface thermocouples based on different materials were fitted at the same OEM injector location, and their temperature swing and mean, together with the transient portion of heat flux were compared to identify the role of the sensor material. A parametric study on surface temperature and transient component of heat flux was also carried out, investigating the effect of engine speed, PCP, gas compositions, coolant/oil temperatures, and the effect of soot on the surface thermocouples. From this heat transfer research the following conclusions were drawn:

1.   It was found that significant two-dimensional effects occur in the Zirconia-based and Aluminium-based surface thermocouples, whereas a smaller magnitude of two-dimensional heat flow was found for the Stainless Steel-based thermocouple.

2.   It was found that the Zirconia-based thermocouple shows a very similar transient component of heat flux to that obtained from the Stainless-Steel based

thermocouple, if two-dimensional effects at the surface of the thermocouples are accounted for. The Aluminium thermocouple which matches the cylinder head material showed a significantly higher heat flux than the other two thermocouples fitted at the same location. No definite physical reason could be found for this high heat flux magnitude reported by the Aluminium thermocouple, but it was hypothesised that the larger diameter of the Aluminium-based thermocouple could have induced local flow disturbances. The mean temperature was the highest for the Zirconia-based thermocouple, followed by Stainless Steel and Aluminium respectively. This is physically understandable by the thermo-physical properties of the constituent materials. The third research question is answered by this and the previous conclusions.

3.   It was concluded that due to physical and analytical limitations, the steady-state component of heat flux computed from the recessed thermocouple measurement was not faithful. Therefore the 1st law of thermodynamics was used with the experimentally obtained in-cylinder pressure to give an estimate of the steady-state component of heat flux expected at the different setpoints tested. A sensitivity analysis was also conducted on this method with regards to the compression ratio and the in-cylinder pressure pegging.

4.   It was found that the transient heat flux component at the OEM injector location has a larger magnitude than that experienced at the custom-drilled location. It is thought that this could be a result of the tumbling motion of the gas close to the central axis of the cylinder, but it was also hypothesised that potentially, local flow disturbances could have occurred at the OEM injector location due to the thermocouple inclination with respect to the cylinder head surface.

5.   At the OEM injector location, the transient component of heat flux was found to drop to zero and negative values very early after compression TDC, whereas at the custom-drilled location, the change in direction of the heat flux occurs much later in the expansion stroke. The negative magnitude of heat flux was also found to be much smaller at the custom-drilled location compared to that at the OEM injector location.

6.   From the two-dimensional analysis on the Aluminium surface thermocouple tested at the OEM injector location, it was found that the magnitude of the negative portion of the transient heat flux (wall to gas) reported by a 2D consideration is less

significant compared to the magnitude of the negative portion of the transient heat flux reported by a 1D consideration on the same sensor. This was also reported in literature [41] for a similar thermocouple base material and hypothesised by the same author [41] that the negative portion of heat flux could possibly be an artefact of the one-dimensional assumption. However, for the Zirconia surface thermocouple tested in this work, the 2D heat flux showed a more pronounced negative heat flux compared to that shown by a 1D consideration on the same sensor. The Stainless-Steel thermocouple showed a similar magnitude of negative heat flux from both the 2D and 1D consideration. Therefore it can be concluded, that whilst the heat flux parallel to the sensor surface may have an effect on the negative portion of heat flux, this negative portion is still existent nonetheless, even if taking care of two-dimensional heat flow. Hence, heat flux parallel to the surface of the eroding thermocouple is not totally responsible for the negative heat flux.

7.   In this dissertation, from conclusion 6, it was hypothesised that the negative portion of heat flux noticed in this work and also in literature could possibly be a function of the sensor conduction cooling time. It was found that when the eroding thermocouple is given a step heat flux and removed, not all thermocouples cool down at the same rate. It was noticed that the Aluminium-based thermocouple cools first, followed by the Stainless Steel-based thermocouple, and finally the Zirconia-based thermocouple. This means that upon arrival of the high boundary layer temperature on compression, the slowest sensor to diffuse the heat through its body will be the one which rejects more heat back to the gas when the temperature of the boundary layer falls below that of the sensor surface; hence results in a larger magnitude of negative heat flux.

8.   It was found that a soot layer covering the surface thermocouples results in a large attenuation in the surface temperature swing, and a consequent significant decrease in the transient component of heat flux. A lag in the angular location of the heat flux peak, and the location of change in the heat flux direction was noted. A decrease in the mean surface temperature was also observed.

9.   Experimental results taken at both the OEM injector location and custom-drilled location showed that an increase in the engine speed resulted in only small increase (often insignificant) in the peak of the transient component of heat flux. The

steady-state component of heat flux computed by the first law also showed an increase with an increase in engine speed.

10. At both surface thermocouple locations, an increase in the PCP showed an increase in the peak of the transient heat flux. The increase in heat flux was found to be relatively small. The steady-state component of heat flux from the 1st law also showed an increase with an increase in PCP.

11. It was noted that an increase in the coolant and oil temperatures resulted in an overall increase in the peak of the transient heat flux component at the OEM injector location. The steady-state component of heat flux from the 1st law showed practically no change with coolant/oil temperature.

12. Running the pressurised motored engine with gases of higher γ resulted in a higher peak of the transient heat flux component at the OEM injector location, but no significant variation at the custom-drilled location. The steady-state component of heat flux from the 1st law showed a linear increase with an increase in γ. The difference in steady-state heat flux between the different gases tested was also not very significant. This conclusion answers part of the second research question.

13. Heat flux modelling showed that global models are able to predict the cycle-averaged heat flux but fail to show a representative angular phasing. Two similar one-dimensional heat flux models were also considered and it was observed that both models are able to represent accurately the phasing of the experimental heat flux, but underestimate greatly the magnitude of the experimentally obtained heat flux at both locations. This conclusion answers the fourth research question.

7.3 Recommendations for Further Study

Based on the results and conclusions that emerged from this dissertation, it was shown that the use of higher gas temperatures in the pressurised motored engine does not result in any measurable differences in the FMEP. It was hypothesised that this is due to the lack of ability of the pressurised motored engine to retrace the phasing of the in-cylinder pressure curve of the fired engine, which therefore reduces the importance of the interaction between the pressure load and the temperature of the lubrication film present at the piston-liner interface. Since at this stage, this

explanation is only a hypothesis, investigation on the matter supported with experimental evidence is sought. Throughout the duration of this project, a side simulation study was conducted by Sammut et al. [83], and briefly presented in Chapter 4, which outlined a possible method of how the interaction effect between the pressure load and thermal load can be investigated with a *'fuelled pressurised motored engine'*, while still ensuring very good robustness of the FMEP measurements.

On the topic of heat transfer, the recommendations for further study given in the forthcoming text would be of more benefit to the interested experimentalist if taken as a form of 'advice'. In this work, it was strived from the very beginning to ensure that the surface thermometry limitations are minimised as much as possible to limit the uncertainties on the determined heat flux. For this matter, literature spanning a long duration of years was consulted and the main factors to keep in sight were identified as being: the spatial location, thermocouple construction, multi-dimensional heat transfer, thermocouple fitment and integration, thermal capacity of the junction, and deposits on the thermocouple surface. These factors were mitigated to the best possible capability during this research work; however it was acknowledged that to satisfy one criterion, another has to be compromised. As a result it is felt that in future work, even more effort should be spent in trying to fulfil each of these criteria to the best possible capability to ensure faithful instantaneous heat flux determination. In this dissertation, two things which were thought to have helped in the evaluation of the heat flux from the measured surface temperature were the understanding of the two-dimensional effects at the eroding thermocouple surface, as well as utilising a method by which the eroding thermocouple junction can be characterised. In this research work, a photography speedlight was found to be convenient for a quick verification of the thermocouple rise time during testing, however in future studies it would be significantly beneficial if a more rigorous setup that allows knowledge of the step heat flux given to the sensor is used instead.

REFERENCES

[1] J. B. Heywood, "Engine Design and Operating Parameters," in *Internal Combustion Engine Fundamentals*.: McGraw-Hill Inc., 1988, ch. 2.5, pp. 48 - 49.

[2] C. Sethu, M. E. Leustek, S. V. Bohac, Z. S. Filipi, and D. N. Assanis, "An Investigation in Measuring Crank Angle Resolved In-Cylinder Engine Friction Using Instantaneous IMEP Method," *SAE Technical Papers 2007-01-3989*, 2007.

[3] D E Richardson, "Review of Power Cylinder Friction for Diesel Engines," *Transactions of the ASME*, vol. 122, 2000.

[4] D Mauke, R Dolt, J Stadler, K Huttinger, and M Bargende, "Methods of Measuring Friction under Motored Conditions with External Charging," Kistler Group, Switzerland, 2016.

[5] G. F. Hohenberg, "Advanced Approaches for Heat Transfer Calculations," *SAE Technical Papers 790825*, 1979.

[6] A. C. Alkidas, "Heat Transfer Characteristics of a Spark-Ignition Engine," *ASME Transactions: Journal of Heat Transfer*, vol. 102, pp. 189-192, 1980.

[7] AJ Torregrosa, V Bermudez, PC Olmeda Gonzalez, and OL Figueroa, "Experimental Assessment for Instantaneous Temperature and Heat Flux Measurements under Diesel Motored Engine Conditions," *Energy Conversion and Management*, pp. 57-66, 2011.

[8] W J A Annand, "Heat Transfer in the Cylinders of Reciprocating Internal Combustion Engines," *Proc. Inst. Mech. Engrs.*, vol. 177, no. 1, 1963.

[9] T LeFeuvre, P S Myers, and O A Uyehara, "Experimental Instantaeous Heat Fluxes in a Diesel Engine and their Correlation," *SAE Technical Papers 690464*, 1969.

[10] G. Borman and K Nishiwaki, "Internal Combustion Engine Heat Transfer," *Progress in Energy and Combustion Science*, vol. 13, no. 1, 1987.

[11] G Woschni, "A Universally Applicable Equation for the Instantaneous Heat Transfer Coefficient in the Internal Combustion Engine," *SAE Technical Paper 670931*, 1967.

[12] E. G. Cocker and W. A. Scoble, "Cyclical Changes of Temperature in a Gas-Engine Cylinder," *The Institution of Civil Engineers, 4061*, December 1913.

[13] V D Overbye, J E Bennethum, O A Uyehara, and P S Myers, "Unsteady Heat Transfer in Engines," *Trans. Soc. Automotive Engineers*, 1961.

[14] D Bendersky, "A Special Thermocouple for Measuring Transient Temperatures ," *Mechanical Engineering*, vol. 75, 1953.

[15] C. Borgnakke, V. S. Arpaci, and R. J. Tabaczynski, "A Model for the Instantaneous Heat Transfer and Turbulence in a Spark Ignition Engine," *SAE Technical Paper, 800287*, 1980.

[16] T. Morel and R. Keribar, "A Model for Predicting Spatially and Time Resolved Convective Heat Transfer in Bowl-in-Piston Combustion Chambers," *SAE Technical Paper, 850204*, 1985.

[17] H. Pfriem, "Periodic Heat Transfer at Small Pressure Fluctuations," National Advisory Committee for Aeronautics, Washington, Technical Memorandum No. 1048 1940.

[18] D. W. Wendland, "The Effect of Periodic Pressure and Temperature Fluctuations on Unsteady Heat Transfer in a Closed System," National Aeronautics and Space Administration, University of Wisconsin, Madison, Wisconsin, NASA CR-72323 1968.

[19] W. J. D Annand and T. H. Ma, "Instantaneous Heat Transfer Rates to the Cylinder Head Surface of a Small Compression-Ignition Engine," *Proc. Inst. Mech. Eng.*, vol. 185, 1970.

[20] G. Woschni and K. Sihling, "Experimental Investigation of the Instantaneous Heat Transfer in the Cylinder of a High Speed Diesel Engine," *SAE Technical Paper 790833*, 1979.

[21] R. W. Goluba and G. L. Borman, "The Effect of Periodic Shock-fronted Pressure Waves on Instantaneous Heat Flux Rates ," *International Journal on Heat and Mass Transfer*, vol. 12, pp. 1281-1293, 1969.

[22] B Lawton, "Effect of Compression and Expansion on Instantaneous Heat Transfer in Reciprocating Internal Combustion Engines," *Proc. Instn. Mech. Enginrs., Part A, Journal of Power and Energy*, vol. 201, pp. 175-186, 1987.

[23] D. J.Oude Nijeweme, J. B. W Kok, C. R. Stone, and L. Wyszynski, "Unsteady in-cylinder heat transfer in a spark ignition engine: experiments and modelling," *Proceedings of the Institution of Mechanical Engineers, Part D: Journal of Automobile Engineering*, vol. 215, pp. 747 - 760, 2001.

[24] R. Greif, T. Namba, and M. Nikanham, "Heat Transfer During Piston Compression Including Side Wall and Convection Effects," *International Journal on Heat and Mass Transfer*, vol. 22, pp. 901-907, 1978.

[25] K. Dao, O. A. Uyehara, and P. S. Myers, "Heat Transfer Rates at Gas-Wall Interfaces in Motored Piston Engine," *SAE Technical Papers 730632*, 1973.

[26] S. Diana, V. Giglio, G. Police, G. Bella, and S. Cordiner, "Heat Transfer Evaluation in 3D Computations of Premixed SI Engines," *SAE Technical Papers, 972876*, 1997.

[27] Z. Han and R. D. Reitz, "A temperature wall function formulation for variable-density turbulent flows with application to engine convective heat transfer modeling," *International Journal on Heat and Mass Transfer*, vol. 40, no. 3, pp. 613 - 625, 1997.

[28] C. Angelberger, T. Poinsot, and B. Delhay, "Improving Near-Wall Combustion and Wall Heat Transfer Modeling in SI Engine Computations," *SAE Technical Paper, 972881*, 1997.

[29] P Gilaber and P Pinchon, "Measurements and Multidimensional Modelling of Gas-Wall Heat Transfer in a SI Engine," *SAE Technical Papers*, 1988.

[30] J. Yang, P. Pierce, J. K. Martin, and D. E. Foster, "Heat Transfer Predictions and Experiments in a Motored Engine," *SAE Technical Paper, 881314*, 1988.

[31] N. D. Whitehouse, "Heat Transfer in Compression-Ignition Engines," *Proceedings of the Institution of Mechanical Engineers*, vol. 185, pp. 963 - 975, June 1970.

[32] T. Morel, P. N. Blumberg, E. F. Fort, and R. Keribar, "Methods for Heat Analysis and Temperature Field Analysis of the Insulated Diesel," *Phase I Progress Report*, August 1984.

[33] J. C. Dent and S. J. Sulaiman, "Convective and Radiative Heat Transfer in a High Swirl Direct Injection Diesel Engine," *SAE Technical Paper, 770407*, 1977.

[34] A. Alkidas, "Thermal Loading of the Cylinder Head of a Spark-Ignition Engine," *Heat Transfer Engineering*, vol. 3, pp. 66-75, 1982.

[35] A. C. Alkidas and R. M. Cole, "Transient Heat Flux Measurements in a Divided-Chamber Diesel Engine," *Journal of Heat Transfer*, vol. 107, no. 2, pp. 439 - 444, 1985.

[36] K. L. Hoag, "Measurement and Analysis of the Effect of Wall Temperature on Instantaneous Heat Flux," *SAE Technical Paper 860312*, February 1986.

[37] J. C. Huang and G. Borman, "Measurements of Instantaneous Heat Flux to Metal and Ceramic Surfaces in a Diesel Engine," *SAE Technical Paper, 870155*, 1987.

[38] C. R. Mure and K. T. Rhee, "Instantaneous Heat Transfer over the Piston of a Motored Direct Injection-Type Diesel Engine," *SAE Technical Paper, 890469*, 1989.

[39] T. L. Hendricks, "Instantaneous Heat Flux Measurements in Internal Combustion Engines," University of Wisconsin - Madison, Wisconsin, PhD Thesis 2011.

[40] C Hennes, Jürgen Lehmann, and Thomas Koch, "Possibilities of Wall Heat Transfer Measurements at a Supercharged Euro VI Heavy-Duty Diesel Engine with High EGR-Rates, an In-Cylinder Peak Pressure of 250 Bar and an Injection Pressure up to 2500 Bar," *SAE Technical Paper 2019-24-0171*, September 2019.

[41] X. Wang, R. Stone, R. Stevens, Y. Arita, and D. Buttsworth, "Finite Element Analysis of Eroding Type Surface Thermocouple with Application to Engine Heat Flux Measurement," *SAE Technical Papers 2006-01-1045*, April 2006.

[42] J Demuynck et al., "Applying Design of Experiments to Determine the Effect of Gas Properties on In-Cylinder Heat Flux in a Motored SI Engine," *SAE Int. J. Engines 5(3):2012*, 2012.

[43] N S Jackson, A D Pilley, and N J Owen, "Instantaneous Heat Transfer in a Highly Rated DI Truck Engine," *SAE Technical Papers 900692*, 1990.

[44] C.C. J. French and K. A. Atkins, "Thermal Loading of a Petrol Engine," *Proceedings of the Institution of Mechanical Engineers*, vol. 187, pp. 1847-1982, June 1973.

[45] N. Uchida and H. Osada, "A New Piston Insulation Concept for Heavy-Duty Diesel Engines to Reduce Heat Loss from the Wall," *SAE Technical Paper, 2017-24-0161*, 2017.

[46] K. S. Chana, T. S. Wilson, and T. V. Jones, "High Bandwidth Heat Transfer Measurements in an Internal Combustion Engine under Low Load and Motored Conditions," in *RTO AVT Symposium on "Advanced Flow Management: Part B – Heat Transfer and Cooling in Propulsion and Power Systems*, Loen, Norway, 2001.

[47] S. Broekaert et al., "Local Heat Flux Measurement Technique for Internal Combustion Engines," in *9th World Conference on Experimental Heat Transfer, Fluid Mechanics and Thermodynamics*, Iguazu Falls, Brazil, 2017.

[48] D R Buttsworth, "Transient Response of an Erodable Heat Flux Gauge using Finite Element Analysis ," *Proceedings of the Institution of Mechanical Engineers Part D (Journal of Automobile Engineering)*, vol. 216, pp. 701-706, 2002.

[49] D. R. Buttsworth, "Assessment of effective thermal product of surface junction thermocouples on millisecond and microsecond time scales," *Experimental Thermal and Fluid Science*, vol. 25, no. 6, pp. 409-420, 2001.

[50] E. J. Lyford-Pike and J. B. Heywood, "Thermal Boundary Layer Thickness in the Cylinder of a Spark-Ignition Engine," *International Journal on Heat and Mass Transfer*, vol. 27, no. 10, pp. 1873 - 1878, January 1984.

[51] R. P. Lucht, D. Dunn-Rankin, T. Walter, T. Dreier, and S. C. Bopp, "Heat Transfer in Engines: Comparison of Cars Thermal Boundary Layer Measurements and Heat Flux Measurements," *SAE Technical Paper, 910722*, 1991.

[52] R. Moffat, "The Gradient Approach to Thermocouple Circuitry Part 1 - Background and Basic Premise," *Temperature—Its Measurement and control in Science and Industry*, vol. 8, no. 3, pp. 24-25, March 1984.

[53] R. Moffat, "The Gradient Approach to Thermocouple Circuitry Part 2 - Illustrations of the Method," vol. 8, no. 4, pp. 23-25, April 1984.

[54] OMEGA. Thermocouple Introduction and Theory. [Online]. https://www.omega.com/techref/

[55] D. R. Buttsworth, R. Stevens, and R. C. Stone, "Eroding Ribbon Thermocouples: Impulse Response and Transient Heat Flux Analysis," *Measurement Science and Technology*, 2005.

[56] S. R. Sanderson and B. Sturtevant, "Transient heat flux measurement using a surface junction thermocouple," *Review of Scientific Instruments*, vol. 73, no. 7, 2002.

[57] E. Schmidt, "Device for the Measurement of Heat," Patent Number: 1528383. 3 3, March 1925.

[58] S. J. Hevey and L. W. Langley, "Schmidt-Boelter Gage," Patent Number: 6,186,661. 13 2, February 2001.

[59] R. Gardon, "An Instrument for the Direct Measurement of Intense Thermal Radiation," *Review of Scientific Instruments*, vol. 24, no. 5, pp. 366 - 370, 1953.

[60] "Bulletin 500 - Coaxial Surface Thermocouple Probes," Medtherm Corporation, Huntsville, Alabama,.

[61] D. N. Assanis, F. A. Friedmann, K. L. Wiese, M. J. Zaluzec, and J. M. Rigsbee , "A Prototype Thin-Film Thermocouple for Transient Heat Transfer Measurements in Ceramic-Coated Com bustion Chambers," *SAE Technical Paper, 900691*, 1990.

[62] O. Aoki et al., "Analysis of Heat Transfer Phenomena on High Response Heat Insulation Coatings by Instantaneous Heat Flux Measurement and Boundary Layer Visualization," *SAE Technical Paper, SAE 2015-01-1996 and JSAE 20159045*, 2015.

[63] E Piccini, S M Guo, and T V Jones, "The Development of a New Direct-Heat-Flux Gauge for Heat-Transfer Facilities," *Measurement Science and Technology* , vol. 11, no. 4, pp. 342 - 349, 2000.

[64] "Eroding Junction Thermocouple - Maintenance," Nanmac Corporation, Holliston, Massachusetts.

[65] M. Farrugia, "Transient Surface Heat Flux Measurements in a Straight Pipe Extension of the Exhaust Port of a Spark Ignition Engine," Oakland University, Rochester, Michigan, PhD Dissertation 2005.

[66] "Self-Renewing Thermocouple E12 Series," Nanmac Corporation, Holliston, Massachusetts, Product Information Sheet.

[67] C. Camci, "Temperature and Heat Transfer Measurements," in *Encyclopedia of Aerospace Engineering*, W. Shyy and R. Blockley, Eds.: John Wiley and Sons, 2010, ch. 11.

[68] K Cornelis et al., "Comparison of Heat Flux Sensors for Internal Combustion Engines on Two Hot Air Gun test rigs and a Test Engine," in *9th International Conference on Heat Transfer, Fluid Mechanics and Thermodynamics*, Malta, 2012.

[69] "HFM-6, HFM-7 & HFM-8 Operator's Manual," Christiansburg, 2015.

[70] A. Grech, T. Sant, and M. Farrugia, "The Effects of Thermocouple Materials and Insulating Mica in an Erodable Surface Thermocouple," in *ASME Summer Heat Transfer Conference*, Jacksonville, Florida, 2008.

[71] "The Stem Effect: Leading Cause of Error in Temperature Measurement," Nanmac Corporation, Holliston, Massachusetts,.

[72] J. A. Gatowski, M. K. Smith, and A. C. Alkidas, "An Experimental Investigation of Surface Thermometry and Heat Flux," *Experimental Thermal and Fluid Science*, vol. 2, pp. 280-292, 1989.

[73] K Ullmann, *Die mechanischen Verluste des schnellaufenden Dieselmotors und ihre Ermittlung mit dem Schleppversuch*. Berlin: VDI-Verlag GmbH, 1939.

[74] W C Pike and D T Spillman, "The Use of a Motored Engine to Study Piston-Ring Wear and Engine Friction," *Proceedings of the Institution of Mechanical Engineers, 178(14)*, pp. 37–44, 1963.

[75] M. Nikanjam and R. Greif, "Heat Transfer During Piston Compression," *ASME Transactions: Journal of Heat Transfer*, July 1978.

[76] H Allmaier et al., "An Experimental Study of the Load and Heat Influence from Combustion on Engine Friction," *International Journal of Engine Research*, vol. 17, no. 3, pp. 347-353, March 2015.

[77] MAHLE International GmbH, "Engine Testing," in *Pistons and Engine Testing*. Stuttgart, Germany: Springer, ch. 7, pp. 117 - 281.

[78] C. Caruana, "Design, Building and Testing of a Pressurised Motoring Diesel Engine Setup for Mechanical Friction Determination," University of Malta, Msida, Masters of Science in Engineering (Mechanical) 2017.

[79] C Caruana, M Farrugia, and G Sammut, "The Determination of Motored Engine Friction by Use of Pressurized 'Shunt' Pipe between Exhaust and Intake Manifolds," *SAE Technical Paper 2018-01-0121*, 2018.

[80] E. Pipitone, A. Beccari, and S. Beccari, "The Experimental Validation of a New Thermodynamic Method for TDC Determination," *SAE Technical Papers 2007-24-0052*, 2007.

[81] T Deuß, "Reibverhalten der Kolbengruppe eines Pkw-Dieselmotors," University, Dissertation 2013.

[82] H. Allmaier, C. Knauder, D. Sanders, and F. M. Reich, "Combining an innovative measurement technique with accurate simulation to analyze engine friction," *MTZ Worldwide*, vol. 77, pp. 66-71, 2016.

[83] G Sammut, M Farrugia, E Pipitone, and C Caruana, "A Simulation Study Assessing the Viability of Shifting the Location of Peak In-Cylinder Pressure in Motored Experiments," *SAE Technical Papers 2020-24-0009*, September 2020.

[84] G. Sammut, E. Pipitone, C. Caruana, and M. Farrugia, "Simulation Study on the Use of Argon Mixtures in the Pressurized Motored Engine for Friction Determination," *SAE Technical Paper, 2020-24-0004*, 2020.

[85] B. W. Millington and E. R. Hartles, "Frictional Losses in Diesel Engines," *SAE Technical Paper, 680590*, 1968.

[86] (2018, November) Mantracourt - T24 Telemetry User Manual. [Online]. https://www.mantracourt.com/products/wireless-strain-gauge-sensor-transmitter/resources

[87] C. Caruana, P. Mollicone, and M. Farrugia, "Development of a Simple Instantaneous Torque Measurement System on a Rotating Shaft," in *2019 IEEE International Conference on Mechatronics (ICM)*, Ilmenau, Germany, 2019, pp. 382-388.

[88] J. P. Azzopardi, "Analysis of Engine Downsizing: An Experimental Investigation of Incylinder Pressure and Knock," University of Malta, Msida, Masters Dissertation 2014.

[89] S Camilleri, "Investigation of Common Rail Diesel Engine," Undergraduate Dissertation, University of Malta, Msida, 2010.

[90] D. A. Kouremenos, C. D. Rakopoulos, D. T. Hountalas, and T. K. Zannus, "Development of a Detailed Friction Model to Predict Mechanical Losses at Elevated Maximum Combustion Pressures," *SAE Technical Papers 2001-01-0333*, 2001.

[91] A. Fitzpatrick, D. Smith, and H. Wagner, "The Single Cylinder OM441LA," *SAE Technical Papers 2000-01-1826*, 2000.

[92] C. Caruana and M. Farrugia, "Balancing of a Four Cylinder Engine for Single Cylinder Operation," in *19th Mechatronika 2020*, Prague, Czech Republic, 2020.

[93] R. N. Sharpe, J. W. David, and E. M. Lowndes, "Determination of Optimal Counterweight Configurations for Multithrow Crankshafts," *SAE Technical Paper 960354*, February 1996.

[94] C. F. Taylor, "Engine Balance and Vibration," in *The Internal-Combustion Engine in Theory and Practice, Volume II: Combustion, Fuels, Materials, Design.*: The Massachusetts Institute of Technology Press, 1985, p. 248.

[95] S. Timoshenko and D. H. Young, "Balancing of a Single-Cylinder Reciprocating Engine," in *Advanced Dynamics.*: McGraw-Hill Book Company, Inc., 1948, pp. 136-142.

[96] J. R. Harkness, "Methods of Balancing Single Cylinder Engines," *SAE Technical Paper 680571*, 1968.

[97] R. Stone, "Mechanical Design Considerations: The disposition and number of the cylinders," in *Introduction to Internal Combustion Engines (4th Edition).*: Palgrave MacMillan, 2012, pp. 345-350.

[98] C. A. F. Parra, "Heat Transfer Investigations in a Modern Diesel Engine," University of Bath, Bath, PhD Thesis 2008.

[99] P. C. Miles and O. Andersson, *Diesel and Diesel LTC Combustion*. DOI: 10.1002/9781118354179.auto120, ISBN: 978-0-470-97402-5: John Wiley & Sons, Ltd., 2014.

[100] J. Song, C. Yao, Y. Liu, and Z. Jiang, "Investigation On Flow Field In Simplified Piston Bowls for Di Diesel Engine," *Engineering Applications of Computational Fluid Mechanics*, vol. 2, no. 3, pp. 354-365, 2008.

[101] C Caruana, M Farrugia, G Sammut, and E Pipitone, "Further Experimental Investigation of Motored Engine Friction Using Shunt Pipe Method," *SAE Technical Paper 2019-01-0930*, 2019.

[102] C Caruana, E Pipitone, M Farrugia, and G Sammut, "Experimental investigation on the use of Argon to improve FMEP determination through motoring method," *SAE Technical Paper - 2019-24-0141, SAE Naples ICE2019 14th International Conference on Engines and Vehicles, Capri, Napoli*, 15th - 19th September, 2019.

[103] C Caruana, M Farrugia, G Sammut, and E Pipitone, "Further Experiments on the Effect of Bulk In-Cylinder Temperature in the Pressurized Motoring Setup Using Argon Mixtures," *SAE Technical Paper, 2020-01-1063*, April 2020.

[104] E Pipitone and A Beccari, "Determination of TDC in internal combustion engines by a newly developed thermodynamic approach," *Applied Thermal Engineering*, pp. 1914 - 1926, 2010.

[105] M. J. Stas, "Thermodynamic Determination of T.D.C. in Piston Combustion Engines," *SAE Technical Paper, 960610*, February 1996.

[106] Y. Nilsson and L. Eriksson, "Determining TDC Position Using Symmetry and Other Methods," *SAE Technical Paper, 2004-01-1458*, 2004.

[107] A Randolph, "Methods of Processing Cylinder-Pressure Transducer Signals to Maximise Data Accuracy," *SAE Technical Paper, 900170*, 1990.

[108] C. Knauder, H. Allmaier, S. Salhofer, and T. Sams, "The impact of running-in on the friction of an automotive gasoline engine and in particular on its piston assembly and valve train," *Proceedings of the Institution of Mechanical Engineers, Part J: Journal of Engineering Tribology, 232(6)*, pp. 749 - 756, 2017.

[109] E. Pipitone, Personal electronic mail communication, March 2019.

[110] C. Knauder, H. Allmaier, D. E. Sander, and T. Sams, "Investigations of the Friction Losses of Different Engine Concepts. Part 1: A Combined Approach for Applying Subassembly-Resolved Friction Loss Analysis on a Modern Passenger-Car Diesel Engine," *Lubricants*, vol. 7, no. 5, April 2019.

[111] J C Livengood, A R Rogowski, and C F Taylor, "The Volumetric Efficiency of Four-Stroke Engines ," *SAE Quarterly Transactions*, vol. 6, no. 4, pp. 617 - 636, October 1952.

[112] J T Kovach, E A Tsakiris, and L T Wong, "Engine Friction Reduction for Improved Fuel Economy," *SAE Technical Papers 820085*, 1982.

[113] T Decuyper et al., "Calibration of a TFG Sensor for Heat Flux Measurements in a S.I. Engine," *SAE Technical Paper, 2015-01-1645*, 2015.

[114] M. L. G. Oldfield, "Guide to Impulse Response Heat Transfer Signal Processing," University of Oxford, Oxford, OUEL Report 2233/2000. Version 6.1 2000.

[115] H. S. Carslaw and J. C. Jaeger, *Conduction of Heat in Solids, Second Edition*.: Oxford University Press. ISBN: 978-0198533689, 1959.

[116] "Understanding FFTs and Windowing," National Instruments, https://download.ni.com/evaluation/pxi/Understanding%20FFTs%20and%20 Windowing.pdf.

[117] B. E. Knight, "The Problem of Predicting Heat Transfer in Diesel Engines," *Proceedings of the Institution of Mechanical Engineers*, vol. 179, no. 3, pp. 99 - 115, June 1964.

[118] H. Hassan, "Unsteady heat transfer in a motored internal combustion engine," Loughborough University of Technology, PhD Thesis 1968.

[119] M. L. G. Oldfield, "Impulse Response Processing of Transient Heat Transfer Gauge Signals," *Journal of Turbomachinery, 021023-1*, vol. 130, no. 2, April 2008.

[120] M. L. G. Oldfield, Personal electronic mail communication, January 2020 - February 2020.

[121] A. S. Gray and C. Uher, "Thermal Conductivity of Mica at Low Temperatures," *Journal of Materials Science*, vol. 12, pp. 959 - 965, 1977.

[122] Y. S. Touloukian, R. W. Powell, C. Y. Ho, and M. C. Nicolaou, "Volume 10: Thermal Diffusivity," in *Thermophysical Properties of Matter*. ISBN: 0-306-67030-5, 1973, p. 548.

[123] F. R. Caldwell, "Thermocouple Materials," National Bureau of Standards, Washington, 1962.

[124] W. D. Callister and D. G. Rethwisch, "Appendix B: Properties of Selected Engineering Materials (Eight Edition)," in *Materials Science and Engineering: An Introduction*.: Wiley & Sons. ISBN 978-0-470-41997-7, 2010, pp. A3 - A30.

[125] W, J D Annand and D Pinfold, "Heat Transfer in the Cylinder of a Motored Reciprocating Engine," *SAE Technical Paper 800457*, 1980.

[126] "GT-Power User's Manual," Gamma Technologies, 2017.

[127] J. Hilsenrath et al., "Tables of Thermal Properties of Gases," U.S. Department of Commerce, Washington, National Bureau of Standards: Circular 564 1955.

[128] Ricardo, "WAVE User Manual," Ricardo, 2017.

[129] C Caruana, M Farrugia, G Sammut, and E Pipitone, "One-dimensional simulation of the pressurized motoring method: friction, blow-by, temperatures and heat transfer analysis," in *IMECHE - Internal Combustion Engines and Powertrain Systems for Future Transport*, West Midlands, Birmingham, 11-12 December 2019.

[130] S Chen and P Flynn, "Development of a Single Cylinder Compression Ignition Research Engine," *SAE Technical Paper 650733*, 1965.

[131] J B Heywood, "Combustion in Compression Ignition Engines," in *Internal Combustion Engine Fundamentals*.: McGraw-Hill, 1988, pp. 508 - 510.

[132] B. E. Poling, J. M. Prausnitz, and J. P. O'Connell, "Thermal Conductivities of Gas Mixtures at High Pressures," in *The Properties of Gases and Liquids. Fifth Edition.*: McGraw Hill, 2000, pp. 10.35 - 10.42.

[133] A. K. Barua and P. Mukhopadhyay, "Thermal Conductivities of Nitrogen-Argon and Oxygen-Argon Gas Mixtures," *British Journal of Applied Physics*, vol. 18, pp. 1307-1310, September 1967.

[134] J. Macek, D. Fuente, and M. Emrich, "A Simple Physical Model of ICE Mechanical Losses," *SAE Technical Papers 2011-01-0610*, 2011.

[135] K. J. Patton, R. G. Nitschke, and J. B. Heywood, "Development and Evaluation of a Friction Model for Spark-Ignition Engines," *SAE Technical Paper, 890836*, 1989.

[136] D. Sandoval and J. B. Heywood, "An Improved Friction Model for Spark-Ignition Engines," *SAE Technical Paper. 2003-01-0725*, 2003.

[137] E. Pipitone, "A New Simple Friction Model for S. I. Engine," *SAE Technical Paper. 2009-01-1984*, 2009.

8 APPENDIX

8.1 ASSESSMENT OF CYCLE-TO-CYCLE VARIABILITY

To have an understanding of the cycle-to-cycle variation that was experienced during the FMEP tests documented in Chapter 4, the standard deviations of different metrics of interest, over a number of cycles were computed and presented in the following tables. The ensemble averaged data presented in Chapter 4 and Chapter 5 of this report was computed over 300 cycles, however in the FMEP mixtures testing defined by Table 4.2, in Chapter 4, ensemble averaged data was taken on 200 cycles. In [78], it was shown that for the same engine tested in this project, using more than 50 cycles for ensemble averaged data computation, resulted in negligible differences in the $IMEP_{360}$, PMEP, FMEP, pressure loss angle and PCP. During the computation of the standard deviation, it was noticed that the test matrix defined by Table 4.1 suffered from a smaller standard deviation than those reported in this section for the test matrix defined by Table 4.2. As a result its standard deviations are not presented in this report.

Although the standard deviations presented give an indication of the cycle-to-cycle variability suffered in the FMEP testing, it should be made clear that they do not represent the total uncertainty suffered in each of the metrics of interest. It is noted that the cumulative uncertainty of each of the metrics presented in Chapter 4 depend on several factors, which their uncertainty is not always known. Some of these unknown uncertainties include; pegging of the in-cylinder pressure signal, unknown mechanical friction resulting from the floating motor housing and windage of the armature, uncertainties associated with thermal shocks in the pressure transducer and uncertainties arising from masking of the pressure transducer sensing holes due to it not being of the flush-mounted type.

8.1.1 Standard deviations of test matrix defined by Table 4.2

Table 8.1. The standard deviation in $IMEP_{360}$.

Standard Deviation in $IMEP_{360}$ [bar]				Engine Speed [rpm]			
				1400	2000	2500	3000
Ratio of Specific Heats (γ)	1.40	PCP [bar]	84 bar	0.0326	0.0295	0.0339	0.0347
			103 bar	0.0292	0.0294	0.0300	0.0347
	1.50		84 bar	0.0317	0.0285	0.0323	0.0326
			103 bar	0.0347	0.0299	0.0293	0.0341
	1.60		84 bar	0.0317	0.0307	0.0313	0.0360
			103 bar	0.0347	0.0366	0.0369	0.0393
	1.67		84 bar	0.0328	0.0363	0.0319	0.0379
			103 bar	0.0375	0.0363	0.0348	0.0339

Table 8.2. The standard deviation in PMEP.

Standard Deviation in PMEP [bar]				Engine Speed [rpm]			
				1400	2000	2500	3000
Ratio of Specific Heats (γ)	1.40	PCP [bar]	84 bar	0.0291	0.0268	0.0274	0.0362
			103 bar	0.0285	0.0283	0.0299	0.0342
	1.50		84 bar	0.0286	0.0289	0.0306	0.0318
			103 bar	0.0272	0.0265	0.0282	0.0384
	1.60		84 bar	0.0286	0.0290	0.0302	0.0377
			103 bar	0.0312	0.0293	0.0327	0.0418
	1.67		84 bar	0.0294	0.0308	0.0315	0.0394
			103 bar	0.0310	0.0310	0.0324	0.0364

Table 8.3. The standard deviation in BMEP.

Standard Deviation in BMEP [bar]				Engine Speed [rpm]			
				1400	2000	2500	3000
Ratio of Specific Heats (γ)	1.40	PCP [bar]	84 bar	0.0462	0.0231	0.0252	0.0424
			103 bar	0.0403	0.0244	0.0236	0.0300
	1.50		84 bar	0.0346	0.0252	0.0284	0.0322
			103 bar	0.0423	0.0269	0.0329	0.0279
	1.60		84 bar	0.0262	0.0246	0.0252	0.0277
			103 bar	0.0290	0.0281	0.0299	0.0301
	1.67		84 bar	0.0368	0.0325	0.0265	0.0297
			103 bar	0.0280	0.0318	0.0277	0.0485

Table 8.4. The standard deviation in FMEP.

Standard Deviation in FMEP [bar]				Engine Speed [rpm]			
				1400	2000	2500	3000
Ratio of Specific Heats (γ)	1.40	PCP [bar]	84 bar	0.0627	0.0447	0.0478	0.0684
			103 bar	0.0572	0.0482	0.0447	0.0555
	1.50		84 bar	0.0583	0.0461	0.0497	0.0571
			103 bar	0.0544	0.0487	0.0502	0.0592
	1.60		84 bar	0.0517	0.0473	0.0516	0.0665
			103 bar	0.0543	0.0575	0.0574	0.0618
	1.67		84 bar	0.0613	0.0509	0.0547	0.0617
			103 bar	0.0573	0.0533	0.0572	0.0671

Table 8.5. The standard deviation in pressure loss angle.

Standard Deviation in Pressure Loss Angle [DegCA]				Engine Speed [rpm]			
				1400	2000	2500	3000
Ratio of Specific Heats (γ)	1.40	PCP [bar]	84 bar	0.04	0.04	0.04	0.05
			103 bar	0.03	0.03	0.03	0.04
	1.50		84 bar	0.04	0.04	0.04	0.05
			103 bar	0.03	0.03	0.03	0.04
	1.60		84 bar	0.04	0.04	0.04	0.04
			103 bar	0.03	0.03	0.04	0.04
	1.67		84 bar	0.04	0.04	0.04	0.05
			103 bar	0.03	0.03	0.03	0.04

Table 8.6. The standard deviation in PCP.

Standard Deviation in PCP [Bar]				Engine Speed [rpm]			
				1400	2000	2500	3000
Ratio of Specific Heats (γ)	1.40	PCP [bar]	84 bar	0.18	0.31	0.16	0.27
			103 bar	0.22	0.26	0.24	0.39
	1.50		84 bar	0.56	0.17	0.27	0.37
			103 bar	0.90	0.36	0.62	0.22
	1.60		84 bar	0.33	0.18	0.18	0.23
			103 bar	0.37	0.46	0.42	0.28
	1.67		84 bar	0.31	1.26	0.21	0.27
			103 bar	0.31	0.55	0.26	0.24